INTERNATIONAL DOCTORAL
SCHOOL OF THE USC

Yolanda
Sabater Algarra

PhD Thesis

Novel Switching Magnetic Materials: From Complexes to Hybrids

Santiago de Compostela, 2024

Doctoral Programme in Chemical Science and Technology

ESCOLA DE DOUTORAMENTO
INTERNACIONAL DA USC

TESIS DOCTORAL

NOVEL SWITCHING MAGNETIC MATERIALS: FROM COMPLEXES TO HYBRIDS

Yolanda Sabater Algarra

Director: Dr. María del Carmen Giménez López

Tutor/a: Prof. Francisco Rivadulla Fernández

PROGRAMA DE DOCTORADO EN CIENCIA Y TECNOLOGÍA QUÍMICA

SANTIAGO DE COMPOSTELA

AGRADECIMIENTOS

La cronología ha sido la decisiva para que me inclinara a escribir los agradecimientos de esta manera. La Yolanda que empezó esta tesis no es la misma que se marcha de Santiago ahora. No sería la persona en la que me he convertido sin la presencia de todos y cada uno de vosotros en mi vida, los que ya me acompañabais y los que aparecisteis en mi camino en el transcurso de estos años.

En primer lugar, gracias a María por acogerme en FunNanoMatlab y ser la causante de que yo decidiera dar el salto y empezar de 0 en Santiago y crecer en mi carrera investigadora. He aprendido muchísimo en estos años, me he convertido en una persona autónoma y con el afán de seguir aprendiendo allá donde vaya. Gracias por enseñarme a hacer las cosas con pasión y a gestionar la frustración cuando las cosas no salían.

El segundo que inclinó la balanza sin duda fue Illya. Mucho de esta tesis es en parte gracias a ti, porque te viniste conmigo sin pensarlo a Galicia y has estado siempre en este camino pedregoso para darme ese pequeño empujón cuando lo he necesitado. Siempre sabes dar con la frase adecuada o hacerme reír a carcajadas hasta que me salen las lágrimas. No te cambiaría por nada ni nadie. Te quiero.

A mis padres, Luis Manuel y María del Mar, gracias por apoyarme en todas las decisiones que he tomado (y que seguiré tomando) aunque probablemente me aleje de Novelda cada vez más. Gracias por creer en mi y dejar que vuele alto pero siempre llevándome de la mano. Os quiero.

Extiendo este agradecimiento al resto de mi familia (la de sangre y la política). Por apoyarme y preocuparos de mi bienestar siempre. Esta tesis la empecé con mis dos abuelas maternas. Por desgracia, la termino sin ninguna de ellas. Sé que me cuidais desde allí arriba. El tiempo me ha hecho arrepentirme de todas las cosas que no os dije lo suficiente. Una parte de vosotras también está aquí, Rogelia y María.

Gracias a toda la gente que me ha acompañado en lo “científico“.

Gracias a Fran, porque has sido mi segundo apoyo en esta temprana etapa investigadora. Por tu predisposición siempre a hablar de ciencia o de cualquier otro tema y a ofrecer tus conocimientos desinteresadamente.

Gracias a Carlos, he aprendido muchísimo de ti en estos años, tanto en lo personal como en lo científico, y aunque mi investigación quedaba alejada de tu campo, siempre me escuchaste, me aportabas ideas y me guiabas por el buen camino. Qué suerte que estuviéramos en el mismo barco.

A Álex, por llegar a mi vida en un punto en el que yo había vivido tantos cambios y por darme las mejores conversaciones, debates y consejos. También me diste un punto crítico en la ciencia y si sigo este camino es sin duda gracias a ti. Por supuesto no puedo olvidarme de Vero (eres luz) y de Roi. Me siento muy afortunada de tener “NO HOMERS” (Alex, Vero, Roisito, Adri, Eu, Illya) en mi vida.

Por último lugar, a Gustavo, gracias por el sprint en la recta final y por ayudar a darle forma a esta tesis.

A todos aquellos que han pasado por el P0L2: Javi, Lucía, Mel y la reciente incorporación, Garoé.

A Eugenia, Marcelo y Noa, os guardo un sitio especial. La pandemia nos quitó mucho pero nos hizo crear “Team One" y ya no os voy a soltar. Habéis sido mi salvavidas en estos años de doctorado y es que entre nosotros sobraban las palabras. Una mirada era suficiente para saber si hacía falta una cerveza en A Taverna o un abrazo.

Eugenia, he tenido la suerte de compartir esta experiencia prácticamente en su totalidad con una gran investigadora como tú. Nunca olvidaré tus primeras clases de orgánica (ni de MestreNova) y todo lo que me has ayudado en este etapa. Parte de esta tesis es también fruto de tu trabajo,

y es que siempre fuiste la “experta en Rayos X”. Rápido te convertiste en amiga y a día de hoy puedo decir que casi en familia.

Marcelo, tu paciencia y generosidad no tienen límites y siempre has estado ahí para mí. Gracias por ser mi respaldo en lo científico y en lo personal, por los planes para sacarme de casa cuando estaba “plof”, todas las comidas y momentos compartidos que me guardo en el corazón. Gracias por convertirte en amigo y en familia.

Noa, llegaste de “sorpresa” y en un momento complicado pero siempre nos las apañamos para salir y conocernos más. Me alegro de que pasaras esos primeros meses con la síntesis, pues me permitieron conocer a la gran persona e investigadora que eres.

Gracias también a todo el personal técnico del CiQUS que siempre me brindaron su ayuda (Laura, Arcadio, Adrián, Noela, Álvaro y Andrea) y al personal de apoyo científico del CACTUS. Muchas veces no nos damos cuenta del trabajo e implicación que hay detrás de las cosas y gran parte de esta tesis no habría sido posible de no ser por ellos.

A Antonio, por tu paciencia y por la facilidad con la que explicabas todos los fundamentos de los rayos X de monocristal cuando es un tema poco accesible. Gracias por todo lo que me has enseñado y que gracias a ello he podido plasmar en esta tesis. Sin duda has hecho que los rayos X se hayan convertido en una de mis partes favoritas de la ciencia. Gracias a Bruno también por tu guía, menuda turra te di con los cristales líquidos.

A Ezequiel, por tantos días de uso de los instrumentos de Raman y por tu disposición siempre para que las medidas salieran bien y las pudiera acabar lo antes posible. El Renishaw conmigo ya está amortizado.

Gracias a Chema, han sido incontables llamadas resolviéndome dudas y hablando de magnetismo. Nunca pensé que medir SQUID a más de 1000 km de distancia fuera tan fácil. Mucho de esta tesis es gracias a que me hayas medido las muestras con tanto cariño, me aportaras ideas y que nunca pusieras impedimento a repetir las medidas dos, tres, cuatro veces.

Gracias a todos los que habéis pasado por el CiQUS y por el P0D7 y habéis estado para sacarme una sonrisa, darme charreta u ofrecerme un café o una cerveza en los días grises: Víctor, Álvaro, Rafa, Naveen, Aitor, Manuel, Manuela, Samuel, Rubén.

Gracias a mis chicas, a Itsaso, Ana García y Ana Carrero. Estáis conmigo todos los días desde que me mudé a Santiago y en estos años hemos crecido juntas. Aprendo mucho de las tres, por vuestra pasión, tenacidad y entrega en todo lo que hacéis y me ayudáis a ser una mejor versión de mi misma. Os quiero.

A mis dos mejores amigos. A Néstor, por estar conmigo prácticamente desde que tengo memoria. Por volver a vernos con la misma euforia de siempre y que siempre encontremos ese nexo de unión aunque la vida nos lleve por caminos diferentes. Gracias por recordarme siempre lo tenaz y persistente que soy cuando a veces dudo de mí. A Víctor, por tu punto de locura y tantas llamadas con las que hemos arreglado el mundo, tu campo siempre será visita obligada.

Gracias a mi equipo de Maxmetal: sobre todo a Irene (mi metalsister), Juanjo, Andrés y Paredes. Y a todas las personas que el mundo periodístico me ha permitido conocer.

Gracias a Jordi, por confiar en mí para la tertulia y hacer que este último año y medio se pasara volando y llegar con ganas al lunes para hacer las entrevistas con vosotros. Gracias por recordarme lo mucho que valgo siempre y por todo lo que me dejas aprender de ti.

En estos seis años, formé parte la gran familia de la Orquesta de la USC. Mi aliciente era no aparcar el violín pero allí he compartido con mucha gente bonita que se me ha quedado grabada en el corazón.

Por último, a mis “magníficos” favoritos: Mercedes, Lola y Fernando’s. Quién iba a decirme que un concurso me traería a tan buena gente y tan cerquita.

"En la vida no todo es avanzar,

a veces un paso atrás,

nunca dudes en cambiar de dirección,

si el camino se acabó.

A cada sueño, cada idea, cada amor

entrégate con pasión

lleva siempre la verdad en tu interior

y tu propia religión".

Víctor García

Tú Mismo – El Sello de los Tiempos (2002) – Warcry

CONTENTS

1 RESUMEN, RESUMO, SUMMARY

1.1 Resumen

La sociedad moderna demanda cada vez más, acceso a tecnologías y dispositivos capaces de almacenar información de manera más eficiente, con mayor capacidad y en un espacio reducido. Para disminuir el tamaño de los dispositivos de almacenamiento de datos y aumentar su capacidad, se requieren unidades biestables más pequeñas (como moléculas). La organización personalizada de moléculas que exhiben biestabilidad magnética en superficies podría conducir en última estancia a puntos de memoria nanométricos, compuertas lógicas u osciladores y resonadores eléctricos. El paso crucial para alcanzar estos objetivos es ensamblar estas moléculas biestables con precisión nanométrica e incluso orientarlas manteniendo su integridad estructural y propiedades.

Los sistemas de transición de espín basados en hierro son un ejemplo paradigmático de materiales biestables. En tales materiales, el estado magnético puede transitar desde una configuración diamagnética de bajo espín (low spin en inglés, LS) hasta una configuración paramagnética de alto espín (high spin en inglés, HS) mediante diversos estímulos externos como la temperatura, la irradiación de luz, presión o potencial.

Numerosos estudios coinciden en que las propiedades de transición de espín están estrechamente ligadas al entorno molecular y a las interacciones que se establecen entre los centros metálicos. Esta comunicación entre centros metálicos se denomina cooperatividad. Estas interacciones suelen ser de naturaleza supramolecular y pueden incluir una variedad de tipos, como enlaces de hidrógeno, enlaces de halógeno, interacciones π-π y fuerzas de Van der Waals. Diversos grupos de investigación han dedicado esfuerzos a establecer correlaciones magneto-estructurales entre este tipo de interacciones y parámetros clave, tales como la temperatura de transición, el carácter de la transición (gradual o abrupta, completa o incompleta) y la presencia de histéresis.

Para este propósito, técnicas de caracterización estructural como la difracción de rayos X de monocristal y la espectroscopia Raman, así como técnicas de caracterización magnética como el SQUID (Dispositivo de Interferencia Cuántica con Superconductividad, Superconducting Quantum Interference Device en inglés), son fundamentales para analizar cambios y características. El progreso científico reciente ha permitido que estas técnicas de caracterización se adapten para obtener información sobre los cambios en la estructura que experimentan los compuestos de transición de espín al someterse a estímulos como luz, presión o temperatura.

Sin embargo, hasta la fecha, no se han establecido reglas generales que permitan predecir y controlar de manera efectiva las propiedades magnéticas en complejos de transición de espín mediante el diseño cuidadoso del entorno molecular del metal. Las constantes de Hammett son un parámetro útil que describe el efecto inductivo de ciertos sustituyentes en posiciones *orto*-, *meta*- y *para*- de un mismo ligando. Aunque las constantes de Hammett son una referencia valiosa, en el campo de los compuestos de transición no tienen en cuenta los efectos del empaquetamiento cristalino ni las interacciones intermoleculares que se establecen al emplear determinados sustituyentes, los cuales son factores clave que influyen

en las propiedades magnéticas. Si bien existen ejemplos donde se ha logrado establecer una correlación clara para ciertos ligandos, estos casos no son generalizables a otros compuestos.

Otro ejemplo representativo de materiales biestables son los imanes mono-moleculares (Single Molecule Magnets, en inglés), y en particular, aquellos que están formados por un solo ion, (Single Ion Magnets, en inglés). En estos compuestos, el átomo magnético puede existir en dos estados de espín magnético, los cuales están separados por una barrera de energía. A temperaturas bajas, los efectos térmicos disminuyen, lo que facilita que los electrones ocupen un estado de menor energía y permita al sistema transitar entre estos dos estados magnéticos. Los imanes mono-moleculares son particularmente interesantes tanto desde una perspectiva teórica, debido a su comportamiento cuántico, como desde un punto de vista práctico. Son considerados como candidatos prometedores para qubits en computación cuántica, así como para el enfriamiento de sistemas a temperaturas extremadamente bajas. Por lo general, estos materiales están compuestos por un ion metálico, comúnmente un lantánido debido a su elevado valor de espín total, lo que contribuye a una barrera energética más significativa. Sin embargo, en las últimas décadas, ha habido un aumento en el estudio de la primera serie de metales de transición con configuración electrónica d^4-d^7, gracias a su mayor disponibilidad y menor coste.

Numerosos estudios han demostrado que la distorsión del entorno intramolecular del ion metálico es fundamental para generar la anisotropía necesaria que induce el comportamiento de imán de un solo ion. Por lo tanto, es esencial continuar explorando el diseño racional de ligandos que nos permita establecer relaciones magneto-estructurales y relacionarlas con la distorsión y anisotropía.

Uno de los principales objetivos de esta tesis es obtener ligandos nitrogenados capaces de inducir el desdoblamiento de los orbitales *d* del metal para observar transiciones de espín, ya sea mediante procedimientos previamente descritos o a través de nuevas rutas propuestas. Una vez obtenidos los ligandos necesarios, se llevará a cabo su complejación con Fe(II). Se estudiará la influencia del diseño de los ligandos (efecto inductivo), las posibles interacciones supramoleculares (Van der Waals, enlaces de hidrógeno y halógeno, interacciones π-π), el efecto de los contraiones y los disolventes en la estructura final del complejo.

Inicialmente se creará una biblioteca de materiales que muestren propiedades de transición de espín, empleando moléculas poco estudiadas o no reportadas hasta la fecha. Se investigará cómo la modificación de los ligandos orgánicos influye en las propiedades magnéticas, analizando las correlaciones magneto-estructurales haciendo énfasis en las interacciones supramoleculares. Además, las estrategias sintéticas propuestas permitirán incorporar nuevas funcionalidades en los compuestos de transición de espín y ajustar sus propiedades magnéticas utilizando estímulos poco convencionales, como cambios de fase o presión.

Asimismo, mediante esta nueva serie de ligandos propuesta, se pretende sintetizar complejos de coordinación de Co(II). Estos ligandos, al establecer potenciales interacciones supramoleculares (intermoleculares), podrían influir en la primera esfera de coordinación (interacciones intramoleculares), lo que resultaría en la modificación de la distorsión octaédrica y la anisotropía en el Co(II), así como en la promoción y ajuste de las propiedades de los imanes de un solo ion inducido por campo.

Estas moléculas, posteriormente, se modificarán químicamente para incorporarlas de forma covalente en derivados de grafeno (óxido de grafeno y óxido de grafeno reducido) con grupos funcionales específicos (ácidos, aminas y α-aminoácidos). El paso crucial para alcanzar estos objetivos es ensamblar estas moléculas biestables con precisión nanométrica e incluso orientarlas manteniendo su integridad estructural y propiedades.

El grafeno, al ser un material bidimensional con propiedades eléctricas y conductoras excepcionales, emerge como una plataforma ideal para la funcionalización covalente con moléculas que incorporen propiedades de transición de espín. Esta funcionalización aprovecharía las características únicas del grafeno, combinándolas con las propiedades magnéticas de las moléculas, para desarrollar dispositivos con aplicaciones en nanoelectrónica y espintrónica molecular.

La organización de materiales magnéticos en grafeno para crear una estructura 2D ha generado un gran interés en la comunidad científica debido a las prometedoras posibilidades que ofrece. Estas láminas de carbono, con alta resistencia química y térmica, así como su alta conductividad eléctrica, proporcionan una plataforma robusta y versátil para la integración de materiales magnéticos. La funcionalización del grafeno con moléculas que exhiben propiedades de transición de espín abre la puerta a la creación de sistemas magnéticos biestables que pueden ser controlados por estímulos externos, como campos magnéticos o eléctricos. Esta capacidad de control es esencial para el desarrollo de dispositivos avanzados, como memorias magnéticas, interruptores moleculares y sensores de alta sensibilidad. Además, la funcionalización covalente del grafeno con moléculas magnéticas evita los problemas asociados con la degradación de las propiedades magnéticas de los materiales. Esto garantiza una mayor estabilidad y durabilidad de los dispositivos, lo cual es crucial para su implementación práctica en aplicaciones tecnológicas.

Hasta la fecha, la mayoría de los trabajos publicados se han centrado en la funcionalización del grafeno para obtener materiales híbridos utilizando una aproximación no covalente, como heteroestructuras de Van der Waals. Aunque esta estrategia ofrece varias ventajas significativas en términos de facilidad de fabricación y versatilidad de los materiales resultantes, la funcionalización covalente permite un mayor control de la estabilidad y la funcionalidad a largo plazo.

Estos resultados se presentan en el **Capítulo 4**, **Resultados y Discusión**, que se divide en cinco secciones que se describirán en detalle a continuación.

En la **sección 4.1**, se sintetizaron tres nuevos ligandos anfifílicos basados en 2,6-di(pirazol-3-il)piridina (3-bpp), funcionalizados con una cadena alquílica de 16 carbonos y con tres grupos terminales diferentes: 2,6-bis(1-hexadecyl-pyrazol-3-yl)pyridine (L1), 16,16'-(pyridine-2,6-diylbis(1H-pyrazole-3,1-diyl))bis(hexadecan-1-ol) (L2) and dimethyl 16,16'-(pyridine-2,6-diylbis(1H-pyrazole-3,1-diyl))dipalmitate (L3). Se sintetizaron y aislaron cristales de los complejos correspondientes de Fe(II): $[Fe(L1)_2](ClO_4)_2$ (**1**), $[Fe(L2)_2](ClO_4)_2$ (**2**) y $[Fe(L3)_2](ClO_4)_2$ (**3**) y se realizaron estudios de difracción de rayos X de monocristal, demostrando que los compuestos presentan una organización lamelar de doble capa para **1** y **2**, y una estructuración menos compacta pero unida por las mismas fuerzas de Van der Waals para el caso de **3**. Este tipo de organización puede dar lugar a que los compuestos presenten propiedades de cristal líquido, en una subclase de materiales denominada metalomesógenos.

Estudios de temperatura variable basados en difracción de rayos X de polvo, espectroscopía Raman, calorimetría diferencial de barrido (DSC) y microscopía óptica polarizada (POM) demostraron que los compuestos experimentan múltiples transformaciones de fase, como transiciones cristal-cristal, cristal a líquido isotrópico o líquido isotrópico a cristal líquido. Las medidas magnéticas mostraron que estos compuestos existen en un estado de alto espín (HS) tanto en el cristal como en el estado de cristal líquido, pero diferentes transiciones de fase están acompañadas por una disminución discreta en la susceptibilidad magnética.

Para demostrar si la transición de espín podría darse a través de otros estímulos como la aplicación de presión, se realizaron estudios de espectroscopía Raman en presión variable. Estos resultados revelaron que los tres compuestos experimentan una transición de alto a bajo espín (HS→LS) bajo presiones notablemente altas, superiores a 2 GPa. La capacidad de alcanzar tales niveles de presión se atribuye a la alta compresibilidad conferida por las cadenas alquílicas presentes en los compuestos.

Estos resultados evidencian que, mediante un diseño cuidadoso de los ligandos, es posible integrar propiedades de cristal líquido y transiciones de espín en metalomesógenos. Esta sinergia entre ambas propiedades abre nuevas oportunidades para el desarrollo de tecnologías avanzadas y la creación de dispositivos con funcionalidades mejoradas.

En la **sección 4.2**, se propuso un diseño sintético novedoso de nuevos compuestos de transición de espín basados en la síntesis de la serie de ligandos del tipo *para*-X-3-bpp y su incorporación en complejos de Fe(II), $[Fe(p\text{-X-3-bpp})_2](ClO_4)_2$ siendo X = F (**F**), Cl (**Cl**), Br (**Br**) y I (**I·H_2O**). Esta serie presenta la particularidad de permitir la investigación conjunta de las interacciones intermoleculares, tales como los enlaces de hidrógeno y halógeno y estudiar su impacto en la cooperatividad y transición de espín. Los experimentos de rayos X, SQUID y Raman, combinados con variaciones de temperatura y presión, establecen una relación magneto-estructural precisa y demuestran cómo la transición se modifica mediante cambios en estas interacciones.

En el caso del **F**, se demostró que la estructura tridimensional presenta únicamente enlaces de hidrógeno y estos estabilizan un estado de espín intermedio, con una primera transición abrupta y una segunda gradual, sin una transición de fase cristalográfica. Sin embargo, el aumento del tamaño del halógeno, como en el caso del **Cl** y el **Br**, permite establecer un enlace de halógeno adicional entre el Cl/Br y el anión perclorato que induce un alto grado de cooperatividad en el sistema traduciéndose en una transición de espín abrupta y con histéresis mínima.

Los estudios magnéticos bajo presión variable revelaron la capacidad de estabilizar un estado de espín intermedio en el caso del **Cl**, lo que demuestra la viabilidad de transicionar de manera reversible entre estados de espín estables: LS ↔ IS ↔ HS. El análisis de la estructura mediante difracción de rayos X de monocristal bajo la presión que estabiliza este estado intermedio (0.51 GPa) permitió identificar de manera inequívoca que la estructura en estado LS presenta dos enlaces de halógeno (uno por cada átomo de halógeno del complejo), mientras que la estructura en estado intermedio (IS) mantiene uno, y la estructura en estado HS pierde ambos. Este hallazgo sugiere que el enlace de halógeno desempeña un papel crucial en sistemas altamente cooperativos. Además, plantea que la frustración de red, introducida por enlaces de hidrógeno altamente direccionales, junto con la pérdida de un enlace de halógeno, contribuye a estabilizar el estado de espín intermedio.

En el caso del compuesto **I·H_2O**, donde se aisló únicamente la estructura hidratada, se pudo observar que las moléculas de solvato establecen interacciones con el ligando, lo que resulta en una reducción del grado de cooperatividad y en la estabilización del estado LS. Esto conduce a una transición gradual incompleta que ocurre por encima de la temperatura ambiente.

Con la experiencia en la síntesis de estos ligandos adquirida en la **sección 4.2**, estos mismos se utilizaron para obtener complejos de coordinación de Co(II) y estudiar sus propiedades como imanes moleculares de un solo ion en la **sección 4.3**.

Se obtuvieron cinco compuestos diferentes en función del halógeno y de los disolventes incluidos, $[Co(p\text{-X-3-bpp})_2](ClO_4)_2$ siendo X: F, Cl, Br, y I y los compuestos obtenidos denominados como **F**, **Cl**, **Br**, **Br·2H_2O** y **I·2H_2O**. Esta serie de compuestos demostraron ser candidatos ideales para estudiar sus propiedades de SIM con campo inducido, demostrando la posibilidad de ajustar la barrera energética mediante la distorsión en el entorno de coordinación del ion metálico en función del sustituyente, así como mediante la relajación de dicha distorsión a través de solvatos.

Para la serie de compuestos anhidros (**F**, **Cl** y **Br**), se observó a través de medidas de susceptibilidad magnética fuera de fase en función de la frecuencia que la barrera de energía aumenta a medida que aumenta el tamaño del halógeno (de **F** a **Br**). Además, se constató que el mecanismo de relajación en el caso del **F** y **Cl** se produce mediante un proceso Raman (fonón-fonón con relajación desde un estado virtual) asistido por Orbach (fonón-fonón con relajación desde un estado excitado), mientras, para el **Br**, la relajación se produce principalmente por Orbach.

Por el contrario, las medidas magnéticas en las estructuras solvatadas (**Br·2H_2O** y **I·2H_2O**) revelaron una considerable disminución en la barrera de energía, y el mecanismo de relajación se produce principalmente mediante un proceso Raman asistido por Orbach.

Las medidas de difracción de rayos X de monocristal resultaron fundamentales para establecer una relación magneto-estructural mediante el análisis de la unidad asimétrica y el empaquetamiento tridimensional. Observamos que, conforme aumenta el tamaño del halógeno, como se detalló en la **sección 4.2**, este establece más interacciones de tipo enlace de halógeno, pasando de ninguna interacción en el caso del **F** a dos interacciones en el caso del **Br**. Estas interacciones son responsables de incrementar la distorsión axial octaédrica del metal, lo que se refleja en el ángulo formado por el enlace trans-N{piridina}-Co-N{piridina} (ϕ). Por otro lado, si las moléculas de agua están presentes en la segunda esfera de coordinación, estas relajan la distorsión axial creada por los enlaces de halógeno, reduciendo la distorsión. Esta distorsión genera una anisotropía axial (D), que a su vez es responsable del fenómeno SIM.

Otro método para alterar las propiedades de transición de espín es investigar la segunda esfera de coordinación y cómo influye en las interacciones establecidas. Por esta razón, varios estudios se han enfocado en examinar cómo cambiar esta segunda esfera de coordinación en compuestos de coordinación, ya sea mediante el cambio de contraiones o de disolventes. En la **sección 4.4**, se seleccionó el ligando *p*-Cl-3-bpp como candidato para estudiar las propiedades magnéticas en una serie de compuestos de transición, siguiendo la fórmula

[Fe(*p*-Cl-3-bpp)$_2$](X)$_2$, donde X: **ClO_4** (reportado en la **Sección 4.2**), **BF_4**, **PF_6**, **NO_3**, **NCS**, **NCSe**, **CF_3SO_3**, **Br** y **I**.

Como se evidenció en la **sección 4.2**, la capacidad del ligando para establecer enlaces de halógeno puede generar una variedad de transiciones de espín menos comunes que estabilizan estados intermedios. Se obtuvieron tres compuestos en su forma anhidra (**BF_4**, **PF_6** y **CF_3SO_3**), y se observó que, para estos tres casos, la correlación magneto-estructural propuesta en la **sección 4.2** concuerda perfectamente. En el caso del **BF_4**, que establece enlaces de hidrógeno y halógeno, se produce una transición abrupta completa, mientras, para el **PF_6**, sin enlace de halógeno, se observa una transición gradual (menos cooperativa), estabilizando un estado intermedio. Finalmente, el **CF_3SO_3**, que incluye dos centros metálicos cristalográficamente independientes, con solo un enlace de halógeno en una red de enlaces de hidrógeno fuertes, disminuye su cooperatividad exhibiendo una transición gradual incompleta.

En el caso de los compuestos solvatados (**NO_3**, **NCS**, **NCSe**, **Br** y **I**), las medidas de susceptibilidad magnética revelaron que, mientras existen en su forma solvatada, se encuentran estabilizados en estado de bajo espín (LS) (**NCS**, **NCSe**, **Br** y **I**) o en estado de alto espín (HS) (**NO_3**). La estabilización de un estado u otro se ha abordado en otros estudios en compuestos derivados del 3-bpp, atribuyéndose a las interacciones π–π. Cuando se establecen interacciones π–π entre los grupos pirazol de las moléculas vecinas, en una disposición conocida como "abrazo de terpiridina", se produce una estabilización del LS. Por el contrario, cuando los complejos [Fe(*p*-Cl-3-bpp)$_2$]$^{2+}$ no presentan interacciones de apilamiento π–π con complejos SCO vecinos, se estabiliza el HS.

En las condiciones de las medidas magnéticas, estos compuestos pueden desolvatarse in situ y presentar transiciones variadas, con más de una transición y naturaleza diferentes (con o sin histéresis, graduales o abruptas). En algunos casos, la caracterización magneto-estructural de los compuestos tras la desolvatación se complica debido a la pérdida de cristalinidad. Solo fue posible obtener la estructura deshidratada en el caso del **NCS**. Durante este proceso, la estructura experimenta cambios debido a la pérdida de enlaces de hidrógeno e interacciones π–π, al tiempo que se forma una nueva interacción Cl···π. Además, la deshidratación provoca la segregación de los centros de Fe(II) en dos unidades cristalográficas independientes, lo que conlleva un cambio en la simetría. A pesar de la reducción en la cooperatividad, se observa una transición de primer orden, que se atribuye a una rehidratación parcial de la muestra o al efecto cooperativo que se mantiene gracias a la interacción Cl···π. Aunque no se cuenta con acceso a la estructura deshidratada de los demás compuestos (**NO_3**, **NCSe**, **Br** y **I**), su comportamiento magnético al deshidratarse es similar al del **NCS**. Por lo tanto, se infiere que el reordenamiento de la estructura al perder las interacciones con el disolvente será análogo.

Finalmente, en la **sección 4.5** y aprovechando la investigación realizada en la serie de compuestos descrita en secciones anteriores, se diseñaron ligandos derivados de la 1-bpp y la 3-bpp utilizando modificaciones de las metodologías sintéticas previamente descritas. Esto condujo a la síntesis de tres series de ligandos con diferentes funcionalidades (ácidos carboxílicos, aminas o α-aminoácidos) para su unión covalente al óxido de grafeno o al óxido de grafeno reducido. La funcionalización con estos ligandos facilitó la posterior incorporación

de complejos de Fe(II) con el fin de estudiar las propiedades de transición de espín sobre el grafeno.

La primera serie de ligandos propuestos se basó en la sustitución por un grupo ácido en la posición *para*- (1-bpp-COOH y 3-bpp-COOH). La reacción consistió en una condensación para obtener el óxido de grafeno comercial (**cGO**) y óxido de grafeno obtenido por el método de Hummer (**hGO**) funcionalizado (**1-GO** y **2-GO**), seguido de su complejación con Fe(II) (**Fe-1-GO** y **Fe-2-GO**). La funcionalización del ligando se confirmó mediante diversas técnicas, como el análisis termogravimétrico (TGA), la espectroscopía Raman y la espectrometría de fotoelectrones inducidos por rayos X (XPS). El análisis termogravimétrico y la espectrometría de fotoelectrones inducidos por rayos X concluyeron la formación del complejo en el caso de **Fe-2-hGO**. Por lo tanto, en este punto se propusieron dos nuevos ligandos, rediseñando la conexión. Para abordar esta cuestión, concebimos funcionalizar la bpp con un grupo amino conectado electrónicamente a través de un grupo espaciador arilo. Además, se planteó la protección del grupo amino de la 3-bpp mediante el uso del grupo protector THP (tetrahidrofurano) con el fin de mejorar su solubilidad y prevenir posibles reacciones secundarias.

Con estos nuevos ligandos se siguieron dos estrategias: (i) a través de la reacción covalente de condensación con el grupo amino, se introdujeron los ligandos 1-bpp-L-NH2 y 3-bpp-THP-L-NH2 en el óxido de grafeno comercial (**3-cGO**, **4-cGO**), seguido de su posterior complejación (**Fe-3-cGO** y **Fe-4-cGO**). Y (ii), utilizando el mismo ligando como punto de partida, se derivatizó para obtener un α-aminoácido terminal (1-bpp-L-Gly y 3-bpp-THP-L- Gly) con el fin de llevar a cabo la reacción covalente de cicloadición 1,3 dipolar, comúnmente conocida como reacción de Prato, en óxido de grafeno reducido (**6-rGO** y **7-rGO**). Posteriormente, se procedió a su complejación con Fe(II) (**Fe-6-rGO** y **Fe-7-rGO**).

La funcionalización con el ligando (**3-cGO**, **4-cGO**, **5-cGO**, **6-rGO** y **7-rGO**) se verificó mediante técnicas como TGA, Raman y XPS. La incorporación de Fe (**Fe-3-cGO**, **Fe-4-cGO**, **Fe-5-cGO**, **Fe-6-rGO** y **Fe-7-rGO**) fue confirmada a través del mapeo elemental por espectroscopía de dispersión de energía de rayos X en combinación con microscopía electrónica de transmisión de barrido (STEM/EDX). El Fe se encuentra formando el complejo de coordinación, distribuido de manera uniforme por toda la muestra, sin la presencia de agregados u otras nanoestructuras. El análisis del estado magnético de los híbridos se llevó a cabo mediante medidas de coeficiente Seebeck a temperatura variable (efecto termoeléctrico) para **Fe-7-rGO**. Estas medidas mostraron que el **Fe-7-rGO** tiene un coeficiente Seebeck el doble del del rGO, lo que sugiere una reducción en el número de defectos asociados a la funcionalización.

En resumen, a lo largo de esta tesis doctoral, se ha llevado a cabo una investigación exhaustiva sobre una librería de compuestos de transición de espín de Fe(II) que exhiben diferentes propiedades magnéticas. Basándose en los resultados obtenidos con estos compuestos, se ha aplicado esta experiencia en la síntesis de nuevos imanes moleculares de Co(II). Además, se ha profundizado en el estudio del comportamiento de estas propiedades al combinarlas con superficies de carbono de forma covalente, como el óxido de grafeno y el óxido de grafeno reducido.

Estos hallazgos son alentadores, sugiriendo que este proyecto podría servir como punto de partida para el diseño y estudio de nuevos materiales con propiedades relevantes para la

fabricación de dispositivos con aplicaciones en nanoelectrónica y espintrónica molecular. Este trabajo ilustra la versatilidad de los compuestos de transición de espín y los imanes moleculares y propone metodologías adaptadas para el desarrollo de grafeno covalentemente funcionalizado, resaltando su potencial aplicación en múltiples campos científicos y tecnológicos.

1.2 Resumo

A sociedade moderna require cada vez máis acceso a tecnoloxías e dispositivos capaces de almacenar información de maneira máis eficiente, con maior capacidade e nun espazo reducido. Para diminuír o tamaño dos dispositivos de almacenamento de datos e aumentar a súa capacidade, requírense unidades biestables máis pequenas (como moléculas). A organización personalizada de moléculas que exhiben biestabilidade magnética en superficies podería conducir en última instancia a puntos de memoria nanométricos, comportas lóxicas ou osciladores e resonadores eléctricos. O paso crucial para alcanzar estes obxectivos é ensamblar estas moléculas biestables con precisión nanométrica e mesmo orientalas mantendo a súa integridade estrutural e propiedades.

Os sistemas de transición de espín de ferro son un exemplo paradigmático de materiais biestables. Nestes materiais, o estado magnético pode transitar dende unha configuración diamagnética de baixo espín (low spin en inglés, LS) ata unha configuración paramagnética de alto espín (high spin en inglés, HS) mediante diversos estímulos externos como a temperatura, a irradiación de luz, presión ou potencial.

Numerosos estudos coinciden en que as propiedades de transición de espín están estreitamente ligadas ao entorno molecular e ás interaccións que se establecen entre os centros metálicos. Esta comunicación entre centros metálicos pode denominarse como cooperatividade. Estas interaccións adoitan ser de natureza supramolecular e poden incluír unha variedade de tipos, como enlaces de hidróxeno, enlaces de halóxeno, interaccións π-π e forzas de Van der Waals. Diversos grupos de investigación dedicaron esforzos a establecer correlacións magnetoestructurais entre este tipo de interaccións e parámetros clave, tales como a temperatura de transición, o carácter da transición (gradual ou abrupta, completa ou incompleta) e a presenza de histérese.

Para este propósito, técnicas de caracterización estrutural como a difracción de raios X de monocristal e a espectroscopia Raman, así como técnicas de caracterización magnética como o SQUID (Dispositivo de Interferencia Cuántica con Superconductividade, Superconducting Quantum Interference Device en inglés), son fundamentais para analizar cambios e características. O progreso científico recente permitiu que estas técnicas de caracterización se adapten para obter información sobre os cambios na estrutura que experimentan os compostos de transición de espín ao someterse a estímulos, como luz, presión ou temperatura.

Sen embargo, ata a data, non se estableceron regras xerais que permitan prever e controlar de maneira efectiva as propiedades magnéticas en complexos de transición de espín mediante o deseño coidadoso do entorno molecular do metal. As constantes de Hammett son un parámetro útil que describe o efecto indutivo de certos substituíntes en posicións *orto*-, *meta*- e *para*- dun mesmo ligando. Aínda que as constantes de Hammett son unha referencia valiosa, no campo dos compostos de transición non se ten en conta os efectos do empaquetamento cristalino nin as interaccións intermoleculares que se establecen ao empregar certos substituíntes, os cales son factores clave que inflúen nas propiedades magnéticas. Aínda que existen exemplos onde se logrou establecer unha correlación clara para certos ligandos, estes casos non son xeralizables a outros compostos.

Outro exemplo representativo de materiais biestables son os imáns monomoleculares (Single Molecule Magnets, en inglés), e en particular, aqueles que están formados por un só ión (Single Ion Magnets, en inglés). Nestes compoñentes, o átomo magnético pode existir en dous estados de espín magnético, os cales están separados por unha barreira de enerxía. A temperaturas baixas, os efectos térmicos diminúen, facilitando que os electróns ocupen un estado de menor enerxía e permitan ao sistema transitar entre estes dous estados magnéticos. Os imáns monomoleculares son particularmente interesantes tanto desde unha perspectiva teórica, debido ao seu comportamento cúantico, como desde un punto de vista práctico. Son considerados como candidatos prometedores para qubits en computación cuántica, así como para o arrefriamento de sistemas a temperaturas extremadamente baixas. Xeralmente, estes materiais están compostos por un ión metálico, comunmente un lantánido debido ao seu elevado valor de espín total, o cal contribúe a unha barreira enerxética máis significativa. Sen embargo, nas últimas décadas, houbo un aumento no estudo da primeira serie de metais de transición con configuración electrónica d^4-d^7, grazas á súa maior dispoñibilidade e menor custo.

Numerosos estudos demostraron que a distorsión do entorno intramolecular do ión metálico é fundamental para xerar a anisotropía necesaria que induce o comportamento de imán dun só ión. Polo tanto, é crucial continuar explorando o deseño racional de ligandos que nos permita establecer relacións magnetoestruturais e relacionalas coa distorsión e anisotropía.

Un dos obxectivos principais desta tese é obter ligandos nitroxenados capaces de inducir o desdobramento dos orbitais *d* do metal para observar transicións de espín, xa sexa mediante procedementos previamente descritos ou novas rutas propostas. Unha vez obtidos os ligandos necesarios, levarase a cabo a súa complexación con Fe(II). Estudarase a influencia do deseño dos ligandos (efecto indutivo), as posibles interaccións supramoleculares (Van der Waals, enlaces de hidróxeno e halóxeno, interaccións π-π), o efecto dos contraíons e os solventes na estrutura final do complexo. Inicialmente crearase unha biblioteca de materiais que mostren propiedades de transición de espín, empregando moléculas pouco estudadas ou non reportadas ata a data. Investigarase como a modificación dos ligandos orgánicos inflúe nas propiedades magnéticas, analizando as correlacións magnetoestruturais facendo énfase nas interaccións supramoleculares. Ademais, as estratexias sintéticas propostas permitirán incorporar novas funcionalidades nos compoñentes de transición de espín e axustar as súas propiedades magnéticas utilizando estímulos pouco convencionais, como cambios de fase ou presión.

Do mesmo xeito, mediante esta nova serie de ligandos proposta, preténdese sintetizar complexos de coordinación de Co(II). Estes ligandos, ao establecer potenciais interaccións supramoleculares (intermoleculares), poderían influír na primeira esfera de coordinación (interaccións intramoleculares), o que resultaría na modificación da distorsión octaédrica e da anisotropía no Co(II), así como na promoción e axuste das propiedades dos imáns dun só ión inducido polo campo.

Estas moléculas, posteriormente, modificaranse quimicamente para incorporalas de forma covalente en derivados de grafeno (óxido de grafeno e óxido de grafeno reducido) con grupos funcionais específicos (ácidos, aminas e α-aminoácidos). O paso crucial para alcanzar estes obxectivos é ensamblar estas moléculas biestables con precisión nanométrica e incluso orientalas mantendo a súa integridade estrutural e propiedades.

O grafeno, ao ser un material bidimensional con propiedades eléctricas e condutoras excepcionais, emerxe como unha plataforma ideal para a funcionalización covalente con moléculas que incorporen propiedades de transición de espín. Esta funcionalización aproveitaría as características únicas do grafeno, combinándoas coas propiedades magnéticas das moléculas, para desenvolver dispositivos con aplicacións en nanoelectrónica e espintrónica molecular.

A organización de materiais magnéticos en grafeno para crear unha estrutura 2D xerou un gran interese na comunidade científica debido ás prometedoras posibilidades que ofrece. Estas láminas de carbono, con alta resistencia química e térmica, así como a súa alta condutividade eléctrica, proporcionan unha plataforma robusta e versátil para a integración de materiais magnéticos. A funcionalización do grafeno con moléculas que exhiben propiedades de transición de espín abre a porta á creación de sistemas magnéticos biestables que poden ser controlados por estímulos externos, como campos magnéticos ou eléctricos. Esta capacidade de control é esencial para o desenvolvemento de dispositivos avanzados, como memorias magnéticas, interruptores moleculares e sensores de alta sensibilidade. Ademais, a funcionalización covalente do grafeno con moléculas magnéticas evita os problemas asociados coa degradación das propiedades magnéticas dos materiais. Isto garante unha maior estabilidade e durabilidade dos dispositivos, o cal é crucial para a súa implementación práctica en aplicacións tecnolóxicas.

Ata a data, a maioría dos traballos publicados centraronse na funcionalización do grafeno para obter materiais híbridos utilizando unha aproximación non covalente, como heteroestructuras de Van der Waals. Aínda que esta estratexia ofrece varias vantaxes significativas en termos de facilidade de fabricación e versatilidade dos materiais resultantes, a funcionalización covalente permite un maior control da estabilidade e a funcionalidade a longo prazo.

Estes resultados preséntanse no **Capítulo 4**, **Resultados e Discusión**, que se divide en cinco seccións que se describirán en detalle a continuación.

Na **sección 4.1**, sintetizáronse tres novos ligandos anfifílicos baseados na 2,6-di(pirazol-3-il)piridina (3-bpp), funcionalizados cunha cadea alquílica de 16 carbonos e con tres grupos terminais diferentes: 2,6-bis(1-hexadecyl-pyrazol-3-yl)pyridina (L1), 16,16'-(piridina-2,6-diylbis(1H-pirazol-3,1-diyl))bis(hexadecan-1-ol) (L2) e dimetilo 16,16'-(piridina-2,6-diylbis(1H-pirazol-3,1-diyl))dipalmitate (L3). Sintetizáronse e illáronse cristais dos complexos correspondentes de Fe(II): $[Fe(L1)_2](ClO_4)_2$ (**1**), $[Fe(L2)_2](ClO_4)_2$ (**2**) and $[Fe(L3)_2](ClO_4)_2$ (**3**) e realizáronse estudos de difracción de raios X de monocristal, demostrando que os compoñentes presentan unha organización lamelar de dobre capa para **1** e **2**, e unha estruturación menos compacta pero unida polas mesmas forzas de Van der Waals para o caso de **3**. Este tipo de organización pode dar lugar a que os compoñentes presenten propiedades de cristal líquido, nunha subclase de materiais denominada metalomesóxenos.

Estudos de temperatura variable baseados en difracción de raios X de po e espectroscopía Raman, calorimetría diferencial de barrido (DSC) e microscopía óptica polarizada (POM) demostraron que os compoñentes experimentan múltiples transformacións de fase, como transicións cristal-cristal, cristal a líquido isotrópico ou líquido isotrópico a cristal líquido. As medidas magnéticas mostraron que estes compoñentes existen nun estado de alto espín (HS) tanto no cristal como no estado de cristal líquido, pero diferentes transicións de fase están acompañadas por unha diminución discreta na susceptibilidade magnética.

Para demostrar se a transición de espín podería darse a través de outros estímulos como a aplicación de presión, realizáronse estudos de espectroscopia Raman en presión variable. Estes resultados revelaron que os tres compoñentes experimentaron unha transición de alto a baixo espín (HS → LS) baixo presións notablemente altas, superiores a 2 GPa. A capacidade de alcanzar tales niveis de presión atribúese á alta compresibilidade conferida polas cadeas alquílicas presentes nos compoñentes.

Estes resultados evidencian que, mediante un deseño coidadoso dos ligandos, é posible integrar propiedades de cristal líquido e transicións de espín en metalomesóxenos. Esta sinerxia entre ambas propiedades abre novas oportunidades para o desenvolvemento de tecnoloxías avanzadas e a creación de dispositivos con funcionalidades melloradas.

Na **sección 4.2**, propúxose un deseño sintético novo de novos compoñentes de transición de espín baseados na síntese da serie de ligandos do tipo *para*-X-3-bpp e a súa incorporación en complexos de Fe(II), [Fe(*p*-X-3-bpp)$_2$](ClO$_4$)$_2$ sendo X = F (**F**), Cl (**Cl**), Br (**Br**) e I (**I·H$_2$O**). Esta serie presenta a particularidade de permitir a investigación conxunta das interaccións intermoleculares, tales como os enlaces de hidróxeno e halóxeno e estudar o seu impacto na cooperatividade e transición de espín. Os experimentos de raios X, SQUID e Raman, combinados con variacións de temperatura e presión, establecen unha relación magnetoestrutural precisa e demostran como a transición se modifica mediante cambios nestas interaccións.

No caso do **F**, demostrouse que a estrutura tridimensional presenta unicamente enlaces de hidróxeno e estes estabilizan un estado de espín intermedio, cunha primeira transición abrupta e unha segunda gradual, sen unha transición de fase cristalográfica. Sen embargo, o aumento do tamaño do halóxeno, como no caso do **Cl** e o **Br**, permite establecer un enlace de halóxeno adicional entre o Cl/Br e o anión perclorato que induce un alto grao de cooperatividade no sistema traducíndose nunha transición de espín abrupta e con histérese mínima.

Os estudos magnéticos baixo presión variable revelaron a capacidade de estabilizar un estado de espín intermedio no caso do **Cl**, o que demostra a viabilidade de transicionar de maneira reversible entre estados de espín estábeis: LS ↔ IS ↔ HS. A análise da estrutura mediante difracción de raios X de monocristal baixo a presión que estabiliza este estado intermedio (0.51 GPa) permitiu identificar de maneira inequívoca que a estrutura en estado LS presenta dous enlaces de halóxeno (un por cada átomo de halóxeno do complexo), mentres que a estrutura en estado intermedio (IS) mantén un, e a estrutura en estado HS perde ambos. Este achado suxire que o enlace de halóxeno desempeña un papel crucial en sistemas altamente cooperativos. Ademais, sinala que a frustración da rede, introducida por enlaces de hidróxeno altamente direccionais, xunto coa perda dun enlace de halóxeno, contribúe a estabilizar o estado de espín intermedio.

No caso do compoñente **I·H$_2$O**, onde se aillou unicamente a estrutura hidratada, puido observarse que as moléculas de solvente establecen interaccións co ligando, o que resulta nunha redución do grao de cooperatividade e na estabilización do estado LS. Isto conduce a unha transición gradual incompleta que ocorre por enriba da temperatura ambiente.

Coa experiencia na síntese destes ligandos adquirida na **sección 4.2**, estes mesmos utilizáronse para obter complexos de coordinación de Co(II) e estudar as súas propiedades como imáns moleculares dun só ion na **sección 4.3**.

Obtivéronse cinco compoñentes diferentes en función do halóxeno e dos solventes incluídos, $[Co(p\text{-X-3-bpp})_2](ClO_4)_2$ sendo X: F, Cl, Br e I e os compoñentes obtidos denominados como **F**, **Cl**, **Br**, **Br·2H₂O** e **I·2H₂O**. Esta serie de compoñentes demostraron ser candidatos ideais para estudar as súas propiedades de SIM con campo inducido, demostrando a posibilidade de axustar a barreira de enerxía mediante a distorsión no entorno de coordinación do ion metálico en función do substituínte, así como mediante a relaxación desta distorsión a través de solventes.

Para a serie de compoñentes anhidros (**F**, **Cl** e **Br**), observouse a través de medidas de susceptibilidade magnética fóra de fase en función da frecuencia que a barreira de enerxía aumenta a medida que aumenta o tamaño do halóxeno (de **F** a **Br**). Ademais, constatouse que o mecanismo de relaxación no caso do **F** e **Cl** prodúcese mediante un proceso Raman (fonón-fonón con relaxación dende un estado virtual) asistido por Orbach (fonón-fonón con relaxación dende un estado excitado), mentres que para o **Br**, a relaxación prodúcese principalmente por Orbach.

Polo contrario, as medidas magnéticas nas estruturas solvatadas (**Br·2H₂O** e **I·2H₂O**) revelaron unha considerable diminución na barreira de enerxía, e o mecanismo de relaxación prodúcese principalmente mediante un proceso Raman asistido por Orbach.

As medidas de difracción de raios X de monocristal resultaron fundamentais para establecer unha relación magnetoestrutural mediante a análise da unidade asimétrica e o empaquetamento tridimensional. Observamos que, conforme aumenta o tamaño do halóxeno, como se detallou na **sección 4.2**, este establece máis interaccións de tipo enlace de halóxeno, pasando de ningunha interacción no caso do **F** a dúas interaccións no caso do **Br**. Estas interaccións son responsables de incrementar a distorsión axial octaédrica do metal, o que se reflicte no ángulo formado polo enlace trans-N{piridina}-Co-N{piridina} (ϕ). Por outra banda, se as moléculas de auga están presentes na segunda esfera de coordinación, estas relaxan a distorsión axial creada polos enlaces de halóxeno, reducindo a distorsión. Esta distorsión xera unha anisotropía axial (D), que a súa vez é responsable do fenómeno SIM.

Outro método para alterar as propiedades de transición de espín é investigar a segunda esfera de coordinación e como inflúe nas interaccións establecidas. Por esta razón, varios estudos enfocáronse en examinar como cambiar esta segunda esfera de coordinación en compoñentes de coordinación, xa sexa mediante o cambio de contraións ou de solventes. Na **sección 4.4**, seleccionouse o ligando *p*-Cl-3-bpp como candidato para estudar as propiedades magnéticas nunha serie de compostos de transición, seguindo a fórmula $[Fe(p\text{-Cl-3-bpp})_2](X)_2$, onde X: **$ClO_4$** (reportado na **Sección 4.2**), **BF_4**, **PF_6**, **NO_3**, **NCS**, **NCSe**, **CF_3SO_3**, **Br** e **I**.

Como se evidenciou na **sección 4.2**, a capacidade do ligando para establecer enlaces de halóxeno pode xerar unha variedade de transicións de espín menos comúns que estabilizan estados intermedios. Obtivéronse tres compostos na súa forma anhidra (**BF_4**, **PF_6** e **CF_3SO_3**), e observouse que, para estes tres casos, a correlación magneto-estructural proposta na **sección 4.2** concorda perfectamente. No caso do **BF_4**, que establece enlaces de hidróxeno e halóxeno, prodúcese unha transición abrupta completa, mentres que para o **PF_6**, sen enlace de halóxeno, obsérvase unha transición gradual (menos cooperativa), estabilizando un estado intermedio. Finalmente, o **CF_3SO_3**, que inclúe dous centros metálicos cristalograficamente independentes, con só un enlace de halóxeno nunha rede de enlaces de hidróxeno fortes, diminúe a súa cooperatividade exhibindo unha transición gradual incompleta.

No caso dos compostos solvatados (**NO_3**, **NCS**, **NCSe**, **Br** e **I**), as medidas de susceptibilidade magnética revelaron que, mentres existen na súa forma solvatada, están estabilizados en estado de baixo espín (LS) (**NCS**, **NCSe**, **Br** e **I**) ou en estado de alto espín (HS) (**NO_3**). A estabilización dun estado ou outro abordouse noutros estudos en compostos derivados do 3-bpp, atribuíndose ás interaccións π–π. Cando se establecen interaccións π–π entre os grupos pirazol das moléculas veciñas, nunha disposición coñecida como "abracemento de terpiridina", prodúcese unha estabilización do LS. Polo contrario, cando os complexos $[Fe(p\text{-}Cl\text{-}3\text{-}bpp)_2]^{2+}$ non presentan interaccións de apilamento π–π con complexos SCO veciños, estabilízase o HS.

Nas condicións das medidas magnéticas, estes compostos poden desolvatarse in situ e presentar transicións variadas, con máis dunha transición e natureza diferentes (con ou sen histérese, graduais ou abruptas). En algúns casos, a caracterización magneto-estructural dos compostos tras a desolvatación complícase debido a perda de cristalinidade. Só foi posible obter a estrutura deshidratada no caso do **NCS**. Durante este proceso, a estrutura experimenta cambios debido a perda de enlaces de hidróxeno e interaccións π–π, ao mesmo tempo que se forma unha nova interacción Cl···π. Ademais, a deshidratación provoca a segregación dos centros de Fe(II) en dúas unidades cristalograficamente independentes, o que conleva un cambio na simetría. A pesar da redución na cooperatividade, obsérvase unha transición de primeiro orde, que se atribúe a unha rehidratación parcial da mostra ou ao efecto cooperativo que se mantén grazas á interacción Cl··· π. Aínda que non se conta con acceso á estrutura deshidratada dos demais compostos (**NO_3**, **NCSe**, **Br** e **I**), o seu comportamento magnético ao deshidratarse é similar ao do **NCS**. Polo tanto, infírese que o reordenamento da estrutura ao perder as interaccións co disolvente será análogo.

Finalmente, na **sección 4.5** e aproveitando a investigación realizada na serie de compostos descrita en seccións anteriores, deseñáronse ligandos derivados da 1-bpp e da 3-bpp utilizando modificacións das metodoloxías sintéticas previamente descritas. Isto conduciu á síntese de tres series de ligandos con diferentes funcionalidades (ácidos carboxílicos, aminas ou α-aminoácidos) para a súa unión covalente ao óxido de grafeno ou ao óxido de grafeno reducido. A funcionalización con estes ligandos facilitou a posterior incorporación de complexos de Fe(II) co fin de estudar as propiedades de transición de espín sobre o grafeno.

A primeira serie de ligandos propostos basouse na substitución por un grupo ácido na posición para- (1-bpp-COOH e 3-bpp-COOH). A reacción consistiu nunha condensación para obter o óxido de grafeno comercial (**cGO**) e o óxido de grafeno obtido polo método de Hummer (**hGO**) funcionalizado (**1-GO** e **2-GO**), seguido da súa complexación con Fe(II) (**Fe-1-GO** e **Fe-2-GO**). A funcionalización do ligando confirmouse mediante diversas técnicas, como análise termogravimétrica (TGA), espectroscopia Raman e espectrometría de fotoelectróns inducidos por raios X (XPS). A análise termogravimétrica e a espectrometría de fotoelectrones inducidos por raios X concluíron a formación do complexo no caso de **Fe-2-GO**. Polo tanto, neste punto propuxéronse dous novos ligandos, redeseñando a conexión. Para abordar esta cuestión, concibimos funcionalizar a bpp cun grupo amino conectado electrónicamente a través dun espaciador arilo. Ademais, plantexouse a protección do grupo amino da 3-bpp mediante o uso do grupo protector THP (tetrahidrofurano) co fin de mellorar a súa solubilidade e previr posibles reaccións secundarias.

Con estes novos ligandos seguíronse dúas estratexias: (i) a través da reacción covalente de condensación co grupo amino, introducíronse os ligandos 1-bpp-L-NH2 e 3-bpp-THP-L-NH2 no óxido de grafeno comercial (**3-cGO**, **4-cGO**), seguido da súa posterior complexación (**Fe-3-cGO** e **Fe-4-cGO**). E (ii), utilizando o mesmo ligando como punto de partida, derivatizouse para obter un α-aminoácido terminal (1-bpp-L-Gly e 3-bpp-THP-L-Gly) co fin de levar a cabo a reacción covalente de cicloadición 1,3 dipolar, comúnmente coñecida como reacción de Prato, en óxido de grafeno reducido (**6-rGO** e **7-rGO**). Posteriormente, procedeuse á súa complexación con Fe(II) (**Fe-6-rGO** e **Fe-7-rGO**).

A funcionalización co ligando (**3-cGO**, **4-cGO**, **5-cGO**, **6-rGO** e **7-rGO**) verificouse mediante técnicas como TGA, Raman e XPS. A incorporación de Fe (**Fe-3-cGO**, **Fe-4-cGO**, **Fe-5-cGO**, **Fe-6-rGO** e **Fe-7-rGO**) confirmouse a través do mapeamento elemental por espectroscopia de dispersión de enerxía de raios X en combinación con microscopía electrónica de transmisión de barrido (STEM/EDX). O Fe atópase formando o complexo de coordinación, distribuído de maneira uniforme por toda a mostra, sen a presenza de agregados ou outras nanoestruturas. A análise do estado magnético dos híbridos levouse a cabo mediante medidas de coeficiente Seebeck a temperatura variable (efecto termoeléctrico) para **Fe-7-rGO**. Estas medidas mostraron que o **Fe-7-rGO** ten un coeficiente Seebeck o dobre do rGO, o que suxire unha redución no número de defectos asociados á funcionalización.

En resumo, ao longo desta tese de doutoramento, levouse a cabo unha investigación exhaustiva sobre unha biblioteca de compostos de transición de espín de Fe(II) que exhiben diferentes propiedades magnéticas. Baseándose nos resultados obtidos con estes compostos, aplicouse esta experiencia na síntese de novos imáns moleculares de Co(II). Ademais, profundizouse no estudo do comportamento destas propiedades ao combinalas con superficies de carbono de forma covalente, como o óxido de grafeno e o óxido de grafeno reducido.

Estes achados son alentadores, suxerindo que este proxecto podería servir como punto de partida para o deseño e estudo de novos materiais con propiedades relevantes para a fabricación de dispositivos con aplicacións en nanoelectrónica e espintrónica molecular. Este traballo ilustra a versatilidade dos compostos de transición de espín e dos imáns moleculares e propón metodoloxías adaptadas para o desenvolvemento de grafeno covalentemente funcionalizado, destacando o seu potencial aplicación en múltiples campos científicos e tecnolóxicos.

1.3 Summary

The modern society increasingly demands access to technologies and devices capable of storing information more efficiently, with greater capacity, and in a reduced space. To decrease the size of data storage devices and increase their capacity, smaller bistable units (such as molecules) are required. The customized organization of molecules exhibiting magnetic bistability on surfaces could ultimately lead to nanometric memory points, logic gates, or electrical oscillators and resonators. The crucial step to achieve these goals is to assemble these bistable molecules with nanometric precision and even orient them while maintaining their structural integrity and properties.

Spin transition systems based on iron are a paradigmatic example of bistable materials. In such materials, the magnetic state can transition from a low spin diamagnetic configuration (LS) to a high spin paramagnetic configuration (HS) through various external stimuli such as temperature, light irradiation, pressure, or potential.

Numerous studies agree that spin transition properties are closely linked to the molecular environment and the interactions established between the metal centers. This communication between metal centers can be termed as cooperativity. These interactions are often supramolecular and can include a variety of types, such as hydrogen bonds, halogen bonds, π-π interactions, and Van der Waals forces. Various research groups have devoted efforts to establish magneto-structural correlations between these types of interactions and key parameters, such as transition temperature, transition character (gradual or abrupt, complete or incomplete), and the presence of hysteresis.

For this purpose, structural characterization techniques such as single-crystal X-ray diffraction and Raman spectroscopy, as well as magnetic characterization techniques such as SQUID (Superconducting Quantum Interference Device), are fundamental for analyzing changes and characteristics. Recent scientific progress has allowed these characterization techniques to be adapted to obtain information about structural changes experienced by spin transition compounds when subjected to stimuli such as light, pressure, or temperature.

However, to date, no general rules have been established to predict and effectively control the magnetic properties in spin transition complexes through the careful design of the metal's molecular environment. Hammett constants are a useful parameter that describes the inductive effect of certain substituents in *ortho*-, *meta*-, and *para*- positions of the same ligand. Although Hammett constants are a valuable reference, in the field of transition compounds, they do not take into account the effects of crystal packing or intermolecular interactions established when using certain substituents, which are key factors influencing magnetic properties. While there are examples where a clear correlation has been established for certain ligands, these cases are not generalizable to other compounds.

Another representative example of bistable materials is single molecule magnets (SMMs), particularly those formed by a single ion (Single Ion Magnets, SIMs). In these compounds, the magnetic atom can exist in two states of magnetic spin, which are separated by an energy barrier. At low temperatures, thermal effects decrease, making it easier for electrons to occupy a lower energy state and allowing the system to transition between these two magnetic states. Single molecule magnets are particularly interesting both from a theoretical perspective, due to their quantum behavior, and from a practical point of view. They are considered promising

candidates for qubits in quantum computing, as well as for cooling systems to extremely low temperatures. Generally, these materials are composed of a metallic ion, commonly a lanthanide due to its high total spin value, which contributes to a more significant energy barrier. However, in recent decades, there has been an increase in the study of the first-row transition metals with electronic configuration d^4-d^7, due to their greater availability and lower cost.

Numerous studies have shown that the distortion of the intramolecular environment of the metallic ion is fundamental to generating the necessary anisotropy that induces single ion magnet behavior. Therefore, it is crucial to continue exploring the rational design of ligands that allow us to establish magneto-structural relationships and relate them to distortion and anisotropy.

One of the main objectives of this thesis is to obtain nitrogen-containing ligands capable of inducing the splitting of the *d* orbitals of the metal to observe spin transitions, either through previously described procedures or via new proposed routes. Once the necessary ligands are obtained, their complexation with Fe(II) will be carried out. The influence of ligand design, potential supramolecular interactions (Van der Waals, hydrogen and halogen bonds, π-π interactions), the effect of counterions, and solvents on the final structure of the complex will be studied.

Initially, a library of materials showing spin transition properties will be created using understudied or unreported molecules to date. The research will investigate how the modification of organic ligands influences magnetic properties, analyzing magneto-structural correlations emphasizing supramolecular interactions. Additionally, the proposed synthetic strategies will allow the incorporation of new functionalities into spin transition compounds and adjust their magnetic properties using unconventional stimuli, such as phase changes or pressure.

Likewise, through this new series of proposed ligands, the aim is to synthesize coordination complexes of Co(II). These ligands, by establishing potential supramolecular (intermolecular) interactions, could influence the first coordination sphere (intramolecular interactions), resulting in the modification of octahedral distortion and anisotropy in Co(II), as well as promoting and adjusting the properties of field-induced single ion magnets.

These molecules will subsequently be chemically modified to covalently incorporate them into graphene derivatives (graphene oxide and reduced graphene oxide) with specific functional groups (acids, amines, and α-amino acids). The crucial step to achieve these goals is to assemble these bistable molecules with nanometric precision and even orient them while maintaining their structural integrity and properties.

Graphene, being a two-dimensional material with exceptional electrical and conductive properties, emerges as an ideal platform for covalent functionalization with molecules incorporating spin transition properties. This functionalization would leverage the unique characteristics of graphene, combining them with the magnetic properties of the molecules, to develop devices with applications in molecular nanoelectronics and spintronics.

The organization of magnetic materials on graphene to create a 2D structure has generated great interest in the scientific community due to the promising possibilities it offers. These carbon sheets, with high chemical and thermal resistance, as well as high electrical

conductivity, provide a robust and versatile platform for the integration of magnetic materials. Functionalizing graphene with molecules exhibiting spin transition properties opens the door to the creation of bistable magnetic systems that can be controlled by external stimuli, such as magnetic or electric fields. This control capability is essential for the development of advanced devices, such as magnetic memories, molecular switches, and high-sensitivity sensors. Additionally, the covalent functionalization of graphene with magnetic molecules avoids problems associated with the degradation of magnetic properties of materials. This ensures greater stability and durability of the devices, which is crucial for their practical implementation in technological applications.

To date, most published works have focused on functionalizing graphene to obtain hybrid materials using a non-covalent approach, such as Van der Waals heterostructures. Although this strategy offers several significant advantages in terms of ease of fabrication, versatility, and stability of the resulting materials, covalent functionalization allows greater control of long-term stability and functionality.

These results are presented in **Chapter 4, Results and Discussion**, which is divided into five sections that will be described in detail below.

In **Section 4.1**, three new amphiphilic ligands based on 2,6-di(pyrazol-3-yl)pyridine (3-bpp), functionalized with a 16-carbon alkyl chain and with three different terminal groups, were synthesized: 2,6-bis(1-hexadecyl-pyrazol-3-yl)pyridine (L1), 16,16'-(pyridine-2,6-diylbis(1H-pyrazole-3,1-diyl))bis(hexadecan-1-ol) (L2), and dimethyl 16,16'-(pyridine-2,6-diylbis(1H-pyrazole-3,1-diyl))dipalmitate (L3). Crystals of the corresponding Fe(II) complexes: $[Fe(L1)_2](ClO_4)_2$ (**1**), $[Fe(L2)_2](ClO_4)_2$ (**2**) y $[Fe(L3)_2](ClO_4)_2$ (**3**) were synthesized and isolated, and single-crystal X-ray diffraction studies were performed, demonstrating that the compounds exhibit a double-layer lamellar organization for **1** and **2**, and a less compact structuring but bound by the same Van der Waals forces for **3**. This type of organization may lead the compounds to exhibit liquid crystal properties, in a subclass of materials called metallomesogens.

Variable temperature studies based on powder X-ray Diffraction, Raman spectroscopy, differential scanning calorimetry (DSC), and polarized optical microscopy (POM) demonstrated that the compounds undergo multiple phase transformations, such as crystal-to-crystal transitions, crystal to isotropic liquid, or isotropic liquid to liquid crystal. Magnetic measurements showed that these compounds exist in a high spin (HS) state both in the crystal and in the liquid crystal state, but different phase transitions are accompanied by a discrete decrease in magnetic susceptibility.

To demonstrate if the spin transition could occur through other stimuli such as the application of pressure, variable pressure Raman spectroscopy studies were conducted. These results revealed that all three compounds experienced a high to low spin (HS→LS) transition under significantly high pressures, exceeding 2 GPa. The ability to reach such pressure levels is attributed to the high compressibility conferred by the alkyl chains present in the compounds.

These results demonstrate that, through careful ligand design, it is possible to integrate liquid crystal properties and spin transitions in metallomesogens. This synergy between both properties opens new opportunities for the development of advanced technologies and the creation of devices with enhanced functionalities.

In **Section 4.2**, a novel synthetic design of new spin transition compounds was proposed based on the synthesis of the ligand series of the *para*-X-3-bpp type and their incorporation into Fe(II) complexes, $[Fe(p\text{-X-3-bpp})_2](ClO_4)_2$ where X = F (**F**), Cl (**Cl**), Br (**Br**) and I (**I·H₂O**). This series allows for the joint investigation of intermolecular interactions, such as hydrogen and halogen bonds, and studying their impact on cooperativity and spin transition. X-ray, SQUID, and Raman experiments, combined with variations in temperature and pressure, establish a precise magneto-structural relationship and demonstrate how the transition is modified by changes in these interactions.

In the case of **F**, it was demonstrated that the three-dimensional structure presents only hydrogen bonds, stabilizing an intermediate spin state, with a first abrupt transition and a second gradual one, without a crystallographic phase transition. However, increasing the halogen size, as in the case of **Cl** and **Br**, allows for an additional halogen bond between Cl/Br and the perchlorate anion, inducing a high degree of cooperativity in the system resulting in an abrupt spin transition with minimal hysteresis.

Magnetic studies under variable pressure revealed the ability to stabilize an intermediate spin state in the case of **Cl**, demonstrating the feasibility of reversibly transitioning between stable spin states: LS ↔ IS ↔ HS. Structure analysis by variable-pressure single-crystal X-ray diffraction stabilizing this intermediate state (0.51 GPa) allowed for the unequivocal identification that the LS state structure presents two halogen bonds (one for each halogen atom of the complex), while the intermediate state (IS) maintains one, and the HS state structure loses both. This finding suggests that the halogen bond plays a crucial role in highly cooperative systems. Additionally, it suggests that network frustration, introduced by highly directional hydrogen bonds, along with the loss of a halogen bond, contributes to stabilizing the intermediate spin state.

In the case of compound **I·H₂O**, where only the hydrated structure was isolated, it was observed that the solvate molecules establish interactions with the ligand, resulting in a reduction of cooperativity and the stabilization of the LS state. This leads to an incomplete gradual transition occurring above room temperature.

With the experience in the synthesis of these ligands acquired in **Section 4.2**, the same ligands were used to obtain Co(II) coordination complexes and study their properties as single ion magnets (SIMs) in **Section 4.3**.

Five different compounds were obtained based on the halogen and included solvents, $[Co(p\text{-X-3-bpp})_2](ClO_4)_2$ where X: F, Cl, Br, and I, and the obtained compounds denoted as **F**, **Cl**, **Br**, **Br·2H₂O** and **I·2H₂O**. This series of compounds proved to be ideal candidates to study their properties of field-induced SIM, demonstrating the possibility of adjusting the energy barrier through distortion in the coordination environment of the metal ion depending on the substituent, as well as through the relaxation of this distortion via solvates.

For the series of anhydrous compounds (**F**, **Cl** and **Br**), it was observed through frequency dependence out-of-phase magnetic susceptibility measurements that the energy barrier increases as the halogen size increases (from **F** to **Br**). Additionally, it was found that the relaxation mechanism in the case of **F** and **Cl** occurs through a Raman (phonon-phonon with relaxation from a virtual state) assisted by Orbach (phonon-phonon with relaxation from an excited state) process, while for **Br**, relaxation mainly occurs through Orbach.

In contrast, magnetic measurements in solvated structures (**Br·2H₂O** and **I·2H₂O**) revealed a considerable decrease in the energy barrier, and the relaxation mechanism mainly occurs through a Raman-assisted Orbach process.

Single-crystal X-ray diffraction measurements were fundamental to establish a magneto-structural relationship by analyzing the asymmetric unit and the three-dimensional packing. It was observed that, as the halogen size increases, as detailed in **Section 4.2**, it establishes more halogen bond interactions, going from no interaction in the case of **F** to two interactions in the case of **Br**. These interactions are responsible for increasing the octahedral axial distortion of the metal, reflected in the angle formed by the trans-N{pyridine}-Co-N{pyridine} bond (ϕ). On the other hand, if water molecules are present in the second coordination sphere, they relax the axial distortion created by the halogen bonds, reducing the distortion. This distortion generates an axial anisotropy (D), which in turn is responsible for the SIM phenomenon.

Another method to alter spin transition properties is to investigate the second coordination sphere and how it influences the established interactions. For this reason, several studies have focused on examining how to change this second coordination sphere in coordination compounds, either by changing counterions or solvents. In **Section 4.4**, the ligand *p*-Cl-3-bpp was selected as a candidate to study the magnetic properties in a series of SCO compounds, following the formula [Fe(*p*-Cl-3-bpp)$_2$](X)$_2$, where X: **ClO$_4$** (reported in **Section 4.2**), **BF$_4$**, **PF$_6$**, **NO$_3$**, **NCS**, **NCSe**, **CF$_3$SO$_3$**, **Br** and **I**.

As evidenced in **Section 4.2**, the ability of the ligand to establish halogen bonds can lead to a variety of less common spin transitions that stabilize intermediate states. Three compounds were obtained in their anhydrous form (**BF$_4$**, **PF$_6$** and **CF$_3$SO$_3$**), and it was observed that, for these three cases, the magneto-structural correlation proposed in **Section 4.2** perfectly matched. In the case of **BF$_4$**, which forms hydrogen and halogen bonds, a complete abrupt transition occurs, whereas for **PF$_6$**, without a halogen bond, a gradual (less cooperative) transition stabilizing an intermediate state is observed. Finally, **CF$_3$SO$_3$**, which includes two crystallographically independent metal centers, with only one halogen bond in a network of strong hydrogen bonds, decreases its cooperativity exhibiting an incomplete gradual transition.

In the case of solvated compounds (**NO$_3$**, **NCS**, **NCSe**, **Br** and **I**), magnetic susceptibility measurements revealed that, while in their solvated form, they are stabilized in a low spin (LS) state (**NCS**, **NCSe**, **Br** and **I**) or a high spin (HS) state (**NO$_3$**). The stabilization of one state or the other has been addressed in other studies on 3-bpp-derived compounds, attributed to π–π interactions. When π–π interactions are established between the pyrazole groups of neighboring molecules, in an arrangement known as "terpyridine embrace", LS stabilization occurs. Conversely, when [Fe(*p*-Cl-3-bpp)$_2$]$^{2+}$ complexes do not exhibit π–π stacking interactions with neighboring SCO complexes, HS stabilization occurs.

Under the conditions of the magnetic measurements, these compounds can undergo in situ desolvation and present varied transitions, with more than one transition and different nature (with or without hysteresis, gradual or abrupt). In some cases, the magneto-structural characterization of the compounds after desolvation is complicated due to the loss of crystallinity. Only the dehydrated structure was obtained in the case of **NCS**. During this process, the structure undergoes changes due to the loss of hydrogen bonds and π–π interactions, while a new Cl···π interaction forms. Additionally, dehydration leads to the

segregation of Fe(II) centers into two independent crystallographic units, resulting in a change in symmetry. Despite the reduction in cooperativity, a first-order transition is observed, attributed to partial sample rehydration or to the cooperative effect maintained by the Cl···π interaction. Although access to the dehydrated structure of the other compounds (**NO_3**, **NCSe**, **Br** and **I**) is not available, their magnetic behavior upon dehydration is similar to that of **NCS**. Therefore, it is inferred that the structure rearrangement upon losing interactions with the solvent will be analogous.

Finally, in **Section 4.5** and leveraging the research conducted on the compound series described in previous sections, ligands derived from 1-bpp and 3-bpp were designed using modifications of previously described synthetic methodologies. This led to the synthesis of three series of ligands with different functionalities (carboxylic acids, amines, or α-amino acids) for covalent attachment to graphene oxide or reduced graphene oxide. Functionalization with these ligands facilitated the subsequent incorporation of Fe(II) complexes for studying spin transition properties on graphene.

The first series of proposed ligands was based on substitution with an acid group in the *para*-position (1-bpp-COOH and 3-bpp-COOH). The reaction involved a condensation to obtain commercial graphene oxide (**cGO**) and graphene oxide obtained by the Hummer method (**hGO**) functionalized (**1-GO** and **2-GO**), followed by their complexation with Fe(II) (**Fe-1-GO** and **Fe-2-GO**). Ligand functionalization was confirmed using various techniques such as thermogravimetric analysis (TGA), Raman spectroscopy, and X-ray photoelectron spectroscopy (XPS). Thermogravimetric analysis and X-ray photoelectron spectroscopy conclude the formation of the complex for **Fe-2-hGO**. Therefore, at this point, two new ligands were proposed by redesigning the connection. To address this issue, we conceived functionalizing bpp with an amino group connected electronically via an aryl spacer. Additionally, protecting the amino group of 3-bpp using the THP (tetrahydrofuran) protecting group was proposed to enhance its solubility and prevent possible side reactions.

With these new ligands, two strategies were followed: (i) through covalent condensation reaction with the amino group, ligands 1-bpp-L-NH2 and 3-bpp-THP-L-NH2 were introduced into commercial graphene oxide (**3-cGO**, **4-cGO**), followed by their subsequent complexation (**Fe-3-cGO** and **Fe-4-cGO**). And (ii), using the same ligand as a starting point, it was derivatized to obtain a terminal α-amino acid (1-bpp-L-Gly and 3-bpp-THP-L-Gly) to carry out the covalent 1,3-dipolar cycloaddition reaction, commonly known as the Prato reaction, on reduced graphene oxide (**6-rGO** and **7-rGO**). Subsequently, complexation with Fe(II) was carried out (**Fe-6-rGO** and **Fe-7-rGO**).

Functionalization with the ligand (**3-cGO**, **4-cGO**, **5-cGO**, **6-rGO**, and **7-rGO**) was verified using techniques such as TGA, Raman, and XPS. The incorporation of Fe (**Fe-3-cGO**, **Fe-4-cGO**, **Fe-5-cGO**, **Fe-6-rGO**, and **Fe-7-rGO**) was confirmed through elemental mapping by energy-dispersive X-ray spectroscopy in combination with scanning transmission electron microscopy (STEM/EDX). Fe is found forming the coordination complex, uniformly distributed throughout the sample, without the presence of aggregates or other nanostructures. The magnetic state analysis of the hybrids was carried out using variable temperature Seebeck coefficient measurements (thermoelectric effect) for **Fe-7-rGO**. These measurements showed that **Fe-7-rGO** has a Seebeck coefficient twice that of rGO, suggesting a reduction in the number of defects associated with functionalization.

In summary, throughout this doctoral thesis, exhaustive research has been conducted on a library of Fe(II) spin transition compounds exhibiting different magnetic properties. Building on the results obtained with these compounds, this experience has been applied to the synthesis of new Co(II) single ion magnets. Additionally, a deeper understanding of the behavior of these properties when combined with carbon surfaces via covalent bonding, such as graphene oxide and reduced graphene oxide, has been explored.

These findings are encouraging, suggesting that this project could serve as a starting point for the design and study of new materials with properties relevant to the manufacturing of devices with applications in nanoelectronics and molecular spintronics. This work illustrates the versatility of spin transition compounds and molecular magnets and proposes methodologies tailored to the development of covalently functionalized graphene, highlighting its potential application in multiple scientific and technological fields.

2 OBJECTIVES

The main objective of this thesis is to develop and study new magnetic switchable materials with advanced functions, specifically focusing on Fe(II) and Co(II) metal complexes that exhibit spin crossover (SCO) or single ion magnet (SIM) properties, and to establish magneto-structural correlation effects. Various external stimuli, such as temperature, pressure, or magnetic fields, will be employed to induce spin transitions and single ion magnet properties in these switchable materials.

To achieve this, we will first focus on the synthesis of new nitrogen-based ligands designed to facilitate metal-ligand interactions within the cation complexes (inner coordination sphere), thereby inducing bistability. These ligands will also be functionalized with different pendant groups to tune intermolecular interactions (outer coordination sphere). Additionally, we will investigate the effect of the charge and structure of various counterions on the packing of the cation complexes to create a new library of magnetic switches. Finally, for the most promising magnetic switchable materials exhibiting SCO, carbon-based materials will be used to interface with them to further investigate and exploit their unique properties.

This doctoral thesis comprises the following general objectives:

(i) Design, synthesis, and characterization of novel ligands suitable for forming complexes with SCO or SIM behavior.

(ii) Synthesis, characterization, and magneto-structural correlation of molecular-based complexes exhibiting SCO or SIM properties.

(iii) Assembly of SCO complexes on graphene through covalent functionalization, and the study of the composition, structure, and magnetic properties of these hybrid carbon nanostructures.

These general objectives are developed into five main sections, detailed below with the specific objectives for each.

In **Section 4.1**, the specific objective is to functionalize the nitrogen-based ligand 3-bpp with a 16-carbon alkyl chain with three different terminal groups (methyl, alcohol, and methyl ester). This will enable the synthesis of spin transition complexes that exhibit liquid crystal properties, in a subclass of materials called metallomesogens. The study aims to investigate whether it is feasible to modulate magnetic properties through different phases (crystal, liquid crystal, and liquid). Moreover, it seeks to examine the impact on magnetic properties under various stimuli such as temperature and pressure.

Section 4.2 focuses on developing a new series of spin transition compounds through the synthesis of *p*-X-3-bpp ligands and incorporating them into Fe(II) complexes, [Fe(*p*-X-3-bpp)$_2$](ClO$_4$)$_2$, where X = F, Cl, Br, and I·H$_2$O. This series of compounds will be utilized to investigate intermolecular interactions such as hydrogen and halogen bonds, analyzing their impact on cooperativity and modulation of spin transitions. Furthermore, the study will explore the influence of pressure on key parameters associated with spin transitions, including T_c, hysteresis effects, and the occurrence of multistep transitions.

Section 4.3 aims to utilize the ligands synthesized in the previous section to investigate Co(II) compounds exhibiting SIM properties. This section focuses on synthesizing five different coordination compounds, resulting in $[Co(p\text{-X-3-bpp})_2](ClO_4)_2$ where X = F, Cl, Br, and I. The study will explore the impact of halogen substitution on octahedral geometry distortion and its effects on energy barriers and relaxation mechanisms through magneto-structural correlations.

Section 4.4 attempts to study the impact on spin transition through changes in the packing of the cation complexes, either by altering counterions or solvents. The ligand *p*-Cl-3-bpp will be selected, and the following compounds, $[Fe(p\text{-Cl-3-bpp})_2](X)_2$, where X: ClO_4 (reported in Section 4.2), BF_4, PF_6, NO_3, NCS, NCSe, CF_3SO_3, Br and I, will be used as candidates for studying the magnetic properties. This will lead to the creation of a series of novel SCO compounds and establish magneto-structural relationships primarily through supramolecular interactions.

Finally, **Section 4.5** aims to interface SCO materials with graphene through covalent interactions by the derivatization of the ligands obtained in previous sections with various functional groups (e.g., alcohols, acids, amides). To confirm successful functionalization, the project will conduct comparative studies of the material at each step of the synthetic route using several techniques, including thermogravimetric analysis, Raman spectroscopy, scanning and transmission electron microscopy, X-ray photoelectron spectroscopy, and electrical conductivity measurements.

3 INTRODUCTION - FUNCTIONAL MAGNETIC MATERIALS: FROM DESIGN TO APPLICATION

3.1 Spin crossover phenomena

Spin crossover (SCO) compounds represent a fascinating class of materials that blur the boundaries between classical chemistry and quantum mechanics. These compounds exhibit the property of exchange their spin state that can be switched between two distinct configurations, typically involving high spin and low spin states. This reversible transformation is driven by external stimuli such as temperature, pressure, light, or even guest molecule interactions.[1–3]

These molecules are commonly composed by transition metal ions with d^4-d^7 electron configuration as they have partially filled *d*-orbitals coordinated to ligands. These ligands are typically organic molecules with donor atoms capable of forming coordinate bonds with the metal ion. The choice of ligands and their arrangement around the metal center plays a crucial role in determining the stability of different spin states.[4–8]

The spin transition arises from the rearrangement of the 3*d* electrons, which occupy different subsets of orbitals resulting from the different coordination environments surrounding the metal center. Among all possible geometries, octahedral geometry is most common by far. In this particular case, the high energy subset (e_g) and the low energy subset (t_{2g}) are separated by an energy gap in this case referred as Δ_{oct}. The transfer of electrons between these two electronic states is known as a spin transition (Figure 3.1.1).

Transition occurs between a high energy –associated with high spin state (HS)– and lower energy level –usually called low spin (LS)– and it is usually accompanied by a dramatic change

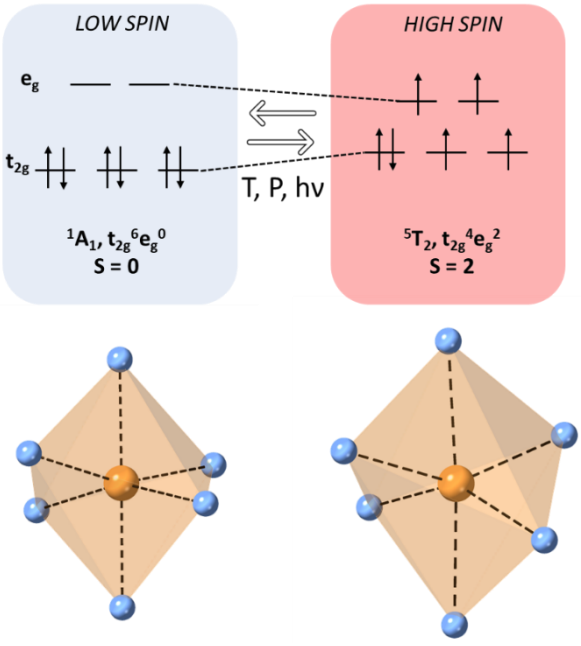

Figure 3.1.1. Schematic representation of two possible spin states depending on its electronic configuration for the case of octahedral Fe(II). At the bottom, octahedral geometry for LS and HS states.

in the structure (geometry and bond distances) and other characteristic physical properties such as magnetism or color.

Spin crossover phenomena have been studied in various metals such as Mn(III),[9] Fe(III),[10] Co(II)[11] and Co(III)[12] complexes, but the family of Fe(II)[13–15] compounds is the most important and numerous due to the maximized total spin change (from LS, S = 0, t_{2g}^6 → HS, S = 2, $t_{2g}^4e_g^2$).

Since this transition usually is reversible and can induce a hysteresis in the process, spin crossover compounds are a good example of bistable molecular switches. Hysteresis is produced by intermolecular cooperativity of the metal centers and SCO can occur in different ways, most common are in a gradual or in an abrupt manner. This transition can be complete, which means 100% interconversion from LS to HS and vice versa, but if there is no complete, transition could be measured by total fraction of converted HS population (Υ_{HS}).[16] Less common transitions are those that involve transition in several steps (multistep) however they have also been reported in systems usually composed by more than a unique metal center (Figure 3.1.2).[17–19]

The ability of SCO compounds to undergo spin state changes has captured the attention of researchers from various disciplines, including chemistry, physics, materials science and engineering. This unique phenomenon holds promise for a range of potential applications, including sensors[20], switches[21], memory devices[22] and even catalysis.[23] The delicate interplay between the molecular structure, electronic configuration and external factors that govern the SCO process makes these compounds a captivating subject for both fundamental studies and practical innovations. The desire to achieve these objectives serves as a major source of motivation for studying SCO. For that reason, one of the biggest challenges is to be harnessed the spin switchable character in a predictable and controlled way. For all this, it is necessary to systematize a way to design SCO compounds. A priori, the ways to control the SCO can be divided in three methods:

- Through coordinating metal center, usually first row transition metal ions.
- Towards synthetic design of the coordinating ligand. From the variety of coordinating atoms, N-donor ligands are most suitable since they are able to decrease crystal field splitting energy (Δ_{oct}) and pairing energy (P) in order to switch two accessible states by thermal effects. Ligand could be designed to potentially establish supramolecular interactions in a crystal lattice structure. In this way, substituent effect and derivatization of same ligand could produce a drastic change in the magnetic properties by steric hindrance effect and modifying energy level splitting.

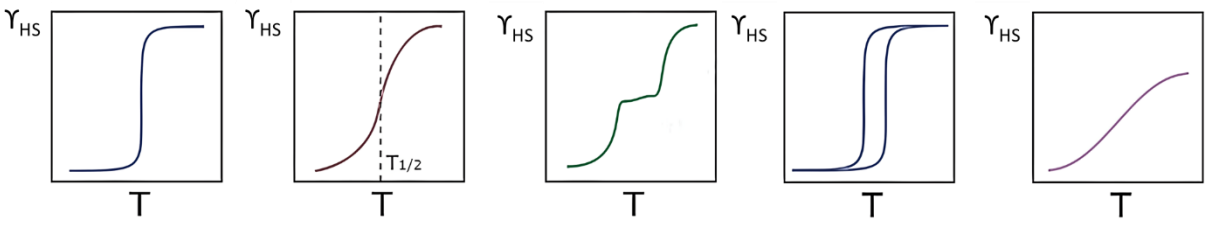

Figure 3.1.2. Different types of spin crossover curves: Left to right — abrupt and complete, gradual and complete, stepped and complete, abrupt and complete with hysteresis, and gradual and incomplete. Reproduced with permission from [16]. Copyright 2020, MDPI.

- Variation of the second coordination sphere, since usually metal center needs a counterion to balance charge. This counterion could be monoatomic, bi, tri, tetranuclear or even more complex. Moreover, if the 3D structure of the complex admits pores to encapsulate solvents, remove or exchange them could affect in the same way as counterion in the spin transition.

3.2 Towards rational design of Fe(II) spin crossover compounds

Our primary focus will be on the examination of Fe(II) metal complexes, as they represent one of the most extensively studied metallic centers and interesting from a magnetic point of view due to their high magnetic moment change. Among the array of geometries observed in Fe(II) complexes, octahedral is most common and our discussion will be centered in this configuration.

3.2.1 Ligand choice to tune Δ_{oct} and field strength

As mentioned above, spin state is heavily influenced by the pairing energy (P) and crystal field splitting energy (Δ_{oct}). For that reason, choice of the coordinating ligand is a key factor in order to tune these two parameters. In an octahedral environment, energy splits in 2 subsets: 3 low energy orbital levels (d_{xy}, d_{xz} and d_{yz}) and 2 high energy orbital levels (d_{x2-y2}, d_{z2}).

Suitable ligands for undergoing spin transition are those with π-acceptor character, which are located in the middle of the spectrochemical serie. These ligands have an empty molecular orbital of low energy and approximately same symmetry as the orbital of the metal center. They usually behave as a highly conjugated system that decreases energy of LUMO (Lowest Unoccupied Molecular Orbital) level. Among all ligands, trischelated aromatic heterocycles with N atoms (i.e. terpyridine) or N-donor bischelated (i.e. bipyridine or phenanthroline) are a good candidates for that purpose.

A traditional method of creating ligands that can trigger SCO in Fe(II) upon coordination involves substituting some six-membered heterocycles found in a LS-inducing ligand with five-membered heterocycles. This alteration decreases the system's σ-donor and π-acceptor properties, increasing the strain in the resulting chelate ring, and reduces the ligand field around the metal center.[24]

SCO phenomenon was discovered for the first time in 1931 by Cambi *et al*. in a dithiocarbamate iron(III) complex.[25] This was first example of thermal spin transition even though concept was not coined until several years later. First studies of SCO mechanism were based on Fe(III), and not was until decade of 60s where a work of SCO based on Co(II) by Busch *et al*. was published.[26] One of the subsequent studies of SCO phenomena were based on bipyridine (2,2' or 4,4')[27,28] and 1,10-phenanthroline[29], which became two of the best-known systems. As the studies of these compounds progressed, it was found that the heterocyclic ligands based on 2-pyridil to either 2- or 4- imidazole, pyrazole or triazole brought the ligand field strength into an ideal range for SCO to be manifest. Their properties and synthetic

modulation to further found SCO complexes has been exploited to create a broad library of novel compounds. Since then, the synthesis of homoleptic octahedral Fe(II) complexes with SCO properties has involved rigorous and extensive exploration of the FeN6 coordination environment especially for those provided by two tridentate pyrazole pyridine-based ligands.

The supramolecular structure that can adopt the SCO systems is a particularly intriguing aspect. Among the families of SCO systems that have been extensively studied, those based on the Fe-*tris*-*triazole* system are notable for their ability to form various nanostructures such as 1D coordination chains and nanoparticles.[30–32] Other extended family of SCO are those which adopt Hofmann-type metal organic framework $[M(L)_2M'(CN)_4]$ (M = Mn^{2+}, Fe^{2+}, Co^{2+}, Ni^{2+}, Cu^{2+}, Zn^{2+}, or Cd^{2+}; M' = Ni^{2+}, Pd^{2+}, or Pt^{2+}), where L can be monodentate ligands or bridging ligands to form 2D or 3D coordination networks, respectively. They show high degree of cooperative since usually their structure is form by more than one active metallic center and a large variety of distinct spin transitions.[33–36]

Although there are a huge range of structures, we will focus this discussion on mononuclear complexes, since it offers an enormous range of synthetic modulation, tunability and processability and it is the aim of this dissertation.

This current work is devoted to a review of the literature describing mononuclear Fe(II) complexes derived from bis and tris-chelated coordinating ligands surrounding octahedrally disposed Fe(II) centers. First, it will highlight how to control spin transition through choice of ligands and its substitution effects. Once establish this first cause, then, how further synthetic derivatization of the ligands or its substitution could modify 3D supramolecular arrangement and, by extension, change the magnetic response. Finally, we will discuss the impact on anion variation in the second coordination sphere and secondary bonding interactions with solvent, affecting cooperativity and thus, spin transition.

3.2.2 Substituent effect and ligand derivatization

In the past few years, it has been described in the literature several studies related to the correlations between strong intermolecular interactions (π-π stacking, hydrogen bonding, Van der Waals interactions, steric hindrance and nature of covalent link between the metal active centers) and SCO characteristics such as: cooperativity, $T_{1/2}$ and T_{LIESST} (LIESST = light-induced excited spin state trapping). $T_{1/2}$ is defined as midpoint temperature where 50% HS fraction is reached. In the case of hysteretic processes, two different values, $T_{1/2\downarrow}$ and $T_{1/2\uparrow}$ are used. Additionally, another parameter, T_c, is used for SCO compounds, indicating the transition temperature at which a significant portion of the molecules undergoes a spin transition. This transition often involves a shift from a low spin state to a high spin state or vice versa. Both $T_{1/2}$ and T_c are extensively used to refer to SCO phenomena. Meanwhile, T_{LIESST} is defined as temperature at which the light-induced spin transition occurs, and it is the minimum of the plot of $d(\chi_M T)/dT$ vs. T.

One of the key factors is to understand how it affects the spin transition between substituents of the same ligand. In contrast to intermolecular interactions, the insertion of the substituents will result in a severe tuning of the SCO through covalent bonds. Moreover, if these substituents are enough bulky, we refer them as derivatize ligands. One of the most useful parameters when studying the effect of the substituent is the Hammett constant, σ, which

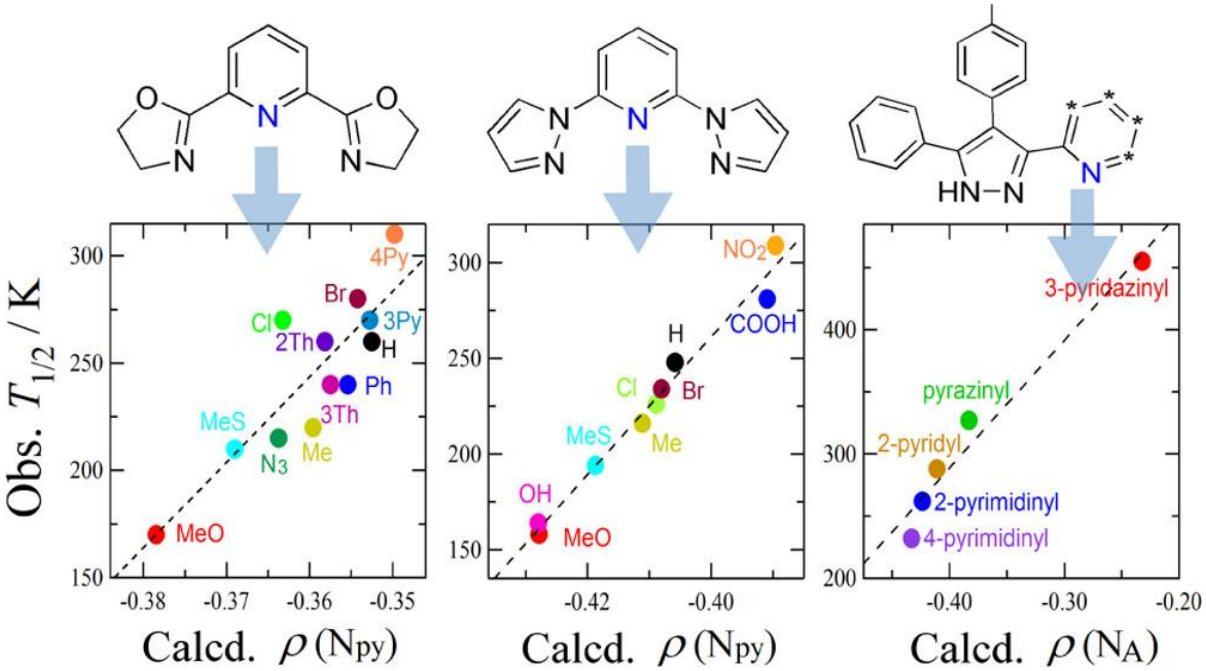

Figure 3.2.1. SCO temperature $T_{1/2}$ for $[Fe(X\text{-}pybox)_2]$ vs ρ (N_{py}) $[Fe(X\text{-}1\text{-}bpp)_2](BF_4)_2$ vs ρ (N_{py}) and $[Fe^{II}(L^{azinyl})_2(NCBH_3)_2]$ vs ρ (N_A). Reproduced with permission from [38]. Copyright 2018, American Chemical Society.

parameterizes the inductive effect and the resonant effects in solution of a substituent usually in *meta*- (σ_m) and *para*-position (σ_p) in the chosen ligand.[37]

T. Ishida and coworkers studied the SCO behavior of 12 derivatives based on $[Fe(X\text{-}pybox)_2](ClO_4)_2$ (pybox = 2,6-bis(oxazolin-2-yl)pyridine) through DFT calculations (Figure 3.2.1) and different substituent in *para* position.[38] They establish a good correlation between σ_p and $T_{1/2}$. Electron donating groups (e.g. MeO, MeS, N_3, Me…) elevate the t_{2g} energy level, resulting in a narrower t_{2g}-e_g energy gap that promotes the high spin state (HS) and reduces $T_{1/2}$. In contrast, electron withdrawing groups (4-Py, 3-Py, Br, Cl…) increase $T_{1/2}$. This correlation was successful again when applying to other SCO families such as $[Fe(X\text{-}1\text{-}bpp)_2](BF_4)_2$ (1-bpp = 2,6-bis(pyrazol-1-yl)pyridine).[39]

Y. Zhu *et al*. investigated various derivatives of thio-pybox with different R in *para*-position (R = Cl, Br, I, OMe and SMe).[40] Through solid-state analyzes, it was discovered that only the Cl substituted exhibits SCO, suggesting that more electronegative atoms can significantly influence SCO. The remaining substituents retained in HS state. Instead, in solution-based measurements, where the effects of crystal lattice packing are suppressed, $T_{1/2}$ demonstrated a linear correlation with the electronegativity of the substituting atoms.

J. Tao *et al.* explored the impact of ligands on Cl- and Me-substituents on *o*-, *m*- and *p*-positions of $[Fe_2(x\text{-}L)_5(NCS)_4]\cdot yMeOH$ (L = N-phenylmethylene-4-amino-1,2,4-triazole).[41] Exploring just the electronic effect of substitution is not enough to provide a satisfactory explanation for the magnetic behavior and it is necessary to appeal to Single Crystal X-Ray Diffraction techniques. The study unveiled that the location of the substitution within the molecular structure led to specific geometric distortions -primarily driven by steric effects-

accompanied by strongest intermolecular interactions C=N···π_{phenyl} play a pivotal role in the spin transition.

Substituent dependence was explored either in asymmetric ligands as in the case of widely known 1,3-bpp (2-(pyrazol-1-yl)-6-(1H-pyrazol-3-yl)pyridine) carried out by G. Aromi *et al*.[42] It provides a study of the impact of one or two methyl substitutions on the pyrazol-1-yl heterocycle, resulting in a strong effect on the transition. To further comprehend the primary reasons behind the $T_{1/2}$ decrease (with one substituent) or $T_{1/2}$ increase (with two substituents), a combination of DFT calculations and in-solution experiments was conducted, revealing that intramolecular steric effects and C-H···π non-covalent interactions play a central role.

For those that imply asymmetric ligands, another investigation was developed by H. Oshio *et al.*, in systems based on $[Fe(H_2L^{1-3})_2](BF_4)_2 \cdot x(solv.)$ (H_2L^{1-3} = 2-[5-(R-phenyl)-1H-pyrazole-3-yl]6-benzimidazole pyridine) being R a phenyl ring with one (**1**), two (**2**) or five (**3**) methyl substituents.[43] The presence of substituent groups influences on how the molecular entities are organized supramolecularly. Notably, a greater number of substituents induce distortions at the metal center, leading to increased dihedral angles and a preference for the high spin state without undergoing a transition.

One of the most studied ligands and its substitution is the 1-bpp, since it is easily to functionalize by each position with a variety of substituents. It has been demonstrated that most of the compounds exhibit transitions near room temperature.[44] We will focus on this ligand since its structural analogue, 3-bpp (2,6-di(pyrazol-3-yl)pyridine), is the main ligand of the thesis. 3-bpp presents some advantages compared to 1-bpp due to the role of NH in establishing H-bonds that contribute to cooperativity, but it has not been extensively studied

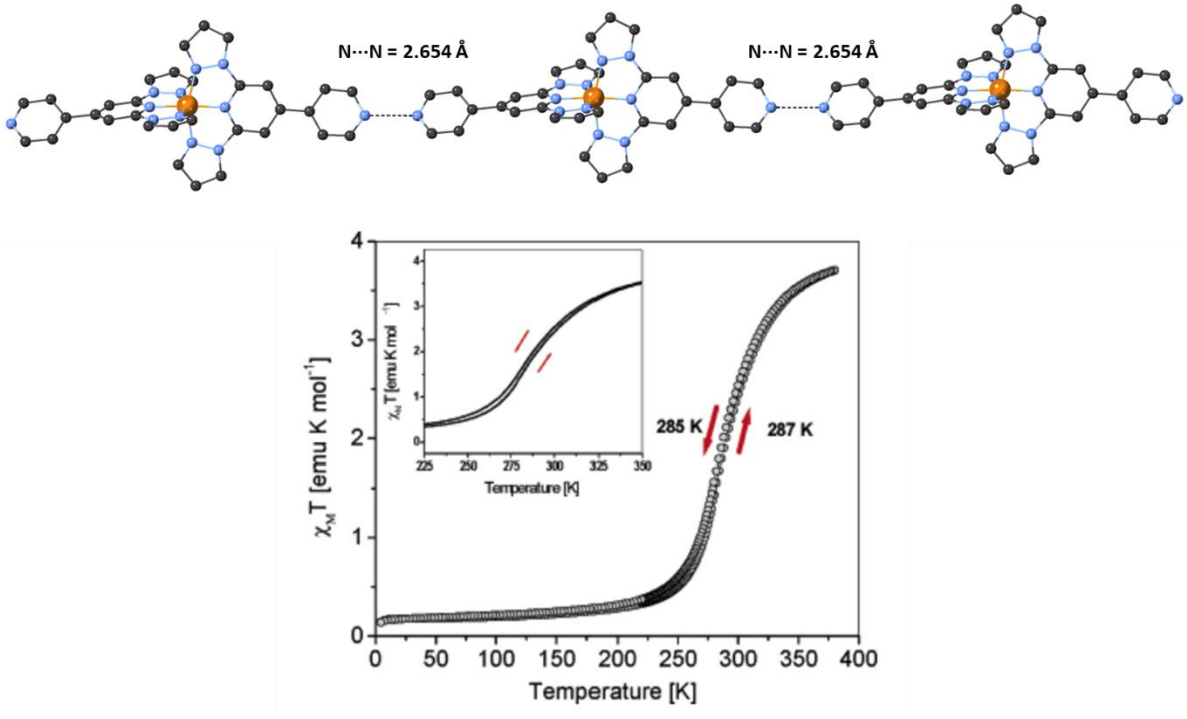

Figure 3.2.2. Top: 3D supramolecular disposition highlighting the N···N distance (hydrogens are omitted for clarity). Bottom: variable temperature magnetic measurements. Image reproduced from [46], Copyright 2016, American Chemical Society.

yet. Many studies have been published on the derivatization of 1-bpp and its impact on the SCO. One of the most relevant works in this field, based on 1-bpp and 3-bpp ligands, is a review article by the same author, M. Halcrow. General aspects concerning the functionalization of 1-bpp, as well as important synthetic and magnetic properties, were compiled.[45]

Concerning 4-substituted pyridine ligands, one of the most relevant from a structural perspective is the *p*-pyridine-1-bpp. This ligand forms a one-dimensional supramolecular polymer held by hydrogen bonds (N-H···N) (Figure 3.2.2).[46] This additional interaction introduces high degree of cooperativity, leading to a complete and abrupt hysteretic transition around room temperature.

Similar behavior is observed when two units of 1-bpp are linked through a 1,4-phenylene group in *para*-position. An oligomer formed by at least six units of Fe is detected by mass spectrometry, as the crystalline structure was not ascertainable. The complex exhibits a hysteretic and abrupt transition near room temperature, albeit not entirely complete due to the residual high spin contribution originating from $[Fe(OH_2)_3]^{2+}$ sites present at the ends of the linear oligomers.[47]

M. Halcrow *et al.* studied the influence of mercapto (bppSH) and disulfide (bppSSbpp) groups in *para*-position of 1-bpp.[48] Interestingly, **1-bpp-SH·$(ClO_4)_2$** salt exhibited a well-defined abrupt hysteretic spin transition, whereas the disulfide derivative (bppSSbpp) created spontaneously from starting bppSH, displays a non-complete gradual spin transition. Although there is not available single crystal data, it is evident that the introduction of an S-S bond obstructs the spin transition, becoming less cooperative. In the case of thioester anchoring group, spin transition occurs in a similar way than pyridine derivative, displaying abrupt transition close to room temperature. Thus, indicating main supramolecular interactions in both compounds are similar and then, they are governing spin transition in analogous manner.[49]

Turning to substitutions on the pyrazole ring, an example of methyl substitution on position 3' and 3" in 1-bpp led to anhydrous form obtained through annealing, exhibiting a thermal spin crossover that occurs in two steps: high spin ↔ mixed-spin ↔ low spin.[50] The significance of this work lies in the identification of a mixed state, which is among the few systems documented. The authors attribute this mixed state to the coexistence of distinct dehydrated and hydrated regions within the bulk material.

Larger substituent groups such as isopropyl or *tert*-butyl result in a pronounced alterations in magnetic properties. In the isopropyl derivative, a high spin state is observed without undergoing a transition due to steric repulsions caused by the isopropyl groups between the two ligands, which hinder the contraction of Fe-N bonds required for the low spin state. The impact of steric hindrance becomes even more substantial in the case of the *tert*-butyl ligand, to the extent that when complexing this ligand with the iron salt, it becomes impossible to form a Fe(II) complex. Instead, the obtained complex is formed by 1 unit of ligand, one molecule of water and one of acetone.[51]

Researchers have push efforts in more complex functionalization with the purpose to introduce anchor groups that potentially introduces some extra interactions with 2D carbon nanostructures such as carbon nanotubes or graphene, in the way to be one step closer to implementation in molecular-based devices.

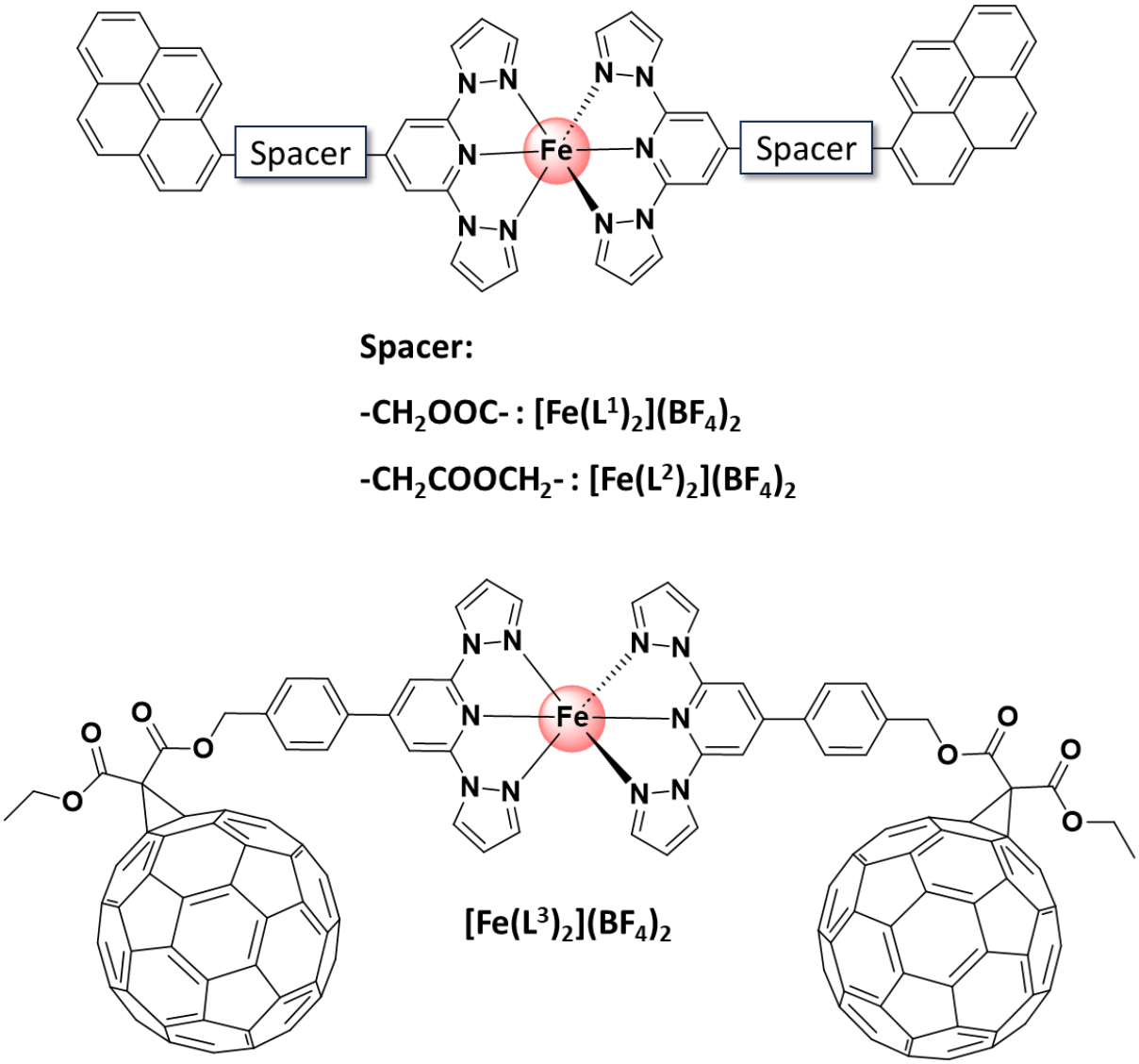

Figure 3.2.3. Chemical structure of SCO complexes of pyrene decorated $[Fe(L^1)_2](BF_4)_2$ and $[Fe(L^2)_2](BF_4)_2$ and fullerene decorated $[Fe(L^3)_2](BF_4)_2$ from [52].

In this context, M. Ruben and coworkers investigated SCO complexes involving fullerene and pyrene-1-bpp.[52] Authors demonstrated space between the active SCO and the anchoring group pyrene plays a crucial role in displaying spin transition character. When a shorter –CH_2OOC– spacer separates the pyrene anchoring group and SCO core, complex shows a non-complete gradual transition up to 400 K. In contrast, when spacer is slightly longer, –CH_2COOCH_2–, the complex remains in HS state across all temperature ranges without undergoing transition. This study concludes that the distance between anchoring group and SCO is influenced by electronic and steric effects arising due to changes in the ligand field around Fe(II). A larger distance between SCO center and pyrene group blocks the transition, generating strong intermolecular interactions among substituents around the switching core. Primary reason for the LS behavior of complex 1 $[Fe(L^1)_2](BF_4)_2$ at 300 K is attributed to the π-acidic nature of L^1 (L^1 = bpp-COOR, R = –CH2-pyrene), which facilitates the transfer of electron density in the ligand via d-π* back-bonding. However, in the case of a longer spacer,

as in the scenario of L^2 (bpp-CH_2OR, R = –$OC(CH_2)$-pyrene), this interaction is absent, favoring a HS state at 300 K and across all studied temperatures. In the case of fullerene linker, a similar result is observed. Bulky fullerene (C_{60}) anchoring group introduces high steric hindrances, blocking SCO (Figure 3.2.3).

Overall, all the aforementioned works provide evidence that the Hammett constant is a good parameter for initially predicting spin transition characteristics, with more electronegative atoms being suitable for modifying spin properties. Moreover, substitutions in *ortho*, *meta*, and *para* positions serve as a major source for obtaining new SCO derivatives, as they enable the creation of new supramolecular interactions that typically enhance cooperativity. However, they can also introduce steric hindrance, which may impede spin transition.

3.2.3 The role of modifying the second coordination sphere

Counterions play a significant role in regulating the SCO phenomenon by mediating crystal packing and tuning intermolecular interactions. These differences could involve a shift in the transition temperature, suppression of the SCO or alter the cooperativity, such as a change from an abrupt to a gradual transition. Solvent molecules, on the other hand, are capable of inducing spin change by coordinating to the transition metal ion or establishing non-direct intermolecular interactions with metal center through anions or ligands. In case of their removal (for instance, through temperature increase or under vacuum conditions), it is possible to promote a concomitant spin transition. This implies that the spin transition occurs subsequent to the removal of solvent molecules. This particular scenario offers a promising mechanism for detecting the presence of guest molecules in these compounds, and their implementation as gas sensors. Crystallographic studies are crucial in providing knowledge of the structural rearrangements that occur during spin transition, as different kinds of phase transitions can accompany SCO originating from counteranions or solvents. Despite is a challenging task, as solvent removal can lead to a loss of crystallinity or the creation of new amorphous phases.

Nevertheless, the impact of the anion and solvation on the systems do not follow a consistent trend and cannot be easily foreseen. Some studies have suggested a possible correlation between the size of the anion and the transition temperature in certain cases, but the validity of this relationship has not been confirmed as a generally rule yet.

3.2.3.1 Anion variation

There are several examples in literature where authors explore influence of anion variations. M. Shores and collaborators have performed a study on the anion dependence of a tripodal ligand in Fe(II) complexes, varying counteranion: OTf^- (**1**), Br^- (**2**), I^- (**3**) and BPh_4^- (**4**).[53] Magnetic studies indicate compounds **1**, **2** and **3** are HS at 300 K and display spin transition. Largest counterions (**1**, **3**), capable of forming hydrogen bonds with the ligands, exhibit a more complete and abrupt spin transition. In case of **2**, the smaller size of the anion stabilizes HS, resulting in a decrease of $T_{1/2}$ and a more gradual transition. On the other hand, groups that do not form hydrogen bonds (**4**), stabilize the HS state in all temperature range, with no observed spin transition (Figure 3.2.4).

Group of W. Linert *et al*. have studied impact of different counterions in 1-*iso*butyltetrazole ligand (i4tz): ClO_4^- (**1**), PF_6^- (**2**), SbF_6^- (**3**), BF_4^- (**4**).[54] Compounds with relatively small counterions size (**1** and **4**) crystallize in same unit cell and space group. Both present a

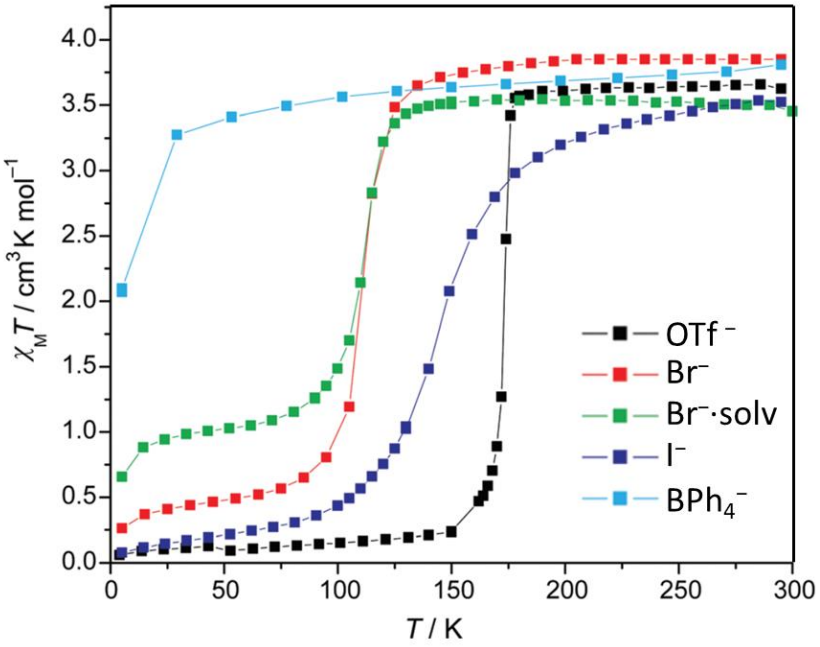

Figure 3.2.4. Temperature dependence of $\chi_M T$ for 1–4. Reproduced with permission from [53]. Copyright 2012, Royal Society of Chemistry.

complete gradual SCO ($T_{1/2}$ = 200 K). Additionally, small size of counterion seems to be crucial to accommodate solvent molecules within the structure. Instead, for larger counterions (**2**, **3**) transition becomes more abrupt and shifts to lower temperature, indicating a stabilization of HS state. Even though there is a considerable size difference between phosphorus (P) and antimony (Sb), the size of the counterion does not appear to be a critical factor in $T_{1/2}$.

Properties of diamine or diimine derivatives with different counterion substitutions were investigated by B. Sun *et al*.[55] In the case of tris(diimine) ligand, four different complexes with non-NH-substituted 4,5 dimethyl imidazole (L1) have been examined: ClO_4^- (**1**), BF_4^- (**2**), PF_6^- (**3**) and SbF_6^- (**4**). Meanwhile, derivative ligand NH-substituted ethyl ester (L2) was only explored with ClO_4^- (**5**). Although complexes **1** and **2** possess a similar structure and counterion arrangement, their magnetic properties differ. Compound **1** undergoes a gradual non-complete transition with $T_{1/2}$ = 175 K. In contrast, **2** displays a complete transition with $T_{1/2}$ shifted to higher temperatures. A comparable trend is observed for compounds **3** and **4**, wherein both exhibit an incomplete and gradual transition, with only a slight shift in $T_{1/2}$. This observation confirms in this case that counterion size is not the predominant factor when establishing a correlation with the temperature of the transition. In the case of L2, no spin transition is observed, and the complex remains in LS state. This is attributed to steric hindrance effects, since the acetic ethyl group constrains the geometry around the metal center, favoring the LS.

Other example of same authors involves the use of L1 = 4,5-dimethy-2-(pyridine-2-yl)imidazole with anionic ligands SCN^-(**1**) or $SeCN^-$(**2**).[56] Through Single Crystal X-Ray Diffraction, they demonstrate that **1** and **2** exhibit nearly identical crystal lattices. Consequently, the differences in magnetic properties between **1** (HS, no transition) and **2** (gradual, $T_{1/2}$ = 214 K) are attributed to the energy level splitting in the ligand field strength generated by the SCN^- or $SeCN^-$ ligands.

An extensive study of a library of counterions has been conducted by S. Brooker *et al*.[57] In this study, they investigated seven different Fe(II) complexes with a PMAT (4-amino-3,5-bis{[(2-pyridylmethyl)-amino]methyl}-4*H*-1,2,4-triazole) ligand, which can provide coordination for six points -3 of them for each of the two Fe(II) centers present in the resulting complex-. The complexes studied include: BF_4^- (**1**), Cl^- (**2**), PF_6^- (**3**), SbF_6^- (**4**), $CF_3SO_3^-$ (**5**), $B(PhF)_4^-$ (**6**) and $C_{16}H_{33}SO_3^-$ (**7**). Magnetic properties of this collection of dinuclear iron(II) complexes are influenced by the choice of anions. While all the compounds demonstrate SCO activity, their SCO behavior differs not only in terms of $T_{1/2}$ but also the completeness and nature of the transition. Interestingly, there is no clear discernible trend between the counteranions and the observed transition patterns.

Other interesting approach for investigating influence of counterion is to obtain a library of products from a reference material with a facile route of synthesis. By utilizing mechanochemistry, derivatives with different counterions can be produced with relatively good yields. This methodology is corroborated by H. Sheperd *et al*.[58] They synthesized $[Fe(atrz)_3]Cl_2$ complex (atrz = 4-amino-1,2,4-triazole) and through solid-state metathesis by grinding means, a counterion exchange was achieved, yielding $[Fe(atrz)_3]Br_2$ and $[Fe(atrz)_3]I_2$. Attempts to produce $[Fe(atrz)_3]F_2$ showed that the obtained structure resembled that of the chlorine compound, indicating that the exchange could not be realized. Magnetic findings confirm larger size of counterion stabilizes HS causing a reduction in $T_{1/2}$ and leading to a more abrupt transition.

Computational calculations help us to understand electronic aspects of how HOMO-LUMO levels can change depending on modifications to the ligand field or the impact of changing the second coordination sphere. Otherwise, these aspects would be very difficult to rationalize. Theorical researchers have pushed efforts in the way to elucidate electronic features in the effect of anion dependence of spin transition through density functional theory. In a recent study, J. Cirera *et al*. have explored anionic SCO system $[Fe(OEt\text{-}L1\text{-}pH)(NCS)_3]^-$ (L1 = tris(pyridin-2-yl)ethoxymethane) replacing axial thiocyanate ligand by similar groups (NCO^-, $NCSe^-$ and $NCBH_3^-$) through theoretical calculations and comparing with experimental reported data.[59] The computed $T_{1/2}$ values reflect a clear trend in ligand strength ($NCO^- < NCS^- < NCSe^- < NCBH_3^-$), which matches with experimental observations for the reported systems.

J. Tuchages and collaborators explored computational aspects derived from density functional theory comparing with previously reported experimental results in a series of $[Fe(trim)_2](X)_2$ (X = F_2 (**1**),[60] Cl_2 (**2**), Br_2 (**3**), I_2 (**4**)) (trim = 4-(4-imidazolylmethyl)-2-(2-imidazolylmethyl)imidazole).[61] Size of halogen plays a pivotal role in determining the inclusion of solvent molecules to occupy vacant spaces within the structure. This effect becomes particularly pronounced in compounds **3** and **4**, prompting them to incorporate MeOH into their structure. Magnetic measurements provide insight into the behavior of these compounds: **1** demonstrates a HS with no transition, **2** shows a gradual complete transition ($T_{1/2}$ = 175 K), while **3** and **4** undergo gradual and complete transitions above room temperature. This behavior can be rationalized by considering that more electronegative atoms diminish electron density on the nitrogen donor atom within the imidazole moiety, consequently, Fe-N bond weakens, thus favoring HS. Following this rationale, when the anion sphere displays a stronger inductive effect, it leads to a lower $T_{1/2}$ for the SCO transition, aligning with experimental observations. DFT calculations provide similar outcomes, indicating that the complex **1** is

strongly stabilized in the HS, while the **4** complex experiences the most substantial stabilization of the LS, as predicted.

Maybe, two of the most significant works in this area are those carried out by M. Halcrow and coworkers.[44,62] We are going to go in deep on these works since they focus on ligand on 3-bpp, which is the key ligand of this dissertation. Different salts of $[Fe(3\text{-bpp})_2]^{2+}$ show a wide variety of thermal transitions, some of them compiled in Table 3.2.1 and Figure 3.2.5. Structural features responsible for these differences remains unclear since the lack of crystallographic characterization. However, it is evident difference in counterion has a strong impact in magnetism, as supported by the examples mentioned above.

These presented works have explored the impact of anions on magnetic behavior and spin transition. It has been observed that larger anions are more prone to establishing intermolecular interactions, thus enhancing cooperativity and producing transitions more abrupt. Moreover, an increase in size can lead to solvent inclusion and induce steric hindrance that impede the transition. In other cases where supramolecular interactions cannot be established due to ligand constraints, different anions can also have a magnetic impact by modifying the ligand field strength. In such cases, computational methods are particularly interesting as they help rationalize energy differences through HOMO-LUMO analysis.

Table 3.2.1. Summary of spin-state transitions undergone by different anhydrous salts of $[Fe(3\text{-bpp})_2]^{2+}$ from [44].

$[Fe(3\text{-bpp})_2](X)_2$	$T_{1/2}$ (K)	ΔT (K)	Character
X = Br	252	4	Abrupt
X = I	203	2	Abrupt
X = NCSe	231	2	Abrupt
X = BF_4	176	10	Abrupt
X = ClO_4	220	0	Gradual
X = PF_6	171	2	Abrupt, 50% conversion
X = OTf	230	0	Gradual, 50% conversion

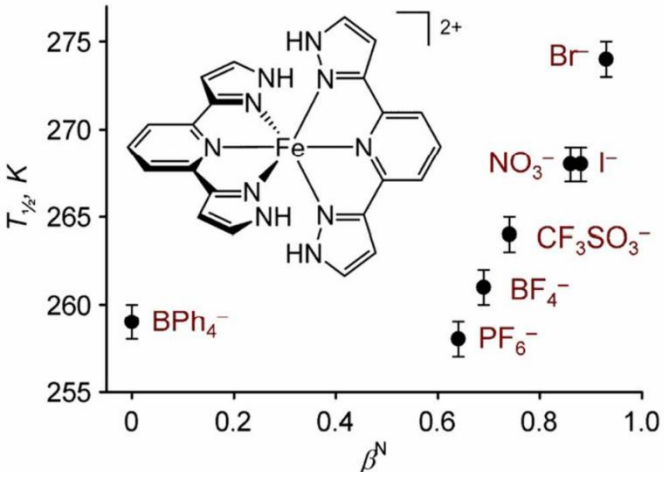

Figure 3.2.5. The spin-crossover equilibrium midpoint temperature ($T_{1/2}$) in $[Fe(3\text{-bpp})_2]X_2$ (3-bpp = 2,6-di{pyrazol-3-yl}pyridine) varies from 259 K when X^- = BPh_4^- to 277 K when X^- = Br^-, in a polar acetone:water solvent mixture. Reproduced with permission from [62]. Copyright 2014, Royal Society of Chemistry.

3.2.3.2 Solvent effect

The inclusion of solvents in the structure of SCO compounds can modulate their SCO behavior by affecting the crystal packing and intermolecular interactions. Solvent molecules can occupy the cavities within the crystal structure, leading to changes in the intermolecular interactions and thus affecting the cooperativity that drive the SCO. Additionally, but less common, solvents can act as ligands, coordinating to the central metal ion, and changing its coordination environment and ligand field, which affects the thermal energy barrier for the SCO process.

Solvents are labile and can be easily removed by increasing the temperature (evaporation) or reabsorbed in a reversible manner. This makes solvent-included SCO compounds attractive for sensing applications, where a change in temperature can trigger the release of the solvent molecules and induce a change in the magnetic properties of the material. The presence of volatile solvate molecules enables the study of desolvated phases and facilitates comparison with their solvated counterparts. However, a primary drawback is the susceptibility of these forms to damage and loss of crystallinity, which complicates structural elucidation.

Recent works have explored these guest-sensitive SCO compounds. E. Coronado and coworkers have studied role of the inclusion of nitromethane in a Fe(II) di[4-(ethylcarboxy)pyrazol-1-yl]pyridine complex.[63] The inherent flexibility of the ethylcarboxy groups leads to the formation of three distinct solvatomorphs depending on the amount of included solvent: 1.5·$MeNO_2$ (**1**), 1·$MeNO_2$ (**2**) and 2·$MeNO_2$ (**3**). The inclusion of one molecule of solvent (**2**) produces a complete gradual transition above 150 K. In this case, desolvated compound exhibits no discernible differences compared to its initial state. Increase in the solvent amount (**1**) results in only 40% of the population undergoing a gradual transition from HS to LS. In the scenario with maximum solvent inclusion (**3**), a gradual transition occurs in 50% of the total HS fraction. Therefore, it can be concluded that the solvent does not impact the transition temperature ($T_{1/2}$) but rather influences the initial distribution of high spin centers. Furthermore, the exchange of solvent in **2** was also explored. When changing nitromethane ($MeNO_2$) for acetic acid (MeCOOH) or acetonitrile (MeCN) no big differences in the transition were observed. However, a totally opposite transition behavior is observed when exchanging nitromethane for acetone (Me_2CO), showing an abrupt transition that is associate with the loss of ca. 60% of acetone in the crystalline structure.

Same authors have explored a hybrid material constructed from a hexavanadate polyoxometalate covalently linked to two 1-bpp ligand.[64] Polyoxometalate derivative in combination with Fe(II) leads to a highly porous 1D network that can reversibly include solvents and facilitate their exchange (**2**). In the initial crystallization media, **2·MeCN** presents a gradual SCO $T_{1/2} \approx 130$ K. Upon exchanging the solvent to **2·$MeNO_2$** or **2·EtOH**, transition remains gradual while shifting to 220 K or 275 K, respectively. However, there is a significant alteration in behavior when other solvents are employed, such as **2·DMF** or **2·PhCN**. In these cases, the transition becomes incomplete, with only a 30% conversion rate. On the other hand, the compound **2·MeOH** remains in a high spin state without undergoing a transition.

Y. Garcia *et al*. investigate ligand bpb (bpb = 1,4-bis(4-pyridyl)benzene) with Fe(II).[65] This new chelating moiety forms a 3D porous structure that resembles to a Hofmann clathrate. Their study was focused on the interaction with two guest molecules, $CHCl_3$ (**1·3$CHCl_3$**) and CH_2Cl_2 (**1·2.5CH_2Cl_2**). In the case of **1·3$CHCl_3$** solvent establishes supramolecular interactions with

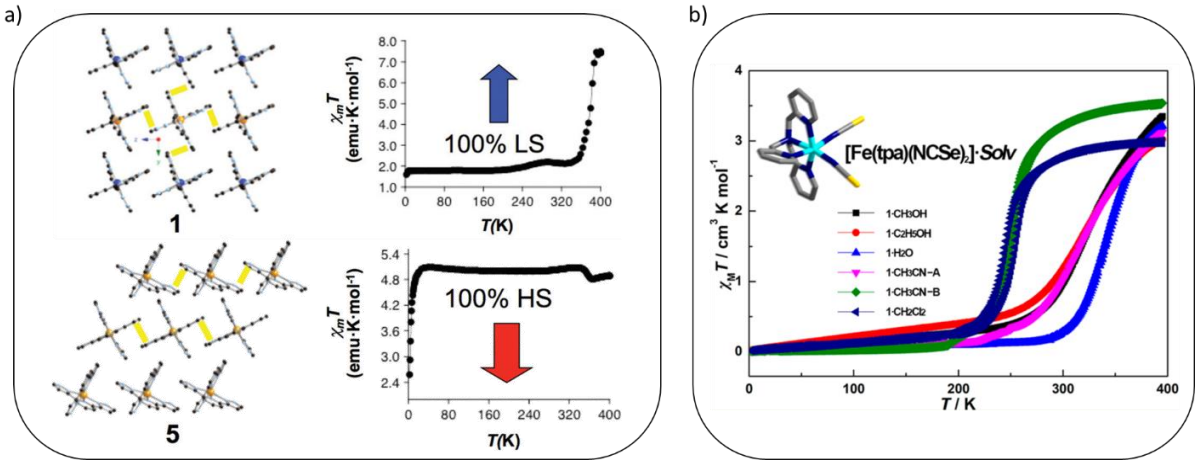

Figure 3.2.6. a) Magneto-structural correlations for 1 and 5 showing the relationship between the different packing diagrams and the variable-temperature magnetic susceptibility (2–400 K) towards the desolvation process. π– π stacking interactions are shown in yellow. Reproduced with permission from [67]. Copyright 2018, Royal Society of Chemistry. b) $\chi_M T$ versus T plots (per Fe unit) of 1·CH_3OH, 1·C_2H_5OH, 1·H_2O, 1·CH_3CN-A, 1·CH_3CN-B, and 1·CH_2Cl_2. Reproduced with permission from [68]. Copyright 20218, American Chemical Society.

chloroform···ligand bpb (hydrogen bond, C-H···Cl) and chloroform···perchlorate (halogen bond, Cl···O). It confers flexibility to the metal center core, leading to elongated metal bond lengths and favoring a HS state. The SCO behavior in this case is characterized by only about 10% gradual SCO occurring below 85 K. On the other hand, interactions in **1·2.5CH_2Cl_2** are weaker -Van der Waals- established between the solvent and bpb ligands. This scenario allows for a two-step non-complete SCO phenomenon to take place between 100 - 250 K.

Paul K. *et al*. have explored the influence of solvents in bidentate imidazolylimine-based complex, $[Fe(L1)_3](ClO_4)_2 \cdot CH_3CN \cdot 0.5H_2O$ where L1 = (1*H*-imidazol-4-yl)-methylene-4methylaniline.[66] In this case, solvents interact strongly both with anions and NH groups of the imidazole. This leads to a two-step transition attributed to a highly connected network through supramolecular contacts enabling elastic interactions and thus, cooperativity. Instead, in case of the desolvalted sample, it shows an abrupt transition ca. 85 K. This drastic change in magnetic behavior can be explained by density increase of the packing due to an arrangement of the lattice when solvate molecules are removed. This arrangement allows an enhancement of elastic communication between adjacent complexes, which in turn the observation of a one-step transition.

The role of solvent molecules in stabilizing LS or HS has been investigated by M. Giménez *et al*.[67] Their study was based on $[Fe(3\text{-bpp})_2]X_2$ complexes being X = $[Cr(CN)_6]$ or $[N(CN)_2]$ and comparing with different reported anions. It was observed if π-π interactions occur within a "terpyridine-embrace" motif, involving interactions with four adjacent iron complexes, structure is stabilized in LS form. Otherwise, if the units of bpp get separated, i.e. increasing anion size, number of aryl-aryl interactions drops drastically and then, HS form is stabilized (Figure 3.2.6a).

J. Tao *et al*. have studied the influence of five different solvents in $[Fe(tpa)(NCSe)_2]$ (**1**) complex (tpa = tris(2-pyridylmethyl)amine): **1·CH_3OH**, **1·C_2H_5OH**, **1·H_2O**, **1·CH_3CN**, and **1·CH_2Cl_2**.[68] Their findings indicated that **1·MeOH**, **1·EtOH** and **1·H_2O** stabilizes the LS state, leading to an increase of $T_{1/2}$. This phenomenon can be attributed to the establishment of hydrogen bonds

such as O-H···Se that contributes to generate different crystal packing (Fe···Fe distances) and π-π interactions. Instead, for non-protonic solvent molecules, **1·CH_2Cl_2**, they stabilize the HS state. In case of **1·CH_3CN** two solvatomorphs (substance that contains solvent molecules within its crystal lattice) were identified, **1·CH_3CN-A** (1·0.5CH_3CN) and **1·CH_3CN-B** (1·CH_3CN). First solvatomorph **CH_3CN-A**, with two independent crystallographic sites, exhibits an isostructural arrangement with **1·MeOH** and **1·EtOH** structures, revealing similar magnetic behavior. Instead, second solvatomorph **CH_3CN-B**, with one crystallographic Fe, shows significant differences in magnetic behavior, stabilizing the LS due to more compact packing and closer π-π interactions (Figure 3.2.6b).

It is noteworthy that the interactions between solvent molecules and complexes are not the only factors to consider. Vapor analytes can also engage in these interactions, earning them the designation of "guest molecules." The interaction between vapor analytes and the complex can result in an intriguing phenomenon called vapochromic effect, characterized by a change in color. This captivating phenomenon has attracted the attention of numerous researchers, as Jose Costa *et al.* published in a recent review of compounds exhibiting this phenomenon.[1]

All these studies confirm the role of solvents in spin transition and highlight that their interaction can range from strong (establishing intermolecular interactions within the lattice), thereby exerting a significant impact on magnetic properties, to weak interactions or solvent exchange, resulting in a negligible impact without inducing significant changes.

3.3 External stimuli as a means of inducing spin crossover behavior

Temperature, light, and pressure are the most common stimuli employed to induce Spin Crossover (SCO) behavior in molecular materials. In addition to these conventional stimuli, there is emerging research on less common triggers such as pH variations and electric fields. Although less explored, works reporting the influence of pH[69] or electric fields[70] on SCO behavior suggest the potential for expanding the scope of stimuli-responsive SCO materials and diversifying their applications in molecular electronics and sensing.

3.3.1 Scan rate temperature dependence

Most of the SCO systems reported are based on the spin switching through thermal effect. Temperature is the most common stimuli since is related with thermal barrier energy (k_BT), proportional to splitting energy between t_{2g} and e_g levels (Δ_{oct}). Many researchers have devoted their efforts to find systems with a switching temperature close to room temperature, which would be the most convenient and manageable when manufacturing a device for daily use and improving energy efficiency.

For that is usual to find in literature most of SCO complexes, testing their behavior through temperature scan rate under an applied field. Despite this, scan rate has been demonstrated to be crucial in order to affect thermal hysteresis, so it is a parameter related with thermally activated mechanisms and mainly associated with the kinetics of the process. Some works have devoted to discussing role of scan rate.

J. Tao and collaborators have explored the influence of scan rate in a system based on [Fe(H_2Bpz_2)$_2$(C9bpy)] (H_2Bpz_2 = dihydrobis(1-pyrazolyl)borate)).[71] They measured magnetic response at different scan rates: 5, 2, 1, 0.5 and 0.05 K·min^{-1}. As the scanning rate decreases, the spin transition completeness becomes more evident. SCO behavior remains similar meanwhile the $T_{1/2}$ value shifts towards lower temperatures. This phenomenon can be elucidated by considering the distribution of relaxation times, and it can be modeled using an Arrhenius-type distribution. The successful fitting of this distribution reveals the presence of a substantial energy barrier, resulting in a slow establishment of spin equilibrium.

T. Ishida *et al*. studied scan rate dependence in tris(2-pyridyl)methanol Fe(II) complex at 10, 2, 1, 0.1 and 0.02 K·min^{-1}.[72] Contrary to the proposed in other works, they found that lower scan rates led to higher $T_{1/2}$ and broader hysteresis. They put forth a possible explanation suggesting a mechanism in which the structural phase transition in a solid comprising polymorph is influenced by the SCO transitions occurring in two distinct phases. This is supported by the observation of a transition occurring in two well-differentiated steps at lower scan rates.

S. Brooker *et al*. explored the influence of scan rate in a triazole-based diiron(II) complex.[73] Experimental findings indicated complex undergoes to HS state to HS-LS mix state. Scan rate experiments reveal a temperature range dependence in the cooling branch, meanwhile heating branch remained invariably. The hysteresis loop showed an increase and cooling branch decreased with the temperature scan. Authors proposed this highly dependence on cooling branch is attributed to an initial vibrational excited state ([HS-HS]*) by the iron(II) centers in the HS state. In this state, one of the centers experiences slightly less distortion and can transition to the LS state, while the other center maintains more distortion. This discrepancy in distortion arises from the restricted nature of the PMPh^{tBu}T ligand, but it causes the latter center to remain in the HS state. However, process of converting the LS (low spin) center to HS (high spin) is not affected by the scan rate likely due to the fact that the conversion releases the inherent ligand strain present in the PMPh^{tBu}T ligand.

Since temperature is by far the most studied stimulus for inducing spin transition, we will focus on other less explored stimuli that we have also investigated in this dissertation, such as light and pressure.

3.3.2 Light-Induced Spin State Trapping (LIESST)

Light-Induced Spin State Trapping (LIESST) refers to the phenomenon where the spin state of a molecule can be trapped into a particular configuration, usually the high energy state, through the application of light. This process involves the absorption of photons by the molecule, which leads to an excitation of the electrons and a subsequent rearrangement of the spin states, usually from LS to HS state. By carefully selecting the wavelength and intensity of the light, researchers can control and manipulate the spin state of the molecule, allowing for precise tuning of its magnetic and optical properties. In the Figure 3.3.1, we represent a scheme of the mechanism through LIESST effect and relaxation (Jablonski diagram).

One of the biggest challenges is to achieve compounds operating at higher temperature, or in other words, with large values of T_{LIESST}, which is the temperature below the metastable high spin state can be trapped and maintained after the initial excitation by light. Above this

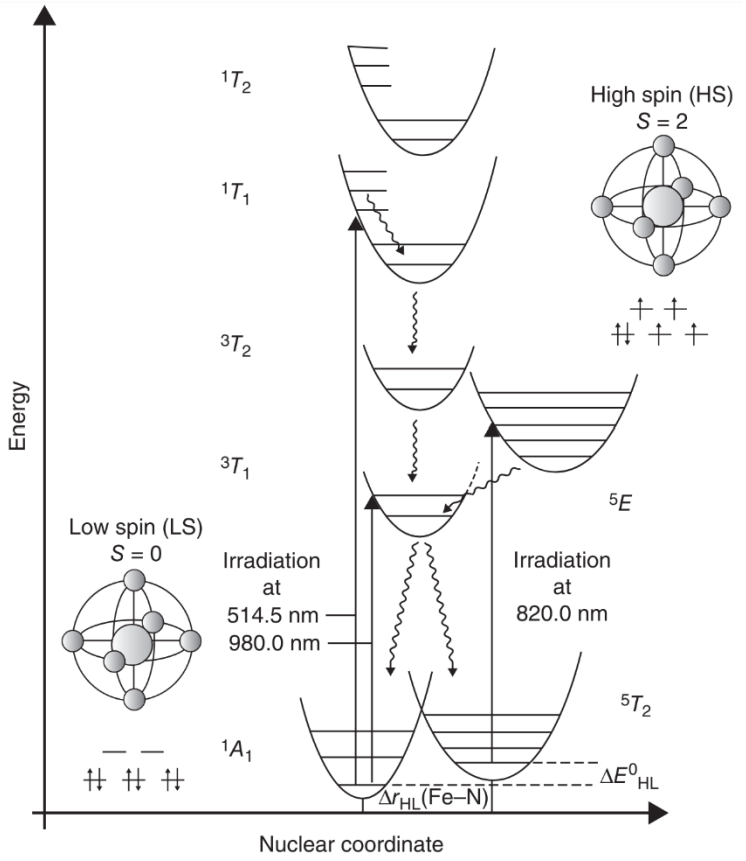

Figure 3.3.1. Jablonski diagram displaying the mechanism of LIESST. Reproduced with permission from [8]. Copyright 2020, Wiley.

temperature, thermal energy is sufficient to cause the system to relax back to the lower energy state. The T_{LIESST} is associated with both T_c and the stability of the high spin (HS) state, leading to a trade-off where higher T_c allows for a broader operating temperature range but results in a lower T_{LIESST}.

This behavior can be explained by Hauser's "inverse energy gap law," which states that higher T_c correspond to faster relaxation of the photoinduced high spin (HS) metastable state.

J. Tang *et al*. have studied the photoconversion yield in two different salts of *p*-aldehyde-1-bpp: **1·ClO₄** ([Fe(bppCHO)$_2$](ClO$_4$)$_2$]) and **1·BF₄** ([Fe(bppCHO)$_2$](BF$_4$)$_2$]).[74] Meanwhile **1·ClO₄** displays a T_{LIESST} of 53 K and a photoconversion of 84%. In contrast, **1·BF₄** exhibits a poor photoconversion of 2.9%. Authors do not provide a definitive explanation for this difference, but it is likely attributed to the presence of hydrogen bonds due to the additional water molecules in **1·BF₄** that are absent in **1·ClO₄**. This results in **1·BF₄** being a more cooperative system, leading to a gradual transition, lowering the $T_{1/2}$. In the case of **1·ClO₄** the transition becomes abrupt hysteresis nearly reaching 400 K. This is another illustration of how the presence or absence of a solvent in the secondary sphere can influence the light-triggered magnetic characteristics.

F. M. Romero *et al.* have reported a complex of Fe(3-bpp)$_2$ with adipate dianion.[75] These combinations lead to a structure with two distinct Fe sites. Photoconversion investigations reveal complex reach 50% of HS and T_{LIESST} of 76 K. Fe ions are located in alternating positions

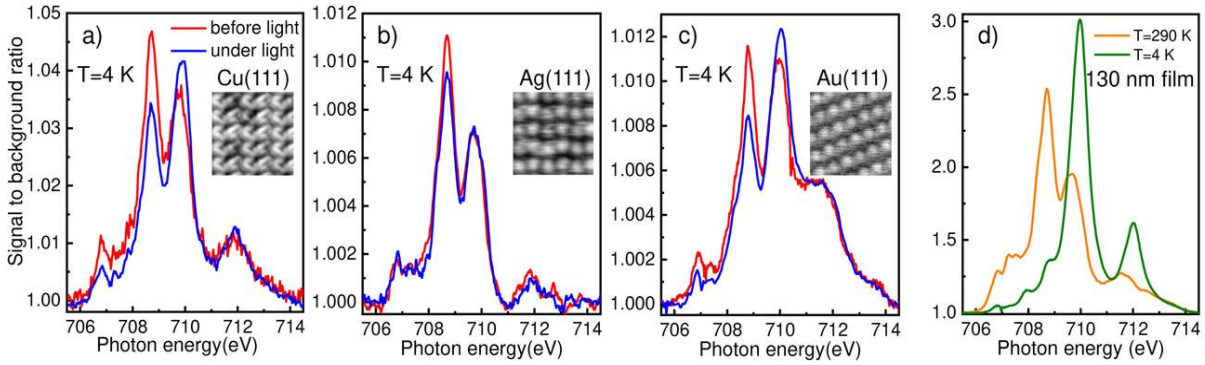

Figure 3.3.2. 4 K X-ray absorption spectra of the $Fe_{II}L_3$ edge before and after illumination of the sample with a blue light for Cu(111) (a), Ag(111) (b) and Au(111) (c). d) Reference spectra recorded at 4 K and 290 K on a 130 nm thick film on a SiO_2 substrate. Reproduced with permission from [77]. Copyright 2020, Wiley.

and it provokes Fe2 remains in the LS state even under light irradiation. Moreover, T_{LIESST} is in the range expected for derivative Fe^{II}3-bpp complexes.[76]

V. Repain and coworkers have reported T_{LIESST} modification of metal complex when predominant interaction is with an interface of metal substrate. For that demonstration 3 different substrates were obtained when depositing Fe^{II}-$[(3,5\text{-}(CH_3)_2Pz)_3BH]_2$ (Pz = pyrazolyl) on (111) Cu, Ag or Au (Figure 3.3.2).[77] First observation of the authors is the complex presents a mixed HS/LS state in comparison with properties of bulk compound. This effect is attributed to deposition, which confers an epitaxial constrain that force Fe^{II} geometry and introduces steric hindrance. Also, an anomalous transition is observed in SCO@Cu and SCO@Au when irradiating with blue light (HS→LS) in contrast of bulk material, where LS→HS occurs. Any switching from HS is observed in SCO@Ag. The proposed mechanism explaining this behavior involves light absorption by the metallic surface and a subsequent change in spin state triggered by low-energy valence photoelectrons, consequently altering the relaxation pathway. This result offers novel insights for the development and understanding of photo-active electronic devices relying on SCO materials.

E. Coronado *et al.* reported a Fe(II) SCO complex based on 1-bpp with unusual high T_{LIESST}.[78] Herein, authors report 1-bpp with carboxylic acid substitutions at the 4' and 4''-pyridil positions which exhibits a SCO near room temperature. This transition is linked to a crystallographic phase transition and also displays a high T_{LIESST} of 120 K with a 100% HS photoconversion, in contrast with only 50% HS conversion achieved by thermal switching. This phenomenon is explained through structural correlation. Firstly, the presence of a rigid bpp ligand causes a distorted high spin (HS) geometry and a symmetry breaking that can lead to a new phase containing HS and LS species. Secondly, the presence of carboxylic acid group promotes the presence of solvent molecules within the structure, creating enough empty space for the distorted HS molecules to transition to the undistorted low spin (LS) state.

Overall, these results deviate from the trend extrapolated from other 1-bpp compounds, which follows the expression first introduced by J.-F. Létard *et al*.[76]:

$$T_{LIESST} = T_0 - 0.3T_{1/2} \quad \textbf{(Eq. 1)}$$

E. Coronado *et al.* described in another work the photomagnetic properties of a Fe(II) complex derivative carboxylic acid of 1-bpp, in this case functionalize in 3-pyridil position.[79] They study

the photoconversion rate of solvated and desolvated complex. Solvated complex presents a non-complete gradual transition above 350 K, thus, complex does not reach saturation under 532 nm light irradiation, with only 15% HS photoconversion with a T_{LIESST} of 40 K. Desolvated complex shifts transition to lower temperature, which is translated in a slightly increase of T_{LIESST}, 50 K.

M. Khusniyaro *et al*. investigated the light-responsive characteristics of a SCO complex that incorporate a photoisomerizable ligand, diarylethene.[80] Researchers examined how these ligands influenced the switching behavior between LS and HS states in the complex by subjecting it to alternating UV and visible light exposure at room temperature. By cyclically exposing UV and visible light, they effectively demonstrated the ability to switch between LS and HS by opening or closing the diarylethene ring. The use of visible light led to a reversal of the transition from LS to HS at the metal center through a process called photocycloreversion. The initial state of the sample involved 32% LS and 68% HS as a result of partial conversion using UV light. However, upon exposing the sample to visible light (wavelength greater than 400 nm) for 8 hours at room temperature, the proportion of HS increased significantly to 83.6%. This observation stands as the first clear confirmation of a reversible SCO phenomenon at the molecular level within a solid-state system under normal conditions. The successful combination of a suitable ligand with a light-responsive metal center facilitated the controlled manipulation of electron states under light exposure, resulting in a reversible switching behavior. Importantly, this switching process occurred at room temperature, within a solid-state environment, and at the molecular scale.

M. Ruben *et al*. documented a novel compound derived from a benzaldehyde-1-bpp derivative. Fe(II) SCO shows a gradual spin transition with a $T_{1/2}$ = 285 K and a T_{LIESST} of 70 K.[81] Results are consistent with same equation formula for bpp compounds (Eq. 1). Additionally, they study if metastable HS state under light irradiation could involve a thermal hysteresis. The sample was exposed to irradiation at a temperature of 10 K until the magnetic signal reached its maximum level. After that, the temperature was gradually increased to 100 K while sustaining the irradiation. The sample was eventually cooled back to 10 K. The results unveiled a thermal hysteresis of 10 K ($T_{\downarrow}$ = 62 K, $T_{\uparrow}$ = 72 K) triggered by light exposure. This observation provided conclusive evidence that the HS phase trapped by light exhibited a considerable degree of cooperative behavior.

J.F.-Létard and coworkers studied a series of related chalcadiazole ligands on Fe(II) SCO compounds.[82] In this work, photomagnetic properties of three different complexes was investigated: $[Fe(^{II})(L^{S})_2(NCS)_2]$ (**A**) or $[Fe(^{II})(L^{S})_2(NCSe)_2]$ (**B**) and $[Fe(^{II})(L^{Se})_2(NCS)_2]\cdot MeOH$ (**C·MeOH**). Compound **A** presents two steps character in relaxation upon heating after irradiation, similar to conventional two-step thermal SCO transition. This is explained through two independent Fe(II) sites in the crystal structure. In the case of **B** and **C·MeOH**, irradiation is produced in one abrupt way indicating LS→HS transition occurs with no intermediate state. A useful tool to unravel kinetics parameters is study relaxation process HS*→LS after irradiation at a certain fix temperature and fit relaxation data by Arrhenius plot. By doing these kinetic study, compound A exhibits two relaxation processes that can be fitted separately since relaxation times scale are enough different. Fitting of both processes result in a similar E_a. Regarding **B** and **C·MeOH** show classical sigmoidal relaxation consistent in a self-acceleration process.

3.3.3 Investigating pressure effects on spin crossover compounds

The preceding discussion primarily focused on thermally and light-induced spin transitions, but it is worth noting that other physical perturbations can also initiate or modify such transitions. Typically, an increase in pressure tends to stabilize the low spin state and thus, increasing the transition temperature or even modifying the width of a hysteresis loop. This phenomenon can be attributed to the volume reduction that occurs during the HS to LS conversion, mainly due to the shorter metal-donor atom distances in the LS form. In fact, pressure can induce a spin transition in high spin systems where a thermal transition does not occur or reveal hidden processes not accessible through thermal variations.

First studies of pressure induced SCO phenomena were carried out by F. Varret in 2001 in system $Fe(btr)_2(NCS)_2$ (btr: 4,4'-bis(1,2,4-triazole)).[83] They report spin transition by optical reflectivity measurements. Transition shifts 60 K up to 2600 bar. In addition, when Fe(II) content of the compound is diluted in a Ni matrix, giving $[Fe_{0.52}Ni_{0.48}(btr)_2(NCS)_2]\cdot H_2O$, T_c shift with pressure is also observed, meanwhile hysteresis width decreases due to less connectivity between Fe domains.

Two years later, J. McGarvey *et al*. reported first piezohysteresis at room temperature in $Fe(pyrazine)[M(CN)_4]$ (M = Ni, Pd, Pt).[84] This work supposed first solid-state measurements using high-pressure Raman spectroscopy to unravel spin transition.

In subsequent years, researchers dedicated their efforts to further investigate the relationship between pressure and spin transition. In 2005, J. A. Real *et al*. published a study discussing the impact of pressure on a novel cyanide-bridged bimetallic polymer $\{Fe(pmd)(H_2O)[Ag(CN)_2]_2\}\cdot H_2O$ (pmd = pyrimidine).[85] This research revealed the responsiveness of the polymer to pressure, leading to adjustable thermal and piezochromic bistability even at room temperature. When pressure increases above 105 Pa, the steep transition persists with higher T_c. While the hysteresis decreased within the pressure range of 0.19 to 0.25 GPa, it subsequently underwent a significant increase (≈ 31 K) between 0.25 and 0.30 GPa, suggesting the occurrence of a phase transition and therefore, alteration in bulk modulus (resistance to volumetric compression or expansion under an applied external pressure). On that sense, this work demonstrates how pressure can be employed to fine-tune the width of thermal hysteresis and/or strategically position of the hysteresis phenomenon.

In 2006, same authors continued studying the magnetic properties under pressure, this time with $Fe[H_2B(pz)_2]_2$ (bipy)} (**1**) and $\{Fe[H_2B(pz)_2]_2(phen)\}$ (**2**) being $[H_2B(pz)_2]^-$: dihydrobis(pyrazolyl)borate; bipy: 2,2'-bipyridine and phen: 1,10-phenanthroline.[86] Pressure experiments reveal a linear dT_c/dP dependence of **1** while in the case of **2**, it shows a non-lineal dependence, in contrast with theoretical expectations. The authors pointed out that this inconsistency is attributed to a possible phase transformation or change in bulk modulus, but no confirmed since further X-Ray measurements were required.

In the following years, Real and coworkers have also contributed to continue exploring this property. In 2014, they reported a 2D coordination polymer $\{Fe(phpy)_2[Ni(CN)_4]\}$ (phpy: 4-phenylpyridine) which undergoes changes under applied pressure.[87] The non-complete transition at ambient pressure is maintained, but the transition becomes more gradual, and the hysteresis more pronounced. This strong non-linearity is attributed to the different interactions that govern the width of hysteresis and the steepness of the transition, that is associated with

the decrease in the interaction parameter (Γ) expressed in the following equation, which connect transition temperature with elastic energy.

$$\frac{dT}{dP} = \frac{\{\Delta V_{HL} + \frac{[d(\Delta_{elast} - \Gamma)]}{dP}\}}{\Delta S}$$ (**Eq. 2**)

Following years have been crucial in the development of theoretical models and extending pressure experiments. In this sense, it is possible to find several works in literature that investigate the role of pressure. For this purpose, compounds that have been thermally characterized previously are chosen, typically exhibiting a single abrupt complete step transition that is suitable for studying pressure dependence.

L-S. Cheng *et al*. analyzed magnetic changes of [Fe(pmea)$(NCS)_2$] (pmea: bis[(2-pyridyl)methyl]-2-(2-pyridyl)ethylamine) under external pressure.[88] The abrupt spin transition gradually shifts to higher temperatures and becomes gradual as pressure increases. To comprehend this phenomenon qualitatively, researchers utilized mean-field theory to examine how external pressure affects the behavior of SCO. This theory obeys Clausius-Clapeyron equation[89,90]:

$$\frac{\partial T_{1/2}}{\partial P} = \frac{\Delta V}{\Delta S_{HL}}$$ (**Eq. 3**)

This theory allows to predict T_c as well as whether the behavior will be gradual or abrupt, although in that case a direct correlation is not evident. Role of supramolecular interactions is tentative to be crucial, but their exact contribution remains undisclosed until development of techniques to access the crystal structure of the SCO compound at different pressures.

Another interesting set of systems suitable for investigations into pressure-related properties are those exhibiting SCO behavior, particularly those that form two-dimensional polymers. An example is the [Fe$(bdpt)_2$]·guest (**1**) (bdpt = 3-(5-bromo-2-pyridyl)-5-(4-pyridyl)-1,2,4-triazole) proposed by X. Chen *et al*.[91] These complexes possess big cavities for accommodating molecules within. To this end, the researchers describe three distinct structures: **1** (anhydrous), **1·MeOH** and **1·EtOH**. All three display two-step abrupt spin transition processes, with the T_c decreasing as the size of the guest molecule increases: T_c (**1·EtOH**) < T_c (**1·MeOH**) < T_c (**1**). Surprisingly, the sharp transition at 200 K retains these characteristics, in contrast to the transition at 150 K, which becomes gradual as the pressure increases. The authors attribute this phenomenon to interactions involving hydrogen bonding and π−π stacking interactions (Figure 3.3.3).

The increasing interest in coordination polymers stems in the last years comes from their ability to break symmetry at the central sites, leading to the generation of diverse metal centers that can result in multi-step transitions.

Regarding the study conducted by S. Neville *et al*.,[92] focused on the compound [$Fe^{II}Pd(CN)_4$(R-1,2,4-trz)$_2$]·$2H_2O$ (R-1,2,4-trz = a 4-functionalized-1,2,4-triazole ligand), it is demonstrated that the inclusion of water molecules within the structure inhibits the spin transition, whereas its removal reveals an abrupt transition. To explore the potential effect of pressure and unveil further transitions, they examine the initial compound under pressure. They observe that the starting HS state becomes a gradual transition up to 0.42 GPa. Up to this pressure, system evolves into two-steps process, culminating in a nearly complete transition. The enhanced

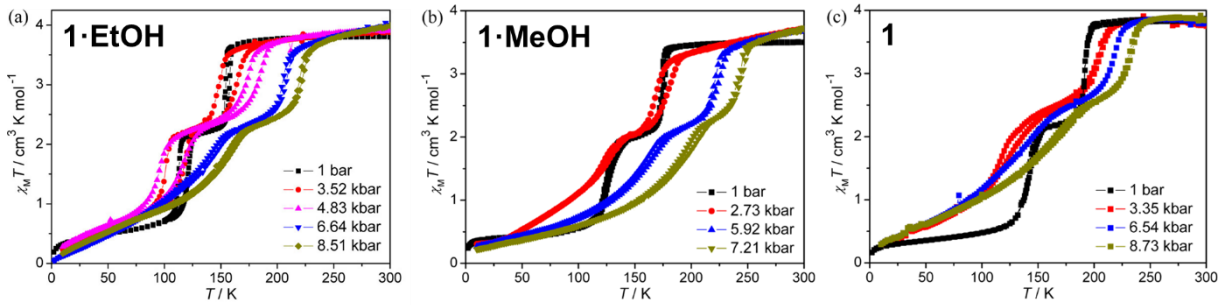

Figure 3.3.3. Pressure effect on the SCO behaviors of (a) 1·EtOH, (b) 1·MeOH, and (c) 1. Reproduced with permission from [91]. Copyright 2012, American Chemical Society.

cooperativity observed with increasing pressure signifies the reinforcement of interactions, such as hydrogen bonding and π-π stacking. This increase in cooperativity demonstrates the role of intermolecular interactions in the thermal spin transition of studied compound.

A recent work has focused on two-dimensional Hofmann-type coordination frameworks $[Fe(L)_2\{M(CN)_4\}]$ (where L = 5-amino isoquinoline) (M = Pt (**1·Pt**) and Pd (**1·Pd**)).[93] Both compounds exhibit comparable abrupt and hysteretic pressure-induced SCO behavior with a shift in the T_c greater than 100 K as pressure increases to 0.8 GPa. The authors proposed that the maintenance of an abrupt transition over the entire pressure range is achieved through the establishment of strong interactions, such as π-π stacking, N−H···C, and C−H···π, which confer strong cooperativity to the system.

All these studies provide evidence that pressure serves as a suitable stimulus for inducing or shifting spin transitions, closely intertwined with changes in the internal structure due to lattice compression (such as alterations in Fe-N bond distances, elastic and supramolecular interactions). In this regard, it is crucial to employ crystallographic techniques capable of elucidating these structural changes to establish correlations and unveil their role in the magnetic response.

3.3.3.1 Barocaloric effect (BCE)

One of the topics within pressure-induced spin transition that has gained significant interest in recent years is undoubtedly the barocaloric effect (BCE), leading to the publication of highly relevant studies. BCE was known for other materials such as alloys[94,95] but the exploration of the BCE in the context of SCO is a relatively recent area of study. The BCE, particularly in SCO systems, is closely associated with the change in entropy since the LS state typically has a more ordered arrangement compared to the HS state. By exploiting the BCE in SCO systems, researchers can manipulate the entropy change to achieve substantial variations in temperature, making them promising candidates for next-generation solid-state refrigeration and cooling applications. Understanding the interplay between the BCE and entropy in SCO systems opens up new opportunities for designing innovative and efficient thermodynamic materials.

Noteworthy progress has been made since K. Sandeman put forward a number of SCO complexes as possible candidates for exhibit BCE. These proposals have been supported by various examples accompanied by experimental data.[96]

In subsequent years, P. von Ranke made significant contributions to the understanding of the BCE during the spin transition from LS to HS from a theoretical point of view.[97,98] Initially, von Ranke proposed a microscopic model that attributed the caloric contribution mainly to phonons. Building upon this, von Ranke and co-authors further refined the model by incorporating electronic, configurational and lattice contributions. Through a well-designed methodology to determine the barocaloric potentials, they theoretically predicted a remarkable effect with an entropy change of 46 $J \cdot K^{-1} \cdot kg^{-1}$ and an adiabatic temperature change of 27 K at a pressure change of 0.1 GPa. These findings showcased the potential for achieving a giant BCE in SCO systems.

This theoretical approach established a precedent in this field, and from this study, first articles in experimental barocalorics start to being published. In 2019, K. Sandeman *et al*. reported first giant BCE in well-studied ligand 1-bpp, in the complex $[Fe(1\text{-}bpp)_2][BF_4]_2$.[99] For facilitate experiments, complex was synthesized by replacing protons with deuterium enabling the viable examination of the BCE using neutron diffraction under hydrostatic pressure. Neutron diffraction and SQUID experiments together reveal non-linear correlation of $T_{1/2}$ with pressure and with calorimetric data, a remarkable barocaloric effect (BCE) of 86 $J \cdot K^{-1} \cdot kg^{-1}$ was discovered. This obtained value significantly surpasses the theoretically anticipated BCE value within SCO compounds. This study set a precedent within the field of barocalorics, prompting the publication of further works in the subsequent years.

P. von Ranke reported in 2020 complex $[CrI_2(depe)_2]$ (depe = 1,2-bis(diethylphosphino)ethane) leading to high values for $\Delta S = 40\ J \cdot K^{-1} \cdot kg^{-1}$.[100] The substantial alteration in entropy is attributed to distinct sources: configurational, magnetic and phonon entropies being the predominant factor of the phonon scattering, stimulated by the considerable volume change during the LS ↔ HS phase transition.

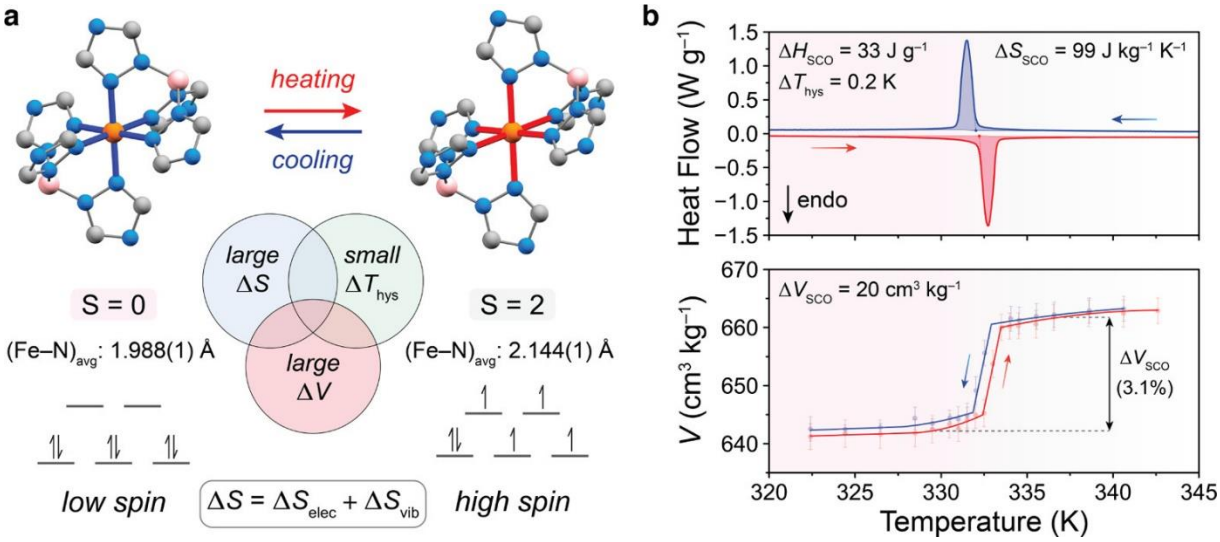

Figure 3.3.4. $Fe[HB(tz)_3]_2$ experiences a thermally triggered spin crossover (SCO) accompanied by a rise in both electronic entropy (ΔS_{elec}) and vibrational entropy (ΔS_{vib}). (b) Differential scanning calorimetry (DSC) conducted at ambient pressure, with heating and cooling rates set at 2 $K \cdot min^{-1}$ (top), along with helium pycnometry measurements (bottom), underscore the significant alterations in entropy and volume during the SCO transition, with minimal hysteresis observed. Reproduced with permission from [103]. Copyright 2022, American Chemical Society.

In 2021, two significant studies emerged. On the one hand, L. Mañosa *et al*. reported a trinuclear spin crossover complex $Fe_3(bntrz)_6(tcnset)_6$ where bntrz = 4-(benzyl)-1,2,4-triazole and tcnset = 1,1,3,3-tetracyano-2-thioethylepropenide.[101] This complex undergoes an abrupt complete transition with a minimal degree of hysteresis. This characteristic combination, an abrupt complete transition coupled with negligible hysteresis, positions this system as an excellent candidate for investigating its barocaloric properties. On that sense, it shows a substantial BCE value, 120 $J \cdot K^{-1} \cdot kg^{-1}$, higher value reported by so far. On the other hand, group of P. von Ranke study barocaloric properties of $\{Fe[H_2B(pz)_2]_2(bipy)\}$ obtaining a value of 83 $J \cdot K^{-1} \cdot kg^{-1}$, similar value than the obtained through theoretical means.[102]

Recent outfindings carried out by J. A. Mason *et al*.[103] provided data for $[Fe(HB(tz)_3)_2]$ ($HB(tz)_3^-$ = bis[hydrotris(1,2,4-triazol-1-yl)borate]). By conducting extensive experiments involving high-pressure calorimetry and diffraction techniques, a significant isothermal entropy change (> 90 $J \cdot K^{-1} \cdot kg^{-1}$) is observed, alongside a minor adiabatic temperature change (> 2 K) (Figure 3.3.4).

In Figure 3.3.5, there are compiled all SCO compounds demonstrating a BCE, organized by their respective values and the year in which they were reported. As a result, significant progress has been made in the field of barocaloric compounds in recent years. The reported SCO compounds have achieved optimal values, even surpassing some refrigerants based on Gd, Ni, or Mn to date. Therefore, it is highly likely that this field of exploration will continue to expand in the coming years improving the achieved values.

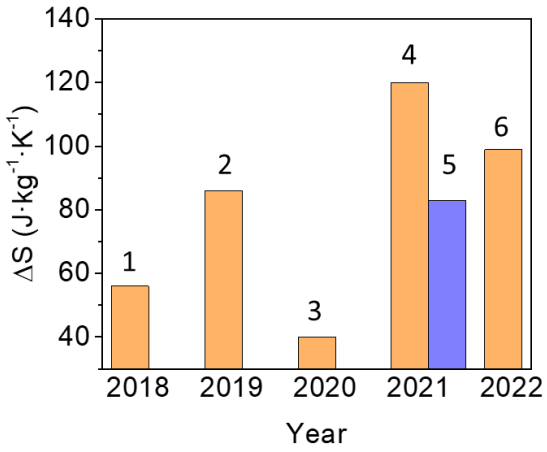

1: $[Fe(hyptrz)_3]\cdot A_2 \cdot H_2O$ *Phys. Rev. B*, **2018**, *98*, 224408
2: $[Fe(1bpp)_2]\cdot(BF_4)_2$ *Adv. Mater.*, **2019**, *31*, 1807334
3: $[CrI2(depe)_2]$ *J. Appl. Phys.*, **2020**, *127*, 165104
4: $Fe(bntrz)_3(tcnset)_6$ *Adv. Mater.*, **2021**, *33*, 2008076
5: $Fe[H_2B(pz)_2]_2(bipy)$ *Phys. Status Solidi B*, **2021**, *258*, 2100108
6: $Fe[HB(tz)_3]_2$ *J. Am. Chem. Soc.*, **2022**, *144*, 6493–6503

Figure 3.3.5. Schematic graph containing the SCO compounds discovered in the last five years that exhibit BCE and their BCE values.

3.4 Applied field as a means of promoting Single Ion Magnet behavior

Single Ion Magnets (SIM) are a subclass of compounds that belong to the broader category, Single Molecule Magnets (SMM), that exhibits magnetic behavior originating from a single magnetic ion. In other words, it is a molecule or complex containing a single paramagnetic ion that behaves like a nanoscale magnet. These SIM are typically composed of a transition metal, or a lanthanide surrounded by various ligands. What makes SIM interesting is their ability to exhibit magnetic bistability, which means they can have two distinct spin states with a significant energy barrier between them. Since their discovery in 1991[104] its study has been intensified due to its potential application in information storage,[105] spintronics[106] and quantum computing.[107]

To function as a single ion magnet, several conditions need to be considered, including a high magnetic anisotropy (D) that ensures the stability of the two spin states and a relatively large effective energy barrier (U_{eff}) between them.

Anisotropy is the preferential alignment of the magnetic moment along a specific direction and can be described as simple as following Hamiltonian based on zero-field splitting:

$$H = g\mu_B SB + D\left(S_z - S^{2/3}\right) + E\left(S_x^2 - S_y^2\right) \text{ (Eq. 4)}$$

where μ_B is the Bohr magneton, D is the axial ZFS parameter, E is the rhombic or transverse ZFS parameter, S is the spin operator and B is the magnetic field vector.

Energy barrier (U_{eff}) is directly related with the total spin number in the ground state, S, and is expressed with the following expression:

$$\text{For integer spin: } U_{eff} = |D| \cdot S^2\ ,\ S \in \mathbb{N} \text{ (Eq. 5)}$$

$$\text{For non-integer spin: } U_{eff} = |D| \cdot \left(S^2 - \frac{1}{4}\right)\ ,\ S \in \mathbb{N} + \frac{1}{2} \text{ (Eq. 6)}$$

Most of the reported studies of SIM were based on lanthanoids for their high total spin number, but in the last decades its study with first row of transition metals with d^4-d^7 electronic configuration has been increased for its abundance and cheaper cost.[108] In most of the cases of compounds that imply electronic transitions within the *d*-orbitals, zero-field relaxation is not produce since system relaxes through fast quantum tunnelling. Therefore, a direct current is needed to observe SIM by AC-susceptibility measurements, in a subfield called as field-induced SIM. Systems based on Co(II) are the most reported, despite other systems containing Fe(II) or Ni(II) have also studied. In the case of molecules with non-integer ground states, such as Co(II), the situation becomes even more intriguing due to the presence of Kramers doublets in the absence of an applied magnetic field. Consequently, the molecule cannot transition from m_s = -S to m_s = +S (Figure 3.4.1a).[109]

The study of spin relaxation through relaxation time measurements (τ) allows us to fit the values to a curve that follows the Arrhenius law. It is not typically a purely thermal process, as there are other relaxation processes related to lattice vibrations through phonons, which have thermal dependence also. The presence or absence of these processes can be deduced from the following equation:

$$\tau^{-1} = \mathrm{A} \cdot \mathrm{T} + \mathrm{C} \cdot \mathrm{T}^{n} + {\tau_0}^{-1} \cdot e^{-U_{eff}/K_B \cdot T} + {\tau_{QTM}}^{-1} \quad (\mathbf{Eq.\ 7})$$

in which A is the coefficient of the direct process, C is the coefficient of the Raman process, third term represents the Orbach process and τ_{QTM} represents the quantum tunneling. Quantum tunneling is suppressed when a magnetic field is applied (Figure 3.4.1b).

To achieve SIM behavior, SIMs are often incorporated into carefully designed ligand frameworks. The ligands surrounding the metal ion help to control its electronic structure and coordination geometry, which influences the strength and stability of the magnetic interactions. The ligand design also plays a crucial role in preventing the unwanted interactions between neighboring SIMs that could lead to the loss of coherence. It is well known the correlation between the molecular symmetry and the anisotropy thus, to explore methods to modulate the distortion of metal complexes could be an instrument to obtain SIM.

There are many examples where the distortion is programmed by the design of the ligand, with tensional or steric restrictions. However, this methodology is very difficult to control due to the existence of supramolecular forces in the crystal structure. Considering the coordination compounds as non-isolated molecules and crystal packing effects in solid state, we can use the supramolecular forces to modify the molecular symmetry by establishing new supramolecular interactions.

Our study encompasses the scope of Co(II) SIM and emphasize the significance of supramolecular interactions and the first coordination sphere and their impact on D and U_{eff}. These factors play a key role in the development and manifestation of SIM behavior. Their understanding is crucial for advancing in the design and synthesis of highly efficient SIM materials with potential applications in information storage and quantum computing.

X. M. Ren *et al*. have explored the impact of various derivatives in a series of three Co(II) mononuclear complexes. These complexes share the ligand based on propyliminophenol but differ in their substitutions: *p*-nitro (**1**), *o*,*p*-dinitro (**2**), or nitro and methoxy (**3**) groups located in either the *para*- and *meta*- positions, respectively.[110] These substitutions result in distinct coordination geometries: **1** adopting a tetrahedral structure; **2** and **3**, octahedral. The different substitutions introduce variations in the distortion around the metal center, directly influencing

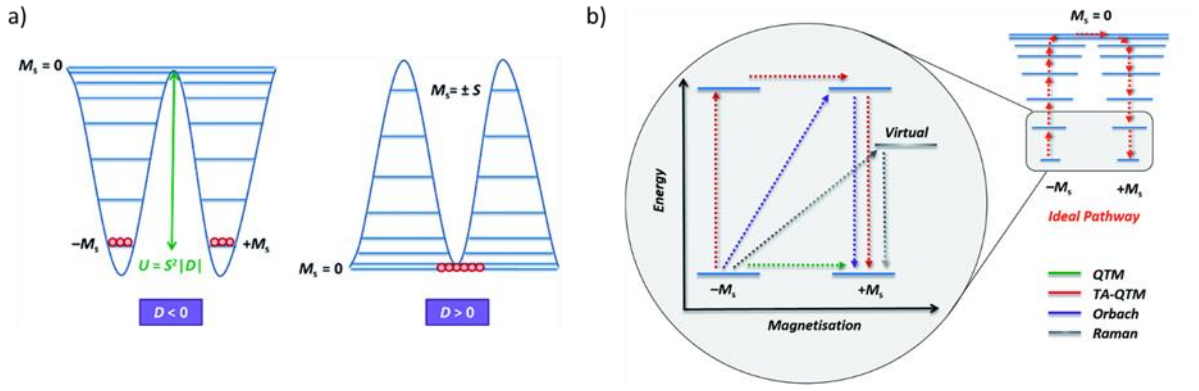

Figure 3.4.1. a) Double-well energy diagram for negative (left) and positive (right) D. b) Schematic representation of possible relaxation pathways in SMM/SIM. Reproduced with permission from [109]. Copyright 2016, Royal Society of Chemistry.

magnetic anisotropy. Complex **1** displays a higher energy barrier (54.9 K), attributed to the shorter Co···Co distance (dipole-dipole interactions). On the other hand, for **2** and **3**, despite having similar coordination environments, distortion is more pronounced in **2** than **3**, resulting in a slightly higher energy barrier (24.3 K for **2** and 19.4 K for **3**). It is worth noting that their magnetic relaxation behavior is not only influenced by coordination geometry, but also affected by intermolecular interactions and molecular vibrations that cannot be fully elucidated in the work only with the structural analysis provided.

S. Gao *et al.* have studied the impact of different substitutions in a pybox-based ligand (**1**-**6**).[111] In that case, researchers can clearly find a relationship between ϕ, which is $N_{pyridine}$–Co–$N_{pyridine}$ (axial position) angle and U_{eff}. As ϕ decreases, leading to a more distorted geometry, U_{eff} increases. Even though complexes **2** and **3** only differ by the presence of a single molecule of acetonitrile in the structure, this slight modification leads to a significant alteration in AC behavior, resulting in distinct energy barriers (with a difference of ca. 5 K).

X-Y. Wang *et al*. have investigated how the introduction of axial ligands affects the anisotropy in Co(II) macrocycles.[112] The macrocycle under study is based on tdmmb ligand (tdmmb = 1,3,10,12-tetramethyl-1,2,11,12-tetraaza[[3](2,6)-pyridino[3](2,9)-1,10-phenanthrolinophane-2,10-diene with H_2O as ligand (**1**) or anionic ligands such as CN^- (**2**), NCS^- (**3**) and SPh^- (**4**). The use of bulkier ligands (**3**, **4**) induces greater deviation from the ideal pentagonal bipyramidal geometry, and consequently increases the energy barrier (Figure 3.4.2).

Up to this point, we have examined the influence of the first coordination sphere on the distorted geometry. However, there is another significant factor that can modify the properties of SIM, and that is the impact of supramolecular interactions. Z. Tian *et al*. have examined how

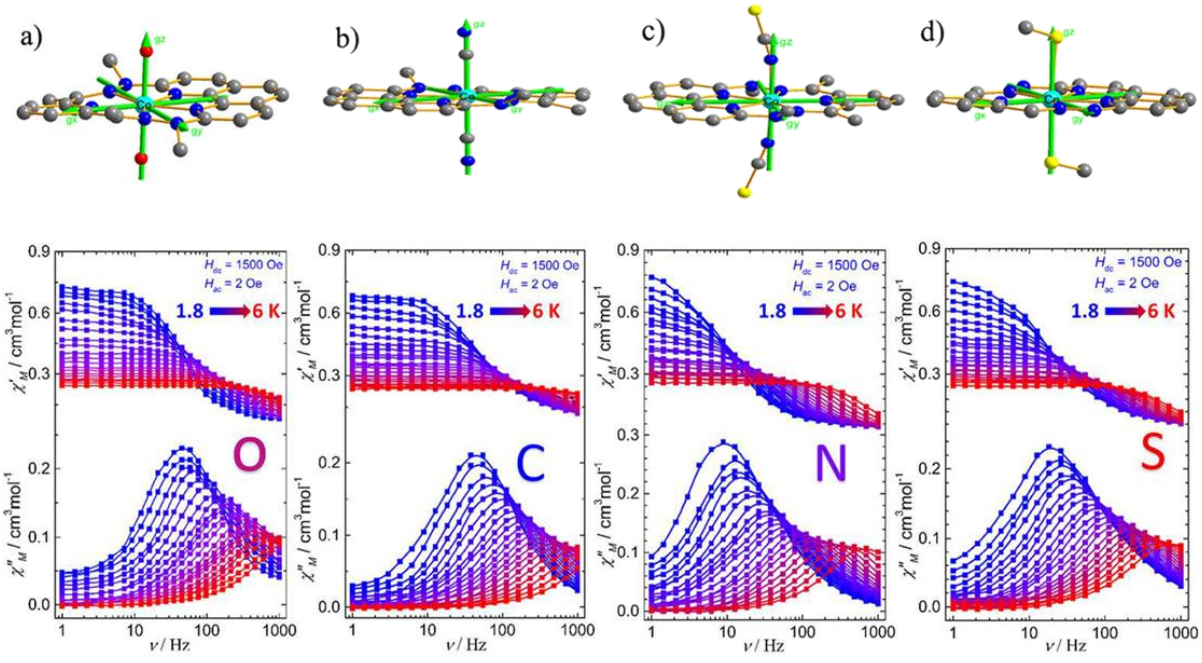

Figure 3.4.2. Orientations of g_x, g_y, and g_z (hard axis) on Co^{II} of complexes 1-4 (a-d). Frequency dependence of the in-phase (χ′) and out-of-phase (χ″) parts of the ac magnetic susceptibilities for 1-4 collected under a 1.5 kOe dc field over the temperature range of 1.8-6.0 K. Reproduced with permission from [112]. Copyright 2016, American Chemical Society.

hydrogen bonds affect the behavior of SIM, using the cpt (4-(p-carboxyphenyl)-1,2,4-triazole) ligand as a basis.[113] X-ray studies have unveiled a 3D arrangement stabilized by hydrogen bonds (O-H···N). This interaction plays a crucial role in introducing additional strain, contributing to the distortion around the metal center, apart from the purely distortion induced by the ligand. This leads to a positive D value, resulting in SIM behavior with a U_{eff} > 40 K.

X. Wang *et al*. provide further evidence for the significant role of these supramolecular interactions by utilizing a Co(II) metal-organic framework coordinated to bpg = meso-α,β-bi(4-pyridyl) glycol.[114] They report two distinct structures depending on the solvent present in the crystal structure, **1** (MeOH) and **2** (DMF). The presence of different solvents does not notably impact the Co(II) center and the interactions within the structure. However, the dynamic magnetic properties of both compounds, exhibit significant differences. Compound **1** displays faster relaxation compared to **2**. These distinctions can be attributed to the supramolecular interactions. In the case of **1**, hydrogen bonds are shorter, resulting in an asymmetry within the two distinct hydrogen bond networks compared to **2**.

K. Dumbar *et al*. explore the influence of axial ligands to fine-tune the octahedral geometry around Co(II) center.[115] In that case, they form $Co(py)_4$ where pyridines are located in equatorial position and anions occupy the axial positions: NCS^- (**1**), Cl^- (**2**) or Br^- (**3**). Primary distortion occurs in the axial positions, resulting in significant and distinct positive D values. This indicates alterations in the axial positions induce an easy-plane magnetic anisotropy and confirms these modifications are an effective way to tune AC magnetic behavior.

S. Das *et al*. also studied role of pyridine in axial position.[116] Depending on the temperature conditions during the reaction, two distinct Co(II) polymorphs are formed, determined by the tilting of the carboxylic group from the benzoic acid. In this case, pyridine does not serve as a parameter for controlling anisotropy, instead, it is controlled through equatorial ligands. Each polymorph results in a different crystal structure, organized by 2D structures (**1**) or 1D (**2**) through hydrogen bonds. Despite the notable differences in crystal packing between these two compounds, the dynamic magnetic properties observed under an applied magnetic field exhibit similarities, with comparable values for energy barriers and relaxation times.

The ligand 1-bpp, which was introduced earlier in the context of Fe(II) SCO compounds, has undergone extensive research due to its potential for inducing SIM behavior. In this context, E. Ruiz and coworkers reported in 2018 that 1-bpp-COOMe (where bpp-COOMe stands for methyl 2,6-di(pyrazol-1-yl)pyridine-4-carboxylate) exhibits slow magnetic relaxation under an applied field of 1 kOe, with an energy barrier of 44 K.[117]

Other derivative of the 1-bpp, 1-bpp-COOH, was reported by E. Coronado *et al*.[118] In contrast, it exhibits a lower energy barrier of 16 K under an applied field of 3 kOe. This observation suggests the presence of alternative relaxation mechanisms rather than relaxation through Orbach mechanism.

Mario Ruben *et al*. extended their investigation into the functionalization of 1-bpp by synthesizing five closely related mononuclear pentacoordinate complexes, each chelates with alkyl tails.[119] AC susceptibility measurements revealed the presence of two relaxation processes in all five compounds. In the case of the low-frequency branch, the peak of the out-of-phase susceptibility was observed within the frequency range of 1 to 10 Hz. This observation indicates that magnetic relaxation occurs at a relatively slow rate, with a relaxation time (τ) of

approximately 0.5 seconds at a temperature of 1.9 K. In contrast with expected times in these type of compounds in the range of 10^{-3}-10^{-6} s.

All these works underscore the importance of distortion around the metal in generating single-ion magnet behavior, particularly in examples involving solvent or ligand exchange effects. This distortion plays a crucial role in influencing the magnetic properties of the materials, highlighting the essential role of the local structural environment in the design and optimization of single-ion magnets.

3.5 Magnetic molecular-based devices

In recent years, the field of magnetic molecular-based devices has emerged as a dynamic area of research, drawing significant attention from scientists and engineers. This exciting frontier in materials science explores the intricate interplay between molecules with unique properties and materials that can adopt role of platform for these molecules. Among an abroad library of molecules, can be included DNA sensors, molecular motors such as rotaxanes, molecular switches such as azobenzene, molecular catalysts such as metal organic frameworks, etc. Different platforms to integrate these molecules are being exploited such as semiconductor surfaces (silicon), metal surfaces (Au or Ag), transition metal dichalcogenides (MoS_2 or WSe_2), insulators (SiO_2), carbon-based materials (graphene, nanotubes), etc.

In this thesis, we will focus on molecules with magnetic properties that can act as a switch between two different magnetic states -both SCO or SIM properties- and carbon-based materials serving as a platform, specifically graphene. Here, we delve into the latest research trends, applications, and the fascinating world of magnetic molecular materials combined with graphene.

Magnetic molecular switches are interesting due to their high sensitivity to external stimuli, making them potential candidates for miniaturization, and their versatility in design. Graphene, a single layer of carbon atoms, possesses extraordinary properties, including electrical and thermal conductivity, mechanical strength, flexibility, and transparency. Its large surface area, impermeability, and biocompatibility contribute to diverse applications in energy storage, electronics, and biotechnology. Graphene's quantum mechanical features and ease of functionalization enhance its versatility, making it a material of great interest for integrating magnetic switches.

The applications of magnetic molecular-based devices are both diverse and promising: data storage, sensors and detectors, quantum technologies or spintronics.[120,121]

In this introduction, we will delve into the advantages and drawbacks of both non-covalent and covalent functionalization strategies applied to graphene, shedding light on the distinctive features that make graphene a compelling candidate for our research endeavors. By exploring these facets, we aim to elucidate the promise and challenges that lie ahead in harnessing the properties of graphene in the realm of magnetic molecular-based devices. Advantages and drawbacks of non-covalent and covalent functionalization of graphene are compiled in Table 3.5.1.[122,123]

In this context, this dissertation aims to explore and evaluate the most relevant works from recent years regarding graphene functionalization with magnets and specifically, SCO systems. SCO molecules, with their switchable magnetic properties, hold great promise for innovative device applications. By carefully selection these important studies, we aim to open up opportunities for new breakthroughs in magnetic molecular devices incorporating graphene.

Table 3.5.1. Advantages and drawbacks of non-covalent and covalent functionalization of graphene.

Graphene		
	Advantages	Drawbacks
Non-covalent functionalization	Preservation of inherent properties Reversibility	Weaker bonding Limited stability
Covalent functionalization	Enhanced stability Tailored properties	Disruption of structure Introduction of defects

The first publications on graphene emerged in the early 21st century. Notably, in 2004, two physicists, Andre Geim and Konstantin Novoselov,[124,125] isolated and characterized graphene through a groundbreaking experiment involving the use of scotch tape and isolating monolayers of graphene. Their pioneering work, published in Science, marked a milestone in the properties of graphene. This achievement in material science culminated in the Nobel Prize in Physics in 2010, awarded to Geim and Novoselov for their revolutionary discovery and contributions to the understanding of graphene's unique properties, opening up new horizons for nanotechnology and materials science. Since then, interest in combining bistable magnetic materials with graphene for device applications has surged, with the earliest reported studies dating back to 2014.

In 2014, Z. Li and colleagues presented a simple method for creating nanocomposites of spin crossover-graphene (SCO-G) using the extensively studied compound $Fe(Htrz)_2(trz)](BF_4)$.[126] They successfully demonstrated that $Fe(Htrz)_2(trz)](BF_4)$ forms nanoparticles with a mean diameter of 50 nm, which were dispersed across the graphene surface. Depending on the ratio SCO:graphene two different hybrids were obtained: **SCO-G1** and **SCO-G2**. To elucidate if the SCO-G retains SCO characteristics, magnetic susceptibility was tested within the temperature range of 300–400 K. SCO phenomena was identified in both SCO NPs and SCO-G nanocomposites, with a minor variation in the percentage of high spin (HS) fraction. This discrepancy can be attributed to differences in the aggregation of the nanoparticles across the graphene sheets from the two different samples **SCO-G1** and **SCO-G2**.

In 2015, W. Kuch and colleagues published the first observation of $[Fe(bpz)_2phen]$ molecules in direct proximity to a highly oriented pyrolytic graphite surface.[127] The research pointed the molecule transitions from an off state (LS) to an on state (HS) upon exposure to green light at a temperature of 6 K, and conversely, revert to the off state when the temperature was raised to 65 K (LIESST effect). Remarkably, this spin transition was observed within a submonolayer of these molecules. Therefore, $[Fe(bpz)_2phen]$ complexes maintain their spin-switching functionality even when immobilized.

During those same years, community continued making efforts to confine the spin transition properties within graphene. S. Hayami *et al*. reported the preparation of non-conductive hybrids, $[Fe(qnal)_2]nGO$ (**1·GO**), and $[Fe(qsal)_2]nGO$ (**2·GO**), through the utilization of electrostatic interactions between negatively charged graphene oxide (GO) and iron(III) complex cations in $[Fe(qnal)_2]Cl$ and $[Fe(qsal)_2]Cl$.[128] The GO hybrids are insulators, whereas

the rGO hybrids (**1·rGO** and **2·rGO**) possess electrical conductivity. Additionally, **1·GO** and **1·rGO** exhibit SCO behavior, with **1·rGO** also showing LIESST effect. Authors effectively managed to regulate the size of metal complex domains on both GO and rGO. These hybrids fall into the rare class of materials that simultaneously exhibit SCO behavior and electrical conductivity.

In 2016, E. Coronado *et al*. published two relevant works in the area centered on spin coating of SCO systems deposited on thin films of graphene. To demonstrate spin state, experiments were conducted through transport measurements in carbon film. In this first example, a collection of reported SCO NPs based on $Fe(Htrz_2)(trz)$ and a chemical alloy $Fe(Htrz)_{2.95}(NH_2trz)_{0.052}$ was introduced into a single layer of graphene. To summarize, they have successfully demonstrated a novel approach for the non-invasive detection of spin-state transitions within a thin film containing SCO nanoparticles. This innovative method entails the measurement of the electrical characteristics of graphene, employing a four-probe field-effect configuration, while the graphene is coated with a monolayer of switchable nanoparticles. Importantly, the graphene resistance exhibits a clear dependence in the range of spin transition reported for the unsupported nanoparticles (320 – 380 K) (Figure 3.5.1).[129]

Once this technique was investigated and corroborated, in parallel, his research group studied charge transport properties of SCO $[Fe(Htrz)_2(trz)](BF_4)$ NPs covered with a silica shell placed in between single-layer graphene electrodes. This class of core-shell SCO nanoparticles exhibits a significant memory effect -hysteresis- in electrical conductance at approximately 40 K, associated with SCO phenomenon. In this specific case, LS state possesses a high conductance value than HS. Importantly, an examination of the hysteresis loop indicates that the presence of the silica shell can alter the activation energies and pre-exponential factors

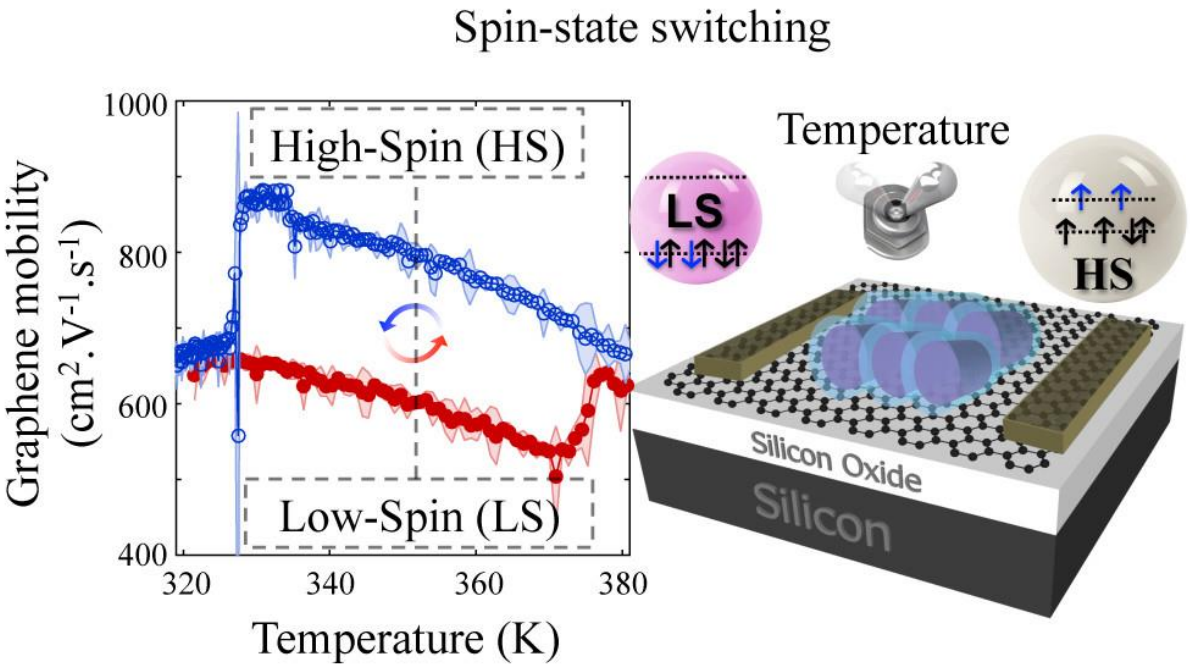

Figure 3.5.1. Schematic of the device with CVD graphene on top of a silicon-silicon oxide substrate and after deposition of a bistable SCO. Resistance per square at the Dirac point as a function of temperature for heating and cooling modes. A wide clockwise hysteresis loop is observed between 327 and 374 K. Reproduced with permission from [129]. Copyright 2016, American Chemical Society.

while maintaining the low spin state as the state with high conductivity. The combination of graphene's versatility and the thermal stability of the hysteresis loop in these core-shell SCO nanoparticles opens up possibilities for future experiments and implementation in a real magnetic nanodevice.[130]

Group of Mario Ruben has been investigating the integration of SCO complexes into a monolayer of graphene, which was obtained through an optimized method to exfoliate graphite powder. The bonding between SCO and graphene is facilitated by π-π interactions, since 1-bpp ligand had incorporated a pyrene group. Their work has been supported by experimental evidence, including Raman and TEM-EDX experiments, which confirm the presence of Fe(II) complexes within the graphene structure. Furthermore, SQUID experiments on the hybrid material, **Gr-SCO**, show that the SCO properties have been preserved. Although there is a slight shift in the $T_{1/2}$, the gradual transition characteristic of SCO materials remains intact. The findings presented in this research could prove valuable in advancing the development of spintronic applications based on SCO materials incorporated through non-covalent interactions.[131]

In early 2022, a team led by E. Coronado *et al*. introduced an innovative method to induce strain in 2D materials. They achieved this by employing thin layers of SCO Van der Waals heterostructures. Their approach involved depositing a mechanically exfoliated layer of Fe-(3-Clpyridine)$_2$[Pt^{II}(CN)$_4$]} on top of FLG (Few-Layer Graphene). They subsequently investigated the electrical transport properties using a four-probe DC setup. The results clearly demonstrate that the thermal spin transition in the SCO layer significantly alters the electrical conductivity of the FLG. This modification is attributed to the extensive change in volume within the SCO layer, which induces strain in the graphene layer in contact and leads to a dramatic alteration in conductivity meanwhile the $T_{1/2}$ is not altered.[132]

In the same year, same research group led by E. Coronado published a work based on the creation of hybrid structures composed of CVD graphene and thin layers of [Fe(Pyrz)$_2$] SCO molecules with sublimation properties. These devices display remarkable characteristics. First, they can efficiently and rapidly induce a photoinduced spin transition (LIESST) in the device, which can be controlled electrically. Consequently, devices exhibit an unprecedented level of durability when exposed to both thermal and light stimuli. In overall, this represents a new method to produce contactless devices that demonstrate exceptionally enhanced light-induced spin switching compared to thermal switching. This enhancement is achieved by incorporating a PMMA intermediate layer between the graphene and the SCO molecular film.[133]

All these efforts have marked the inception within a relatively emerging domain and have set a precedent by demonstrating the feasibility of incorporating SCO properties into graphene obtaining kind of synergy while preserving the distinctive characteristics of each material.

4 RESULTS AND DISCUSSION

4.1 Pressure-Induced Spin Crossover Metallomesogens bearing Long Alkyl Chains

4.1.1 Background

Spin crossover complexes (SCO) are coordination compounds that undergo a reversible change in their electronic spin state of the metal center in response to external stimuli, such as temperature, pressure, or light irradiation.[2,6,8] In these complexes, the central metal ion can switch between high spin (HS) and low spin (LS) states, making them increasingly important in materials science and physics research.[107,120] They hold potential applications in information storage,[134] sensors,[31,133] and switches.[3] Structural modifications allow for modulation of the SCO transition, resulting in various SCO behaviors, including hysteric first-order, gradual second-order, or multistep transitions.[17,135,136]

Controlling the SCO nature and its characteristic temperature is a primary focus in molecular-based magnetism and involves employing various strategies to modify the electronic configuration of the central metal ion. One approach to achieve this is through ligand design, where the choice of ligands surrounding the metal center influences the strength of the metal-ligand interaction, affecting the energy difference between high spin (HS) and low spin (LS) states.[38,39,41] Another strategy involves fine-tuning the molecular environment and leveraging cooperative effects within the crystal lattice, which can impact on the spin crossover behavior. Within this context, intermolecular interactions and solvent effects have been subjects of significant research interest.[44,45,64,65]

An alternative pathway to control spin transition is through phase transitions, utilizing methodologies such as synthesizing liquid crystals (metallomesogens),[137,138] gels,[139,140] self-assembled monolayers,[141] Langmuir-Blodgett films,[142,143] etc. One option involves designing ligands or counterions with long alkyl chains, particularly within a subclass known as soft materials or metallomesogens.[144,145] The introduction of long alkyl chains typically does not impede spin transitions, but it may lead to transitions that are less abrupt compared to non-alkylated analogues.[146] In some extreme cases, if the alkyl chains absorb the deformation of SCO cores without effectively transmitting it through the lattice, the transition may be inhibited. On the other hand, it has been reported that flexible substituents can induce various types of "exotic" spin transitions, such as reverse spin transition (rST)[147] or a reduction in magnetic susceptibility through phase transformations, including crystal-to-crystal, crystal-to-liquid crystal, or crystal-isotropic liquid transitions.[148,149] However, the investigation of SCO behavior in soft materials incorporating flexible molecular units has been relatively limited, despite the potential of such compounds to exhibit distinctive magnetic characteristics resulting from the synergy between SCO behavior and the flexible nature of the involved substituent.[150] Because of the high compressibility imparted by alkyl chains to the structure, these systems represent promising candidates for investigating spin transition properties under an external stimulus such as pressure.[151,152]

Herein, we report three new amphiphilic ligands based on the extensively studied 2,6-di(pyrazol-3-yl)pyridine (3-bpp), which is functionalized with a 16-carbon alkyl chain and features various terminal groups: 2,6-bis(1-hexadecyl-pyrazol-3-yl)pyridine (L1), 16,16'-

(pyridine-2,6-diylbis(1H-pyrazole-3,1-iyl))bis(hexadecan-1-ol) (L2) and dimethyl 16,16'-(pyridine-2,6-diylbis(1H-pyrazole-3,1-diyl))dipalmitate (L3). We have synthesized and isolated crystals of the corresponding Fe(II) complexes: $[Fe(L1)_2](ClO_4)_2$ (**1**), $[Fe(L2)_2](ClO_4)_2$ (**2**) and $[Fe(L3)_2](ClO_4)_2$ (**3**). Single crystal X-ray diffraction (SCXRD) studies reveal that compound **1** and **2** are arranged in a bilayer lamellar organization with an anti-anti-anti (aaa) conformation. In contrast, compound **3** adopts a less densely packed structure with an anti-gauche-anti (aga) disposition, leading to the absence of the lamellar structure. However, interchain interaction is preserved through Van der Waals forces, albeit to a lesser degree. Variable temperature studies based on powder XRD, Raman spectroscopy, Differential Scanning Calorimetry (DSC) and Polarized Optical Microscopy (POM) demonstrate that the isolated crystals undergo multiple transformations such as crystal-to-crystal, crystal to isotropic liquid or isotropic liquid to liquid-crystal that agrees with previously reported amphiphilic compounds.[153] It is worth noting that the liquid crystal properties were characterized once the initial crystalline structure reaches disordered in an isotropic liquid. Magnetic measurements show that these compounds exist in a high spin state in both the crystal and the liquid crystal states. However, different phase transitions are accompanied by a decrease in magnetic susceptibility up to 300 K. Variable-pressure Raman spectroscopy undoubtedly confirms that the complexes can undergo a spin transition above 2 GPa, demonstrating the high compressibility of the alkyl chain within the crystal lattice, which enables lattice reorganization across an extensive pressure range before undergoing spin transition.

4.1.2 Synthesis

The synthesis of the ligand 3-bpp was carried out starting from the 2,6-diacetylpyridine following a previously reported synthetic route.[154] For obtaining the corresponding alkyl-functionalized 3-bpp, the N-pyrazole alkylation was performed using the corresponding Br-alkyl chain following a described method in literature.[155] L1, L2 and L3 were obtained in a relatively good yield. Metal complexes were obtained through the complexation of the corresponding tridentate ligand in CH_2Cl_2 and the stoichiometric amount of $Fe(ClO_4)_2 \cdot 6H_2O$ in EtOH. High-quality anhydrous crystals of compounds **1**, **2** and **3** suitable for single crystal X-ray diffraction were obtained through slow evaporation of the solvent mixture (CH_2Cl_2/EtOH) and isolated by filtration with a good yield. These crystals were subsequently analyzed using elemental analysis (CHN) and FT-IR spectroscopy. Thermal stability of the isolated crystal was examined in the range of 25 – 200 °C using thermogravimetric analysis (TGA), confirming the anhydrous character of the compounds. Synthetic procedure details can be found in Section 6.1.1 and 6.1.2.

4.1.3 Single Crystal X-Ray Diffraction (SCXRD) measurements

The crystal structure of all the compounds at 100 K was determined using single-crystal XRD techniques. Compounds **1** and **2** are isomorphic and crystallize in an orthorhombic space group P2/n, while **3** crystallizes in a tetragonal system**,** a primitive $I4_1/a$ space group (Table 6.1.1 – Table 6.1.3). The corresponding asymmetric units for all the compounds are shown in Figure 6.1.16 and Figure 6.1.17. The average Fe-N bond lengths obtained at 100 K are 2.184 Å (**1**), 2.172 Å (**2**), 2.164 Å (**3**) that are in agreement with the values expected for Fe(II) in HS (Table 6.1.4).[156] In all cases, Fe(II) display a distorted $\{FeN_6\}$ octahedral geometry. The

octahedral distortion can be quantified through Σ_{Fe} parameter, which is the sum of the deviations from cis N-Fe-N angles from 90°.[157] Σ_{Fe} values observed at 100 K are 146.07° (**1**), 139.05° (**2**), 143.09° (**3**). The correlation between a higher Σ_{Fe} parameter value and an increased Fe-N bond distance is noteworthy. The ϕ angle, which is the angle between $N_{pyridine1}$-Fe-$N_{pyridine2}$ (axial positions), could be also indicated of a distorted {FeN6} octahedral geometry. Compounds **1** (ϕ = 178.18°) and **2** (ϕ = 178.13°) exhibit deviations from an ideal octahedral geometry, unlike **3** (ϕ = 180.00).[68] To explain these differences, it is necessary to analyzed intermolecular interactions (Table 6.1.5).

An analysis of the packing of compounds **1** and **2** in the crystal reveals that they are ordered in a lipid layer-like arrangement (Figure 4.1.1) with an interdigitation of the alkyl chains of around 4.3 Å for **1** and 4.1 Å for **3**. This interdigitation is characteristic of Van der Waals interactions between the alkyl chains, previously observed in other amphiphilic complexes.[148,158] In this lipid layer-like arrangement, the closest Fe···Fe distance is approximately 9 Å, whereas the farthest Fe···Fe separation between layers is around 20 Å for compound **1** and 21 Å for compound **2**. Additionally, in compound **2**, an extra hydrogen bond interaction is established through the OH group, forming an O-H···O (perchlorate) interaction. Despite this additional interaction, the position of the perchlorate ions occupying the interstitial space outside the interdigitation of the alkyl chains remains largely unchanged compared to compound **1**.

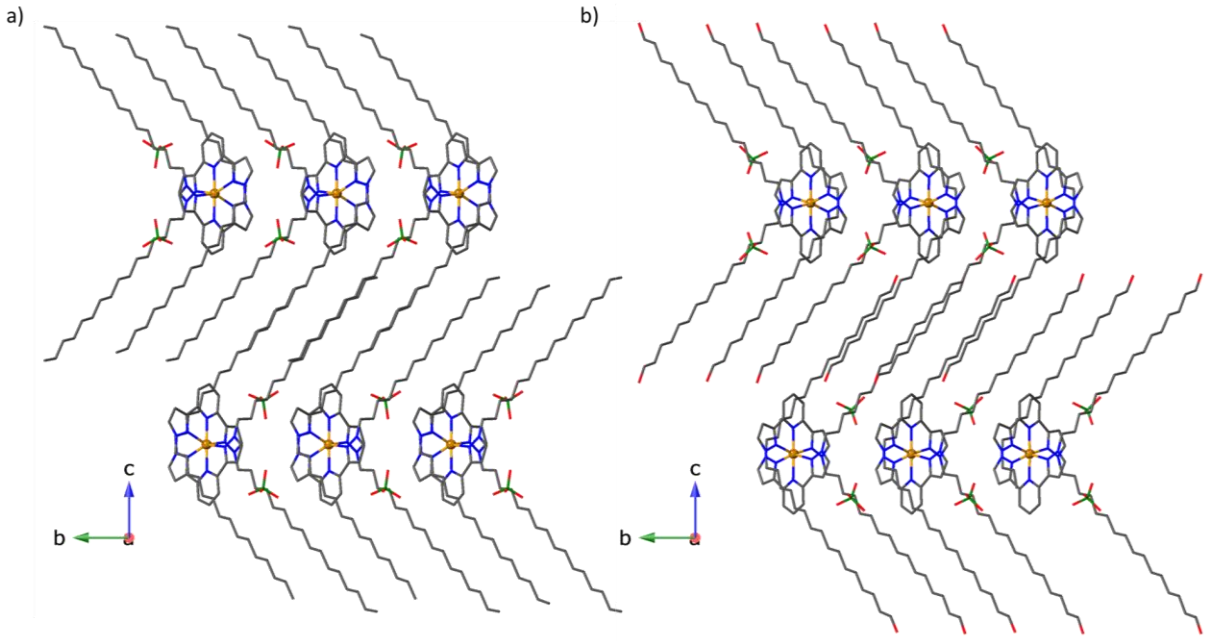

Figure 4.1.1. Ball and stick representation of the cationic layers of the Fe^{II} complexes stacked via Van der Waals along the *c* axis for compounds **1** (a) and **2** (b). Hydrogens and anions are omitted for clarity. Carbons are in grey, nitrogen in blue, oxygen in red, chlorine in green, and iron in orange.

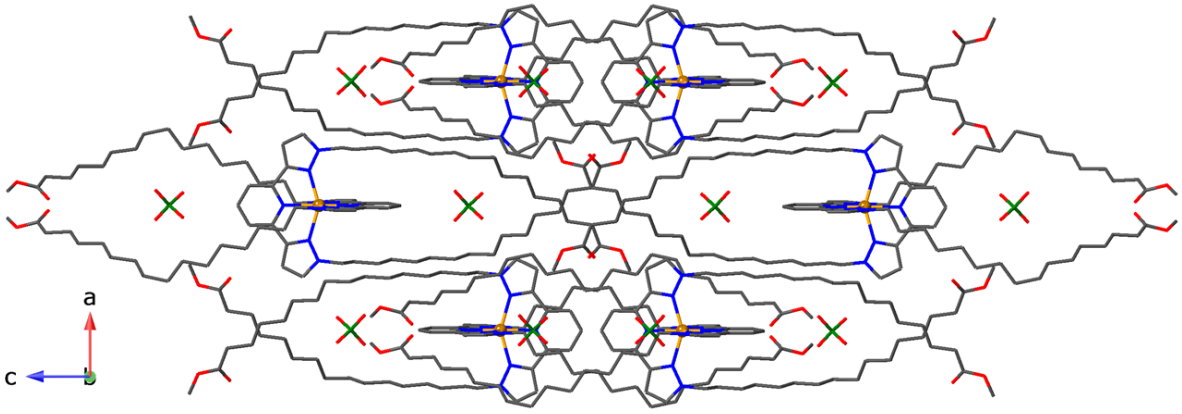

Figure 4.1.2. Ball and stick representation of the cationic layers of the Fe^{II} complexes stacked via Van der Waals along the *c* axis for compound **3**. Hydrogens and anions are omitted for clarity. Carbons are in grey, nitrogen in blue, oxygen in red, chlorine in green, and iron in orange.

For compound **3** the presence of a terminal ester group forces the alkyl chains substituents to be tilted (in a gauche form) in the 12-C of the chain (Figure 4.1.2). As the ester chain undergoes distortion, it forms an empty cavity between two opposing derivate bpp units, which is then occupied by the perchlorate ions, leading to their positioning away from the metal center. The packing in the *ab* plane is facilitated by Van der Waals forces between adjacent chains (4.9 Å), a distance significantly greater than the typical distance for lamellar organization (approximately 4 Å). Meanwhile, in the *c* direction, the chains are oriented toward each other between two adjacent bpp units, resulting in repulsion between ester groups, which is preferred in this direction. The shortest Fe···Fe distance corresponds to 13.289 Å in all three directions.

The disparities in crystal packing appear to be a crucial factor in forming a liquid crystal state. However, further characterization of these crystals is necessary to confirm this hypothesis.

4.1.4 Differential Scanning Calorimetry (DSC) and Polarized Optical Microscopy (POM) studies

Complexes **1**-**3** underwent investigation via DSC. However, to unequivocally identify each phase transition, POM experiments were carried out under identical experimental conditions (with heating and cooling rates of 2 °C·min^{-1}). Figure 4.1.3 presents the DSC data for the three compounds, along with corresponding images of each phase obtained through POM. It is noteworthy that Cr, Cr*, and Cr** labels denote three distinct crystalline phases, while the LC and IL labels signify a liquid-crystal-like phase and an isotropic liquid, respectively. Single crystals of the ligands (L1, L2, and L3) were analyzed using DSC and POM, revealing a solid-liquid fusion process followed by liquid-solid solidification. This confirms that the ligands themselves do not exhibit liquid crystal properties (Figure 6.1.18 - Figure 6.1.20). DSC and POM measurements conducted under the same conditions for compounds **1**-**3** showed a significant contrast compared to what was previously observed for the single crystal ligands. Additionally, phase transitions and temperatures vary depending on the functionalized terminal group, highlighting their dependence on the functional terminal group. Compound **1** exhibits at 90 °C and 114 °C two different crystal-to-crystal transformations (Cr → Cr*; Cr*→Cr**). Both processes have a similar enthalpy value (Table 4.1.1). Complete fusion of the complex is

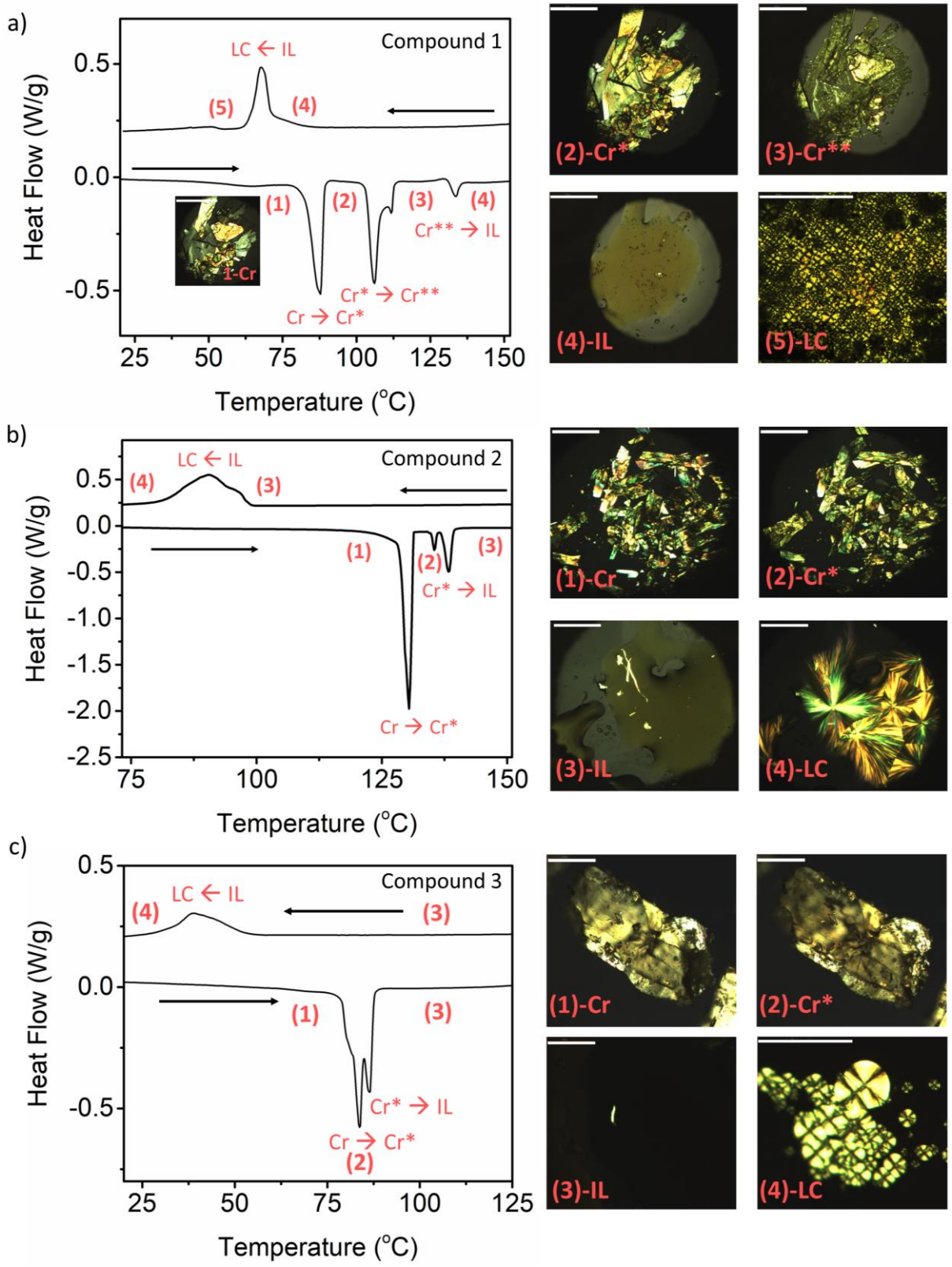

Figure 4.1.3. a) DSC measurements of **1** (a), **2** (b) and **3** (c) remarking each state and transition associated with a phase transformation. At the right part, polarized optical microscope images of different states. Cr, Cr* and Cr** refer to three different crystalline phases, LC is liquid crystal and IL, isotropic liquid. The scale bar corresponds to 200 μm.

achieved at 140 °C (Cr**→IL) being an endothermic process with a much lower enthalpy value. Fusion can be characterized as an isotropic liquid that shows no activity under polarized light. As the enthalpy associated with the Cr** to IL transition (4.49 kJ/mol) is lower compared to the crystal-to-crystal transformation, this suggests that Cr** exhibits a highly disordered packing, resulting in a lower energy requirement to reach the liquid state. On cooling, a liquid crystal state is started to be formed at 90 °C and remains stable until room temperature (Figure 4.1.3a). The pattern of the liquid crystal observed suggests the possibility of a smectic phase.[159] Compound **2** presents a single exothermic Cr→Cr* transformation at 130 °C with a large enthalpy value. This process is unusually exothermic when compared to compound **1**, where the structure and packing are similar. Thus, the difference observed in compound **2** appears to stem from supramolecular interactions of the hydrogen bonding type, which enhance its cohesion, explaining the higher exothermic nature of the process. For compound **2**, melting occurs at 150 °C (3-IL). Upon cooling, the liquid crystal state begins to form at 102 °C and persists until reaching room temperature. However, this semicrystalline state exhibits a liquid-crystal-like appearance with a distinct pattern compared to compound **1**, featuring a typical Maltese cross shape (Figure 4.1.3b). Compound **3** presents a crystal-to-crystal (Cr→Cr*) transformation before fusion. Melting is achieved at 100 °C (2-IL), notably lower temperature than **1** and **2**. Crystallization is observed on cooling starting at 58 °C until room temperature. Nonetheless, liquid crystal shows different pattern than compound **1** and **2**, typical of lamellar organizations. The experiments confirm that before fusion, the crystals undergo solid-solid transformations (Figure 4.1.3c). Moreover, it becomes apparent that the efficiency of liquid crystal transformation diminishes over successive cycles, accompanied by a shift in the peak of liquid crystal formation in DSC towards lower temperatures. This phenomenon arises from the recrystallization process, wherein crystals develop characteristic crack lines after multiple heating-cooling cycles, leading to reduced cooperativity within the system during phase transitions, thus promoting the appearance of dislocations (Figure 6.1.21 - Figure 6.1.23).[160]

Table 4.1.1. Thermodynamic parameters calculated from DSC for **1**-**3**.

1			**2**			**3**		
Process	**T (°C)**	**ΔH (kJ/mol)**	**Process**	**T (°C)**	**ΔH (kJ/mol)**	**Process**	**T (°C)**	**ΔH (kJ/mol)**
Cr → Cr*	87	49.37	**Cr → Cr***	130	83.8	**Cr → Cr***	84	53.7
Cr* → Cr**	110	45.12	**Cr* → IL**	136	19.1	**Cr*→IL**	87	22.05
Cr → IL**	133	4.49	**IL → LC**	90	91.69	**IL → LC**	39	19.5
IL → LC	67	39.92						

4.1.5 Variable-Temperature Powder X-Ray Diffraction (VT-PXRD) measurements

Phase transition changes were closely monitored using variable temperature powder XRD for compounds **1**-**3**, validating the transition temperatures observed in DSC and POM

experiments. It is noteworthy that the temperature required to induce liquid crystal formation was only reached for compound **3**.

The X-ray diffraction (XRD) profile and unit cell parameters for compound **3** at various temperatures are depicted in Figure 4.1.4a,b. At room temperature, sample displayed a distinct pattern typical of a crystalline substance. As it cooled from the isotropic liquid phase (90 °C), it exhibited a diffuse pattern characteristic of directional alignment, with noticeable variations in intensity. Subsequent systematic cooling revealed a sharpening of the intensity of the low-angle signal observed at 30 °C. At this temperature, PXRD pattern show two sets of diffuse anisotropic arcs (Figure 4.1.4c). The broad diffuse peak observed at wider angles, with a d-spacing of 4.05 Å, indicates the chain-chain correlation that contributes to the liquid-like appearance in the mesophase.[146]

For compounds **1** and **2**, no discernible transformations are observed; instead, notable peak shifts and an expansion of the unit cell parameters are evident. The diffractogram of compound **1** at 30 °C agrees well with the simulated powder pattern of the P2/n phase. As the temperature increases, the most notable change occurs in the peak at 2θ = 4.40°, which corresponds to lamellar packing in the crystalline arrangement of various materials.[137,161] At 80 °C, the coexistence of the Cr and Cr* structures are observed, and finally, at 110°C, the Cr** structure start to become amorphous. At 130 °C, although nearly amorphous, the structure retains a predominant order along the (00l) direction, where the chains are stacked assuming the crystalline structure maintains its monoclinic arrangement (P2/n). It is hypothesized that a liquid with oriented molecules exists, and upon solidifying, as observed in the cooling process, compound **1** crystallizes in an oriented or columnar fashion. Variable-temperature XRD measurements and simulated XRD pattern are provided in Figure 6.1.26 - Figure 6.1.30.

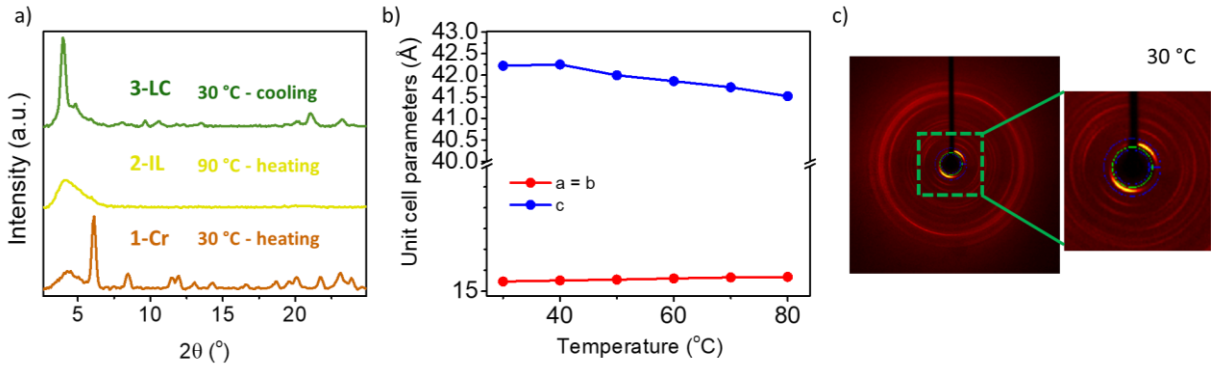

Figure 4.1.4. a) Variable temperature PXRD patterns of **3** recorded 30 and 90 °C on heating mode and 30 °C on cooling. b) Unit cell parameters variation of **3** showing shortening of *c*-axis through phase transitions. c) X-Ray pattern of the liquid crystal phase of 3 at 30 °C.

4.1.6 Magnetic measurements for the crystals and liquid crystals formed in 1-3 after heating

Thermal variation of the magnetic susceptibility (χ_M) measurements for compounds **1**-**3** were carried out in the 2 – 400 K temperature range to monitor crystal-to-crystal and crystal-to-liquid crystal phase transitions. As shown in Figure 4.1.5, compounds **1** and **3** exhibited different values for the product of the molar magnetic susceptibility with temperature ($\chi_M T$) for the crystal

and liquid crystal phases, with a characteristic drop in values after heating at 400 K. Before heating at 400 K, the initial $\chi_M T$ values found for **1** and **3** at 300 K were 3.89 and 3.25 emu·K·mol^{-1}, respectively. These values agree with the reported Curie values for Fe(II) centers in HS (3.25 – 4.06 emu·K·mol^{-1}) and the Fe-N bond distances found from single-crystal XRD measurements. A decrease in the $\chi_M T$ values is observed after 360 K for **1** and 357 K for **3**, reaching $\chi_M T$ values of 3.44 emu·K·mol^{-1} (**1**) and 3.01 emu·K·mol^{-1} (**3**) at 400 K (a decrease of approximately 10% and 16%, respectively). The temperatures at which $\chi_M T$ values change closely match the phase transition temperatures observed during the conversion of the Cr state to the corresponding Cr* state in the heating process for the DSC measurements. The changes observed in the magnetic measurements have previously been linked to a space group transformation, consistent with the crystal transformations observed in DSC and POM from 80 °C onwards. No alterations in the $\chi_M T$ values were observed after subsequent heating-cooling cycles, indicating that the crystal transformations occur irreversibly.

On the contrary, for compound **2** such change was not observed displaying the same $\chi_M T$ values before and after heating at 400 K as crystal-to-crystal transformation is not achieved under these conditions. This agrees with the single exothermic Cr→Cr* transformation observed for **2** at 130 °C from DSC measurements. It is noteworthy that all the measured phases exhibit a decrease in the $\chi_M T$ values upon cooling, indicative of spin-orbit coupling.

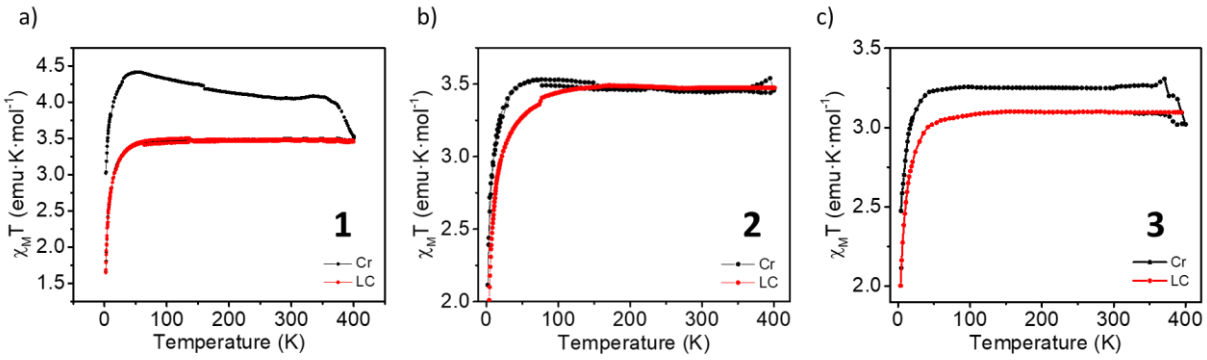

Figure 4.1.5. Temperature dependent $\chi_M T$ for **1**, **2** and **3** compounds. Samples were measured in both crystalline and liquid crystal phases after melting and cooling the compound down to room temperature. Cycle of the measurement was: Cr: 2 – 400 – 2 K; LC: 2 – 400 – 2 K at a heating/cooling rate 2 °C/min.

4.1.7 Raman spectroscopy: variable-temperature and variable-pressure measurements

Variable-temperature Raman spectroscopy was performed to distinguish additional characteristics of the formed liquid crystal phases, as no spin transition-associated changes are expected in this temperature range. Measurements were conducted in both cooling and heating modes using a temperature rate of 2 °C/min to ensure thorough observation of changes. However, while changes in bands associated with (C=N str, C=C str, 1650 cm^{-1}), (C=C str, -CH2- def, 1500 cm^{-1}), and (aromatic, 1000 cm^{-1}) were observed, these changes are attributed to the mobility of chains within the crystalline structure but are inconclusive in confirming fusion, liquid crystal formation, or precisely identifying the liquid crystal phase (Figure 4.1.6a-c, Figure 6.1.31 - Figure 6.1.33).[162,163]

Furthermore, as no spin transition has been observed under thermal variation, we propose that pressure could serve as a viable stimulus to induce a spin transition in the system, particularly at elevated pressures, given the high compressibility conferred by the chains. The only available method for such high-pressure investigations exceeding 1 GPa is the diamond anvil cell, allowing for the study through Raman spectroscopy.

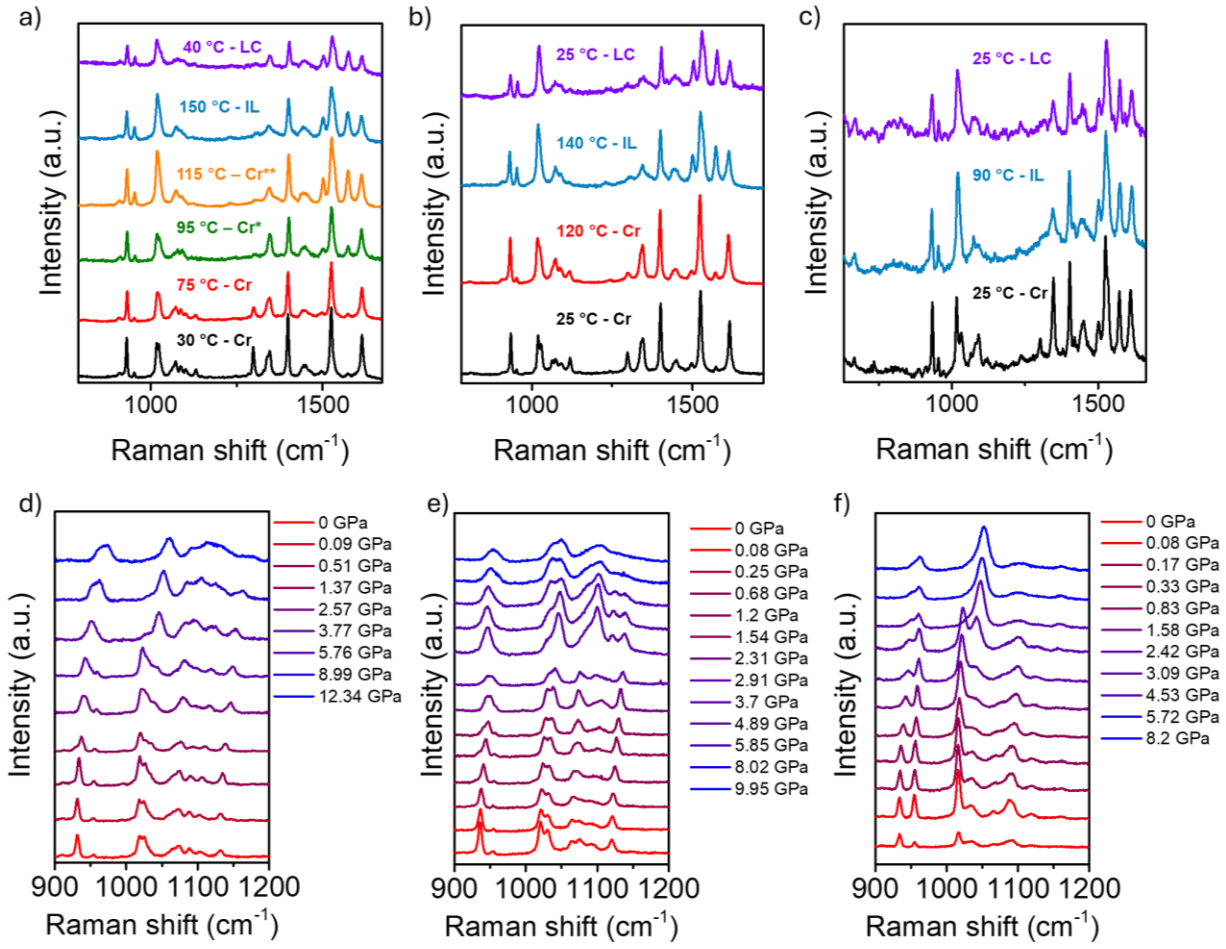

Figure 4.1.6. Variable-temperature Raman spectra on heating mode for **1** (a), **2** (b) and **3** (c). Variable-pressure Raman spectra for **1** (d), **2** (e) and **3** (f).

The temperature-dependent changes in the structure associated with the spin-state transition can be tracked by observing the Fe(II)–$N_{pyridine}$ stretching band in the Raman spectrum.[164] The Raman peak associated with pyridine ring breathing, coupled to the Fe(II)–N bond, occurs at ≈ 1020 cm^{-1} at room temperature. This signal shifts to a higher frequency in the LS state, reflecting the contraction of the Fe-N bond. Consequently, Raman spectroscopy proves valuable in monitoring the LS to HS transition and provides insights into the mechanism of the spin transition.

Experiments conducted confirms high compressibility of the alkyl chains within the crystal lattice prompting the complexes to undergo a spin transition within a high-pressure range, more than 3 GPa in the case of **1** and **3** and up to 2 GPa in the case of **2** (Figure 4.1.6d-f). This pressure range is uncommon for inducing spin transitions and is primarily linked to the significant compression of the alkyl chain.[99,101,103] The pressure range of the spin transition is

illustrated in Figure 4.1.7. In the case of **1**, the transition is observed above 3.77 GPa, indicating that the system is capable of reorganizing and compressing over a broad range of pressures until the transition occurs as can be seen in the shift of the bands as pressure increases. In the case of compound **2**, the transition occurs at 2.31 GPa. As the system is less compressible, these differences in compression primarily rely on variances in supramolecular forces, with an additional hydrogen bond established in this particular case. This bond introduces a degree of structural restriction, thereby diminishing compression of the alkyl chain part. Finally, **3** presents similar pressure ranges as compound **2** even differences in the crystal packing, but similar in the supramolecular interactions.

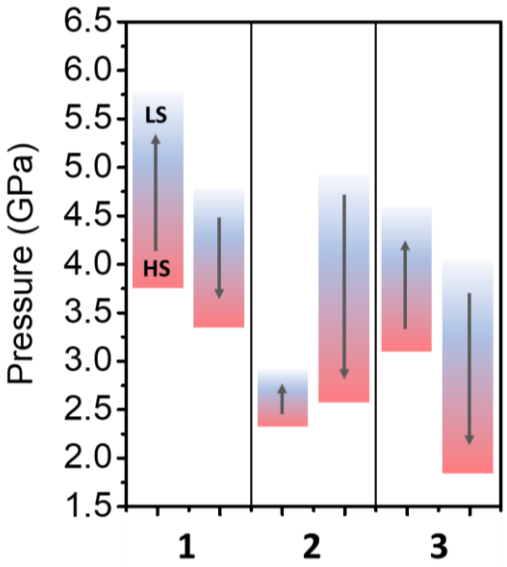

Figure 4.1.7. Pressure range for the spin transition for compounds **1**, **2** and **3** on press (arrow pointing up) and release mode (arrow pointing down).

4.1.8 Conclusions

In conclusion, this work explores the modulation of magnetic properties in Fe(II) metallomesogens, specifically focusing on the SCO transition influenced by pressure as an external stimuli. The incorporation of alkyl chains in these materials is investigated, revealing that alkyl chains do impede the spin transition, even with different functionalization.

The study introduces three novel Fe(II) metallomesogens with different terminal groups on a ligand functionalized with a 16-carbon alkyl chain. Crystallographic analysis demonstrates distinct arrangements in their crystalline structures, with terminal group of the alkyl chains playing a crucial role in the packing and organization of the complexes. The compounds exhibit multiple transformations at variable temperatures, assuming various semi-crystalline or liquid crystal-like phases typical for amphiphilic compounds.

DSC and polarized microscopy experiments further confirm the temperature-dependent phase transitions and the formation of liquid crystal phases in the complexes. The ligands alone do not display liquid crystal properties, emphasizing the role of metal complexes in inducing such behavior, influenced by the nature of terminal groups.

The magnetic properties of the complexes are investigated through SQUID measurements, revealing a high spin state in both crystal and liquid crystal phases. Variable-temperature Raman spectroscopy and variable-pressure Raman spectroscopy provide insights into the structural changes associated with the spin-state transition. The high compressibility of the alkyl chains is explored under applied pressure conditions, leading to spin transitions observed at pressures exceeding 2 GPa.

Overall, the comprehensive study sheds light on the interplay between molecular design, structural modifications, and external stimuli in controlling the spin transition behavior of Fe(II) metallomesogens. These findings contribute to the understanding of these materials for potential applications in advanced technologies and device functionalities.

4.2 Elucidating the Nature of Intermediate Spin States in SCO under Pressure

4.2.1 Background

The bistability associated to the low spin (LS)/high spin (HS) states in spin crossover molecular materials offers possibilities for applications in molecular switches, memories[21] and molecular-based spintronic devices[22], or energy harvesting.[103] Key for many of these applications is the ability to control the order of the phase transition, *i.e.* the possibility to design materials with either an abrupt first-order transition with a given thermal hysteresis, multiple spin-state transitions (hysteretic or not), or continuous spin crossovers.

There is a consensus that cooperativity among the local changes in the metal-ligand bond, introduced through long-range elastic interactions in molecular crystals, transform the continuous SCO into an abrupt first-order transition.[136,165,166] This is easily understood based on a Landau-type expansion of the free energy around the spin transition, in which the order parameter (the fraction of ions in the HS state) is coupled to the volume of the lattice.[167,168] If, associated to the spin transition the system undergoes a structural transformation, an intermediate spin state may stabilize for a strong enough coupling of the spin and crystallographic order parameters.[169] This intermediate phase consists of an ordered pattern of ions in their HS and LS states, with different proportions resulting in multistep spin state transitions.[135]

The stable intermediate spin states can be also understood from the perspective of elastic frustration: accommodating the different bond distances of the HS and LS to their equilibrium lengths might be difficult in certain crystal arrangements, resulting in a bond-mismatch and frustration. Paez-Espejo *et al.*[170] showed that this effect may be invoked as the microscopic cause of the stabilization of the intermediate spin state, and hence of the two-step transitions. In their model, the frustration enters the elastic energy through a parameter that measures the mismatch between the equilibrium bond-lengths in the HS and LS states. The authors showed that increasing the elastic frustration parameter reduces the spin transition temperature, at the time that changes it from first-order to two-step, or multistep. At HS/LS=1 in the intermediate spin state, spatial modulations minimize the elastic energy, as it happens in other spin crossover materials like $LaCoO_3$.[171] Several stable patterns, resulting in well-defined multistep transitions for other proportions of HS/LS were identified in elastic models when introducing longer range interactions.[172]

However, there is no obvious path to translate "*cooperativeness*" or "*frustration*" into actual crystalline coordination and molecular packing, which chemists may use as a guide to advance in the synthesis of these important class of materials. It seems, however, that some kind of bonding anisotropy introduced through directional and strong H-bonds, or the presence of guest molecules which introduce Van der Waals interactions, may frustrate the lattice bonding.

Here, we show that the spin state transition can be controlled, precisely, in a series of Fe(II) complexes coordinated to a new family of *para*-substituted 3-bpp: (**F**, **Cl**, **Br** and **I·H₂O**), $[Fe(p\text{-X-3-bpp})_2]^{2+}$ (X = F, Cl, Br, or I). We report the first synthetic route for *para*-X-3-bpp (X = F, Cl, Br, I). In octahedral Fe(II) complexes, the spin-state transition is accompanied by a large lattice expansion due to the occupation of the antibonding e_g states: LS, $t_{2g}^6 e_g^0$ (S=0) to HS, $t_{2g}^4 e_g^2$

(S=2). This effect is reinforced when coordinated by N-donor ligands, which make Fe(II)−N particularly suitable for studying the effect of cooperativity (and pressure) in the nature of the spin-state transition.[8]

We used high-pressure to fine tune the intermolecular interactions in this new family of Fe(II) spin crossover materials, which were studied by magnetization, Raman spectroscopy and X-ray diffraction experiments. Our results show that the size of the halogen bond can be used to determine the number and strength of anisotropic intermolecular connectivity in $[Fe(p\text{-X-3-bpp})_2]^{2+}$, which allowed us to control the nature of the spin-state transition, from continuous, to hysteretic first-order, or multistep. The results presented in this section are an important step forward for the design of spin crossover molecular materials with the desired spin-state transition.

4.2.2 Synthesis

Spin crossover molecular materials based on 2,6-bispyrazolpyridines (bpp) ligands are well documented in the literature.[44] However, whereas 1-bpp have been extensively studied because it can be easily functionalized,[39,48,173–176] 2,6-di(pyrazol-3-yl)pyridines (3-bpp) and specifically its *para* functionalization remains shortly studied since its high reactivity through free amines. However, introducing a halogen atom at the *para* position is an effective way of changing the intermolecular interactions without affecting the nearest neighborhood of the Fe(II) site.

Here we propose the first synthetic route for *para*-X-3-bpp (X = F, Cl, Br, I). The synthesis of the ligand 3-bpp is usually carried out starting from the 2,6-diacetylpyridine following previously reported procedure.[154] In this case, to obtain the *para*-substituted ligands, two distinct routes were designed due to the different stability of the halogenated pyridine under the reaction conditions. The ligand *p*-F-3-bpp was obtained in 3 steps in high yields. First, the fluorination of *p*-nitro-2,6-dichloropyridine using TBAF lead to fluorinated compound $\mathbf{L^F}$. A Suzuki-Miyaura reaction with 1-(Tetrahydro-pyran-2-yl)-5-(4,4,5,5-tetramethyl-[1,3,2]dioxaborolan-2-yl)-1H-pyrazole), prepared according to the bibliography,[177] was used to obtain bispyrazole 3 and a later THP deprotection reaction in acid medium to obtain compound 4 without further purification (Scheme 6.2.1). Ligands *p*-X-3-bpp (X = $\mathbf{L^{Cl}}$, $\mathbf{L^{Br}}$ or $\mathbf{L^{I}}$) were obtained from the corresponding *p*-substituted pyridine using a combination of previously described synthesis (Scheme 6.2.2). First, through a Minisci reaction 2,6-diacetylpyridine derivatives were obtained in moderated (6a-b) or low yields (6c). The next step consists of the condensation of the para-halogenated-2,6-diacetylpyridine with N,N-dimethylformamide dimethyl acetal to, finally, obtain the desired final ligands (8a-c) through a cyclization with hydrazine monohydrate. These last two steps were performed in quasi-quantitative yields and the compounds were isolated without further purification.[178,179]

After this synthetic route we obtained single crystals of the Fe(II) compounds coordinated to halogen functionalized 3-bpp in the *para*-position: $[Fe(p\text{-X-3-bpp})_2](ClO_4)_2$ (X = L^F (**F**), L^{Cl} (**Cl**), L^{Br} (**Br**) and L^I (**I·H₂O**); see Figure 4.2.1a). Note that in this structure the protons and the halogen in the pyrazole rings confer the possibility of establishing different types of interconnectivities between the molecules, thus modifying the cooperativity/frustration of the

molecular assembly, which makes this family of molecular material especially suitable for the kind of study planed in this section.

Millimeter-size crystals of the metal complexes were obtained by slow evaporation of the solvent from H_2O:MeOH 1:1 at room temperature (Figure 4.2.1b). In the case of **F**, after collecting an anhydrous complex, the dihydrate was also isolated from the crystallization media, **F·2H₂O**. For **Cl** and **Br** only dehydrated form was obtained, while only the hydrate form was isolated in the case of the **I** complex. Thermal stability of the complexes was analyzed by thermogravimetric analysis (Figure 6.2.26).

In Section 6.2.1, comprehensive chemical characterization is presented for the synthesis of the ligands, encompassing ^{1}H, ^{13}C, and DEPT-135 NMR data, as well as mass spectrometry results. Section 6.2.2 compiles the physical characterization of the metal complexes, including elemental analysis and infrared spectra.

4.2.3 Single-Crystal X-Ray Diffraction (SCXRD) studies

Single-crystal X-ray Diffraction (SCXRD) at 100 K show that the **F**, **Cl** and **Br** complexes are isomorphic, with the orthorhombic space group *Pbca*. Regarding the hydrated **I·H₂O** and **F·2H₂O** structures, both display the same orthorhombic space group, $P2_12_12_1$ (Table 6.2.1-Table 6.2.2).

All compounds present same general crystallographic asymmetric unit consisting in one molecule of $[Fe(p\text{-X-3-bpp})_2](ClO_4)_2$ (X = F, Cl, Br) with only one symmetry independent Fe(II) site. Additionally, the unit cell of **F·2H₂O** and **I·H₂O** complexes includes two or one water molecules, respectively (Figure 6.2.27). The halogen effect is noticed as a continuous increase

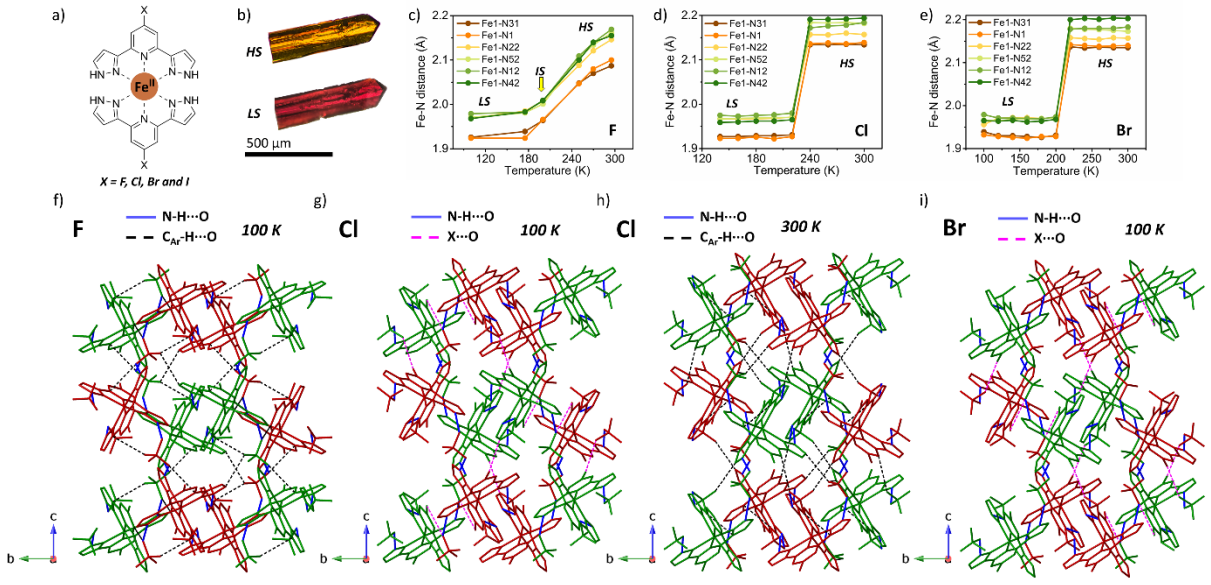

Figure 4.2.1. Structure of the para-functionalized X-3-bpp ligand (a). Optical microscopy image of a **Cl** crystal in the HS and LS state, showing a change in color (b). Evolution of the Fe-N distances across the spin-state transition for the **F** (c), **Cl** (d), and **Br** (e) compounds. Stick representation of molecular packing of **F** complex in the LS. The H-bonded molecular networks are shown in different colors (red/green) (f). Structures of **Cl** in LS (g) and HS (h) and for **Br** in LS (i). N-H···O bonds are shown as blue lines, C-H···O bonds as dashed black line and halogen bond in dashed pink line.

of the Fe−N length, from **F** to **Br**, although the most relevant effect of the halogen functionalization occurs in the second coordination sphere.[157] Upon heating to 300 K, mean bond lengths increase to 2.136 Å (**F**), 2.165 Å (**Cl**), 2.166 Å (**Br**). Elongation of bond lengths suggests all spin centers undergo spin transition in the range 100 - 300 K (Figure 4.2.1c-e). The gradual increase over a wide temperature range of **F** suggests an intermediate state before total transition since average Fe-N at 200 K is 1.993 Å, intermediate value between the reported values for LS and HS states. On the other hand, there is a steep change observed in **Cl** and **Br**, indicating an abrupt transition.

Regarding hydrated compounds, average Fe-N bond lengths are 1.954 Å (**F·2H$_2$O**) higher than anhydrous form, and 1.951 Å (**I·H$_2$O**), both indicating there are in the LS form at 100 K. The 0.014 Å increment in average Fe-N bond length (1.965 Å) in case of **I·H$_2$O** at 300 K indicates spin transition does not occur below this temperature (Table 6.2.7).

In all cases, Fe(II) ion is situated within a distorted {FeN6} octahedron. The octahedral distortion can be quantified through Σ_{Fe} parameter, which is the sum of the deviations from cis N-Fe-N angles from 90º. Some works have reported higher values of Σ_{Fe} are characteristic from weaker ligand field and a stabilization of HS and vice versa.[180] Σ_{Fe} values at 100 K are 95.65° (**F**), 94.76° (**Cl**), 97.33° (**Br**) and 93.73° (**I·H$_2$O**) at 300 K 133.66° (**F**), 147.18° (**Cl**), 147.95° (**Br**) and 97.47° (**I·H$_2$O**) indicating transition of **Br** occurs at lower temperature in comparison of **F** and **Cl**. The slight increase in **I·H$_2$O** is other indicative that transition does not occur below 300 K. **Cl** compound shows a discrepancy, which can be quantified also in the bite angle N_{pz}-Fe-N'_{pz} (ψ) being **Br** (157.74°) < **F** (158.01°) < **Cl** (158.37°), which increase upon heating due to volume increase. To explain this discrepancy, it is necessary to appeal not only the first coordination sphere but also the predominant interactions in the second coordination sphere (Table 6.2.8).[157]

A similar trend in unit cell parameters is observed in three compounds: the *a*-axis tends to be the most compressive and shortens due to the proximity of Fe···Fe along this direction, while the *b* and *c*-axes expand as a result of weakening hydrogen bond interactions with increasing temperature. The cell volume increases in all cases, as expected in HS. However, in the case of **F**, there is a significant volume expansion (> 4%) compared to **Cl** (> 1.6%) and **Br** (> 1.2%) (Figure 6.2.31).

The **F** complex at 100 K establishes 5 N_{pz}-H···O_{ClO4} bonds with an average distance N-H···O ≈ 2.845 Å which generates two identical interpenetrating three-dimensional networks that are related to each other by an inversion center. These networks are connected through H-bonds (C_{pyr}-H···O_{ClO4} and C_{pz}-H···O_{ClO4}) (Figure 4.2.1f). Upon heating, the system forms an additional H-bond at ≈ 200 K, stabilizing an intermediate phase (IS) with two quasi-independent sublattices. Very important, X-ray diffraction analysis does not show any change in the space group in the IS phase, which maintains only one Fe(II) center. The additional H-bond and the connection through C-H···O bonds of the **F** complex are lost at room temperature.

Cl and **Br** compounds show a halogen bond (Cl_{bpp}···O_{ClO4} = 3.102 Å or Br_{bpp}···O_{ClO4} = 3.364 Å), as well as the 6 H-bonds at 100 K (Figure 4.2.1g,i). The H-bond distances increase slightly with respect to **F**, in **Cl** (N-H···O ≈ 2.903) Å) and **Br** (N-H···O ≈ 2.915 Å). Interestingly, the **Cl** compound loses the halogen bond at room temperature, forming two identical interpenetrating structure that resembles the intermediate temperature phase observed in **F** at 200 K (Figure

4.2.1h). In the case of **Br**, the 3D structure is maintained in the whole temperature range, from 100 K to room temperature.

Finally, in **I·H₂O** only 3 of the NH groups of the pyrazoles form a H-bond with the ClO_4^-, the fourth being replaced by N-H···O bonding with the oxygen of a water molecule (N-H···O ≈ 2.940 Å). The same happens in the hydrated complex of **F·2H₂O**.

4.2.4 Magnetic Susceptibility measurements

The temperature dependence of $\chi_M T$ for the complexes is shown in Figure 4.2.2a. The T_c decreases and the nature of the spin transition changes, in a good correspondence with the differences in the structure observed by X-ray diffraction: **I·H₂O**, with only 3, long N-H···O_{ClO4} bonds, shows a continuous second order transition, from a 100% LS fraction to an approximately 50% HS fraction at 400 K ($\chi_M T$ = 1.92 emu·K·mol^{-1}). Increasing the number of shorter H and X-bonds drives the system into a hysteretic first order (**Br** and **Cl**), characteristic of coupled lattice and spin degrees of freedom, with total spin conversion. Finally, for the very short distances of **F** purely consisting of hydrogen bonds, an intermediate plateau separates a hysteretic first-order transition with higher connectivity at low temperature from a continuous one at high temperature. The value of $\chi_M T$ upon cooling from 325 K (≈3.5 emu·K·mol^{-1}) to 200 K ($\chi_M T$ ≈ 1.9 emu·K·mol^{-1}) is consistent with an intermediate spin state in this material. Note that this intermediate spin state coincides with the intermediate phase identified in X-ray diffraction, where the pattern of H-bonds stabilizes two identical interpenetrating three-dimensional networks at 200 K. However, different to previous reports, spin state is not associated to a crystallographic transition.[17–19] The strength of the H-bonds and their precise influence on the nature of the spin-state transition can be further tested by introducing guest molecules.

In case of hydrated sample **F·2H₂O**, the first cycle between 2 K and 400 K presents a gradual spin transition from 325 K to (100% HS) to 128 K (100% LS). A hysteresis cycle is observed at 178 K (ΔT = 12 K, $\chi_M T$ = 0.65 emu·K·mol^{-1}) that implies only 18% HS population present hysteresis, reaching 100% HS state at 335 K in a gradual transition (T_c = 228 K). Additionally, the second cycle aligns with the recorded date for the anhydrous form **F**, as the first cycle surpasses the dehydration temperature under SQUID conditions. After two cycles, the sample underwent analysis by single crystal X-ray diffraction to demonstrate solvent molecule loss, thus corroborating the dehydration hypothesis. It was confirmed that the compound remains stable after dehydration under SQUID conditions and exhibits the same crystallographic parameters as **F**. Notably, the average bond distances increase compared to the anhydrous phase, and one of the H-bonds with the ClO_4^- ion is replaced by water. This alteration in the H-bond interaction results in an increased temperature of the SCO, alongside a reduction in the LS-IS hysteresis and enhanced stability of the intermediate state (Figure 6.2.38). Magnetic behavior was confirmed by DSC measurements (see Section 6.2.5).

The LS to HS photoconversion was investigated by irradiating crystals at 10 K (λ_{exc} = 630 nm). A drastic increase in the magnetic signal was observed after irradiation. The value of **F** after irradiation is 2.73 emu·K·mol^{-1}, consistent with 80% of the centers reaching the metastable HS

state. **Cl** and **Br** reach 3.5 emu·K·mol^{-1}, consistent with total conversion to the metastable HS state. In the case of **I·H$_2$O**, the value reached after irradiation is 2.45 emu·K·mol^{-1} (70% HS).

These results align with magnetic measurements, indicating that the metastable HS state remains stable across a wide temperature range, with relaxation processes following first-order kinetics in systems exhibiting an abrupt spin transition, such as **Cl** and **Br**. Conversely, less cooperative systems, **F** and **I·H$_2$O** show incomplete saturation of the HS metastable state and non-linear relaxation, resulting in lower T_{LIESST} (Figure 6.2.37a).

4.2.5 Variable-Temperature Raman Spectroscopy measurements

The microscopic changes in the structure associated to the spin-state transition can be followed through the temperature dependence of the Fe(II) – $N_{pyridine}$ stretching band in the Raman spectrum. The pyridine ring breathing, coupled to the Fe(II) – N bond distance, shows a Raman peak at ≈ 1020 cm^{-1}, at room temperature; this signal appears at higher frequency in the LS state, due to the contraction of the Fe-N bond. Therefore, Raman spectroscopy can be used to follow the LS to HS transition in [Fe(*p*-X-3-bpp)$_2$]$^{2+}$ and help us to deciphering some features about mechanism of the spin transition.[164]

In the **F** complex, the peaks of the LS and HS state coexist in the temperature region of the χ_MT plateau, which confirms the coexistence of HS and LS Fe(II) centers in the IS (Figure 4.2.2b). In the **Br** and **Cl** complexes, spin transition is abrupt in accordance with the magnetic susceptibility (Figure 4.2.2c,d). Besides, in the case of **Br**, the Fe(II)–$N_{pyridine}$ stretching band, at 1025 cm^{-1} splits in two different vibrational modes when transition to LS state (1030 and 1040 cm^{-1}). This phenomenon is attributed to an anisotropic axial strain.[181]

Finally, in **I·H$_2$O**, the two bands corresponding to the LS and HS states coexist, and move very gradually without shifting, which suggests a crossover rather than a true phase transition (Figure 4.2.2e).

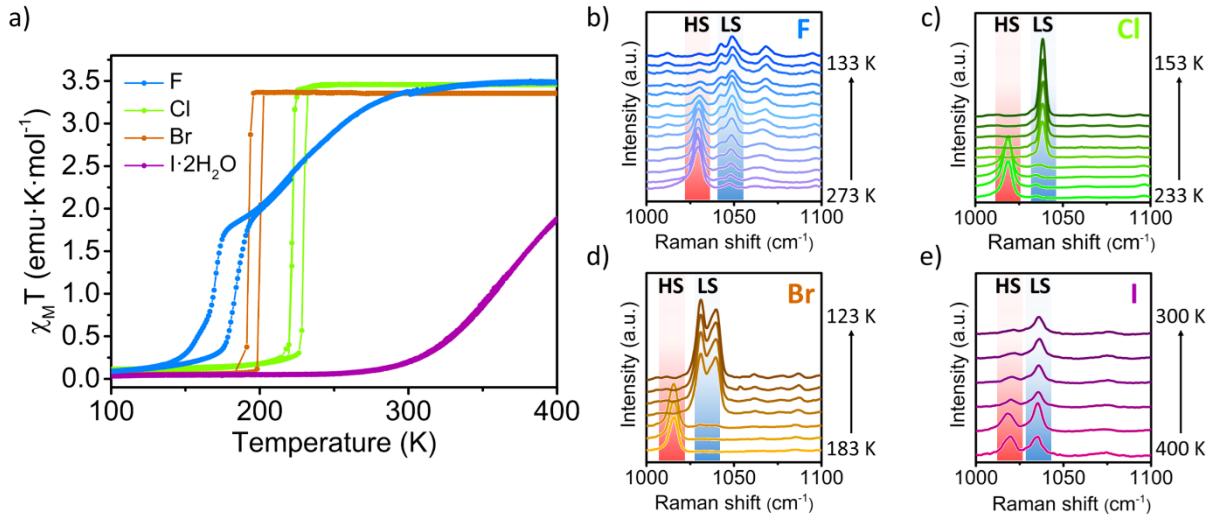

Figure 4.2.2. a) Temperature dependent χ_MT for F, Cl, Br and I·H$_2$O compounds. For the case of I·H$_2$O, the transition to the HS cannot be completed at 400 K, the highest available in our magnetometer. Raman spectra recorded on cooling of F (b), Cl (c), Br (d) and I·H$_2$O (e) in the 1000-1100 cm^{-1} range. The order and magnitude of the temperature scan is indicated to the right of each panel.

Section 6.2.6 provides the Raman spectra for **F**, **Cl**, **Br**, and **I·H₂O** in both cooling and heating modes, covering the temperature range associated with the spin transition.

Therefore, *para*-halogen substitution in the 3-bpp ligand, allows a very fine control in the intermolecular connectivity of Fe(II) sites, through the number and strength of hydrogen and halogen bonds, which is translated into a systematic variation of the nature of the spin-state transition. Additionally, pressure serves as a particularly suitable control parameter for this type of study, as it can induce changes in supramolecular interactions. Consequently, it may modify the sign of the quadratic parameter in the Landau expression for compressible lattices, especially when the coupling between the spin order parameter and the lattice volume is sufficiently significant. Such modifications can drive a second-order phase transition into a first-order one without requiring a crystallographic transformation to act directly upon the atomic lattice, thus avoiding the added complexity of chemical doping.

4.2.6 Variable-Pressure Magnetic Susceptibility and Raman Spectroscopy studies

As shown in Figure 4.2.3, the general effect of pressure is to increase the stability of the IS state. In the case of **F** (Figure 4.2.3a,d), a very small pressure stabilizes the IS state at room temperature, with the IS state being observed across a wide pressure range.

For **Cl** (Figure 4.2.3b), increasing pressure beyond 0.1 GPa transforms the first-order hysteretic transition into a two-step transition, with a plateau at $\chi_M T$ corresponding to an intermediate spin of HS/LS ≈ 1. This plateau spans over a wider temperature range as the applied pressure increases, demonstrating that pressure stabilizes the intermediate spin state. Note that in **Cl**, the H-bond network of the HS state at room temperature is quite similar to the H-bond network in **F**. High pressure Raman spectroscopy (Figure 4.2.3e) confirms the coexistence of the HS and LS ions in the intermediate spin state stabilized at high pressure in **Cl**. This behavior is completely reversible, recovering the single-step transition after releasing the pressure (Figure 6.2.39). Therefore, pressure drives the **Cl** complex between different spin states $\{Fe^{LS}\} \leftrightarrow \{Fe^{IS}\} \leftrightarrow \{Fe^{HS}\}$, reversibly and at room temperature, in what constitutes a kind of pressure-driven switch spin system. This unusual behavior can be correlated to the structural and subtle color changes of **Cl** under pressure (Figure 4.2.4a-c): high-pressure X-ray diffraction of the **Cl** compound confirms that the crystal structure of IS state, between 0.51 – 0.59 GPa at 300 K, maintains the same space group as the LS and HS phases. There is not a significant difference in the Fe-N distances between IS and LS phase (Table 6.2.13-Table 6.2.14).

Finally, for **Br**, the first-order transition is kept over the entire pressure range, with an increasing hysteresis from 6 K at 0 GPa, to 16 K at 0.95 GPa (Figure 4.2.3c,f).

In Section 6.2.9, the Raman spectra of **F**, **Cl** and **Br** are provided across the entire pressure range studied, from 0 to approximately 12 GPa. By tracking the variation of the characteristic bands of HS (1019 cm^{-1}) and LS (1039 cm^{-1}), it is possible to discern a trend regarding the compressibility of the HS and LS phases in each of the compounds. As expected, the HS phase (more extended) exhibits higher compressibility compared to the already "compressed" LS phase. Furthermore, it is noteworthy that the characteristic LS band, which split in the case of **Br** in the variable-temperature experiments, does not display the same splitting in the LS

phase attained under pressure, suggesting that pressure reduces bond anisotropy, thereby forcing the bond in a preferred direction.

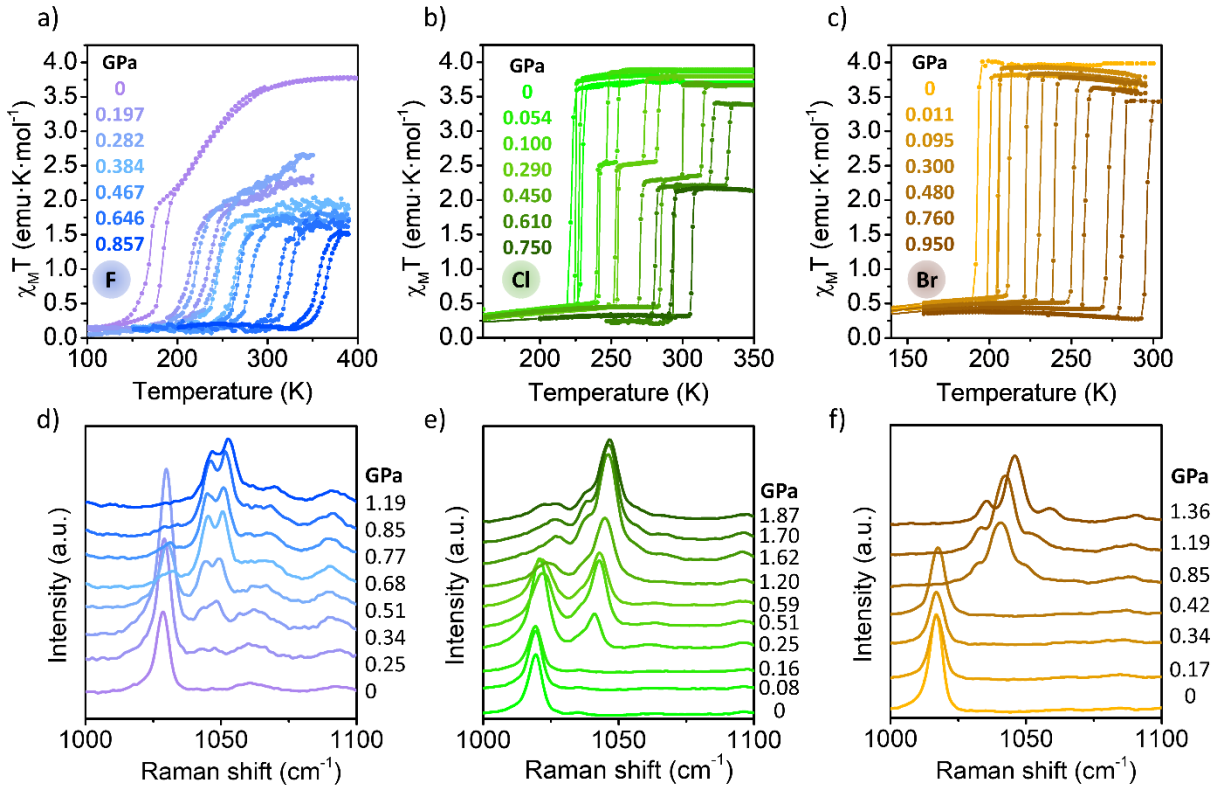

Figure 4.2.3. Top: $\chi_M T$ versus temperature for **F** (a), **Cl** (b) and **Br** (c) at different pressures. There is a small background of $\chi_M T \approx 0.25$ emu·K·mol^{-1}. Bottom: Room temperature Raman spectra for **F** (d), **Cl** (e) and **Br** (f) at different pressures. The comparison of panel b) and e) shows the coexistence of the LS and HS peaks in the intermediate pressure range of the **Cl** system, characteristic of the intermediate spin state.

4.2.7 Variable-Pressure Single Crystal X-Ray Diffraction measurements

The high-pressure results for the different spin states of **Cl** show that a crystallographic transformation, with two different Fe(II) sites, is not a prerequisite for the stabilization of an intermediate spin state. It is a delicate balance of the strength and number of N-H···ClO_4^- H-bonds what determines the nature of the phase transition. This, in turn, can be controlled either by the size of the halogen in the *para*-position of the 3-bpp ligands, or by pressure. With the shorter H-bonds of the series, the excitation of higher-volume HS centers in the **F** as the T_c is

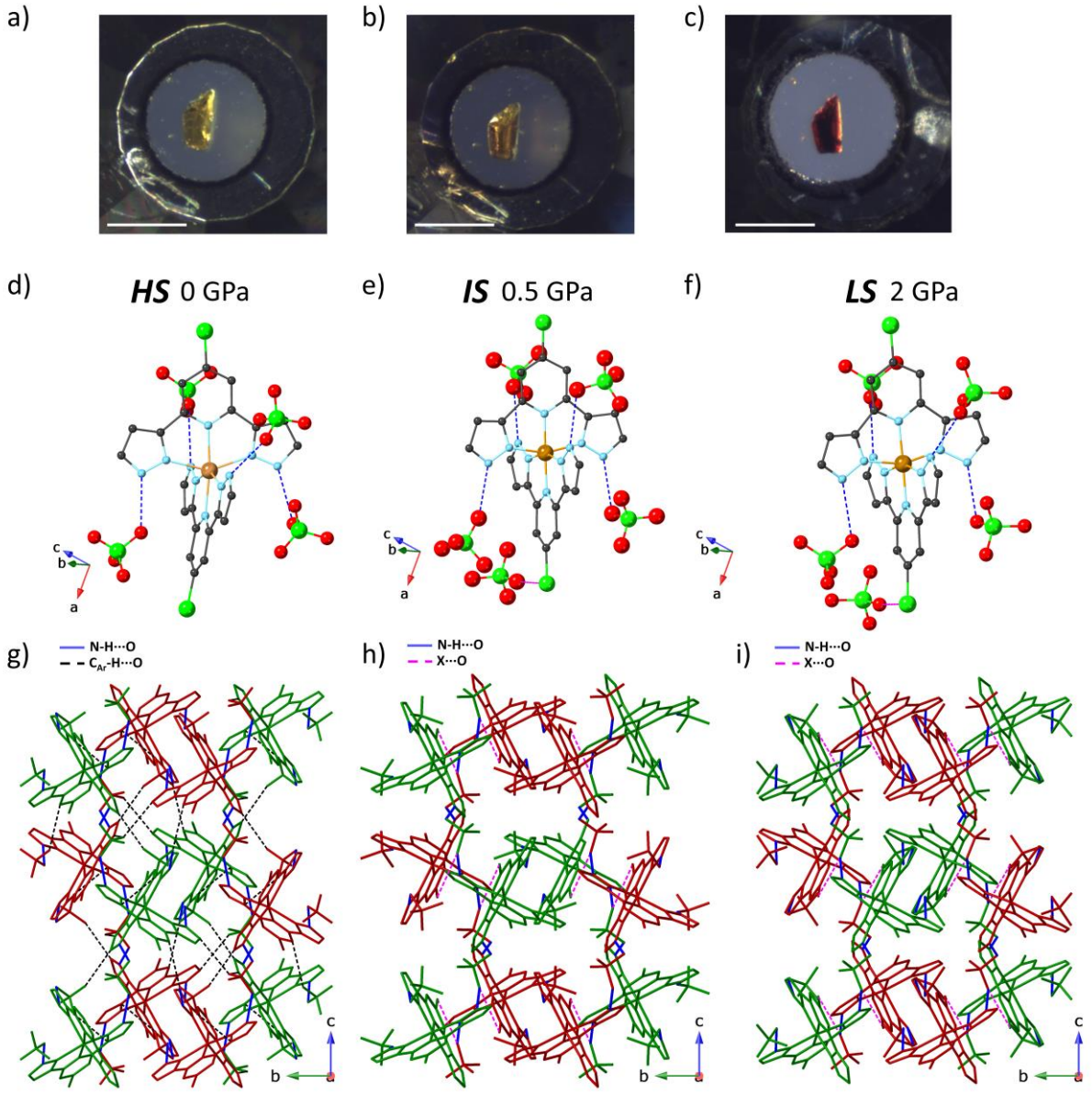

Figure 4.2.4. Images of a single crystal of **Cl** compound in DAC cell at 0 GPa (a), 0.5 GPa (b) and 2 GPa (c) applied pressure. Scale bar is 200 μm. Ball and stick representation of the second coordination sphere of **Cl** at d) 0, e) 0.5 and f) 2 GPa. Stick representation of the 3D supramolecular structure of **Cl** at g) 0, h) 0.5 and i) 2 GPa. In general, chlorine is green, oxygen is red, nitrogen is light-blue, carbon is grey, and iron is light brown. Hydrogen atoms are omitted for clarity. N-H···O bonds are shown as blue lines, C-H···O bonds as dashed black line and halogen bond in dashed pink line.

approached from the LS side, will introduce a strong bonding anisotropy. The lattice solves this problem stabilizing the IS at 50% population of HS and LS through a spontaneous segregation of two sublattices with very weak interactions. This structure must be the most favorable, in the elastic energy terms, like the spontaneous segregation of HS and LS ions in ordered patterns predicted by Paez Espejo *et al*.[170] and J. Cruddas *et al*.[172]

Replacing **F** by **Cl** increases slightly the length of the H-bonds, and the HS state resembles the IS state of **F** (Figure 4.2.4d,g). Increasing pressure reduces the H-bonds and establishes a new interaction, a halogen bond, leading towards a situation close to that in **F**, and stabilizes an intermediate spin state, and the temperature range of stability of the IS state grows with pressure (Figure 4.2.4e,h). An increase in pressure in LS does not result in the formation of a second halogen bond (Figure 4.2.4f,i). These results demonstrate that the anisotropy introduced by H-bonds frustrates the elastic interactions in the lattice during the LS-to-HS transition. Therefore, ligands and counterions with a large number of H-bonding active sites should promote multistep spin state transitions.[18,19,182]

4.2.8 Conclusions

We have developed a novel series of functionalized *p*-X-3-bpp ligands (where X = F, Cl, Br, and I) aimed at influencing the nature of the spin-state transition in Fe(II) coordination compounds. This modulation is achieved by finely balancing intermolecular H-bond and X-bond interactions, which are dictated by the size of the halogen. Larger halogens (Cl, Br, and I) facilitate the establishment of halogen bond interactions (X···O), while the smallest one (F) does not exhibit this phenomenon.

This effect is intricately linked with the ability of SCO systems to undergo volume expansion during the SCO transition, directly impacting the supramolecular interactions involved. We have demonstrated that sufficiently strong H-bonds, such as those in **F**, stabilize an intermediate spin state without a crystallographic phase transition.

Furthermore, our studies on the high-pressure IS and LS phases of **Cl** have revealed that induced halogen bonding plays a pivotal role in highly cooperative systems. This suggests that lattice frustration introduced by highly directional H-bonds, coupled with the loss of one halogen bond, stabilizes the intermediate spin state.

Finally, we have shown the feasibility of reversibly transitioning between different stable spin states $\{Fe^{LS}\} \leftrightarrow \{Fe^{IS}\} \leftrightarrow \{Fe^{HS}\}$ at room temperature using pressure, representing a novel form of pressure-driven spin switching.

These findings offer invaluable insights for the development of ligands that can effectively control the nature of SCO by potentially establishing supramolecular interactions. Such insights are essential for predicting and controlling the switching properties of this important class of molecular materials.

4.3 Tuning field-induced Single Ion Magnet Properties via Co(II) Halogen Ligand Substitutions

4.3.1 Background

Single Ion Magnets (SIM) are a group within the family of Single Molecule Magnets (SMM).[104] Since their discovery in 1991[183] their study has been intensified due to their potential application in information storage,[105] spintronics[106] and quantum computing.[107] Usually, these materials are composed by a metal ion -typically a lanthanoid-, but, in the last decades the study with first row of transition metals with d^4-d^7 electronic configuration has been increased for its abundance and cheaper cost.[108]

For the case of those that imply electronic transitions within the *d*-orbitals, zero-field relaxation usually occurs very rapidly due to quantum tunnelling.[184] To observe SIM behavior, which typically involves long-lived magnetic states or slow relaxation processes, an external perturbation is often necessary to prevent or slow down the rapid relaxation mechanisms. Applying a direct current (DC) magnetic field is one such perturbation commonly used in experiments, in a subfield called as field-induced SIM.

Systems based on Co(II) are the most reported,[110,185] despite other systems containing Fe(II)[186] or Ni(II)[187] have been also studied. Cobalt(II) presents two different possible half-integer spin states (S = 1/2 or S = 3/2) and has been discovered to exhibit zero-field SMM behavior in different coordination geometries such as tetrahedral,[188] trigonal prismatic,[189] lineal[190,191] or octahedral.[111] In the case of an octahedral environment, SIM phenomena are observed when distortion is accused resulting in breaking the degeneracy of the energy levels.[113] A well-studied series of SIM are those with [Co(II)N6] coordination environment in which some of the nitrogen donors are forming part of a heterocycle.[192–195]

It is well known the correlation between the molecular symmetry and the anisotropy, thus, to explore methods to modulate the distortion of metal complexes could be an instrument to obtain SIM behavior.[196] There are many examples of distorted geometries with rigid ligands where, the distortion is programmed by the ligand with tensional restrictions.[197] However, this methodology is very difficult to control due to the existence of supramolecular forces in the crystal structure.[198] Considering the coordination compounds as non-isolated molecules and crystal packing effects in solid state, we can use the supramolecular forces to modify the molecular symmetry by establishing new supramolecular interactions.

One highly versatile polydentate ligand known for establishing intermolecular interactions is 2,6-bis(pyrazol-3-yl)pyridine (3-bpp).[44] This ligand possesses two NH groups that strongly tend to form hydrogen bonds with anions, solvents, or neighboring molecules. Examples abound of Spin Crossover (SCO) systems involving Fe(II)[48,199] and Co(II)[200] based on this ligand, where the NH groups significantly influence the magnetic properties of the system. However, this functionality is not enough to induce a distortion on the metal complex. While numerous examples of functionalization exist for the isomer 1-bpp,[117–119,201] 3-bpp remains largely unexplored and represents a challenge in this field due to the heightened reactivity of its NH positions, making direct functionalization difficult to achieve. Halides (F, Cl, Br, I) are particularly useful functional groups for establishing halogen bonds, interactions that have not been extensively studied. These bonds, formed by electrophilic halogens, are characterized

by a strong directional character. In Section 4.2, we have demonstrated that these ligands, in the presence of Fe(II), can modulate spin transition through the supramolecular interactions established (hydrogen and halogen bonds).

Substitution in the *para*-position is crucial due to its direct impact on the metal complex. This position aligns with the axial direction of the octahedral geometry, thereby inducing a single ion magnet effect. Introducing halogen functionalization in the 3-bpp molecule allows for the combination of halogen bonds with hydrogen bonds, enhancing the overall interactions and potentially influencing the magnetic properties of the system.

In this work, we explore the influence of these *para*-halogen-substituted 3-bpp ligands in SIM behavior. We focus on the study of these ligands involved in the obtaining of Co(II) metal complexes $[Co(p\text{-X-3-bpp})_2](ClO_4)_2$ (X = **F, Cl, Br, Br·2H₂O, I·2H₂O**) and the analysis of the 3D structures obtained by Single-Crystal X-Ray Diffraction (SCXRD) results. Distortion of a perfect octahedral environment confers to these systems unique properties and big differences in the magnetic behavior, which could influence the size of the barrier to reversal of magnetization and their slow relaxation process. The study and understanding of these structural differences would aid in comprehending the variances observed in the magnetic behavior of the compounds. Thus, we will endeavor to establish correlations and/or trends between structural parameters, such as single ion anisotropy and orbital splitting, among other factors. Understanding these relationships may shed light on the modulation of energy barriers and the mechanisms underlying slow relaxation of the magnetization. Thus, we contribute new evidence for a rational control in the design of single ion magnets.

4.3.2 Synthesis

Ligands *p*-X-3-bpp (X = F, Cl, Br or I) were obtained according to the procedure outlined in Section 6.2.1. Metal complexes were obtained by direct synthesis of corresponding ligand and the stoichiometric amount of $Co(ClO_4)_2 \cdot 6H_2O$ in methanol at room temperature. Crystals were isolated by slow evaporation of the organic solvent in a relatively good yield. We found five different crystals depending on its substituted halogen $[Co(p\text{-F-3-bpp})_2](ClO_4)_2$ (**F**), $[Co(p\text{-Cl-3-bpp})_2](ClO_4)_2$ (**Cl**), $[Co(p\text{-Br-3-bpp})_2](ClO_4)_2$ (**Br**), $[Co(p\text{-Br-3-bpp})_2](ClO_4)_2 \cdot 2H_2O$ (**Br·2H₂O**), $[Co(p\text{-I-3-bpp})_2](ClO_4)_2 \cdot 2H_2O$ (**I·2H₂O**).

The crystal structure analysis revealed that compounds **F** and **Cl** were obtained in their anhydrous forms while compound **Br** appeared in two well-defined crystal structures. Acicular crystals were found for compound **Br·2H₂O**, whereas cubic crystals were obtained for the compound **Br** in a 1:3 ratio. On the other hand, only the hydrated form was observed for the compound **I·2H₂O**. We appreciate a clear tendency to accommodate water molecules in the secondary coordination sphere as the larger size of the halogen, thus the bromine ligand represents a transition point between anhydrous-hydrated structure stability.

These compounds were characterized using common solid-state analysis techniques such as FT-IR, EA and SCXRD, as detailed in Section 6.3.1. Thermal stability was studied using thermogravimetry thermal analysis (TGA). The results indicated that **F-I·2H₂O** exhibited thermal stability in the range of 25 °C – 220 °C. Moreover, it reveals solvent removal is produced before in **Br·2H₂O** than in **I·2H₂O** (Figure 6.3.6).

4.3.3 Single-Crystal X-Ray Diffraction (SCXRD) measurements

Single-crystal X-ray Diffraction (SCXRD) was used to determine the crystal structure of all the compounds at 100 K. Group of anhydrous compounds **F, Cl** and **Br** (Figure 4.3.1) and hydrated ones **Br·2H₂O** and **I·2H₂O** (Figure 4.3.2) are isomorphic in orthorhombic space group *Pbca* (Table 6.3.1 and Table 6.3.2). All anhydrous compounds present same general crystallographic asymmetric unit consisting in one unit of $[Co(p\text{-}X\text{-}3\text{-}bpp)_2](ClO_4)_2$ (X = F, Cl, Br, I). Additionally, in case of hydrated complexes, **Br·2H₂O** and **I·2H₂O**, the asymmetric unit cell includes two water molecules.

In all cases, Co(II) ion is situated within a distorted CoN6 octahedron. The deviation of the CoN_6 coordination environment from a regular octahedral geometry is expected to influence the magnetic properties of the metal complexes. This deviation becomes evident when analyzing the distortion indices Σ and Θ for the Co^{II} complexes. Σ measures the deviation of a metal ion from an ideal octahedral geometry considering the sum of the deviation of the 12 cis N–Co–N angles from 90°, while Θ indicates its distortion from an octahedral towards a trigonal prismatic structure as the sum of the 24 N–Co–N angles measured on the projection of two triangular faces of the octahedron along their common pseudo-threefold axis.[157] Both indices were obtained using the OctaDist program[202] and their values deviate significantly from Σ = Θ = 0, which would indicate a perfect octahedral geometry. In both parameters, we observe a clear trend toward greater distortion from **F** to **Br**. If water molecules are introduced into the coordination sphere, with **Br·2H₂O** and **I·2H₂O**, the distortion decreases significantly.

In the specific case of these compounds, the angles that reveal the most information are θ and ϕ, which measures the angular Jahn-Teller distortion, the ideal values for a perfect octahedral environment θ = 90° and ϕ = 180°. Regarding anhydrous compounds, the metal coordination environment shows a pronounced distortion from an octahedral geometry as shown Σ and Θ

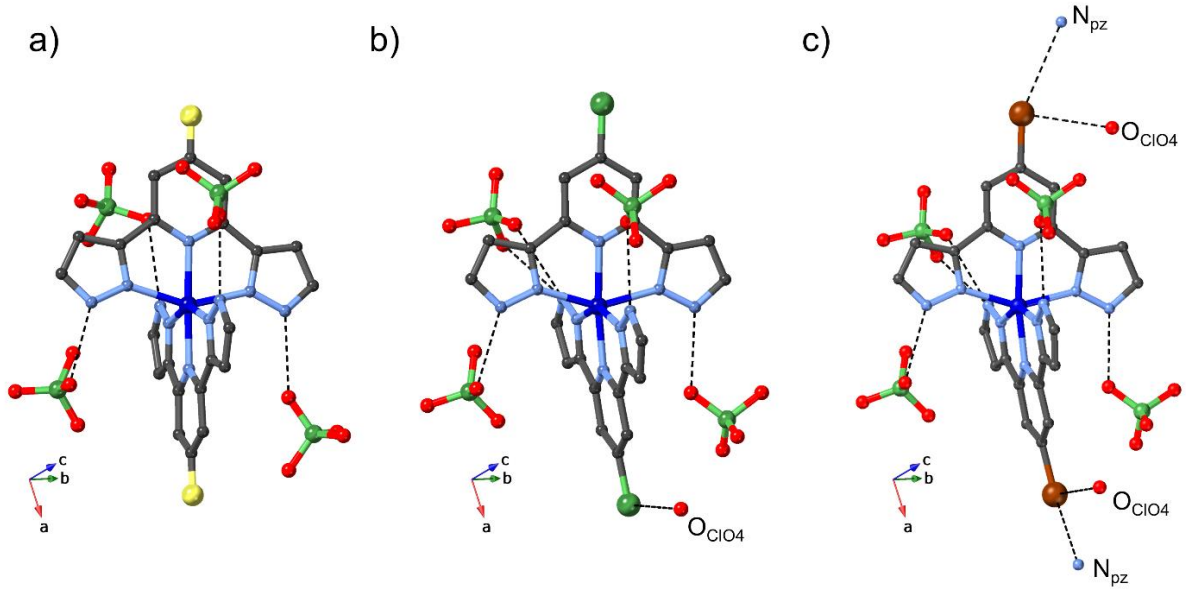

Figure 4.3.1. Second coordination sphere of compounds **F** (a), **Cl** (b), **Br** (c). Second coordination sphere has been depicted to illustrate influence of interactions with halogen in overall distortion. Hydrogen and halogen bond are depicted as dashed black line. Colors: carbon is grey, nitrogen is blue, oxygen is red, cobalt is dark blue, fluor is yellow, chlorine is green, and bromine is brown. Hydrogens are omitted for clarity.

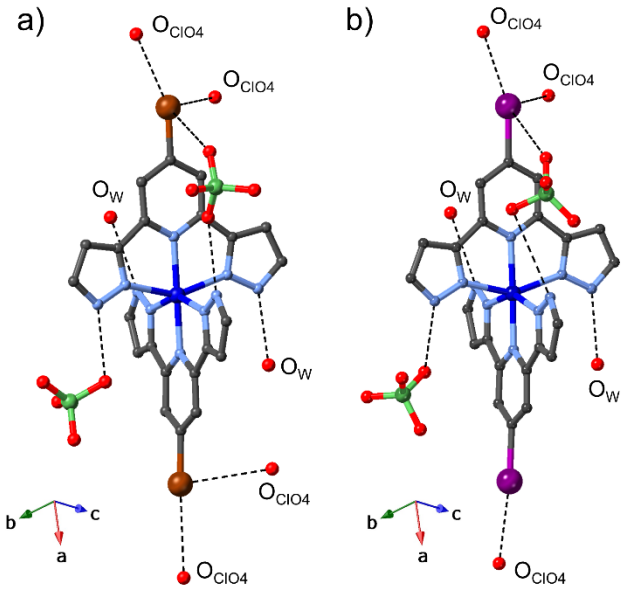

Figure 4.3.2. Second coordination sphere of compounds **Br·2H₂O** (a) and **I·2H₂O** (b). Second coordination sphere has been depicted to illustrate influence of interactions with halogen in overall distortion. Hydrogen and halogen bond are depicted as dashed black line. Colors: carbon is grey, nitrogen is blue, oxygen is red, cobalt is dark blue, bromine is brown, and iodine is purple. Hydrogens are omitted for clarity.

parameters. Whereas hydrated ones present a pseudo-octahedral geometry close to the ideal octahedral. Effect of the distortion is clearly observed in the trans-N{pyridine}-Co-N{pyridine} angle ϕ (ϕ = 175.24° (**F**); 173.97° (**Cl**) and 172.53° (**Br**)). Hydrated complexes **Br·2H₂O** and **I·2H₂O** show new supramolecular interactions through the water molecules providing relaxation to the structure (ϕ = 178.27° (**Br·2H₂O**) and 178.60° (**I·2H₂O**)) (Table 6.3.3).

The Co-N bond length for all the compounds at 100 K are between 2.058 and 2.163 Å (Table 6.3.4) which is the characteristic value of the HS configuration for the Co(II) ions. The halogen effect is noticed as a slightly continuous increase of the Co-N lengths, from **F** (Co-N = 2.117 Å), **Br** (Co-N = 2.127 Å) and **I·2H₂O** (Co-N = 2.136 Å).[118,198]

To better understanding the octahedral distortion of the compounds, we focused on supramolecular arrangement and crystal packing. Hydrogen bonds between N_{pz}-H···O (O_{ClO4} and/or O_w) are present in all the complexes. In addition, as halogen size increases, atoms establish extra halogen bond (X···O_{ClO4}) interactions. We observed establishment of halogen bond in the case of **Cl** and **Br**, corresponds with an increase in the octahedral distortion. It must be pointed out that in the fluor-derivative there is no halogen bond in the crystal structure (Figure 4.3.1a). This fact explains why the compound **F** presents the minimum distorted structure among the anhydrous forms.[203] Moreover, this finding reveals that the halogen bond is the driving force to the structure distortion because, N_{pz}-H···O_{ClO4} hydrogen bond does not provide enough strain to the crystal structure and barely alter the octahedral geometry.

At 100 K, **F** organizes in two identical interpenetrating three-dimensional networks. These networks are assembled intranetwork through hydrogen bonds N_{pz}-H···O_{ClO4} with an average distance N-H···O ≈ 2.732 Å. These networks are connected between them through weaker interactions such as H-bonds (C_{pyr}-H···O_{ClO4} and C_{pz}-H···O_{ClO4}, ≈ 3.263 Å), π-π pyridine-pyridine (C_g-C_g, 4.668 Å) and halogen-π (F-$C_{g\text{-pyrazole}}$, 3.528 Å). Figure 4.3.3 depicts the 3D

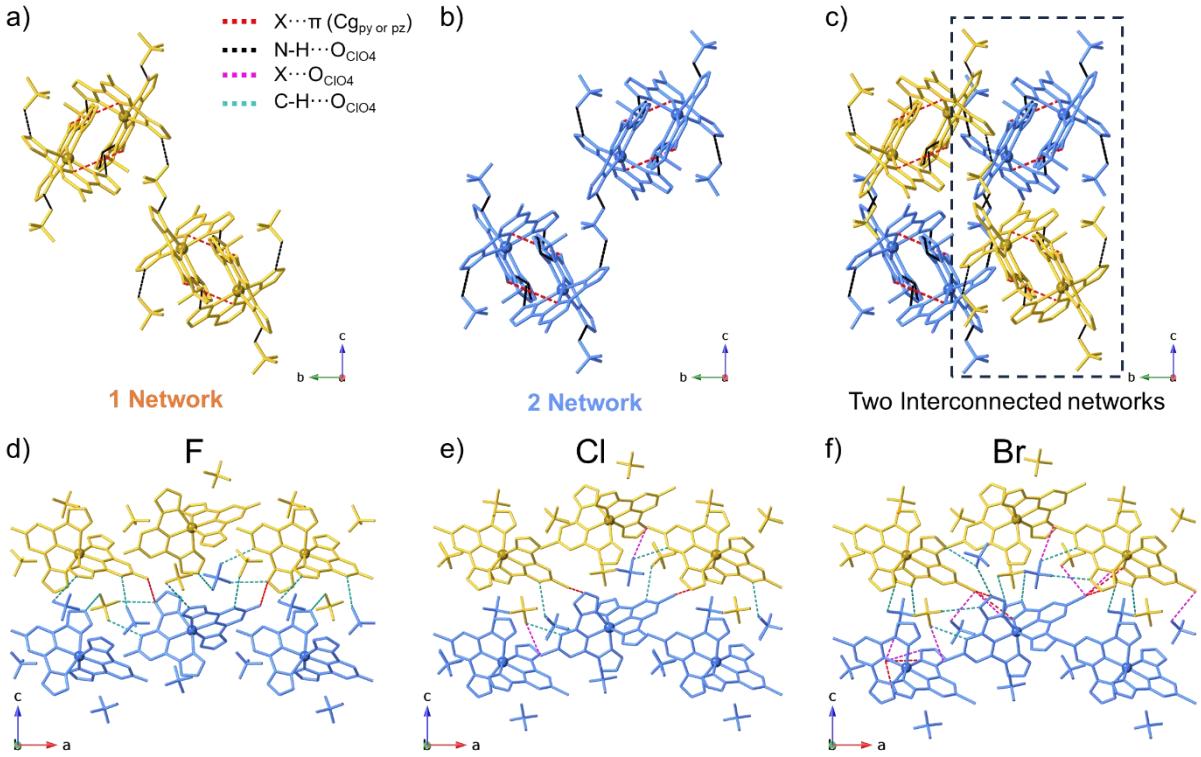

Figure 4.3.3. Illustration of the 3D packing in **F** with two networks (a, b) and the interconnection to form two interpenetrating networks (c). Main connection between two networks of **F** (d), **Cl** (e) and **Br** (f).

packing of F, showcasing two distinct networks (Figure 4.3.3a-d) and their interpenetration within the resulting 3D structure (Figure 4.3.3c). This arrangement in two interpenetrating networks is maintained in the case of **Cl** and **Br**, but additionally there is an extra halogen bond established. To highlight the interactions involved in the internetwork connection, connection between both networks of **F**, **Cl**, and **Br** were illustrated to emphasize their differences (Figure 4.3.3d-f).

In the case of **Cl**, main connection intranetwork assemblies through hydrogen bond (N_{pz}-H···O_{ClO4} ≈ 2.916 Å). As the halogen size increases, an additional intranetwork interaction of the halogen-π type is also established (Cl1-$C_{g\text{-pyridine}}$, 4.146 Å). Interactions along internetworks are established through weaker interactions such as halogen bond (Cl1···O1_1, 3.283 Å); H-bonds (C_{pyr}-H···O_{ClO4} and C_{pz}-H···O_{ClO4}, ≈ 3.298 Å), π-π pyridine-pyridine (C_g-C_g, 4.384 Å) and halogen-π (Cl-$C_{g\text{-pyrazole}}$, 3.596 Å).

The **Br** complex was obtained in two distinct forms, each with different compositions. The larger size of the halogen allows for sufficient space in the crystal packing to accommodate water molecules within the crystal structure. Consequently, we obtained an anhydrous form (**Br**) and a hydrated form (**Br·2H₂O**).

Packing of **Br** is analogous to that of the **Cl** structure. Main connection intranetwork assemblies through hydrogen bond (N_{pz}-H···O_{ClO4} ≈ 2.877 Å). As the halogen size increases, an additional intranetwork interaction of the halogen-π type is also established (Br1-$C_{g\text{-pyridine}}$, 3.989 Å). Interactions along internetworks are established through weaker interactions such as halogen bond (Br···O ≈ 3.428 Å); H-bonds (C_{pyr}-H···O_{ClO4} and C_{pz}-H···O_{ClO4}, ≈ 3.295 Å), π-π pyridine-

pyridine (C_g-C_g, 4.345 Å) and halogen-π (Br-$C_{g\text{-pyrazole}}$, 3.606 Å). Some insights can be drawn from these results. It is important to note that only one **Cl** of the ligands establishes a halogen bond, whereas in the case of **Br**, each Br atom in each bpp unit forms a halogen bond. Additionally, π-π interactions decrease in length as the halogen size increases. Moreover, the size of the halogen does not consistently correlate with the Co···Co shorter distances, suggesting that supramolecular interactions also play a role. For instance, the Co···Co shorter distances are 8.288 Å for **F**, 8.443 Å for **Cl**, and 8.319 Å for **Br**.

However, in the case of hydrated forms, a new set of supramolecular interactions emerges. These are established between the water molecules, perchlorates, and halogen atoms, respectively, in the bromo and iodo derivatives. Additionally, they present halogen bonds. Specifically, in **Br·2H$_2$O** (Br1, Br2···O_{ClO4}) and **I·2H$_2$O** (I1, I2···O_{ClO4}).This significant increase in hydrogen bond interactions results in the formation of a unique three-dimensional network. In the case of **Br·2H$_2$O and I·2H$_2$O** shortest Co···Co distances (8.225 Å) are located through *b* axis, in a longitudinal disposition of complexes in the same orientation. Meanwhile, the orientation in the *bc* plane is achieved by bilayers of complexes related by a two-fold axis that stack in pairs through an inversion axis. In the form {AB}{AB}^{i}, where A and B are related by a C_{2v}. The new hydrogen bonds act as an extra connection or spacer among the components of the crystal structure, thus reducing the tension in the crystal structure and the subsequent distortion in the metal complexes (Figure 6.3.10 - Figure 6.3.11).

We can conclude that octahedral distortion can be modulated by tuning supramolecular interactions. This distortion is induced by a synergistic effect of halogen substitution, as well as the total interactions established within the crystal lattice. Considering the close relationship between molecular asymmetry and anisotropy, we can anticipate variations in their magnetic behavior.

4.3.4 Direct-Current Magnetic measurements

To understand the influence of the halogen and the supramolecular interactions over the properties of the metal complexes we performed Magnetic Studies in solid state in a Superconducting Quantum Interference Device (SQUID) and Physical Property Measurement System (PPMS).

The direct-current magnetic properties of **F**, **Cl**, **Br**, **Br·2H$_2$O** and **I·2H$_2$O** were studied on crystalline samples slightly pressed and wrapped with Teflon in the range of 2 − 300 K under 1 kOe employing a SQUID using sweep mode and a scan rate of 2 K·min^{-1} (Figure 4.3.4). At room temperature, the χ_MT (χ_M: molar susceptibility; T: absolute temperature) values are 2.63 emu·K·mol^{-1} for **F**, 2.98 emu·K·mol^{-1} for **Cl**, 2.77 emu·K·mol^{-1} for **Br**, 3.06 emu·K·mol^{-1} for **Br·2H$_2$O** and 3.59 emu·K·mol^{-1} for **I·2H$_2$O**. Upon cooling from 300 K to 2 K, the χ_MT values decreased monotonously to 1.59, 1.51, 1.81, 2.02, 2.22 emu·K·mol^{-1} for **F-I·2H$_2$O**, respectively. The sharp decrease in χ_MT at low temperatures is commonly attributed to the depopulation of Kramer's excited state levels caused by zero-field splitting (ZFS),[204] in the absence of any close contacts between complexes that might allow for intermolecular exchange interactions. These obtained values are higher than the theoretical value of 1.875 emu·K·mol^{-1} for a spin-only high spin cobalt(II) ion (S=3/2, g=2.0). The experimental range of 2.1-3.4 emu·K·mol^{-1} for anisotropic Co(II) centers is consistent with the obtained results except for **I·2H$_2$O**, χ_MT value

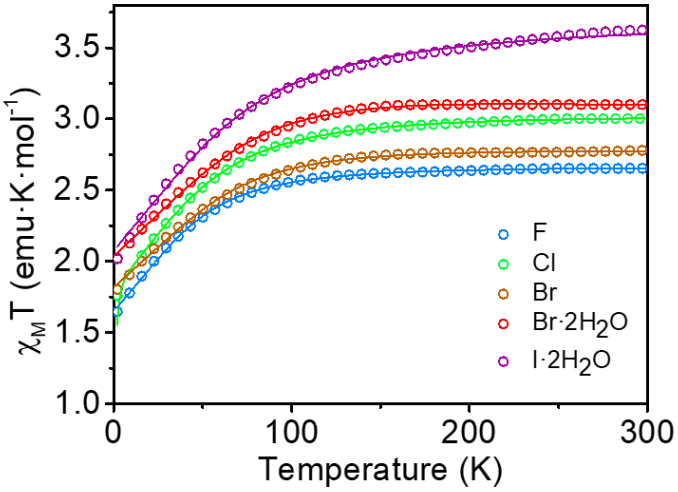

Figure 4.3.4. Temperature dependence of $\chi_M T$ between 2 and 300 K for complexes **F**, **Cl**, **Br**, **Br·2H₂O** and **I·2H₂O** at 1 kOe.

is significantly higher than the expected value obtained experimentally for Co^{2+}, due to an unexpected higher orbital angular contribution. Sample was measured under different applied field to corroborate this effect and discard field effects and $\chi_M T$ value obtained was the same.

The field-dependent magnetization of complexes **F**-**I·2H₂O** was determined in the range of 1-5 T at 2, 3, 5 and 7 K (Figure 6.3.12). At 2 K and in a magnetic field of 5 T, magnetization data of 2.15, 2.48, 2.56, 2.88 and 2.67 $N_A\mu_B$ were obtained for **F**, **Cl**, **Br**, **Br·2H₂O** and **I·2H₂O**. The experimental results obtained are lower than the expected values for a high spin Co(II) (S = 3/2) (g = 2.2 and M_{sat} = 3.3). These differences rely on the different magnetic anisotropy of the analyzed compounds. Zero-field splitting (ZFS) parameters were obtained the temperature and field-dependent magnetization data using PHI program[205] based on the following spin Hamiltonian:

$$H = g\mu_B SB + D\left(S_z - S^{2/3}\right) + E\left(S_x^2 - S_y^2\right) \qquad (\mathbf{Eq.\,1})$$

where μ_B is the Bohr magneton, D is the axial ZFS parameter, E is the rhombic or transverse ZFS parameter, S is the spin operator and B is the magnetic field vector.

The data underwent fitting, and the optimal parameters are detailed in Table 6.3.5. To ensure a robust fit, the g-factor was fixed through calculated $\chi_M T$ values at 300 K, with g-factor set at 2.37 (**F**), 2.52 (**Cl**), 2.43 (**Br**), 2.55 (**Br·2H₂O**), and 2.77 (**I·2H₂O**). The resulting D and E parameters are consistent with other reported cobalt(II) systems, aligning with positive D values indicative of an easy-plane anisotropy.[206–208] The progression of D values from **F** to **Br** correlates with the octahedral distortion evident in X-ray analysis. Although the hydrated compounds exhibit elevated D values despite less pronounced distortion, solvent effects may contribute additional anisotropy. Notably, the **I·2H₂O** compound stands out with a negative E value, potentially accounting for the unusually high $\chi_M T$ value. The observation of non-saturation of magnetization with a high-field indicates the presence of a strong magnetic anisotropy for all the complexes, which is further confirmed by the lack of superposition of the magnetization values in the reduced magnetization plots ($M/N_A\mu_B$ versus HT^{-1}) between 2−7 K (Figure 6.3.13).[209,210]

4.3.5 Alternating Current Magnetic measurements

To probe the dynamic magnetic behavior of the Co(II) complexes **F-I·2H₂O**, alternating-current (ac) susceptibility studies were carried out. These measurements were first performed under a zero-dc field (with an oscillating field of 5 Oe) between 2–10 K. No out-of-phase signal for the magnetic susceptibility (χ_M'') could be detected in the absence of an applied dc magnetic field at 10 kHz, which was attributed to efficient quantum tunneling of the magnetization (QTM). However, at the same frequency (10 kHz) under a dc applied magnetic field between 0.1–2.1 T, these complexes show a maximum for the temperature-dependence in-phase (χ_M') and out-of-phase (χ_M'') ac susceptibility between 2–10 K (Figure 6.3.14 - Figure 6.3.19). In the absence of an external magnetic field, the magnetic moments of the Co(II) ions may orient randomly, leading to a lack of coherent magnetic behavior. However, when subjected to an external magnetic field, the magnetic moments of the Co(II) ions align, enabling the observation of single ion magnetism phenomena such as slow relaxation of magnetization that originates from hyperfine interactions or dipole interactions with the spin centers.[211]

The high spin Co(II) (S=3/2) is a Kramers ion, these types of ions typically undergo relaxation via alternative thermal relaxation mechanisms rather than quantum tunneling when subjected to a direct current (dc) applied field.[212] Frequency-dependent ac signals were observed under 1000 Oe for **F**, **Cl** and **I·2H₂O**; 500 Oe for complex **Br** and 250 Oe for **Br·2H₂O**; thus, indicating efficient suppression of the QTM effect and field-induced slow magnetic relaxation.

Considering the results registered, for complexes **F**, **Br** and **Br·2H₂O** maximum appeared between 1 kOe and 3 kOe while, on the other hand, complex **Cl** and **I·2H₂O** behave in the range of 1 kOe and 6 kOe. From the analysis of those measurements, to monitor the relaxation process, optimal applied dc magnetic fields of 1 kOe were selected to suppress quantum tunneling relaxation and to compare the magnetic properties of compounds **F-I·2H₂O** under similar conditions when performing the temperature and frequency dependence measurements for both χ_M' and χ_M''.

Maximum out-of-phase (χ'') susceptibilities frequency-dependent ac data under 1 kOe dc field, suggest a slow relaxation of the magnetization and a SIM behavior for the given temperature range 2-5 K. Effect of solvent molecules create a clear change in relaxation, for the case of **Br** and **Br·2H₂O** (Figure 4.3.5. Only one relaxation process was observed in all compounds at the same conditions (Figure 4.3.5e,g). Additionally, as maximum of **Br** was observed even at small applied dc field, maximum out-of-phase (χ'') susceptibilities frequency-dependent ac data under 250 Oe was measured (Figure 6.3.25).

Also, Cole-Cole plots were constructed from the frequency-dependent ac data (Figure 6.3.20 - Figure 6.3.24). The data were fitted using CC-FIT software.[213,214] The fitted values of χ_T (isothermal susceptibility), χ_s (adiabatic susceptibility), τ and α are summarized in Table 6.3.6 and Table 6.3.7). For complexes **F-I·2H₂O**, curves display typical semicircles at low temperatures, indicating a relatively narrow distribution of the relaxation time.

To examine Orbach relaxation process, Eq. 2 was employed to analyze the parameters for complex **F-I·2H₂O**:

$$\tau^{-1} = {\tau_0}^{-1} \cdot e^{-U_{eff}/K_B \cdot T} \qquad (\mathbf{Eq.\ 2})$$

where τ_0 is the pre-exponential factor, U_{eff}/K_B represents the energy barrier and T is the temperature of the system. Spin-reversal energy barrier ($U_{eff}//K_B$) and pre-exponential factor are compiled in Table 4.3.1.

To examine whether other processes are involved in relaxation process, were considered: direct (*AT*), Raman (CT^n) and Orbach relaxation (Eq. 3):

$$\tau^{-1} = \mathrm{A} \cdot \mathrm{T} + \mathrm{C} \cdot \mathrm{T}^n + {\tau_0}^{-1} \cdot e^{-U_{eff}/K_B \cdot T} \qquad (\mathbf{Eq.3})$$

in which A is the coefficient of the direct process, C is the coefficient of the Raman process, and the third term represents the Orbach process. Best agreement with experimental data becomes possible with two relaxation mechanisms involving Orbach and Raman. Best fitting parameters for complexes **F-I·2H₂O** found are compiled in Table 4.3.1. These values suggest that the predominant relaxation mechanism is Orbach, wherein spin reversal occurs through a thermal barrier. In the anhydrous series, the contribution of Raman diminishes significantly as the halogen size increases, evident from the low values of τ_0. Additionally, there is a minor contribution from the Raman process, particularly notable in the context of hydrated compounds. These relaxation processes are widely reported in literature for other cobalt(II) and iron(II) single ion magnets (SIMs).[110,209,212]

We observed a clear trend between the two groups of compounds: anhydrous and hydrated. In complexes **F**, **Cl** and **Br**, the activation energy U_{eff}/K_B increases as we vary the halogen size F > Cl > Br and the number of halogen bonds, and thus, the octahedral distortion increases. For complexes **F** and **Cl,** the activation barrier is 13.17 K and 14.29 K respectively, indicating a Raman-assisted Orbach process. However, for complex **Br**, the activation barrier increases to 20.63 K making the process Orbach or quasi-Orbach assisted mechanism. Regarding hydrated complexes **Br·2H₂O** and **I·2H₂O**, water molecules play a pivotal role by introducing novel supramolecular interactions. These interactions serve to mitigate octahedral distortions, resulting in a quasi-octahedral coordination geometry. This unique characteristic aids in lowering the energy barrier for slow magnetic relaxation, indicating a dominant Raman-like process in the studied temperature range. This distinction underscores that the magnetic dynamics are influenced not only by magnetic anisotropy but also by the surrounding ligands coordinated to the metal center.

Table 4.3.1 Main relaxation parameters for **F − I·2H₂O**. Orbach parameters were calculated from the high temperature regime. Orbach and Raman parameters were extracted from all temperature fitting.

	Orbach		**Orbach + Raman**			
	τ_0 (s)	**U_{eff}/k_B (K)**	**C ($s^{-1}\cdot K^{-n}$)**	**n**	**τ_0 (s)**	**U_{eff}/k_B (K)**
F	$3.41E^{-06}$	5.49	$9.81E^{+03}$	1.22	$1.09E^{-06}$	13.17
Cl	$2.21E^{-06}$	7.836	$3.03E^{+03}$	2.08	$2.29E^{-06}$	14.29
Br	$2.16E^{-07}$	20.63	$1.00E^{+02}$	3.43	$1.10E^{-07}$	25.83
Br·2H₂O	$2.75E^{-06}$	6.99	$2.58E^{+02}$	3.51	$1.24E^{-05}$	3.70
I·2H₂O	$1.60E^{-06}$	9.28	$2.47E^{+03}$	2.17	$6.56E^{-06}$	7.91

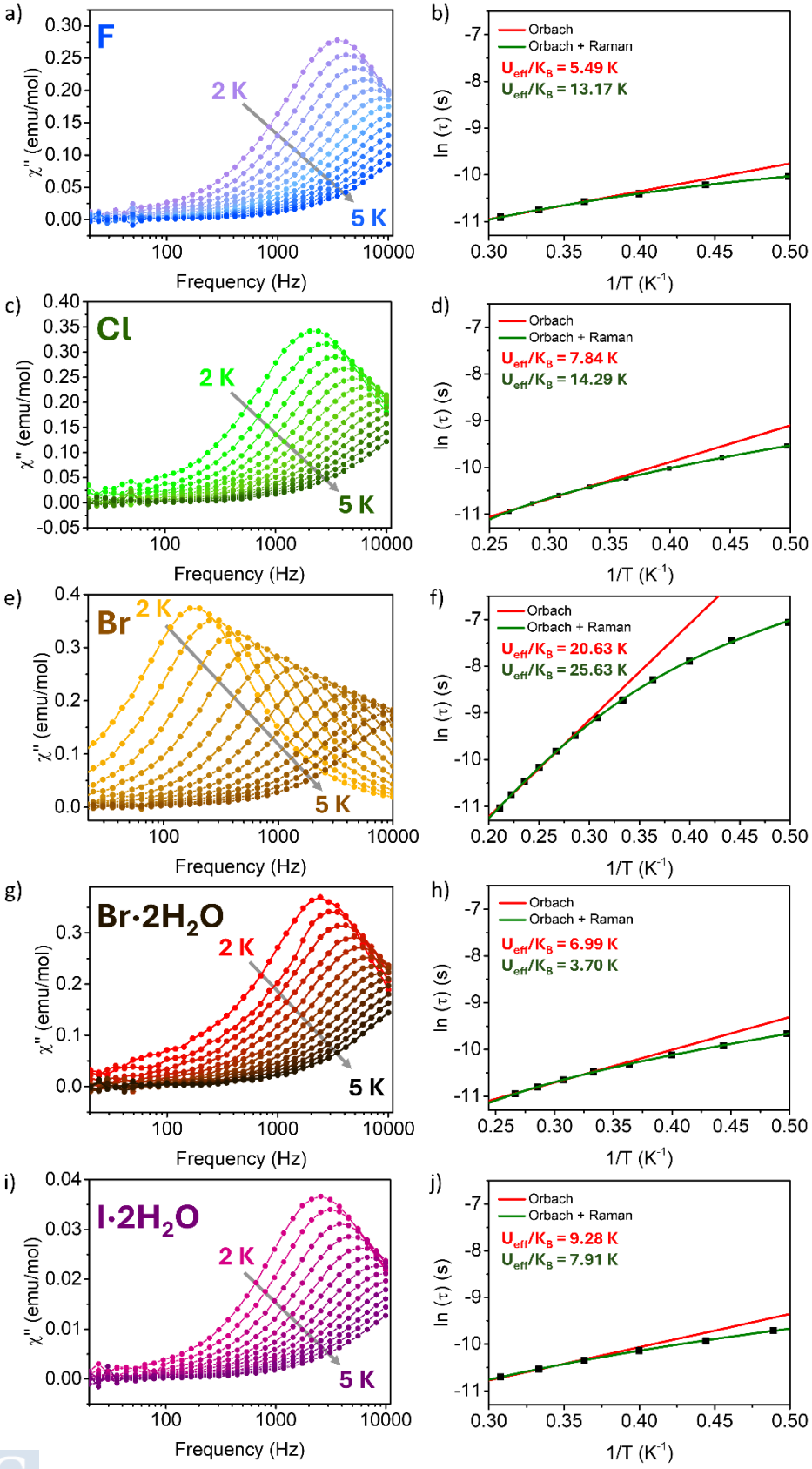

Figure 4.3.5. Frequency-dependent of out-of-phase (χ'') ac susceptibility and Arrhenius plots constructed from data for **F** (a-b), **Cl** (c-d), **Br** (e-f), **Br·2H₂O** (g-h) and **I·2H₂O** (i-j) in the range between 2 – 5 K.

4.3.6 Conclusions

In summary, we employed a novel methodology developed in Section 4.2 to obtain halogen-substituted 2,6-bis(1H-pyrazol-3-yl)pyridine (*p*-X-3-bpp). The potential of these novel ligands was explored in five different Co(II), **F−I·2H$_2$O**, focusing on the impact of *para*-halogen-substituted ligands and supramolecular interactions. These complexes have been synthesized and fully characterized through usual common solid-state techniques. The five obtained crystals present the same space group. The significant impact of halogen size on the inclusion of solvents in the second coordination sphere was observed. As the size increases, particularly evident in the bromo derivative, it becomes possible to isolate crystals in both hydrated and anhydrous forms. However, in the case of the largest halogen, the iodo derivative, only the hydrated form was isolated.

Through a combination of structural analysis, magnetic measurements, and relaxation mechanism studies, magneto-structural correlations can be extracted. Firstly, the introduction of *para*-halogen-substituted ligands enables the modulation of octahedral distortion in cobalt(II) complexes, key for inducing single ion magnet behavior. Supramolecular interactions, including hydrogen bonds and halogen bonds, play a pivotal role in shaping the crystal packing and molecular symmetry of these complexes, ultimately influencing their magnetic properties.

Slow magnetic relaxation behavior of **F−I·2H$_2$O** was obtained through further investigations of dynamic magnetic properties under 1 kOe dc applied field. Results demonstrated that these 5 complexes exhibit slow magnetic relaxation. The analysis of the ac magnetic data reveals the predominant involvement of Orbach relaxation, assisted by Raman processes. Additionally, the possibility of accommodating solvation molecules, such as water, introduces the ability to control magnetic behavior by relaxing the octahedral environment and favoring thermal relaxation processes, decreasing the thermal barrier in favor of relaxation through the Raman mechanism.

Overall, the study advances our understanding of the structural and magnetic properties of cobalt(II) complexes, highlighting the intricate interplay between molecular architecture, supramolecular interactions, and magnetic behavior. The present work shows that the magnetic anisotropy and the slow relaxation dynamics of Co(II) complexes can be fine-tuned by structural modification of the series of halogen derivatives.

4.4 Fine-tuning of the spin transition through the counterion selection

4.4.1 Background

Spin crossover compounds are those belonging to d^4-d^7 electronic configuration. These systems can switch between two spin states under an external stimulus such as temperature, light, pressure, or a magnetic field.[2,6] This spin state can involve a change in the magnetic or optical properties as well as significant differences in the structure (metal-donor bonds). These features convert SCO systems in ideal candidates for act as molecular switches that can be implemented in emerging applications for sensing, actuators or spintronics.[8]

Numerous studies have demonstrated that cooperativity within these systems leads to hysteresis phenomena and alterations in switching temperature.[215–217] Cooperativity, in this context, denotes the degree to which neighboring molecules or units within a crystal lattice or molecular assembly affect each other. As we discussed in Section 4.2, directional halogen bonds induce cooperativity leading to one steep step or two step transition. Also, some studies have been dedicated to exploring the role of the halogen bond in cooperativity.[218] Meanwhile, extended hydrogen bond networks lead to gradual and high temperature transition.[219]

For decades, anions have served as chemical templates in supramolecular chemistry, facilitating the creation of 3D scaffolds with intricate connectivity. This approach relies on the directional nature of interactions and their diverse geometries.[220,221] For the past two decades, extensive research has been conducted on the impact of counterions on spin transitions across a diverse range of ligands.[53,54,57,67] A wide range of $[Fe(3\text{-bpp})_2]^{2+}$ salts have exhibited diverse thermal and photochemical spin transitions.[44]

Here, we present eight new SCO systems based on the scaffold 2,6-di(pyrazol-3-yl)pyridine (3-bpp), which is a well-known precursor in the field of SCO materials. These structures have been extensively studied over the last decade and they have showed SCO and magnetic properties highly dependent on the second coordination sphere. This strong dependence relies on the ability of the 3-bpp to establish hydrogen bonds with solvents and/or counterions through two $HN_{pyrazol}$ groups. To increase the potential to create new supramolecular interactions we functionalized the 3-bpp with a chlorine atom in the *para* (4-chloro-2,6-di(1H-pyrazol-3-yl)pyridine) (*p*-Cl-3-bpp), a strategic position to establish new intermolecular interactions. Given the cooperative nature of this SCO complex, this novel ligand stands as an ideal candidate for exploring new methodologies to achieve on-demand control of the spin transition.

In this study, we present the synthesis, structure, magnetic, and spectroscopic properties of novel members within the $[Fe(p\text{-Cl-3-bbp})_2](X)_2$ family where X includes: **ClO_4** (reported in Section 4.2), **BF_4**, **PF_6**, **NO_3**, **NCS**, **NCSe**, **CF_3SO_3**, **Br** and **I**. These compounds are labeled according to the specific counterion used. Investigating these structural differences is crucial for understanding the variations observed in the magnetic behavior of these compounds and for establishing magneto-structural correlations. Our aim is to identify correlations and trends among cooperativity parameters, primarily focusing on hydrogen bonds, halogen bonds, π-π interactions, among other factors. Insight into these relationships may illuminate the modulation of spin transitions, aiding in the comprehension of cooperative mechanisms and enabling researchers to tailor-make SCO complexes.

4.4.2 Synthesis

The ligand *p*-Cl-3-bpp was synthetized following the previously described method in Section 6.2.1., where, starting from the 4-chloropyridine hydrochloride, the desired product is obtained through three synthetic steps in an overall yield of 45%.

To obtain the target compounds two different methodologies were applied depending on the counterion. Most of the compounds were obtained following a described method where, the metal complex [Fe(*p*-Cl-3-bpp)$_2$]Cl$_2$ is prepared by direct synthesis between the ligand *p*-Cl-3-bpp and the stoichiometric amount of $FeCl_2$ and, the counterion exchange is performed adding the potassium or sodium salt (2 eq.) of the desired counterion dissolved in hot water over the metal complex solution in methanol.[76,222,223] Red crystals, suitable for SCXRD were obtained for **PF$_6$**, **BF$_4$**, **SCN**, **SeCN**, **NO$_3$** and **CF$_3$SO$_3$**. Metal complex [Fe(*p*-Cl-3-bpp)$_2$](ClO$_4$)$_2$ (**ClO$_4$**) was obtained as described in Section 6.2.2. In the case of **Br** and **I** an alternative procedure was followed. From the complex [Fe(*p*-Cl-3-bpp)$_2$](ClO$_4$)$_2$, the counterion exchange was performed adding the stoichiometric amount of the corresponding potassium salt (KBr or KI) dissolved in methanol forcing the precipitation of the $KClO_4$. Compounds were isolated as crystals after filtration of $KClO_4$ and the slow evaporation of the solvent. In this second methodology the same volume of water was added after separation of the $KClO_4$ to obtain red crystals.

4.4.3 Single-Crystal X-Ray Diffraction (SCXRD) measurements

Single-Crystal X-ray Diffraction (SCXRD) was used to determine the crystal structure of all compounds at 100 K. We observe that, in a general manner, the asymmetric unit of all compounds contain one [Fe(*p*-Cl-3-bpp)$_2$]$^{2+}$ coordination entity and two counterions. Just for the case of **NCS** and **I**, the asymmetric unit is formed by half unit of the coordination entity. The second coordination sphere composition relies heavily on the anion radii and 3D disposition of the ligands, consequence of the direct interactions of NH with counterions (Figure 4.4.1). As can be appreciated on Table 6.4.1−Table 6.4.2, the crystal system and the space group are not the same for all compounds. Five of these structures (**ClO$_4$**, **BF$_4$**, **PF$_6$**, **NCS and I**) present an orthorhombic crystal system. Three of them (**ClO$_4$**, **BF$_4$**, **PF$_6$**) in a primitive Pbca space group and **NCS** and **I** in a Pbcn space group. Instead, compounds **Br**, **NO$_3$** and **CF$_3$SO$_3$** crystallize in a monoclinic crystal system in a $P2_1$, $P2_1/n$ and $P2_1/c$ space group respectively. **NCSe** presents a triclinic crystal system in $P\bar{1}$ space group. It can be noticed crystal system and space group is clearly affected by the geometry of the counterion and the capability of the structure to accommodate solvent molecules. Suggesting that introducing water molecules is more feasible in the case of smaller counterions (**NO$_3$**, **NCS**, **NCSe**, **Br** and **I**).

Except for **NO$_3$**, all complexes exhibit a typical range bond distances for LS for Fe(II), in the range of 1.90 Å. **NO$_3$** is the only compound that shows HS spin bond distances**.** Selected Fe-N bond distances are listed in Table 6.4.3 and Table 6.4.4.[224]

In all cases, Fe(II) ion is situated within a distorted FeN6 octahedron. To estimate the octahedral distortion, several parameters can be used. All these parameters are expected to influence the magnetic properties of the metal complexes. Σ measures the deviation of a metal ion from an ideal octahedral geometry considering the sum of the deviation of the 12 cis N–Co–N angles from 90°, while Θ indicates its distortion from an octahedral towards a trigonal

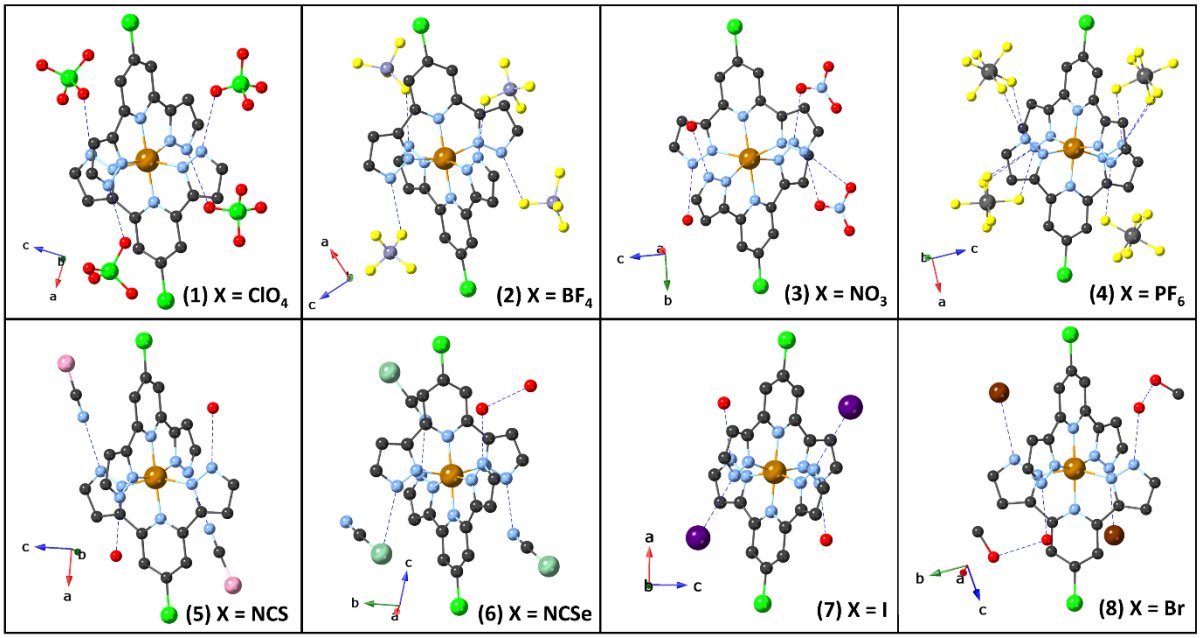

Figure 4.4.1. Representation of first and second-sphere coordination interactions of all the complexes. Hydrogen bonds are represented as dashed blue lines. The color code used is as follows: nitrogen (blue), carbon (grey), oxygen (red), chlorine (green), iron (orange), boron (light grey), fluorine (yellow), sulfur (pale pink), selenium (pale green), iodine (violet), and bromine (brown).

prismatic structure as the sum of the 24 N–Co–N angles measured on the projection of two triangular faces of the octahedron along their common pseudo-threefold axis.[157] Both indices were obtained using the OctaDist program[202] and their values deviate significantly from Σ = Θ = 0, which would indicate a perfect octahedral geometry (Table 6.4.5). **NO_3** compound differs from the rest considerably, with the largest angle ϕ and ψ of deviation, other indicative that it exhibits HS state at 100 K.[180,225]

We can identify several common features in the 3D arrangement of these structures. In all cases, the NH groups of the pyrazoles establish hydrogen bonds either with counterions or with solvent molecules (water or methanol). In dehydrated structures, the anions interact with two units of independent complexes. However, if solvent molecules are present, the NH groups also form interactions with them, and the interaction between units of complexes occurs via anion-solvent hydrogen bonds. Additionally, halogen bonds formed through Cl_{bpp} are only established in dehydrated compound. There are also halogen bonds between counterions and solvent molecules, but these do not directly affect the ligand field around the metal. Finally, when the geometry of the anion allows, π-π interactions occur between pyrazoles and pyridines. All these characteristics contribute to the network formed by hydrogen and halogen bonds and the connectivity between the different 3-bpp units, resulting in distinct lattice connections. For clarity and correlation, our discussion will primarily focus on dehydrated structures followed by hydrated ones.

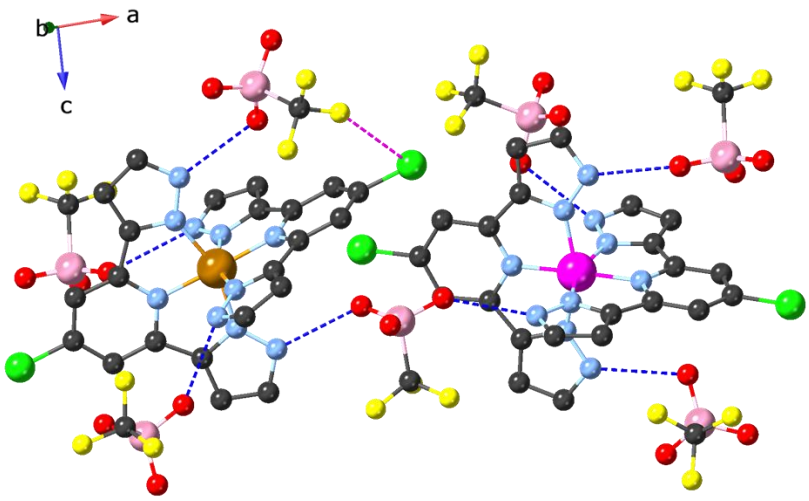

Figure 4.4.2. Asymmetric of **CF_3SO_3** depicted with second sphere coordination interactions. Hydrogen bonds are represented as dashed blue lines and halogen bonds as dashed violet lines. The color code used is as follows: nitrogen (blue), carbon (grey), oxygen (red), chlorine (green), iron 1 (orange), iron 2 (violet), fluorine (yellow), and sulfur (pale pink).

4.4.3.1 Anhydrous structures

Crystal structure of compound **ClO_4** was previously described in Section 4.2 (labeled as **Cl**), this compound arranges in two identical interpenetrating three-dimensional networks AA^i and it resembles the structure of **BF_4**. The intranetwork connection is composed by hydrogen bonds (N_{pz}-H···O_{ClO4} ≈ 2.903 Å (**ClO_4**) and N_{pz}-H···F_{BF4} ≈ 2.73 Å (**BF_4**)) (pz: pyrazole) while the internetwork in this case is through halogen bond (Cl_{bpp}···O_{ClO4} = 3.102 Å or Cl_{bpp}···F_{BF4} = 3.15 Å).

For the case of **PF_6**, that structure resembles the **F** mentioned in Section 4.2. **PF_6** complex at 100 K establishes N_{pz}-H···O_{ClO4} bonds with an average distance of 3.02 Å. This interaction favours that structure grows in two identical interpenetrating three-dimensional networks that are related to each other by an inversion center, in AA^i manner. These networks are connected between them through H-bonds (C_{py}/C_{pz}-H···O_{ClO4}) (py: pyridine). Main difference is no halogen bond is established in this structure, becoming two interpenetrating networks in a less connected degree.

In the case of **CF_3SO_3**, hydrogen bonding occurs through N_{pz}-H···O_{CF3SO3} and N_{pz}-H···O_w (2.80 Å), additionally, a halogen bond Cl_{bpp}···F_{CF3SO3} (3.118 Å) is established. It is important to highlight that this is the only compound in this series that presents two independent crystallographic Fe(II) centers (Figure 4.4.2). Curiously, the halogen bond is only formed in one of the Cl_{bpp} ligands of the asymmetric unit. Due to these interactions, the compound forms a three-dimensional network where the Fe···Fe distances are similar in all three directions (10 Å), connecting through the network of anion-water.

4.4.3.2 Hydrated structures

In case of **NO_3**, hydrogen bond connection is through N_{pz}-H···O_w (2.728-2.819 Å) and N_{pz}-H···O_3N (2.728-3.077 Å). The strong hydrogen bonding interactions lead to the formation of 2D molecular clusters ("layers") consisting of molecules (complex+anion+H_2O), which extend

along the plane defined by the *b*-axis and the diagonal of the *a* and *c* axes. The layers of molecules stack upon each other through C-H···O type interactions. The π-π interactions are weak, as the shortest distance in this case is established between pyrazole-pyridine (4.431 Å), which is significantly higher than the typical distance of ~ 4 Å.

NCS establishes N_{pz}-H···N_{NCS} (2.779 Å), N_{pz}-H···O_w (2.754 Å) and O_w-H···S_{NCS} (2.405 Å). In this case, the complex organizes into layers (with the shortest Fe···Fe distances at 8.597 Å). Within the layer, the most significant connections are established through hydrogen bonds, involving complex-anion-H_2O-complex interactions, or through a network of water molecules, complex-H_2O-anion-H_2O-anion-complex. Additionally, the layers establish a π-π interaction between pyrazoles (3.879 Å). The main connection between layers in this case is through water molecules.

NCSe establishes N_{pz}-H···N_{NCS} (2.7789 Å) and N_{pz}-H···O_w (2.754 Å) and O_w-H···S_{NCS} (2.405 Å). The primary interlayer connections arise from hydrogen bonds, creating a network of complex-water-anion-complex interactions and π-π interactions between pyrazoles (3.787 and 3.698 Å). Water molecules are arranged alternately, leading to a lack of connection between layers and resulting in a separation between them, which generates two distinct regions in an AB manner.

In the **Br** complex, MeOH and H_2O create an extended hydrogen bond network. Hydrogen bonds are established through O_w-H···O_{MeOH}: 2.731 Å, O_w-H···Br: 3.33 Å, N_{pz}-H···O_w: 2.69 Å, and N_{pz}-H···Br: 3.25 Å. Additionally, there are two halogen bonds between the Br··· O_w (3.21 Å). The packing of the structure resembles that of **NCSe**. Complexes are arranged in layers where connections are made through complex-anion-solvent-anion-complex interactions, as well as π-π interactions between adjacent pyrazoles (3.503 Å) being the shortest π-π distance of this series.

Compound **I** organizes into a three-dimensional network with main interactions (N_{pz}-H···O_w: 2.779 Å; N_{pz}-H···I: 3.528 Å; O_w-H···I: 3.54 Å), favoring π-π stacking between adjacent pyrazoles (3.998 Å), which aligns the structure along the *c*-axis with the shortest Fe···Fe distances (8.4 Å).

In Figure 6.4.9 - Figure 6.4.16, the packing of all the structures is illustrated. The 3D representations emphasize π-π interactions and hydrogen and halogen bonds.

4.4.4 Magnetic studies

Magnetic studies were conducted on a collection of slightly pressed single crystals and wrapped with Teflon at a magnetic field of 1 T within a temperature range of 2-400 K, utilizing a scan rate of 2 K·min^{-1} for both cooling and heating modes. A perforated Teflon capsule was employed to facilitate the dehydration of the samples. The thermal stability of the complexes and the presence of solvent molecules in the initial structures were assessed via thermogravimetric analysis (Figure 6.4.17). The thermogravimetric analysis confirms that all compounds are stable up to 400 K. We observe that the solvated samples lose the solvents before 100 °C, so it is expected that their dehydration will occur under the experiment conditions inside the SQUID. Moreover, this dehydration can be observed in Figure 4.4.3 by noting a change between the first and second cycles. This is attributed to a desolvation

process, and we have attributed it to the obtaining of the anhydrous sample. Therefore, both the initial (solvated) sample and the desolvated sample in the second cycle have been treated in the graphs as well.[226–228]

Given the observation that the obtained hydrated or non-hydrated samples depend on the chosen counteranion, our discussion primarily delves into the distinct treatment of anhydrous samples and hydrated ones.

4.4.4.1 Anhydrous complexes

Magnetic behavior of four compounds obtained in their anhydrous form (**ClO_4**, **BF_4**, **PF_6** and **CF_3SO_3**) is illustrated in Figure 4.4.3a.

If we focus on **ClO_4** and **BF_4** both compounds present $\chi_M T$ = 3.86 emu·K·mol^{-1}, with a $T_{1/2}$ = 227 K. This value is consistent with a high spin iron(II) ($t_{2g}^4 e_g^2$, S = 2) configuration. Both compounds present a hysteresis loop with an ΔT = 8 K and 15 K respectively with a complete spin transition (γ_{HS}, 100%).

PF_6 presents a gradual two step transition. First, from 235 to 287 K, reaching a value of $\chi_M T$ = 1.79 emu·K·mol^{-1}, consistent with a 50% population in HS. This gradual transition is followed by second gradual from 287 K to 325K, reaching a $\chi_M T$ value of 3.45 emu·K·mol^{-1} above this temperature (γ_{HS}, 100%). A hysteresis loop is observed in both transitions (ΔT_1 = 4 K, ΔT_2 = 5 K). This two-step transition could suggest compound transits through an intermediate state (LS-IS-HS) of mixed-spin (S=1) instead of a single transition (LS-HS).

Finally, **CF_3SO_3** shows a non-complete gradual transition ($T_{1/2}$ = 242 K) from a (γ_{HS}, 66%, 300 K) to (γ_{HS}, 10%, 100 K).

4.4.4.2 Hydrated form

Some of these structures were obtained in their solvated or hydrated forms (we refer to hydrated if composed solely of water molecules). In Figure 4.4.3b-f, we focused on the magnetic behavior of hydrated compounds **NO_3**, **NCS**, **NCSe**, **Br** and **I** respectively, represented in a first scan rate on heating mode from 2 K to 400 K (violet lines). After the first cycle reaching 400 K, we assume the second cycle represents the obtaining of the anhydrous compound (magenta).

For the family of compounds: **NCS, NCSe, Br** and **I** an abrupt spin transition with a similar T_c (ca. 325 K) is observed in the first cycle. All four compounds remain in 100% LS configuration (t_{2g}^6, S = 2) up to 300 K. Instead, **NO_3** is in high spin configuration ($\chi_M T$ = 3.87 emu·K·mol^{-1}).

This desolvation is evident as there is a significant magnetic change after measuring the second cycle, as can be observed in Figure 4.4.3b-f. **NO_3** converts into a two-stepped non-complete transition. Meanwhile after the loss of solvent (Figure 4.4.3b), **NCS, NCSe, Br** and **I** exhibit a drastic change in magnetic behavior, displaying a wide complete transition (**NCS**) (Figure 4.4.3c) or non-complete transition (**NCSe**, **Br** and **I**) centered at 300 K (Figure 4.4.3d-f).

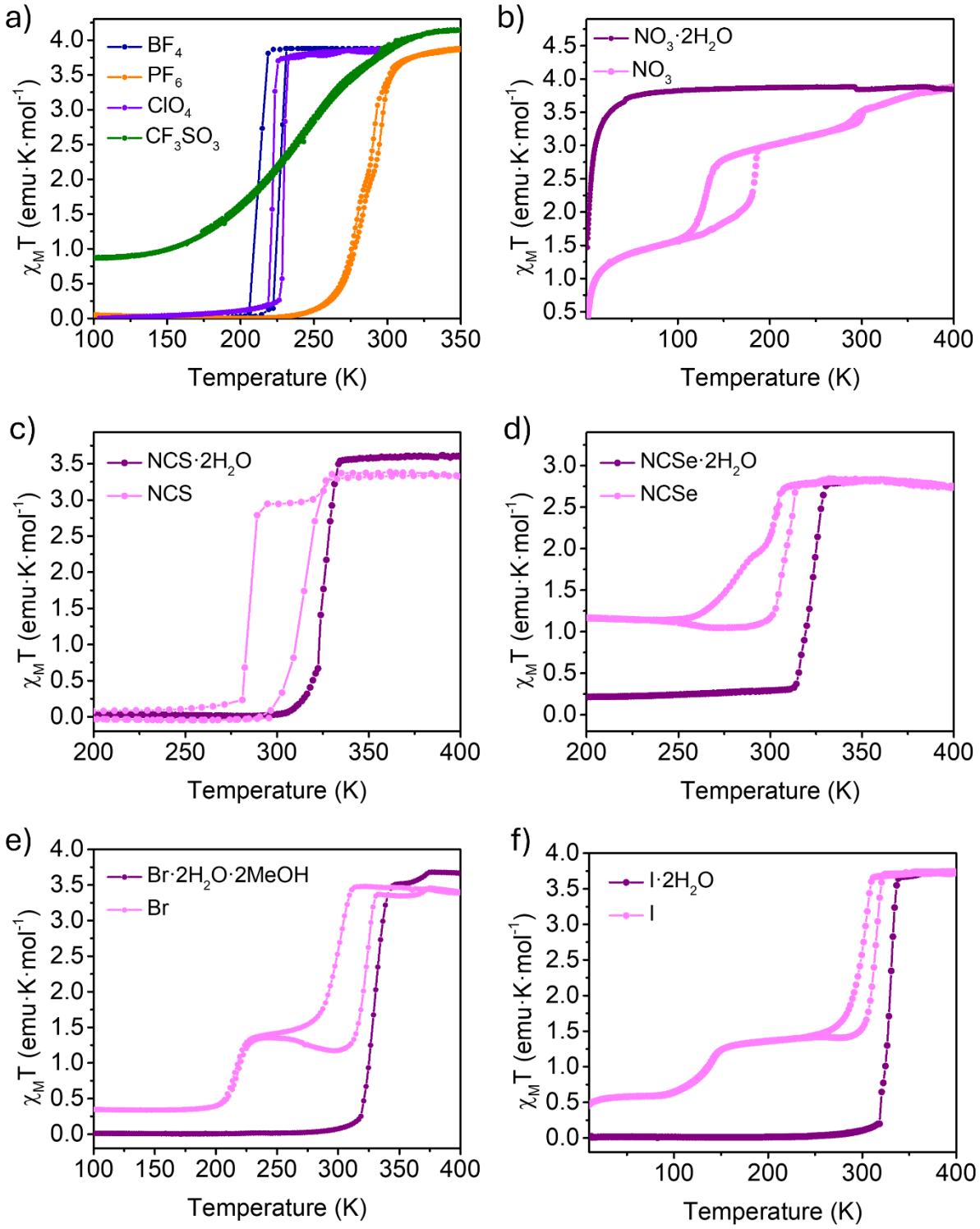

Figure 4.4.3. Temperature dependence of $\chi_M T$ for all complexes. Anhydrous compounds **ClO_4**, **BF_4**, **PF_6** and **CF_3SO_3** are represented in (a) showing one cycle: 2 K – 400 K – 2 K. Hydrated compounds are represented individually: **NO_3** (b), **NCS** (c), **NCSe** (d), **Br** (e) and **I** (f). The violet line represents first heating cycle (2 – 400 K). Upon desolvation, second cycle on both cooling and heating is represented in light magenta color.

Upon desolvation of **NO_3** (Figure 4.4.3b), the complex experiences a partial spin transition, shifting from 100% to 50% HS, occurring in two gradual steps. The first step, centered at 298 K, exhibits a hysteresis of 7 K, while the second step, centered at 179 K, displays a broader hysteresis of 50 K. After second transition at 179 K, the compound maintains a 50% HS state.

The desolvation of **NCS** leads to a single hysteretic step transition, resulting in a complete conversion of Fe(II) centers from low spin (LS) to high spin (HS) ($\chi_M T$ = 3.367 emu·K·mol^{-1}). This transition is centered at 285 K with a hysteresis of 29 K (Figure 4.4.3c).

The anhydrous **NCSe** exhibits a similar behavior, with transition occurring at 288 K and a hysteresis of 29 K. However, in this instance, the transition is incomplete. Even in the first cycle, the value of $\chi_M T$ reached (2.83 emu·K·mol^{-1}) is insufficient to assume a 100% population of high spin (HS) centers, compared to the theoretical value of 3.00 emu·K·mol^{-1}. Assuming an ideal value of $\chi_M T$ with a minimal orbital contribution (μ_{eff} = 5.1 μ_B), $\chi_M T$ should reach 3.25 emu·K·mol^{-1}. Thus, at 400 K, the total HS population corresponds to approximately 90% (2.83 emu·K·mol^{-1}). During the second cycle, the transition shifts from 90% to 35% HS (1.15 emu·K·mol^{-1}) (Figure 4.4.3d).

In the case of **Br**, after desolvation, the compound exhibits two-step transitions. The first transition is abrupt, with a T_c of 297 K and a hysteresis of 25 K, occurring from 100% to 40% high spin (HS) state (from $\chi_M T$ = 3.45 to 1.38 emu·K·mol^{-1}). This is followed by a gradual transition encompassing 30% of the overall transition (from $\chi_M T$ = 1.38 to 0.34 emu·K·mol^{-1}). The gradual transition does not exhibit hysteresis, whereas the abrupt one does, accompanied by a slight decrease in $\chi_M T$ prior to the abrupt transition (Figure 4.4.3e).

Desolvated **I** exhibits similarities with **Br**. The compound exhibits two-step transitions. The first transition is abrupt, with a T_c of 298 K and a hysteresis of 16 K, occurring from 100% to 40% high spin (HS) state (from $\chi_M T$ = 3.72 to 1.41 emu·K·mol^{-1}). This is followed by a gradual transition encompassing 15% of the overall transition (from $\chi_M T$ = 1.41 to 0.58 emu·K·mol^{-1}). The gradual transition does not exhibit hysteresis, whereas the abrupt one does, accompanied by a slight decrease in $\chi_M T$ prior to the abrupt transition (Figure 4.4.3f).

Photo-response of all compounds were investigated at 10 K under the irradiation with 640 nm light and all compounds exhibit Light-Induced Excited Spin-State Trapping (LIESST) although total conversion (100% HS) is only achieved for **BF_4** and **PF_6**. Relaxation of the photo-induced state for the rest of the complexes occurred in the range of 60 to 97 K, with a median value of T_{LIESST} approximately 80 K, which is notably high compared to values reported for other compounds in the literature.[229–232]

Moreover, it is important to note that for compounds exhibiting two different compositions, solvated and unsolvated, they exist a difference in T_{LIESST} between these two phases. However, in neither case do they achieve complete photoconversion. Additionally, it is noteworthy that the photo-relaxation from the photoexcited HS state to the thermal LS state is not always a single-step process. Each compound exhibits different dynamic relaxations occurring in multiple steps, from first order to second order, which may be a consequence of the multi-step thermal transitions observed in these compounds under varying thermal conditions.[233]

Figure 6.4.26. compiled all LIESST of all complexes and Table 4.4.1 presents the primary magnetic parameters for the 9 different compounds. The compounds are categorized based on whether they are anhydrous or solvated, as well as their in situ desolvation. Additionally,

Table 4.4.1. Primary magnetic parameters for the all the compounds based on SQUID and LIESST measurements. The compounds are categorized based on whether they are anhydrous or solvated form, as well as their in situ desolvation.

Anhydrous					
Complex	**T_c (K)**	**ΔT (K)**	**HS fraction (%)**	**Character**	**T_{LIESST} (K)**
ClO_4	227	8	100	Abrupt	75
BF_4	227	15	100	Abrupt	75
PF_6	T_c1: 277	4	50	Abrupt two step	59
	T_c2: 297	5	50		
CF_3SO_3	242	-	66	Gradual	88
Solvated form					
Complex	**T_c (K)**	**ΔT (K)**	**HS fraction (%)**	**Character**	**T_{LIESST} (K)**
$NO_3 \cdot 2H_2O$	-	-	100	-	-
$NCS \cdot 2H_2O$	326	-	100	Abrupt	81
$NCSe \cdot 2H_2O$	323	-	100	Abrupt	76
$I \cdot 2H_2O$	329	-	100	Abrupt	80
$Br \cdot 2H_2O \cdot MeOH$	330	-	100	Abrupt	78
In situ desolvation					
Complex	**T_c (K)**	**ΔT (K)**	**HS fraction (%)**	**Character**	**T_{LIESST} (K)**
NO_3	T_c1: 179 T_c2: 298	7, 50	40 7	Abrupt two step	97
NCS	285	29	100	Abrupt one step	81
NCSe	288	29	60	Abrupt one step	-
I	T_c1: 216 T_c2: 297	16, 0	40 15	Two step: one abrupt and one gradual	-
Br	T_c1: 216 T_c2: 297	25, 0	40 30	Two step: one abrupt and one gradual	78

critical temperature, hysteresis, high spin fraction, nature of the transition, and T_{LIESST} are listed for each compound.

Additionally, spin transition and desolvation were also confirmed by DSC measurements (Figure 6.4.27). In the cases of **BF_4**, **PF_6**, and **CF_3SO_3**, which are unsolvated, transitions were observed in the first cycle, although the magnitude (enthalpy of the process) varies significantly in each case. For **NCS** and **NCSe**, transitions were detected in the second cycle after desolvation, whereas for **NO_3**, **Br** and **I**, desolvation and transition occur at similar temperatures, with both peaks appearing in the first cycle. Interestingly, subsequent cycles did not exhibit later transitions, even though the sample was exposed to three cycles of heating and cooling.

In order to directly examine the pressure influence on the spin transition and to explore potential future applications in barocalorics applications for these compounds, we conducted preliminary high-pressure DSC (HP-DSC) experiments on the **PF_6** sample under isobaric conditions, up to 70 bar (Figure 4.4.4) in collaboration with Prof. Beceiro from Coruña University. As expected, the onset of the phase transition shifts towards higher temperatures as pressure increases, yielding a dT/dP value of 28 $K \cdot kbar^{-1}$. This value falls within the range of other reported values,[103] implying the promising potential of this series of compounds as candidates for further exploration regarding their barocaloric properties.

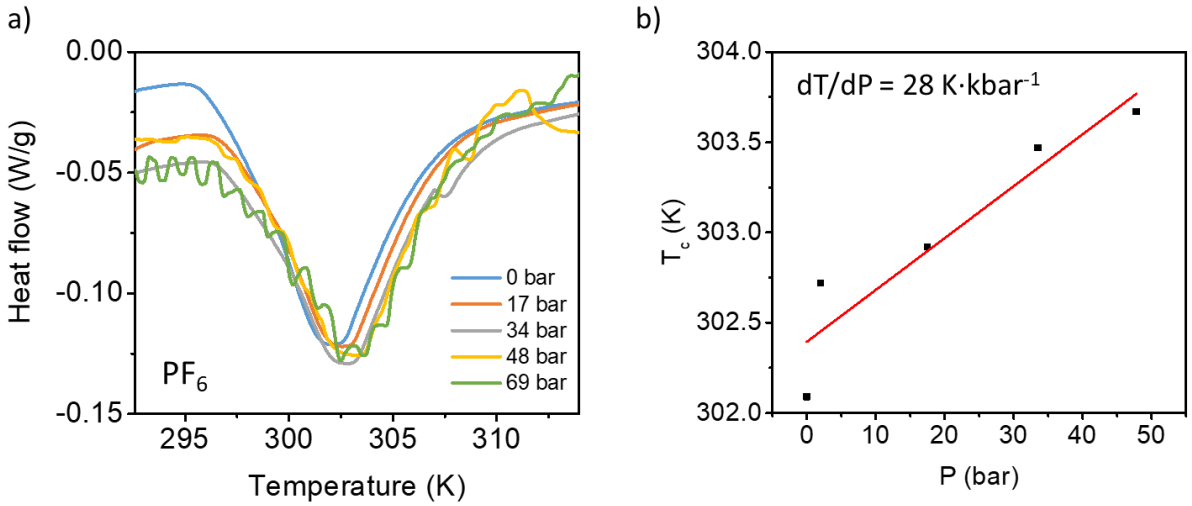

Figure 4.4.4. DSC measurements for **PF_6** under applied hydrostatic pressure with heating and cooling rates of 10 °C/min (a). T_c pressure-dependence (b). We denote 0 bar as the ambient pressure.

4.4.5 Raman Spectroscopy measurements

Variable-temperature Raman spectroscopy, served as a qualitative method to validate the occurrence of spin transitions in metal complexes and to identify associated structural features. To monitor the spin transition and discern between high spin (HS) and low spin (LS) states, we relied on assignments supported by previously reported DFT calculations, particularly utilizing the characteristic diagnostic bands at 1019 cm^{-1} (HS) and 1039 cm^{-1} (LS), which correspond to the pyridine ring breathing coupled to Fe(II)–N vibrations.[164,234,235] Notably, these vibrational modes are consistent across both complexes due to the similar octahedral

environment surrounding Fe(II). This assignment aligns with similar investigations examining Raman spectra and SCO in other bpp derivatives.[236–238]

The estimation of the HS/LS fraction as a function of temperature was achieved through the analysis of the relative area of the respective peaks. Across a wide range of measured temperatures, the coexistence of HS and LS states was observed, in agreement with magnetic measurements (Figure 4.4.5). For anhydrous samples exhibiting abrupt transitions (such as **ClO_4** and **BF_4**), the observed transition temperatures were consistent with magnetic data, albeit with slight deviations attributable to thermal inertia within the Linkham device. In the case of **PF_6**, three distinct states -LS, intermediate spin (IS), and HS- were identified within a similar temperature range (Figure 4.4.5a-c).

In the investigation of hydrated samples, samples were subjected to a heating cycle up to 400 K to facilitate solvent loss, conducted under a nitrogen atmosphere, as the primary focus was on the anhydrous forms. However, it was observed that under the experimental conditions, even with a flux of inert atmosphere, compounds quickly reabsorbed solvent molecules, making it impossible to measure changes associated with the anhydrous samples in some cases.

Nevertheless, it was possible to isolate intermediate states for **NO_3**, **NCS**, **NCSe**, **CF_3SO_3** and **I**. By integrating the relative area of both peaks, it was determined that **NO_3** and **CF_3SO_3** exhibited a 50-50% HS/LS state, while **I** displayed a 38-62% HS/LS ratio. **NCS** and **NCSe**, on the other hand, exhibited a 75-25% HS/LS ratio. Finally, in the case of **Br**, although some spectral shifts were observed, a clear spin transition was not evident. This is an anomaly, as **Br** at room temperature should exhibit a low spin (LS) state, but Raman spectra shows is in a high spin (HS) state. This can be attributed to desolvation occurring when subjected sample to inert atmosphere conditions even at room temperature (Figure 4.4.5d-i).

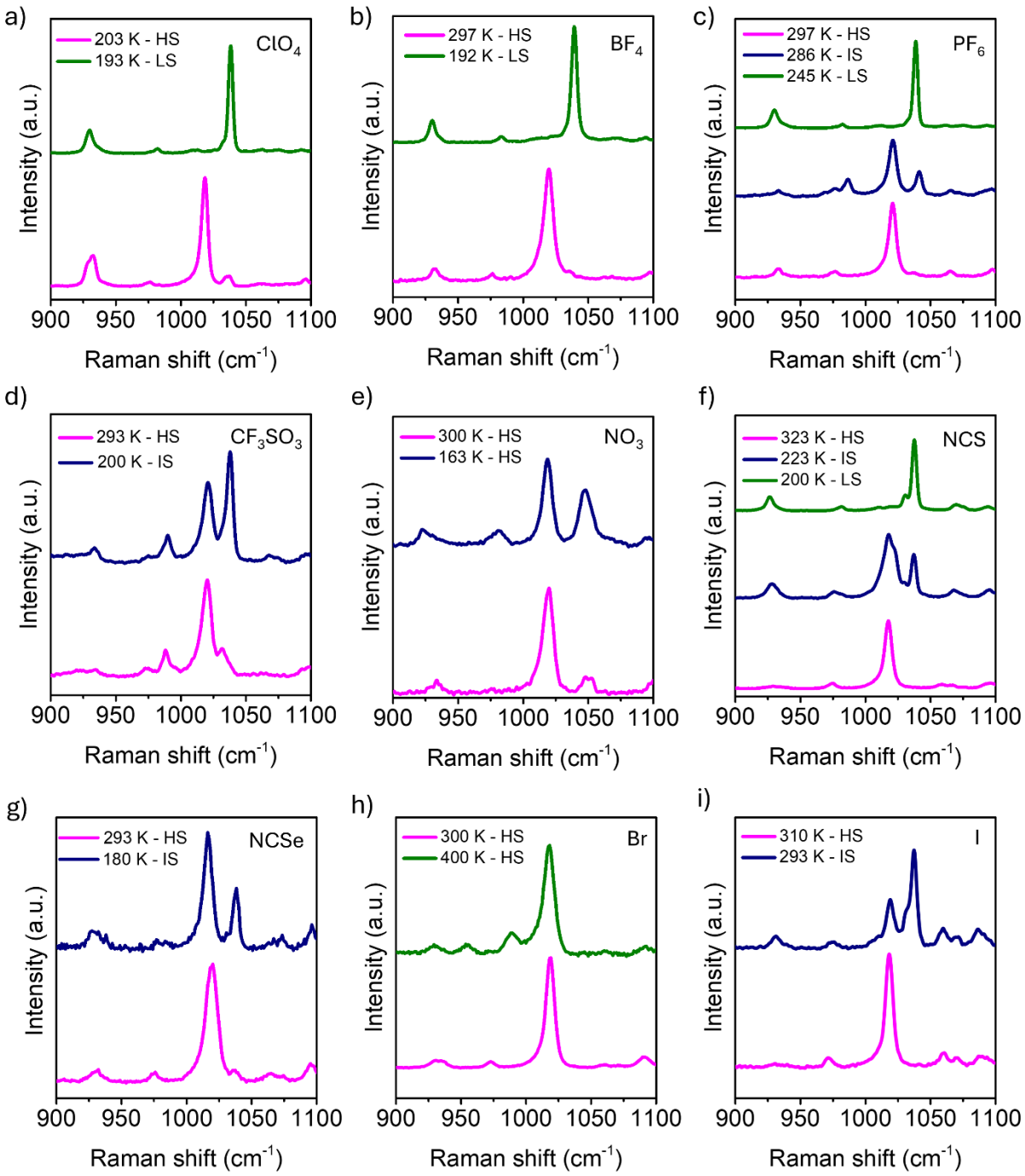

Figure 4.4.5. Variable-temperature Raman spectra under 785 nm excitation showing the 900 to 1100 cm^{-1} region. Temperatures were selected in order to illustrate low spin (LS), intermediate spin (IS) and high spin (HS). List of compounds: **ClO_4** (a), **BF_4** (b), **PF_6** (c), **CF_3SO_3** (d), **NO_3** (e), **NCS** (f), **NCSe** (g), **Br** (h) and **I** (i).

4.4.6 Magneto-structural correlation

Drawing on the results from Section 4.2, it is possible to establish some magneto-structural correlations in the series of *p*-Cl-3-bpp complexes. On one hand, in anhydrous compounds, such as **ClO_4** and **BF_4**, the presence of halogen bond, alongside intra/internetwork hydrogen bonds, confers a high level of cooperativity to the system. This cooperative effect manifests in an abrupt transition with minimal hysteresis. In contrast, in cases where halogen bonding is absent, as observed with **PF_6**, the system exhibits a lower degree of cooperativity (resulting in a less interconnected 3D lattice). Here, the transition unfolds in two distinct steps with a gradual transition.

Establishing a magneto-structural correlation becomes a more challenging task for structures containing solvents. However, previous studies have shown that hydrated compounds may exist in either the HS or LS state depending on aryl-aryl interactions via π–π stacking with four neighboring iron complexes, giving rise to which is known as terpyridine embrace motif.[67] In the case of **NCS**, **NCSe**, **Br** and **I**, aryl-aryl interactions occur between adjacent pyrazole rings, with four Fe(II) complexes neighbors, which are found within the range of 3.50-4.00 Å, hence all of them are in the LS state in their hydrated form. Meanwhile, these interactions are not established in the case of **NO_3**, which is in the HS state (Figure 4.4.6).

We observe that for the four hydrated structures (**NCS**, **NCSe**, **Br** and **I**), the solvent loss is concomitant with a complete spin transition near room temperature (above 300 K). These results demonstrate that the phenomenon of spin conversion is associated with the complex desolvation process.

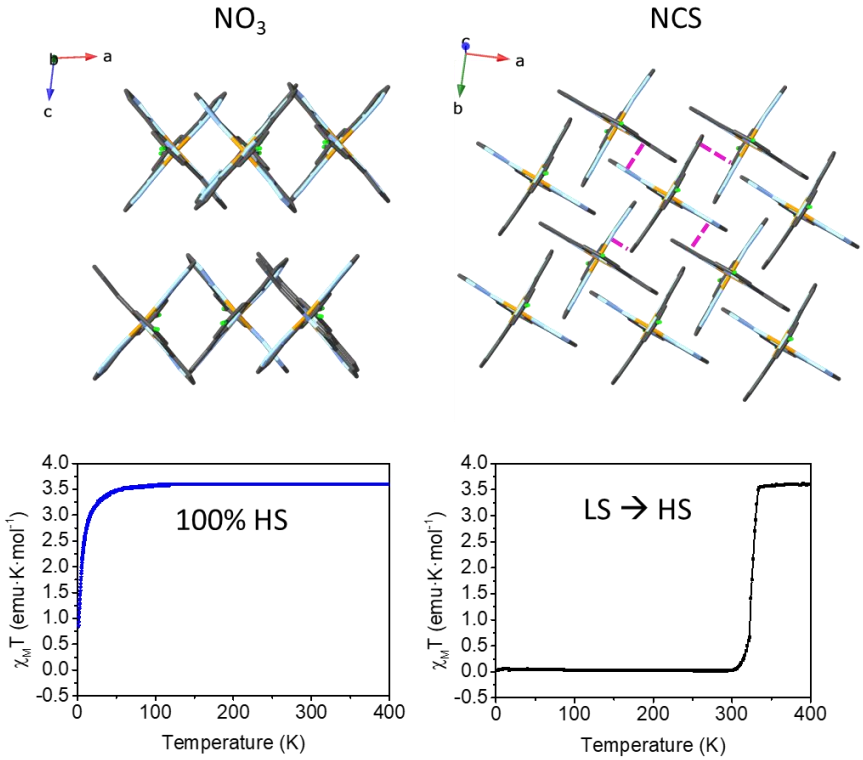

Figure 4.4.6. Magneto-structural correlation between NO_3 and NCS showing the relationship between different packing diagrams within a 2D single layer comprising $[Fe(p\text{-Cl-3-bpp})_2]^{2+}$ SCO units, alongside variable-temperature magnetic susceptibility ranging from 2 to 400 K. Ball-and-stick representations of **NO_3** and **NCS** are depicted, highlighting π–π stacking interactions between bpp ligands of neighboring $[Fe(p\text{-Cl-3-bpp})_2]^{2+}$ units in magenta.

When studying dehydrated samples in situ, it becomes more challenging to establish a structural correlation, as the crystals were measured at room temperature (via SCXRD), but they experienced a loss of crystallinity, and it was only possible to extract structural information in the case of **NCS**.

When dehydrated, **NO_3** exhibits two incomplete gradual transitions. In this case, it remains plausible since the system does not form halogen bonds, leading to decreased cooperativity. As a result, both transitions demonstrate a high hysteresis, and furthermore, the transitions are not complete. Nonetheless, we can infer, without identifying which interactions are maintained, that the network retains some degree of connectivity since both transitions are distinguishable.

Upon dehydration, **NCS** undergoes a complete transition to the HS state. This dehydration can be confirmed through X-ray structure analysis. The structure becomes less connected as part of the hydrogen bonds and π–π interactions are lost, although a new $Cl_{bpp}\cdots\pi$ interaction is formed. Dehydration in this case leads to the segregation of Fe(II) centers into two distinct crystallographic Fe(II) per asymmetric unit. This also results in a symmetry change from an orthorhombic to a monoclinic space group. Despite the decrease in cooperativity, which might suggest the observation of a second-order (gradual) transition, a first-order transition is still observed. This could be attributed to either i) the sample undergoing rehydration during measurement or ii) the $Cl_{bpp}\cdots\pi$ interaction confers cooperativity in the system (Figure 4.4.7).

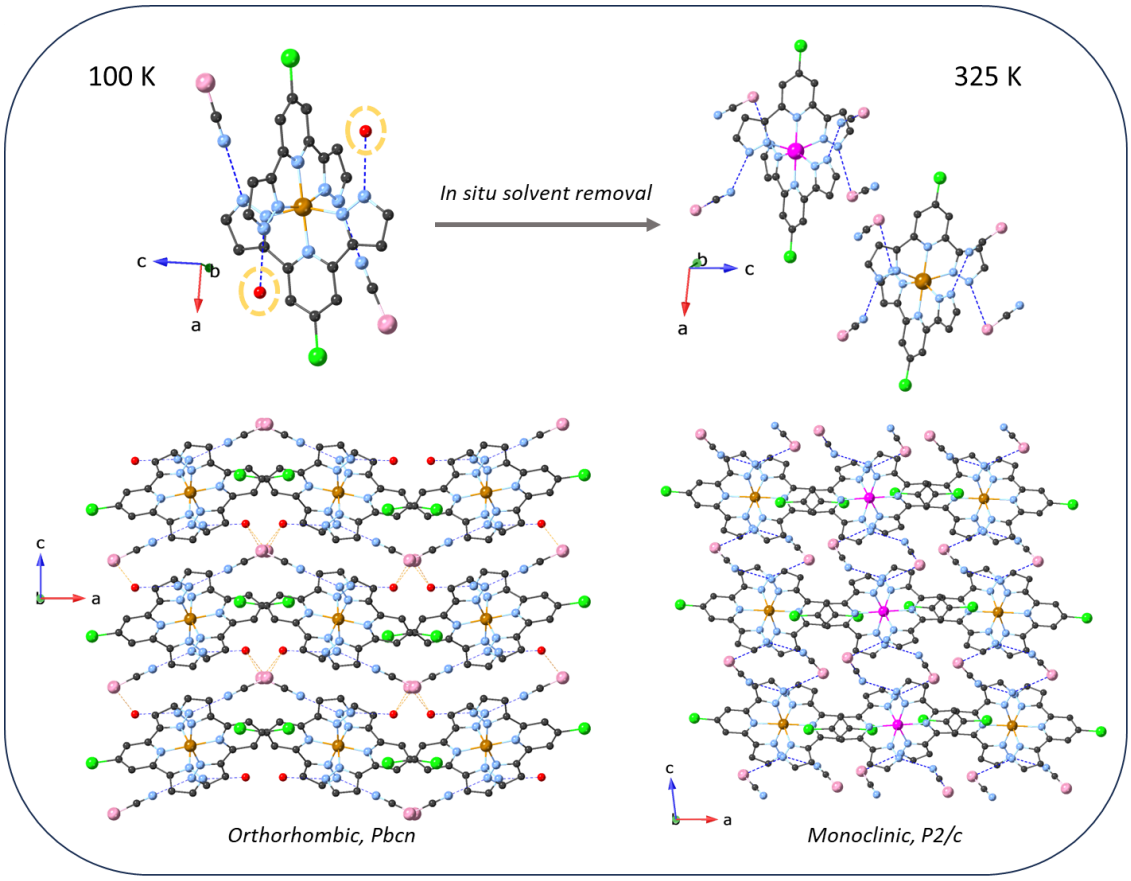

Figure 4.4.7. Comparison of the asymmetric unit and 3D packing of **NCS·2H₂O** and **NCS**. Desolvation was carried out in situ X-Ray diffractometer. The color code used is as follows: nitrogen (blue), carbon (grey), oxygen (red), chlorine (green), iron 1 (orange), iron 2 (violet), and sulfur (pale pink).

For **NCSe**, we suggest that upon dehydration, some internetwork connections are lost, favoring a less cooperative process, as evidenced by an incomplete gradual transition in the second cycle.

In the case of **Br**, the strongest interactions are localized within the layer. Intermolecularly, the $Cl_{bpp}\cdots\pi$ interaction prevails between layers, which, although weak, may persist upon dehydration as it does not depend on solvent molecules. This may impart some cooperativity to the network, resulting in two steps upon dehydration (one gradual and one abrupt). However, the increase in $\chi_M T$ observed at 300 K could also be due to partial rehydration.

The magnetic behavior of **I** is similar to that of **Br**, differing only in a shift in $T_{1/2}$. Despite differences in crystal packing, cooperativity may be similar since both anions have the same geometry and charge. Additionally, it is possible that the compound undergoes partial rehydration during the second heating cycle.

4.4.7 Conclusions

In this study, we introduce eight novel SCO systems based on the 2,6-di(pyrazol-3-yl)pyridine (3-bpp) scaffold, renowned for its SCO properties highly dependent on the second coordination sphere. Functionalization with a chlorine atom, strategically positioned, enhances the potential for new intermolecular interactions, thereby facilitating control over spin transitions. Detailed synthesis methodologies elucidate the preparation of these compounds, highlighting the importance of counterion selection and solvent effects on crystal structures.

Single-crystal X-ray diffraction (SCXRD) analysis provides insights into the structural diversity of these SCO compounds, revealing intricate coordination environments influenced by anion radii and ligand geometry. Magnetic studies, complemented by differential scanning calorimetry (DSC) and thermogravimetric (TGA) analyzes, elucidate the thermal and solvent-induced spin transitions, showcasing the versatility of these compounds in responding to external stimuli. Raman spectroscopy corroborates the occurrence of spin transitions, with variable-temperature studies revealing the coexistence of HS and LS states across a range of temperatures. Magneto-structural correlations highlight the role of intermolecular interactions in governing spin transitions, with halogen and hydrogen bonds playing crucial roles in modulating cooperativity and transition behaviors. Magneto-structural correlations further underscore the influence of solvent effects on spin transitions, with solvent loss accompanying complete spin conversions in hydrated structures.

Overall, this comprehensive investigation provides valuable insights into the synthesis, structure, and properties of novel SCO compounds, shedding light on the interplay between molecular architecture and spin transition behaviors. These findings not only advance our fundamental understanding of SCO phenomena but also pave the way for the design and development of functional materials for next-generation applications in molecular electronics and spintronics.

4.5 Integrating Bistable Behavior into 2D Carbon Structures

4.5.1 Background

Graphene is an allotrope form of carbon, essentially a monolayer of sp2 carbon atoms packed in a 2D honeycomb lattice. Since its discovery in 2004,[124,125] this carbon-based material has become a very important material because of the countless applications including flexible electronics, sensors, transparent conductive films, thermoelectric devices, capacitors, batteries, fuel cells, spintronic devices, high-frequency circuits, toxic material removal…[122,239–243]

Many efforts are focused on obtaining well-defined sheets of graphene, that include methods such as micromechanical or chemical exfoliation of graphite,[244] chemical vapor deposition (CVD) growth, chemical, electrochemical, thermal, or reduction of graphene oxide (GO) to obtained the reduced graphene oxide (rGO).[245,246] GO and rGO, among others, show different properties mainly because of the presence of oxygen defects on the surface which also originates an increase on the reactivity. GO presents a high degree of oxygen-containing functional groups on its surface, which provide reactive sites for further chemical modification, enabling tailored properties and applications. RGO exhibits improved processability due to the introduction of oxygen-functional groups, enhancing dispersibility in solvents and showing enhanced chemical reactivity compared to pristine graphene. This requires a commitment, as the introduction of defects decreases the electrical properties, but this increase in reactivity makes it easier to incorporate molecules that provide additional functionality to the graphene.[247]

The implementation of metal complexes —especially those with spin crossover properties— onto two-dimensional substrates to achieve synergy between these materials, has posed a significant challenge in spintronics for the past two decades, particularly when considering a non-covalent approach. The incorporation of metal complexes exhibiting SCO properties holds promise for creating multifunctional materials with adjustable magnetic properties. Some of the most relevant works attempting to obtain these hybrids have already been compiled in Section 3.5. This advancement opens doors to applications in magnetic storage devices, spintronics, and magnetic sensors.[121]

Most studies reported have focused on a non-covalent approach. Therefore, proposing new covalent mechanisms for their functionalization presents a challenge. Different approaches to conjugate coordinating motives to 2D materials, depending on the nature of the surface either graphene or graphene derivatives like GO or rGO have been proposed.[126,128,131] Two of the most widely employed methods to perform covalent functionalization of graphene and rGO are the use of diazonium salts[248,249] or click chemistry.[250] In the case of GO, condensation reactions stand out as the most prevalent method for modification. These reactions typically entail the interaction of amines, hydroxyl, or carboxylic groups on the linker, leading to the formation of amide or ester functionalities. This method has proven to be both the simplest and most widely adopted approach, owing to its ease of implementation and widespread applicability.[251,252]

In contrast, our proposal introduces a groundbreaking covalent strategy employing chelating ligands tailored for the integration of SCO complexes. Based on the preceding information, we have developed five distinct bpp ligands derived from 1-bpp and 3-bpp. The initial series comprises bpp molecules functionalized at the *para*-position with a carboxylic acid, specifically

2,6-bis(pyrazolyl)pyridine-4-carboxylic acid (1-bpp-COOH[79] and 3-bpp-COOH), intended for attachment to graphene oxide (GO) via hydroxyl groups to form an ester linkage. Drawing inspiration from these compounds, we attempted a similar strategy to produce an amine derivative suitable for coupling to the carboxylic acid groups of GO. However, due to the low nucleophilicity of the amine group, a redesign of the connection was necessary. To address this, we devised a bpp motif containing an amine group electronically connected via a spacer. This functionalization was achieved through Sonogashira coupling with 4-ethynylaniline to the appropriate *para*-halogenated bpp. It is worth noting that proper protection of the pyrazole groups is essential for 3-bpp to prevent undesired side reactions and improve solubility (Scheme 4.5.1).

Finally, we delved into covalent functionalization in rGO. Our aim was to assess whether reducing defects significantly contributes to achieving a higher degree of functionalization. In this regard, we employed 1,3-dipolar Cycloaddition on rGO, a reaction successfully applied in functionalization of carbon nanostructures. This process entails the addition of 1,3-dipoles, like azomethine ylides, onto the π-conjugated structure of graphene, preferentially occurring at its edges. This leads to the formation of covalent bonds between the graphene lattice and the dipolarophile. By carefully controlling reaction conditions and the characteristics of the 1,3-dipole and dipolarophile, selective functionalization of graphene can be achieved, enabling precise adjustment of its electronic, optical, and chemical properties.[253–255]

One common method for obtaining azomethine ylide involves the decarboxylation of terminal glycine in the presence of formaldehyde. A glycyl group within the previously synthesized amine-substituted bpp was chosen for the functionalization. Direct alkylation proved challenging to control, prompting us to explore reductive amination as a successful alternative for obtaining specifically designed NH_2-terminated α-amino acids.

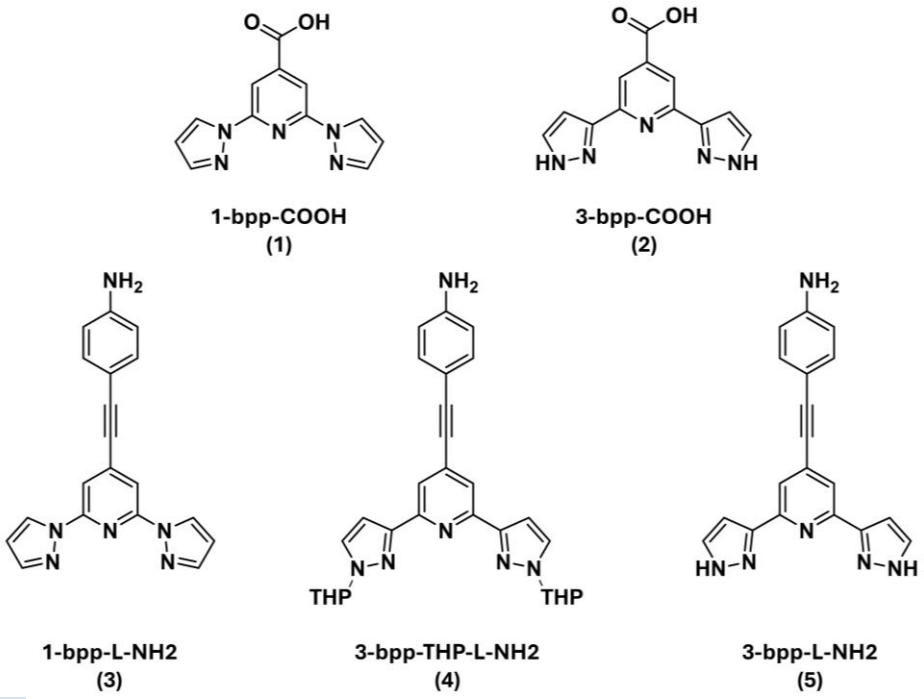

Scheme 4.5.1. Chemical structure of the ligands employed in this section for the covalent functionalization of the graphene oxide.

For the sake of clarity, the following table compiles all materials utilized in this section, along with the corresponding starting graphene, ligand and resulting hybrid materials, including those with ligands or complexes, along with the labels used for referencing each material.

Table 4.5.1. Compilation of all materials described in Section 4.5.3 and Section 4.5.4.

Graphene	Ligand	Functionalized-ligand	Functionalized-complex
Graphene oxide from Hummer's method (hGO)	1-bpp-COOH (1)	1-hGO	Fe-1-hGO
	3-bpp-COOH (2)	2-hGO	Fe-2-hGO
Commercial graphene oxide (cGO)	1-bpp-COOH (1)	1-cGO	Fe-1-cGO
	3-bpp-COOH (2)	2-cGO	Fe-2-cGO
	1-bpp-L-NH2 (3)	3-cGO	Fe-3-cGO
	3-bpp-THP-L-NH2 (4)	4-cGO	Fe-4-cGO
	3-bpp-L-NH2 (5)	5-cGO	Fe-5-cGO
Reduced graphene oxide (rGO)	1-bpp-L-Gly (6)	6-rGO	Fe-6-rGO
	3-bpp-THP-L-Gly (7-THP)	7-THP-rGO	-
	3-bpp-L-Gly (7)	7-rGO	Fe-7-rGO

4.5.2 Functionalizing graphene oxide through covalent bonding

4.5.2.1 Graphene oxide synthesis from a water-enhanced Hummer's method (hGO)

In order to evaluate the chemical functionalization of graphene oxide with carboxylic and amine derivative ligands, two different graphene oxide materials were used. The first graphene oxide was synthesized from the Hummer's method, following a reported synthetic procedure from literature starting from graphite (Figure 4.5.1).[256] This method entails the oxidation of graphene layers, which increases the distance between the layers, facilitating their exfoliation. The obtained graphene oxide (labelled as hGO) was compared with commercial graphene oxide purchased from Graphenea (labelled as cGO).[253,257]

To obtain hGO, natural graphite powder (1.0 g of graphite sheets, Pure Flake (Superior Graphite 2900M, particle sizes in the range of 10 to 100 µm)) was added to a mixture of water (12 mL) and concentrated sulfuric acid (46 mL, < 10 °C) in a 250 mL flask with mechanical agitation. After cooling down the solution to < 10 °C, $KMnO_4$ (3.0 g) was added. Successively, the reaction system was transferred to a 40 °C oil bath and vigorously stirred for 2 h. Then, the oxidation product was slowly poured into 300 mL ice/water mixture under agitation to keep a low temperature. Then, 5 mL of H_2O_2 (30 %) were added dropwise, turning the color of the solution from dark brown to yellow. The mixture was then filtered and washed with 1:9 HCl aqueous solutions (50 mL, 3 times) to remove metal ions. The resulting solid was dried in air and dispersed in 500 mL water to form a hGO aqueous dispersion. Successively, the hGO dispersion was then centrifuged for 20 min twice to remove the unexfoliated particles. The solid was filtered under vacuum and dried by filtering through a 0.45 µm hydrophilic PTFE membrane.

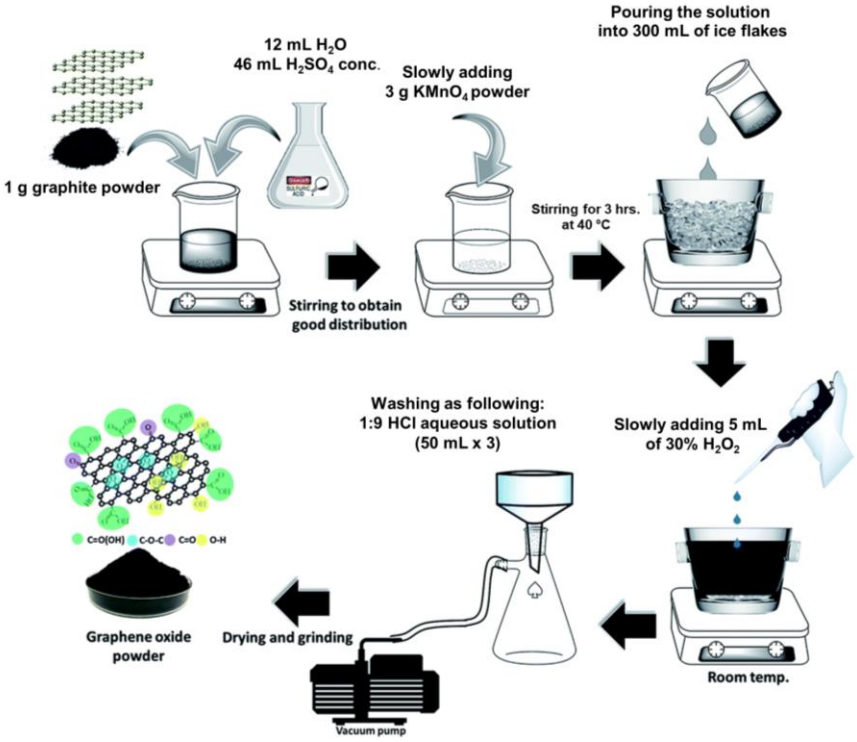

Figure 4.5.1. General scheme of the experimental procedure of Hummer's method. Reproduced with permission from [257]. Copyright 2020, Royal Society of Chemistry.

Thermogravimetric analysis in air reveals that the graphite oxidation process reduces stability, indicating that in both cases, cGO and hGO, the material is oxidized. The degree of oxidation can be estimated based on the weight loss observed within the range between 200 – 300 °C, which is related to the elimination of oxygen functional groups. A slight difference exists between the two samples. cGO exhibits a higher oxidation degree, with a value of 34%, compared to hGO, which has a value of 23%. The combustion of graphene sheets in cGO begins at 400 °C, while in hGO, at 600 °C. This difference is attributed to variations in the size of the graphene sheets, which are larger in the case of hGO (Figure 4.5.2a).

Raman spectroscopy is particularly well-suited for examining the degree of functionalization in graphene by analyzing the D and G bands. D-band arises due to defects and disorder in the graphene lattice, such as vacancies, edges, and functional groups. The intensity of the D-band is proportional to the density of defects and the degree of disorder in the graphene structure. Therefore, an increase in the intensity of the D band indicates a higher degree of functionalization -or oxidation- and structural disorder induced by functional groups. In contrast, G-band is associated with the doubly degenerate E_{2g} phonon mode of sp^2 carbon atoms in the graphene lattice. It represents the in-plane vibrational motion of carbon atoms bonded in a hexagonal lattice. The G-band is highly sensitive to the sp^2 hybridization and the integrity of the graphene structure. Changes in the G-band, such as peak position and width, can provide information about the degree of functionalization and defects. One of the most commonly used metrics for quantifying the degree of functionalization is the ratio of the intensity of the D-band to that of the G-band (I_D/I_G) obtained by Raman spectroscopy. This ratio serves as a measure of the disorder-induced structural changes relative to the pristine graphene lattice. An increase in the I_D/I_G ratio indicates a higher degree of functionalization and structural modification.[258] The Raman spectra (Figure 4.5.2b) further confirms that graphite is highly graphitized as it exhibits minimal defects (I_D/I_G = 0.04). However, after the oxidation, the defect level increases in both the hGO and cGO. Similar to the TGA results, Raman analysis also suggests that cGO has more defects than hGO, with I_D/I_G ratios of 0.89 and 0.84, respectively.

XPS was used to analyze the quality and defects in hGO by assessing the carbon (C) and oxygen (O) content, and estimating the presence of aldehyde, alcohols, and carboxylic groups (Figure 6.5.11).

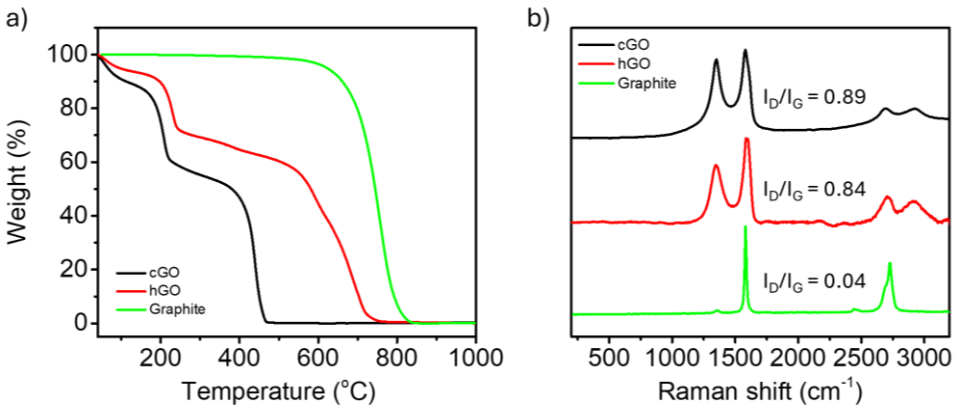

Figure 4.5.2. TGA measurements (a) and Raman spectra (b) for cGO, hGO and starting graphite. TGA was performed at 4 °C/min in air and Raman spectra were acquired using a 514 nm laser wavelength, 10% of laser power, 30 s of exposition and 5 accumulations.

4.5.3 Covalent modified graphene oxide – carboxylic acid derivatives ligands

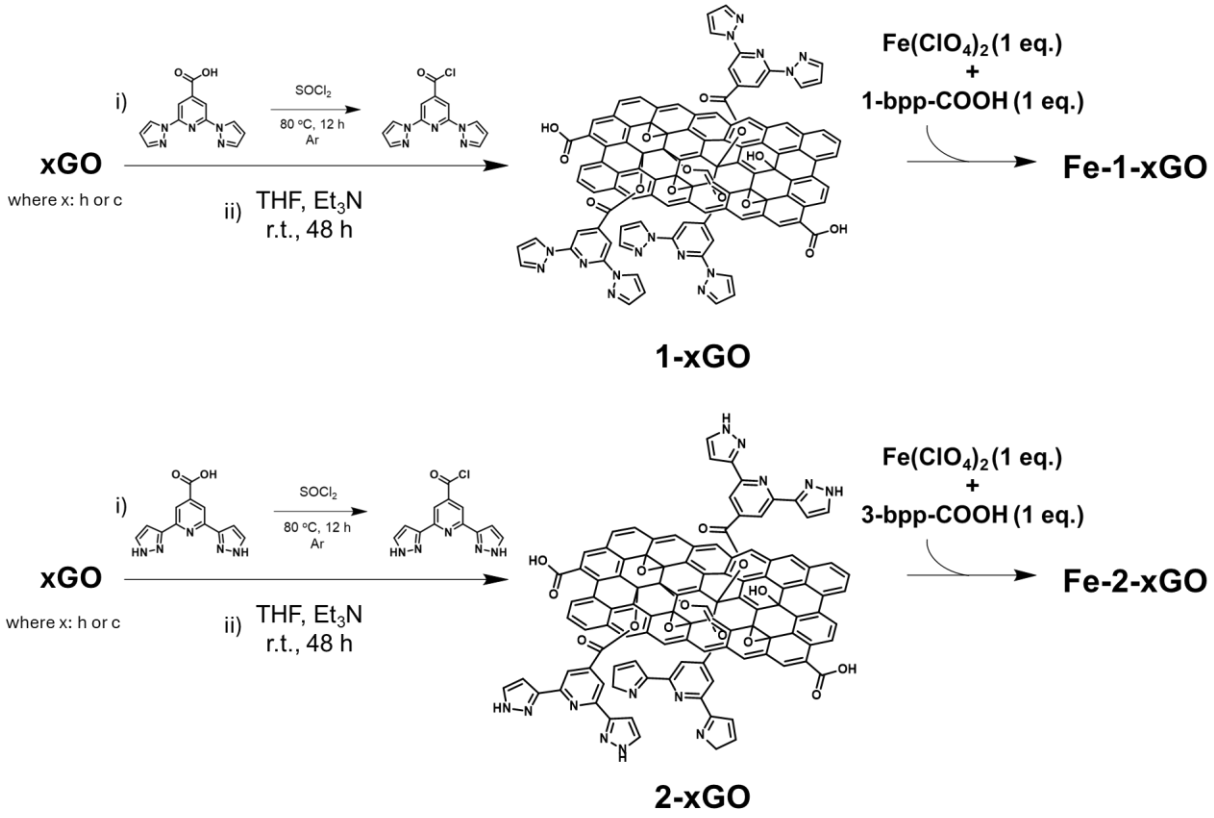

Scheme 4.5.2. General scheme of the synthesis for the obtention of 1-xGO, 2-xGO, Fe-1-xGO and Fe-2-xGO, x is either h (i. e. hGO) or c (cGO).

With these carboxylic ligands, functionalization of GO was performed with both hGO and cGO to compare their functionalization efficiency. The chemical reaction was conducted under same conditions. Scheme 4.5.2 summarizes covalent functionalization reaction for 1-xGO, 2-xGO, Fe-1-xGO and Fe-2-xGO, where x: h or c. The coupling process began with the activation of 2,6-bis(pyrazolyl)pyridine-4-carboxylic acid through thionyl chloride heating under reflux for 12 hours to generate the reactive acyl chloride. Excess thionyl chloride was then removed under vacuum while maintaining the ligand under an inert atmosphere. Subsequently, the coupling reaction was carried out by mixing both compounds (wt %: 2:1 GO:ligand) in the presence of triethylamine (TEA) and tetrahydrofuran (THF) at room temperature for 48 hours. After this period, 1-xGO and 2-xGO were filtered using a 0.45 µm hydrophobic PTFE membrane and washed three times with methanol to remove excess of unreacted ligand. The degree of functionalization was determined via thermogravimetric analysis.

Once functionalization of the GO substrate was determined, the complex formation was conducted by in situ treatment of 1-xGO and 2-xGO with the $Fe(ClO_4)_2$ salt and one equivalent of 1-bpp-COOH or 3-bpp-COOH, thereby completing the octahedral coordination sphere of the metal center, obtaining Fe-1-xGO and Fe-2-xGO. Coupling was performed on both cGO and hGO. In the TGA analysis, a comparison between 1-hGO and Fe-1-hGO is compared with the ligand (1-bpp-COOH) and hGO (Figure 4.5.3a). The alteration in the TGA profile of 1-hGO, serves as an indicator of functionalization. The degree of functionalization can be estimated

by analyzing the difference in defect loss areas between 200 – 300 °C. Subtracting the defect contribution from hGO to 1-hGO reveals a functionalization of 3% for hGO. However, upon forming the complex Fe-1-hGO, minimal change is observed, suggesting unsuccessful complexation. The identical methodology was applied to 1-cGO and Fe-1-cGO (Figure 4.5.3b). TGA analysis of 1-cGO demonstrates a higher degree of functionalization, around 5%. This increase in functionalization appears logical, given that GO exhibits more defects (and consequently, OH^- groups) accessible for covalent bonding with the ligand. In the case of Fe-1-cGO, the metal content (Fe^{2+}) is approximately 10%. Fe^{2+} was quantified from the residue obtained at 1000 °C. Under these experimental conditions, it is considered that the residue exists in the form of Fe_3O_4 and from these it is possible to calculate the metal residue in the sample. This quantity exceeds the theoretical amount expected from complete functionalization (assuming 5% of ligand functionalization should yield 1-2% of Fe^{2+}).

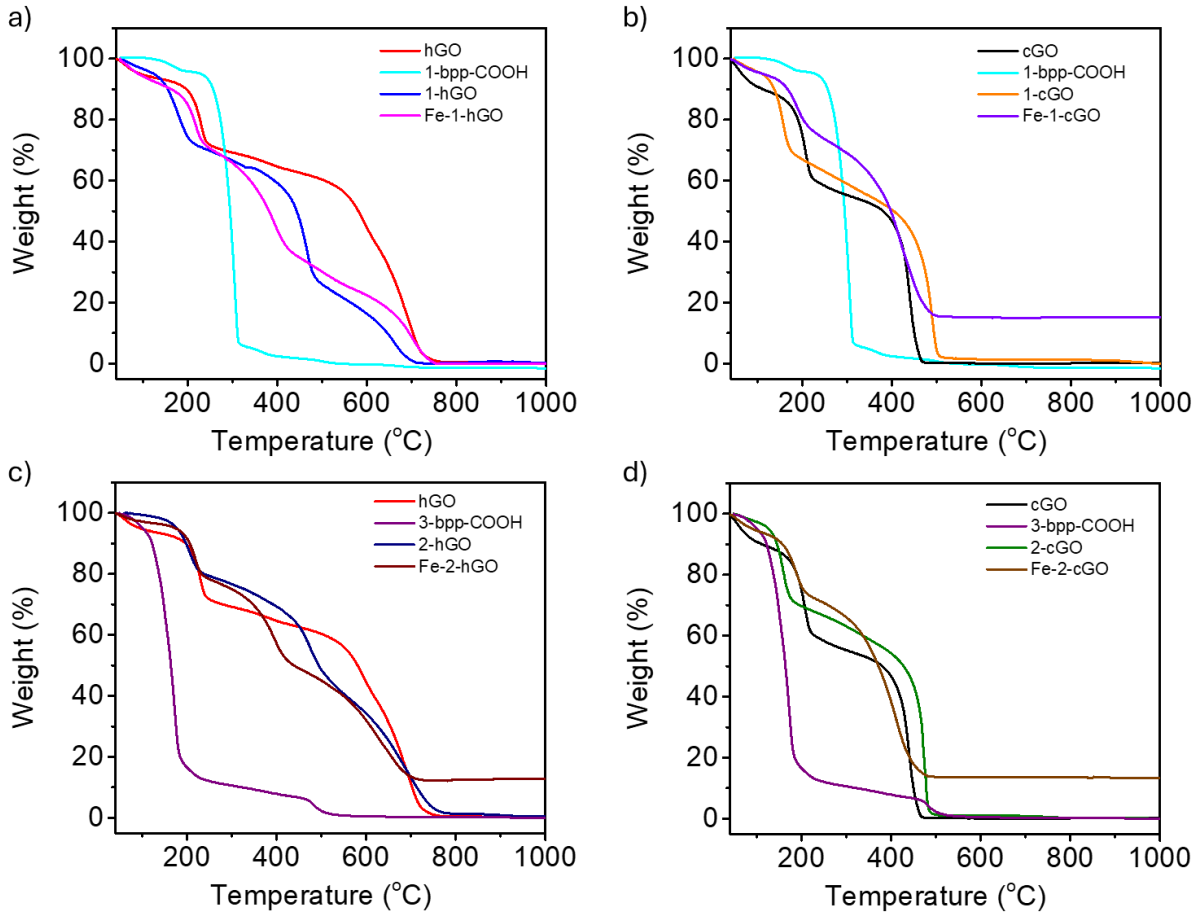

Figure 4.5.3. TGA analysis for 1-GO and Fe-1-GO comparing with 1-bpp-COOH and hGO (a) and cGO (b). 2-GO and Fe-2-GO are compared with 3-bpp-COOH and hGO (c) and cGO (d). Measurements were performed in the range of 40 – 1000 °C at a scan rate of 4 °C/min under air.

TGA analysis of 2-hGO and Fe-2-hGO is compared with the ligand 3-bpp-COOH and hGO in Figure 4.5.3c. Sample comparison with cGO is presented in Figure 4.5.3d. In both scenarios, a similar level of functionalization is observed: 5% for 2-hGO and 4% for 2-cGO. In this case, functionalization appears to enhance the stability since the combustion of the graphene sheets (hGO (600 °C) and cGO (450°C)) in the functionalized samples shifts towards higher temperatures.

After complexation, the residual metal content of Fe^{2+} is 9% for both. Once again, this surpasses the theoretical value. This is hypothesized to be due to an excess of non-covalently attached metal, even after washing, as 1 equivalent of ligand is added for complex formation.

Raman spectroscopy reveals slight differences from covalently modified graphene oxide. The Raman spectra of the ligands 1-bpp-COOH and 3-bpp-COOH were also measured to identify some of the characteristic bands and determine whether they are present in the covalently modified graphene. However, in this case, none of these bands were identified in the spectra. The spectra are provided in Figure 6.5.13. In the case of hGO, the I_D/I_G ratio slightly decreases when it is covalently bonded to the ligand (1-hGO) and with the metal complex (Fe-1-hGO) (Figure 4.5.4a). On the other hand, with cGO, the decrease in defects is higher with both the ligand and the metal complex (1-cGO and Fe-1-cGO) (Figure 4.5.4b). This change in the I_D/I_G ratio is small if we expect covalent functionalization. Other studies have reported changes in this ratio of over 10%.[123,259]

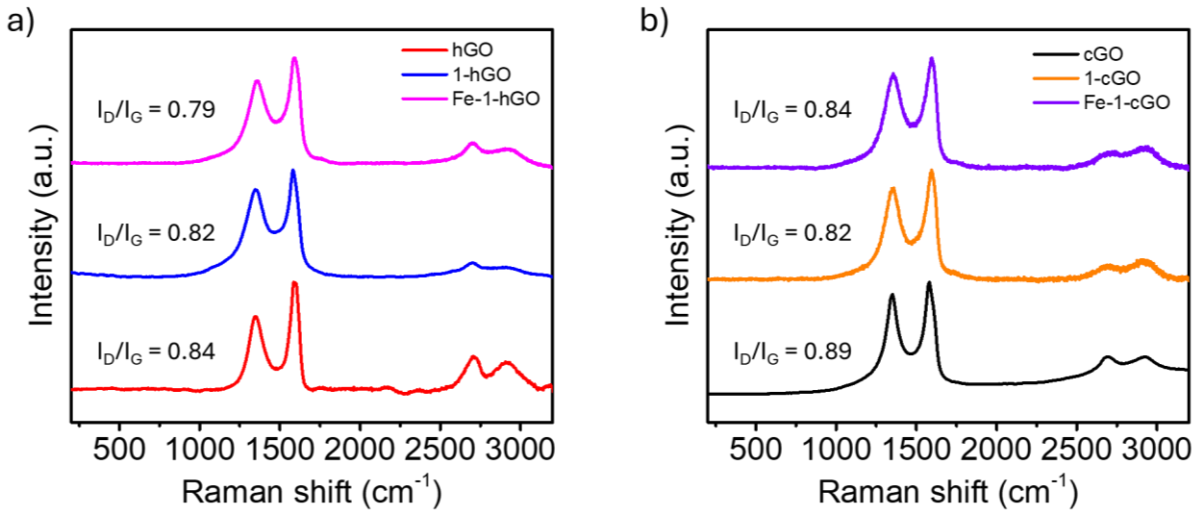

Figure 4.5.4. Raman spectra of hGO, 1-hGO and Fe-1-hGO (a) and cGO, 1-cGO and 1-Fe-cGO (b). Experiments were performed with a 514 nm 50% of laser power, 30 s of exposition and 5 accumulations.

In the case of 2-GO and Fe-2-GO, the I_D/I_G ratio decreases when it is covalently bonded to the ligand and with the metal complex. The change is considerable in the case of hGO, with a decrease in the I_D/I_G from 0.84 to 0.59 (2-hGO) and 0.61 (Fe-2-hGO) (Figure 4.5.5a). On the other hand, with cGO, the decrease is lower when it is covalently modified with both the ligand and the metal complex (2-cGO and Fe-2-cGO) (Figure 4.5.5b). This fact could suggest the functionalization was successful in the case of hGO.

XPS experiments were performed for 1-hGO (Figure 4.5.6), Fe-1-hGO (Figure 4.5.7), 2-hGO (Figure 4.5.8) and Fe-2-hGO (Figure 4.5.9). In addition to the expected carbon (C) and oxygen (O) signals, nitrogen (N) 1s band was observed in all samples at 399 and 401 eV. These bands are attributed to aromatic nitrogen bonds associated with pyridine (pyridinic-N, 399 eV) and C=N or pyrrolic-N (401 eV).[260] This suggests the presence of the molecule in the hybrid material, but it does not provide information on whether covalent bonding occurs. The elemental content of the material surface is presented in Table 4.5.2. The nitrogen content aligns with the degree of functionalization estimated by TGA analysis, as nitrogen comprises approximately 25% of the total ligand. Therefore, the material may exist in both covalent and

non-covalent forms. In contrast, we expected to observe some Fe^{2+} in Fe-1-hGO; however, iron was not detected in that sample. On the contrary, Fe^{2+} was detected in the Fe-2-hGO sample, with an atomic percentage of 0.43%, equivalent to a weight functionalization of approximately 1.5%, which aligns quite well with the observations in TGA.

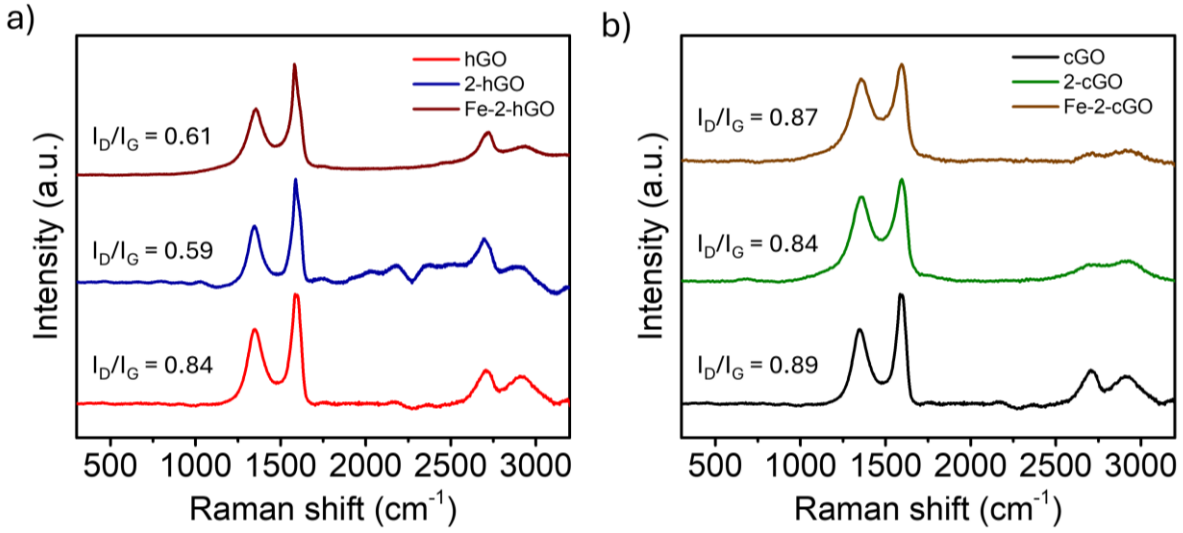

Figure 4.5.5. Raman spectra of hGO, 2-hGO and Fe-2-hGO (a) and cGO, 2-cGO and 2-Fe-cGO (b). Experiments were performed with a 514 nm 50% of laser power, 30 s of exposition and 5 accumulations.

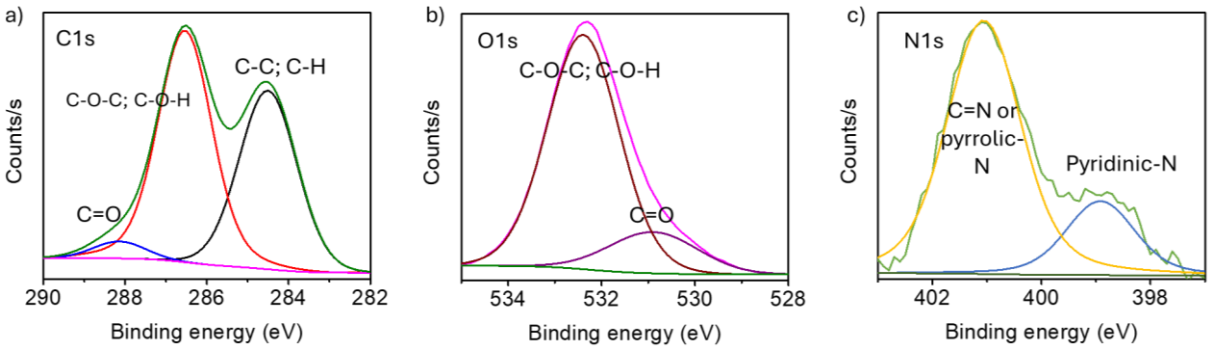

Figure 4.5.6. High resolution XPS spectra of a) C 1s, b) O 1s and c) N 1s for 1-hGO. Charge correction for the C 1s spectrum was set at the binding energy of 284.8 eV.

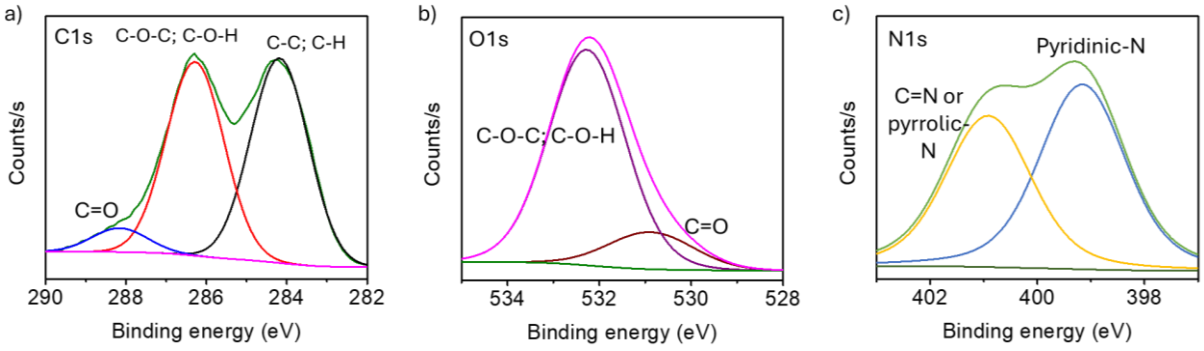

Figure 4.5.7. High resolution XPS spectra of a) C 1s, b) O 1s and c) N 1s for Fe-1-hGO. Charge correction for the C 1s spectrum was set at the binding energy of 284.8 eV.

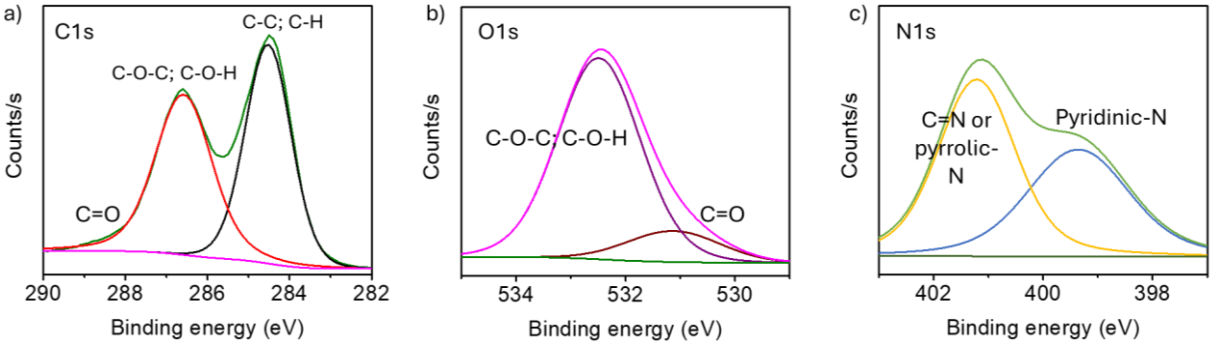

Figure 4.5.8. High resolution XPS spectra of a) C 1s, b) O 1s and c) N 1s for 2-hGO. Charge correction for the C 1s spectrum was set at the binding energy of 284.8 eV.

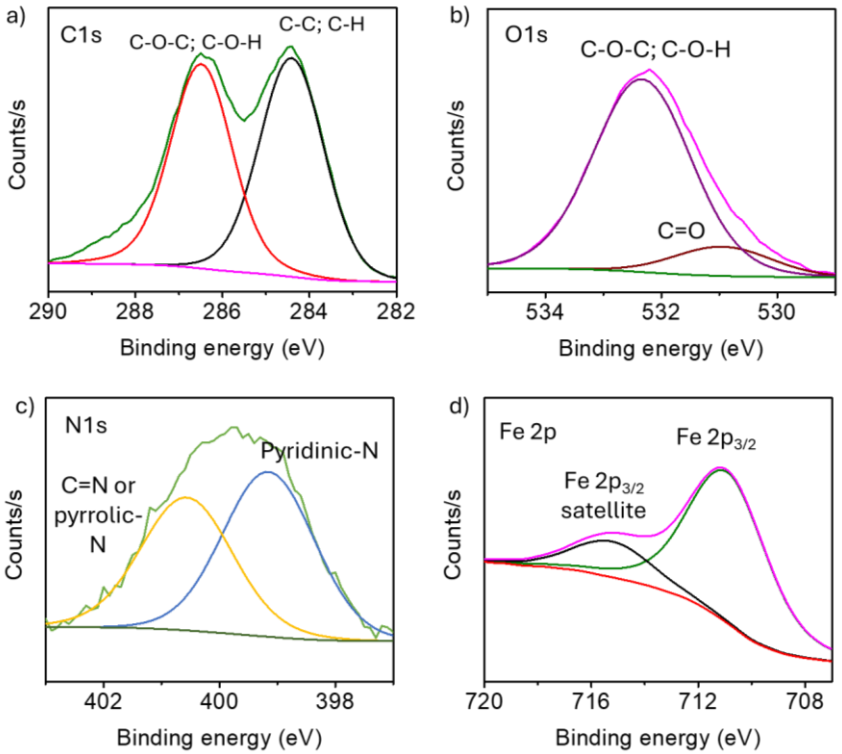

Figure 4.5.9. High resolution XPS spectra of a) C 1s, b) O 1s, c) N 1s and d) Fe 2p for Fe-2-hGO. Charge correction for the C 1s spectrum was set at the binding energy of 284.8 eV.

Table 4.5.2. Quantification of the elemental surface composition of 1-hGO, Fe-1-hGO and 2-hGO

	1 - hGO	**Fe-1-hGO**	**2-hGO**	**Fe-2-hGO**
At. % C	66.87	66.27	71.62	67.38
At. % O	29.77	27.90	25.05	28.07
At. % N	1.75	1.84	1.38	2.97
At. % Fe	-	-	-	0.43
At. Rest	1.6	4.01	27	1.15

As iron was not detected for the case of Fe-1-hGO, we conducted additional experiments to confirm the covalent functionalization. HPLC-MS was performed to study the activation of the carboxylic acids (1-bpp-COOH and 3-bpp-COOH) with thionyl chloride. We observed that the formation of the acyl chloride intermediate occurred only in the case of 1-bpp-COOH, suggesting that the activation of 3-bpp-COOH was not carried out. Consequently, the covalent functionalization cannot be confirmed. Since the presence of metal could not be confirmed in the case of Fe-1-GO, and the covalent coupling of 3-bpp-COOH exhibits low efficiency due to the limited activation of its carboxylic acid, this method was discarded.

4.5.4 Covalent modified graphene oxide – amine derivatives ligands

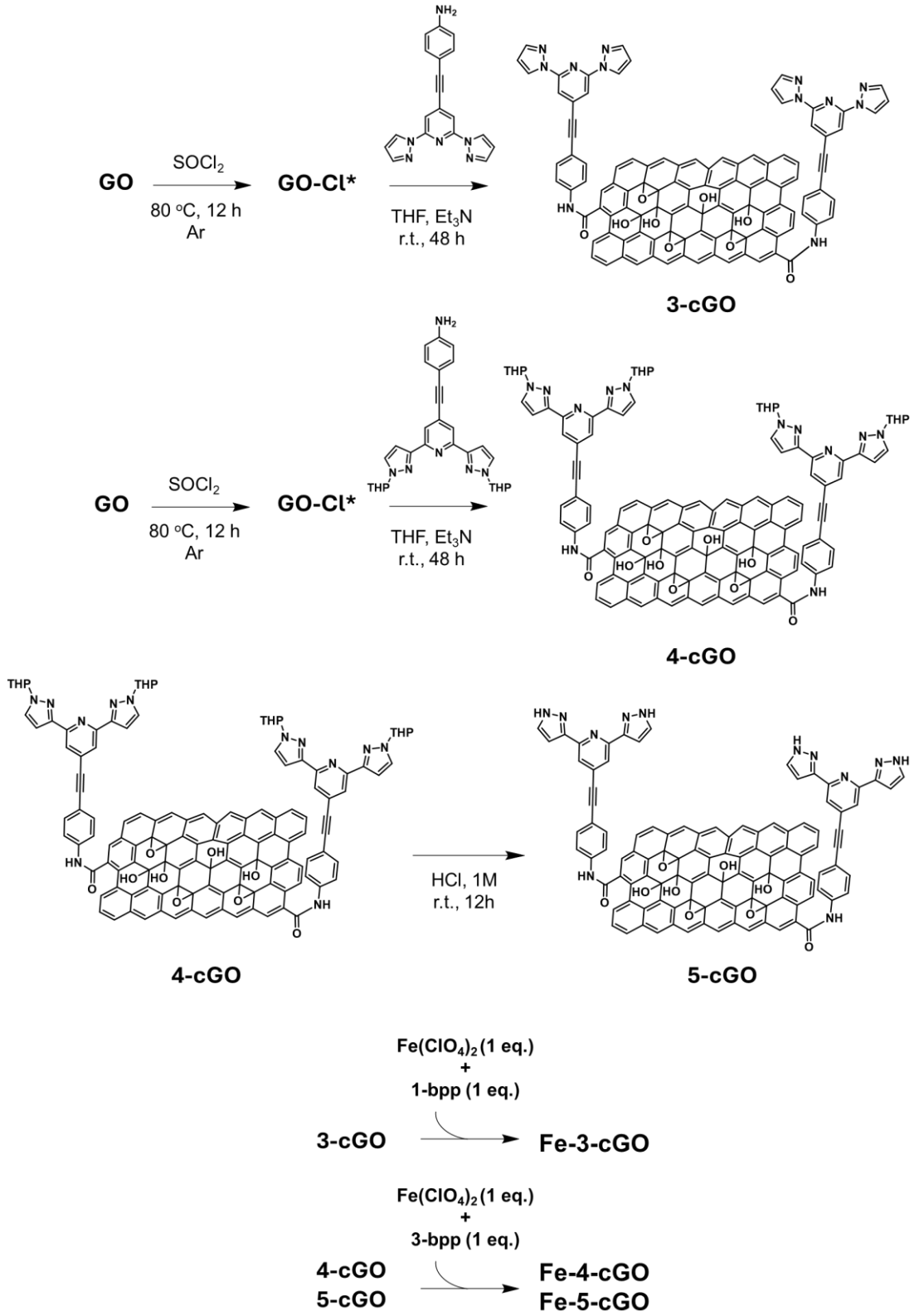

Scheme 4.5.3. General scheme of the synthesis for the obtention of 3-cGO, 4-cGO, 5-cGO, Fe-3-cGO, Fe-4-cGO, and Fe-5-cGO. Synthesis of 5-cGO was performed in-situ by the deprotection of 3-bpp-THP-L-NH2 in HCl 1M media and with a deep cleansing.

To attach the amine-derivative bpp to the carboxylic acids on the surface of cGO, we followed the different strategy from the previous method. The carboxylic groups of the graphene were activated in the presence of thionyl chloride under reflux to form the corresponding acyl chloride. Excess thionyl chloride is then removed under vacuum, maintaining the activated graphene oxide under an inert atmosphere. Subsequently, the coupling reaction is carried out by mixing the amine ligand with cGO (wt %: 2:1 GO:ligand) in the presence of triethylamine (TEA) and tetrahydrofuran (THF) at room temperature for 48 hours. After the reaction, the graphene oxide is filtered using a 0.45 µm hydrophobic PTFE membrane and washed three times with methanol to remove excess unreacted ligand. In this strategy, we only employed cGO for the covalent modification. Scheme 4.5.3 summarizes covalent functionalization reaction for 3-cGO, 4-cGO, 5-cGO, Fe-3-cGO, Fe-4-cGO and Fe-5-cGO.

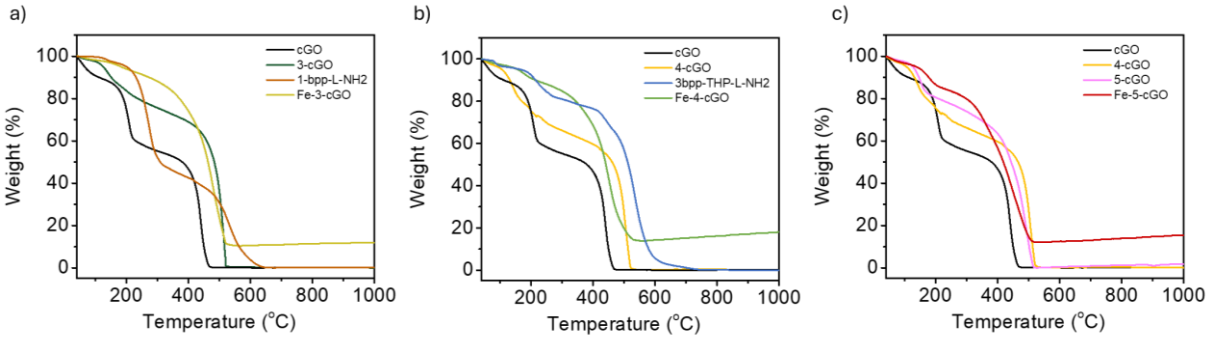

Figure 4.5.10. TGA analysis for 3-cGO and Fe-3-cGO comparing with ligand 1-bpp-L-NH2 (a); 4-cGO, Fe-4-cGO and ligand 3-bpp-THP-L-NH2 (b) and 4-cGO, 5-cGO and Fe-5-GO (c). All samples were compared with the starting material cGO. Measurements were performed in the range of 40 °C – 1000 °C at a scan rate of 4 °C/min under air.

In Figure 4.5.10, the TGA analysis of 3-cGO, 4-cGO, 5-cGO, Fe-3-cGO, Fe-4-cGO and Fe-5-cGO is compared with respect to the ligand (1-bpp-L-NH2 or 3-bpp-THP-L-NH2) and cGO. In the case of 3-cGO (Figure 4.5.10a), analyzing weight loss at 200 °C – 300 °C can estimate a 5% of functionalization. When the complex is formed (Fe-3-cGO), the metal residue of Fe^{2+} corresponds to 7.87%. In the case of 4-cGO (Figure 4.5.10b), we estimate functionalization to be 7%, with an Fe^{2+} residue (Fe-4-cGO) of 10.16%. For 5-cGO (Figure 4.5.10c), the deprotection of THP has been carried out in situ, then it is compared with the previous hybrid, 4-cGO. The removal of THP protection does not significantly alter the TGA profile. Consequently, TGA is not a suitable technique to determine if the deprotection has occurred. In this particular case, the Fe^{2+} loading is 8.75%.

The Raman spectra analysis reveals that all materials, including 3-cGO (Figure 4.5.11a), 4-cGO (Figure 4.5.11b), and 5-cGO (Figure 4.5.11c), exhibit a notably high degree of defects, as indicated by the unexpectedly elevated I_D/I_G ratio (1.04 for 3-cGO, 1 for 4-cGO, and 0.96 for 5-cGO). However, upon formation of the complex, these defects exhibit a consistent decrease of defects (0.81 for Fe-3-cGO, 0.93 for Fe-4-cGO, and 0.73 for Fe-5-cGO). Some studies confirm that the use of thionyl chloride reduces sp^2 domains and edge defects as a result of a reduction in some C=C bonds in graphene oxide, which could be the reason for an increase in the I_D/I_G ratio.[245,261] Based on our understanding, the effect of complexation should not impact the decrease in defects. Therefore, it is possible that this reduction may be attributed to the presence of complexes and/or freely adsorbed non-covalent ligands on the graphene surface.

XPS analysis was conducted to quantitatively assess the incorporation of nitrogen content. The high resolution C1s spectra exhibit typical bands corresponding to various oxygen functional groups. Upon undergoing condensation, the intensities of the C=O and COOH peaks decrease due to the creation of amide bonds. The significant reduction in the C-O-C component suggests potential activation of OH groups of GO by thionyl chloride, followed by the attachment of NH2-terminated linker through the formation of O-S(O)-N linkage. The incorporation of nitrogen is confirmed by the presence of two distinct bands in both 3-cGO and 4-cGO (Figure 4.5.12 and Figure 4.5.13).

The elemental content of the material surface is presented in Table 4.5.3. The nitrogen content exceeds with the degree of functionalization estimated by TGA analysis, as nitrogen comprises approximately 25% of the total ligand. Considering the atomic percentage, the nitrogen content should not exceed 1%. The greatest discrepancy is observed for compound 4-cGO, as the nitrogen content exceeds more than twice the expected amount from functionalization.

Combined energy dispersive X-Ray and scanning transmission electron microscopy (STEM-EDX) techniques were used to map carbon, oxygen, nitrogen, and iron in Fe-3-cGO and Fe-5-cGO. As illustrated in Figure 6.5.15 - Figure 6.5.16, the presence of iron is evident throughout both samples, with iron uniformly distributed across the graphene flakes, without the formation of aggregates or nanoparticles.

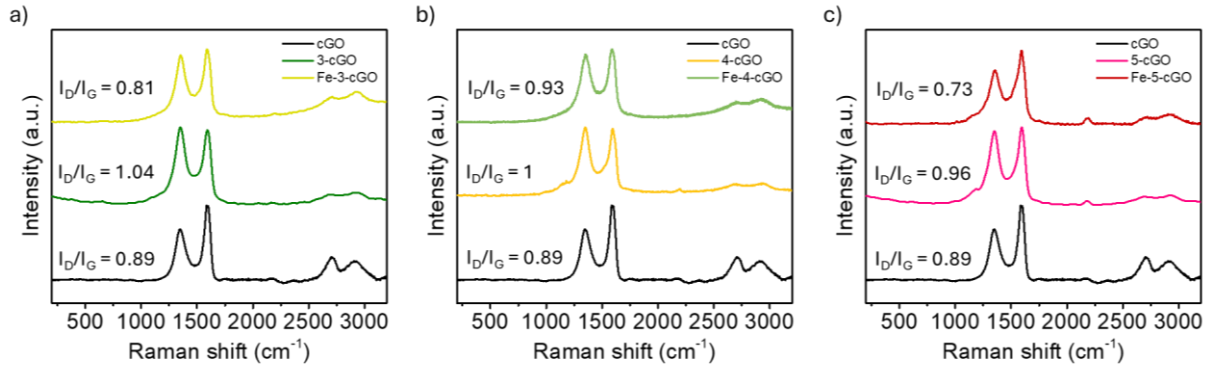

Figure 4.5.11. Raman spectra of cGO, 3-cGO and Fe-3-cGO (a) cGO, 4-cGO and 4-Fe-cGO (b) and cGO, 5-cGO and Fe-5-cGO. Experiments were performed with a 514 nm 50% of laser power, 30 s. of exposition and 5 accumulations.

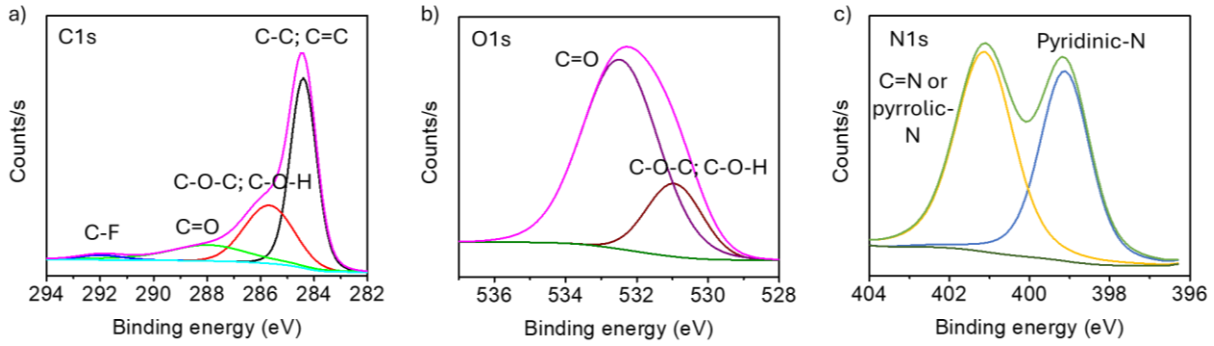

Figure 4.5.12. High resolution XPS spectra of a) C 1s, b) O 1s and c) N 1s for 3-cGO. Charge correction for the C 1s spectrum was set at the binding energy of 284.8 eV. Note that in 3-cGO, a band assigned to C-F is observed at 292 eV, likely attributable to contamination from the PTFE membranes used for filtration of the hybrids.

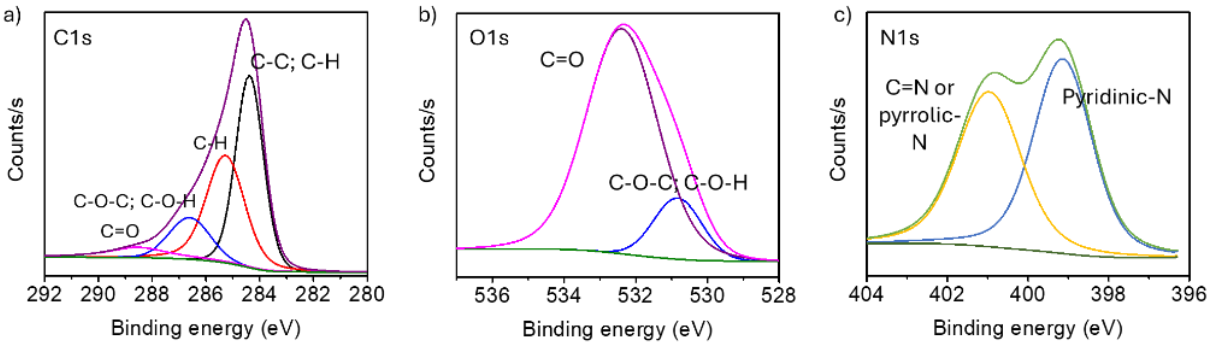

Figure 4.5.13. High resolution XPS spectra of a) C 1s, b) O 1s and c) N 1s for 4-cGO. Charge correction for the C 1s spectrum was set at the binding energy of 284.8 eV.

Table 4.5.3. Quantification of the elemental surface composition of 3-cGO and 4-cGO

	3 - cGO	**4 - cGO**
At. % C	79.27	76.87
At. % O	13.3	14.32
At. % N	3.44	6.16
At. Rest	4.01	2.64

4.5.5 Covalent modified reduced graphene oxide (rGO) - 1,3-DC of azomethine ylide on rGO

Reduced graphene functionalization was prepared following a previous described method in literature.[253] 50 mg of rGO were used to carry out the reaction. 1.5 equivalent (% weight) with respect to graphene of modified NH2-terminated α-amino acid derivative (Scheme 4.5.4) and paraformaldehyde was added to the graphene suspension in dry NMP (0.5 mg/ml). The reaction mixture was heated at 125 °C under magnetic stirring and inert conditions, while the reagents were added each 24 h for 5 days. The resulting mixture was filtered with a 0.45 µm hydrophobic PTFE membrane, and the solid was washed thoroughly with methanol. The product was dried under vacuum oven at 50 °C. In the case of 7-rGO, a prior step involved deprotecting the THP group by stirring it in 1M HCl and then filtering the solution was performed (Scheme 4.5.5).

Functionalization was determined via thermogravimetric analysis. The complex formation was conducted by in situ treatment of rGO with the respective $Fe(ClO_4)_2$ salt and one equivalent of 1-bpp or 3-bpp, thereby completing the octahedral coordination sphere of the metal center, obtaining Fe-6-rGO and Fe-7-rGO.

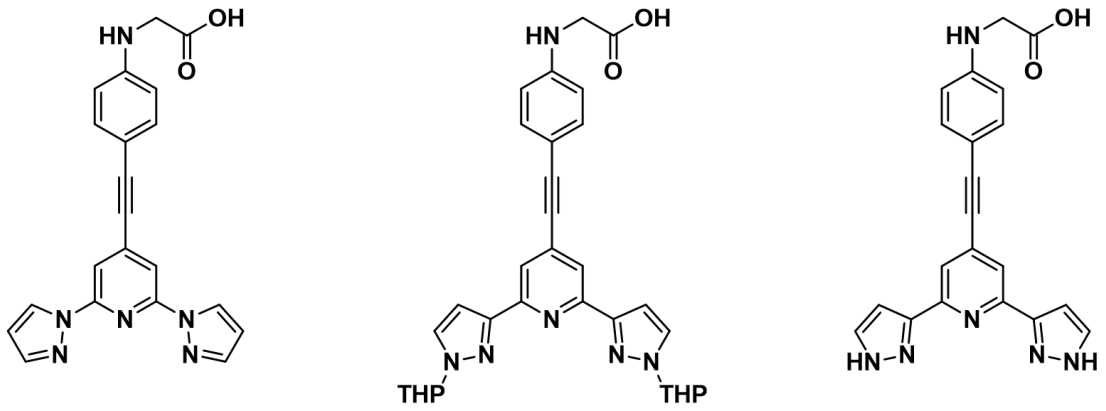

1-bpp-L-Gly (6) **3-bpp-THP-L-Gly (7-THP)** **3-bpp-L-Gly (7)**

Scheme 4.5.4. Chemical structure of the ligands employed in this section for the covalent functionalization of the reduced graphene oxide.

In Figure 4.5.14, the TGA analysis conducted in air for 6-rGO and Fe-6-rGO is compared with the ligand 1-bpp-L-Gly and rGO (Figure 4.5.15a). On the contrary, 7-rGO is compared to the previous step with the protected ligand (Figure 4.5.14b). Ligands 1-bpp-L-Gly and 3-bpp-THP-L-Gly were also measured under air and nitrogen conditions (Figure 6.5.12). To gain further insight into weight loss linked to functionalization, additional TGA analysis was carried out under nitrogen conditions. Based on these findings, the functionalization of 6-rGO and Fe-6-rGO yield ca. 16% (Figure 4.5.15a). For 7-THP-rGO results in a 14%, meanwhile for 7-rGO and Fe-7-rGO ca. 12% (Figure 4.5.15b). This functionalization is much higher than for the method followed with GO, which highlights that this method may be more efficient in terms of covalent functionalization. The notable structural transformations occurring throughout the chemical processing from pristine graphite to graphene oxide (hGO), and subsequently to reduced GO, are provided in Figure 4.5.16.

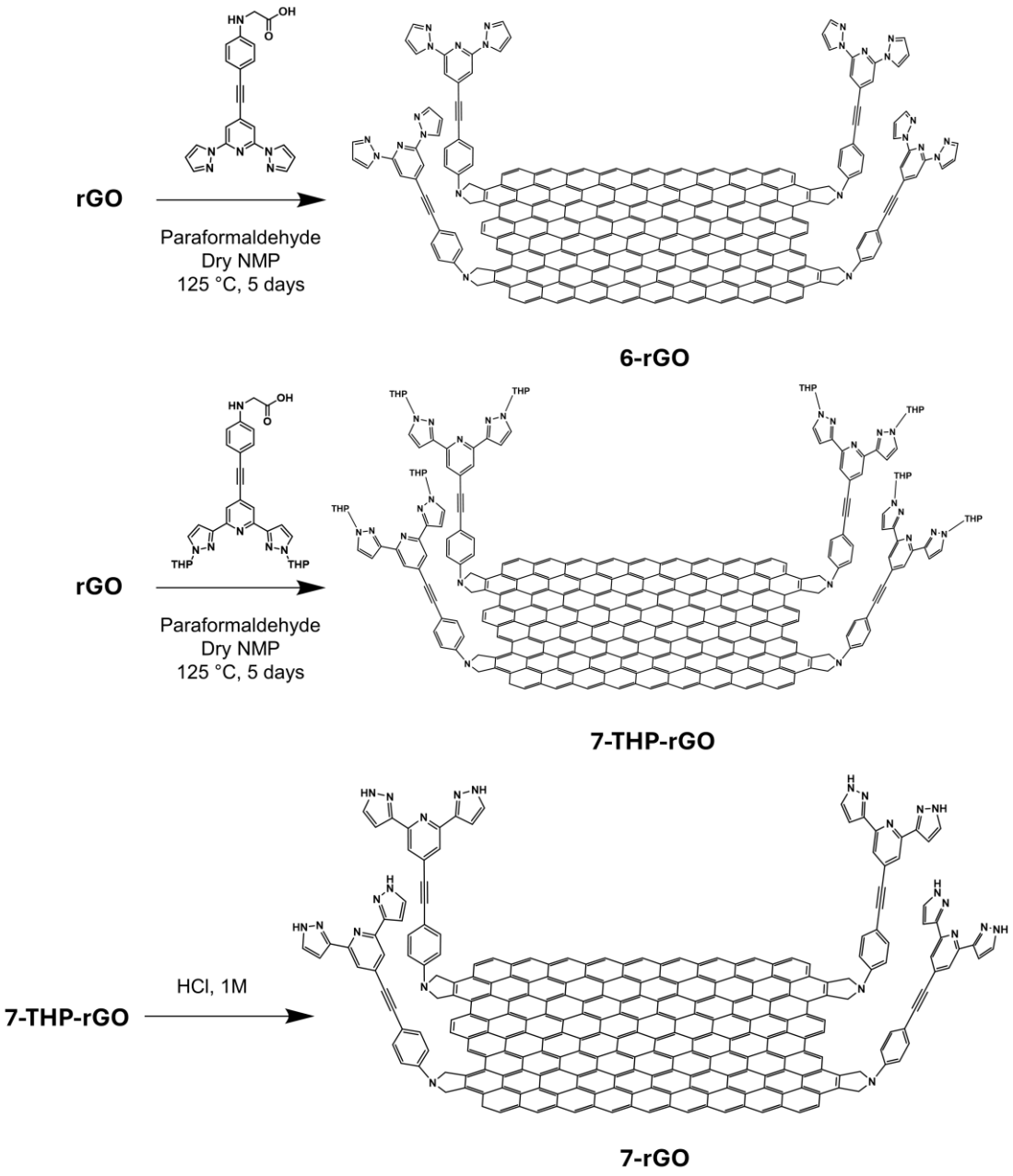

$Fe(ClO_4)_2$ (1 eq.)
+
1-bpp (1 eq.)

6-rGO → **Fe-6-rGO**

$Fe(ClO_4)_2$ (1 eq.)
+
3-bpp (1 eq.)

7-rGO → **Fe-7-rGO**

Scheme 4.5.5. General scheme of the synthesis for the obtention of 6-rGO, 7-rGO, Fe-6-rGO and Fe-7-rGO.

Upon from graphite transition to hGO, the G band undergoes broadening and a shift to 1594 cm^{-1}. Additionally, the emergence of the D band at 1363 cm^{-1} signifies a reduction in the size of the in-plane sp^2 domains, likely attributed to extensive oxidation. The Raman spectrum of rGO retains both G and D bands, positioned at 1584 cm^{-1} and 1352 cm^{-1}, respectively. Notably, rGO exhibits an escalated I_D/I_G ratio compared to hGO. This shift implies a diminution in the average size of the sp^2 domains following the reduction process. Such a phenomenon could be elucidated by the creation of new graphitic domains post-reduction, characterized by smaller dimensions.[245] We consider it pertinent to highlight this aspect since the I_D/I_G ratio reverses upon chemical transformation from GO to rGO.

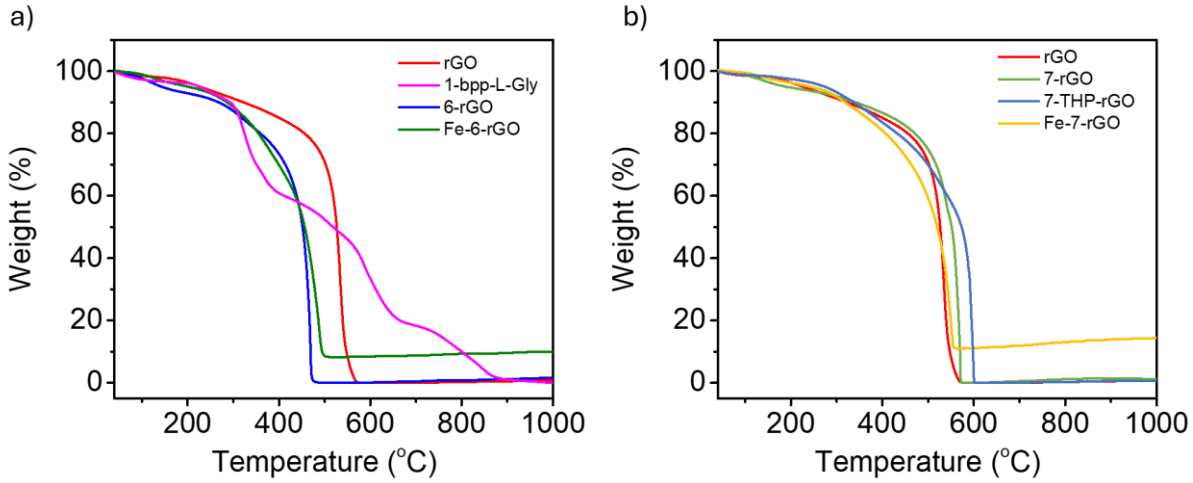

Figure 4.5.14. TGA analysis for rGO, 6-rGO, Fe-6-rGO and 1-bpp-L-Gly (a) and rGO, 7-rGO, 7-THP-rGO and Fe-7-rGO (b). Measurements were performed in the range of 40 – 1000 °C at a scan rate of 4 °C/min under air.

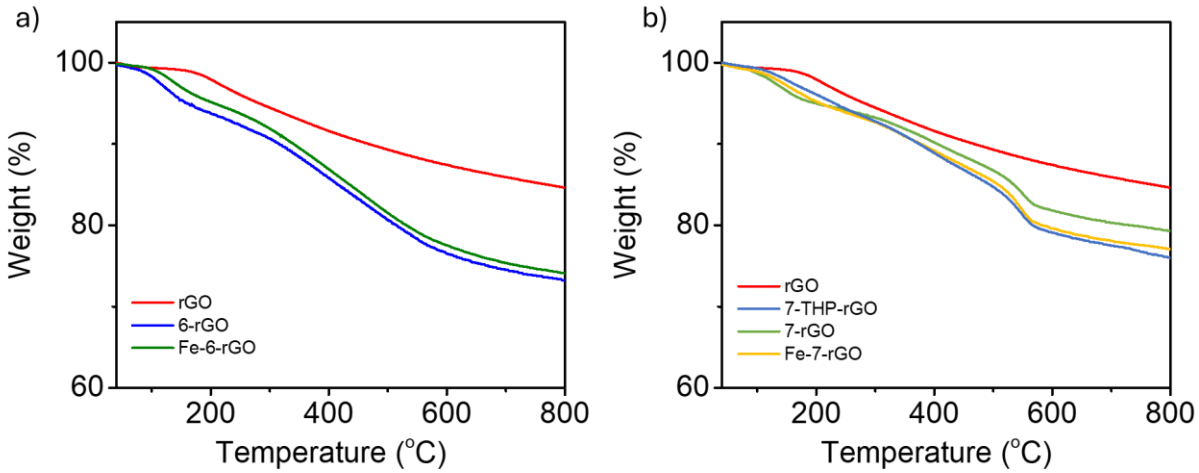

Figure 4.5.15. TGA analysis for rGO, 6-rGO, Fe-6-rGO and 1-bpp-L-Gly (a) and rGO, 7-rGO, 7-THP-rGO and Fe-7-rGO (b). Measurements were performed in the range of 40 - 1000 °C at a scan rate of 4 °C/min under N_2.

For the case of rGO, previous works in the literature assess covalent modifications substantially alter the D band.[262] To have better control of the functionalization, Raman spectroscopy was performed on the four different samples: 6-rGO, Fe-6-rGO, 7-rGO, and Fe-7-rGO, with a mapping of each one. The spectra were acquired using a 532 nm laser, 5 mW of power, 5 accumulations, and 2 s exposure time. All measurements were performed in 10x10

μm areas. 100 spectra were measured to gather statistics, and data processing was carried out using Matlab. The maximum of the D band (in the range of 1300 to 1450 cm^{-1}) and the maximum of the G band (in the range of 1550 to 1700 cm^{-1}) were extracted, and their ratio was calculated. Statistical analysis was performed on this quotient, and a histogram with Gaussian fitting was generated to determine the overall I_D/I_G ratio of the sample. This allows us to obtain additionally a Raman map of the D to G intensity ratio, I_D/I_G showing the patterning of a graphene. The single spectrum of each material is shown in Figure 4.5.17. The histograms shown in Figure 4.5.18 demonstrate the heterogeneity of the samples, while also revealing a clear trend that fits well with a Gaussian curve. In the case of 6-rGO, the I_D/I_G ratio decreases considerably upon functionalization, reaching values between 1.07 and 1.12 (Figure 4.5.18a), indicating successful functionalization. A less pronounced change is observed when iron is complexed, as in the case of Fe-6-rGO, where the I_D/I_G ratio remains similar at around 1.05 (Figure 4.5.18b). For the case of 7-rGO, I_D/I_G ratio is similar than 6-rGO, of 1.13 and the I_D/I_G ratio of Fe-7-rGO does not change dramatically, in a 1.15 (Figure 4.5.18c,d). Raman spectra of the ligands 1-bpp-L-Gly and 3-bpp-THP-L-Gly were also recorded (Figure 6.5.14).

The elemental content to determine the presence of nitrogen was carried out through SEM-EDX (see Section 6.5.6). In the case of 6-rGO, the nitrogen content is consistent with the expected functionalization, 1.51%. However, for the Fe-6-rGO and Fe-7-rGO cases, the nitrogen content is very high in comparison, almost 10%, indicating that there may be non-covalently adsorbed compounds. In the case of 7-rGO, nitrogen was not detected in the sample. However, since iron was detected in Fe-7-rGO, we opted to examine the nitrogen content using a combination of energy dispersive X-Ray and scanning transmission electron microscopy (STEM-EDX) techniques to map carbon, oxygen, and nitrogen. STEM-EDX mapping unveiled the distribution of carbon, oxygen, and nitrogen content across all the sample (Figure 6.5.17).

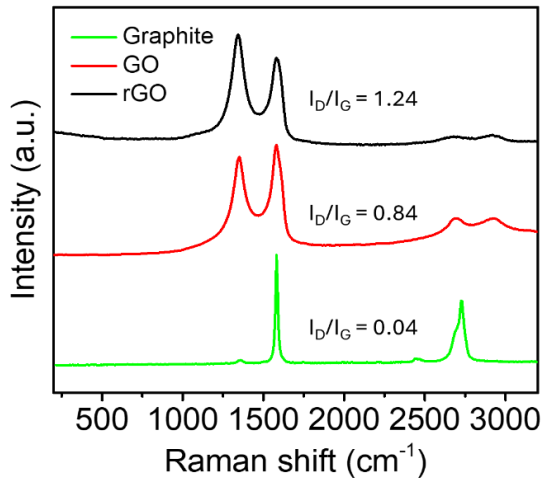

Figure 4.5.16. Raman spectra of graphite flakes, graphene oxide and reduced graphene oxide. Raman was performed with 532 nm laser.

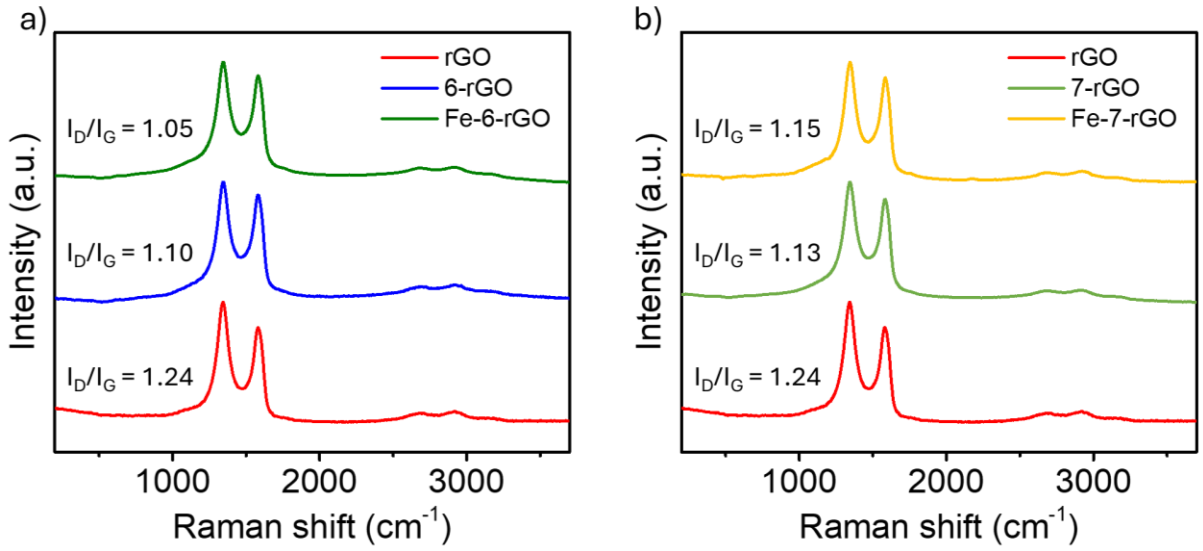

Figure 4.5.17. Raman spectra of rGO, 6-rGO and Fe-6-rGO (a) rGO, 7-rGO and Fe7-rGO (b). Experiments were performed with a 514 nm 50% of laser power, 30 s of exposition and 5 accumulations.

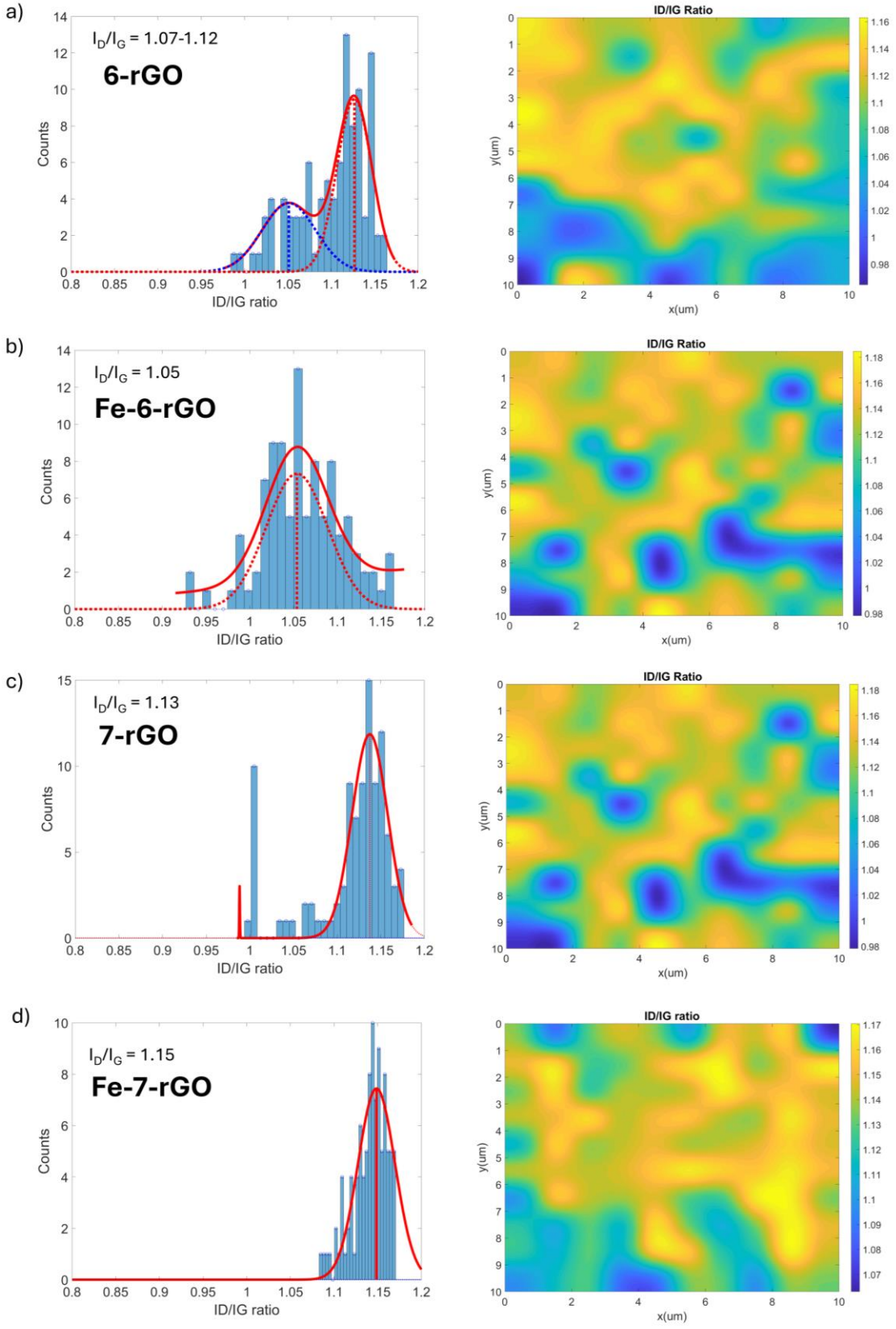

Figure 4.5.18. Raman statistics of 6-rGO (a), Fe-6-rGO (b), 7-rGO (c) and Fe-7-rGO (d).

4.5.6 Exploring spin states in covalent graphene via thermoelectric analysis

One of the main challenges in measuring the magnetic properties of these hybrid systems lies in the lack of sensitivity. This is due to the minimal amount of deposited (active) material on carbon, typically less than 5%, which hinders detection using routine magnetic techniques to determine spin states such as those employed in this thesis, including SQUID, DSC, Raman, or X-ray methods. Several attempts were made to measure these samples using SQUID, as it is the most sensitive among the mentioned techniques. However, the contribution of graphene induces a diamagnetic effect that masks any potential detection of the magnetic state of the 2D hybrid SCO system.

For this purpose, we decided to measure the electrical and thermal properties of the hybrid material through Seebeck effect measurements in the temperature range between 100 and 300 K in collaboration with Dr. Rafael Ramos from my group. To this end, the hybrid carbon sample is compacted, as when subjected to appropriate pressure, the finely powdered hybrid material sinters and forms a tablet. The key consideration is to ensure the material is as uniform as possible, devoid of cracks (grain boundaries), to facilitate continuous electrical transport throughout. Employing this technique involves thoroughly mixing one milligram or less of the finely powdered sample. The sample can be ground using a mortar and pestle or in a small ball mill. Subsequently, the sample is pressed into a special die at pressures ranging between 700 and 1000 kg/cm^2 until a black disc is obtained.[263]

The Seebeck effect was measured using a customized 6-contact setup. In this setup current is passed through a heater (2 contacts) which generates the temperature gradient (ΔT) measured with thermocouples (2 contacts), and the Seebeck voltage is measured (2 contacts). The sample selected for the experiment was Fe-2-rGO, as $[Fe(3\text{-}bpp)_2](ClO_4)_2$ homoleptic complex exhibits an abrupt spin transition below room temperature, and therefore, we would expect to observe a change in graphene. This measurement will help us achieve two distinct objectives. Firstly, the Seebeck coefficient (S) of the initial material (rGO) and the functionalized material will differ due to the latter's covalent modification. Additionally, if the metallic centers undergo spin transition within the studied temperature range (100-300 K), this will induce a localized volume change in the graphene, resulting in variations in conductivity. Consequently, these changes will manifest as a transition or a discontinuity in the observed data.

We performed the Seebeck measurement by selecting five different gradients at these voltages: 0.8 V, 1.2 V, 1.5 V, 2.0 V, 2.5 V, with a ramp from 300 to 100 K at 2 K/min. The Seebeck coefficient of rGO was measured as a background, yielding a value at 300 K of 8.59 µV/K, which falls within the expected range for rGO with a high oxygen content.[264] The Seebeck coefficient at 300 K of Fe-7-rGO is 13.09 µV/K, more than double, indicating a reduction in the number of defects and possibly a consequence of functionalization. However, no discontinuity was observed in the measurement, thus indicating the spin transition cannot be confirmed (Figure 4.5.19).

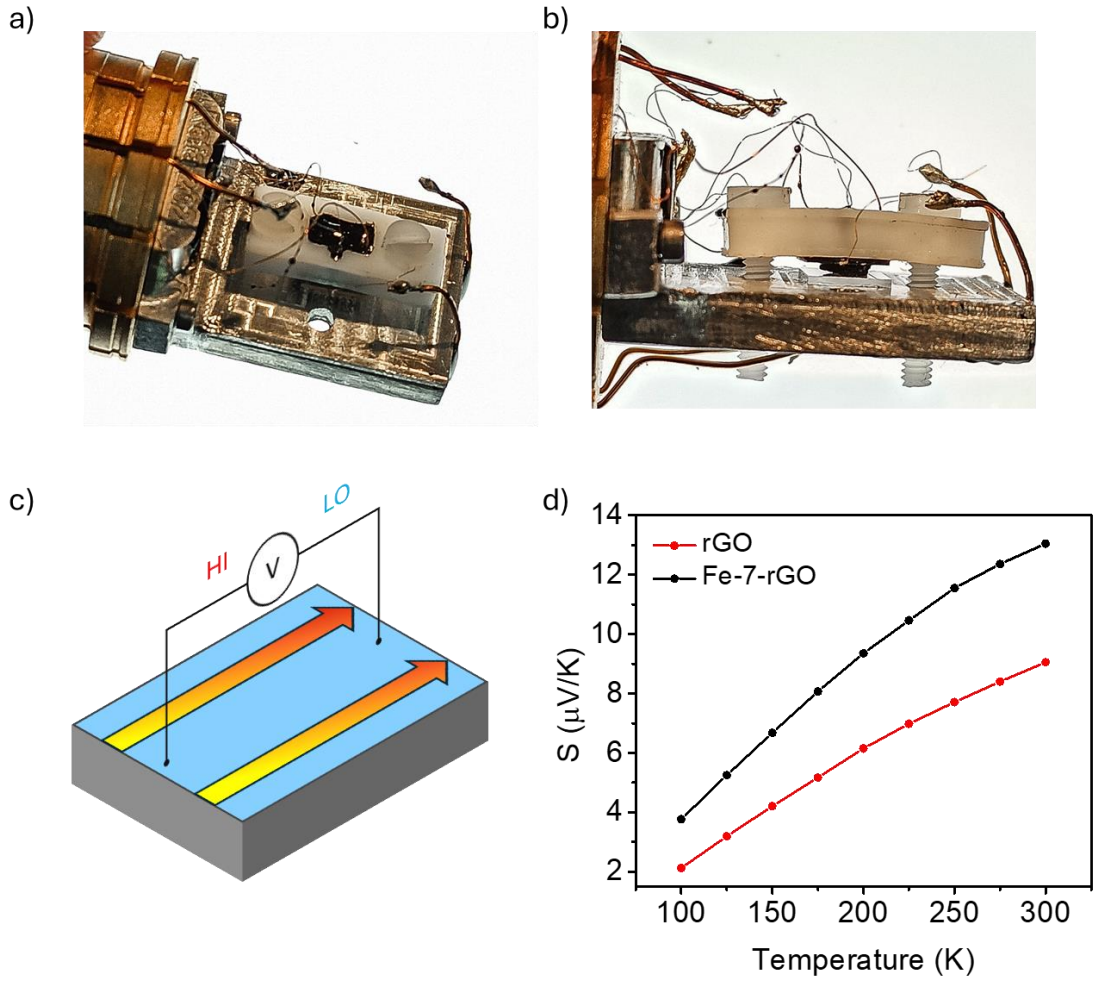

Figure 4.5.19. Experimental customized setup for measuring the Seebeck effect to integrate with a PPMS (Physical Property Measurement System) (a, b). Scheme of the fundamental basics of the technique (c) and measurement of the Seebeck coefficient of rGO and Fe-7-rGO (d).

4.5.7 Conclusions

This study explores various methods for functionalizing two types of graphene (graphene oxide and reduced graphene oxide) using adapted methodologies reported for synthesizing new ligands ideal for these reactions. Initially, graphene oxide synthesis was conducted following the well-known Hummer method from graphite. This graphene oxide (hGO) was compared with commercially available graphene oxide (cGO), and both materials were assessed. Through TGA and Raman spectroscopy, it was observed that hGO exhibits lower degree of oxidation and yields larger flake sizes compared to the commercial counterpart. Concerning the functional groups, both materials were analyzed via XPS analysis, indicating an equal number of oxygen functionalities with comparable intensities. Covalent functionalization of graphene oxide was accomplished through a condensation reaction utilizing two distinct methodologies.

Initially, the target ligand with an acid functional group (1-bpp-COOH and 3-bpp-COOH) was utilized to form the corresponding acyl chloride, followed by its incorporation onto graphene through a condensation reaction. Subsequently, with the second methodology, the acyl chloride was formed by leveraging the carboxylic acid groups present in the graphene oxide,

and the target ligand was modified with amine groups for the corresponding condensation (1-bpp-L-NH2 and 3-bpp-L-NH2). In this case, the 3-bpp ligand was protected with THP to prevent side reactions.

For both 1-xGO and 2-xGO (where x: h or c), TGA demonstrated that the functionalization of 1-cGO was greater than that of 1-hGO. However, upon adding Fe to form the complex, the metal residue obtained is much higher than expected if only considering covalent functionalization. Therefore, functionalization does occur, but it is difficult to differentiate between what is established covalently and what remains adsorbed in a supramolecular manner upon complexation. This functionalization was confirmed by XPS, where the nitrogen content matches with only covalent functionalization. However, when forming the complex, Fe was observed by XPS in the case of Fe-2-hGO. Finally, Raman spectroscopy does not provide clear evidence of functionalization, but there is a change in the I_D/I_G ratio.

For the ligands containing an amine group, testing was conducted with cGO (3-cGO, 4-cGO and 5-cGO). TGA results reveal that functionalization does occur for all three cases. However, the deprotection of THP is challenging to observe. Upon forming the metallic complex, residue is indeed obtained in all three compounds. Raman spectroscopy indicates a reversal in the I_D/I_G ratio, which is attributed to the use of thionyl chloride. This decrease in defects is also observed by XPS, as the content of C-O-C and C-O-H drastically decreases. The N signal in XPS confirms the incorporation of nitrogen, and both signals match the bonds present in the attached molecule (N-pyridine and N-pyrrole). However, the elemental content is higher than expected considering only covalent functionalization. The elemental content of iron was further confirmed using STEM/EDX.

Subsequently, rGO was selected for study due to its superior electrical conductivity compared to GO, which is essential for investigating transport properties associated with spin transitions. A suitable method for functionalizing rGO involves 1,3-dipolar cycloaddition. We modified the ligands used to covalently modify GO by introducing alkylation via reductive amination. Functionalization of rGO, resulting in 6-rGO and 7-rGO, was confirmed through TGA and a statistical analysis of the I_D/I_G ratio using Raman spectroscopy. These results demonstrate that covalent functionalization occurs more efficiently through the 1,3-dipolar cycloaddition reaction in rGO than the condensation method for GO.

Despite observing that the formation of the complex does not alter the I_D/I_G ratio, suggesting that the complex may not have formed, iron content was detected via SEM/EDX. Preliminary measurements of the spin state of the hybrid Fe-7-rGO were attempted through Seebeck effect measurements. Differences between rGO and Fe-7-rGO were observed, attributed to functionalization. However, the results did not yield clear information about the spin state of the material.

5 GENERAL CONCLUSIONS

The research presented in this thesis explores the control of bistable behavior through molecular design, leading to structural modifications. By systematically investigating the design of Fe(II) and Co(II) coordination complexes and evaluating magneto-structural correlations, this research unveils how subtle alterations in molecular architecture, such as the incorporation of alkyl chains or halogen substitutions, can profoundly influence spin transition or single ion magnet relaxation dynamics. Another source of bistability is the application of an external stimulus such as pressure, which offers the advantage of inducing spin transitions in systems that may not undergo transitions under thermal conditions. Therefore, several sections of this thesis focus on studying magnetic properties dependent on pressure. Additionally, the investigation extends to explore the incorporation of these switchable molecules into graphene via covalent functionalization, employing a variety of physicochemical techniques to precisely identify functional groups and metal complexes on graphene.

In **Section 4.1**, the focus was on understanding the modulation of magnetic properties in Fe(II) metallomesogens. The incorporation of alkyl chains in these materials was investigated, revealing that the presence of alkyl chains in the crystals impedes a thermal spin transition below 400 K, even with different functionalizations. Single-crystal diffraction analysis provided insights into the distinct arrangements in their crystalline structures, with terminal groups of the alkyl chains playing a crucial role in packing and organization.

Further investigations through DSC and polarized microscopy confirmed temperature-dependent phase transitions and the formation of liquid crystal phases. Magnetic properties were explored using SQUID measurements and variable-temperature Raman spectroscopy, unveiling a high spin state in both crystal and liquid crystal phases. Variable-pressure Raman spectroscopy provided structural insights associated with the spin-state transition, with spin transitions observed at pressures exceeding 2 GPa. These compounds are able to reach such high pressure values thanks to the compressibility provided by the alkyl chains.

In **Section 4.2**, a novel series of functionalized *p*-X-3-bpp ligands were developed to influence the nature of spin state transitions in Fe(II) coordination compounds. Through a combination of X-Ray, SQUID, and Raman experiments, along with variations in temperature and pressure, a precise magneto-structural relationship was established, highlighting the significant impact of intermolecular H-bond and X-bond interactions dictated by the size of the halogen on cooperativity and a variety of spin transition: from gradual to one or two step-transition.

In **Section 4.3**, the same methodology used to obtain halogen-substituted ligands as in the previous section was employed to investigate the synthesis of Co(II) complexes, aiming to influence single ion magnet properties. Structural analysis, magnetic measurements, and relaxation mechanism studies revealed magneto-structural correlations, demonstrating the modulation of octahedral axial or equatorial distortion crucial for inducing single ion magnet behavior. Supramolecular interactions, including hydrogen bonds and halogen bonds, played essential role in shaping crystal packing and molecular symmetry, thereby influencing magnetic properties.

In **Section 4.4**, eight novel SCO systems based on the *p*-Cl-2,6-di(pyrazol-3-yl)pyridine (*p*-Cl-3-bpp) scaffold and employing a variety of different counterions to influence the second coordination sphere were introduced. Insights into their structural diversity were provided through Single-Crystal X-Ray Diffraction analysis, while magnetic studies elucidated thermal and light-induced spin transitions, demonstrating the versatility of these compounds in responding to external stimuli. Raman spectroscopy supported the observations of spin transitions, with magneto-structural correlations emphasizing the significance of intermolecular interactions in governing spin transitions.

Lastly, **Section 4.5** explored three different methodologies for functionalizing graphene, specifically graphene oxide and reduced graphene oxide. Covalent functionalization was achieved through condensation reactions in the case of GO and 1,3-dipolar cycloaddition reactions in the case of rGO, providing insights into the challenges and opportunities involved in functionalizing graphene for spin transition studies. TGA, Raman spectroscopy, and XPS analysis provided valuable information regarding functionalization processes. Preliminary studies of the magnetic state of the hybrid graphene were conducted using measurements of both thermal and electrical conductivity over a wide temperature range.

Overall, this thesis represents a significant contribution to the advancement of our understanding of spin transition and single ion magnet phenomena and their implications for material design and development. Through systematic investigations of Fe(II) metallomesogens, Co(II) complexes, novel SCO systems, and functionalized graphene, this study unveils the potential of molecular engineering strategies in tailoring magnetic properties for various applications. The findings presented herein not only deepen our comprehension of these bistable molecules but also offer innovative pathways for designing functional materials with customized magnetic functionalities. As we embark on the next phase of exploration, armed with newfound knowledge and innovative methodologies, the prospects for transformative advancements in molecular magnetism and multifunctional materials science are boundless.

6 METHODOLOGY

Materials and Methods

All reagents were purchased from commercial sources (Sigma Aldrich, Alfa Aesar, Acros and Fluorochem) and used without further purification. All reactions dealing with air and moisture-sensitive compounds were carried out in an oven-dried flask under an argon atmosphere with dry solvents. The abbreviation “rt” refers to reactions carried out approximately at 23 °C. Analytical grade solvents were used as a spreading solvent and pure water (Milli-Pore; 18.2 MΩcm) was employed.

Purity of ligands was checked by **NMR** spectra were recorded in $CDCl_3$, purchased from Eurisotop at 300 MHz (*Varian*) or 500 MHz (*Bruker*), unless other solvent is specified. NMR spectra were analyzed using MestreNova© NMR data processing software (www.mestrelab.com). The following abbreviations are used to indicate signal multiplicity: s, singlet; d, doublet; t, triplet; q, quartet; dd, double doublet; m, multiplet. Mass spectra (MALDI, ESI-MS) was recorded at the CACTUS facility of the University of Santiago de Compostela in an *Agilent 6410B-QQQ* equipment. **RP-UHPLC-MS** analysis were carried out in an *Agilent Technologies 1260 Infinity III* chromatograph in tandem with an *Agilent Technologies 6120* mass spectrometer, using gradient elution (5-95% B) of the mobile phase (A: H2O 0.1% TFA; B: ACN 0.1% TFA).

Elemental analysis measurements were performed in an *Elemental LECO CHNS-932* analyzer in Elemental Chemical Analysis Laboratory of SiDI facilities of the Universidad Autónoma de Madrid. **Infra-red spectra** were measured using a *Bruker Alpha FTIR* spectrometer with a platinum ATR module. **TGA analyzes** were performed on a *Mettler Toledo TGA/DSC 3+ STARe* system analyzer. Samples for TGA analyzes were heated in air or N_2 up to 1000°C with a heating scan rate of 4 °C/min. **DSC** experiments were performed in a *TA Instrument DSC 25* apparatus with warming and cooling rates equal to $4 \cdot K \cdot min^{-1}$ unless other rate specified. Variable-pressure DSC experiments of Section 4.4 were performed in collaboration with Prof. Jorge López Beceiro and Prof. Ramon Artiaga from CITENI-Proterm Group. The **Raman** spectra were performed with *RENISHAW* Raman microscope with diode laser (785 nm) or in a *WiTec Confocal Alpha300+R* with diode laser (532 nm). Raman mappings were performed on a *Bruker Senterra II* confocal in collaboration with the group of Prof. Emilio Pérez from IMDEA Nanociencia. Raman mappings were analyzed using a MATLAB script developed in-house with the assistance of Dr. Víctor Leborán. Variable temperature experiments were performed using a *Linkham THS94* cell.

Single-crystal X-ray diffraction was measured on a Bruker D8 Venture Photon III C14 κ--geometry diffractometer system equipped with an *Incoatec high brillance IμS 3.0 microsource* (MoKα, λ = 0.71073 Å). Both Raman and Single-crystal X-ray diffraction under pressure were performed using a Diamond Anvil Cell (**DAC**) (*Almax EasyLab*) with an applied pressures in the range of 0 to 18 GPa using a rubi standard for pressure elucidation. **Powder X-Ray diffraction** was measured on a *Panalytical-EMPYREAN* equipped with a theta/theta-two goniometer, tube with Cu anode, *PXCEL3D* type hybrid solid state detector, 5-axis sampling platforms, for flat sample and for liquid samples and high- and low-resolution multilayer mirror optics. **Crysta images** were recorded using a *Leica DM2700M* equipped with a temperature controller *Linkham LTS420*.

Scanning electron microscopy (SEM) and **energy-dispersive X-ray spectroscopy (EDX)** analysis were performed on a *ZEISS EVO LS 15* with EDX module (*Oxford Inca x-act* with 129 eV of resolution and WD 8.5 mm). **High-resolution transmission electron microscopy (HR-TEM)** was performed on a *JEOL JEM F200* microscope equipped with a cold field-emission gun (Cold-FEG) operated at 200 kV with an ultra-high-resolution pole piece. TEM images were acquired using a *Gatan OneView* camera. **Energy Dispersive X-ray Spectroscopy (EDX)** was performed with a *Centurio Large Angle Silicon Drift Detector* (SDD) that collects X-rays from a detection area of 100 mm^2. Copper grids were used for HR-TEM measurements. **X-Ray Photoelectron Spectroscopy (XPS)** analysis of the samples was performed using a Thermo Scientific *ESCALAB 250Xi* equipped with monochromated Al Kα (hν = 1486.68 eV) radiation, operated at 220W, 14.6 kV, spot size 650μm. The XPS spectra were collected at pass energies 100eV and 40eV for survey spectra and individual elements respectively. The energy step for individual elements was 0.1eV. The XPS spectra were peak-fitted using Avantage data processing software. For peak fitting the Shirley-type background subtraction was used. All the XPS peaks are to be referenced to adventitious carbon C1s, C-C peak at 284.8 eV. Quantification has been done using sensitivity factors provided by the Avantage library. Charge neutralization was achieved with both low energy electron and argon ion Flood guns (0.5eV, 100 μA and 25 μA current respectively) during XPS measurements.

The **magnetic susceptibility measurements and direct current magnetic measurements** were performed using a *Quantum Design MPMS-XL5* SQUID magnetometer equipped with a 5 T magnet. Field dependent/reduced magnetization measurements were performed in a field range of 0-5 T and over the temperature range 1.8-16 K. Parameters of the ZFS spin Hamiltonian *g*, *D*, *E* were calculated with PHI program.[205] The **magnetic susceptibility measurements** under an applied pressure were performed using a clamp-type piston-cylinder pressure cell. Applied pressures were in the range 0 – 1.3 GPa and sample was placed in a Teflon capsule along with a pressure transmitting oil and a Sn pressure gauge as a reference. **LIEEST (Light-Induced Excited Spin-State Trapping)** experiments were performed irradiating samples during 6 hours with a green laser (640 nm) with a power of 15 mW.

Alternating current (ac) susceptibility measurements were carried out using a *Quantum Design PPMS-9* under an oscillating ac field of 1.55 Oe and ac frequencies ranging from 1 to 10 kHz. Cole-Cole results were fitted with CC-FIT software.[213,214] Crystalline samples were slightly pressed and wrapped with Teflon. Temperature-dependent susceptibility experiments were carried out under a static magnetic field of 1 T, unless otherwise state, and in the temperature range 2-300 K.

6.1 Pressure-Induced Spin Crossover Metallomesogens bearing Long Alkyl Chains

6.1.1 Synthesis of the ligands

2,6-bis(pyrazol-3-yl)pyridine was synthesized according to a method previously described in the literature.[154]

2,6-bis(1-hexadecyl-pyrazol-3-yl)pyridine (L1) was prepared according to a previous literature method.[155] A mixture of 2,6-bis(pyrazol-3-yl)pyridine (500 mg, 2.3 mmol) and sodium hydride (380 mg, 60%, 9.5 mmol, 4 eq.) is dissolved in 30 mL of dry DMF. This mixture is heated up to 70°C during 90 min. After that, 1-bromohexadecane (2.9 mL, 9.5 mmol) is added and the reaction was heated to reflux (153 °C) for 2 days. The solvent was removed under vacuum. The crude was dissolved in chloroform and washed with water (3 x 50 mL) and NH_4Cl (1 x 50 mL). The solvent was removed under reduced pressure and the product was purified by column chromatography on silica gel with chloroform-methanol (20:1 v/v) as eluent to obtain the product as a white solid. Analytical data were in accordance with those previously published. Yield: 65%

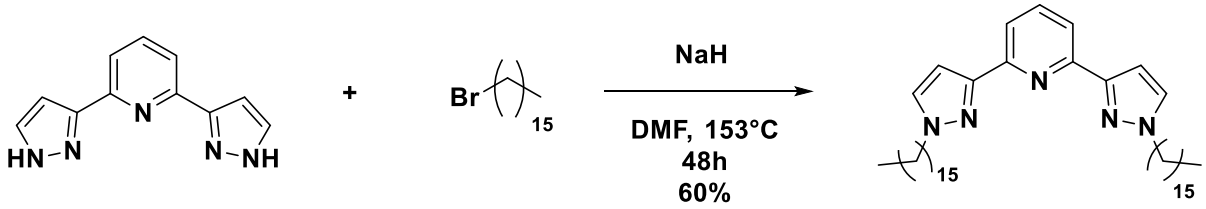

Scheme 6.1.1. Scheme reaction of 2,6-bis(1-hexadecyl-pyrazol-3-yl)pyridine (L1).

^{1}H NMR (300 MHz, Chloroform-*d*): δ 7.87 (d, *J* = 7.7 Hz, 2H), 7.72 (t, *J* = 8.5, 1H), 7.42 (d, *J* = 2.3 Hz, 2H), 7.01 (d, *J* = 2.3 Hz, 2H), 4.17 (t, *J* = 7.2 Hz, 4H), 1.91 (t, *J* = 7.0 Hz, 4H), 1.62 (s, 4H), 1.25 (d, *J* = 2.5 Hz, 48H), 0.91 (t, J = 6.9 Hz, 4H).

^{13}C NMR (126 MHz, $CDCl_3$): 152.08, 137.02, 130.30, 118.40, 104.53, 52.67, 32.05, 30.63, 29.81, 29.78, 29.75, 29.68, 29.61, 29.49, 29.28, 26.77, 22.82, 14.24.

MS (EI$^+$): m/z: 660 [M$^+$], 683 [M+Na]$^+$

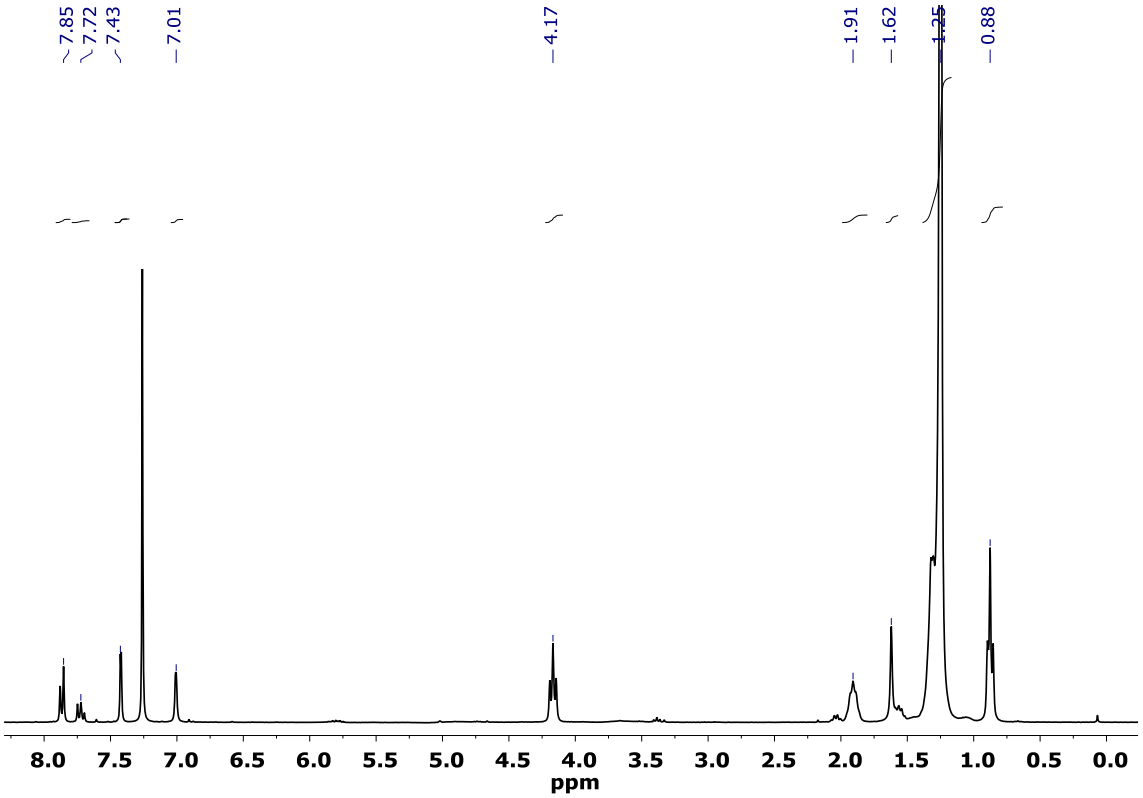

Figure 6.1.1. ^{1}H NMR spectrum of compound L1.

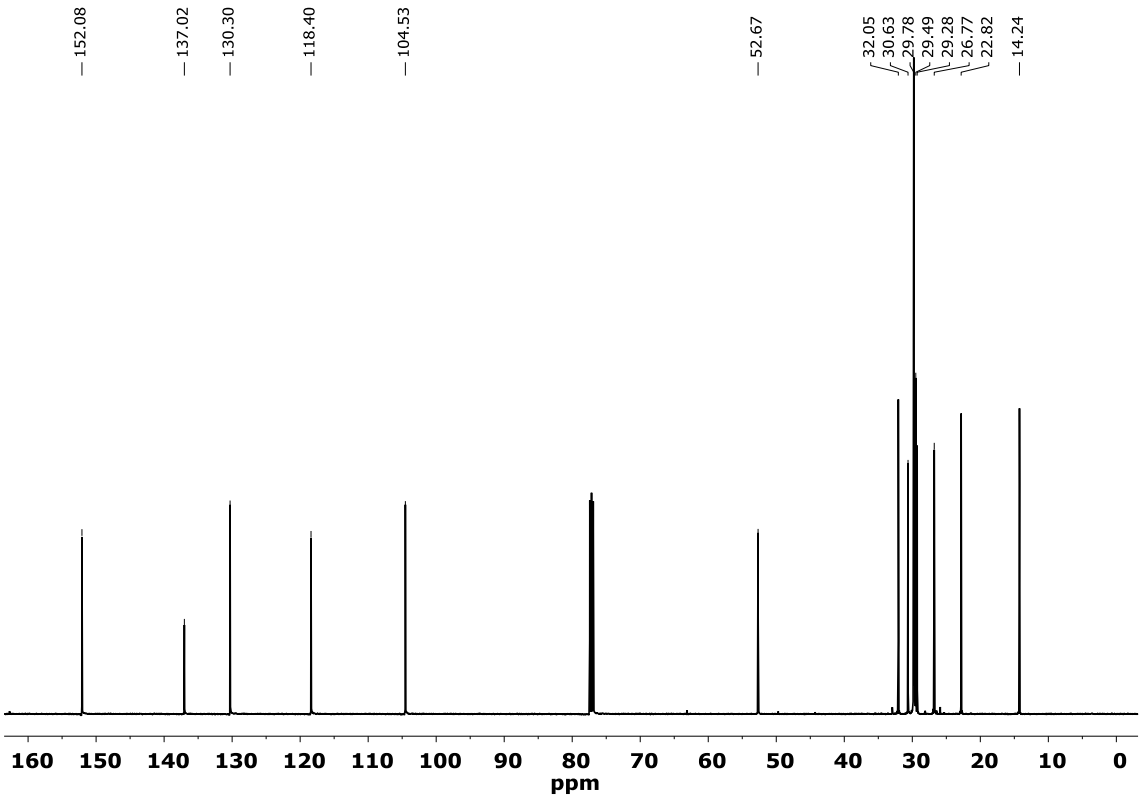

Figure 6.1.2. ^{13}C NMR spectrum of compound L1.

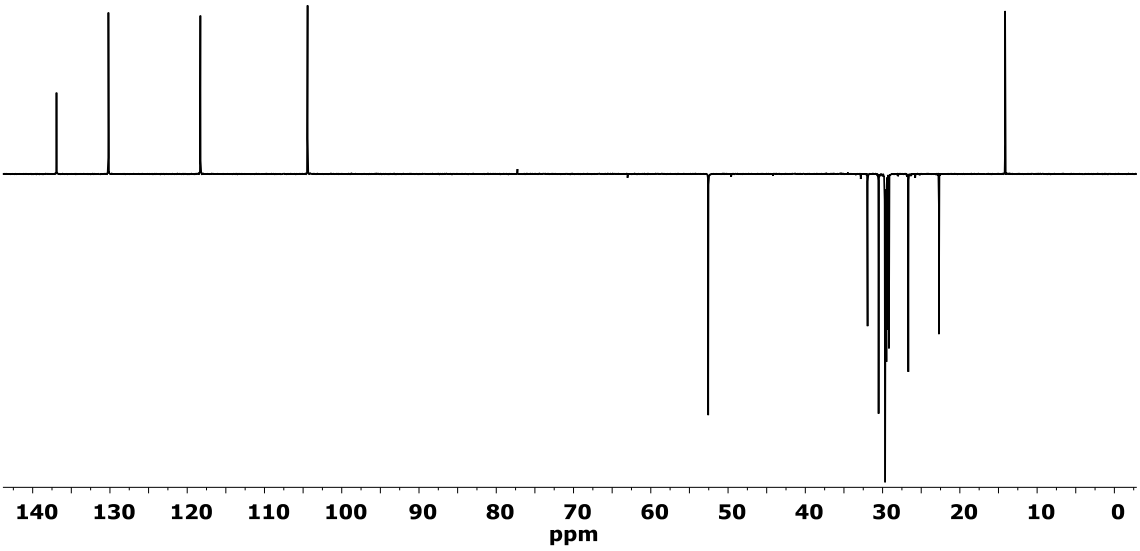

Figure 6.1.3. DEPT-135 of compound L1.

16,16'-(pyridine-2,6-diylbis(1H-pyrazole-3,1-diyl))bis(hexadecan-1-ol) (L2): a mixture of 2,6-bis(pyrazol-3-yl)pyridine (500 mg, 2.3mmol) and sodium hydride (60%, 284 mg, 7.11 mmol, 3 eq.) in 60 mL dry DMF was heated up to 70 °C under Ar atmosphere during 90 min. After 90 minutes, 16-bromohexadecan-1-ol (2.21g, 6.9 mmol, 3 eq.) was added carefully keeping the system under Ar and let react for 24 h at 60 °C.

The solvent was removed under vacuum. The crude was dissolved in dichloromethane and washed with water (3 x 50 mL) and brine (1 x 20 mL), dried over Na_2SO_4, filtered, and evaporated to dryness. The pure product was obtained after recrystallization of the crude in dichloromethane/hexane. Yield: 82%

Scheme 6.1.2. Scheme reaction of 16,16'-(pyridine-2,6-diylbis(1H-pyrazole-3,1-diyl))bis(hexadecan-1-ol) (L2).

^{1}H NMR (500 MHz, Chloroform-*d*): 7.86 (d, *J* = 7.8 Hz, 2H), 7.72 (dd, *J* = 8.2, 7.3 Hz, 1H), 7.42 (d, *J* = 2.3 Hz, 2H), 6.99 (d, *J* = 2.3 Hz, 2H), 4.17 (t, *J* = 7.3 Hz, 4H), 3.62 (t, *J* = 6.7 Hz, 4H), 1.91 (tq, *J* = 9.0, 5.5, 4.8 Hz, 4H), 1.74 (s, 4H), 1.54 (dt, *J* = 7.9, 6.5 Hz, 4H), 1.41 – 1.19 (m, 44H).

^{13}C NMR (126 MHz, $CDCl_3$): 152.09, 137.08, 130.36, 118.45, 104.56, 63.20, 52.70, 32.95, 30.64, 29.76, 29.73, 29.70, 29.66, 29.59, 29.56, 29.28, 26.78, 25.88.

MS (EI$^+$): m/z: 692.58 [M$^+$]

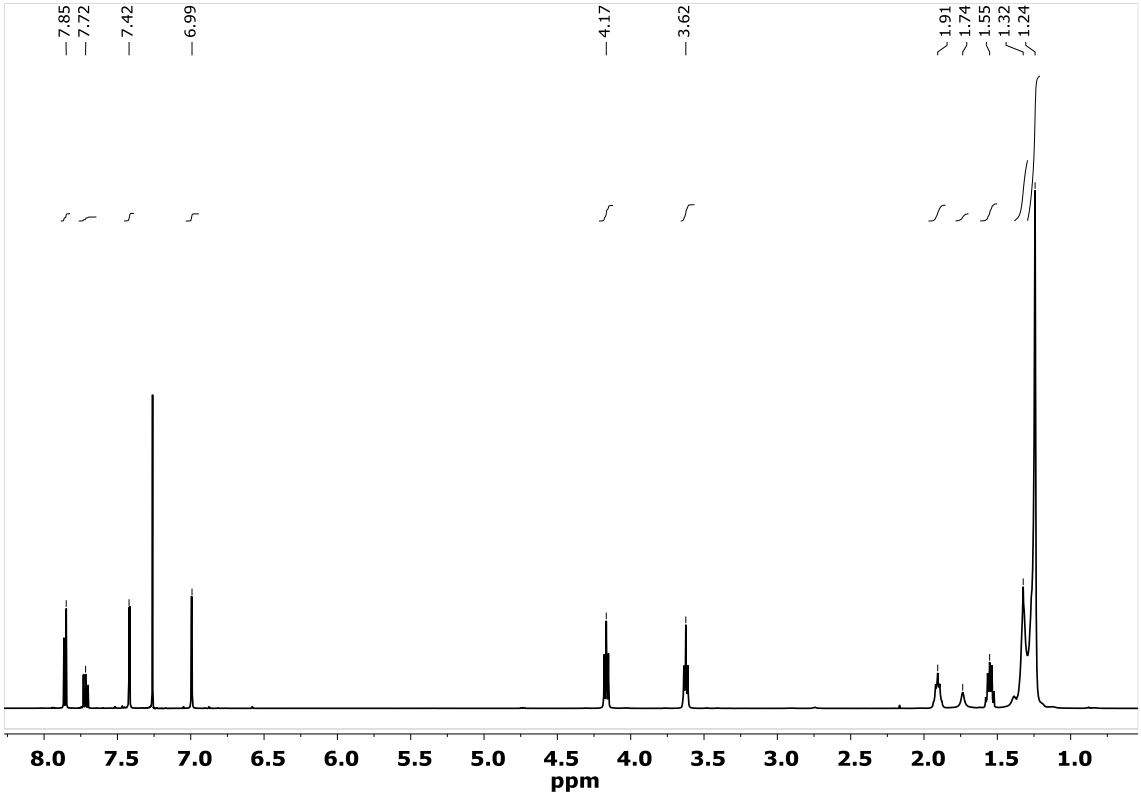

Figure 6.1.4. ^{1}H NMR spectrum of compound L2.

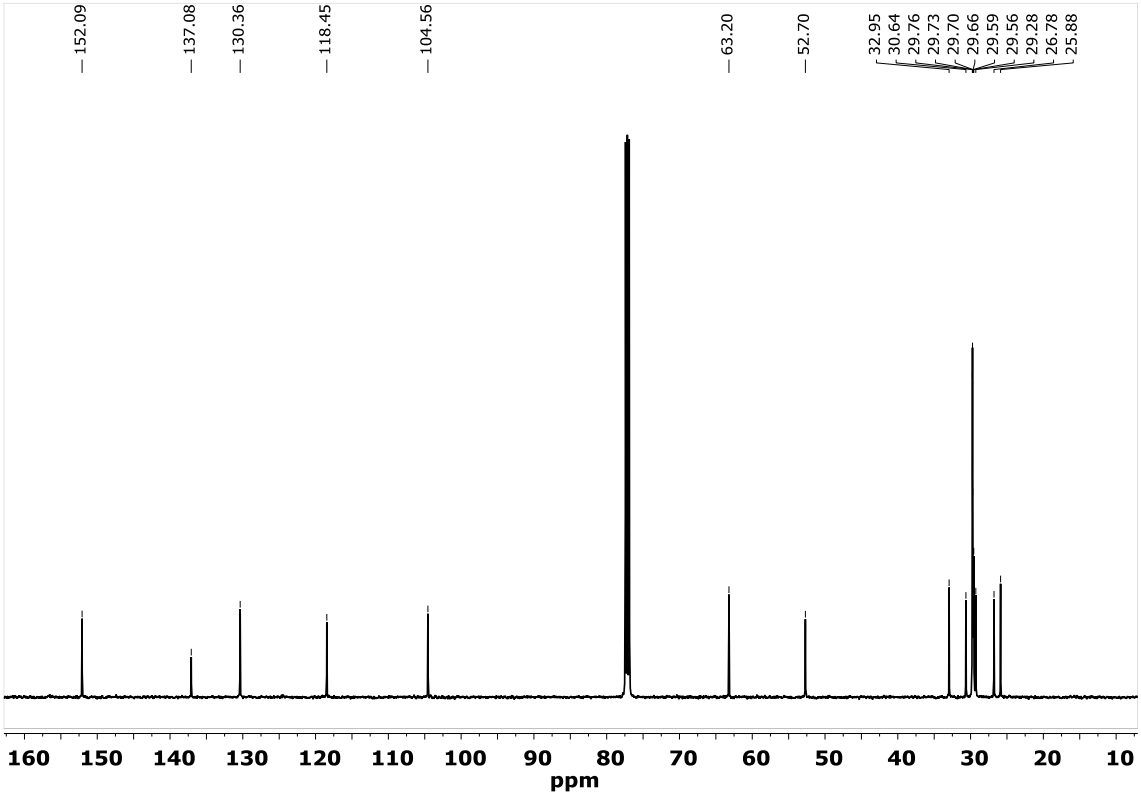

Figure 6.1.5. ^{13}C NMR spectrum of compound L2.

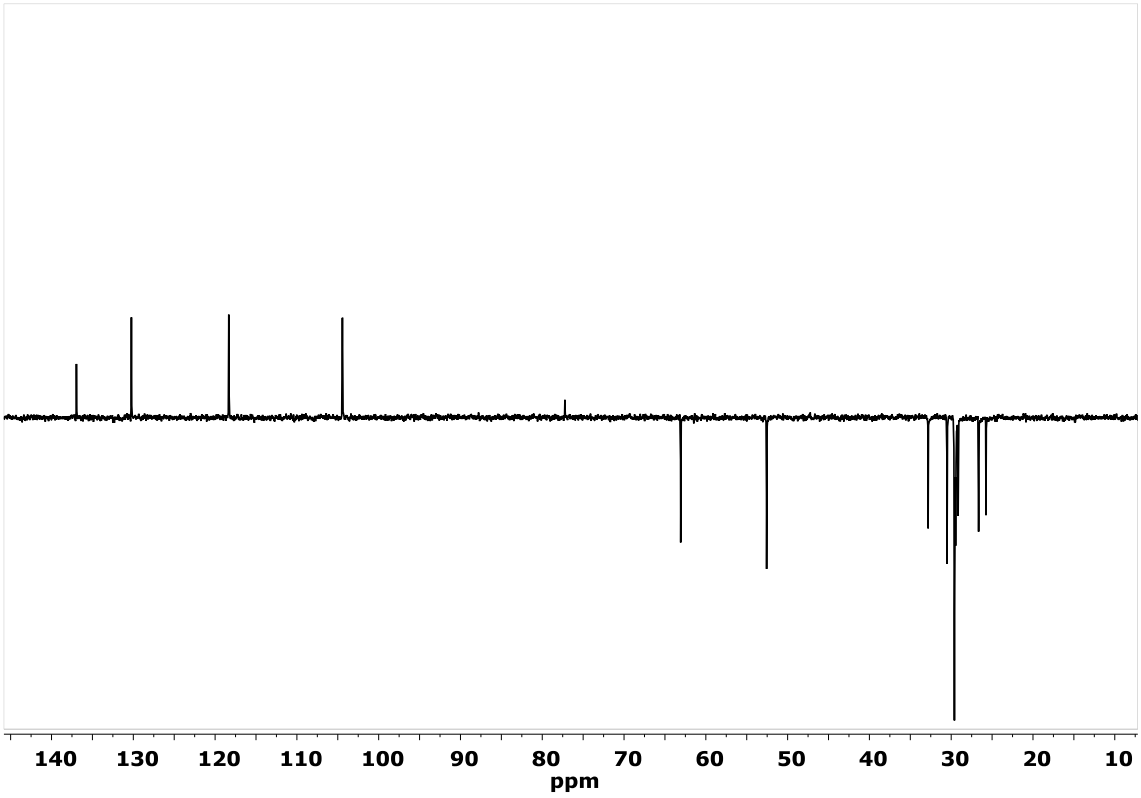

Figure 6.1.6. DEPT-135 NMR spectrum of compound L2.

Dimethyl 16,16'-(pyridine-2,6-diylbis(1H-pyrazole-3,1-diyl))dipalmitate (L3): A mixture of 2,6-bis(pyrazol-3-yl)pyridine (500 mg, 2.3mmol) and sodium hydride (60%, 276 mg, 6.9 mmol, 3 eq.) in 60 mL dry DMF was heated up to 70 °C under Ar atmosphere during 90 min. After this time, methyl 16-bromohexadecanoate (2.46g, 7.08 mmol, 3 eq.) was added carefully keeping the system under Ar and let react during 2 days at reflux (153 °C).

After two days, the solvent was removed under vacuum. The crude was dissolved in chloroform and washed with water (3 x 50 mL) and NH_4Cl (1 x 50 mL). The organic phase was dried over Na_2SO_4, filtered, and evaporated to dryness.

The solvent was removed under reduced pressure and the product was purified by column chromatography on silica gel with dichloromethane-methanol (30:1 v/v) as eluent to obtain the product as a brown solid. Yield: 66%

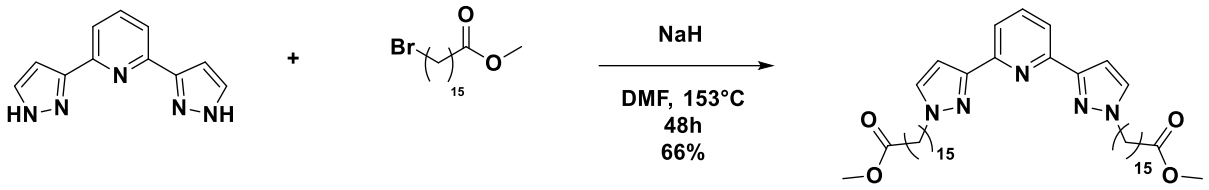

Scheme 6.1.3. Scheme reaction of dimethyl 16,16'-(pyridine-2,6-diylbis(1H-pyrazole-3,1-diyl))dipalmitate (L3).

^{1}H NMR (300 MHz, Chloroform-*d*) δ 7.86 (d, *J* = 8.2 Hz, 2H), 7.71 (dd, *J* = 8.5, 7.0 Hz, 1H), 7.41 (d, *J* = 2.3 Hz, 2H), 6.99 (d, *J* = 2.2 Hz, 2H), 4.16 (t, *J* = 7.2 Hz, 4H), 3.65 (s, 6H), 2.29 (t, *J* = 7.5 Hz, 4H), 1.90 (t, *J* = 7.0 Hz, 4H), 1.64 – 1.57 (m, 4H), 1.35 – 1.20 (m, 44H).

^{13}C NMR (126 MHz, $CDCl_3$) δ 174.49, 152.00, 137.18, 130.36, 118.48, 104.63, 52.70, 51.56, 34.25, 30.63, 29.75, 29.71, 29.67, 29.61, 29.57, 29.38, 29.28, 26.78, 25.09.

MS (EI$^+$): m/z: 748.57 [M$^+$]

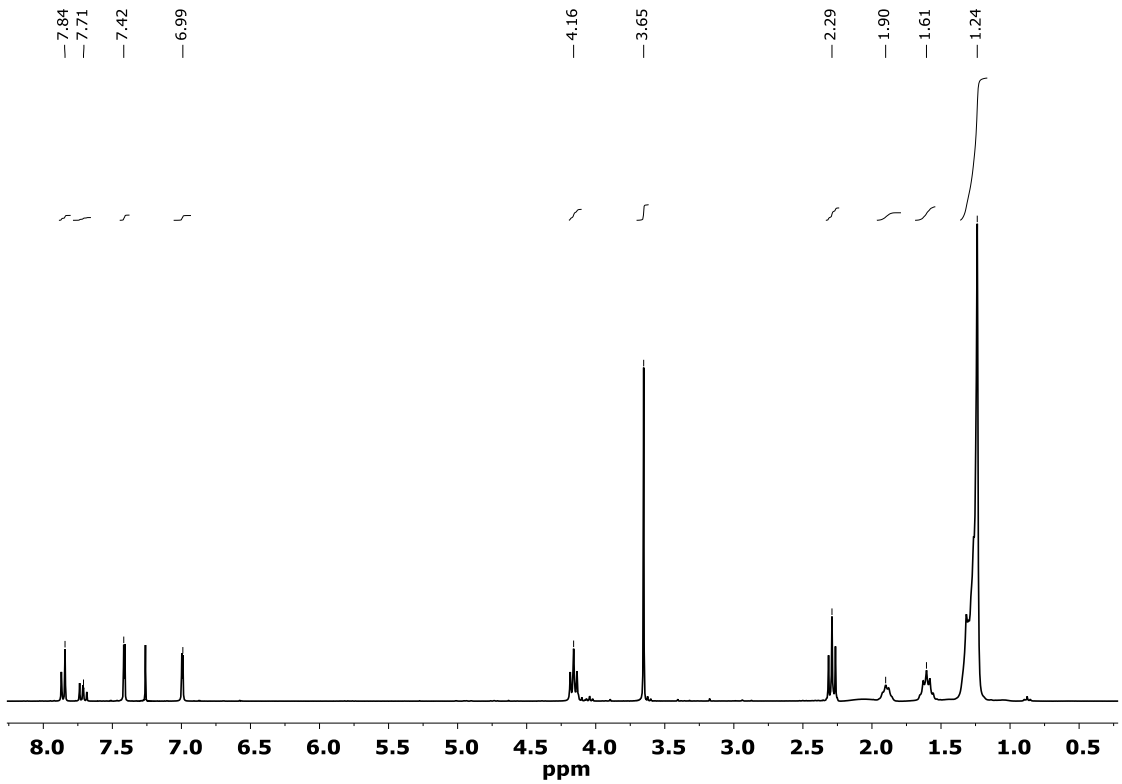

Figure 6.1.7. ^{1}H NMR spectrum of compound L3.

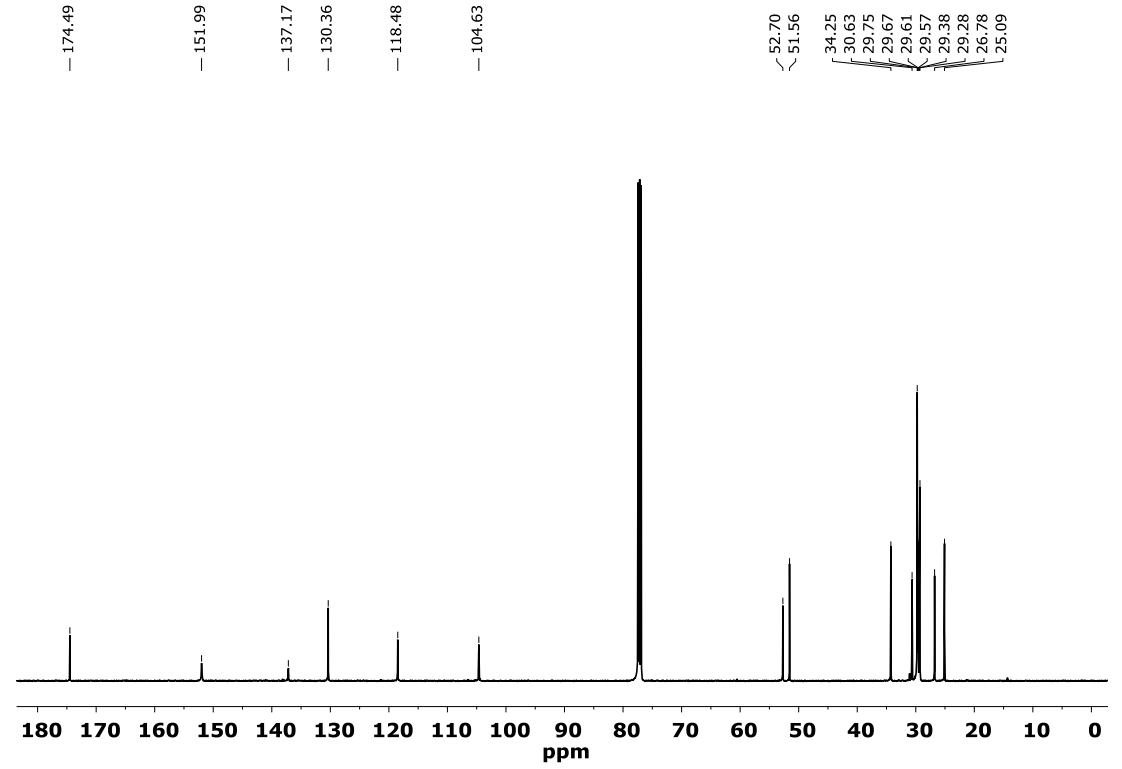

Figure 6.1.8. ^{13}C NMR spectrum of compound L3.

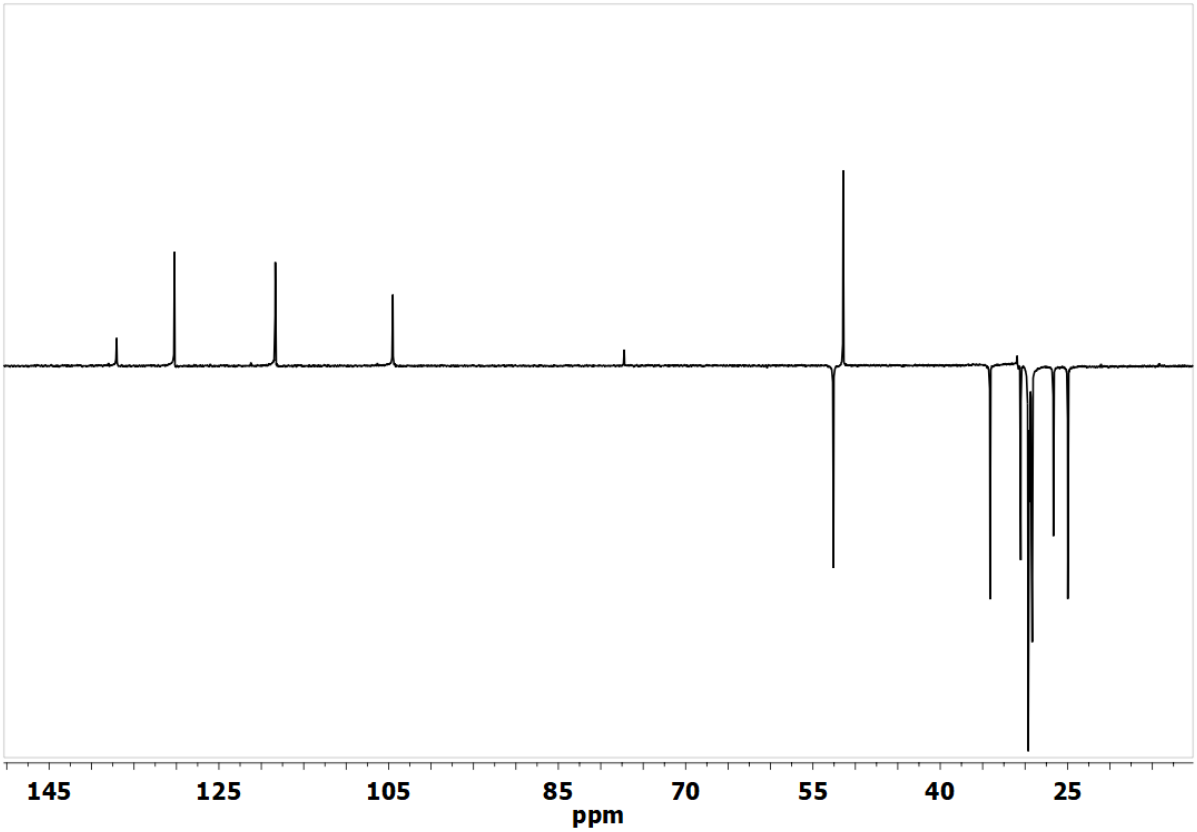

Figure 6.1.9. DEPT-135 NMR spectrum of compound L3.

6.1.2 Synthesis of the complexes

[Fe(L1)$_2$](ClO$_4$)$_2$ [1]: A methanolic solution of Fe(ClO$_4$)$_2$·6H$_2$O (0.05 mmol, 1 eq.) was added to a solution of ligand L1 (0.10 mmol, 2 eq.) in CH$_2$Cl$_2$ (10 mL) with stirring for a further one hour. Crystals, suitable for single crystal X-Ray analysis, were obtained by slow evaporation of the organic solvent mixture (DCM/EtOH) and isolated by filtration in good yield. Yield: 63%.

IR: 2918 (vs), 2850 (vs), 1610 (m), 1570 (m), 1468 (m), 1446 (s), 1358 (s), 1238 (s), 1068 (vs), 788 (s), 718 (s), 622 (s).

Elemental analysis (%) calcd for C$_{86}$H$_{146}$Cl$_2$FeN$_{10}$O$_8$ (1574.92): C, 65.59; H, 9.34; N, 8.89; found: C, 64.81; H, 9.95; N, 8.78.

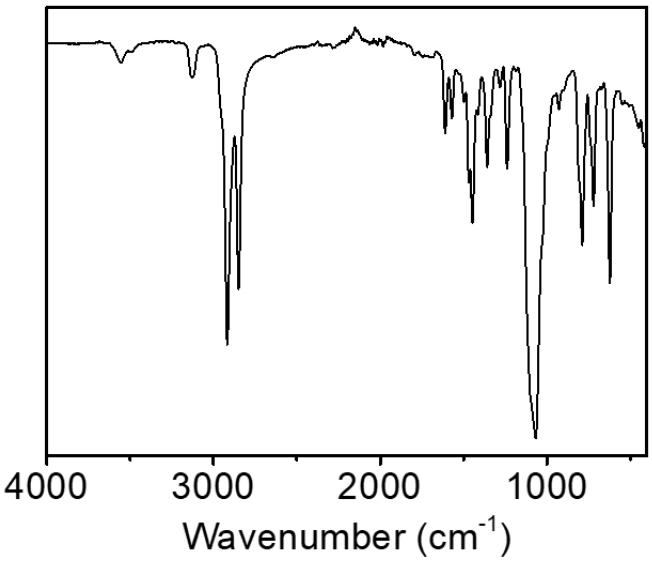

Figure 6.1.10. FT-IR of complex 1.

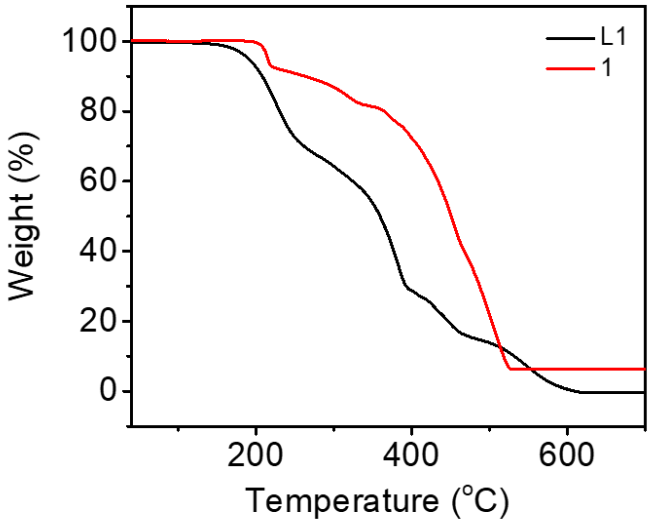

Figure 6.1.11. TGA measurements at 4 °C/min of ligand L1 and complex 1 under air.

$[Fe(L2)_2](ClO_4)_2$ [2]: A methanolic solution of $Fe(ClO_4)_2 \cdot 6H_2O$ (0.05 mmol, 1 eq.) was added to a solution of ligand L2 (0.10 mmol, 2 eq.) in CH_2Cl_2 (10 mL) with stirring for a further one hour. Crystals, suitable for single crystal X-Ray analysis, were obtained by slow evaporation of the organic solvent mixture (DCM/EtOH) and isolated by filtration in good yield. Yield: 80%.

IR: 3534 (m), 3132 (w), 2919 (vs), 2845 (vs), 1617 (w), 1574 (w), 1467 (w), 1446 (w), 1356 (w), 1242 (w), 1086 (m), 1065 (m), 805 (w), 628 (w).

Elemental analysis (%) calcd for $C_{86}H_{146}Cl_2FeN_{10}O_{12}$ (1638.92): C, 63.03; H, 8.98; Cl, 4.33; found: C, 62.97; H, 8.95; N, 4.28

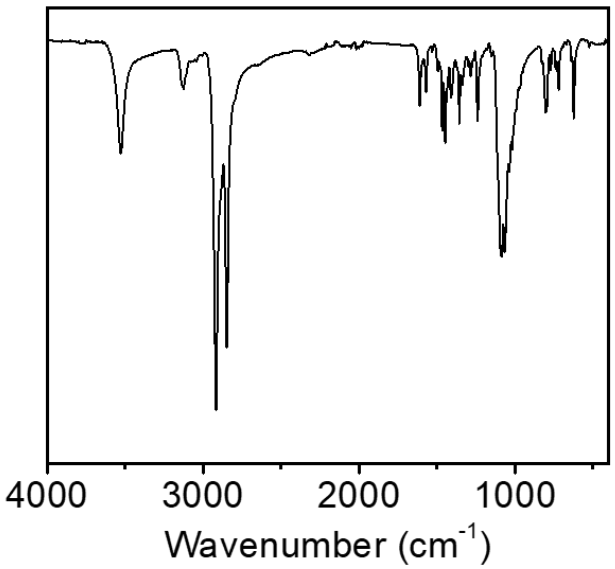

Figure 6.1.12. FT-IR of complex 2.

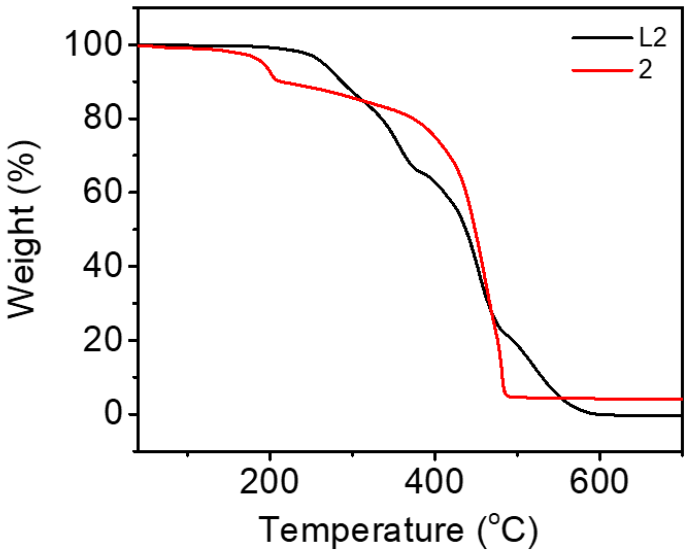

Figure 6.1.13. TGA measurements at 4 °C/min of ligand L2 and complex 2 under air.

$[Fe(L3)_2](ClO_4)_2$ [3]: A methanolic solution of $Fe(ClO_4)_2 \cdot 6H_2O$ (0.05 mmol, 1 eq.) was added to a solution of ligand L3 (0.10 mmol, 2 eq.) in CH_2Cl_2 (10 mL) with stirring for a further one hour. Crystals, suitable for single crystal X-Ray analysis, were obtained by slow evaporation of the organic solvent mixture (DCM/EtOH) and isolated by filtration in good yield. Yield: 70%.

IR: 3130 (m), 3111 (m), 2922 (s), 2851 (s), 1722 (s), 1607 (m), 1570 (m), 1449 (m), 1358 (m), 1243 (m), 1090 (s), 808 (m), 622 (m)

Elemental analysis (%) calcd for $C_{90}H_{146}Cl_2FeN_{10}O_{16}$ (1750.91): C, 61.74; H, 8.41; N, 8.00; found: C, 61.97; H, 8.95; N, 8.28

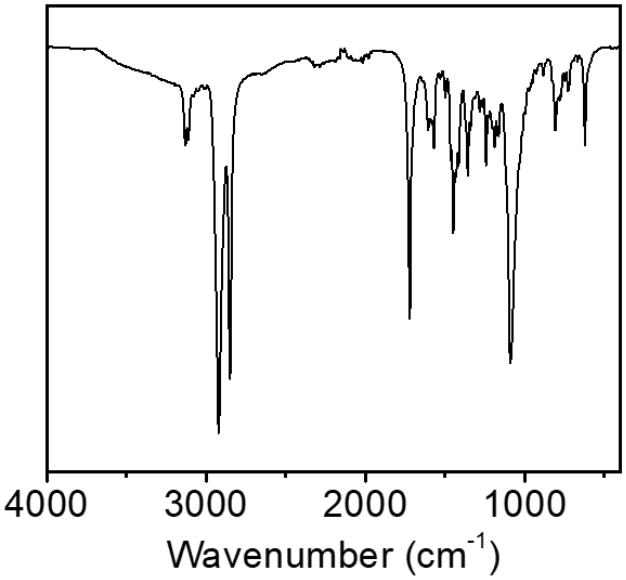

Figure 6.1.14. FT-IR of complex 3.

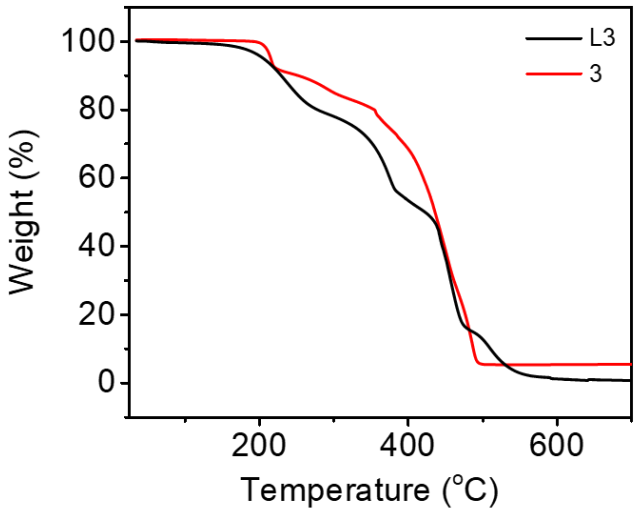

Figure 6.1.15. TGA measurements at 4 °C/min of ligand L3 and complex 3 under air.

6.1.3 Single Crystal X-Ray Diffraction (SCXRD)

Crystallographic data for all the complexes were deposited in the Cambridge Structural Database (CSD) with the following deposit numbers: CCDC-2352225 for 1; CCDC-2352227 for 2; CCDC-2352226 for 3.

Table 6.1.1. Crystallographic data and structure refinement of single crystal X-Ray analysis for complex 1.

	1
Chemical Formula	$C_{86}H_{146}Cl_2FeN_{10}O_8$
Size (mm^3)	0.020 x 0.150 x 0.180
Formula weight (g/mol)	1574.87
Crystal system	monoclinic
Space group	P2/n
a [Å]	11.5641(7)
b [Å]	9.6178(7)
c [Å]	39.463(3)
α [°]	90
β [°]	91.336(4)
γ [°]	90
V [$Å^3$]	4387.9(5)
Z	2
Dx [g/cm^3]	1.192
Temperature [K]	100(2)
Tmax/Tmin	0.9540, 0.6730
Absortion coeff. [mm^{-1}]	2.392
F (000)	1712
Θ range [°]	2.24 to 74.49
Reflections collected	66931
Independent reflections	8946
GOF on F2	1.065
Final R indices [I > 2σ(I)]	R1 = 0.1055, wR2 = 0.2606
R indices (all data)	R1 = 0.1279, wR2 = 0.2719

Table 6.1.2. Crystallographic data and structure refinement of single crystal X-Ray analysis for complex 2.

	2
Chemical Formula	$C_{86}H_{146}Cl_2FeN_{10}O_{12}$
Size (mm^3)	0.010 x 0.120 x 0.180
Formula weight (g/mol)	1638.87
Crystal system	monoclinic
Space group	P2/n
a [Å]	11.4476(4)
b [Å]	9.5627(4)
c [Å]	40.6556(14)
α [°]	90
β [°]	91.026(3)
γ [°]	90
V [$Å^3$]	4449.9(3)
Z	2
Dx [g/cm^3]	1.223
Temperature [K]	100(2)
Tmax/Tmin	0.9760 and 0.6710
Absortion coeff. [mm^{-1}]	2.413
F (000)	1776
Θ range [°]	2.17 to 58.92
Reflections collected	31354
Independent reflections	6410
GOF on F2	1.042
Final R indices [I > 2σ(I)]	R1 = 0.0850, wR2 = 0.2195
R indices (all data)	R1 = 0.1446, wR2 = 0.2626

Table 6.1.3. Crystallographic data and structure refinement of single crystal X-Ray analysis for complex 3.

	3
Chemical Formula	$C_{90}H_{146}Cl_2FeN_{10}O_{16}$
Size (mm^3)	0.080 x 0.090 x 0.220
Formula weight (g/mol)	1750.91
Crystal system	tetragonal
Space group	I 41/a
a [Å]	14.9695(8)
b [Å]	14.9695(8)
c [Å]	43.925(3)
α [°]	90
β [°]	90
γ [°]	90
V [$Å^3$]	9843.0(12)
Z	4
Dx [g/cm^3]	1.182
Temperature [K]	100(2)
Tmax/Tmin	0.9790, 0.9430
Absortion coeff. [mm^{-1}]	0.272
F (000)	3776
Θ range [°]	2.67 to 30.51
Reflections collected	321792
Independent reflections	7504
GOF on F2	1.054
Final R indices [I > 2σ(I)]	R1 = 0.0374, wR2 = 0.0916
R indices (all data)	R1 = 0.0517, wR2 = 0.1015

Table 6.1.4. Fe1-N distances for all the compounds at 100 K.

1		2		3	
Bond	**Distance (Å)**	**Bond**	**Distance (Å)**	**Bond**	**Distance (Å)**
Fe1-N1	2.143(5)	**Fe1-N1**	2.189(5)	**Fe1-N1**	2.1917(9)
Fe1-N11	2.200(5)	**Fe1-N5**	2.211(5)	**Fe1-N3**	2.1357(13)
Fe1-N41	2.207(4)	**Fe1-N6**	2.115(5)		

Table 6.1.5. Main distortion angles of all the compounds at 100 K.

	1	2	3
Σ	146.07	139.05	143.09
Θ	469.13	456.85	449.76
θ	84.48	83.88	90.00
Ψ	147.85	149.13	148.46
ϕ	178.18	178.13	180.00

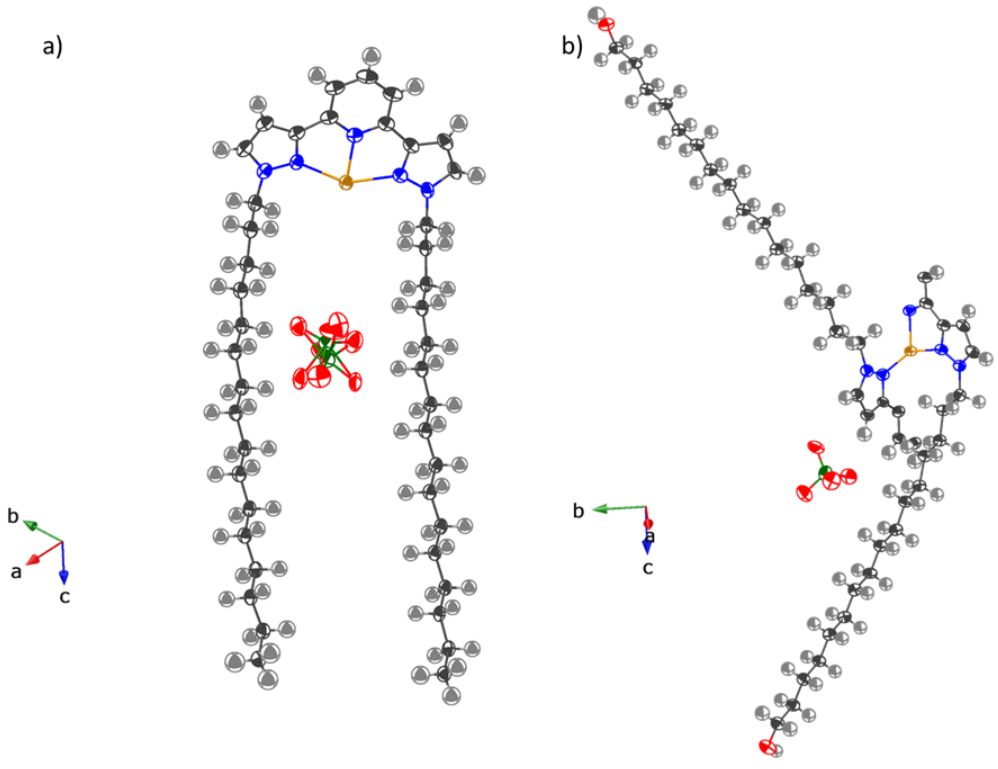

Figure 6.1.16. ORTEP representation (30% probability) of asymmetric unit of 1 (a), 2 (b). Iron is brown, carbon is dark grey, nitrogen is blue, oxygen is red, chlorine is green, and hydrogen is light grey.

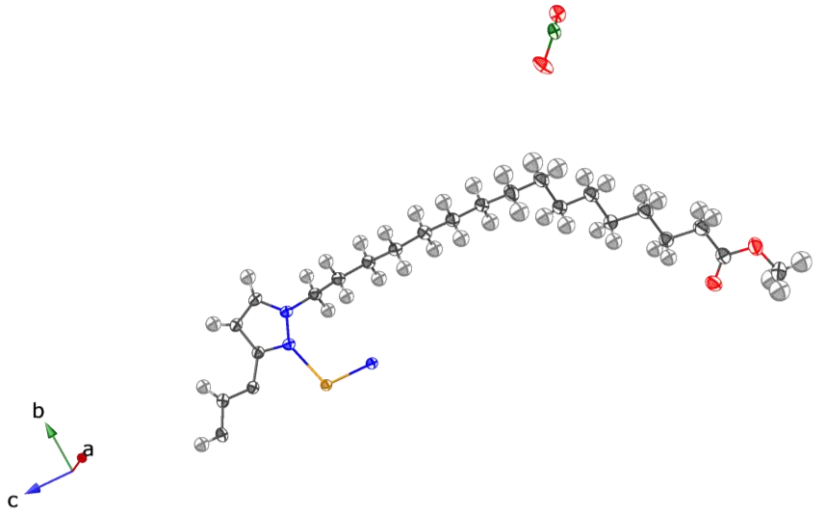

Figure 6.1.17. ORTEP representation (30% probability) of asymmetric unit of 3. Iron is brown, carbon is dark grey, nitrogen is blue, oxygen is red, chlorine is green, and hydrogen is light grey.

6.1.4 Differential Scanning Calorimetry (DSC)

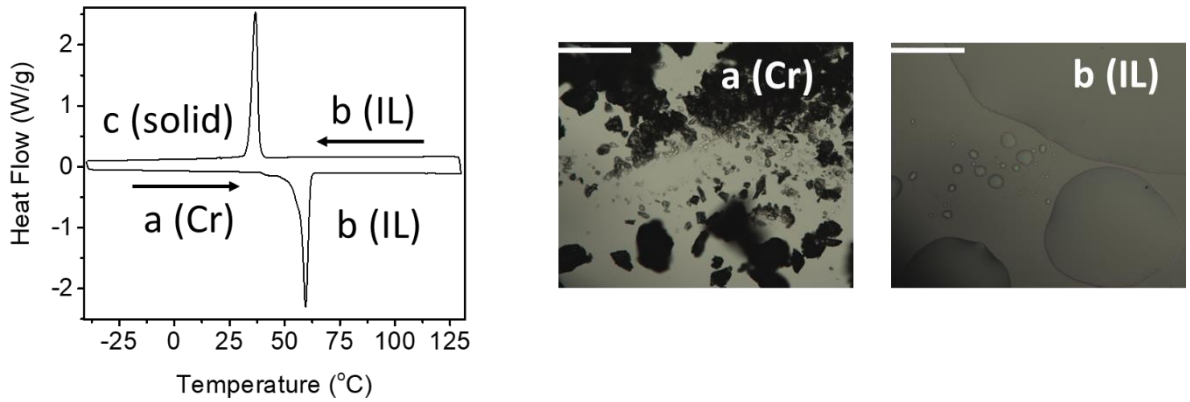

Figure 6.1.18. DSC and POM images of L1 in a heating/cooling rate of 2 °C·min^{-1}. Scale bar is 200 µm.

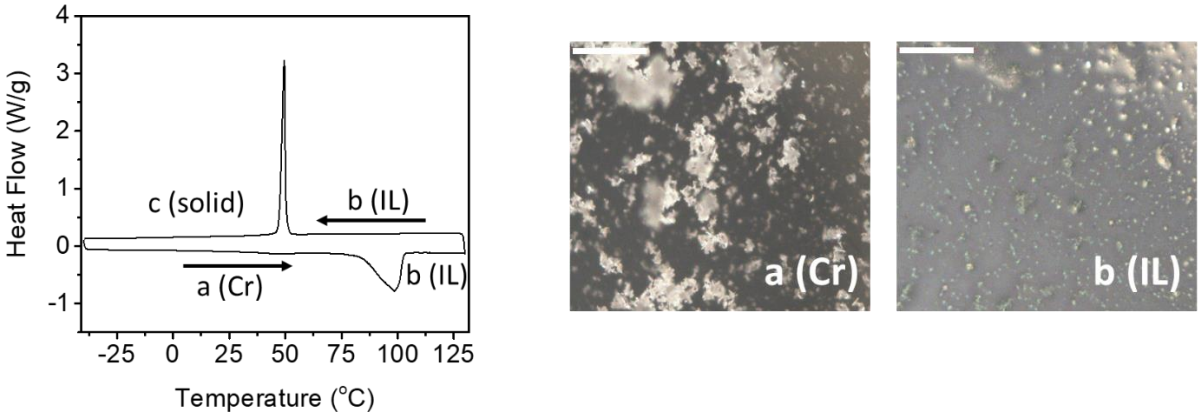

Figure 6.1.19. DSC and POM images of L2 in a heating/cooling rate of 2 °C·min^{-1}. Scale bar is 200 µm.

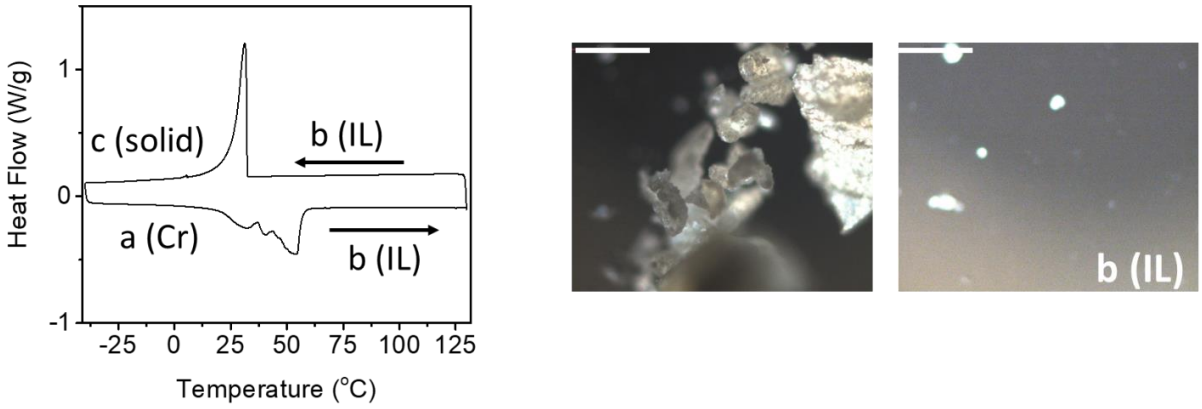

Figure 6.1.20. DSC and POM images of L3 in a heating/cooling rate of 2 °C·min^{-1}. Scale bar is 200 µm.

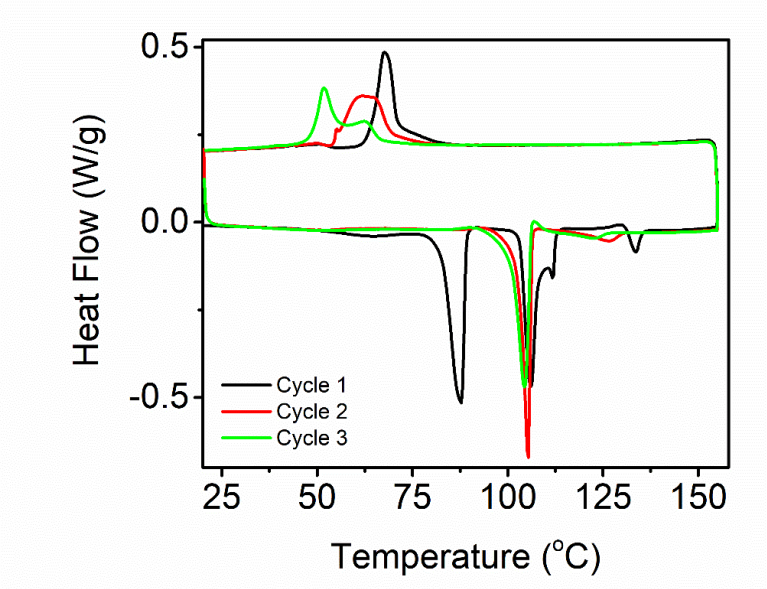

Figure 6.1.21. DSC of complex 1 with 3 cycles performed. Measurement was done in a heating/cooling rate of 2 °C/min under N_2 atmosphere.

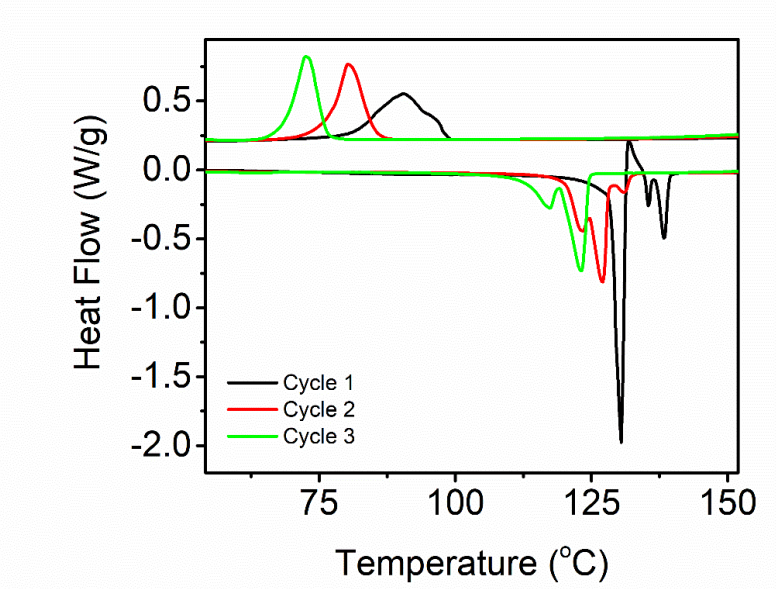

Figure 6.1.22. DSC of complex 2 with 3 cycles performed. Measurement was done in a heating/cooling rate of 2 °C/min under N_2 atmosphere.

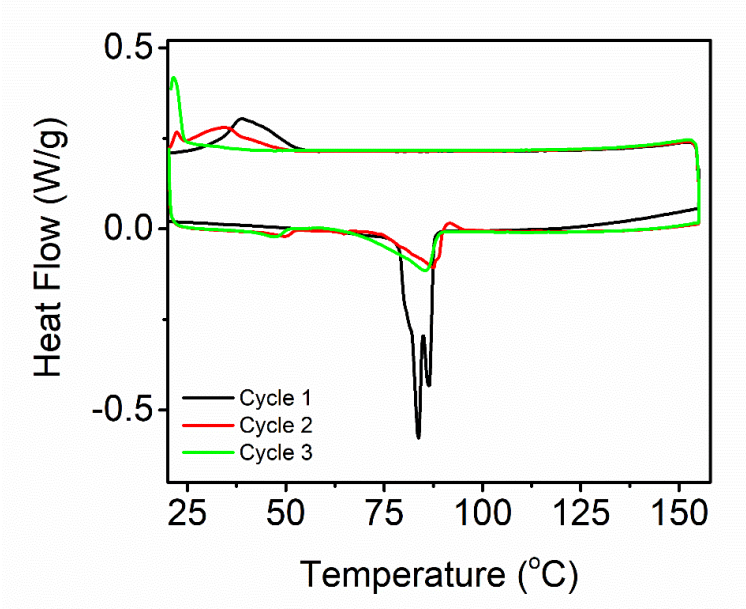

Figure 6.1.23. DSC of complex 3 with 3 cycles performed. Measurement was done in a heating/cooling rate of 2 °C/min under N_2 atmosphere.

6.1.5 Variable-Temperature Powder X-Ray Diffraction (VT-PXRD)

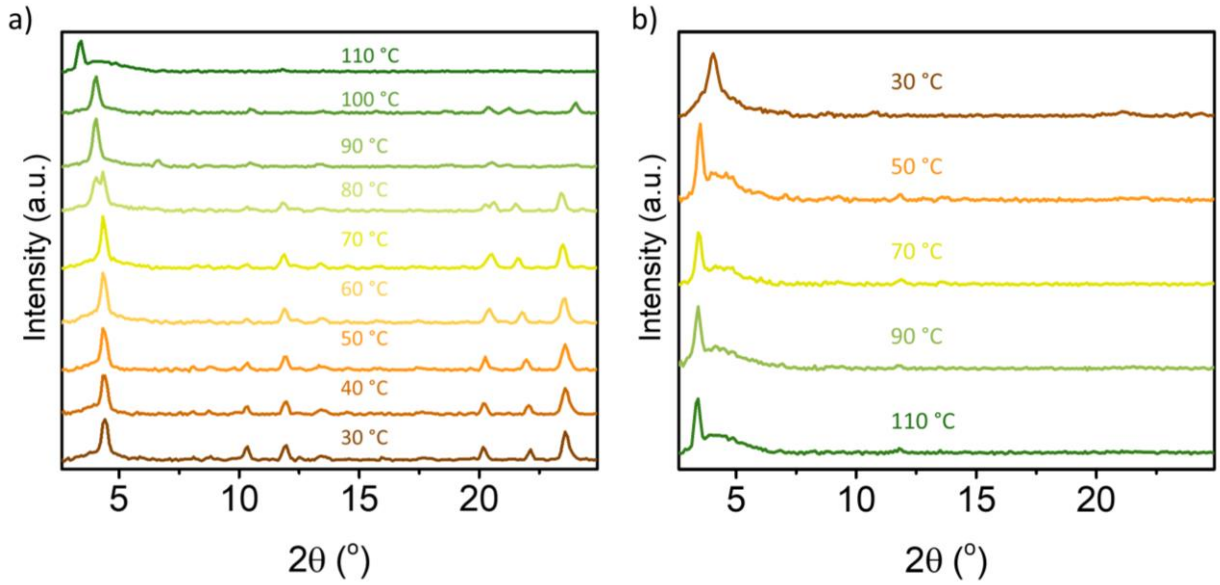

Figure 6.1.24. Variable temperature PXRD patterns of 1 recorded between 30 – 110 °C on heating mode (a) and cooling mode (b) at a scan rate of 2 °C/min. Patterns were measured each 10 °C for heating and each 20 °C for cooling down.

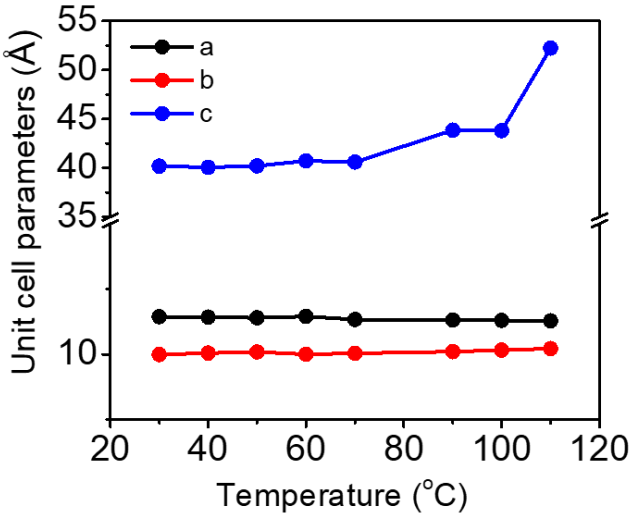

Figure 6.1.25. Temperature-dependent unit cell parameters of 1.

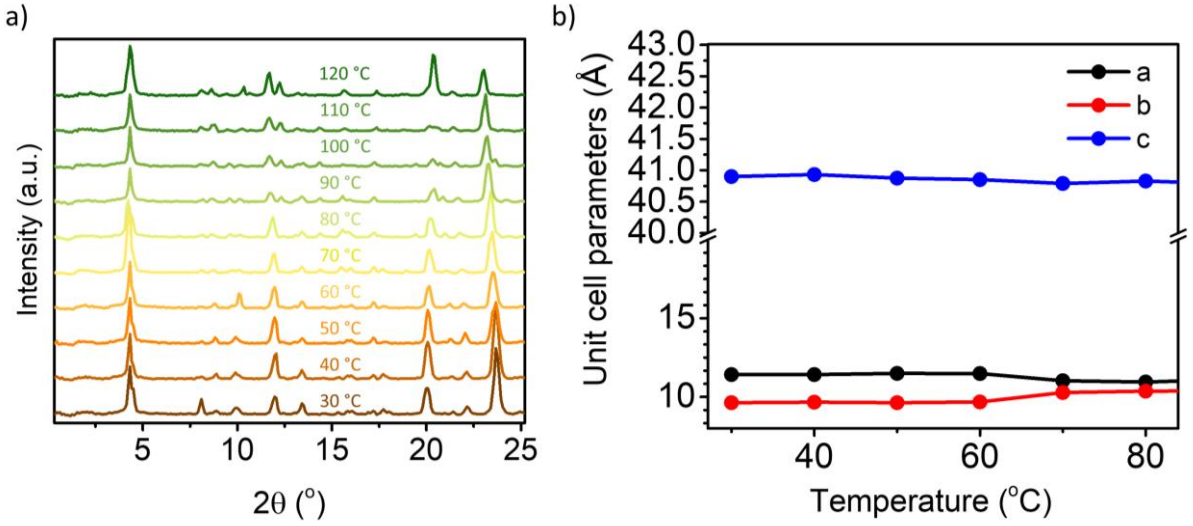

Figure 6.1.26. Variable temperature PXRD patterns of 2 recorded between 30 – 120 °C on heating mode (a) at a scan rate of 2 °C/min. Patterns were measured each 10 °C. Temperature-dependent unit cell parameters of 2 (b).

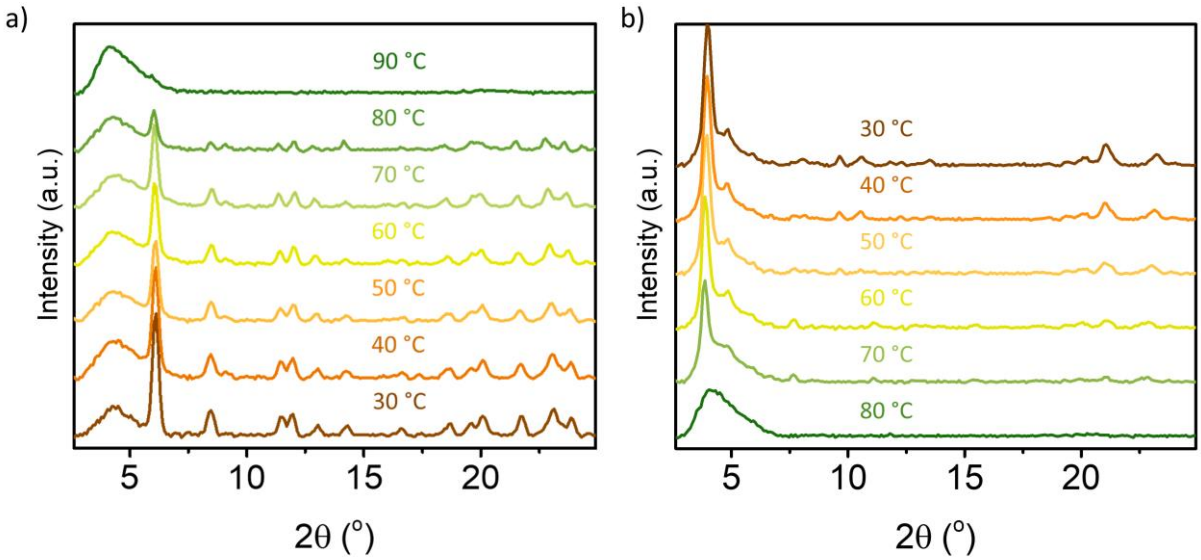

Figure 6.1.27. Variable temperature PXRD patterns of 3 recorded between 30 – 90 °C on heating mode (a) and cooling mode (b) at a scan rate of 2 °C/min. Patterns were measured each 10 °C for heating and cooling down.

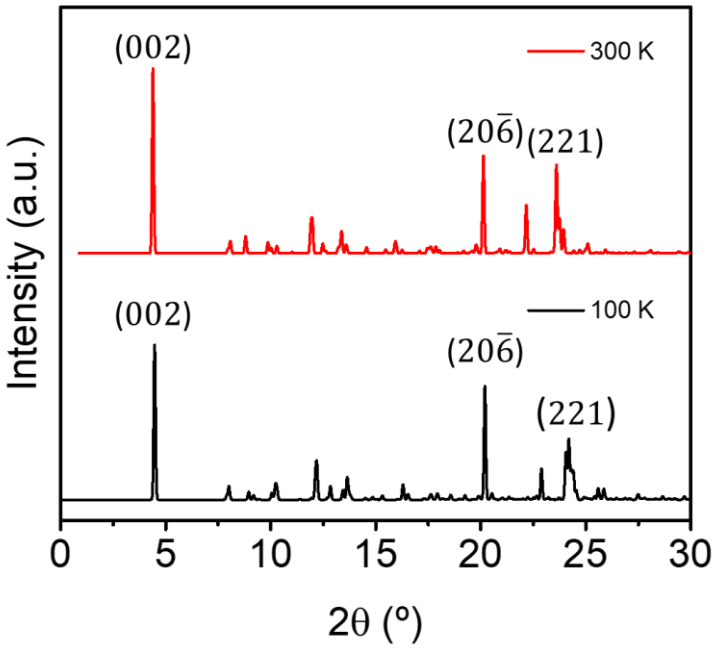

Figure 6.1.28. Simulation XRD pattern for 1 at 100 and 300 K.

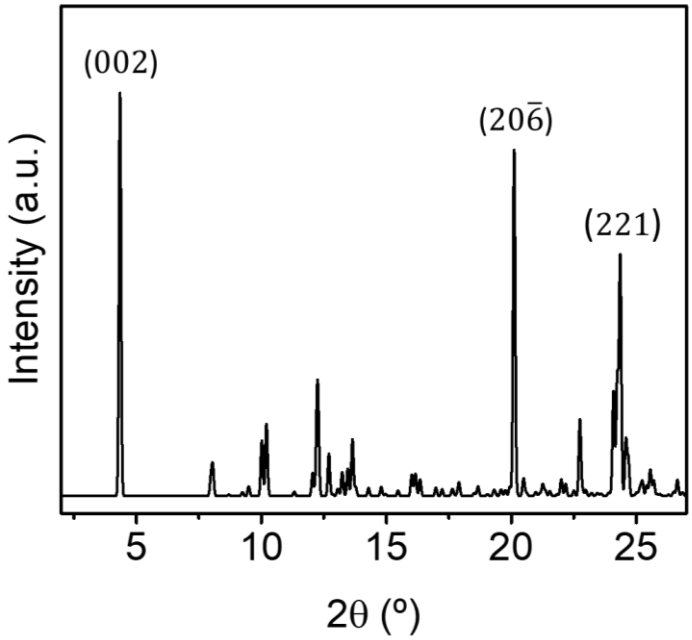

Figure 6.1.29. Simulation XRD pattern for 2 at 100 K.

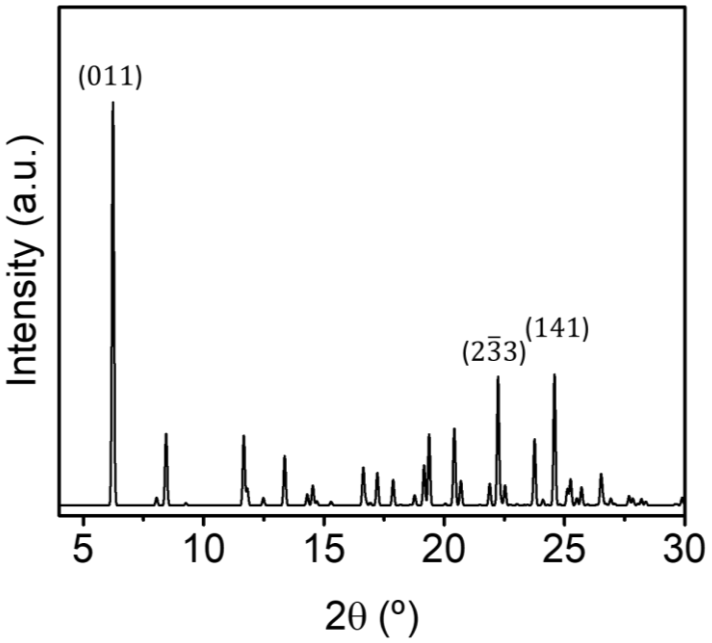

Figure 6.1.30. Simulation XRD pattern for 3 at 100 K.

6.1.6 Raman Spectroscopy

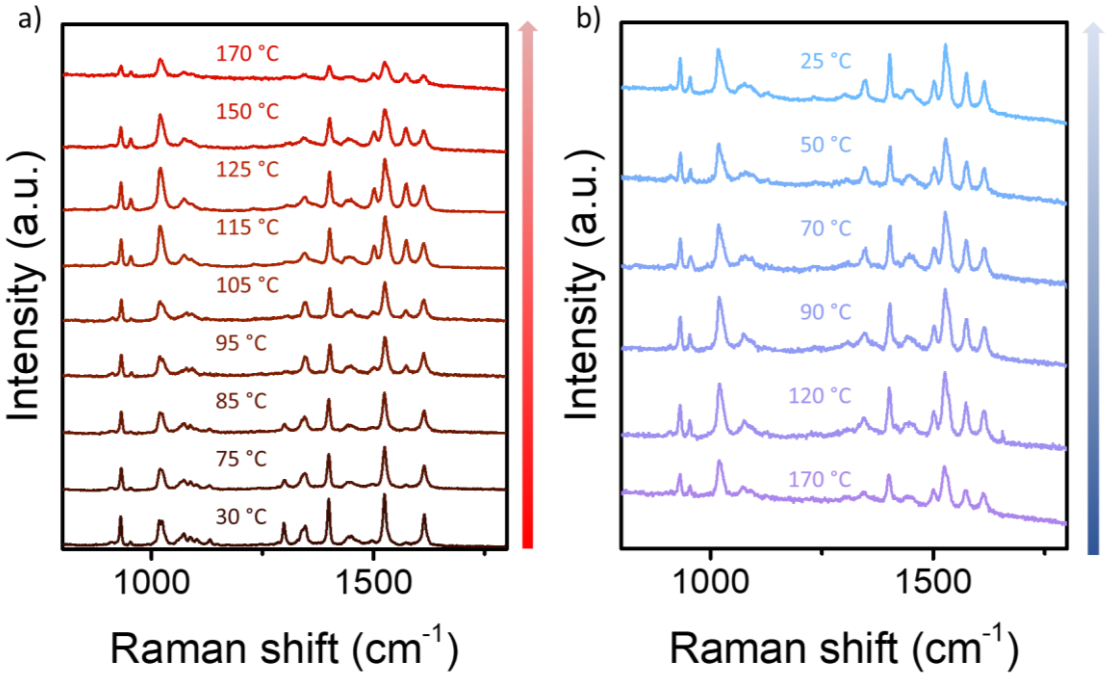

Figure 6.1.31 Raman spectra on heating (a) and cooling mode (b) for complex 1 at a scan rate of 2 °C/min.

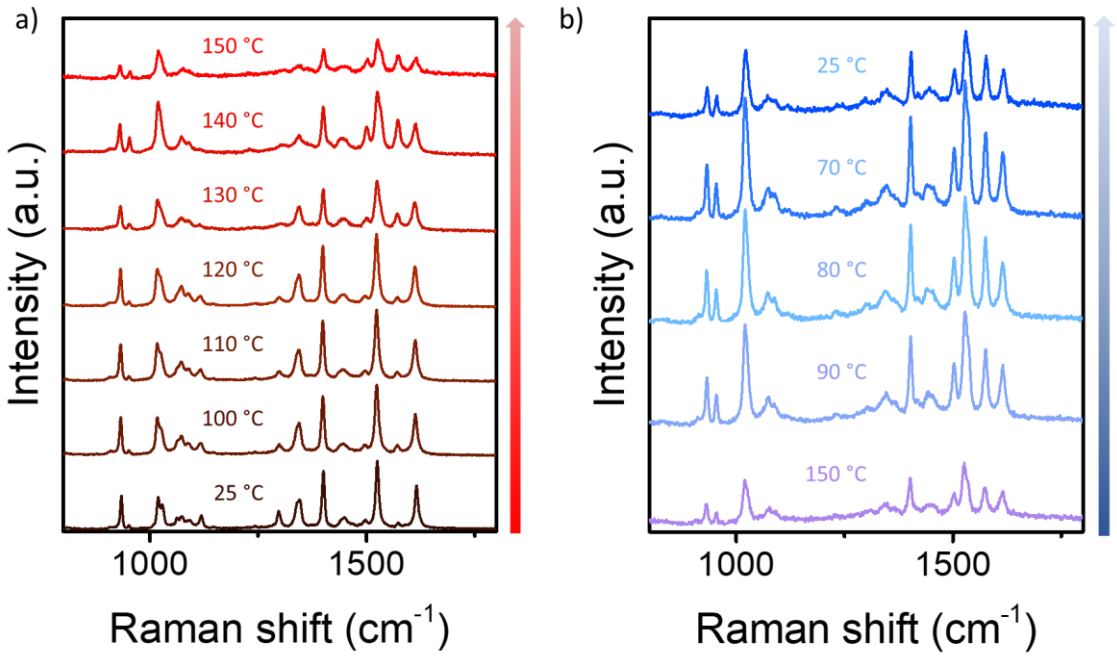

Figure 6.1.32. Raman spectra on heating (a) and cooling mode (b) for complex 2 at a scan rate of 2 °C/min.

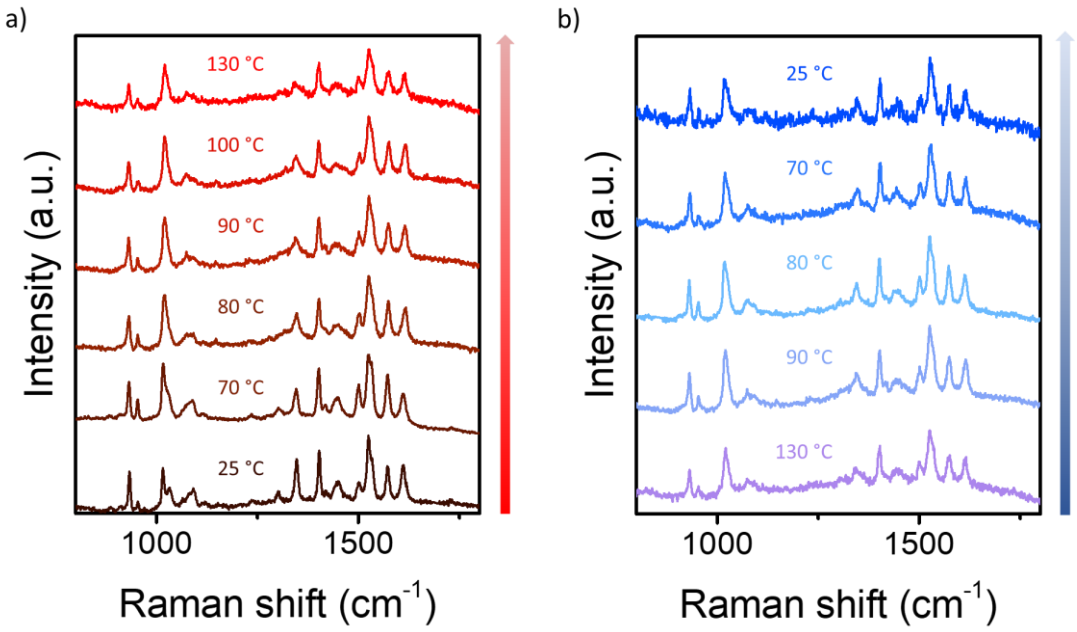

Figure 6.1.33. Raman spectra on heating (a) and cooling mode (b) for complex 3 at a scan rate of 2 °C/min.

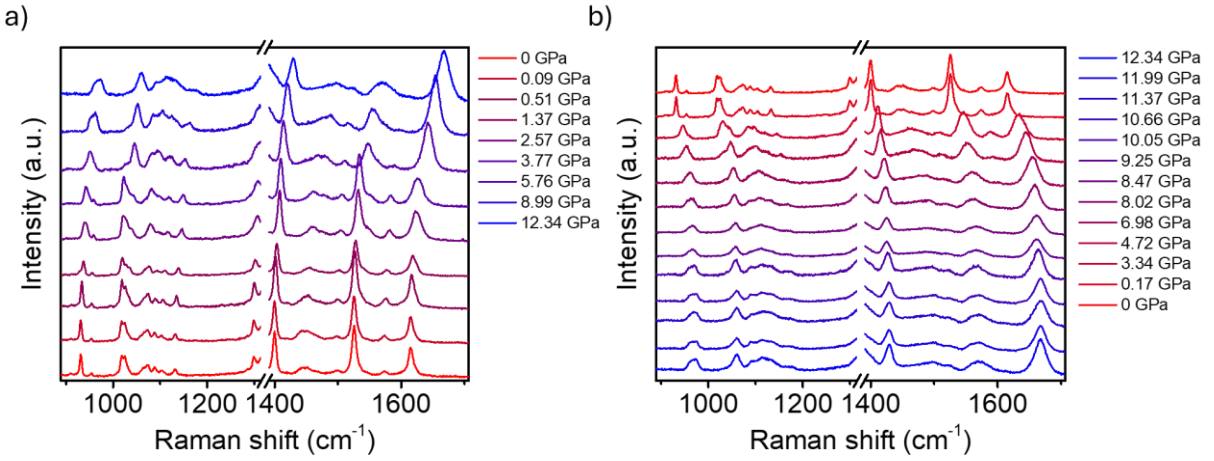

Figure 6.1.34. Variable Pressure Raman spectra of 1 at press (a) and release (b) mode.

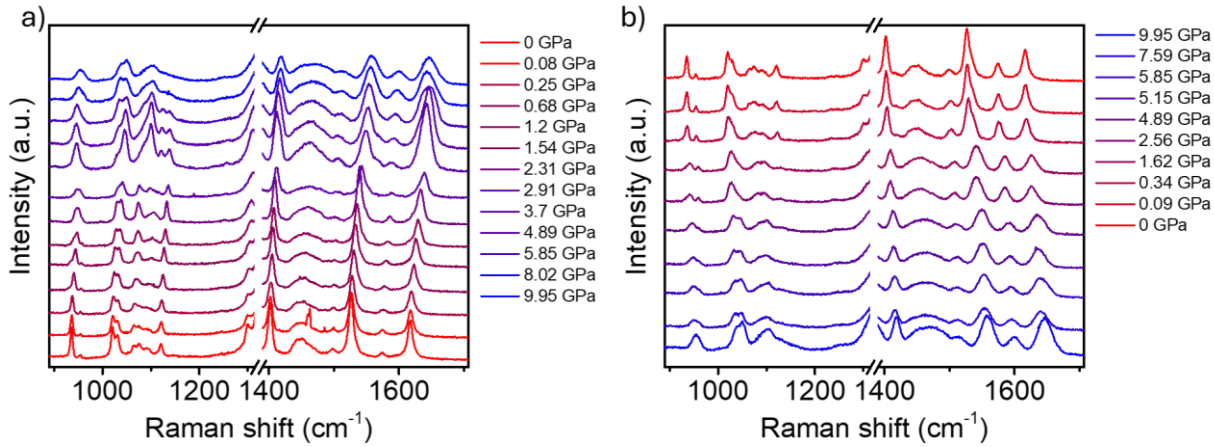

Figure 6.1.35. Variable Pressure Raman spectra of 2 at press (a) and release (b) mode.

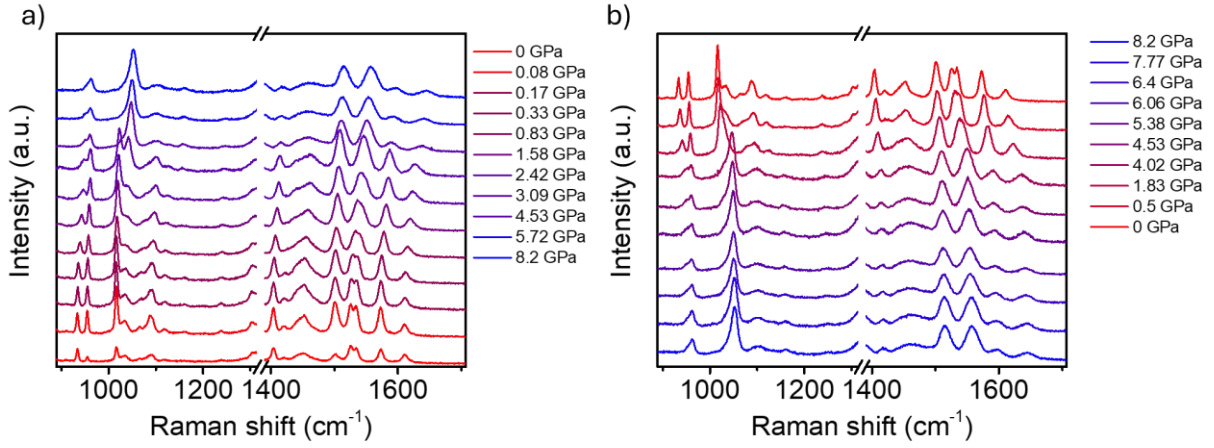

Figure 6.1.36. Variable Pressure Raman spectra of 3 at press (a) and release (b) mode.

6.2 Elucidating the Nature of Intermediate Spin States in SCO under Pressure

6.2.1 Synthesis of the ligands

6.2.1.1 Synthesis of 4-fluoro-2,6-di(1H-pyrazol-3-yl)pyridine (4)

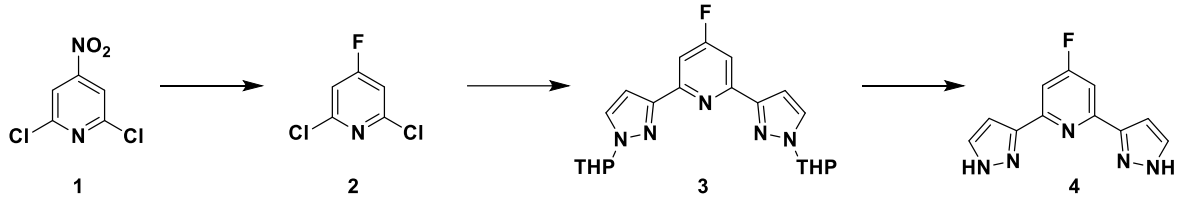

Scheme 6.2.1. Synthetic route to obtain (4).

6.2.1.2 Synthesis of 2,6-dichloro-4-fluoropyridine (2)

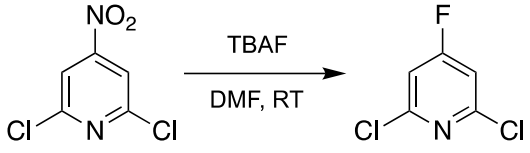

1 **2**

2,6-Dichloro-4-nitropyridine (1.0 g, 5.2 mmol, 1.0 eq.) was dissolved in 10 mL of dry DMF. Then 1 M TBAF in THF solution (10.36 mL, 10.36 mmol, 2.0 eq.) was added and the reaction at 0 °C and the mixture was stirred for 30 min at room temperature. The reaction was poured into 50 mL of brine and extracted with ethyl acetate (3 × 40 mL). Combined organic extract was dried over Na_2SO_4 and the solvent was removed under reduced pressure. 2,6-dichloro-4-fluoropyridine was obtained as a white solid 776.8 mg (90% Yield).

^{1}H NMR (300 MHz, $CDCl_3$, δ): 7.05 (d, $^{3}J_{HF}$ = 7.54 Hz, 2H, H_a and $H_{a'}$).

^{13}C NMR (75MHz, $CDCl_3$, δ): 169.89 (C, d, *J* = 267.56 Hz), 152.16 (C, d, *J* = 12.07 Hz), 111.63, (CH, d, *J* = 21.58 Hz).

^{19}F NMR (282 MHz, $CDCl_3$, δ): -96.86 (s)

ESI-MS m/z (relative intensity): $[M+H]^+$ calcd.for $[C_5H_3Cl_2FN]^+$ 165.96; found: 165.92 (100%).

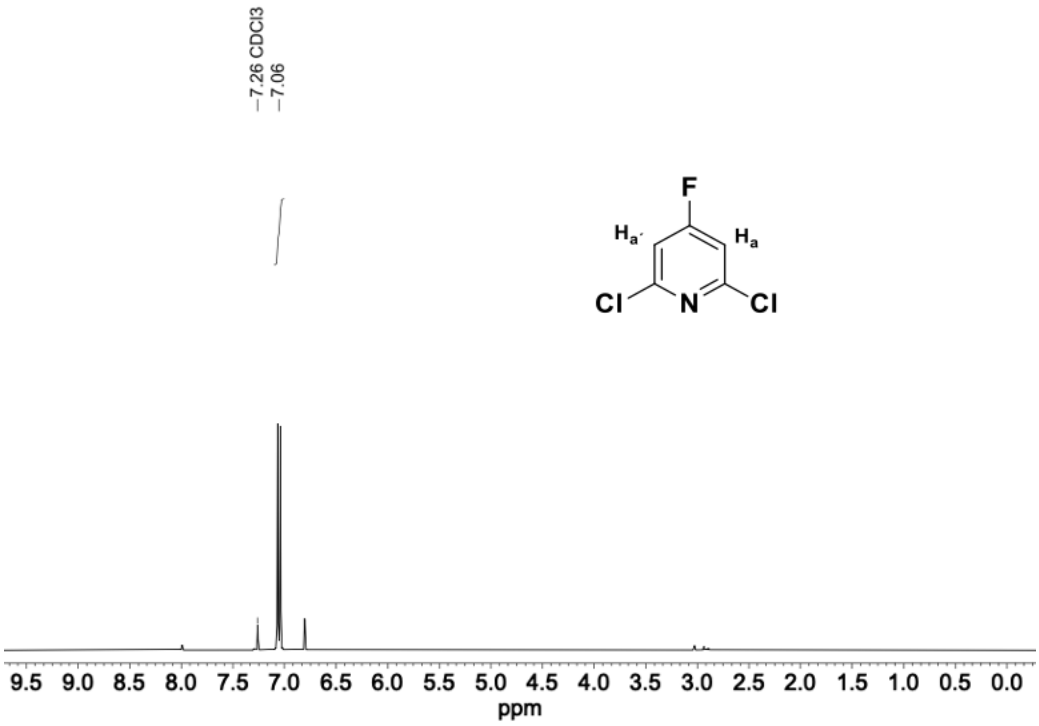

Figure 6.2.1. ^{1}H NMR of compound 2.

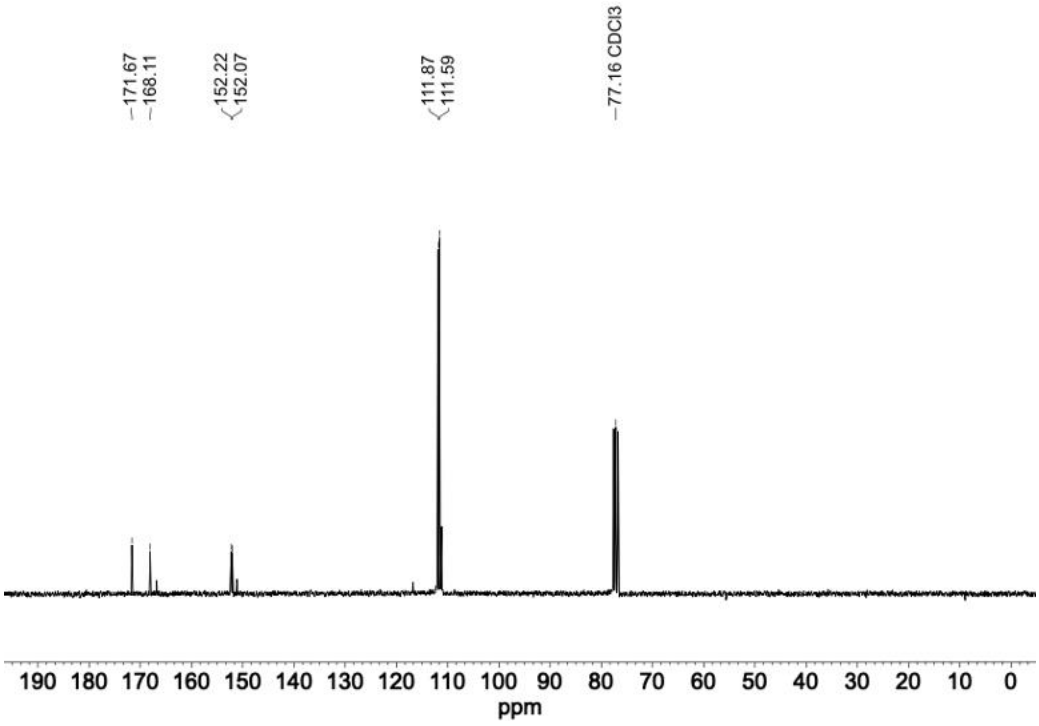

Figure 6.2.2: ^{13}C NMR of compound 2.

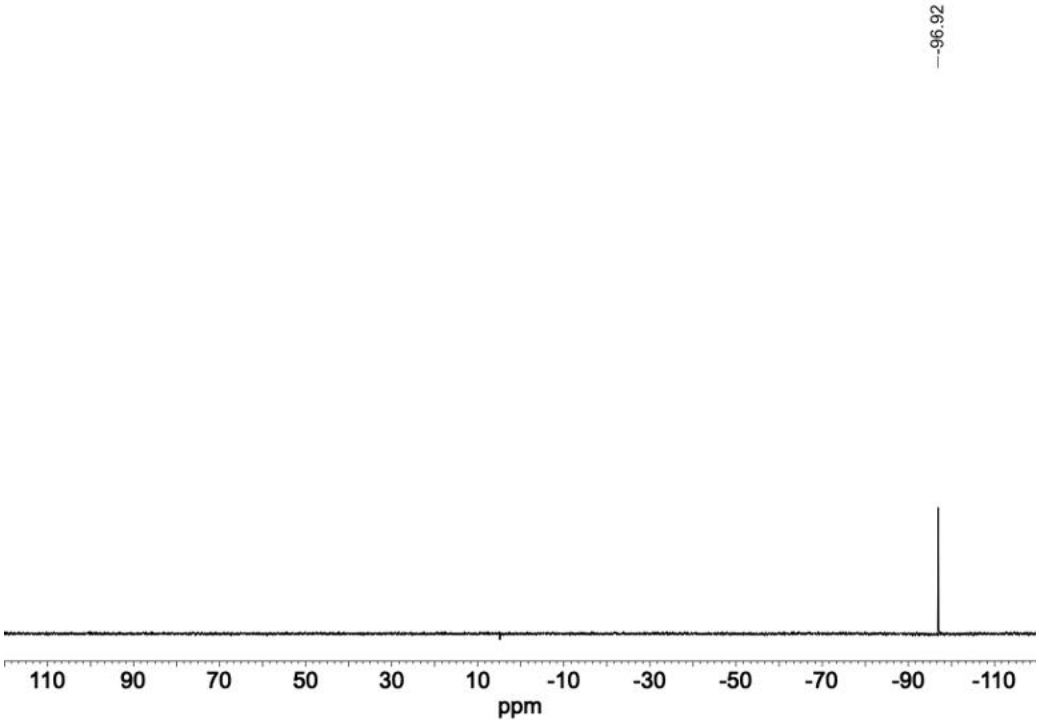

Figure 6.2.3: ^{19}F NMR of compound 2.

6.2.1.3 Synthesis of 4-fluoro-2,6-di(1H-pyrazol-3-yl)pyridine (4).

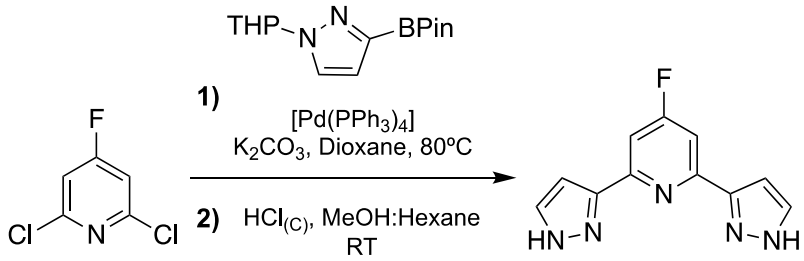

2 **4**

1-(Tetrahydro-pyran-2-yl)-5-(4,4,5,5-tetramethyl-[1,3,2]dioxaborolan-2-yl)-1H-pyrazole (1.69 g, 6.07mmol, 2.5 eq.), 4-fluoro-2,6-dichloropyridine (400 mg, 2.43 mmol, 1 eq.), K_2CO_3 (1.34 g, 9.72 mmol, 4 eq.) and $[Pd(PPh_3)_4]$ (280 mg, 0.243 mmol, 0.1 eq.) were dissolved in dry 1,4-dioxane (72 mL) under a nitrogen atmosphere. The mixture was then heated at 80 °C for 24 hours before being poured into diethyl ether (100 mL) and brine (100 mL). The combined organic layer was separated, dried over Na_2SO_4 and evaporated to give a brown oil. The oil was dissolved in a mixture of methanol (20 mL) and hexane (20 mL) and a few drops of conc. Hydrochloric acid were added. The mixture was stirred for 24 hours at room temperature before being separated and the methanol layer evaporated to leave a sticky brown oil. This was then sonicated in diethyl ether and the precipitate was washed with $CHCl_3$ to leave an off-white precipitate. 543 mg (97% yield)

^{1}H NMR (300 MHz, DMSO-d_6, δ): 11.61 (s, 2H, H_d and $H_{d'}$), 7.79 (d, *J* = 2.1Hz, 2H, H_c and $H_{c'}$), 7.69 (d, *J* = 10 Hz, 2H, H_a and $H_{a'}$), 7.08 (d, *J* = 2.1 Hz, 2H, H_b and $H_{b'}$)

^{13}C NMR (75 MHz, DMSO-d_6, δ): 171.1, 167.7, 153.2, 153.1, 146.5, 133.9, 105.5, 105.2, 104.3

^{19}F NMR (282 MHz, DMSO-d$_6$, δ): -102.76 (t, *J* = 10.2 Hz)

ESI-MS *m/z* (Relative intensity): $[M+H]^+$ calcd. for $[C_{11}H_9FN_5]^+$ 230.08; found: 230.09 (100%).

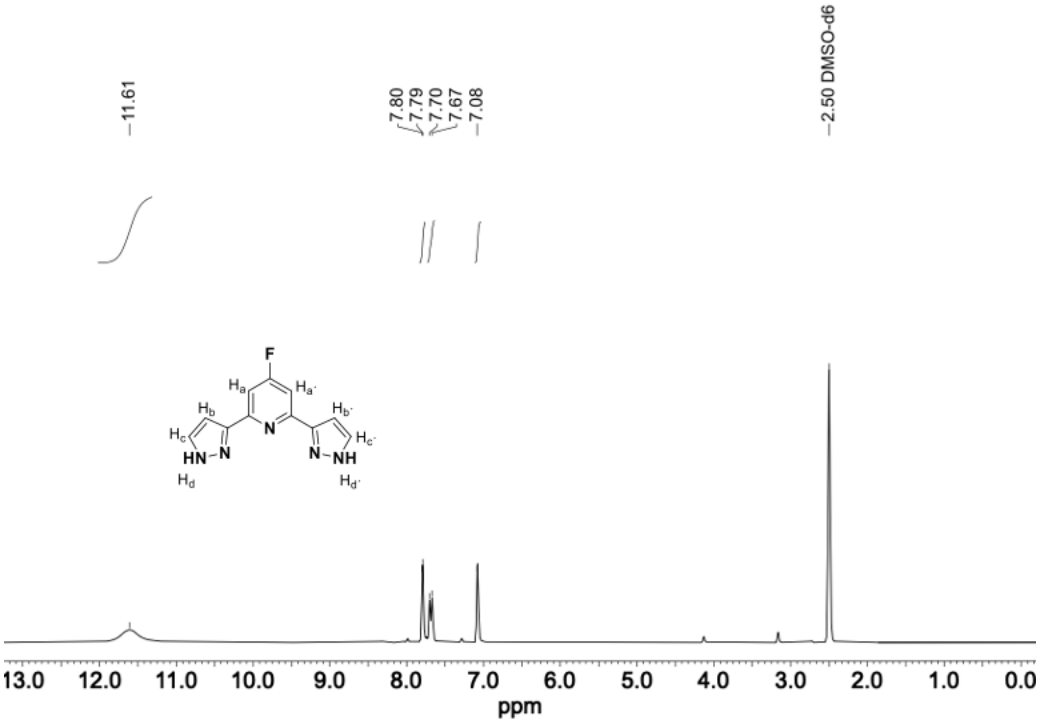

Figure 6.2.4: ^{1}H NMR of compound 4.

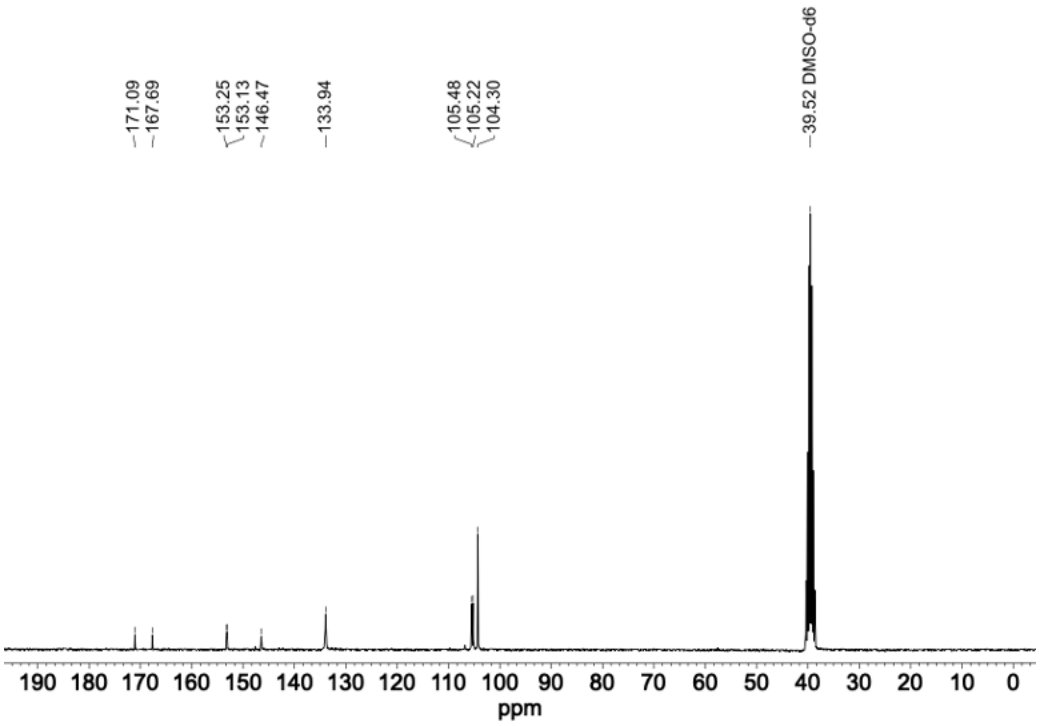

Figure 6.2.5: ^{13}C NMR of compound 4.

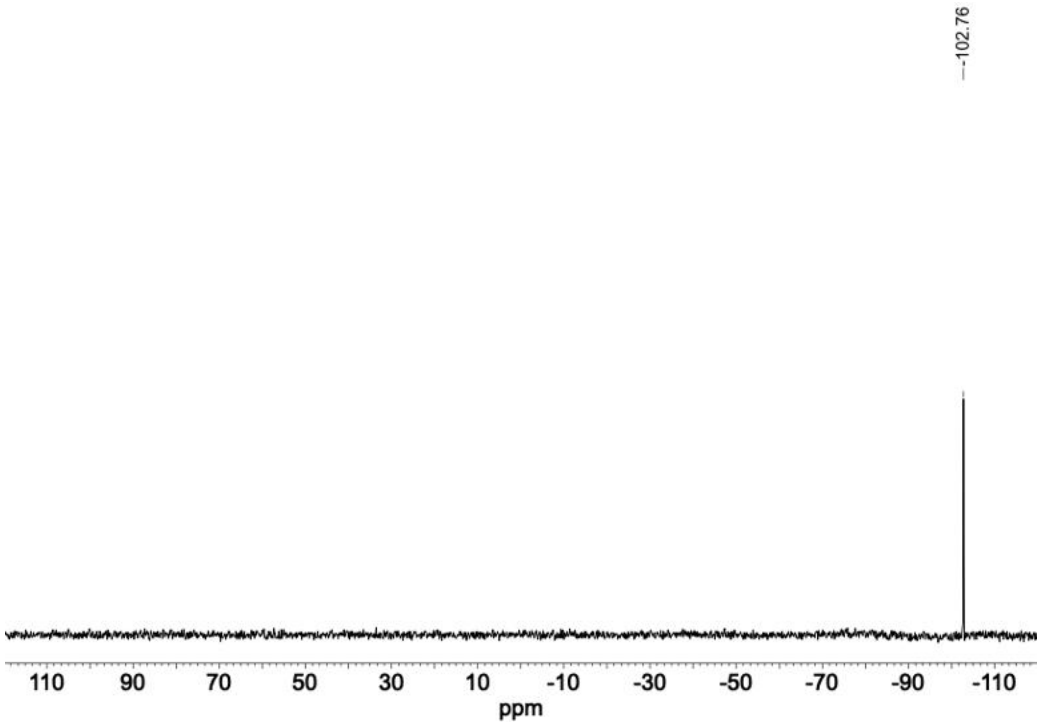

Figure 6.2.6: ^{19}F NMR of compound 4.

6.2.1.4 Synthesis of 1,1'-(4-halogenpyridine-2,6-diyl)bis(ethan-1-one) (6a-c)

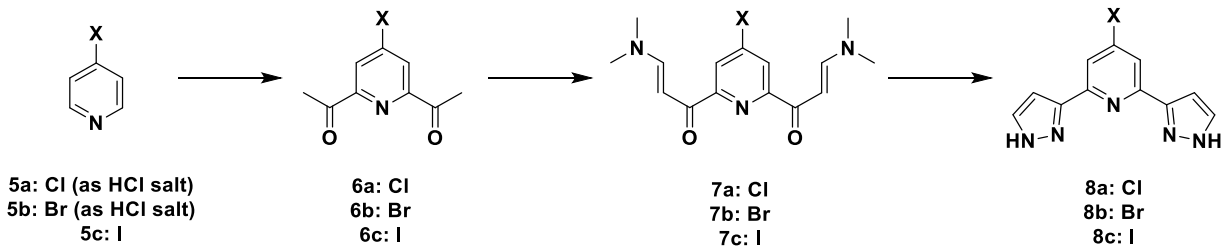

Scheme 6.2.2. Synthetic route to obtain ligands 8a-c.

6.2.1.5 Synthesis of 2, 6-diacetyl-halogenpyridines (6a-c)

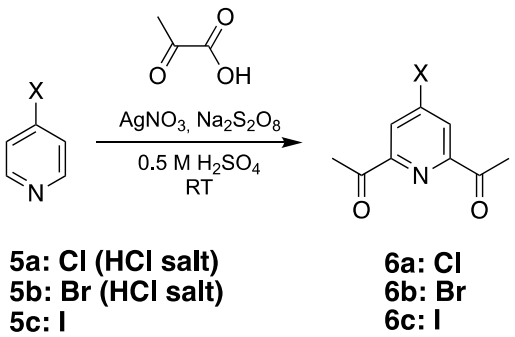

Synthesis of 6a: In a round-bottom flask, 4-chloropyridine hydrochloride (5.0 g, 33.3 mmol, 1.0 eq.) was dissolved in 50 mL of deionized water and this solution was then basified to pH=9 using saturated solution of Na_2CO_3. Then, this basified solution was extracted with CH_2Cl_2 (3 x 25 mL) and then the organic phase was extracted with 0.5 M sulfuric acid (3 x 55 mL). Then, pyruvic acid (11.75 g, 133.3 mmol, 4.0 Equiv.), $AgNO_3$ (567 mg, 3.33 mmol, 0.1 eq.) dissolved in 50mL of deionized water and sodium persulfate (31.6 g, 133.3 mmol, 4.0 eq.) were added. Reaction was let to react overnight. After this time, yellow-green solution and a dark green precipitate was obtained. The mixture was filtered, and the precipitate was washed using CH_2Cl_2 (25 mL). The filtrate was then basified to pH=10 using aqueous saturated solution of NaOH, which led to a color change (dark red/orange). The resulting filtrate was let to cool to room temperature and then extracted with CH_2Cl_2 (3 x 50 mL). The organic phase was dried over sodium sulphate, filtered and solvent removed under vacuum. The product was purified by column chromatography in CH_2Cl_2 to obtain white crystalline solid with 28% of yield. Spectroscopic properties matched with the previously reported.[179]

Synthesis of 6b. In a round-bottom flask, 4-bromopyridine hydrochloride (5 g, 25.7 mmol, 1.0 eq.) was dissolved in 38 mL of deionized water and this solution was then basified to pH=9 using saturated solution of Na_2CO_3. Then, this basified solution was extracted with CH_2Cl_2 (3 x 12 mL) and then the organic phase was extracted with 0.5 M sulfuric acid (3 x 42 mL). Then, pyruvic acid (9.1 g, 102.8 mmol, 4.0 eq.), $AgNO_3$ (437 mg, 2.57 mmol, 0.1 eq.) dissolved in 25 mL of deionized water and sodium persulfate (18.38 g, 77.1 mmol, 3.0 eq.) were added. Reaction was let to react overnight. After this time, yellow-green solution and a dark green precipitate was obtained. The mixture was filtered, and the precipitate was washed using CH_2Cl_2 (25 mL). The filtrate was then basified to pH=10 using aqueous saturated solution of NaOH, which led to a color change (dark red/orange). The resulting filtrate was let to cool to room temperature and then extracted with CH_2Cl_2 (3 x 50 mL). The organic phase was dried over sodium sulphate, filtered and solvent removed under vacuum. The product was purified by column chromatography in CH_2Cl_2 to obtain white crystalline solid with 24% of yield. Spectroscopic properties matched with the previously reported.[1]

Synthesis of 6c. 4-iodinepyridine (5 g, 24.4 mmol, 1.0 eq.) was dissolved in 125 mL of 0.5 M sulfuric acid. To this solution, pyruvic acid (8.6 g, 97.6 mmol, 4.0 Equiv.), silver nitrate (415 mg, 2.44 mmol, 0.1 eq.) dissolved in 50 mL of deionized water and sodium persulfate (23.13 g, 97.6 mmol, 4.0 eq.) were added. Reaction was let to react overnight. After this time, yellow-green solution and a dark green precipitate was obtained. The solution was filtered, and the precipitate was washed using CH_2Cl_2 (25 mL). The filtrate was then basified to pH=10 using aqueous saturated solution of NaOH, which led to a color change (dark red/orange). The resulting filtrate was let to cool to room temperature and then extracted with CH_2Cl_2 (3 x 50 mL). The organic phase was dried over sodium sulphate, filtered and solvent removed under vacuum. The product was purified by column chromatography in CH_2Cl_2 to obtain a white crystalline with a yield of 14%. Spectroscopic properties matched with the previously reported.[1]

6.2.1.6 Synthesis of 1,1'-(4-halogenpyridine-2,6-diyl)bis(3-(dimethylamino)prop-2-en-1-one) (7a-c)

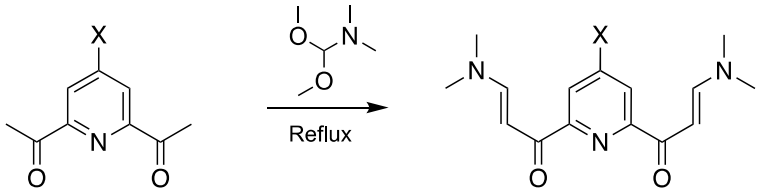

6a: Cl
6b: Br
6c: I

7a: Cl
7b: Br
7c: I

In a round-bottom flask, 1.0 equiv. of diacetyl-halogenpyridine (6a-c) and 44 eq. of N,N-dimethylformamide dimethyl acetal were added and refluxed overnight. The reaction was cooled to room temperature and solvent was evaporated. The yellow solid obtained was then dissolved in 5 mL of chloroform and then hexane was added to precipitate the solid. The solid was recovered by centrifugation and dried under vacuum.

7a. 4-Chloro-2,6-diacetylpyridine (2.5 g, 12.65 mmol, 1.0 eq.) and N,N-dimethylformamide dimethyl acetal (66.35g, 556 mmol, 44.0 Equiv.). 3.19 g (82% yield).

^{1}H NMR (300 MHz, $CDCl_3$, δ): 8.20 (s, 2H, He+e'), 7.93 (d, *J* = 12.7 Hz, 2H, Hc+c'), 6.54 (d, *J* = 12.5 Hz, 2H, Hd+d'), 3.20 (s, 6H, Hb+b'), 3.00 (s, 6H, Ha+a')

^{13}C NMR (75 MHz, $CDCl_3$, δ): 184.7, 155.8, 154.4, 145.6, 123.2, 90.7, 44.8, 36.8.

ESI-MS *m/z* (relative intensity): $[M+H]^+$ calcd. for $[C_{15}H_{19}ClN_3O_2]^+$ 308.12; found 308.11 (100%), 310.11 (32.2%).

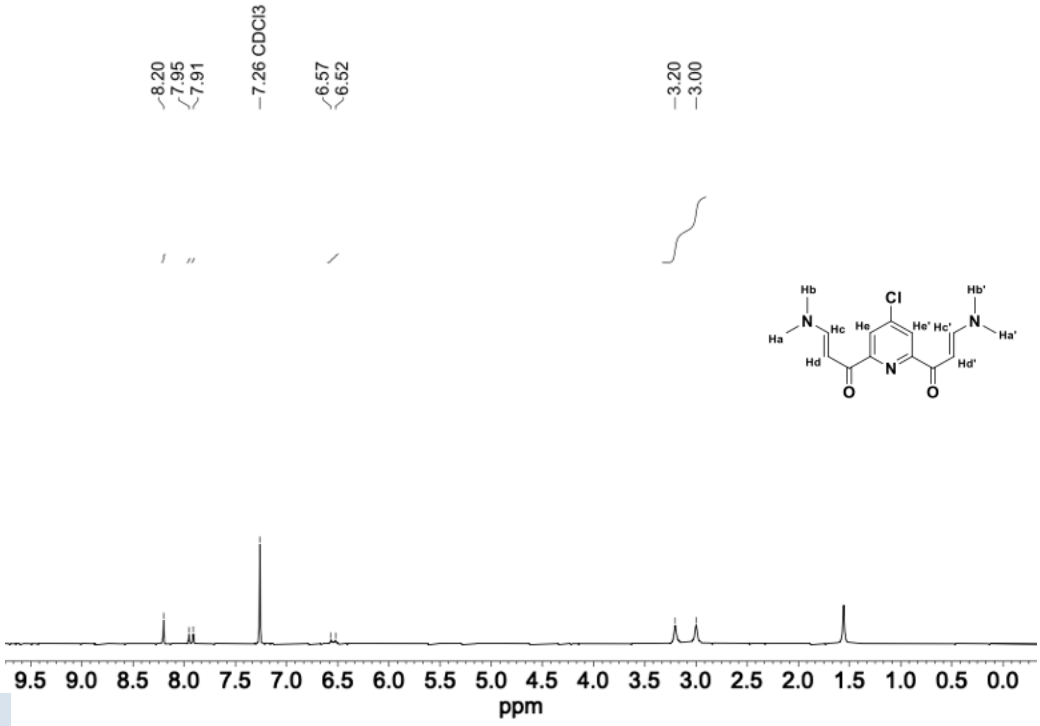

Figure 6.2.7: ^{1}H NMR spectrum of compound 7a.

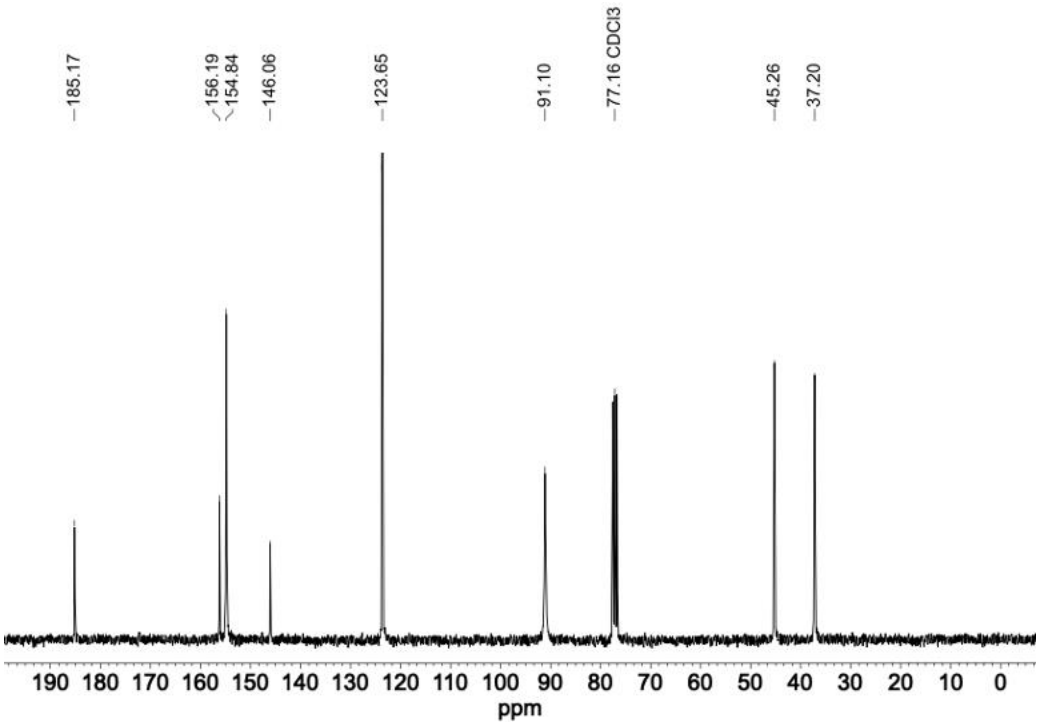

Figure 6.2.8: ^{13}C NMR spectrum of compound 7a.

7b. 4-Bromo-2,6-diacetylpyridine (2.1 g, 8.7 mmol, 1.0 eq.) and N,N-dimethylformamide dimethyl acetal (45.68 g, 383 mmol, 44.0 eq.). 2.44 g (80% yield).

^{1}H NMR (300 MHz, $CDCl_3$, δ): 8.36 (s, 2H, He+e'), 7.93 (d, *J* = 12.7 Hz, 2H, Hc+c'), 6.53 (d, *J* = 13.0 Hz, 2H, Hd+d'), 3.20 (s, 6H, Hb+b'), 2.99 (s, 6H, Ha+a')

^{13}C NMR (75 MHz, $CDCl_3$, δ): 185.4, 155.9, 155.0, 134.9, 126.9, 91.3, 45.4, 37.3

ESI-MS *m/z* (relative intensity) $[M+H]^+$ calcd. for $[C_{15}H_{19}BrN_3O_2]^+$ 352.07 ; found 352.07 (100%), 354.06 (97.1%).

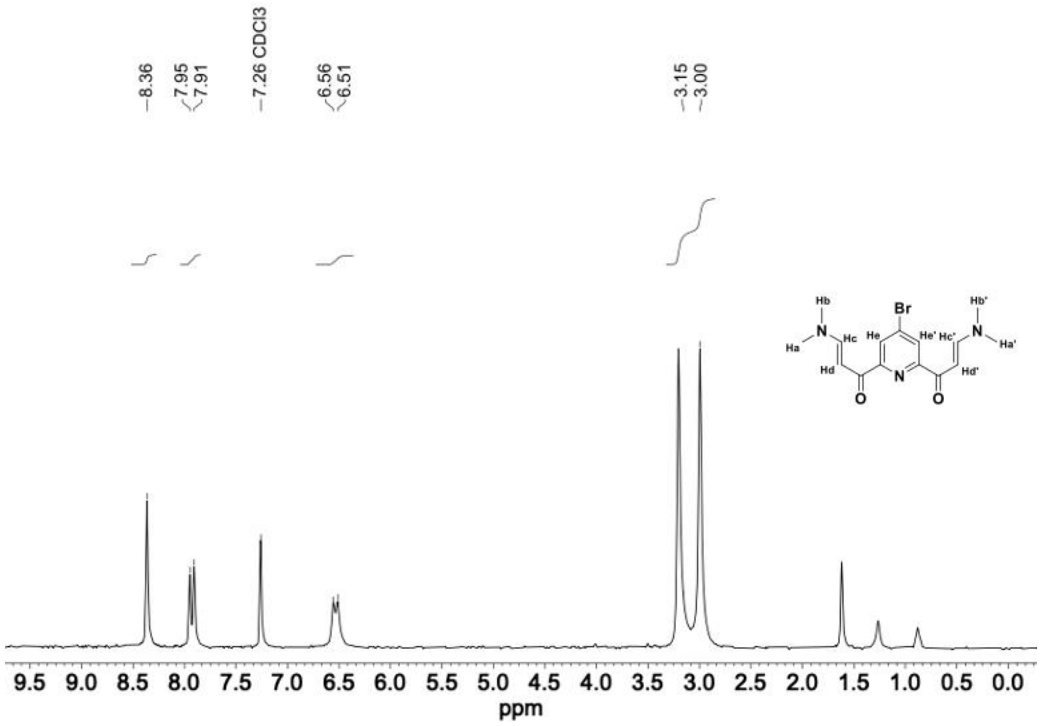

Figure 6.2.9: ^{1}H NMR spectrum of compound 7b.

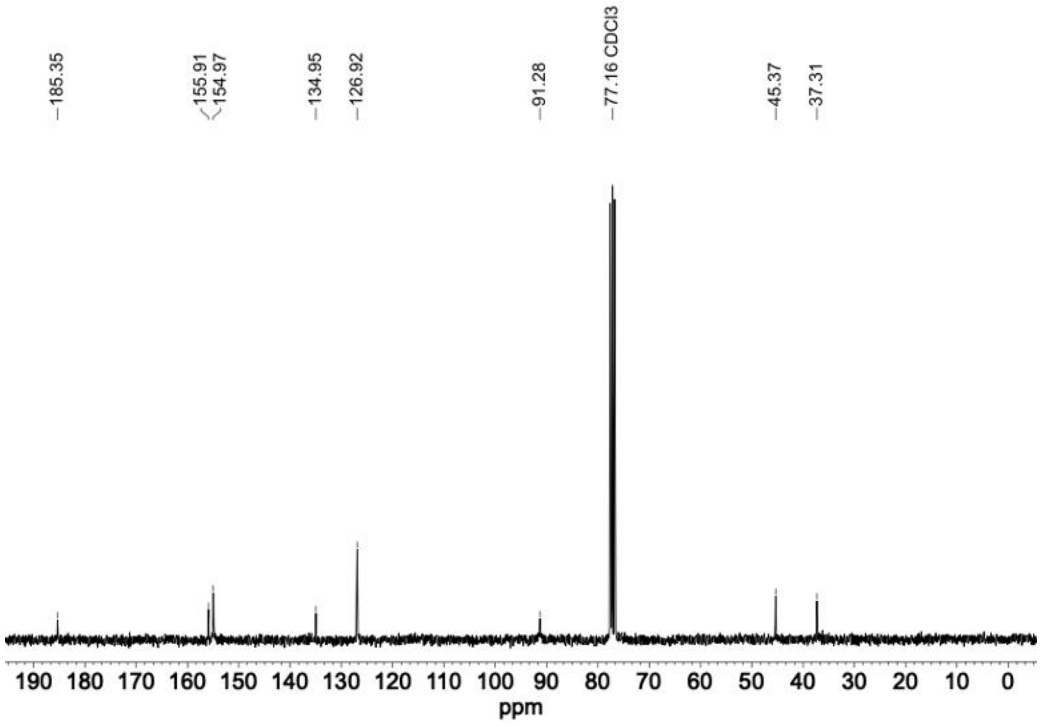

Figure 6.2.10: ^{13}C NMR spectrum of compound 7b.

7c. 4-Iodo-2,6-diacetylpyridine (1 g, 3.46 mmol, 1.0 eq.) and N,N-dimethylformamide dimethyl acetal (18.14 g, 152 mmol, 44.0 Equiv.). 1.24 g (90% yield)
^{1}H NMR (300 MHz, $CDCl_3$, δ): 8.57 (s, 2H, He+e'), 7.92 (d, *J* = 12.7 Hz, 2H, Hc+c'), 6.52 (d, *J* = 12.7 Hz, 2H, Hd+d'), 3.20 (s, 6H, Hb+b'), 2.99 (s, 6H, Ha+a')

^{13}C NMR (75 MHz, $CDCl_3$, δ): 185.1, 155.0, 154.8, 132.6, 107.2, 91.0, 77.6, 77.2, 76.7, 45.2, 37.2

ESI-MS *m/z*: (relative intensity: $[M+H]^+$ calcd. for $[C_{11}H_{19}IN_5]^+$ 400.05; found 400.06 (100%).

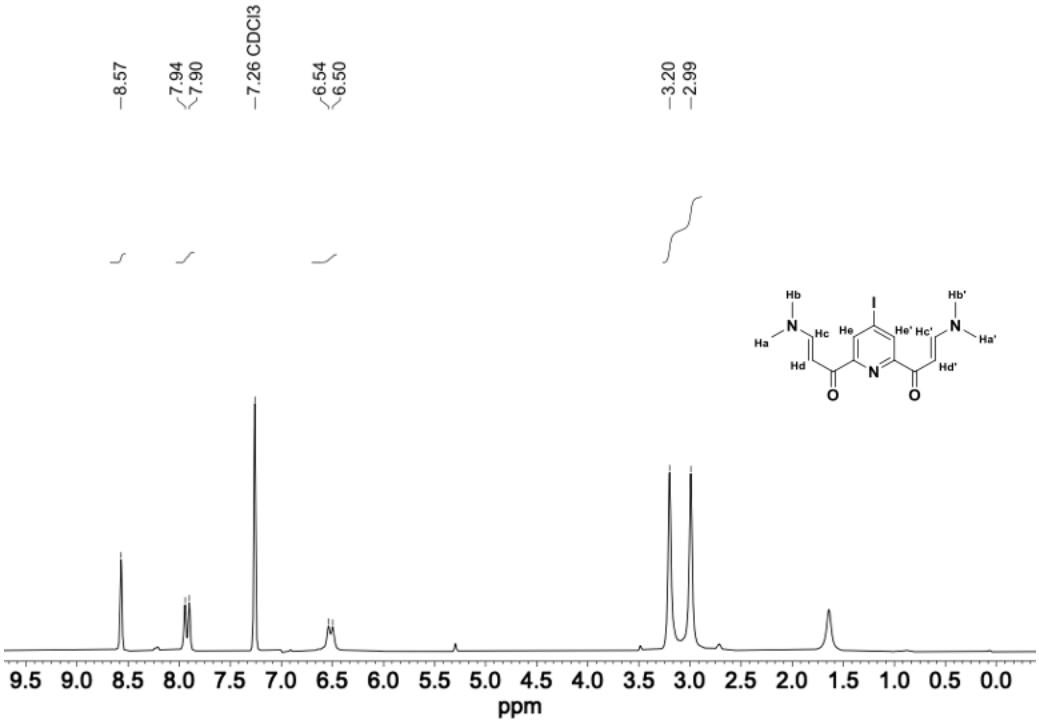

Figure 6.2.11: ^{1}H NMR spectrum of compound 7c.

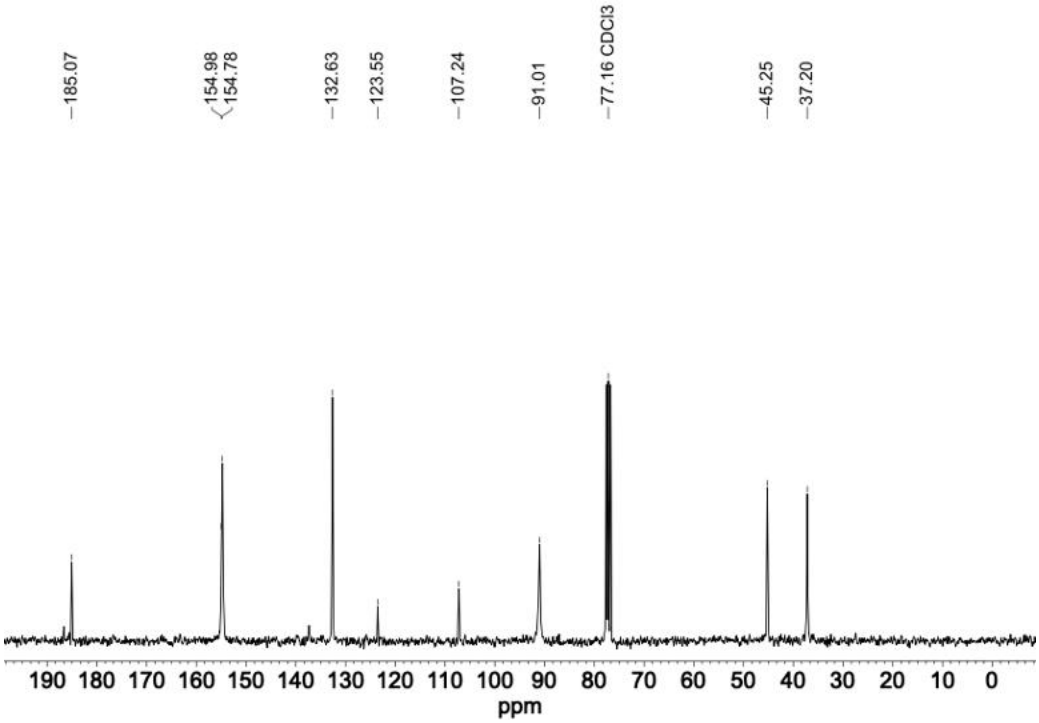

Figure 6.2.12: ^{13}C NMR spectrum of compound 7c.

6.2.1.7 Synthesis of 4-halogen-2,6-di(1H-pyrazol-3-yl)pyridine (8a-c)

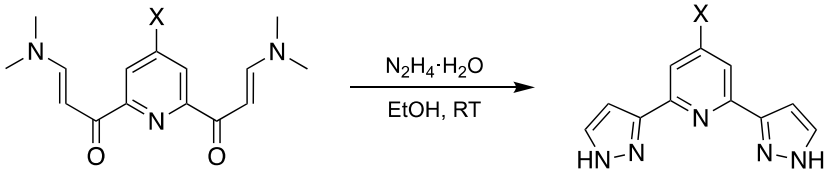

7a: Cl
7b: Br
7c: I

8a: Cl
8b: Br
8c: I

In a round-bottom flask were dissolved 1 eq. of 7a-c in EtOH. Then 3 eq. of $N_2H_4 \cdot H_2O$ were added, and the reaction was stirred for 3 days at room temperature. After this time, a white solid appears, water was added and the solid was filtered under vacuum. The solid was washed with water and the white solid was then dried under vacuum.

Synthesis of 8a. 1,1'-(4-chloropyridine-2,6-diyl)bis(3-(dimethylamino)prop-2-en-1-one) (2.5 g, 8.14 mmol, 1.0 eq.), $N_2H_4 \cdot H_2O$ (1.2 g, 24.42mmol, 3.0 eq.) in 60 mL of EtOH. 99% Yield.

^{1}H NMR (300 MHz, DMSO-d_6 δ): 13.60 (s, 1H, Ha) 13.56 (s, 1H, Ha), 13.17 (s, 1H, Ha'), 7.87 (s, 2H, Hb+b'), 7.63 (s, 2H, Hc+c'), 7.36 – 6.72 (m, 2H, Hd+d').

^{13}C NMR (75 MHz, DMSO-d_6, δ): 153.5, 149.8, 149.0, 148.5, 144.8, 144.0, 143.5, 140.3, 140.0, 130.0, 117.8, 117.6, 116.9, 104.4, 103.6.

ESI-MS *m/z*: (relative intensity): $[M+H]^+$ calcd. for $[C_{11}H_9ClN_5]^+$ 246.05; found 246.09 (100%), 248.05 (31.7%).

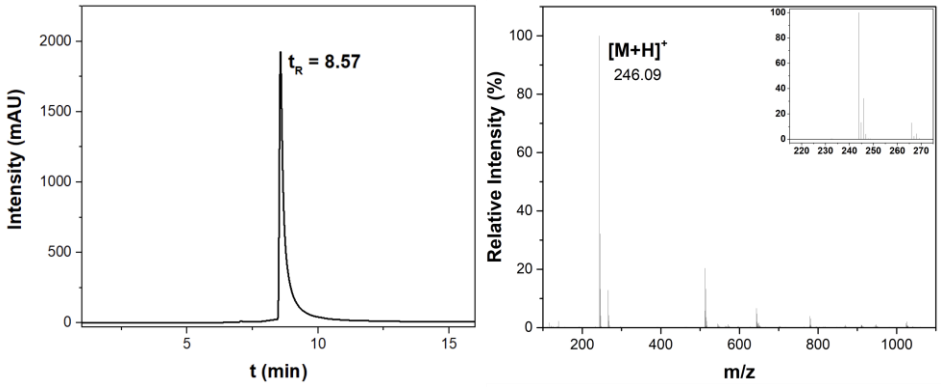

Figure 6.2.13: Left, RP-UHPLC of compound 8a; right, MS of chromatographic peak t_R = 8.57'.

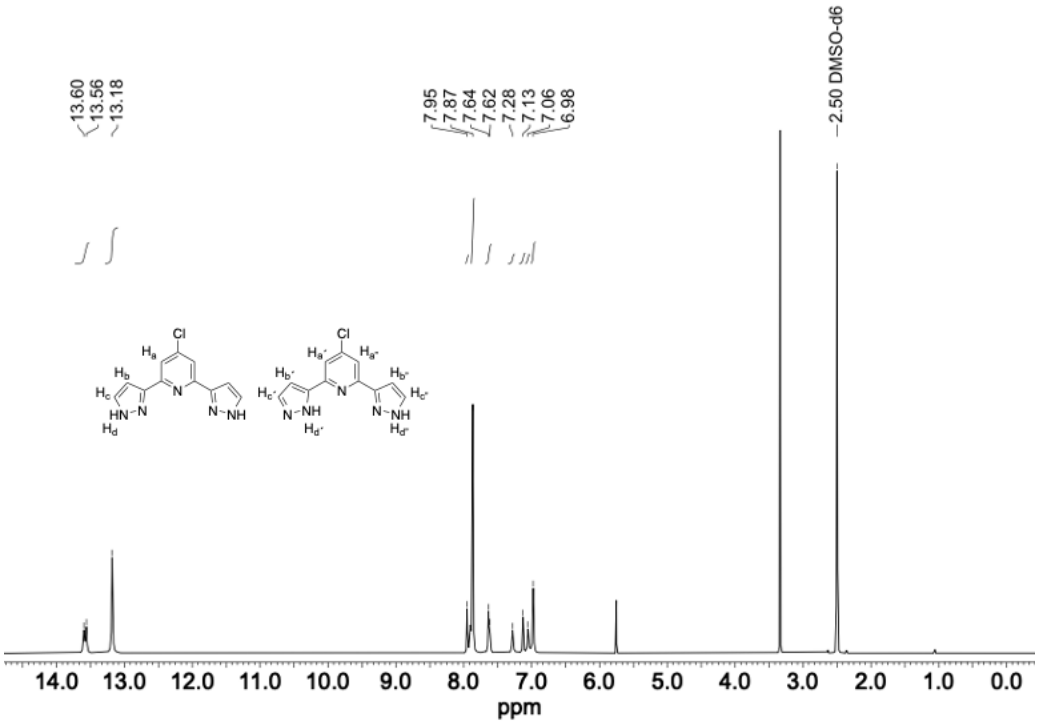

Figure 6.2.14: ^{1}H NMR spectrum of compound 8a.

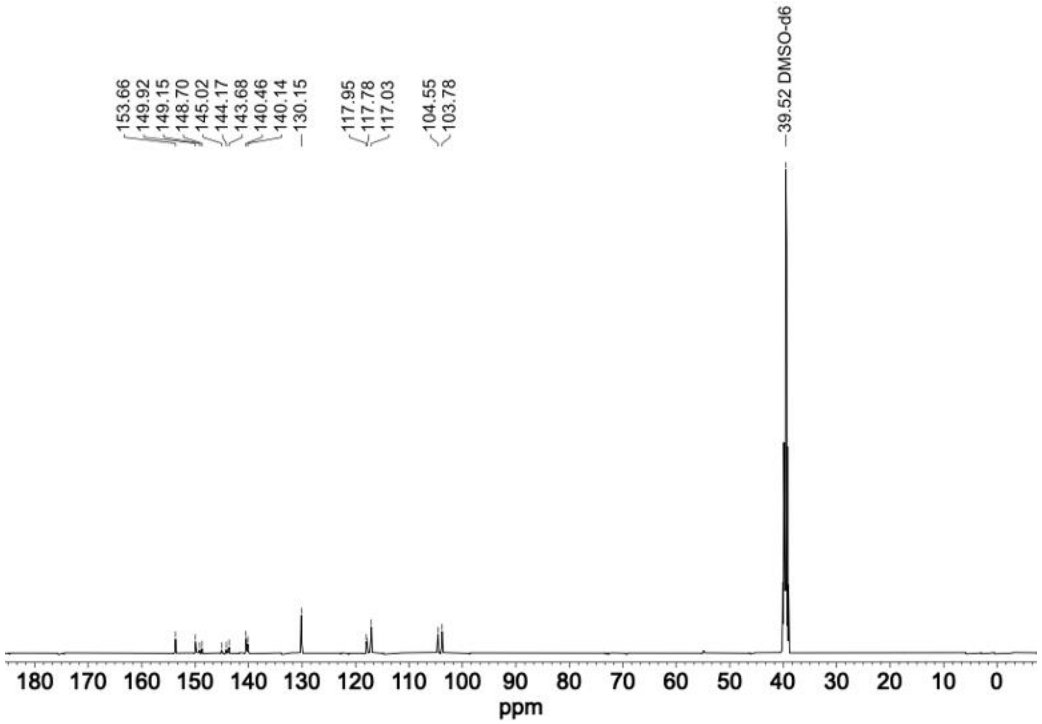

Figure 6.2.15: ^{13}C NMR spectrum of compound 8a.

Synthesis of 8b. 1,1'-(4-bromopyridine-2,6-diyl)bis(3-(dimethylamino)prop-2-en-1-one) (2.5 g, 7 mmol, 1.0 eq.), $N_2H_4 \cdot H_2O$ (1.06 g, 21.0 mmol, 3.0 eq.) in 60 mL of EtOH. 99% yield.
^{1}H NMR (**300 MHz, DMSO-d_6 δ**) 13.56 (s, 1H, Ha), 13.19 (s, 1H, Ha'), 8.02 (s, 2H, Hd+d'), 7.86 (s, 1H, Hb), 7.63 (s, 1H, Hb'), 7.36 – 6.84 (m, 2H, Hc+c')
^{13}C NMR (**75 MHz, DMSO-d_6 δ**) δ 153.5, 149.8, 149.0, 148.5, 140.6, 140.1, 134.2, 133.3, 132.9, 130.2, 120.9, 120.2, 104.6, 103.9
ESI-MS *m/z*: (relative intensity): $[M+H]^+$ calcd. for $[C_{11}H_9BrN_5]^+$ 290.00; found 290.08 (100%), 292.08 (96.3%).

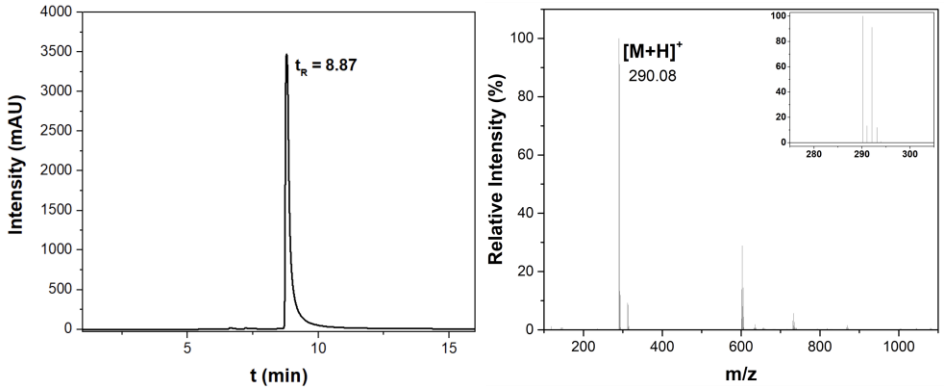

Figure 6.2.16: Left, RP-UHPLC of compound 8b; right, MS of chromatographic peak t_R = 8.87'.

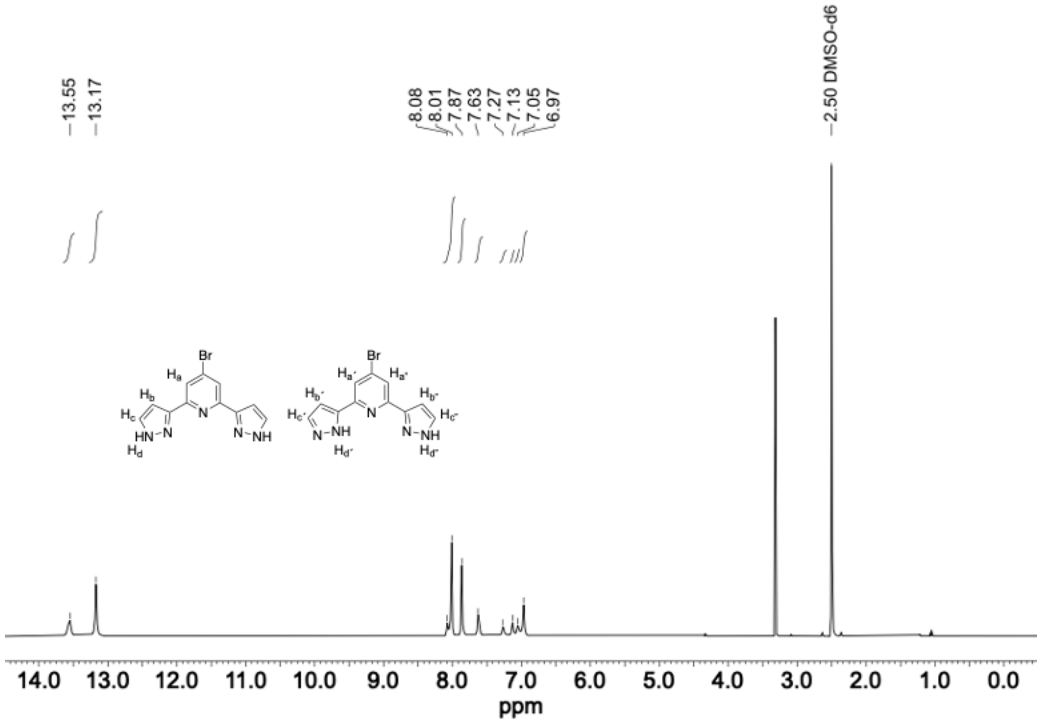

Figure 6.2.17: ^{1}H NMR spectrum of compound 8b.

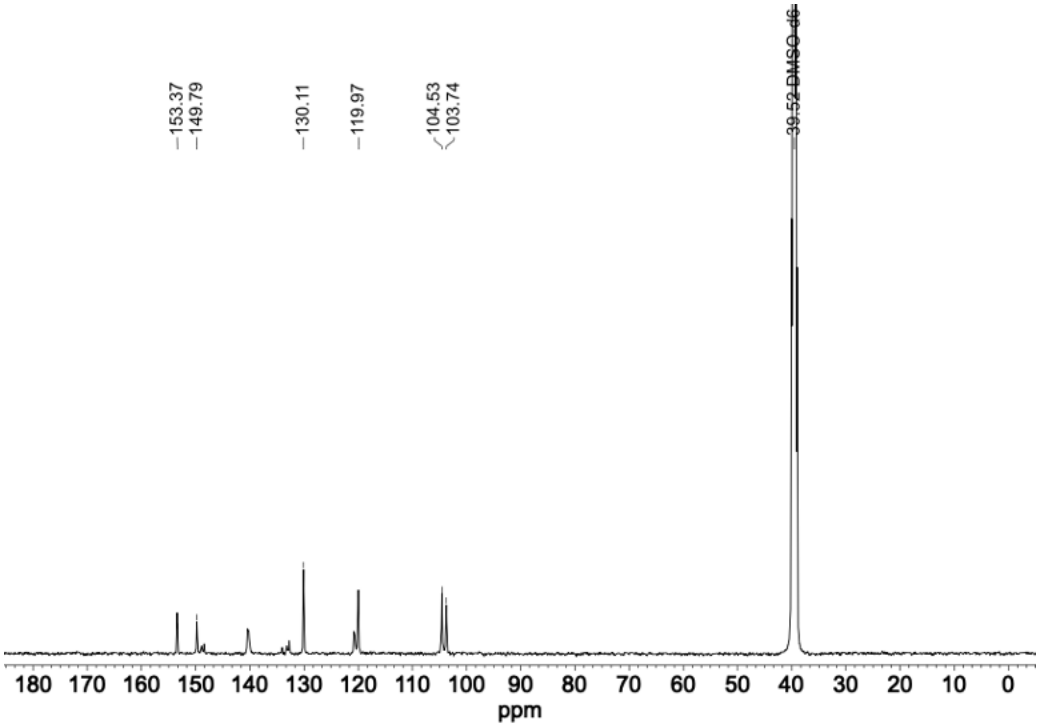

Figure 6.2.18: ^{13}C NMR spectrum of compound 8b.

Synthesis of 8c. 1,1'-(4-iodopyridine-2,6-diyl)bis(3-(dimethylamino)prop-2-en-1-one) (2.5 g, 6.26 mmol, 1.0 eq.), $N_2H_4 \cdot H_2O$ (1.06 g, 21.0 mmol, 3.0 eq.) in 60 mL of EtOH. 97% Yield.

^{1}H NMR (300 MHz, DMSO-d_6, δ): 13.52 (s, 1H, Ha), 13.15 (s, 1H, Ha'), 8.20 (d, *J* = 4.6 Hz, 2H, Hd+d'), 7.85 (s, 1H, Hb), 7.61 (s, 1H, Hb'), 7.36 – 6.71 (m, 2H, Hc+c')

^{13}C NMR (75 MHz, DMSO-d_6, δ): 155.98, 155.78, 148.53, 139.50, 137.69, 131.85, 131.33, 128.28, 128.01, 117.25, 116.17, 49.94, 42.48, 39.48, 39.31, 39.15, 38.98, 38.81, 38.65, 38.48

ESI-MS *m/z* (Relative intensity): $[M+H]^+$ calcd. for $[C_{11}H_9IN_5]^+$ 337.99; found 337.92 (100%).

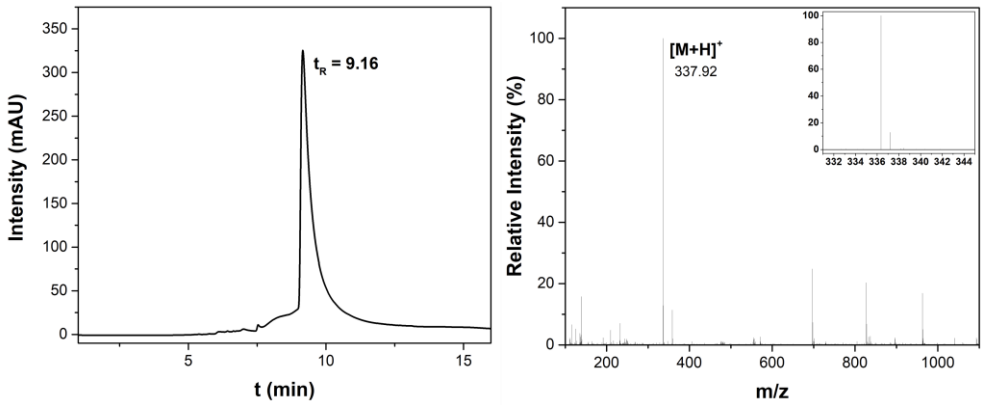

Figure 6.2.19: Left, RP-UHPLC of compound 8c; right, MS of chromatographic peak t_R = 9.16'

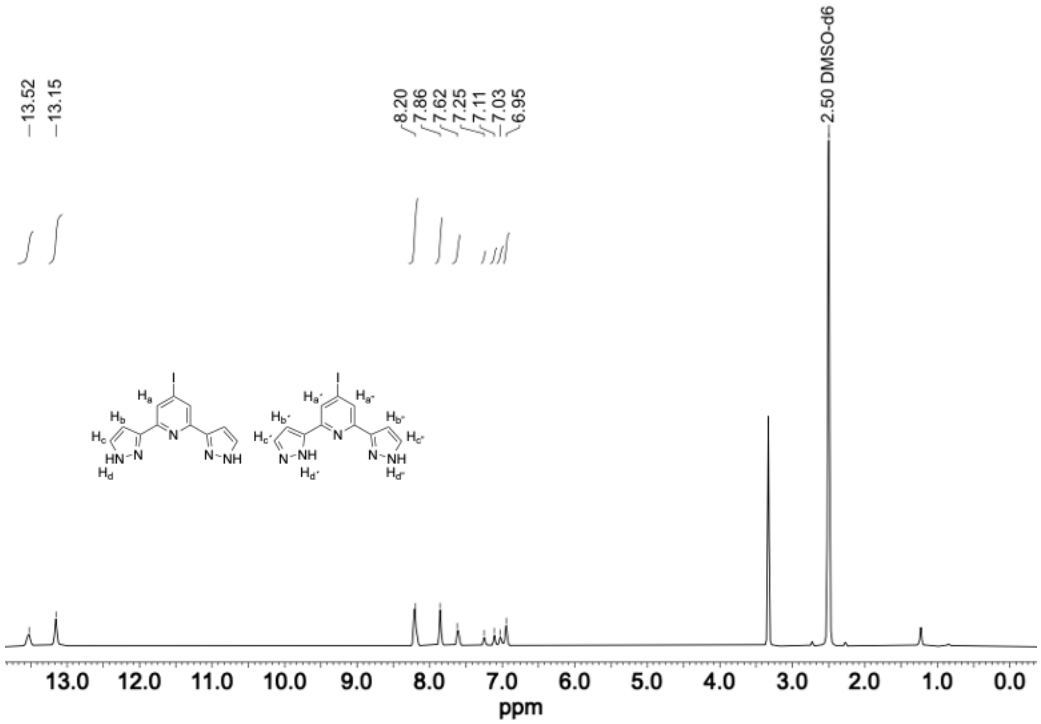

Figure 6.2.20: ^{1}H NMR spectrum of compound 8c.

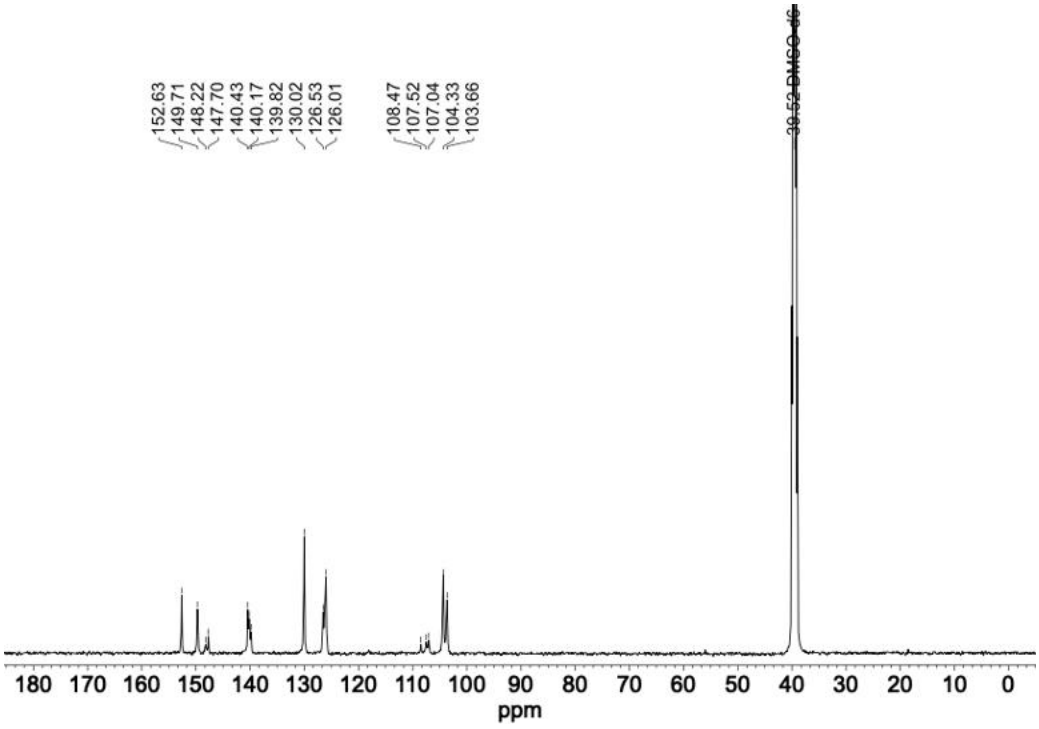

Figure 6.2.21: ^{13}C NMR spectrum of compound 8c.

6.2.2 Synthesis metal complexes

General procedure:

Ligand *p*-X-3-bpp (100.0 mg, 1.0 eq.) was dissolved in 20 mL of methanol, to this solution, $Fe(ClO_4)_2 \cdot 6H_2O$ (0.5 eq.) dissolved in 5 mL of methanol was added dropwise under magnetic stirring. After 1 hour stirring at room temperature under inert atmosphere the solution was transferred into a beaker, and 25 mL of water were added. The solution was allowed to evaporate slowly to obtain crystals suitable for X-Ray diffraction after 3-4 days.

F: Orange crystals, 65% Yield

Elemental analysis (%) calcd. for $C_{22}H_{18}Cl_2F_2FeN_{10}O_9$ (731.19 g·mol^{-1}): C, 36.14; H, 2.48; N, 19.16; found: C, 36.63; H, 2.48; N, 19,16

IR: 3584 (m), 3244 (s), 3144 (m), 3087 (m), 1618 (m), 1587 (m), 1413 (m), 1221 (m), 1073 (s), 1050 (s), 780 (m), 620 (m)

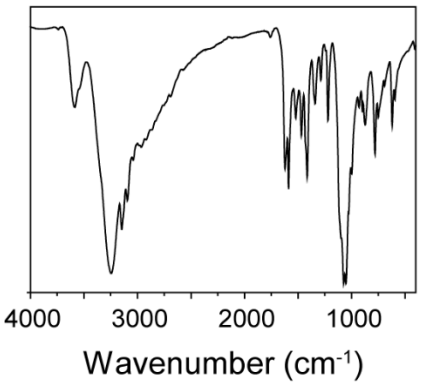

Figure 6.2.22. FT-IR of complex [Fe(*p*-F-3-bpp)$_2$](ClO$_4$)$_2$ (F).

Cl: Orange-red crystals 71% Yield

Elemental analysis (%) calcd. for $C_{22}H_{16}Cl_4FeN_{10}O_8$ (743.93 g·mol^{-1}): C, 35.42; H, 2.16; N, 18.77, found: C, 35.48; N, 2.41; H, 18.92

IR: 3241 (s), 1601 (m), 1556 (m), 1399 (s), 1268 (m), 1215 (m), 1073 (s), 1051 (s), 777 (m), 620 (m)

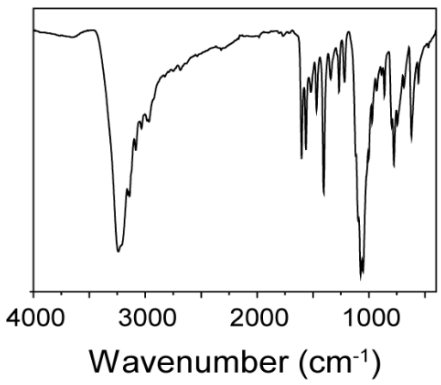

Figure 6.2.23: FT-IR of complex [Fe(*p*-Cl-3-bpp)$_2$](ClO$_4$)$_2$ (Cl).

Br: Red-orange crystals 68% Yield

Elemental analysis (%) calcd. for $C_{22}H_{16}Br_2Cl_2FeN_{10}O_8$ (834,99 g·mol^{-1}): C, 31.65; H, 1.93; N, 16.78; found: C, 31.65, H, 1.93; N, 16.78

IR: 3240 (s), 3069 (m), 3030 (m), 1596 (s), 1561 (s), 1465 (m), 1400 (s), 1265 (m), 1212 (m), 1078 (s), 1047 (s), 781 (m), 742 (m), 615 (m)

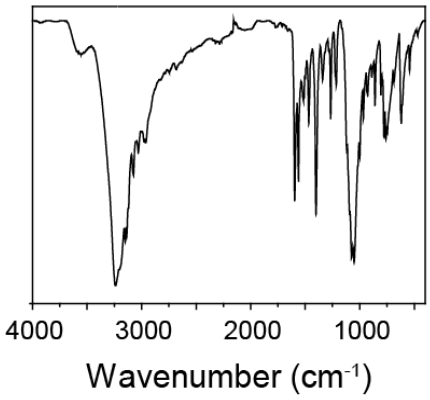

Figure 6.2.24: FT-IR of complex [Fe(*p*-Br-3-bpp)$_2$](ClO$_4$)$_2$ (Br).

I·H$_2$O: Red crystals, 73% Yield

Elemental analysis (%) calcd. for $C_{22}H_{18}Cl_2FeI_2N_{10}O_9$ (947,00 g·mol^{-1}): C, 27.90; H, 1.92; N, 14.79; found: C, 28.06; H, 2.15; N, 14.90

IR: 3598 (m), 3528 (m), 3190 (s), 3158 (s), 2918 (m), 1594 (m), 1526 (m), 1498 (m), 1406 (m), 1086 (s), 1034 (s), 922 (m), 850 (m), 772 (m), 618 (m)

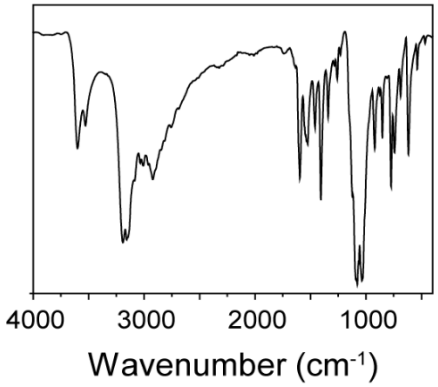

Figure 6.2.25: FT-IR of complex [Fe(*p*-I-3-bpp)$_2$](ClO$_4$)$_2$·H$_2$O (I·H$_2$O).

6.2.3 Thermogravimetric analysis (TGA)

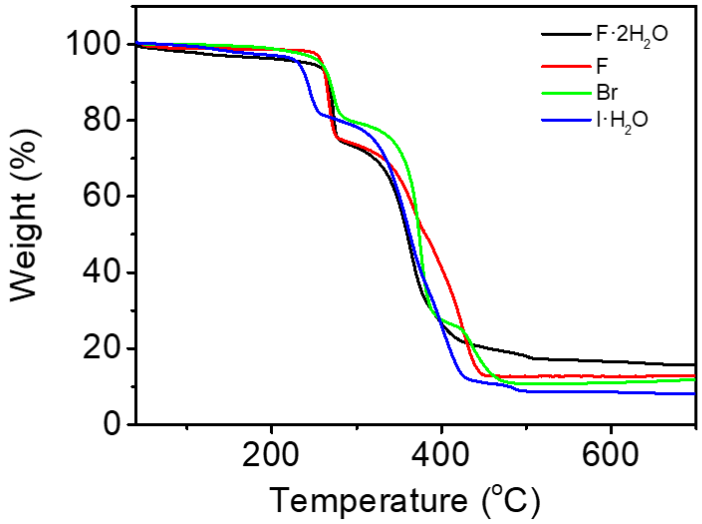

Figure 6.2.26: TGA measurements at 4 °C/min of complex F, F·2H₂O, Br and I·H₂O under air. For complex Cl was not possible to perform since it was found that the perchlorate counterion is not stable in the presence of this ligand under heating conditions.

6.2.4 Single Crystal X-Ray Diffraction (SCXRD)

Crystallographic data for all the complexes were deposited in the Cambridge Structural Database (CSD) with the following deposit numbers. All structures were resolved at 100 K unless otherwise specified. CCDC-2355017 for F; CCDC-2355018 for F·2H2O; CCDC-2355019 for Cl; CCDC-2355020 for Br; CCDC-2355021 for I·H2O.

From CCDC-2355022 to CCDC-2355027 for F (100, 175, 200, 250, 270 and 295 K).

From CCDC-2355028 to CCDC-2355036 for Cl (140, 160, 180, 200, 220, 240, 260, 280, 300 K).

From CCDC-2355028 to CCDC-2355036 for Br (120, 140, 160, 180, 200, 220, 240, 260, 280, 300 K).

CCDC-2355047 for I·H_2O (100 K); CCDC-2355048 for I·H_2O (300 K).

CCDC-2355049 for Cl (0.51 GPa, IS); CCDC-2355050 for Cl (2 GPa, LS).

Table 6.2.1. Crystallographic data and structure refinement of single crystal X-Ray analysis for complexes F and F·2H_2O.

	F	**F·2H_2O**
Chemical Formula	$C_{22}H_{16}Cl_2F_2FeN_{10}O_8$	$C_{22}H_{20}Cl_2F_2FeN_{10}O_{10}$
Size (mm^3)	0.017 x 0.060 x 0.098	0.077 x 0.135 x 0.139
Formula weight	713.20	749.23
Crystal system	Orthorhombic	Orthorhombic
Space group	*Pbca*	*P 2_1 2_1 2_1*
a [Å]	19.1557(7)	8.3074(3)
b [Å]	16.7306(5)	8.5129(3)
c [Å]	16.9943(7)	40.4540(13)
α [°]	90	90
β [°]	90	90
γ [°]	90	90
V [$Å^3$]	5446.4(3)	2860.91(17)
Z	8	4
Dx [mg/m^3]	1.740	1.739
Temperature [K]	100	100
Tmax/Tmin	0.9860, 0.9230	0.9410, 0.8970
Absortion coeff. [mm^{-1}]	0.833	0.802
F (000)	2880	1520
Θ range [°]	2.01 to 26.44	2.01 to 34.37
Reflections collected	131285	232344
Independent reflections	5596	12000
GOF on F2	1.069	1.102
Final R indices [I > 2σ(I)]	R1 = 0.0624, wR2 = 0.1545	R1 = 0.0484, wR2 = 0.1234
***R* indices (all data)**	R1 = 0.0940, wR2 = 0.1723	R1 = 0.0555, wR2 = 0.1268

Table 6.2.2. Crystallographic data and structure refinement of single crystal X-Ray analysis for complexes Cl, Br and I·H_2O.

	Cl	**Br**	**I·H_2O**
Chemical Formula	$C_{22}H_{16}Cl_4FeN_{10}O_8$	$C_{22}H_{16}Br_2Cl_2FeN_{10}O_8$	$C_{22}H_{18}Cl_2FeI_2N_{10}O_9$
Size (mm^3)	0.029 x 0.079 x0.162	0.094 x 0.177 x 0.214	0.020 x 0.150 x 0.190
Formula weight	746.10	835.02	947.01
Crystal system	Orthorhombic	Orthorhombic	Orthorhombic
Space group	*Pbca*	*Pbca*	*P 2_1 2_1 2_1*
a [Å]	19.0138(14)	19.0542(10)	13.7603(14)
b [Å]	16.7893(11)	16.9140(10)	14.5341(14)
c [Å]	17.8747(15)	18.0484(11)	15.3067(15)
α [°]	90	90	90
β [°]	90	90	90
γ [°]	90	90	90
V [$Å^3$]	5706.1(7)	5816.7(6)	3061.2(5)
Z	8	8	4
Dx [mg/m^3]	1.737	1.907	2.055
Temperature [K]	100	100	100
Tmax/Tmin	0.9720, 0.8590	0.733, 0.520	0.9470, 0.6230
Absortion coeff. [mm^{-1}]	0.970	3.516	2.752
F (000)	3008	3296	1832
Θ range [°]	2.28 to 26.45	1.966 to 27.210	2.43 to 32.58
Reflections collected	31602	137294	54915
Independent reflections	5842	6469	11126
GOF on F2	1.142	1.139	1.032
Final R indices [I > 2σ(I)]	R1 = 0.1094, wR2 = 0.1925	R1 = 0.0953, wR2 = 0.1948	R1 = 0.0257, wR2 = 0.0546
***R* indices (all data)**	R1 = 0.1425, wR2 = 0.2066	R1 = 0.01188, wR2 = 0.1948	R1 = 0.0298, wR2 = 0.0568

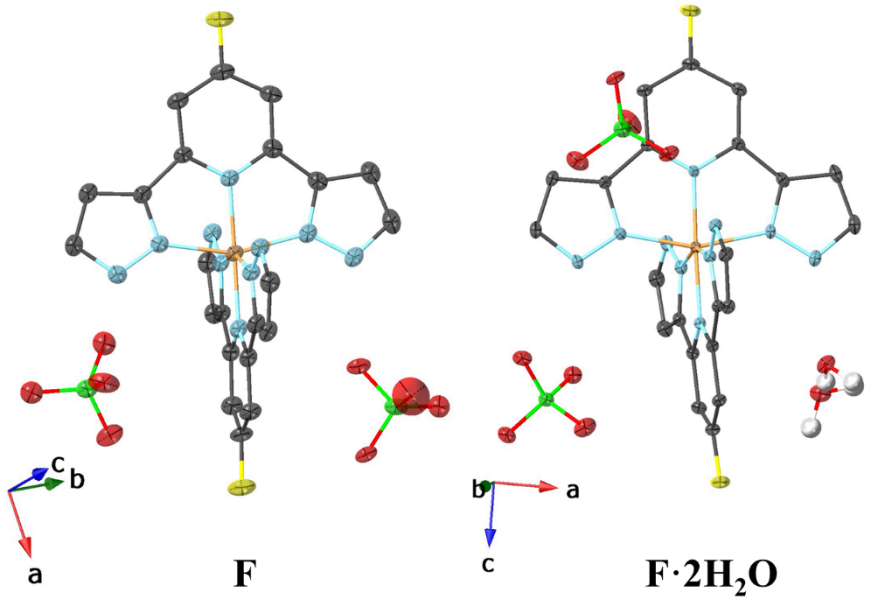

Figure 6.2.27. ORTEP representation (30% of probability) of asymmetric unit of F and F·2H_2O. Hydrogen atoms are omitted for clarity except for water molecules. Iron is clear brown, carbon is black, nitrogen is blue, oxygen is red, and fluorine is yellow.

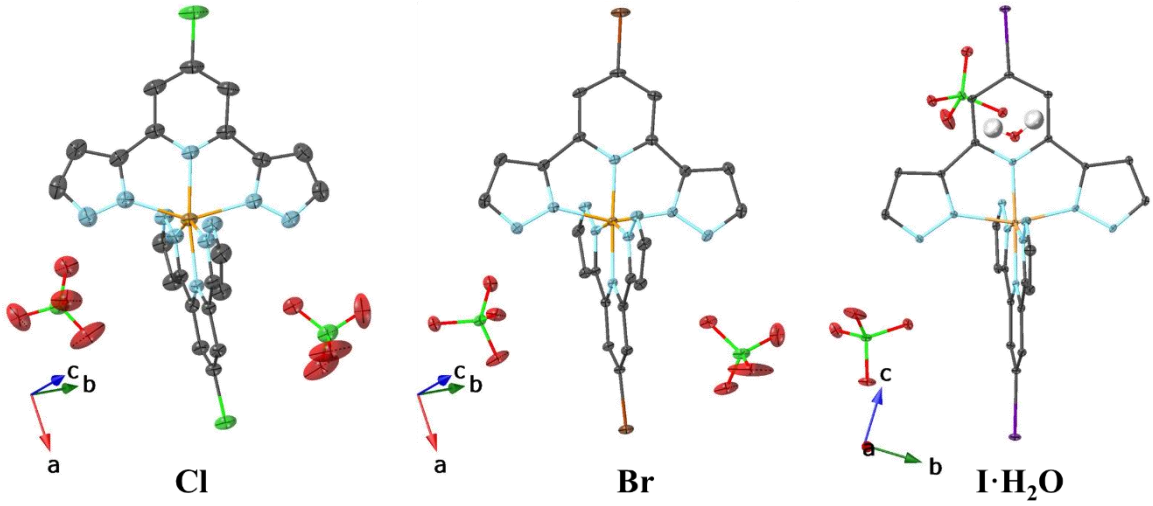

Figure 6.2.28. ORTEP representation (30% probability) of asymmetric unit of Cl, Br, and I·H_2O. Hydrogen atoms are omitted for clarity except for water molecules. Iron is orange, carbon is grey, nitrogen is blue, oxygen is red, fluorine is yellow, chlorine is green, bromine is dark brown, and iodine is purple.

Table 6.2.3. Fe1-N distances for all the compounds at 100 K.

	F	F·2H$_2$O	Cl	Br	I·H$_2$O
Bond	**Distance (Å)**	**Distance (Å)**	**Distance (Å)**	**Distance (Å)**	**Distance (Å)**
Fe1-N1	1.921(4)	1.927(3)	1.922(6)	1.932(6)	1.921(2)
Fe1-N12	1.969(5)	1.977(3)	1.982(6)	1.979(8)	1.963(2)
Fe1-N22	1.966(3)	1.969(3)	1.957(7)	1.956(7)	1.968(2)
Fe1-N42	1.967(3)	1.960(3)	1.955(7)	1.966(7)	1.968(3)
Fe1-N31	1.920(4)	1.927(3)	1.947(6)	1.937(8)	1.922(3)
Fe1-N52	1.970(3)	1.968(3)	1.962(7)	1.964(7)	1.962(3)

Table 6.2.4. Fe1-N distances for F at different temperatures.

F						
Bond length (Å)						
T (K)	**Fe1-N1**	**Fe1-N31**	**Fe1-N22**	**Fe1-N12**	**Fe1-N42**	**Fe1-N52**
100	1.924(1)	1.979(2)	1.969(3)	1.926(3)	1.971(1)	1.968(4)
175	1.924(7)	1.983(1)	1.985(2)	1.939(3)	1.981(2)	1.983(3)
200	1.966(4)	2.008(1)	2.008(1)	1.964(5)	2.001(1)	2.009(1)
250	2.047(3)	2.109(5)	2.088(2)	2.048(8)	2.105(6)	2.100(9)
270	2.080(0)	2.139(6)	2.121(2)	2.070(4)	2.134(4)	2.140(1)
295	2.100(0)	2.169(8)	2.146(6)	2.087(6)	2.161(2)	2.155(6)

Table 6.2.5. Fe1-N distances for Cl at different temperatures.

Cl						
Bond length (Å)						
T (K)	**Fe1-N1**	**Fe1-N31**	**Fe1-N22**	**Fe1-N12**	**Fe1-N42**	**Fe1-N52**
140	1.9218(16)	1.9269(16)	1.9680(18)	1.9742(18)	1.9619(17)	1.9686(18)
160	1.9242(16)	1.9303(16)	1.9682(18)	1.9783(18)	1.9624(17)	1.9685(18)
180	1.9238(16)	1.9270(18)	1.9675(18)	1.9774(18)	1.9609(19)	1.9681(19)
200	1.9242(18)	1.9289(18)	1.970(2)	1.9769(19)	1.9624(19)	1.969(2)
220	1.9273(18)	1.9318(18)	1.969(2)	1.981(2)	1.965(2)	1.970(2)
240	2.1375(18)	2.1365(18)	2.158(2)	2.1736(19)	2.192(2)	2.184(2)
260	2.1376(18)	2.1350(19)	2.159(2)	2.175(2)	2.192(2)	2.183(2)
280	2.1373(19)	2.135(2)	2.157(2)	2.179(2)	2.191(2)	2.185(3)
300	2.136(2)	2.138(2)	2.161(3)	2.180(3)	2.194(3)	2.182(3)

Table 6.2.6. Fe1-N distances for Br at different temperatures.

Br						
Bond length (Å)						
T (K)	**Fe1-N1**	**Fe1-N31**	**Fe1-N22**	**Fe1-N12**	**Fe1-N42**	**Fe1-N52**
100	1.932(6)	1.937(8)	1.956(7)	1.979(8)	1.966(7)	1.964(7)
120	1.928(3)	1.930(3)	1.971(3)	1.971(3)	1.964(3)	1.964(3)
140	1.926(3)	1.930(3)	1.972(3)	1.971(3)	1.966(3)	1.968(3)
160	1.924(3)	1.928(3)	1.972(3)	1.970(3)	1.962(3)	1.969(3)
180	1.928(3)	1.926(3)	1.970(3)	1.969(3)	1.964(3)	1.970(3)
200	1.928(3)	1.931(3)	1.971(3)	1.974(3)	1.968(3)	1.971(3)
220	2.142(3)	2.137(3)	2.158(3)	2.178(3)	2.200(3)	2.180(3)
240	2.140(3)	2.134(3)	2.156(3)	2.181(3)	2.203(3)	2.178(3)
260	2.138(3)	2.136(3)	2.155(3)	2.180(3)	2.201(3)	2.178(3)
280	2.139(3)	2.135(3)	2.158(3)	2.180(3)	2.205(3)	2.174(4)
300	2.140(3)	2.135(3)	2.156(4)	2.183(4)	2.203(4)	2.174(4)

Table 6.2.7. Fe1-N distances for I·H_2O at different temperatures.

I·H_2O						
Bond length (Å)						
T (K)	**Fe1-N1**	**Fe1-N31**	**Fe1-N22**	**Fe1-N12**	**Fe1-N42**	**Fe1-N52**
100	1.922(3)	1.917(3)	1.967(3)	1.967(3)	1.963(4)	1.968(3)
300	1.941(5)	1.930(5)	1.977(5)	1.987(5)	1.968(6)	1.983(6)

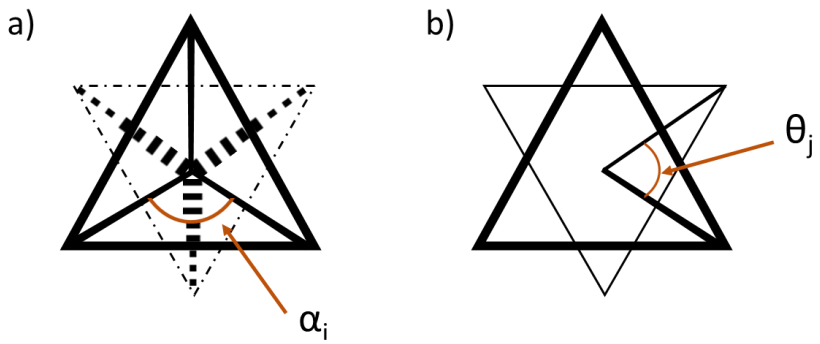

Figure 6.2.29. Representation of angles used to calculate the distortion indices obtained by OctaDist (Σ and Θ) for an octahedral coordination complex following the provided expressions.

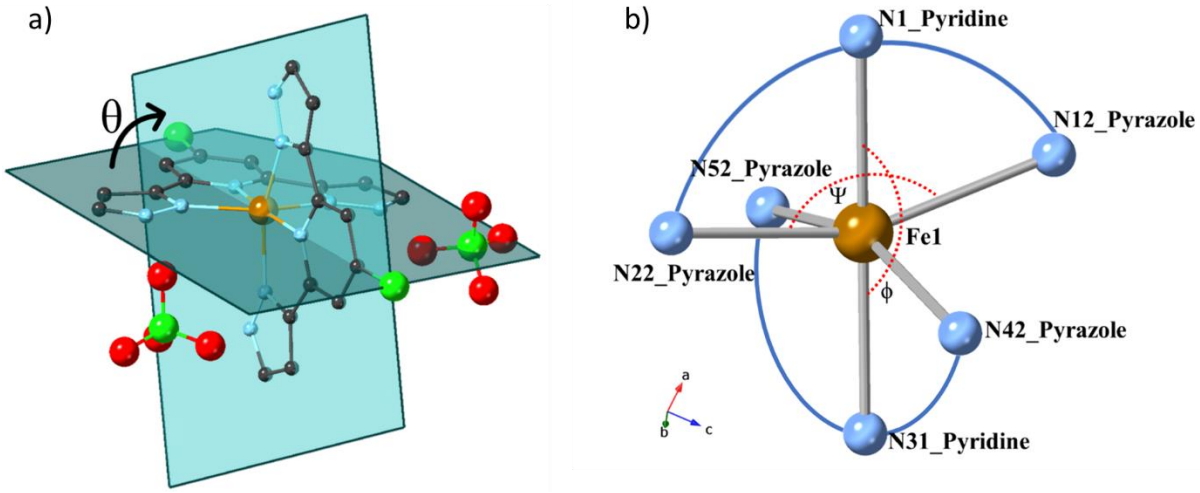

Figure 6.2.30. a) Schematic representation of dihedral angle between two ligands (θ). The plane of each ligand was defined as the least-squares plane through its sixteen aromatic C/N atoms. b) Schematic representation of the octahedral Fe core to represent all the Fe1-N bonds in all the compounds. Ψ and ϕ angles are represented in red dash line.

Table 6.2.8. Main angles of all the compounds at 100 K and 300 K.

	F		$F{\cdot}2H_2O$	Cl		Br		$I{\cdot}H_2O$	
T (K)	**100**	**300**	**100**	**100**	**300**	**100**	**300**	**100**	**300**
Σ (°)	95.65	133.66	94.81	94.76	147.18	97.33	147.95	93.73	97.47
Θ (°)	313.73	456.87	317.85	311.85	488.01	324.86	501.93	309.73	317.61
Θ (°)	89.62	91.87	89.58	89.54	89.33	89.53	88.42	89.42	88.85
Ψ (°)	158.01	149.37	158.34	158.37	147.53	157.74	147.37	158.29	157.73
ϕ (°)	177.90	173.88	177.85	177.02	172.04	176.74	171.09	178.51	178.84

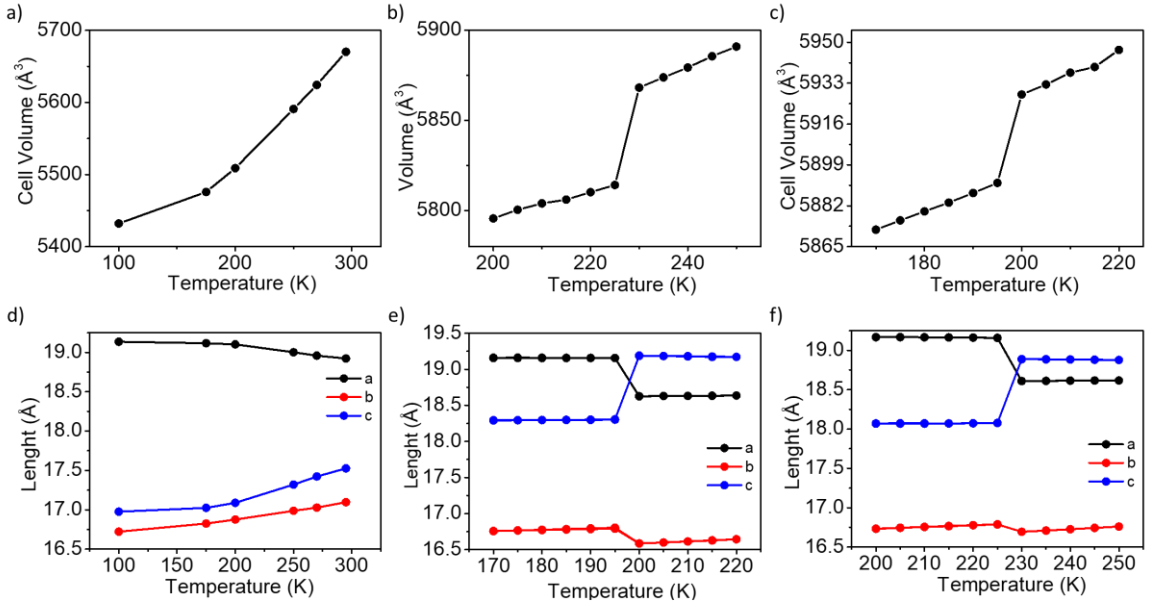

Figure 6.2.31. Variation in volume for a) F, b) Cl and c) Br; and in unit cell parameters (a, b, c) for d) F, e) Cl and f) Br with the temperature.

Table 6.2.9. Crystallographic data and structure refinement of SCXRD analysis for F at 200 and 295 K.

	F (200 K)	**F (295 K)**
Chemical Formula	$C_{22}H_{16}Cl_2F_2FeN_{10}O_8$	$C_{22}H_{16}Cl_2F_2FeN_{10}O_8$
Size (mm^3)	0.038 x 0.151 x 0.193	0.038 x 0.151 x 0.193
Formula weight	713.20	713.20
Crystal system	Orthorombic	Orthorombic
Space group	*Pbca*	*Pbca*
a [Å]	19.1028(10)	18.9233(8)
b [Å]	16.8759(9)	17.0962(8)
c [Å]	17.0883(10)	17.5267(9)
α [°]	90	90
β [°]	90	90
γ [°]	90	90
V [$Å^3$]	5508.9(5)	5670.2(5)
Z	8	8
Dx [mg/m^3]	1.720	1.671
Temperature [K]	200	295
Tmax/Tmin	0.9690, 0.8570	0.9700, 0.8610
Absortion coeff. [mm^{-1}]	0.823	0.800
F (000)	2880	2880
Θ range [°]	2.00 to 26.52	1.98 to 25.03
Reflections collected	81182	32699
Independent reflections	5689	5022
GOF on F2	1.083	1.028
Final R indices [I > 2σ(I)]	R1 = 0.0666, wR2 = 0.1573	R1 = 0.0646, wR2 = 0.1558
***R* indices (all data)**	R1 = 0.0860, wR2 = 0.1680	R1 = 0.1169, wR2 = 0.1840

6.2.5 Differential Scanning Calorimetry (DSC)

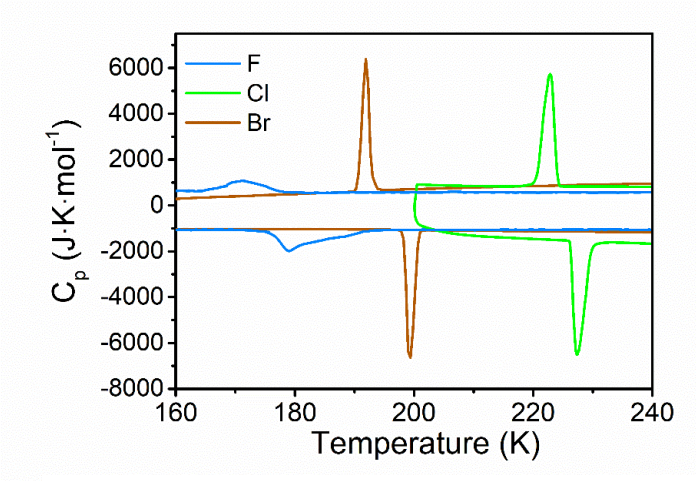

Figure 6.2.32. DSC measurements of compounds F, Cl and Br.

Table 6.2.10. SCO midpoint ($T_{1/2}$) temperature and hysteresis for compounds F, Cl, Br and I·H_2O.

	F		Cl	Br	I·H_2O
	2 steps		1 step	1 step	1 step (incomplete)
Character	**Gradual**	**Abrupt**	**Abrupt**	**Abrupt**	**Gradual**
$T_{1/2\downarrow}$ (K)	235	168	221	192	393
$T_{1/2\uparrow}$ (K)	-	184	229	200	-
Thermal hysteresis (K)	0	16	8	8	0

Table 6.2.11. Calorimetric parameters for compounds F, Cl and Br.

F			Cl			Br		
T (K)	**ΔH (kJ·mol^{-1})**	**ΔS (J·K^{-1}·mol^{-1})**	**T (K)**	**ΔH (kJ·mol^{-1})**	**ΔS (J·K^{-1}·mol^{-1})**	**T (K)**	**ΔH (kJ·mol^{-1})**	**ΔS (J·K^{-1}·mol^{-1})**
$T_{\downarrow}$= 171	3.215	7.23	$T_{\downarrow}$=225	11.17	50.31	$T_{\downarrow}$=192	12.12	63.12
$T_{\uparrow}$=179	5.99	13.71	$T_{\uparrow}$=229	11.12	48.55	$T_{\uparrow}$=199	12.14	61.00

6.2.6 Variable-Temperature Raman Spectroscopy

Table 6.2.12. Raman vibrational modes identified as a marker of spin transition.

Vibrational Mode	ν_{LS}/cm^{-1}	ν_{HS}/cm^{-1}
Pyridine breathing Fe(II) – N stretch	1039	1019
NCH in-plane ring stretch Fe(II)-N stretch	1159	1154
C=C stretch pyridine	1615	1601

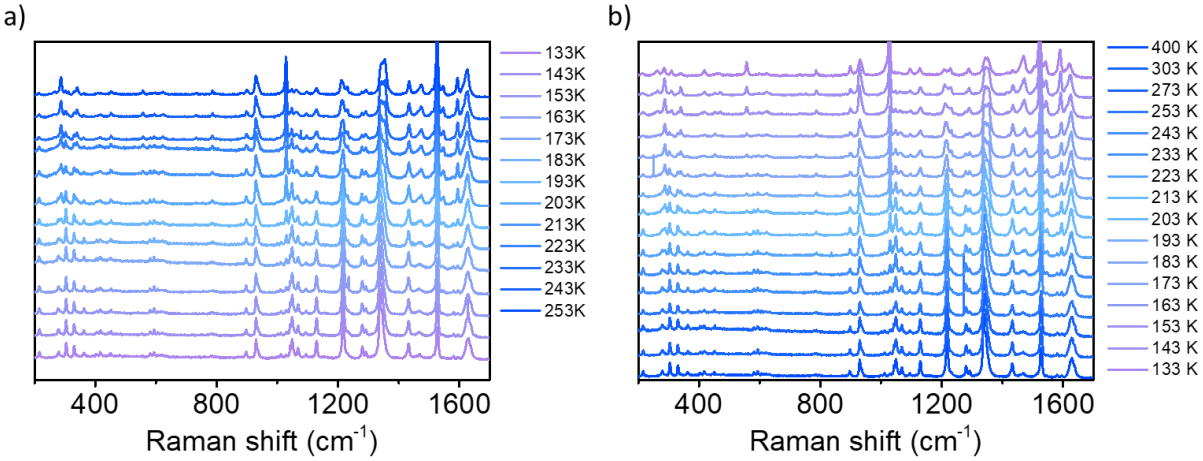

Figure 6.2.33. Raman spectra on heating (a) and cooling (b) mode of F.

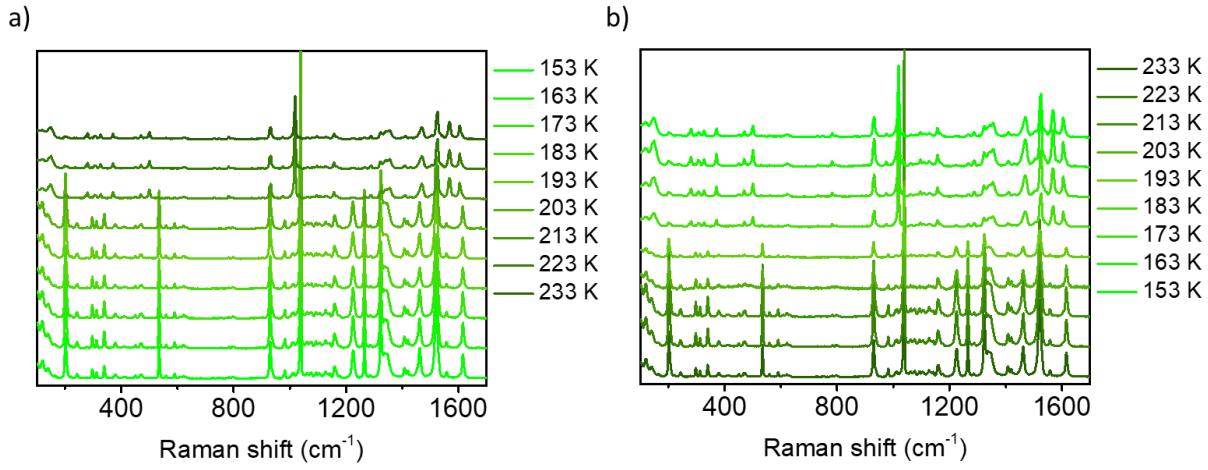

Figure 6.2.34. Raman spectra on heating (a) and cooling (b) mode of Cl.

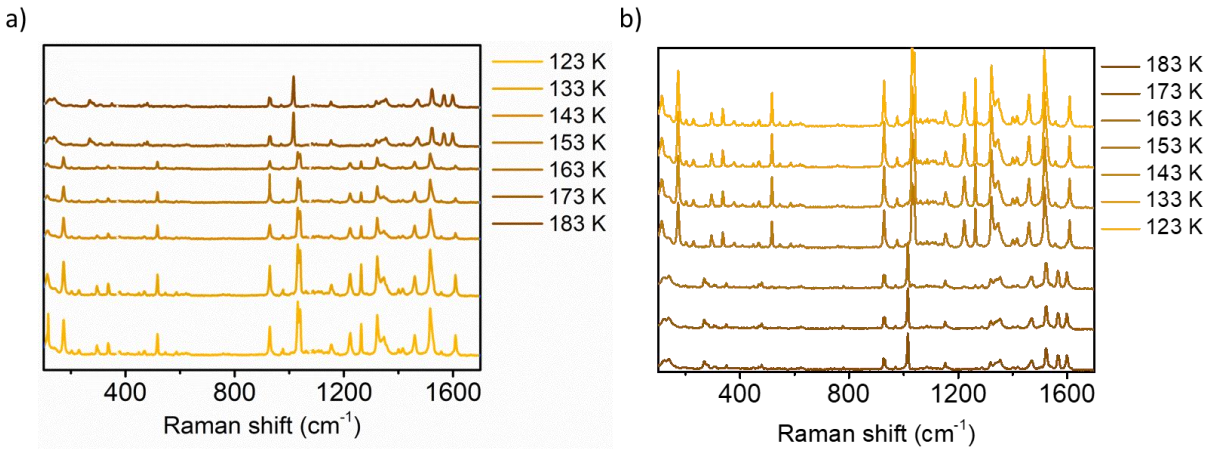

Figure 6.2.35. Raman spectra on heating (a) and cooling (b) mode of Br.

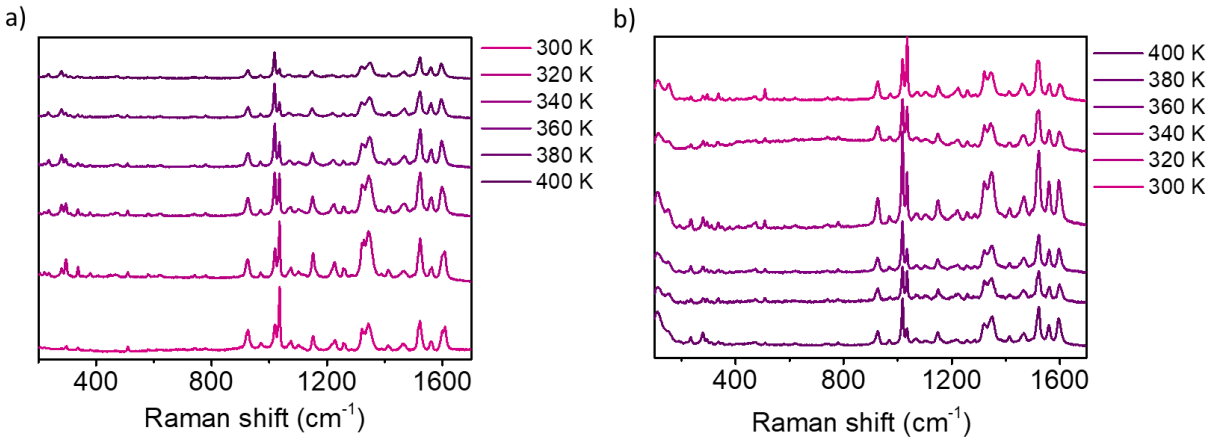

Figure 6.2.36. Raman spectra on heating (a) and cooling (b) mode of I·H_2O.

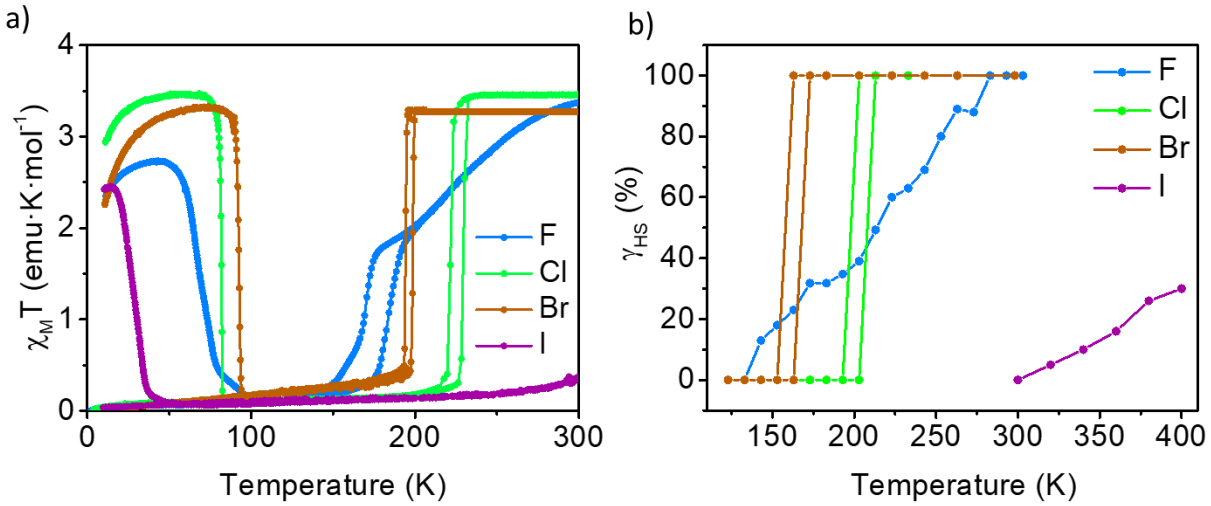

Figure 6.2.37. a) Thermal dependence of $\chi_M T$ under irradiation (metastable HS at 10 K) and after irradiation upon heating/cooling at 0.4 K/min in the dark. b) High spin fraction (Y_{HS}) calculated from Raman measurements.

6.2.7 Magnetic measurements

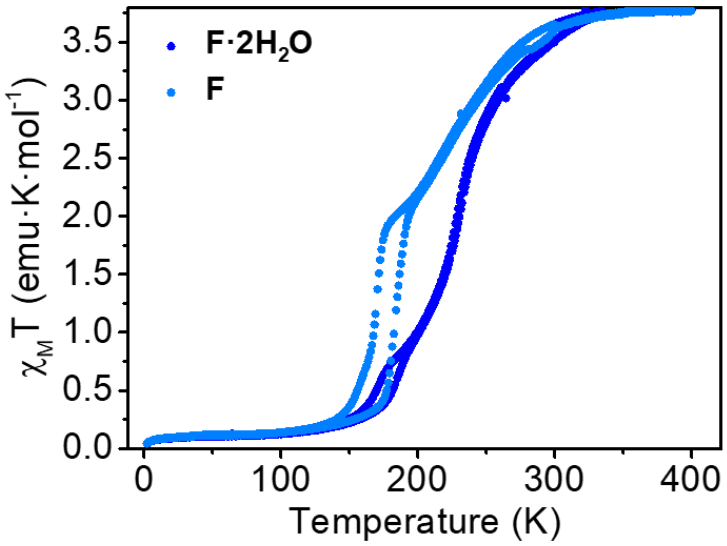

Figure 6.2.38. $\chi_M T$ vs Temperature measurement of F and F·2H₂O.

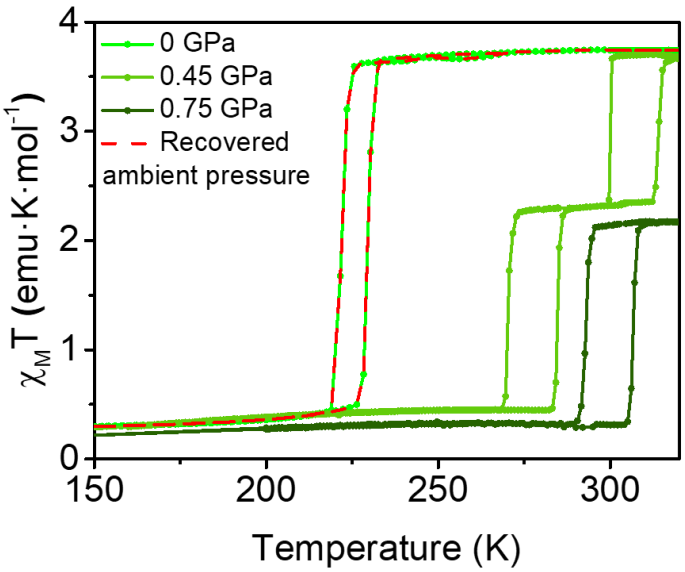

Figure 6.2.39. Recovered ambient pressure for Cl.

6.2.8 Variable-Pressure Single Crystal X-Ray Diffraction

Table 6.2.13. Crystallographic data and structure refinement of single crystal X-Ray analysis for complex **CI** at IS phase (0.51-0.59 GPa) and LS phase (2 GPa). Crystals were measured inside DAC cell.

	CI	**CI**
	0.51-0.59 GPa	**2 GPa**
Chemical Formula	$C_{22}H_{16}Cl_4FeN_{10}O_8$	$C_{22}H_{16}Cl_4FeN_{10}O_8$
Size (mm^3)	0.050 x 0.174 x 0.193	0.050 x 0.174 x 0.193
Formula weight	746.10	746.10
Crystal system	Orthorhombic	Orthorhombic
Space group	*Pbca*0	*Pbca*
a [Å]	19.2671(7)	18.8794(17)
b [Å]	16.5683(7)	16.3421(14)
c [Å]	16.7845(14)	16.954(3)
α [°]	90	90
β [°]	90	90
γ [°]	90	90
V [$Å^3$]	5358. (5)	5230.8
Z	8	8
Dx [mg/m^3]	1.850	1.895
Temperature [K]	300	300
Tmax/Tmin	0.9500/0.8250	0.9490/0.8220
Absortion coeff. [mm^{-1}]	1.033	1.059
F (000)	3008	3008
Θ range [°]	2.11 to 21.83	2.16 to 19.78
Reflections collected	66291	18368
Independent reflections	1905	1446
GOF on F2	1.148	1.064
Final R indices [I > 2σ(I)]	R1 = 0.0718, wR2 = 0.1959	R1 = 0.0773, wR2 = 0.1811
***R* indices (all data)**	R1 = 0.1042, wR2 = 0.2443	R1 = 0.1241, wR2 = 0.2226

Table 6.2.14. Fe1-N distances for **Cl** at different pressures.

P (GPa)	Fe1-N1 (Å)	Fe1-N12 (Å)	Fe1-N22 (Å)	Fe1-N31 (Å)	Fe1-N52 (Å)	Fe1-N42 (Å)
0.51 – 0.59 (IS)	1.907(11)	2.010(19)	1.935(18)	1.910(10)	1.976(11)	1.953(12)
2 (LS)	1.899(18)	2.04(3)	1.97(3)	1.955(17)	1.969(17)	1.964(18)

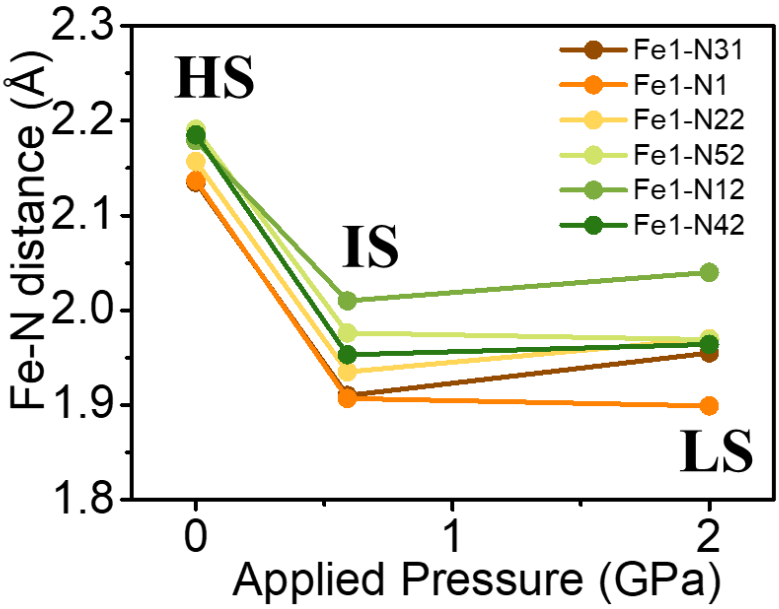

Figure 6.2.40. Variation in Fe-N distances with the applied pressure for Cl.

6.2.9 Variable-Pressure Raman Spectroscopy

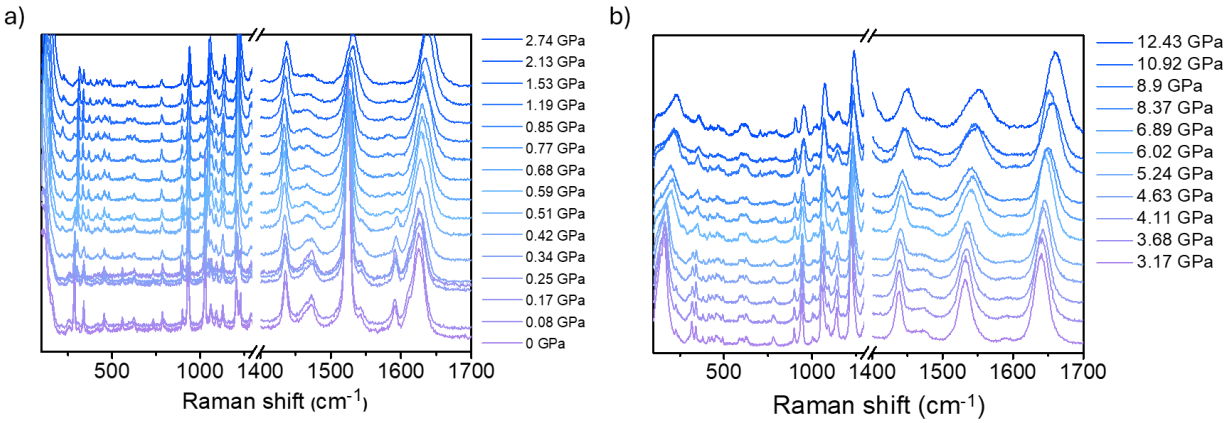

Figure 6.2.41. Variable Pressure Raman spectra of F at low pressure range (a) and high-pressure range (b).

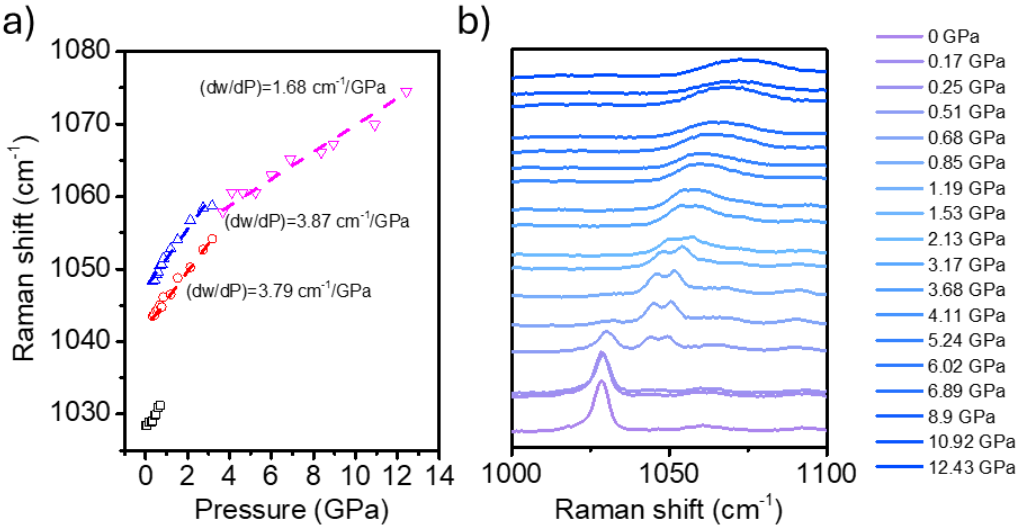

Figure 6.2.42. Variable Pressure Raman spectra of F. Raman shift of the characteristics HS (1018 cm^{-1}) and LS (1039 and 1046 cm^{-1}) bands vs. pressure (a) shift of these bands at variable pressure in the 1000-1100 cm^{-1} range (b). A shift of up to 3.68 GPa is attributed to a highly deformed phase.

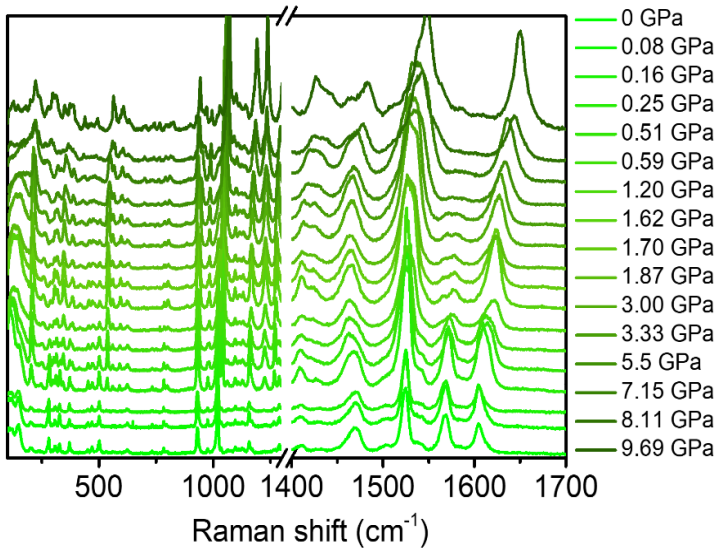

Figure 6.2.43. Variable Pressure Raman spectra of Cl.

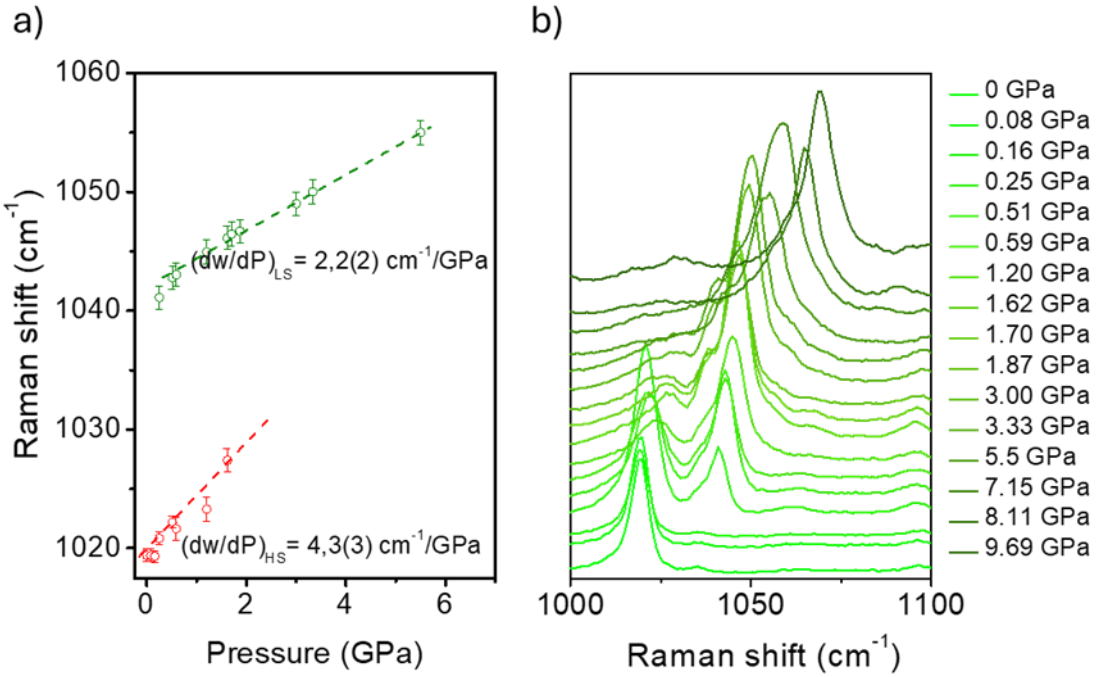

Figure 6.2.44. Variable Pressure Raman spectra of Cl. Raman shift of the characteristics HS (1018 cm^{-1}) and LS (1039 cm^{-1}) bands vs. pressure (a) shift of these bands at variable pressure in the 1000-1100 cm^{-1} range (b). A shift of up to 3.33 GPa is attributed to a highly deformed phase.

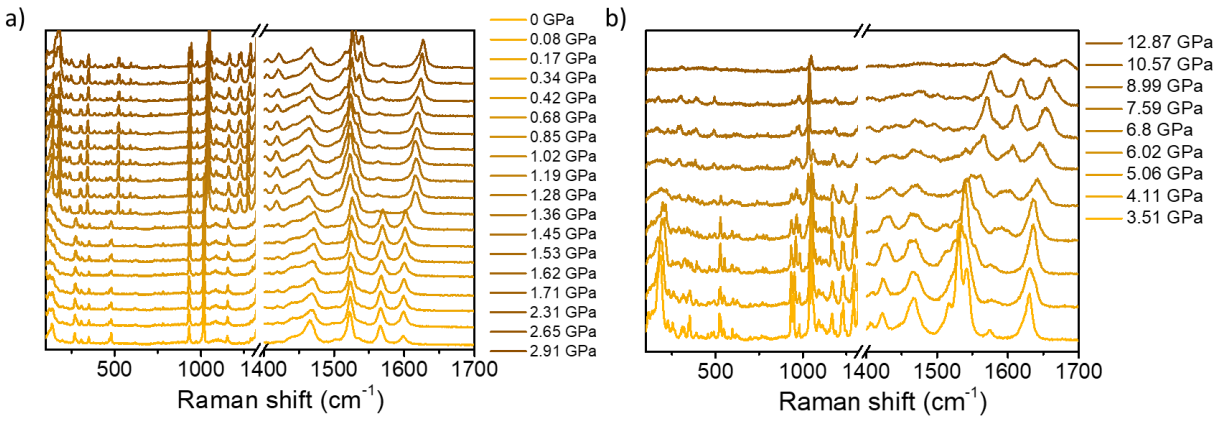

Figure 6.2.45. Variable Pressure Raman spectra of Br at low pressure range (a) and high-pressure range (b).

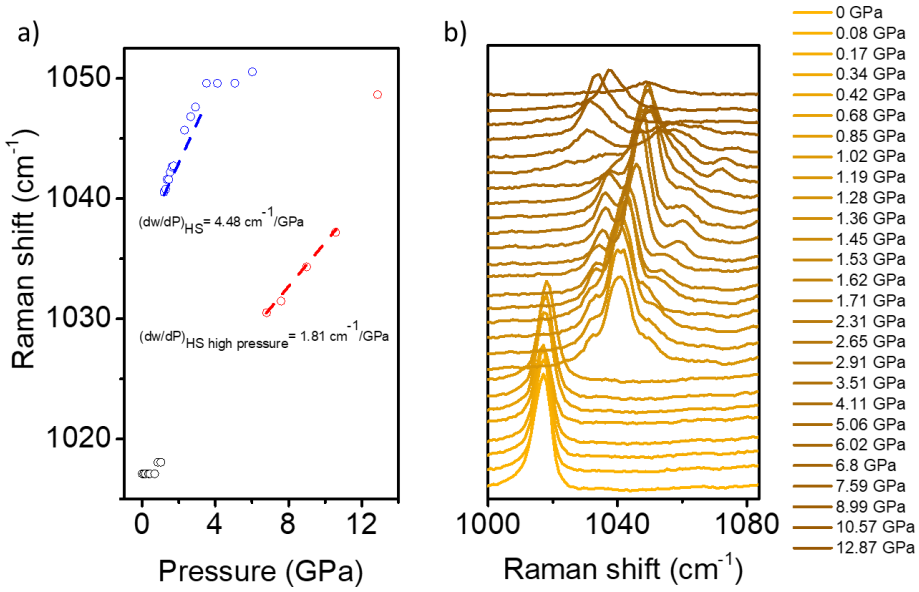

Figure 6.2.46. Variable Pressure Raman spectra of Br. Raman shift of the characteristics HS (1018 cm^{-1}) and LS (1039 cm^{-1}) bands vs. pressure (a) shift of these bands at variable pressure in the 1000-1100 cm^{-1} range (b). A shift of up to 4.11 GPa is attributed to a highly deformed phase.

6.3 Tuning field-induced Single Ion Magnet Properties via Co(II) Halogen Ligand Substitutions

6.3.1 Synthesis of metal complexes

General procedure: Ligand *p*-X-3-bpp (0.436 mmol, 1.0 eq.) was suspended in 10 mL of MeOH, over this mixture were added (0.218 mmol, 0.5 eq.) of $Co(ClO_4)_2 \cdot 6H_2O$ dissolved in 1 mL of MeOH and the mixture was stirred at room temperature for 1 hour. The ligand got dissolved through de coordination reaction and the solution became red-orange.

F: Orange crystals (125 mg, 80% yield)

Elemental analysis (%) calcd for $C_{22}H_{16}Cl_2F_2CoN_{10}O_8$ (716.26): C, 36.89; H, 2.25; N, 19.56; found: C, 36.84; H, 2.27; N, 19.52

IR: 3562 (s), 3248 (vs), 3139 (vs), 3084 (vs), 1640 (vs), 1589 (vs), 1520 (s), 1418 (s), 1221 (s), 776 (s), 617 (s)

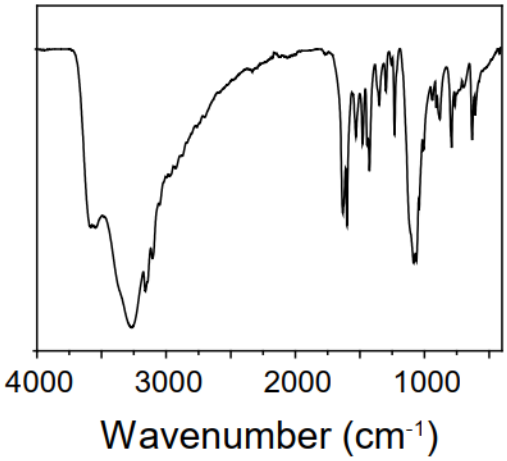

Figure 6.3.1. Infrared spectra of F.

Cl: Orange crystals (125 mg, 77% yield)

Elemental analysis (%) calcd for $C_{24}H_{19}Cl_4CoN_{11}O_8$ (743.93): C, 36.48; H, 2.42; N, 19.50; found: C, 36.40; H, 2.42; N: 19.50

IR: 3523 (s), 3239 (vs), 3137 (s), 3085 (s), 1602 (s), 1564 (s), 1404 (vs), 1072 (vs), 1052 (vs), 775 (s), 617 (s)

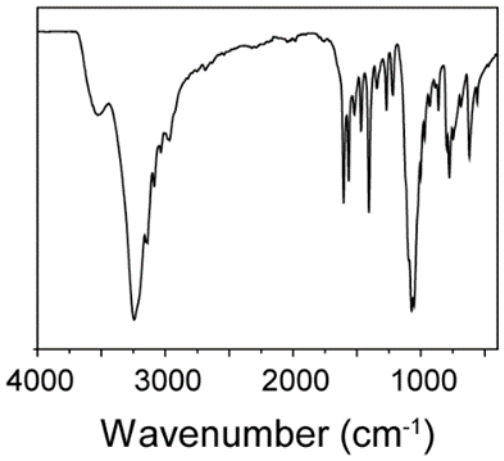

Figure 6.3.2. Infrared spectra of Cl.

Br: orange crystals (cubes) (100 mg, 55%)

Elemental analysis (%) calcd for $C_{22}H_{16}Br_2Cl_2CoN_{10}O_8$ (834,99): C, 31.53; H, 1.92; N, 16.71; found: C, 31.58; H, 1.98; N, 16.77

IR: 3239 (vs), 3144 (s), 3074 (s), 1601 (s), 1561 (s), 1404 (s), 1265 (s), 1074 (vs), 1052 (vs), 776 (s), 755 (s), 619 (s)

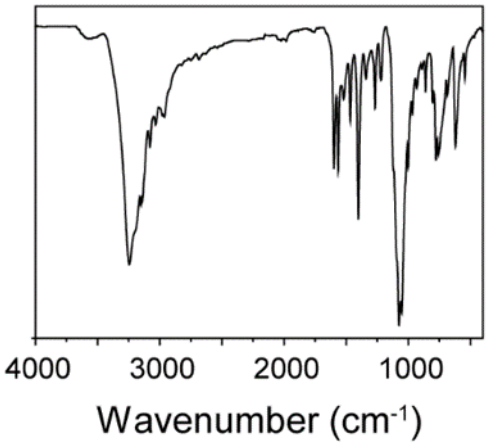

Figure 6.3.3. Infrared spectra of Br.

Br·2H$_2$O: orange crystals (acicular) (30 mg, 16.5%)

Elemental analysis (%) calcd for $C_{22}H_{18}Br_2Cl_2CoN_{10}O_9$ (856.09): C, 30.87; H, 2.12; N, 16.36; found: C, 30.81; H, 2.15; N, 16.31

IR: 3575 (vs), 3501 (s), 3235 (vs), 2960 (s), 1598 (s), 1562 (s), 1470 (s), 1401 (vs), 1069 (vs), 1052 (vs), 770 (s), 619 (s)

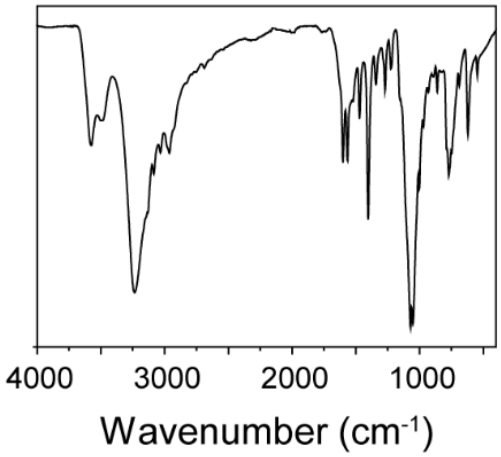

Figure 6.3.4. Infrared spectra of Br·2H_2O.

I·2H_2O: orange crystals (acicular) (150 mg, 72%)

Elemental analysis (%) calcd for $C_{22}H_{18}Cl_2CoI_2N_{10}O_9$ (950.09): C, 27.90; H, 1.92; N, 14.79; found: C, 27.81; H, 1.95; N, 14.78

IR: 3487 (vs), 3234 (vs), 2958 (s), 1593 (s), 1557 (s), 1399 (s), 1065 (vs), 1049 (vs), 770 (s), 735 (s), 618 (s)

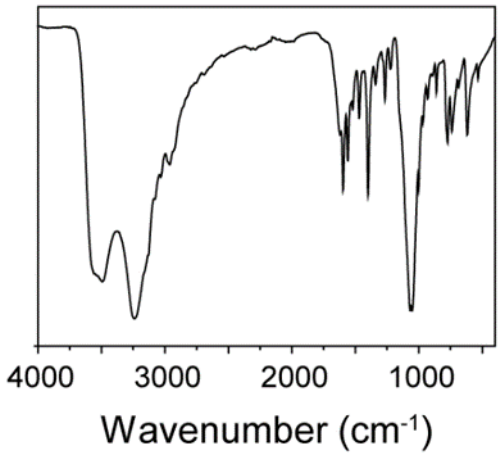

Figure 6.3.5. Infrared spectra of I·2H_2O.

6.3.2 Thermogravimetric analysis (TGA)

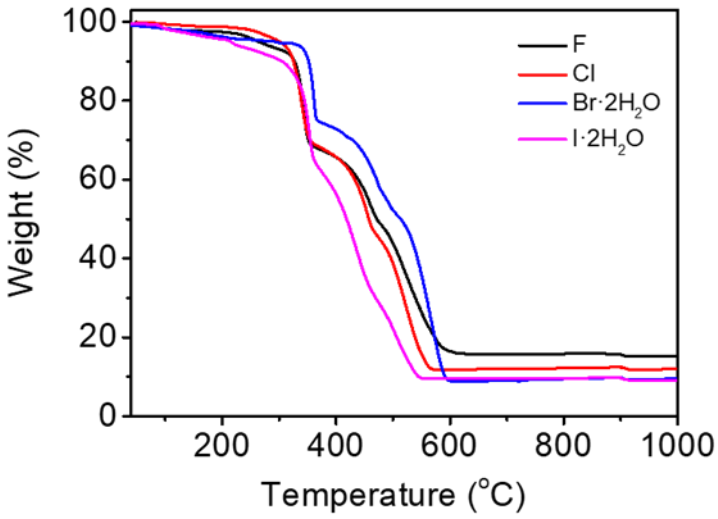

Figure 6.3.6. TGA measurements at 4 °C/min of complex F, Cl, Br·2H_2O and I·2H_2O under air. It was not feasible to perform the Br complex experiment, as it was discovered that the perchlorate counterion becomes unstable in the presence of this ligand under heating conditions.

6.3.3 Single Crystal X-Ray Diffraction (SCXRD)

Crystallographic data for all the complexes were deposited in the Cambridge Structural Database (CSD) with the following deposit numbers: CCDC-2242322 for F; CCDC-2242319 for Cl; CCDC-2242321 for Br; CCDC-2242320 for Br·2H_2O and CCDC-2242323 for I·2H_2O.

Table 6.3.1. Crystallographic data and structure refinement of single crystal X-Ray analysis for complexes F, Cl and Br.

	[Co(*p*-F-3-bpp)$_2$](ClO$_4$)$_2$	**[Co(*p*-Cl-3-bpp)$_2$](ClO$_4$)$_2$**	**[Co(*p*-Br-3-bpp)$_2$](ClO$_4$)$_2$**
Chemical Formula	$C_{22}H_{16}Cl_2CoF_2N_{10}O_8$	$C_{22}H_{16}Cl_4CoN_{10}O_8$	$C_{22}H_{16}Br_2Cl_2CoN_{10}O_8$
Size (mm^3)	0.025 x 0.091 x 0.220	0.080 x 0.100 x 0.150	0.087 x 0.147 x 0.149
Formula weight (g/mol)	716.28	749.18	838.10
Crystal system	Orthorhombic	Orthorhombic	Orthorhombic
Space group	Pbca	Pbca	Pbca
a [Å]	18.8524(7)	18.6748(4)	18.7039(5)
b [Å]	16.7704(7)	16.3783(4)	16.4084(4)
c [Å]	17.1603(8)	18.8224(4)	19.0687(5)
α [°]	90	90	90
β [°]	90	90	90
γ [°]	90	90	90
V [Å^3]	5425.4(4)	5757.0(2)	5852.2(3)
Z	8	8	8
Dx [mg/m^3]	1.754	1.729	1.902
Temperature [K]	100	100	100
Tmax/Tmin	0.9780. 0.8240	0.9220. 0.8600	0.7470. 0.6190
Absortion coeff. [mm^{-1}]	0.912	1.034	3.566
F (000)	2888	3016	3304
Θ range [°]	2.01 to 28.34	2.18 to 28.33	1.97 to 33.19
Reflections collected	139338	43449	115625
Independent reflections	6769	7165	11138
GOF on F2	1.185	1.020	1.017
Final R indices [I > 2σ(I)]	R1 = 0.1278. wR2 = 0.2482	R1 = 0.0339. wR2 = 0.0695	R1 = 0.0305. wR2 = 0.0589
R indices (all data)	R1 = 0.1390. wR2 = 0.2530	R1 = 0.0529. wR2 = 0.0759	R1 = 0.0536. wR2 = 0.0657

Table 6.3.2. Crystallographic data and structure refinement of single crystal X-Ray analysis for complexes Br·2H_2O and I·2H_2O.

	([Co(*p*-Br-3-bpp)$_2$](ClO$_4$)$_2$)·2H_2O	**([Co(*p*-I-3-bpp)$_2$](ClO$_4$)$_2$)·2H_2O**
Chemical Formula	$C_{22}H_{18.74}Br_2Cl_2CoN_{10}O_{9.37}$	$C_{22}H_{18.98}Cl_2CoI_2N_{10}O_{9.49}$
Size (mm^3)	0.035 x 0.082 x 0.437	0.021 x 0.067 x 0.244
Formula weight (g/mol)	862.75	958.94
Crystal system	Orthorhombic	Orthorhombic
Space group	Pbca	Pbca
a [Å]	13.3694(3)	13.7964(5)
b [Å]	16.1452(4)	16.1047(6)
c [Å]	27.6762(7)	27.9483(11)
α [°]	90	90
β [°]	90	90
γ [°]	90	90
V [Å^3]	5974.0(3)	6209.7(4)
Z	8	8
Dx [mg/m^3]	1.919	2.051
Temperature [K]	100	100
Tmax/Tmin	0.8870. 0.3100	0.9440. 0.5500
Absortion coeff. [mm^{-1}]	3.499	2.782
F (000)	3413	3711
Θ range [°]	2.11 to 30.09	2.07 to 28.34
Reflections collected	75970	322576
Independent reflections	8742	7736
GOF on F2	1.025	1.101
Final R indices [I > 2σ(I)]	R1 = 0.0419. wR2 = 0.0787	R1 = 0.0495. wR2 = 0.1141
R indices (all data)	R1 = 0.0766. wR2 = 0.0893	R1 = 0.0627. wR2 = 0.1230

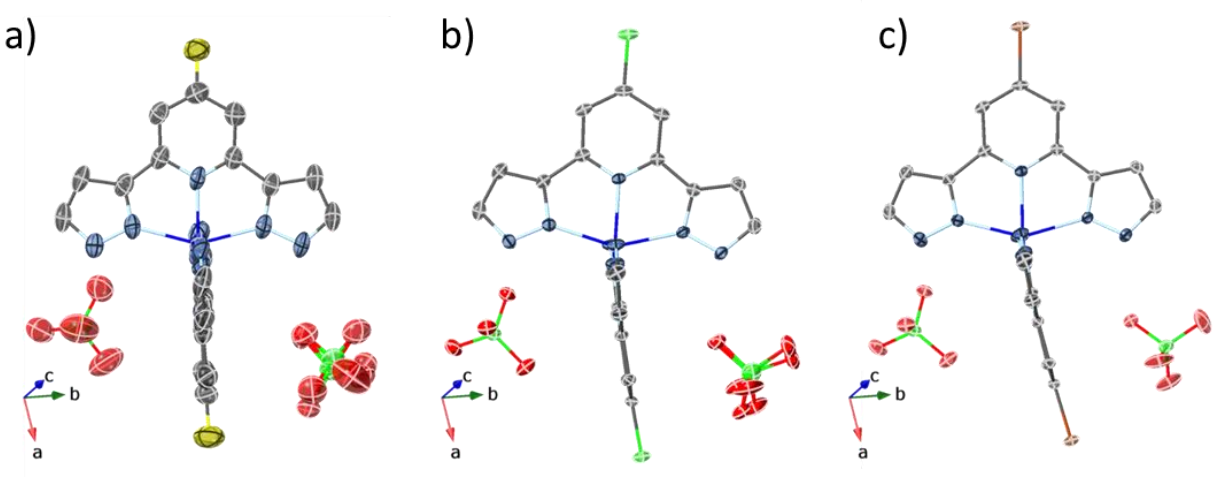

Figure 6.3.7. Ball and stick representation of compound F, Cl and Br. The separation of the ligands form the dash line represent the distortion of the octahedral geometry. Hydrogen atoms are omitted for clarity. Carbon is grey, nitrogen is blue, oxygen is red, cobalt is dark blue, chlorine is green, fluorine is yellow, and bromine is brown.

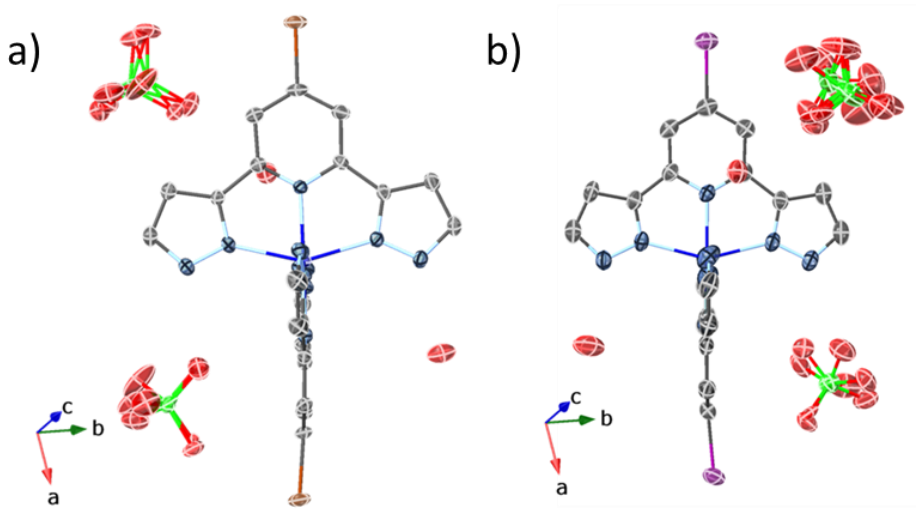

Figure 6.3.8. Ball and stick representation of compound Br·2H_2O and I·2H_2O. The separation of the ligands from the dash line represents the distortion of the octahedral geometry. Hydrogen atoms of the complex are omitted for clarity. Carbon is grey, nitrogen is blue, oxygen is red, cobalt is dark blue, chlorine is green, iodine is purple, and bromine is brown.

Table 6.3.3. Main distortion parameters of all the compounds at 100 K.

Angle (°)	F	Cl	Br	Br·2H₂O	I·2H₂O
Σ	128.40	133.84	134.12	131.41	130.67
Θ	412.13	442.94	458.88	418.37	415.67
θ	88.423	87.798	87.282	95.864	95.724
Ψ	151.03	150.26	150.07	150.55	150.66
ϕ	175.24	173.97	172.53	178.27	178.60

Table 6.3.4. Co1-N distances for all the compounds at 100 K.

Bond	F	Cl	Br	Br·2H₂O	I·2H₂O
Co1-N	Distance (Å)	Distance (Å)	Distance (Å)	Distance (Å)	Distance (Å)
Co1-N31	2.0583(59)	2.0896(15)	2.0922(15)	2.0801(22)	2.0729(41)
Co1-N52	2.1451(71)	2.1540(18)	2.1524(15)	2.1466(25)	2.1410(39)
Co1-N42	2.1499(56)	2.1537(18)	2.1629(15)	2.1515(25)	2.1485(42)
Co1-N1	2.0587(59)	2.0911(15)	2.0919(14)	2.0762(22)	2.0677(41)
Co1-N22	2.1329(69)	2.1292(16)	2.1281(16)	2.1378(23)	2.1395(34)
Co1-N12	2.1582(68)	2.1387(17)	2.1372(15)	2.1567(23)	2.1509(37)

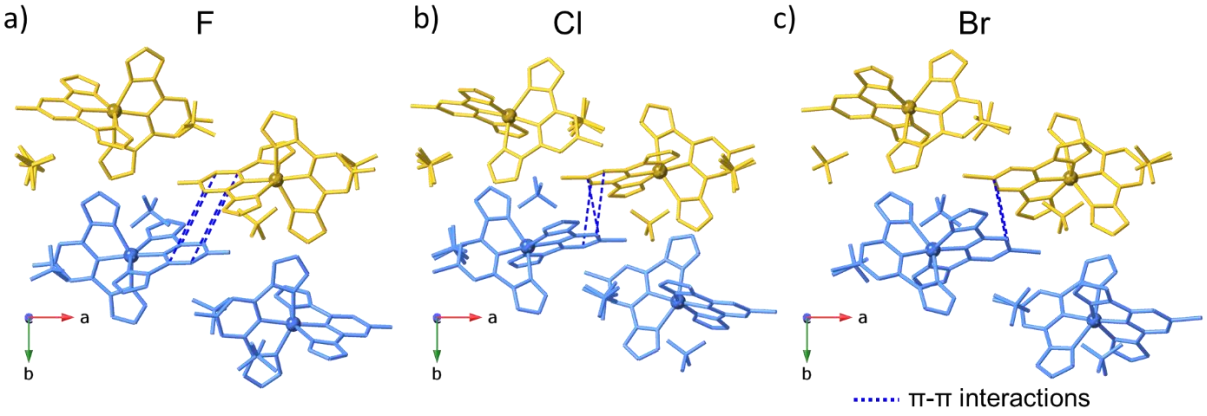

Figure 6.3.9. Illustration of π-π interactions established in F (a), Cl (b) and Br (c).

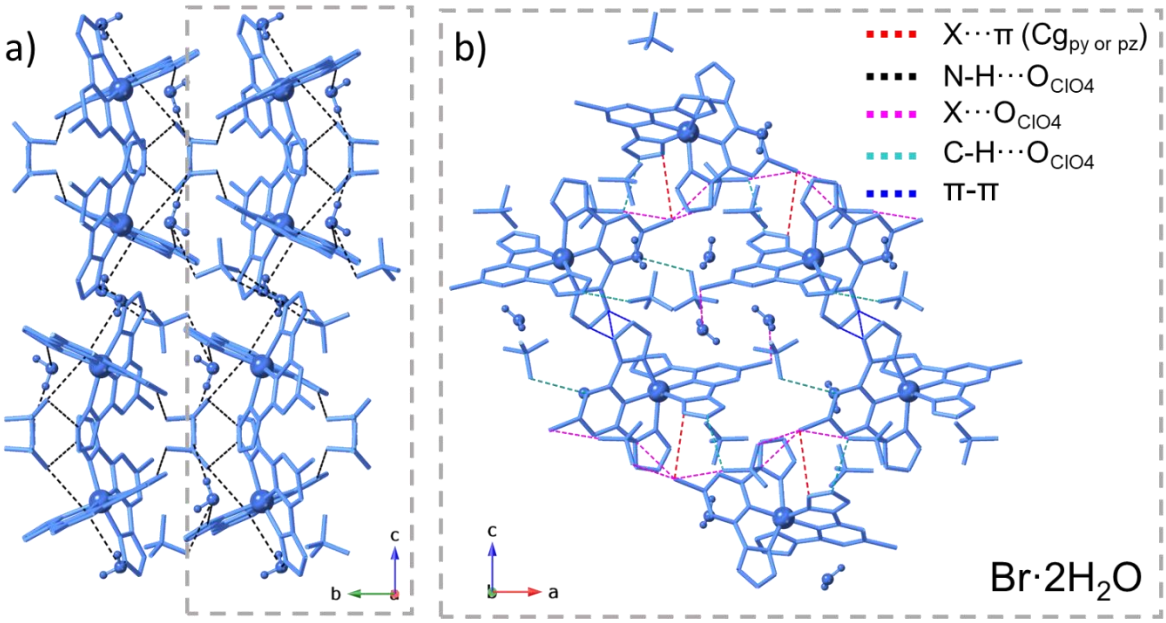

Figure 6.3.10. a) Packing of Br·2H$_2$O through bc plane (a) and ac plane (b). Main intermolecular interactions are depicted.

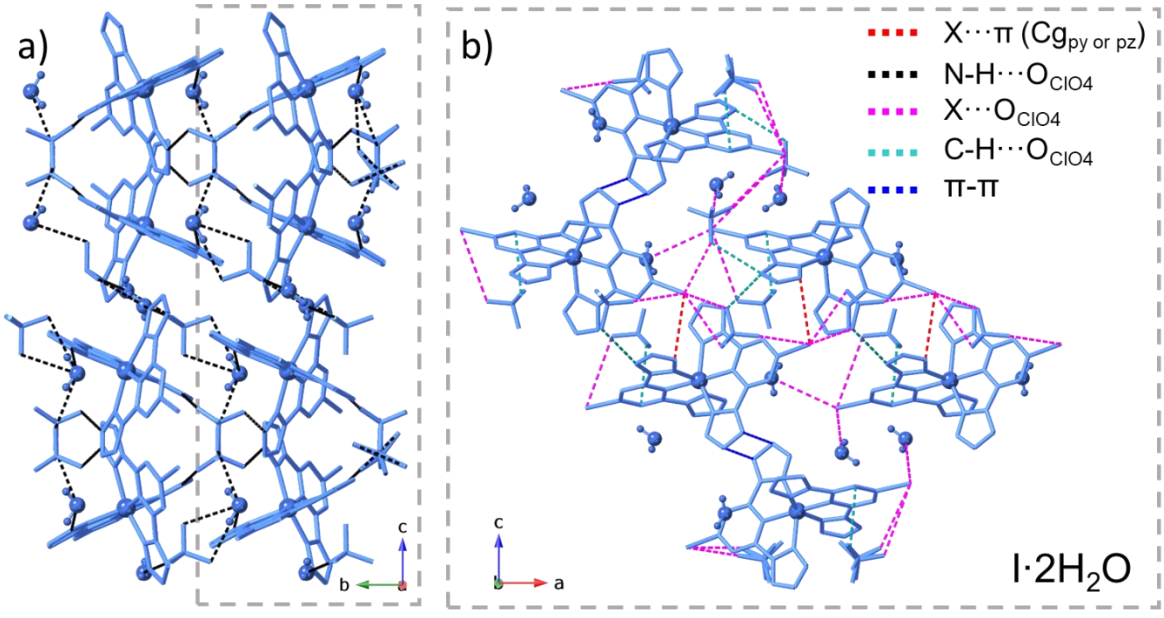

Figure 6.3.11. a) Packing of I·2H$_2$O through bc plane (a) and ac plane (b). Main intermolecular interactions are depicted.

6.3.4 Magnetic measurements

Table 6.3.5. Main parameters of the Zero Field Splitting Hamiltonian fitted using PHI program.

	g	D (cm^{-1})	E (cm^{-1})
F	2.37	15.18	0.08
Cl	2.52	20.61	0.05
Br	2.43	28.23	0.10
$Br \cdot 2H_2O$	2.55	29.73	0.24
$I \cdot 2H_2O$	2.77	40.26	-0.17

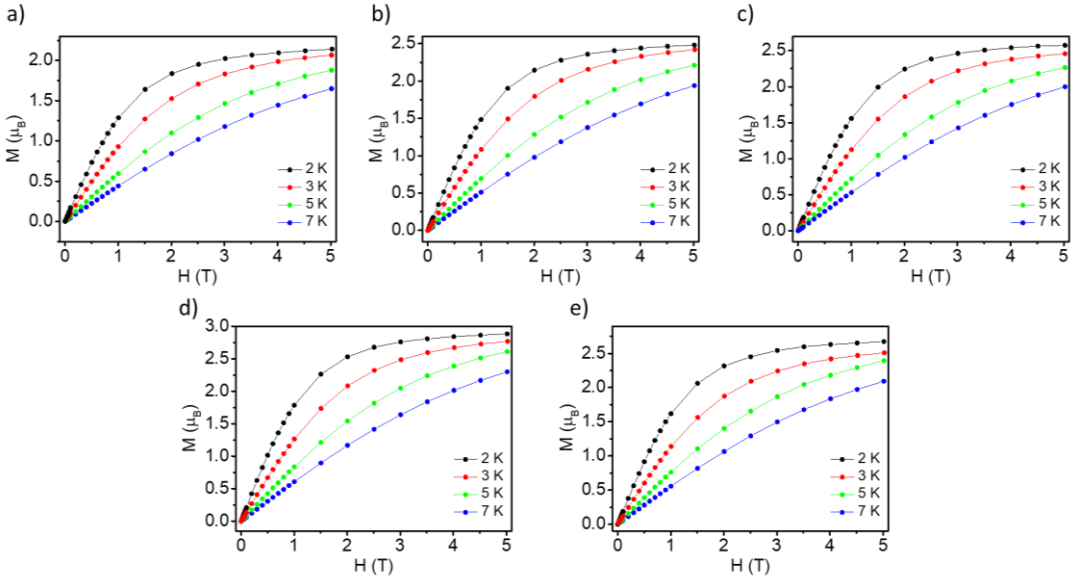

Figure 6.3.12. Experimental M vs H plots at 2, 3, 5 and 7 K for F (a), Cl (b) and Br (c), $Br \cdot 2H_2O$ (d) and $I \cdot 2H_2O$ (e).

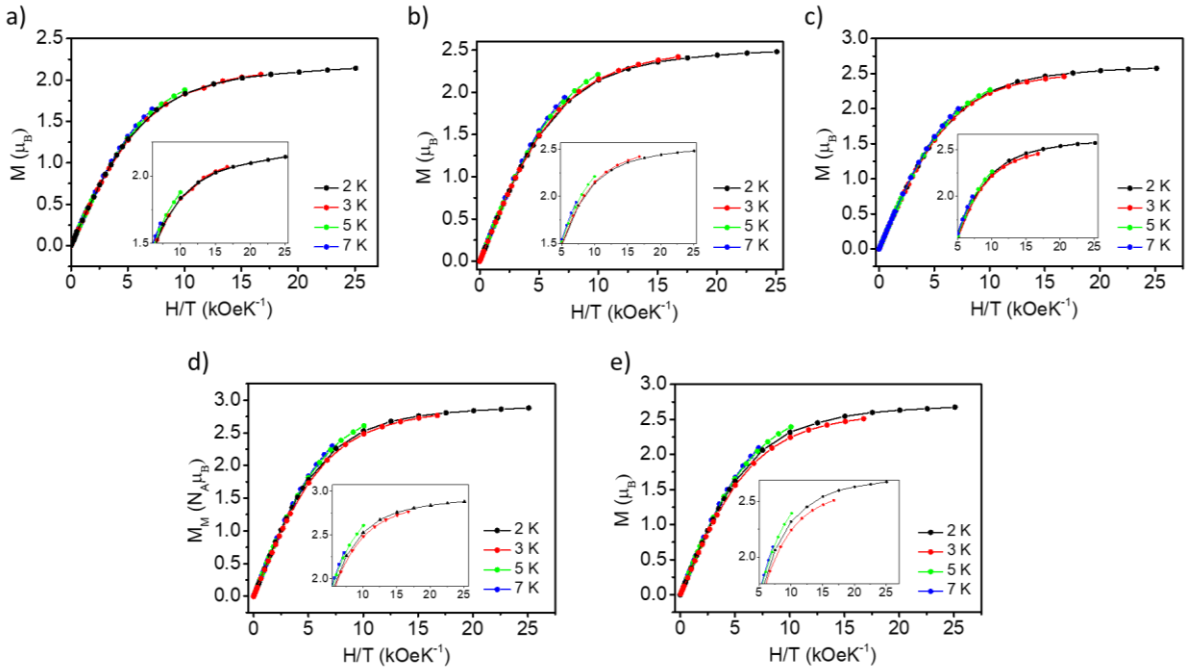

Figure 6.3.13. Experimental M vs HT^{-1} plots at 2, 3, 5 and 7K for F (a), Cl (b) and Br (c), Br·2H_2O (d) and I·2H_2O (e). Inset: M vs H/T plot in the high applied magnetic field region to illustrate the non-superposition of the curves.

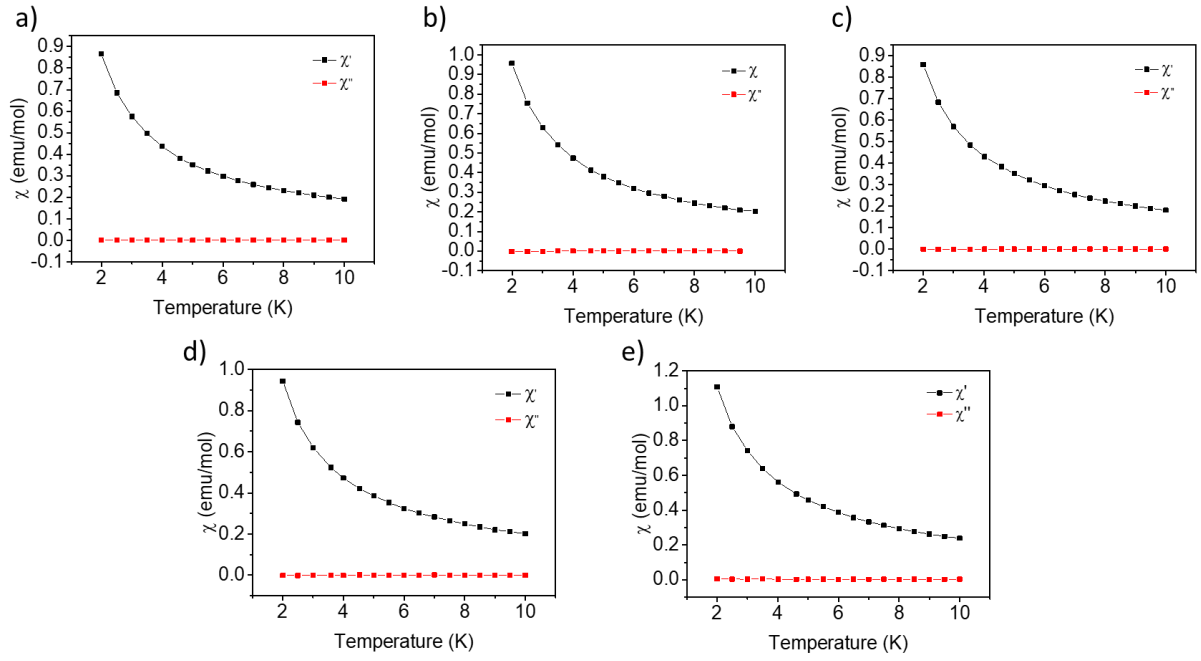

Figure 6.3.14. Zero field dependent in-phase and out-of-phase ac susceptibility for complex over the temperature range 2-10 K under an applied frequency of 110 Hz.

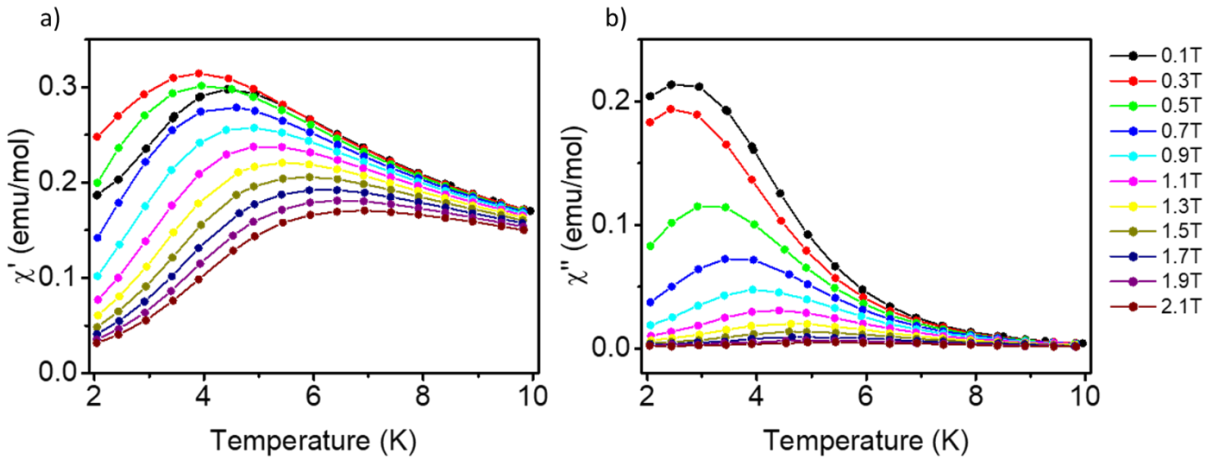

Figure 6.3.15. Field dependent in-phase (a) and out-of-phase (b) ac susceptibility for complex F over the temperature range 2-10 K under an applied frequency of 10 kHz.

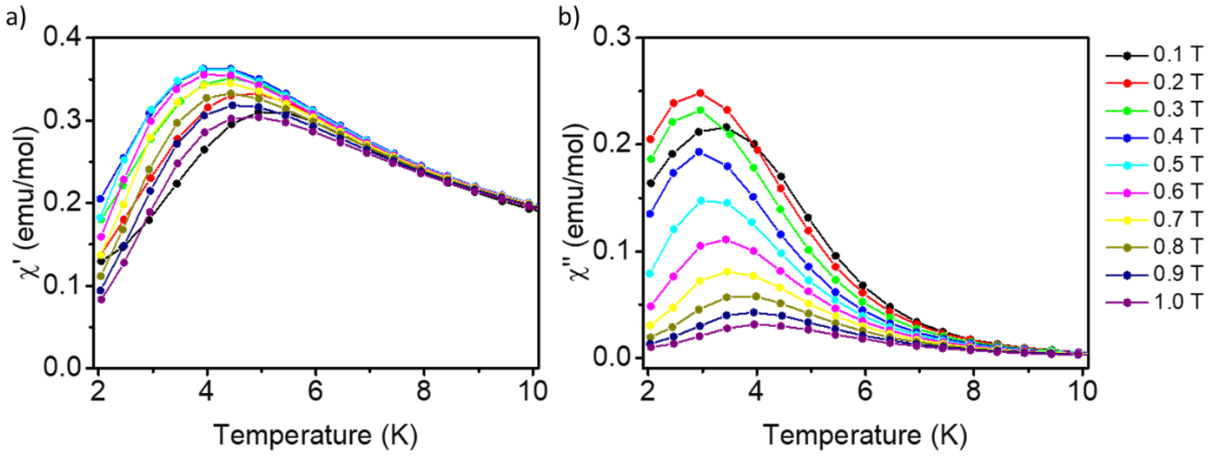

Figure 6.3.16. Field dependent in-phase (a) and out-of-phase (b) ac susceptibility for complex Cl over the temperature range 2-10 K under an applied frequency of 10 kHz.

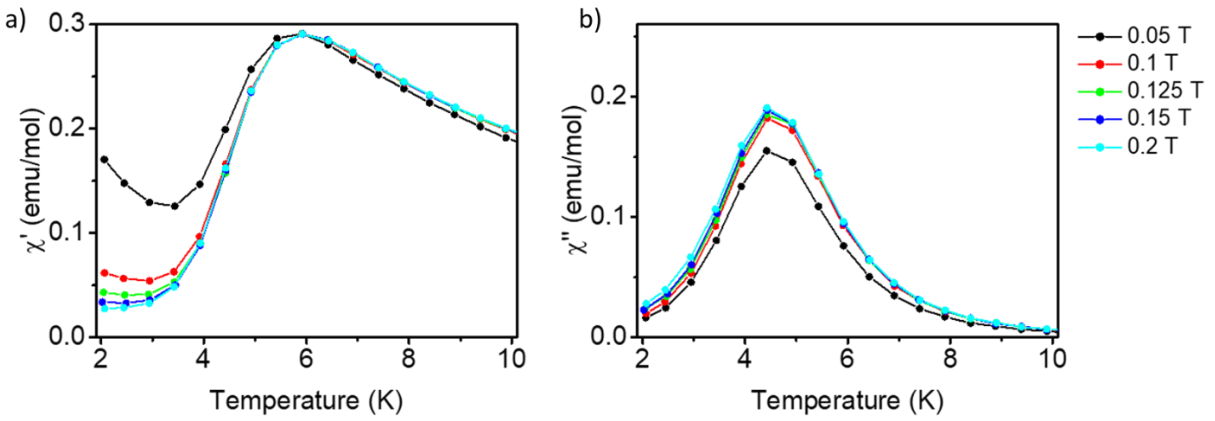

Figure 6.3.17. Field dependent in-phase (a) and out-of-phase (b) ac susceptibility for complex Br over the temperature range 2-10 K under an applied frequency of 10 kHz.

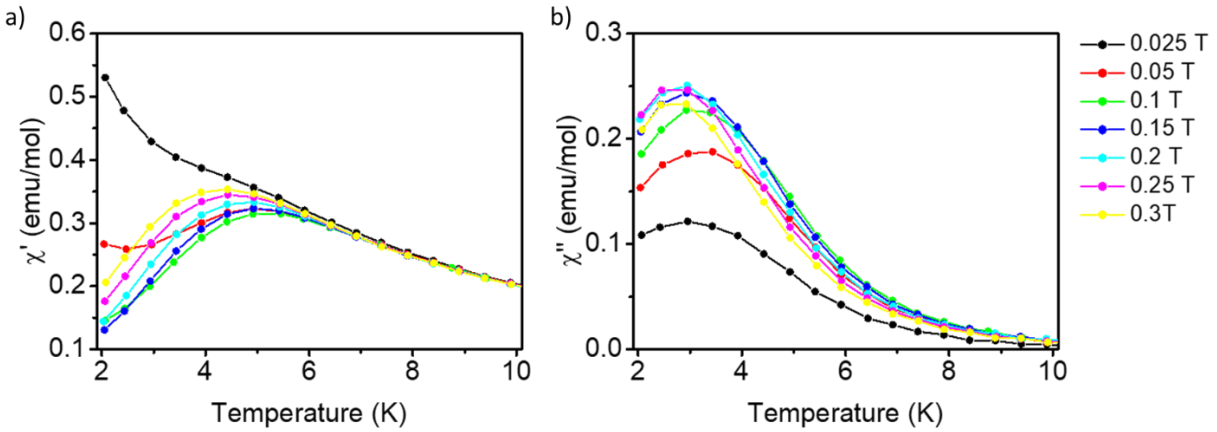

Figure 6.3.18. Field dependent in-phase (a) and out-of-phase (b) ac susceptibility for complex Br·2H_2O over the temperature range 2-10 K under an applied frequency of 10 kHz.

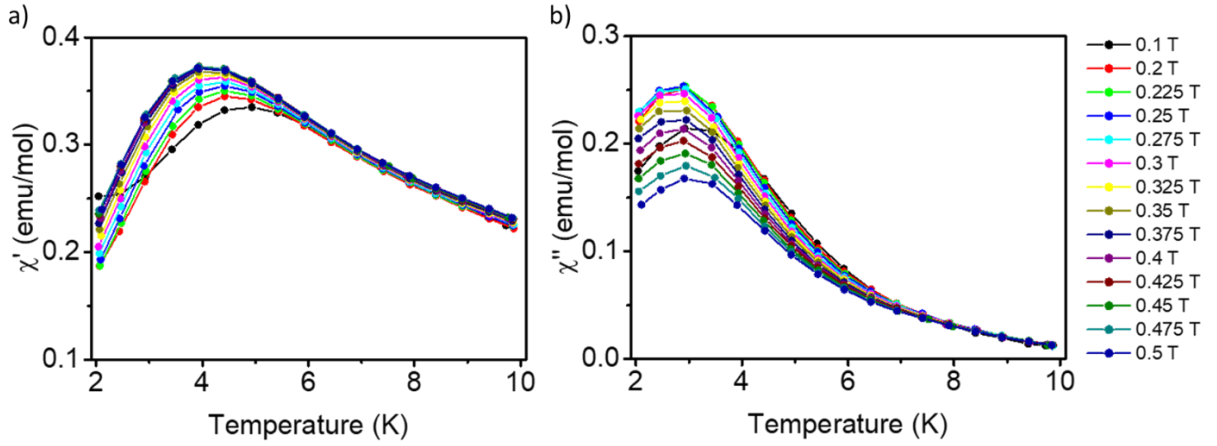

Figure 6.3.19. Field dependent in-phase (a) and out-of-phase (b) ac susceptibility for complex I·2H_2O over the temperature range 2-10 K under an applied frequency of 10 kHz.

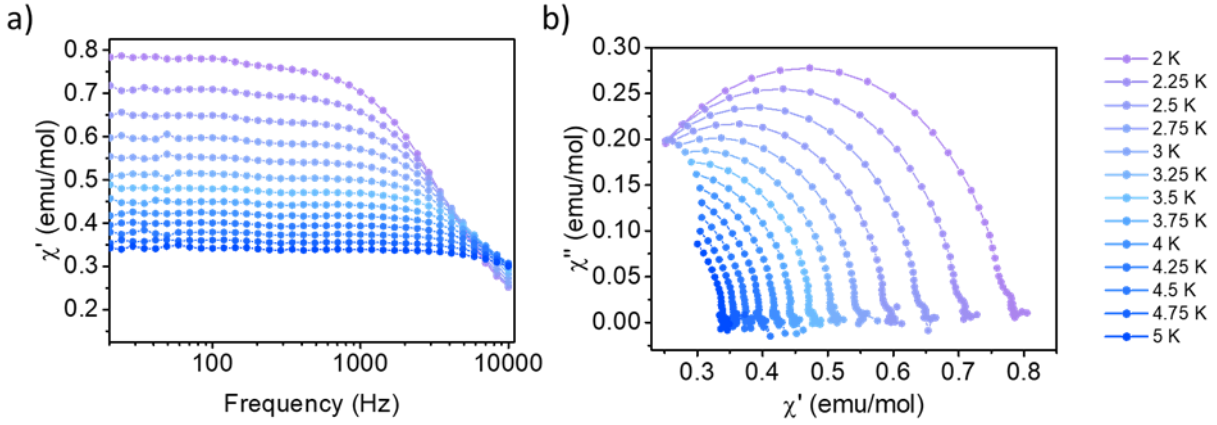

Figure 6.3.20. Frequency dependent in-phase (a) and Argand plots derived from the frequency-dependent ac susceptibility data at various temperatures (b) under an applied dc field of 1000 Oe in a range of 2-5 K for F.

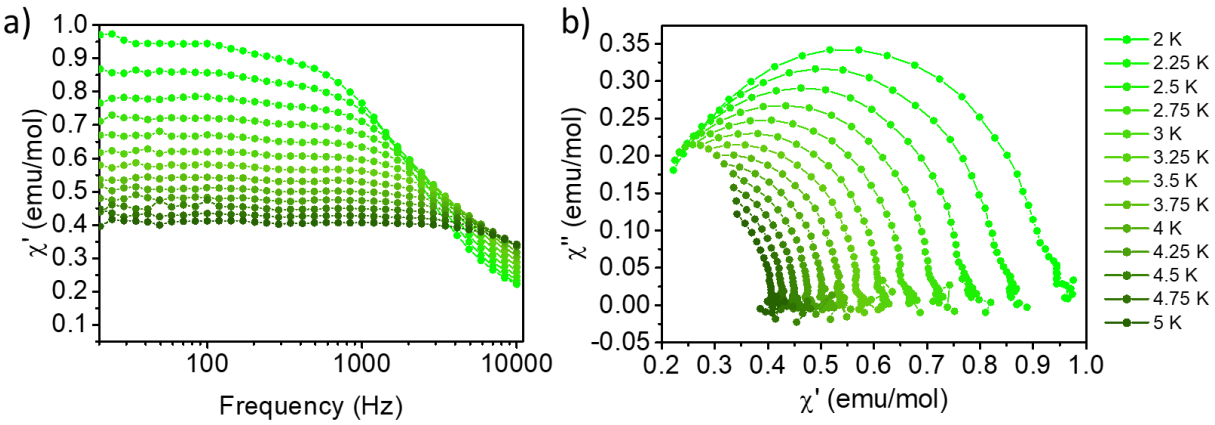

Figure 6.3.21. Frequency dependent in-phase (a) and Argand plots derived from the frequency-dependent ac susceptibility data at various temperatures (b) under an applied dc field of 1000 Oe in a range of 2-5 K for Cl.

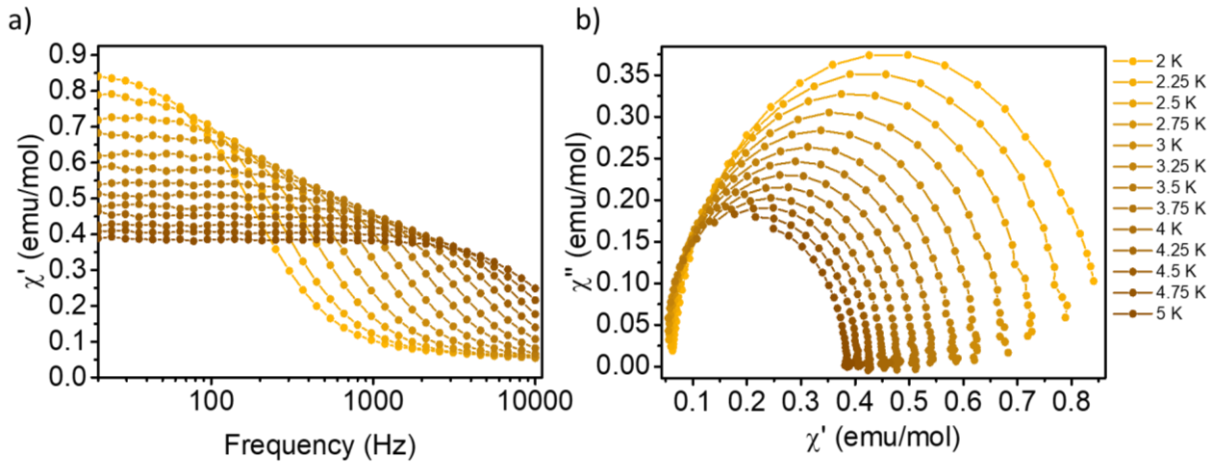

Figure 6.3.22. Frequency dependent in-phase (a) and Argand plots derived from the frequency-dependent ac susceptibility data at various temperatures (b) under an applied dc field of 1000 Oe in a range of 2-5 K for Br.

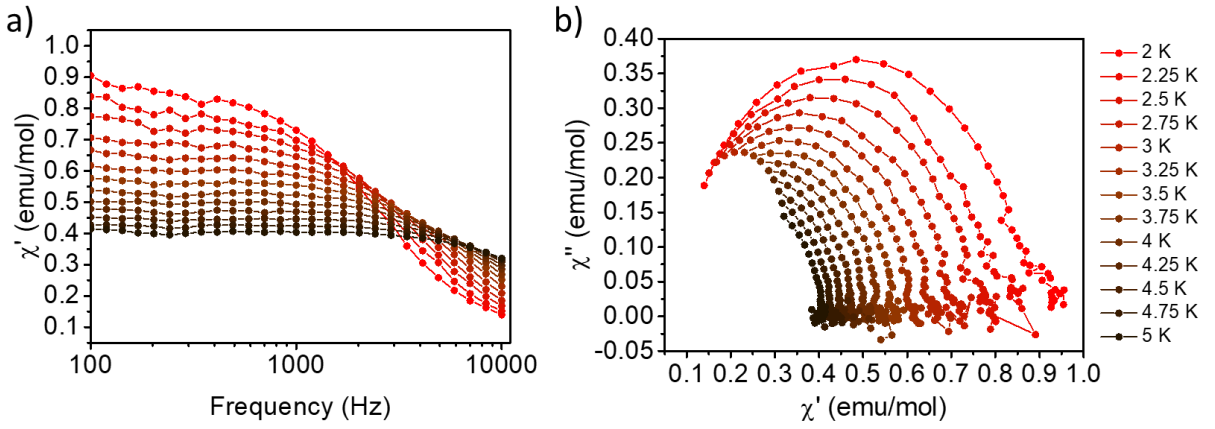

Figure 6.3.23. Frequency dependent in-phase (a) and Argand plots derived from the frequency-dependent ac susceptibility data at various temperatures (b) under an applied dc field of 1000 Oe in a range of 2-5 K for Br·2H_2O.

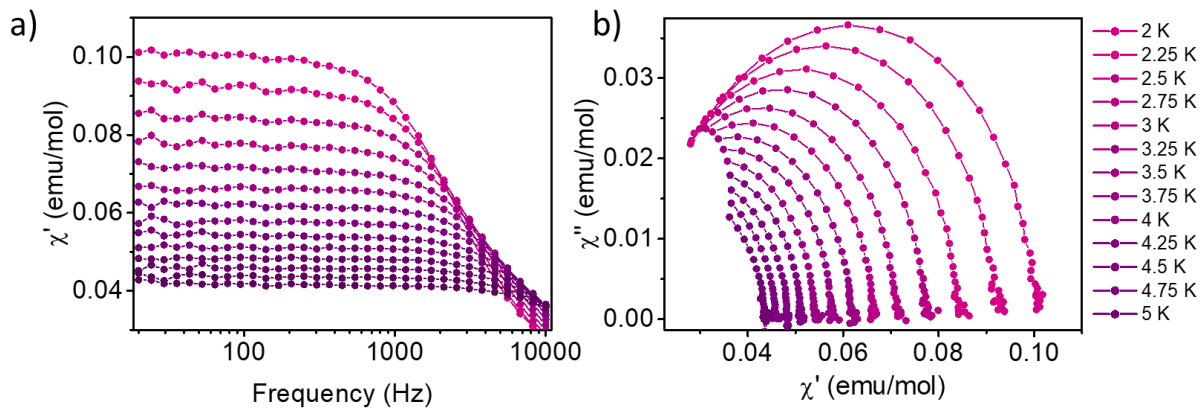

Figure 6.3.24. Frequency dependent in-phase (a) and Argand plots derived from the frequency-dependent ac susceptibility data at various temperatures (b) under an applied dc field of 1000 Oe in a range of 2-5 K for I·2H_2O.

Table 6.3.6. Relaxation fitting parameters from the least-square fitting of the Cole-Cole plots of F, Cl and Br according to the generalized Debye model.

$[Co(p\text{-F-3-bpp})_2](ClO_4)_2$				
T / K	**χ_S / cm^3 mol^{-1}**	**χ_T / cm^3 mol^{-1}**	**τ / s**	**α**
2.00401	0.17707	1.00308	4.39608E-5	0.10108
2.25193	0.16412	0.90894	3.64973E-5	0.08668
2.50071	0.15073	0.83064	3.03838E-5	0.07978
2.75045	0.14341	0.76208	2.55858E-5	0.06815
3.00047	0.13198	0.70579	2.14462E-5	0.06683
3.25041	0.12958	0.65358	1.83137E-5	0.05367
$[Co(p\text{-Cl-3-bpp})_2](ClO_4)_2$				
T / K	**χ_S / cm^3 mol^{-1}**	**χ_T / cm^3 mol^{-1}**	**τ / s**	**α**
2.01291	0.13372	0.95764	7.1772E-5	0.12441
2.25624	0.13062	0.86115	5.5819E-5	0.0963
2.50429	0.12287	0.78454	4.4378E-5	0.08424
2.74991	0.11871	0.72223	3.62921E-5	0.07519
3.00012	0.11349	0.66685	2.9917E-5	0.06824
3.24971	0.1096	0.6185	2.49533E-5	0.06075
3.50096	0.10681	0.57754	2.09873E-5	0.05533
3.75014	0.10436	0.53883	1.77084E-5	0.04569
$[Co(p\text{-Br-3-bpp})_2](ClO_4)_2$				
T / K	**χ_S / cm^3 mol^{-1}**	**χ_T / cm^3 mol^{-1}**	**τ / s**	**α**
2.005382	0.06075	0.86211	8.56328E-4	0.04718
2.264823	0.0587	0.7959	5.85777E-4	0.0307
2.501502	0.0533	0.73062	3.74989E-4	0.02246
2.750590	0.05107	0.67739	2.50892E-4	0.01841
2.999327	0.04752	0.6237	1.62791E-4	0.01103
3.247667	0.04499	0.58228	1.11247E-4	0.01401
3.499075	0.04286	0.54219	7.60042E-5	0.00904
3.748109	0.04096	0.50874	5.42787E-5	0.01097
3.998882	0.03924	0.47776	3.85649E-5	0.01094
4.246140	0.03652	0.45206	2.84224E-5	0.01818
4.498102	0.03844	0.42606	2.15272E-5	0.00839
4.741902	0.02996	0.40602	1.61353E-5	0.0261

Table 6.3.7. Relaxation fitting parameters from the least-square fitting of the Cole-Cole plots of Br·2H_2O and I·2H_2O according to the generalized Debye model.

[Co(*p*-Br-3-bpp)$_2$](ClO$_4$)$_2$·2H_2O				
T / K	**χ_S / cm^3 mol^{-1}**	**χ_T / cm^3 mol^{-1}**	**τ / s**	**α**
2.009	0.01497	0.92095	6.37047E-5	0.15502
2.25397	0.01005	0.83483	4.89397E-5	0.14428
2.50234	0.01432	0.77511	4.04613E-5	0.13177
2.7514	0.02019	0.71066	3.33405E-5	0.11394
3.00244	0.02631	0.65905	2.8106E-5	0.09953
3.25249	0.03104	0.61376	2.37401E-5	0.0915
3.50206	0.03656	0.57307	2.02762E-5	0.0798
3.75145	0.04431	0.53576	1.76676E-5	0.06059
[Co(*p*-I-3-bpp)$_2$](ClO$_4$)$_2$·2H_2O				
T / K	**χ_S / cm^3 mol^{-1}**	**χ_T / cm^3 mol^{-1}**	**τ / s**	**α**
2.04491	0.20288	1.00958	6.09078E-5	0.06068
2.25149	0.18465	0.91954	4.87749E-5	0.04972
2.50103	0.16891	0.84548	3.94914E-5	0.05335
2.75201	0.15709	0.77696	3.23241E-5	0.05049
3.00091	0.14634	0.71518	2.66649E-5	0.04894
3.24978	0.1418	0.66364	2.25903E-5	0.04137
3.49968	0.12699	0.62009	1.87799E-5	0.05199
3.74858	0.12748	0.57739	1.63109E-5	0.03714

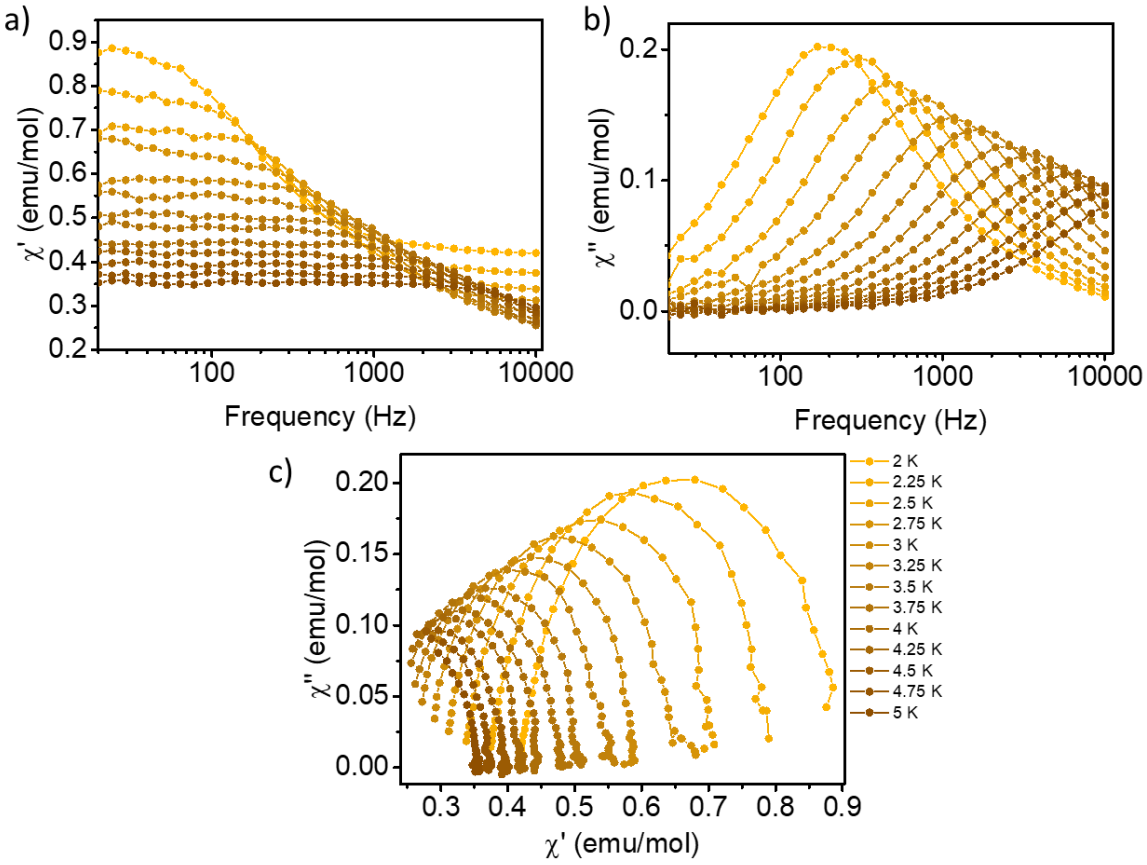

Figure 6.3.25. Frequency dependent in-phase (a), out-of-phase (b) and Argand plots derived from the frequency-dependent ac susceptibility data at various temperatures (c) under an applied dc field of 250 Oe in a range of 2 − 5 K for Br·2H_2O.

6.4 Fine tuning of the spin transition through the counterion selection

6.4.1 Synthesis of metal complexes

Synthesis of BF_4: [Fe(*p*-Cl-3-bpp)$_2$](BF_4)$_2$

Ligand *p*-Cl-3-bpp (86 mg, 0.33 mmol) was suspended in methanol (10 mL). To this solution, $Fe(BF_4)_2 \cdot 6H_2O$ (60 mg, 0.165 mmol) dissolved in 1 mL of methanol was added dropwise over the methanolic ligand suspension. The addition of the iron salt led the dissolution of the ligand and caused a rapid formation of the complex with a color change to orange. After 1 hour stirring, solution was transferred into a beaker. Solution was covered with Parafilm in order to allow crystallization by slow evaporation. Brown crystals suitable for X-Ray diffraction was collected after 3 days.

IR: 3305 (s), 3255 (s), 3154 (m), 3141 (m), 1604 (s), 1563 (s), 1469 (m), 1405 (s), 1266 (m), 1042 (m), 1020 (s), 934 (m), 779 (s).

Elemental analysis (%) calcd. For $C_{22}H_{16}B_2Cl_2F_8FeN_{10}$ (720.79): C, 36.66; H, 2.24; N, 19,43: found: C, 36.62; H, 2.28; N, 19.42.

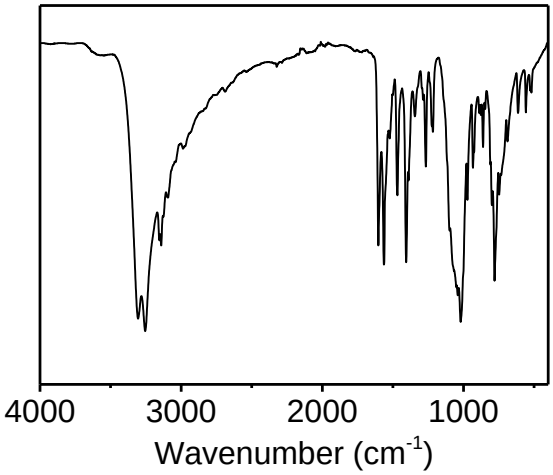

Figure 6.4.1. Infrared spectra of BF_4.

Synthesis of PF_6: [Fe(*p*-Cl-3-bpp)$_2$](PF_6)$_2$

Ligand *p*-Cl-3-bpp (420mg, 2 mmol) was suspended in hot ethanol (5 mL). To this solution, $FeCl_2$ (126 mg, 1 mmol) dissolved in 15 mL of hot water was added over the ethanolic ligand suspension. The addition of the iron salt led the dissolution of the ligand and caused a rapid formation of the complex with a color change to orange. Finally, a warm aqueous solution of NH_4PF_6 (326 mg, 2 mmol) in 15 mL of hot water was added over first solution rapidly. Solution was sealed and let crystallized at 4 °C overnight. Brown crystals suitable for X-Ray diffraction was collected after 1 days.

IR: 3367 (s), 3156 (m), 1604 (s), 1565 (m), 1465 (m), 1405 (s), 1351 (m), 1263 (m), 1107 (m), 828 (s), 776 (m), 552 (s).

Elemental analysis (%) calcd. For $C_{22}H_{16}Cl_2F_{12}FeN_{10}P_2$ (835.96): C, 31.57; H, 1.93; N, 16.73; found: C, 31.57; H, 1.94; N, 16.71.

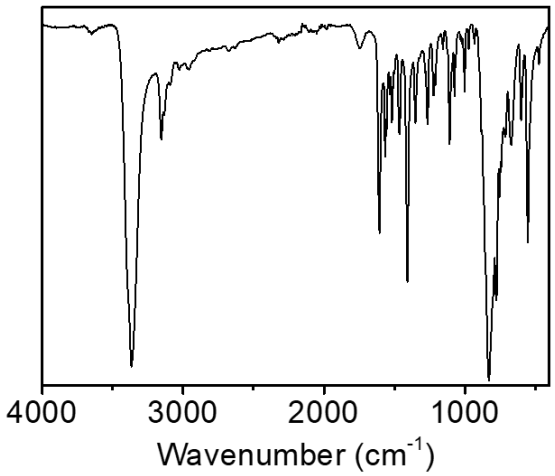

Figure 6.4.2. Infrared spectra of PF_6.

Synthesis of NO_3: [Fe(*p*-Cl-3-bpp)$_2$](NO_3)$_2$

Ligand *p*-Cl-3-bpp (200 mg, 0.816 mmol) was suspended in hot ethanol (5 mL). To this solution, $FeCl_2$ (51.7 mg, 0.408 mmol) dissolved in 8 mL of hot water was added over the ethanolic ligand suspension. The addition of the iron salt led the dissolution of the ligand and caused a rapid formation of the complex with a color change to orange. Finally, a warm aqueous solution of $NaNO_3$ (69 mg, 0.816 mmol) in 8 mL of hot water was added over first solution rapidly. Solution was sealed and let crystallized at 4 °C overnight. Yellow crystals suitable for X-Ray diffraction was collected after 1 days.

IR: 3545 (w), 3397 (w), 3139 (m), 3069 (m), 2943 (m), 2917 (m), 1601 (m), 1557 (m), 1474 (w), 1339 (s), 1260 (m), 1108 (m), 1060 (m), 999 (m), 795 (m), 782 (m)

Elemental analysis (%) calcd. For $C_{22}H_{16}Cl_2F_{12}FeN_{12}O_6$ (670.00): C, 39.37; H, 2.40; N, 25.04; found: C, 39.46; H, 2.45; N, 24.97.

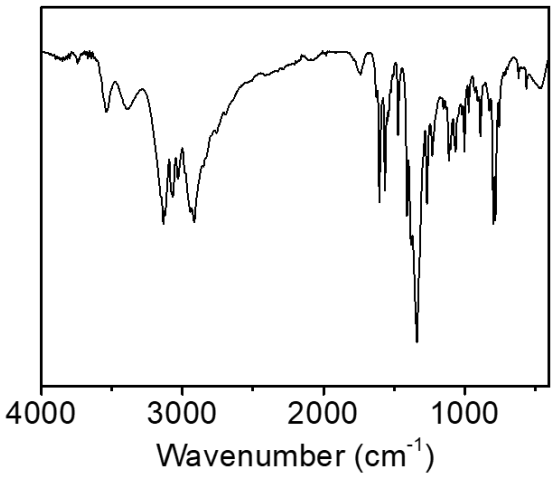

Figure 6.4.3. Infrared spectra of NO_3.

Synthesis of NCS: [Fe(*p*-Cl-3-bpp)$_2$](NCS)$_2$

Ligand *p*-Cl-3-bpp (100 mg, 0.407 mmol) was suspended in hot ethanol (5 mL). To this solution, $FeCl_2$ (25.79 mg, 0.203 mmol) dissolved in 8 mL of hot water was added over the ethanolic ligand suspension. The addition of the iron salt led the dissolution of the ligand and caused the rapid formation of the complex with a color change to orange. Finally, a warm aqueous solution of KNCS (40 mg, 0.407 mmol) in 8 mL of hot water was added over first solution rapidly. Solution was sealed and let crystallized at 4 °C overnight. Dark red-black crystals suitable for X-Ray diffraction was collected after 1 days.

IR: 3392 (m), 3314 (m), 3313 (m), 2743 (m), 2089 (s), 1610 (m), 1550 (m), 1464 (m), 1403 (m), 1337 (m), 1260 (w), 1106 (w), 869 (m), 786 (m), 771 (m), 751 (m)

Elemental analysis (%) calcd. For $C_{24}H_{18}Cl_2FeN_{12}OS_2$ (661.98): C, 42.31; H, 2.66; N, 24.67; found: C, 42.36; H, 2.65; N, 24.67.

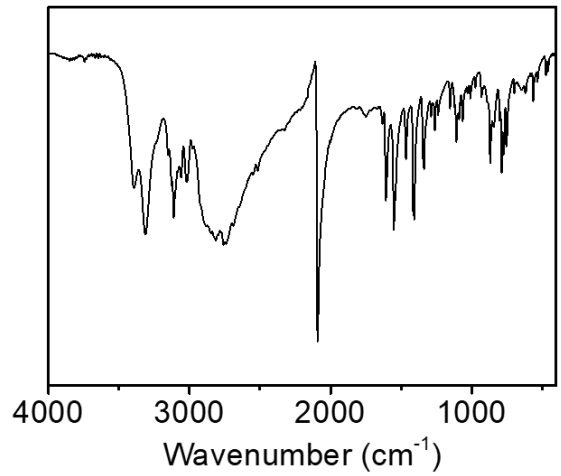

Figure 6.4.4. Infrared spectra of NCS.

Synthesis of NCSe: [Fe(*p*-Cl-3-bpp)$_2$](NCSe)$_2$

Ligand *p*-Cl-3-bpp (100 mg, 0.407 mmol) was suspended in hot ethanol (5 mL). To this solution, $FeCl_2$ (25.79 mg, 0.203 mmol) dissolved in 8 mL of hot water was added over the ethanolic ligand suspension. The addition of the iron salt led the dissolution of the ligand and caused a rapid formation of the complex with a color change to orange. Finally, a warm aqueous solution of KNCSe (58.64 mg, 0.407 mmol) in 8 mL of hot water was added over first solution rapidly. Solution was sealed and let crystallized at 4 °C overnight. Dark red-black crystals suitable for X-Ray diffraction was collected after 1 days.

IR: 3300 (m), 3109 (s), 3078 (s), 2856 (s), 2817 (s), 2097 (s), 2058 (s), 1608 (m), 1549 (m), 1403 (s), 1334 (m), 1109 (m), 784 (m), 771 (m), 750 (m)

Elemental analysis (%) calcd. For $C_{24}H_{18}Cl_2FeN_{12}OSe_2$ (775.88): C, 37.19; H, 2.34; N, 21.68; found: C, 36.18; H, 2.39; N, 21.58.

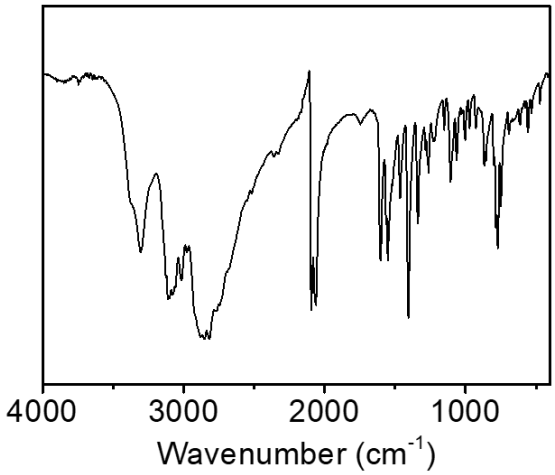

Figure 6.4.5. Infrared spectra of NCSe.

Synthesis of Br: [Fe(*p*-Cl-3-bpp)$_2$](Br)$_2$

Ligand *p*-Cl-3-bpp (100 mg, 0.407 mmol) was suspended in methanol (5 mL). To this solution, $Fe(ClO_4)_2 \cdot 6H_2O$ (73.65 mg, 0.203 mmol) dissolved in 8 mL of methanol was added over the methanolic ligand suspension. The addition of the iron salt led the dissolution of the ligand and cause a rapid formation of the complex, resulting in a color change to orange. A methanolic solution of KBr (145 mg, 1.221 mmol) was added dropwise, leading to the rapid formation of a white precipitate. The solution was stirred for 1 hour; the white solid was filtered off, and the solution was sealed and allowed to crystallize. Brown crystals suitable for X-Ray diffraction were collected after slow evaporation of the solvent.

Elemental analysis (%) calcd. For $C_{22}H_{22}Br_2Cl_2FeN_{13}O_3$ (757.90): C, 34.72; H, 2.91; N, 18.41; found: C, 34.76; H, 2.95; N, 18.47.

IR: 3440 (m), 3362 (m), 3313 (s), 3052 (n), 2930 (m), 1604 (s), 1564 (m), 1464 (w), 1405 (m), 1340 (w), 1266 (w), 1112 (w), 1067 (w), 1005 (w), 798 (m), 780 (m)

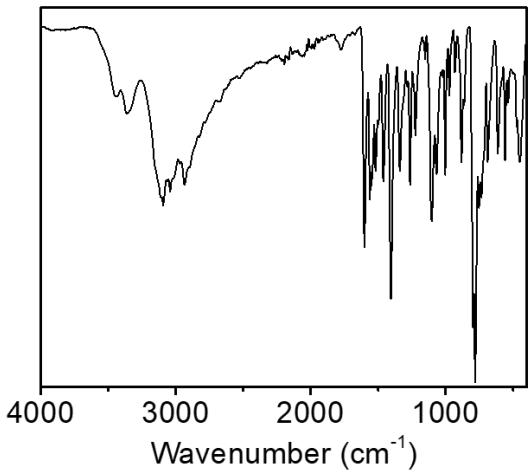

Figure 6.4.6. Infrared spectra of Br.

Synthesis of CF_3SO_3: [Fe(*p*-Cl-3-bpp)$_2$](CF_3SO_3)$_2$

Ligand *p*-Cl-3-bpp (100 mg, 0.407 mmol) was suspended in hot ethanol (5 mL). To this solution, $FeCl_2$ (25.79 mg, 0.203 mmol) dissolved in 8 mL of hot water was added over the ethanolic ligand suspension. The addition of the iron salt led the dissolution of the ligand and caused a rapid formation of the complex with a color change to orange. Finally, a warm aqueous solution of $NaCF_3SO_3$ (70 mg, 0.407 mmol) in 8 mL of hot water was added over first solution rapidly. Solution was sealed and let crystallized at 4 °C overnight. Dark red-black crystals suitable for X-Ray diffraction was collected after 1 days.

Elemental analysis (%) calcd for $C_{24}H_{16}Cl_2F_6FeN_{10}O_6S_2$ (843.93): C, 34.10; H, 1.91; N, 16.57; found: C, 34.06; H, 1.97; N, 16.64

IR: 3422 (s), 3144 (s), 1610 (m), 1566 (m), 1470 (w), 1409 (m), 1339 (w), 1291 (s), 1248 (s), 1221 (s), 1160 (s), 1017 (s), 788 (m), 774 (m), 634 (m)

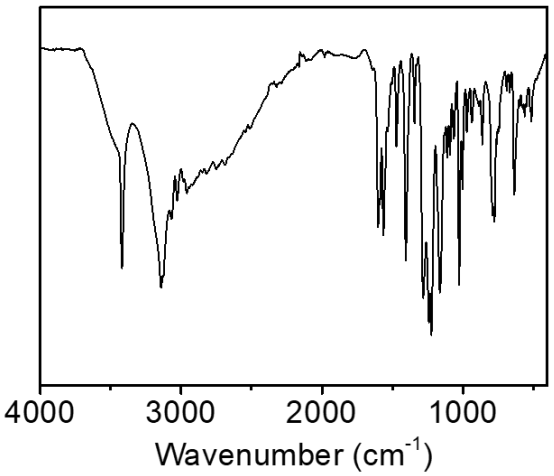

Figure 6.4.7. Infrared spectra of CF_3SO_3.

Synthesis of I: [Fe(*p*-Cl-3-bpp)$_2$](I)$_2$

Ligand *p*-Cl-3-bpp (100 mg, 0.407 mmol) was suspended in methanol (5 mL). To this solution, $Fe(ClO_4)_2 \cdot 6H_2O$ (73.65 mg, 0.203 mmol) dissolved in 8 mL of MeOH was added over the methanolic ligand suspension. The addition of the iron salt led the dissolution of the ligand and cause a rapid formation of the complex, resulting in a color change to orange. A methanolic solution of KI (202 mg, 1.221 mmol) was added dropwise, leading to the rapid formation of a white precipitate. The solution was stirred for 1 hour; the white solid was filtered off, and the solution was sealed and allowed to crystallize. Brown crystals suitable for X-Ray diffraction were collected after slow evaporation of the solvent.

Elemental analysis (%) calcd for $C_{22}H_{20}Cl_2F_6FeN_{10}O_2I_2$ (837.03): C, 31.57; H, 2.41; N, 16.73; found: C, 31.08; H, 2.42; N, 16.54

IR: 3449 (m), 3362 (s), 3121 (s), 3106 (s), 3043 (s), 2940 (s), 1605 (m), 1550 (w), 1414 (m), 1340 (w), 1098 (m), 862 (2), 788 (m)

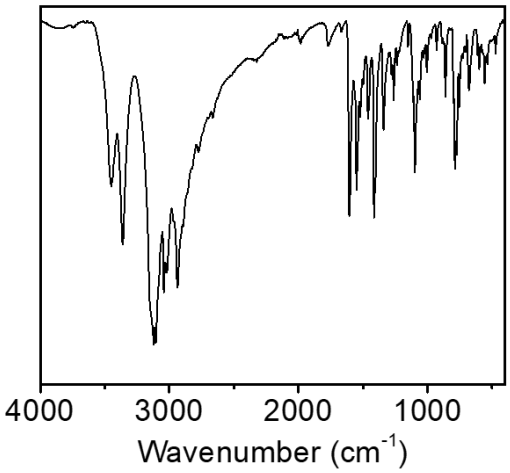

Figure 6.4.8. Infrared spectra of I.

6.4.2 Single Crystal X-Ray Diffraction (SCXRD)

Crystallographic data for all the complexes were deposited in the Cambridge Structural Database (CSD) with the following deposit numbers. All structures were resolved at 100 K unless otherwise specified. CCDC-2354940 for BF_4; CCDC-2354939 for BF_4 (300 K); CCDC-2354942 for PF_6; CCDC-2354941 for NO_3; CCDC-2354943 for NCS; CCDC-2354944 for NCSe; CCDC-2354945 for Br; CCDC-2354946 for I and CCDC-2354947 for CF_3SO_3.

Table 6.4.1. Crystallographic data and structure refinement of single crystal X-Ray analysis for complexes BF_4, NO_3, PF_6 and NCS.

	[Fe(*p*-3-bpp-Cl)$_2$](BF$_4$)$_2$	**[Fe(*p*-3-bpp-Cl)$_2$](NO$_3$)$_2$·2H$_2$O**	**[Fe(*p*-3-bpp-Cl)$_2$](PF$_6$)$_2$**	**[Fe(*p*-3-bpp-Cl)$_2$](NCS)$_2$·2H$_2$O**
Chemical Formula	$C_{22}H_{16}B_2Cl_2F_8FeN_{10}$	$C_{22}H_{20}Cl_2FeN_{12}O_8$	$C_{22}H_{26}Cl_2F_{12}FeN_{10}P_2$	$C_{24}H_{20}Cl_2FeN_{12}O_2S_2$
Size (mm^3)	0.24 x 0.26 x 0.12	0.010 x 0.132 x 0.254	0.018 x 0.044 x 0.154	0.044 x 0.125 x 0.162
Formula weight	720.82	707.25	837.14	699.39
Crystal system	Orthorhombic	Monoclinic	Orthorhombic	Orthorhombic
Space group	Pbca	$P2_1/n$	Pbca	Pbcn
a [Å]	18.8527(5)	9.1657(6)	19.2195(8)	18.9233(12)
b [Å]	16.5410(5)	16.6609(11)	16.7682(6)	9.7896(8)
c [Å]	17.9284(6)	18.9713(13)	18.4117(7)	16.1893(12)
α [°]	90	90	90	90
β [°]	90	98.984(3)	90	90
γ [°]	90	90	90	90
V [Å^3]	5590.8(3)	2861.5(3)	5933.7(4)	2999.1(4)
Z	8	4	8	4
Dx [mg/m^3]	1.713	1.642	1.874	1.549
Temperature [K]	100	100	100	100
Tmax/Tmin	0.825 / 0.909	0.9920 / 0.8260	0.9840 / 0.8730	0.9630 / 0.8720
Absorption coeff. [mm^{-1}]	0.820	0.784	0.909	0.867
F (000)	2880	1440	3328	1424
Θ range [°]	2.272 to 35.04	2.49 to 26.43	2.21 to 25.71	2.15 to 32.03
Reflections collected	12332	6168	279567	73542
Independent reflections	9863	5536	8837	5216
GOF on F2	1.036	1.172	1.037	1.047
Final R indices [I > 2σ(I)]	R1 = 0.0929, wR2 = 0.0843	R1 = 0.0777, wR2 = 0.1424	R1 = 0.0673, wR2 = 0.1089	R1 = 0.0320, wR2 = 0.0736
R indices (all data)	R1 = 0.0515, wR2 = 0.0353	R1 = 0.0906, wR2 = 0.1475	R1 = 0.1403, wR2 = 0.1340	R1 = 0.0444, wR2 = 0.0802

Table 6.4.2. Crystallographic data and structure refinement of single crystal X-Ray analysis for complexes NCSe, I_2, Br_2 and CF_3SO_3.

	[Fe(*p*-3-bpp-Cl)$_2$](NCSe)$_2$·2H$_2$O	[Fe(*p*-3-bpp-Cl)$_2$](I)$_2$·2H$_2$O	[Fe(*p*-3-bpp-Cl)$_2$](Br)$_2$·2H$_2$O·2MeOH	[Fe(*p*-3-bpp-Cl)$_2$](CF$_3$SO$_3$)$_2$
Chemical Formula	$C_{24}H_{20}Cl_2FeN_{12}O_2Se_2$	$C_{22}H_{20}Cl_2FeI_2N_{10}O_2$	$C_{24}H_{28}Br_2Cl_2FeN_{10}O_4$	$C_{24}H_{16}Cl_2F_6FeN_{10}O_6S_2$
Size (mm^3)	0.027 x 0.076 x 0.099	0.093 x 0.133 x 0.142	0.069 x 0.124 x 0.207	0.108 x 0.140 x 0.147
Formula weight (g/mol)	793.19	837.03	807.13	845.34
Crystal system	Triclinic	Orthorhombic	Monoclinic	Monoclinic
Space group	$P\bar{1}$	Pbcn	$P2_1$	$P2_1/c$
a [Å]	8.2010(4)	17.1487(7)	7.8994(4)	19.4493(9)
b [Å]	8.2106(4)	10.7985(5)	12.3214(6)	17.1429(8)
c [Å]	23.0226(10)	15.7349(6)	16.6339(8)	18.8862(9)
α [°]	98.1379(18)	90	90	90
β [°]	97.4108(19)	90	99.324(3)	93.284(2)
γ [°]	91.2722(18)	90	90	90
V [Å^3]	1520.51(12)	2913.8(2)	1597.61(14)	6286.6(5)
Z	2	4	2	8
Dx [mg/m^3]	1.732	1.908	1.678	1.786
Temperature [K]	100	100	100	100
Tmax/Tmin	0.9210 / 0.7480	0.7770 / 0.6870	0.8100 / 0.5580	0.9110 / 0.8820
Absortion coeff. [mm^{-1}]	3.111	2.860	3.188	0.878
F (000)	784	1616	808	3392
Θ range [°]	2.51 to 34.40	2.23 to 33.19	2.07 to 30.50	1.88 to 27.55
Reflections collected	114526	111092	45170	139579
Independent reflections	12764	5592	9727	20144
GOF on F2	1.026	1.120	1.028	1.049
Final R indices [I > 2σ(I)]	R1 = 0.0337, wR2 = 0.0812	R1 = 0.0272, wR2 = 0.0647	R1 = 0.0497, wR2 = 0.1102	R1 = 0.0517, wR2 = 0.1157
R indices (all data)	R1 = 0.0459, wR2 = 0.0867	R1 = 0.0366, wR2 = 0.0701	R1 = 0.0729, wR2 = 0.1199	R1 = 0.0706, wR2 = 0.1268

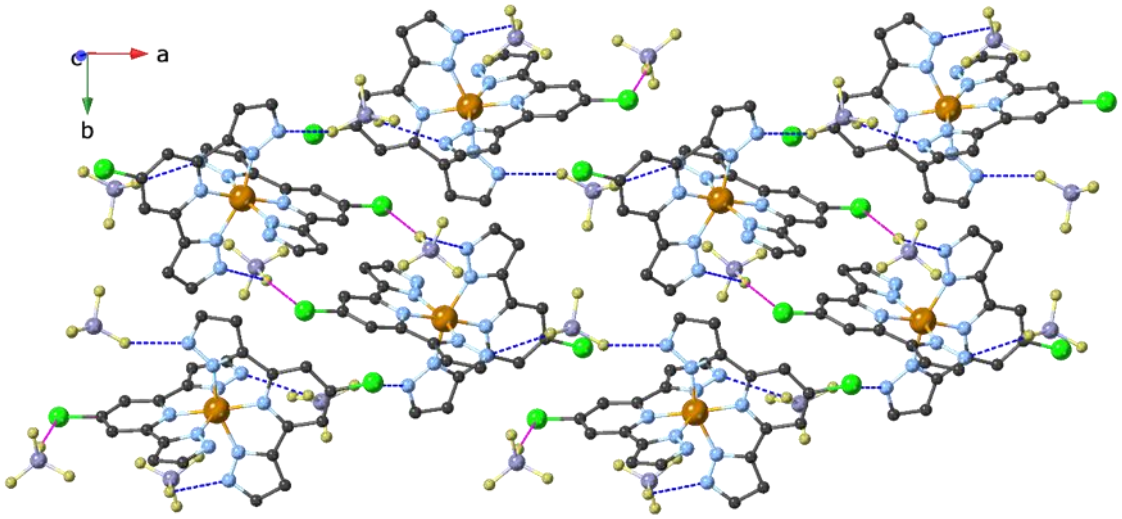

Figure 6.4.9. 3D packing of BF_4 through ab plane. Hydrogen bonds are depicted in dashed blue and halogen bond in dashed pink. Iron is clear brown, carbon is black, nitrogen is blue, chlorine is green, boron is grey, and fluorine is yellow.

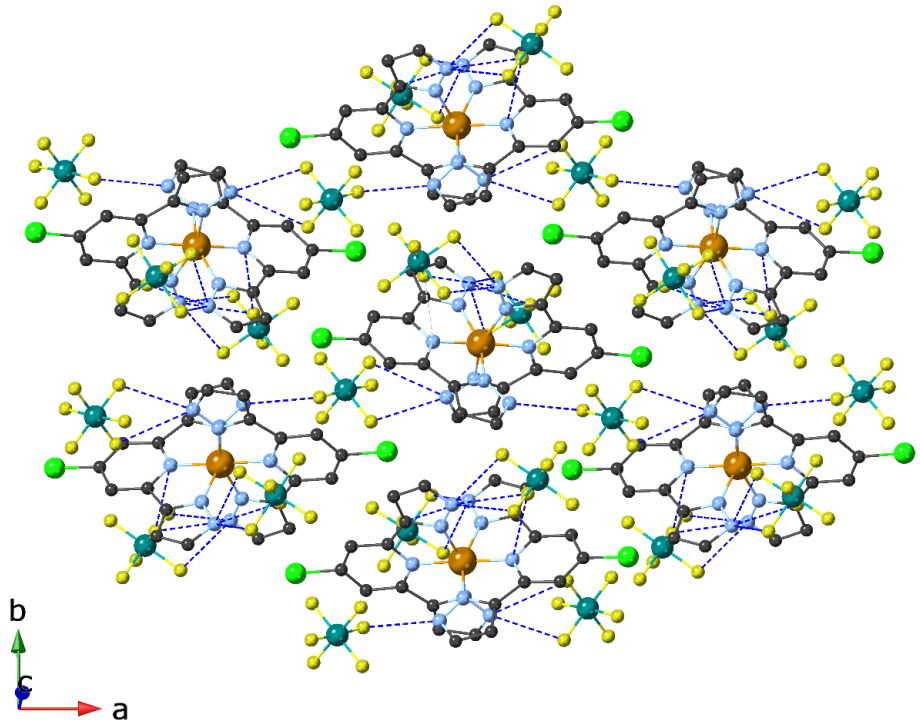

Figure 6.4.10. 3D packing of PF_6 through ab plane. Hydrogen bonds are depicted in dashed blue. Iron is clear brown, carbon is black, nitrogen is blue, chlorine is green, phosphorous is bluish-green and fluorine is yellow.

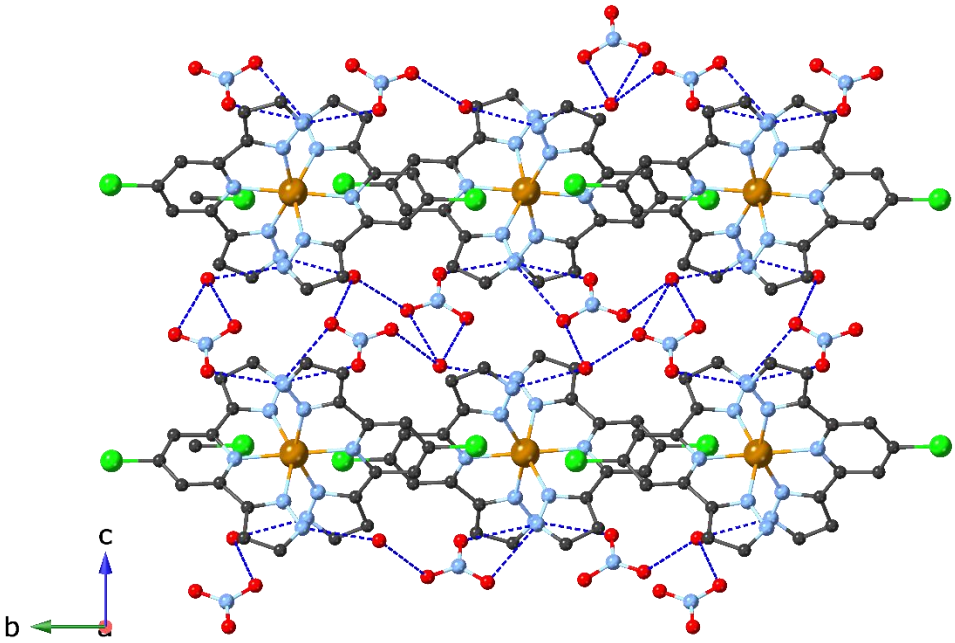

Figure 6.4.11. 3D packing of NO_3 through bc plane. Hydrogen bonds are depicted in dashed blue. Iron is clear brown, carbon is black, nitrogen is blue, chlorine is green, oxygen is red, and fluorine is yellow.

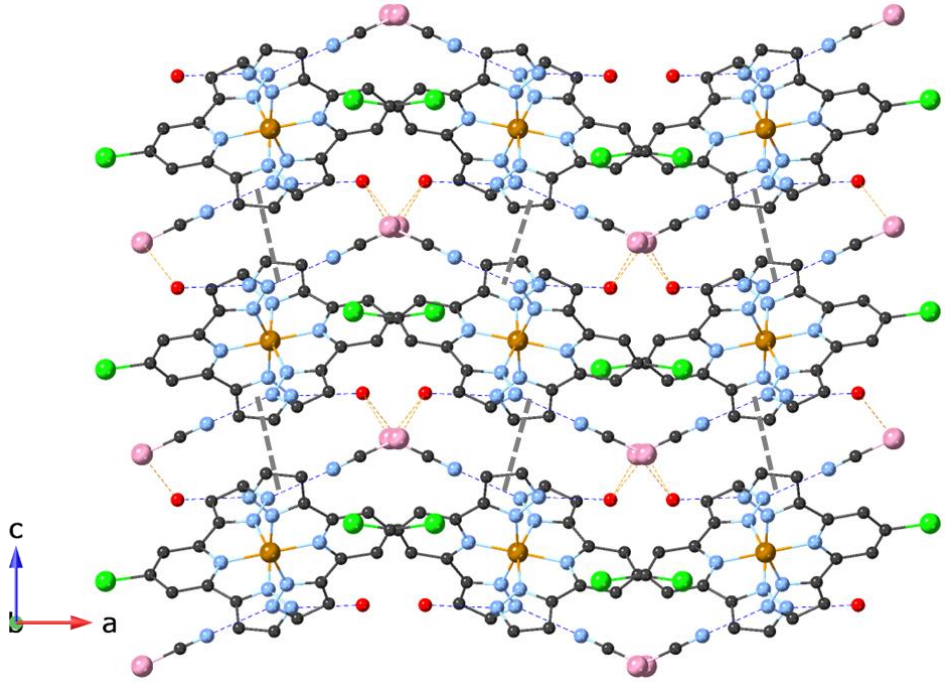

Figure 6.4.12. 3D packing of NCS through ac plane. Hydrogen bonds are depicted in dashed blue and S-O interaction as dashed orange line. π-π interactions are represented from centroid-centroid in dashed grey line. Iron is clear brown, carbon is black, nitrogen is blue, chlorine is green, oxygen is red, and sulfur is pale pink.

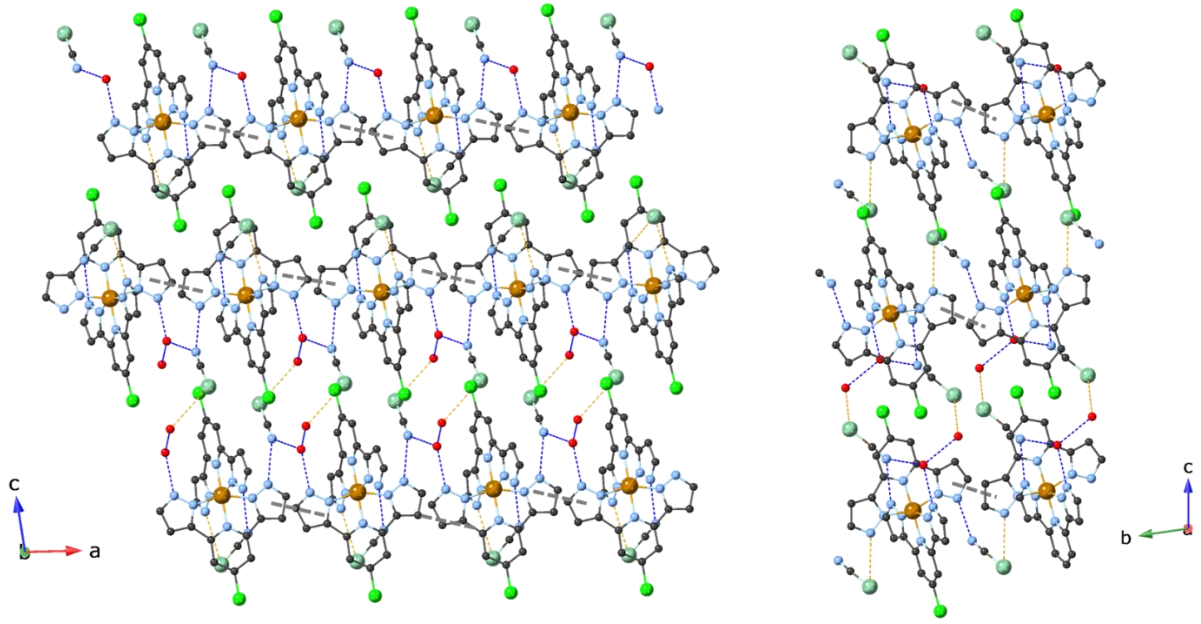

Figure 6.4.13. 3D packing of NCSe through ac and bc plane. Hydrogen bonds are depicted in dashed blue and Se-O interaction as dashed orange line. π-π interactions are represented from centroid-centroid in dashed grey line. Iron is clear brown, carbon is black, nitrogen is blue, chlorine is green, oxygen is red, and selenium is pale green.

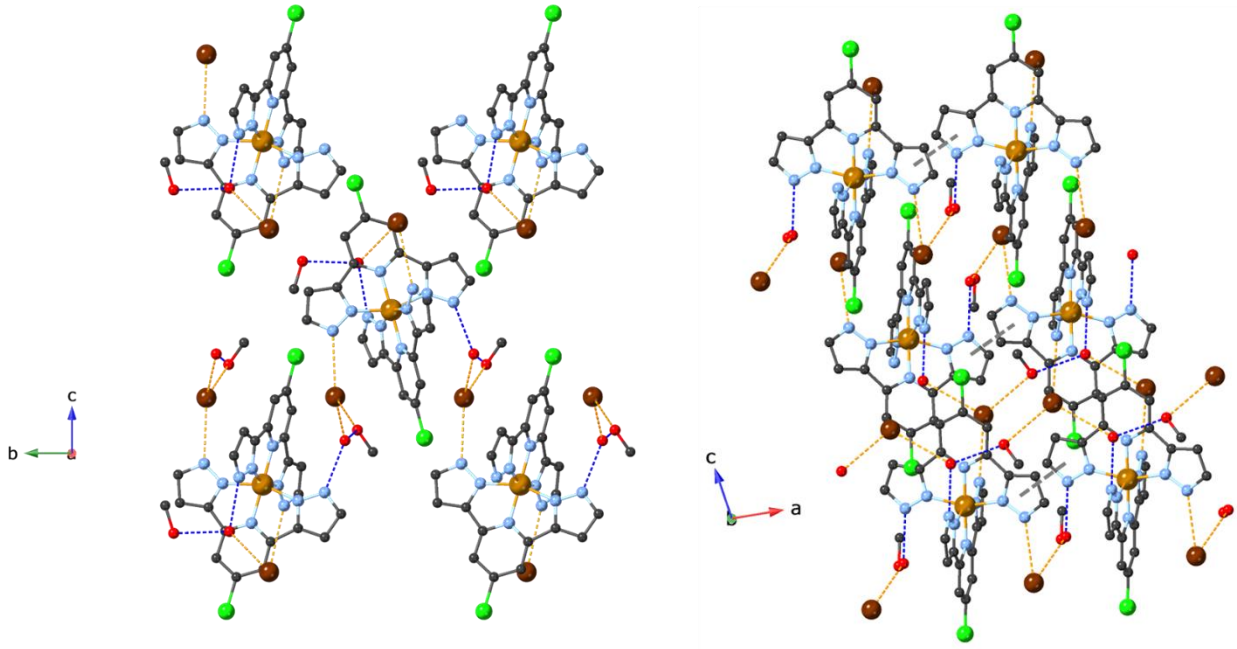

Figure 6.4.14. 3D packing of Br through bc and ac plane. Hydrogen bonds are depicted in dashed blue and Br-O interaction as dashed orange line. π-π interactions are represented from centroid-centroid in dashed grey line. Iron is clear brown, carbon is black, nitrogen is blue, bromine is brown, oxygen is red.

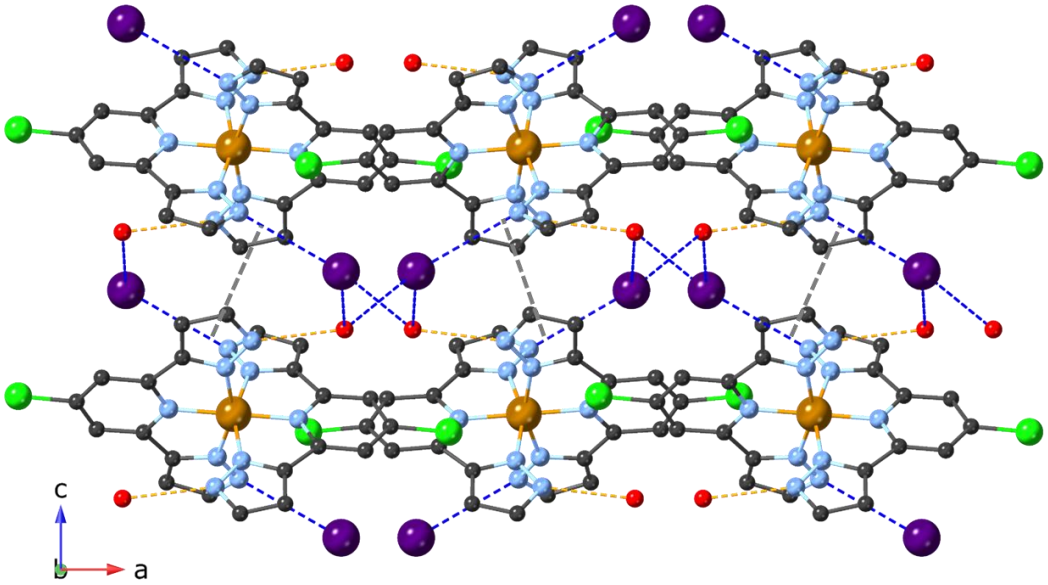

Figure 6.4.15. 3D packing of I through ac plane. Hydrogen bonds are depicted in dashed blue and I-O interaction as dashed orange line. π-π interactions are represented from centroid-centroid in dashed grey line. Iron is clear brown, carbon is black, nitrogen is blue, chlorine is green, oxygen is red, and iodine is purple.

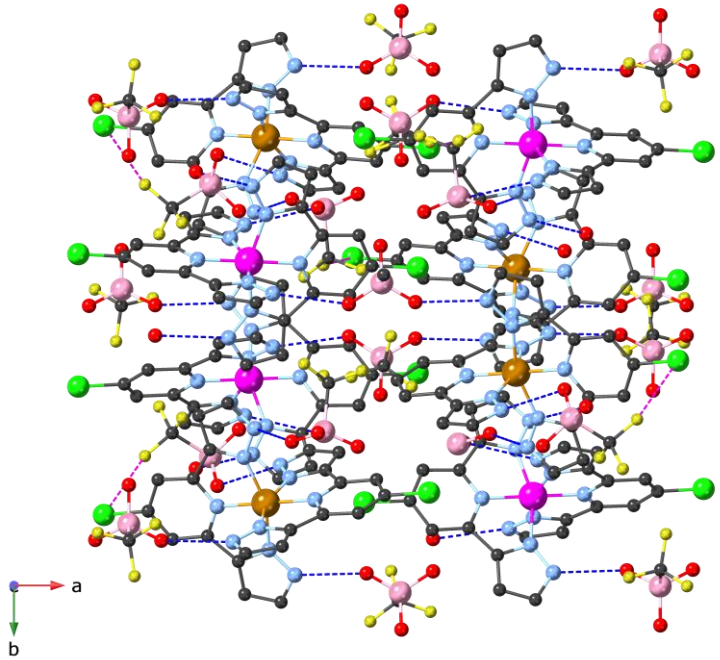

Figure 6.4.16. Packing of CF_3SO_3 through ab plane. Hydrogen bonds are depicted in dashed blue and Cl-F interaction as dashed pink line. Iron is clear brown (1) and violet (2), carbon is black, nitrogen is blue, chlorine is green, oxygen is red, fluorine is dark-yellow, and sulfur is light-pink.

Table 6.4.3. Fe-N bond lengths for all the compounds at 100 K.

	BF_4	PF_6	$(NO_3)_2 \cdot 2H_2O$	$(NCS)_2 \cdot 2H_2O$
Bond	**Lenght (Å)**	**Lenght (Å)**	**Lenght (Å)**	**Lenght (Å)**
Fe1-N1	1.926(1)	1.924(4)	2.140(5)	1.927(0)
Fe1-N12	1.978(1)	1.979(5)	2.200(5)	1.960(6)
Fe1-N22	1.968(1)	1.956(5)	2.201(5)	1.961(2)
Fe1-N42	1.961(1)	1.960(6)	2.189(6)	
Fe1-N31	1.929(1)	1.919(4)	2.146(5)	
Fe1-N52	1.969(1)	1.960(5)	2.193(6)	

Table 6.4.4. Fe-N bond lengths for all the compounds at 100 K.

	$(NCSe)_2 \cdot 2H_2O$	$(CF_3SO_3)_2$	$(Br)_2 \cdot 2H_2O \cdot 2(CH_4O)$	$(I)_2 \cdot 2H_2O$
Bond	**Lenght (Å)**	**Lenght (Å)**	**Lenght (Å)**	**Lenght (Å)**
Fe1-N1	1.929(6)	1.920(3)	1.929(5)	1.923(9)
Fe1-N12	1.980(3)	1.968(3)	1.968(5)	1.955(9)
Fe1-N22	1.968(1)	1.957(3)	1.968(5)	1.966(0)
Fe1-N42	1.980(1)	1.971(3)	1.978(5)	
Fe1-N31	1.930(8)	1.918(3)	1.931(5)	
Fe1-N52	1.964(2)	1.957(3)	1.978(5)	

Table 6.4.5. Main octahedral distortion parameters of all the compounds at 100 K.

Angle	BF_4	PF_6	NO_3	NCS	NCSe	CF_3SO_3		Br	I
						Fe1	Fe2		
θ (º)	90.07	88.04	83.21	93.67	90.69	90.92	92.84	97.90	98.79
Ψ (º)	158.34	158.12	100.94	158.28	157.83	158.81	158.56	158.13	158.51
ϕ (º)	176.97	178.09	169.91	178.60	177.22	178.48	178.11	178.71	178.36
Θ (º)	316.76	313.82	520.37	314.35	322.54	300.44	308.78	320.59	315.51
Σ (º)	94.79	95.85	155.74	96.59	97.21	92.48	92.63	101.21	99.16

6.4.3 Thermogravimetric analysis (TGA)

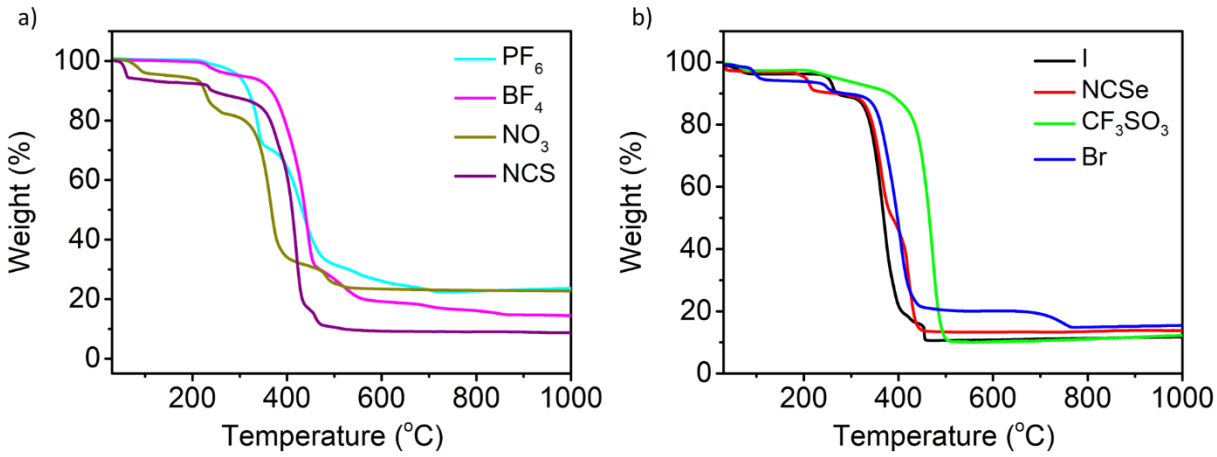

Figure 6.4.17. TGA measurements at 4 °C/min for all complexes under air conditions in the range of 40-1000 °C.

6.4.4 Variable-Temperature Raman Spectroscopy

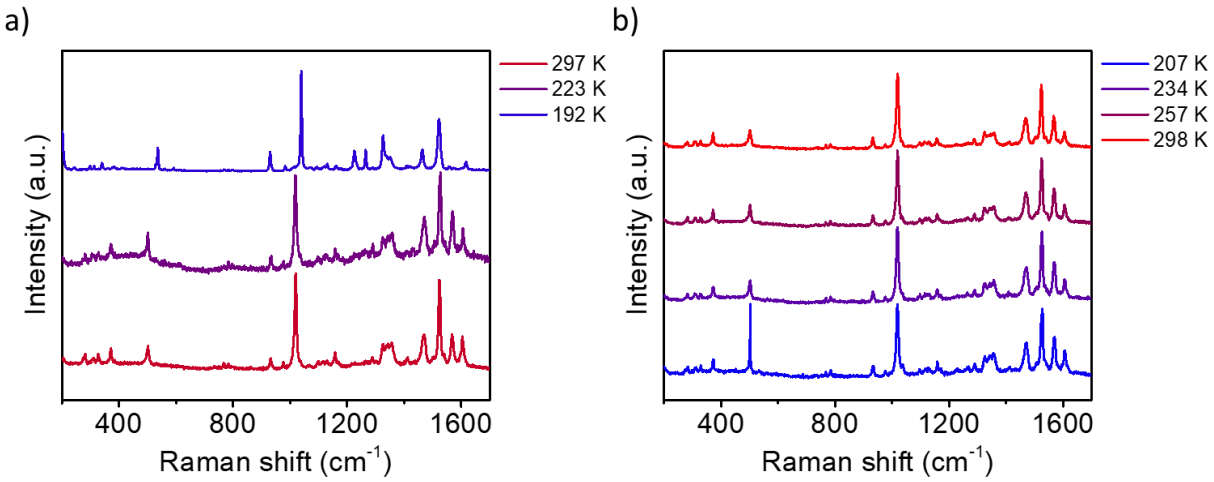

Figure 6.4.18. Variable-Temperature Raman Spectra for BF_4 on cooling (a) and heating (b) mode. Sequence was (K): 297-223-192-207-234-257-298 (on a cooling/heating rate of 4 K·min^{-1}).

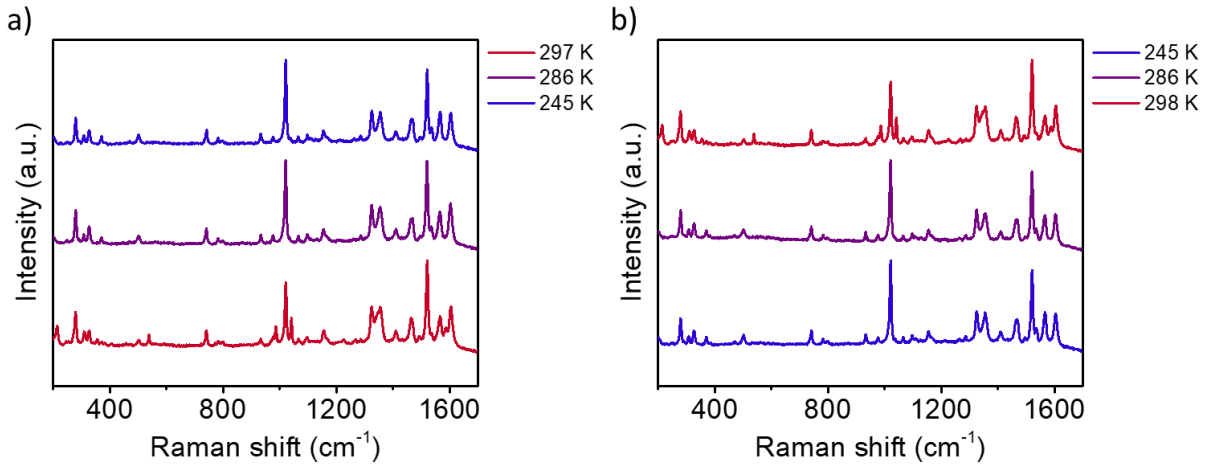

Figure 6.4.19. Variable-Temperature Raman Spectra for PF_6 on cooling (a) and heating (b) mode. Sequence was (K): 297-286-245-286-298 (on a cooling/heating rate of 4 K·min^{-1}).

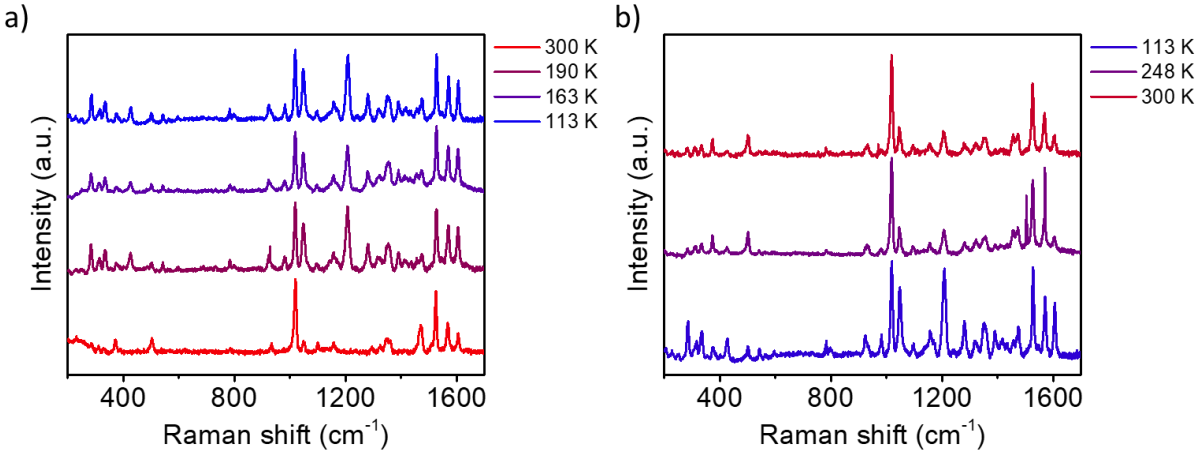

Figure 6.4.20. Variable-Temperature Raman Spectra for NO_3 on cooling (a) and heating (b) mode. Sequence was (K): 300-190-163-113-248-300 (on a cooling/heating rate of 4 K·min^{-1}).

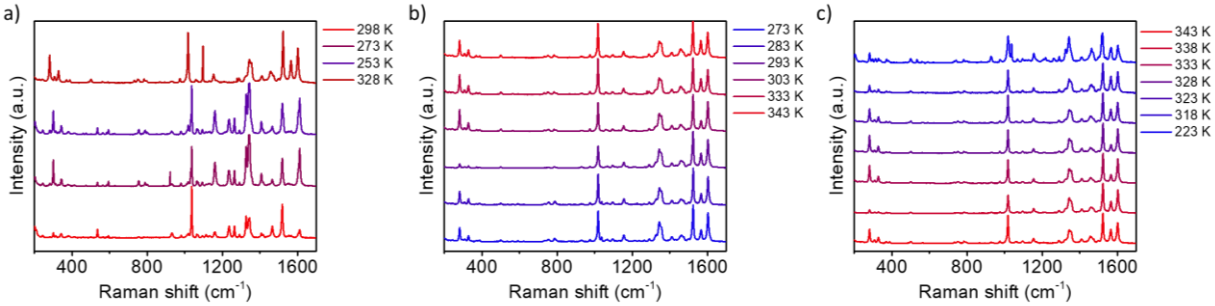

Figure 6.4.21. Variable-Temperature Raman Spectra for NCS on cooling (a), heating (b) and cooling (c) mode. Sequence was (K): 298-273-253-328(dehydration)-248-300 (on a cooling/heating rate of 4 K·min^{-1}).

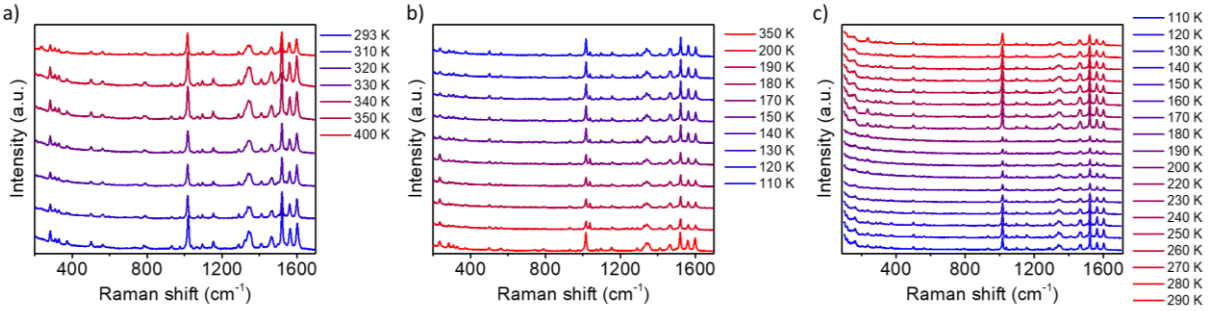

Figure 6.4.22. Variable-Temperature Raman Spectra for NCSe on heating (a), cooling (b) and heating (c) mode. Sequence was (K): 293-310-320-330-340-350-400-350-200. 200 to 110 and 110 to 290 K in steps of 10 K (on a cooling/heating rate of 4 K·min^{-1}).

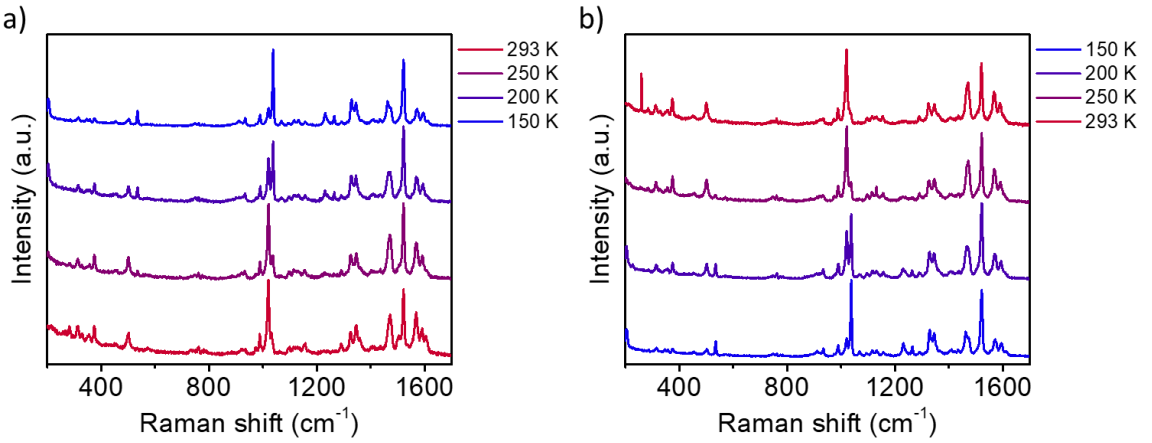

Figure 6.4.23. Variable-Temperature Raman Spectra for CF_3SO_3 on cooling (a) and heating (b) mode. Sequence was (K): 293-250-200-150-200-250-293 (on a cooling/heating rate of 4 K·min^{-1}).

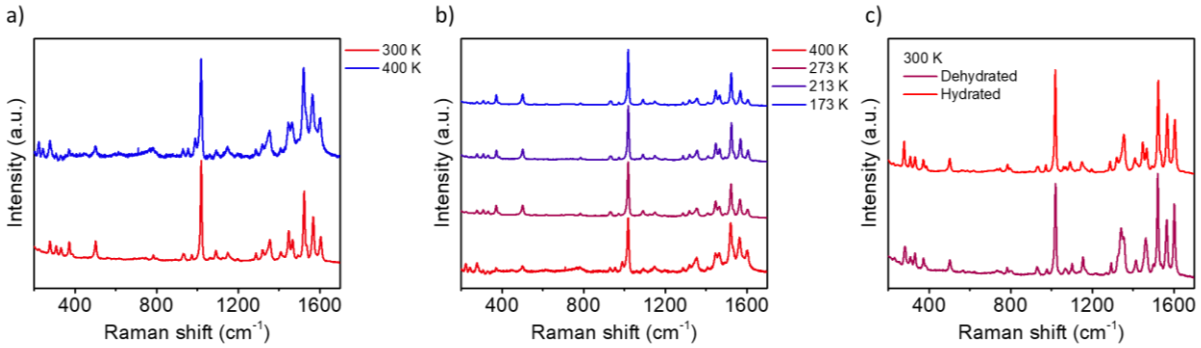

Figure 6.4.24. Variable-Temperature Raman Spectra for Br on heating (a) and cooling (b) mode. Sequence was (K): 300-400-273-213-173 (on a cooling/heating rate of 4 K·min^{-1}). c) Partially dehydration of the sample led to a different color of the sample, one spectrum of each zone at 300 K was recorded to illustrate differences.

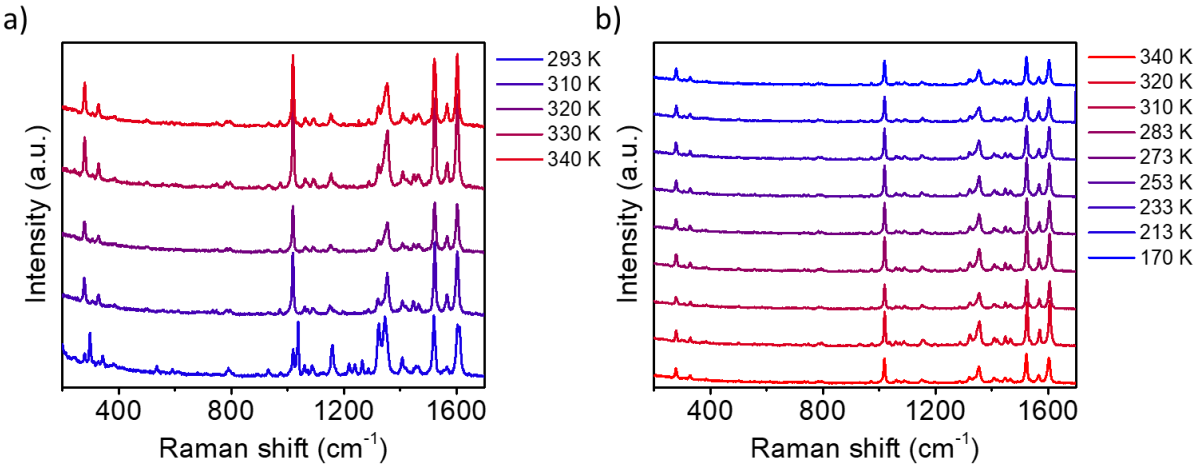

Figure 6.4.25. Variable-Temperature Raman Spectra for I on heating (a) and cooling (b) mode. Sequence was (K): 293-310-320-330-340-320-310-283-273-253-233-213-170 (on a cooling/heating rate of 4 K·min^{-1}).

6.4.5 Light-Induced Excited Spin State Trapping (LIESST)

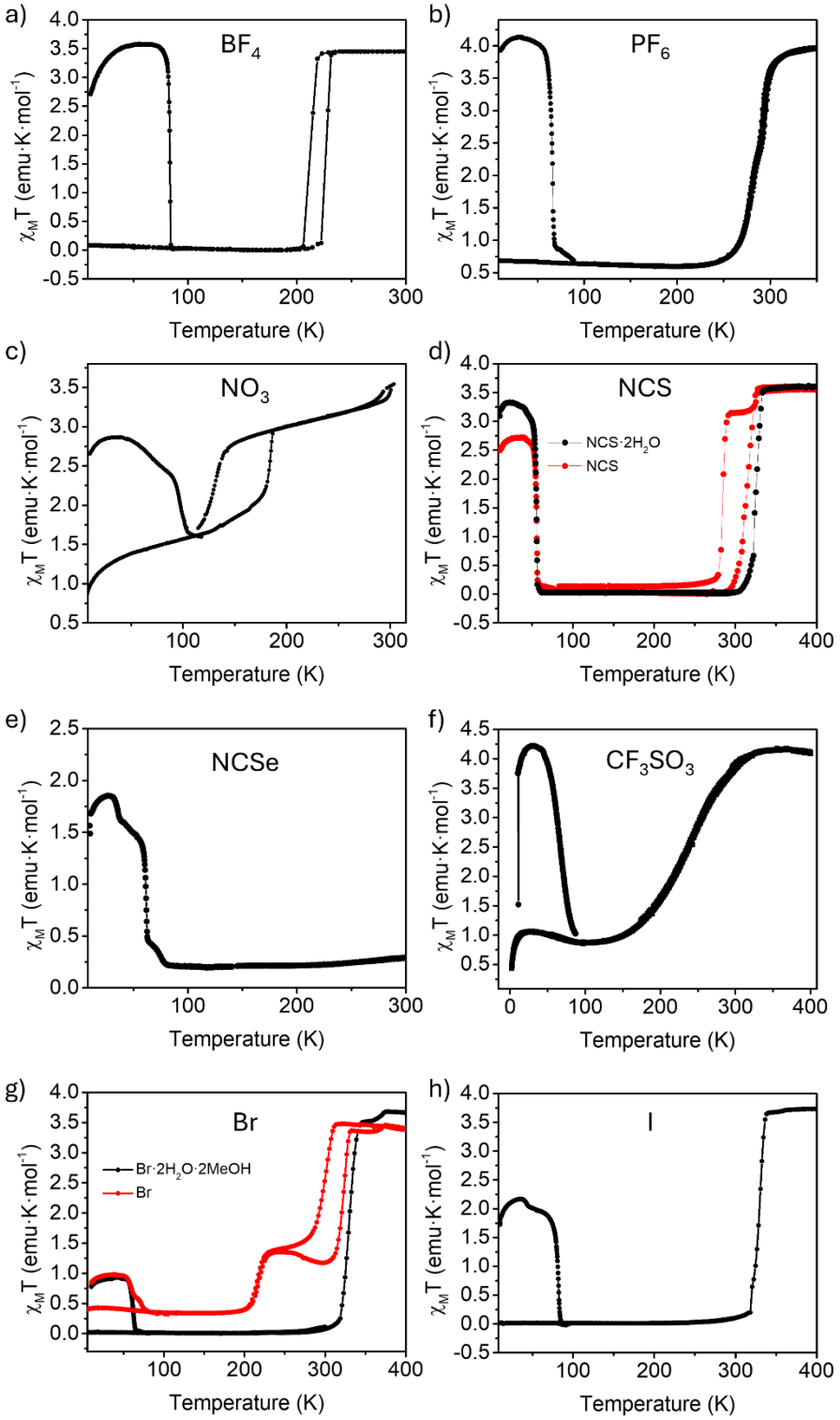

Figure 6.4.26. Temperature dependence $\chi_M T$ for all complexes under irradiation at 10 K, followed by subsequent heating-cooling in the dark. For both NCS and Br, both hydrated and anhydrous forms were recorded.

6.4.6 Differential Scanning Calorimetry (DSC)

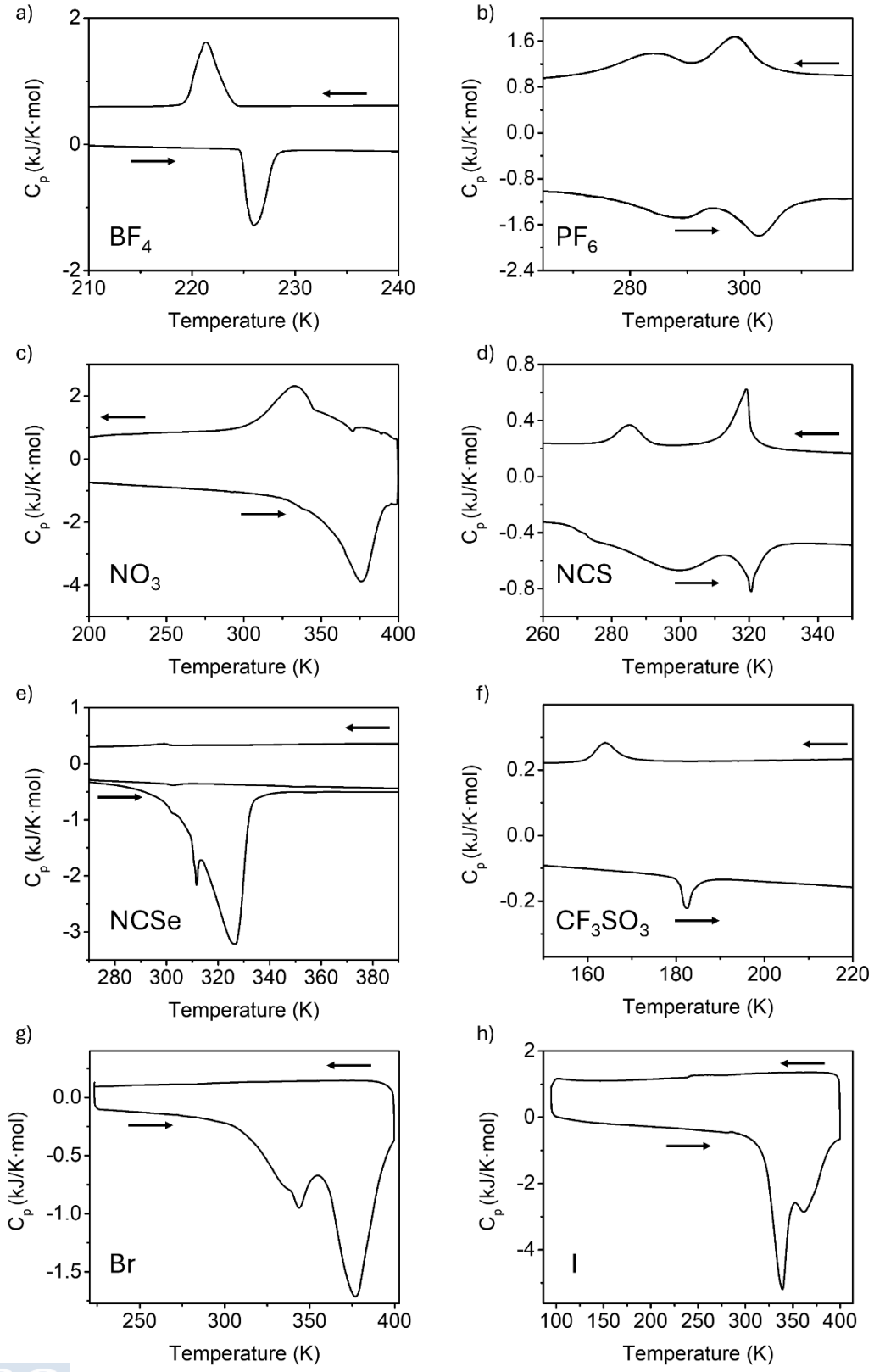

Figure 6.4.27. DSC for all complexes. Measurements were performed on first heating and then cooling at 4 °C/min. Arrows indicate the direction of the experiment. In some cases, only dehydration was observed.

6.5 Integrating Bistable Behavior into 2D Carbon Structures

6.5.1 Synthesis of the ligands

6.5.1.1 Carboxylic acid derivatives

Synthesis of 2,6-di(1H-pyrazol-1-yl)isonicotinic acid (1-bpp-COOH)

To a suspension of NaH (60% in mineral oil) (1.25 g, 31.2 mmol, 6.0 eq.) in 40 mL of anhydrous DMF was added a solution of pyrazole (1.77 g, 21.0 mmol, 5.0 eq.) in 10 mL of anhydrous DMF at room temperature under inert conditions. The resulting suspension was heated up to 60 °C for 60 min and 2,6-dichloro-isoniconic acid (1.01 g, 5.2 mmol, 1.0 eq.) was added in one portion. The brown mixture was then heated up to 150 °C under argon overnight. DMF was removed at low pressure and the brownish solid was dissolved in 20 mL of DCM, 100 mL of hexane were added, and the insoluble brownish impurities were filtered off while the clear solution was evaporated to afford the pure product (1.10 g, 83% yield).

^{1}H NMR (300 MHz, DMSO-d6, δ): 8.90 (s, 1H), 8.89 (s, 1H), 8.18 (d, 3J = 2.3 Hz, 2H), 7.85 (d, J = 1.0 Hz, 2H), 6.60 (dd, J = 2.5, 1.7 Hz, 2H).

^{13}C NMR (75 MHz, DMSO-d6, δ): 166.33 (C), 155.01 (C), 149.53 (C), 142.32 (CH), 127.90 (CH), 108.84 (CH), 108.09 (CH).

HRMS (ESI) m/z: $[M + H]^+$ calcd. for $[C_{12}H_{10}N_5O_2]^+$ 256.0829, found 256.0879.

Synthesis of 2,6-di(1H-pyrazol-3-yl)isonicotinic acid (3-bpp-COOH)

A dry 500 mL round-bottom flask under Ar atmosphere was charged with 1-(Tetrahydro-pyran-2-yl)-5-(4,4,5,5-tetramethyl-[1,3,2]dioxaborolan-2-yl)-1H-pyrazole (5.01 g, 17.78 mmol, 2.50 eq.), 2,6-dichloroisonicotinic acid (2.00 g, 7.11 mmol, 1.0 eq.), K_2CO_3 (3.90 g, 28.4 mmol, 4.0 eq.), $[Pd(PPh_3)_4]$ (820 mg, 0.71 mmol, 0.1 eq.) in 250 mL of dry THF and the mixture was heated at 80 °C. After 24 hours the reaction was quenched with 200 mL of brine and extracted with diethyl ether (3 × 100 mL). The combined organic layers were separated, dried over Na_2SO_4 and the solvent was removed under vacuum to give the desired THP-protected compound as a brownish oil. (1.68 g, 55% yield) .

The oil was diluted in a methanol (20 mL) hexane (20 mL) mixture and a few drops of concentrated hydrochloric acid were added under stirring. The reaction was stirred for 24 hours at room temperature before being separated and the methanol layer evaporated to leave a yellowish sticky solid. This solid was sonicated in diethyl ether and a powdered yellow solid appeared. This solid was washed with $CHCl_3$ to give the target product as an off-white precipitate. (980 mg, 54% yield).

^{1}H NMR (300 MHz, DMSO-d6, δ): 8.24 (s, 2H), 7.80 (d, J = 2.2 Hz, 2H), 7.09 (d, J = 2.2 Hz, 2H).

^{13}C NMR (75 MHz, DMSO-d6, δ): 166.62 (C), 151.89 (C), 140.52 (C), 134.02 (CH), 117.30 (CH), 105.66 (CH), 104.52 (CH).

HRMS (ESI) m/z: $[M + H]^+$ calcd. for $[C_{12}H_{10}N_5O_2]^+$ 256.0829, found 256.0886.

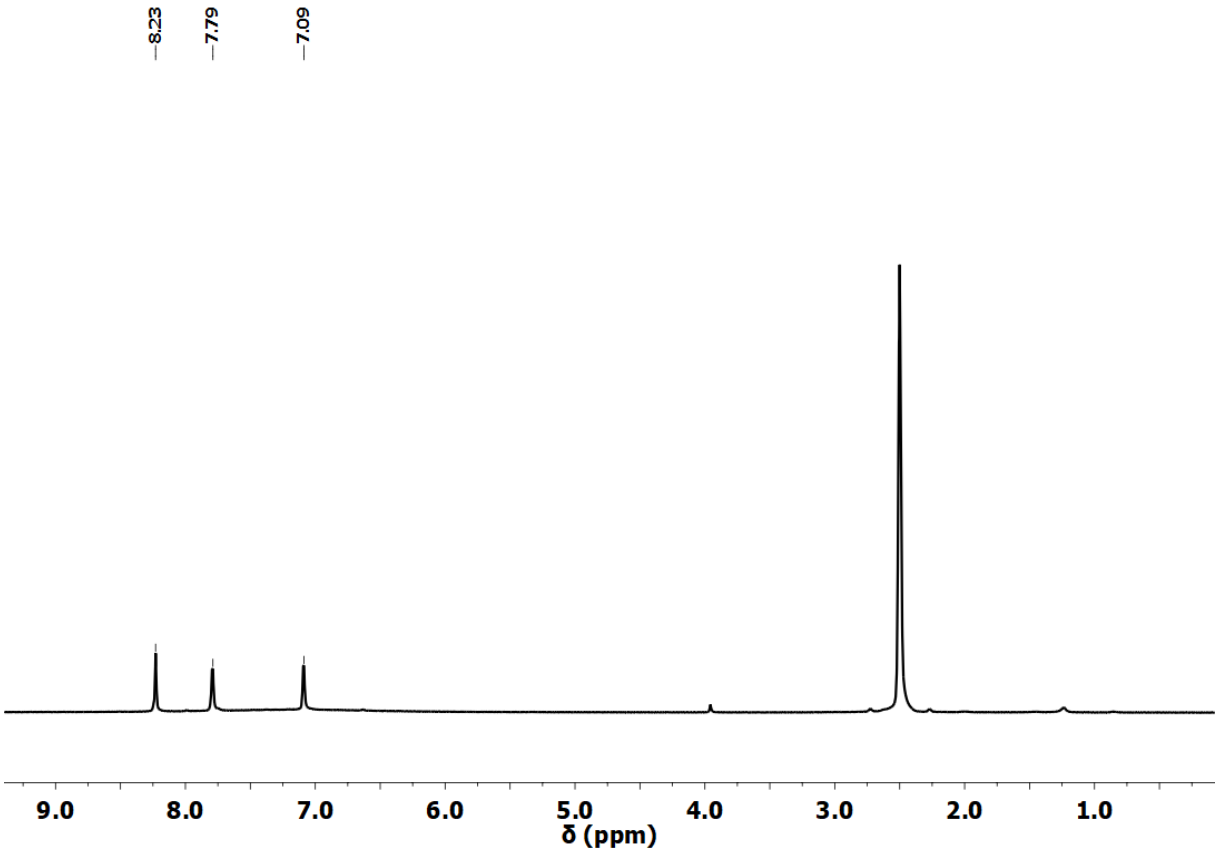

Figure 6.5.1. ^{1}H NMR spectrum of 2,6-di(1H-pyrazol-3-yl)isonicotinic acid (3-bpp-COOH).

6.5.1.2 Amine derivative ligands

Synthesis of 4-((2,6-di(1H-pyrazol-1-yl)pyridin-4-yl)ethynyl)aniline (1-bpp-L-NH2)

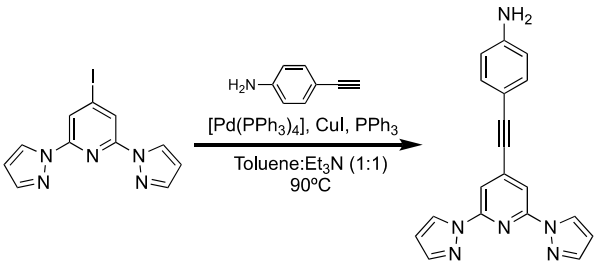

A dry 100 mL Schlenk flask under Ar atmosphere, was charged with 4-iodo-2,6-di(1H-pyrazol-1-yl)pyridine (1.34 g, 3.97 mmol, 1.0 eq.), 4-Ethynylaniline (512 mg, 4.37 mmol, 1.1 eq.) CuI (30.0 mg, 0.159 mmol, 0.04 eq.), $[Pd(PPh_3)_4]$ (253.2 mg, 0.079 mmol, 0.02 eq.) and PPh_3 (104.0 mg, 0.40 mmol, 0.1 eq.) in 20 mL of dry Et_3N and 20 mL of dry toluene and the mixture was stirred at 80 °C for 48 h. The reaction mixture was left to reach RT, poured into a solution of $(NH_4)Cl$ (sat) stirred for 30 min. The aqueous layer was extracted with ethyl acetate (3 x 30 mL). The combined organic layers were washed with brine (80 mL) and dried with $MgSO_4$, after filtration the solvent was removed under vacuum to afford the desired compound as an orange solid without further purification (1.18 g, 91%).

^{1}H NMR (300 MHz, DMSO-d^{6}): δ(ppm) 8.77 (d, ^{3}J = 2.5 Hz, 2H), 7.76 (d, ^{4}J = 0.9 Hz, 2H), 7.02 (s, 2H), 6.72 (br, 2H), 6.72 (br, 2H), 6.53 (m, 2H).

^{13}C NMR (75 MHz, DMSO-d^{6}): 158.84 (C), 150.40 (C), 141.68 (CH), 127.58 (CH), 107.44 (CH), 93.29 (CH).

MS-ESI-TOF: m/z calculated for $[C_{11}H_{11}N_6]^+$ 326.36, found 326.25.

Synthesis of 4-bromo-2,6-bis(1-(tetrahydro-2H-pyran-2-yl)-1H-pyrazol-3-yl)pyridine

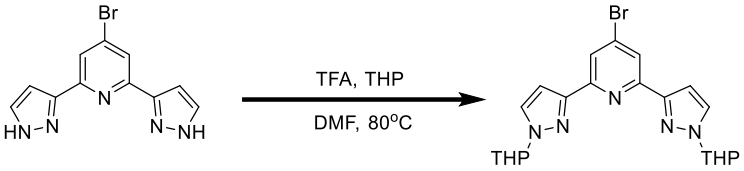

An oven dried 50 mL Schlenk flask with a stir bar was charged with 4-bromo-2,6-di(1H-pyrazol-3-yl) (1 g, 3.44 mmol, 1 eq.) and trifluoroacetic acid dropwise (11.5 µl, 0.344 mmol, 0.1 eq.) under Ar atmosphere. 50 mL of dry DMF was added and the mixture was let to stir during 5 min. Finally, 3,4-dihydro-2H-pyran (0.937 mL, 10.32 mmol, 3 eq.) and the mixture was set to stirring at 80 °C during 12h.

After 12 h, solvent was evaporated, and 30 mL of DI water was added. Mixture was neutralized with NaOH 1M until pH 7 and extracted with chloroform (3 x 30 mL). Organic phase was separated, dried over sodium sulfate and solvent was removed under reduced pressure. The product was purified by column chromatography in hexane:ethyl acetate to obtain white solid with 97% of yield.

^{1}H NMR (500 MHz, Chloroform-d) δ 8.12 (s, 2H), 7.62 (d, J = 2.5 Hz, 2H), 7.03 (d, J = 2.5 Hz, 2H), 5.39 (dd, J = 9.7, 2.6 Hz, 2H), 4.06 (m, 2H), 3.69 (td, J = 11.1, 2.9 Hz, 2H), 2.16 (m, 2H), 2.06 (m, 4H), 1.68 (ddd, J = 12.2, 9.1, 3.3 Hz, 4H), 1.59 (tt, J = 9.6, 2.7 Hz, 2H).

^{13}C NMR (126 MHz, Chloroform-d): δ 153.25 (C), 151.48 (C), 133.79 (C), 129.50 (CH), 122.02 (CH), 105.82 (CH), 88.28 (CH), 68.18 (CH_2), 31.00 (CH_2), 25.33 (CH_2), 22.75 (CH_2).

MS (ESI) *m/z*: [M+H]$^{+}$ calcd for $C_{21}H_{24}BrN_5O_2$ 457.11; found: 458.11.

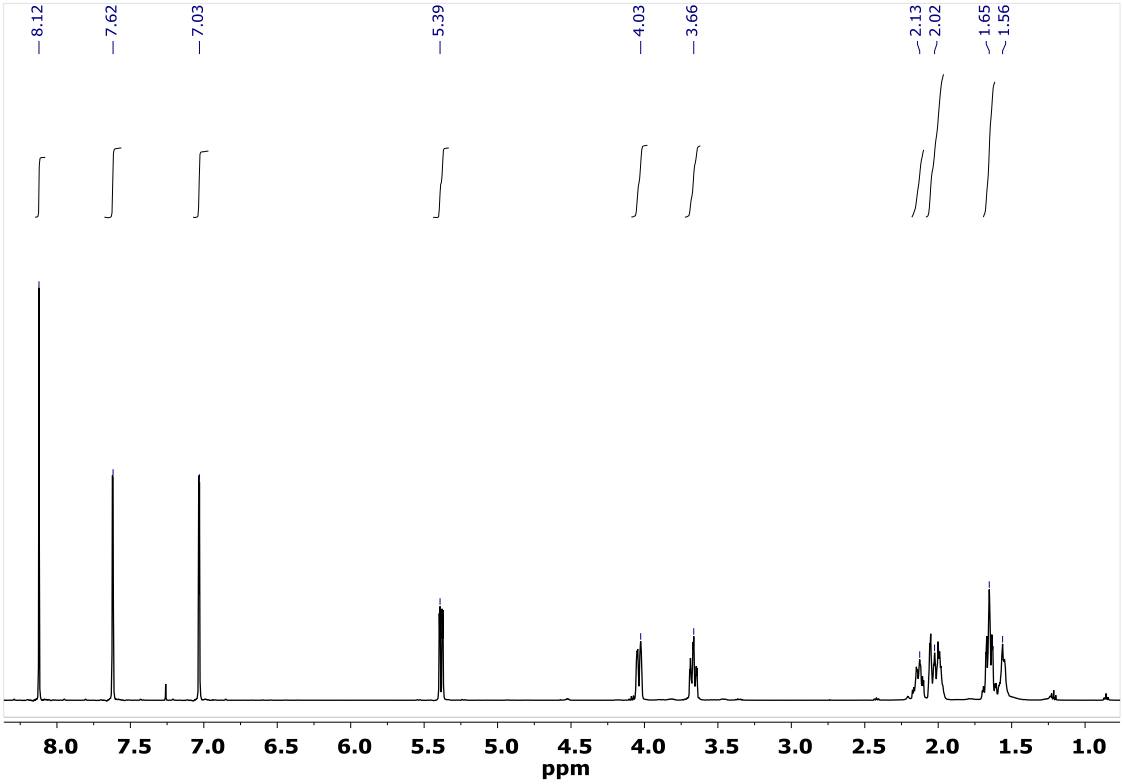

Figure 6.5.2. ^{1}H NMR spectrum of 4-bromo-2,6-bis(1-(tetrahydro-2H-pyran-2-yl)-1H-pyrazol-3-yl)pyridine.

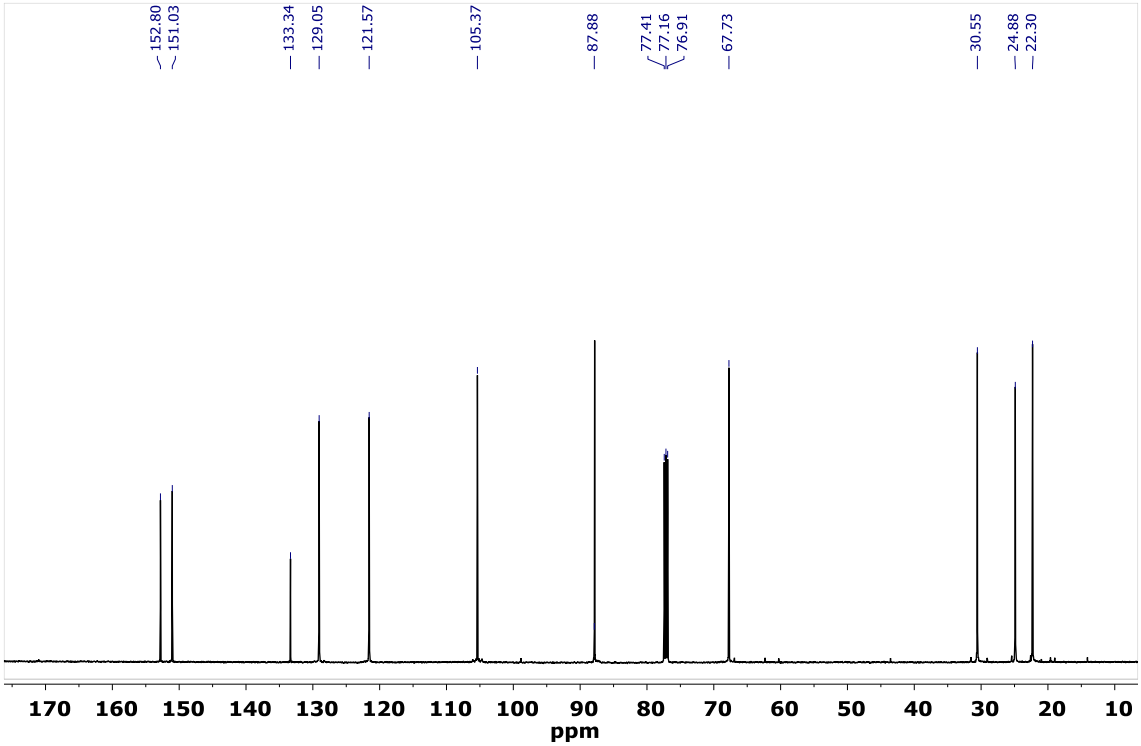

Figure 6.5.3. ^{13}C NMR spectrum of 4-bromo-2,6-bis(1-(tetrahydro-2H-pyran-2-yl)-1H-pyrazol-3-yl)pyridine.

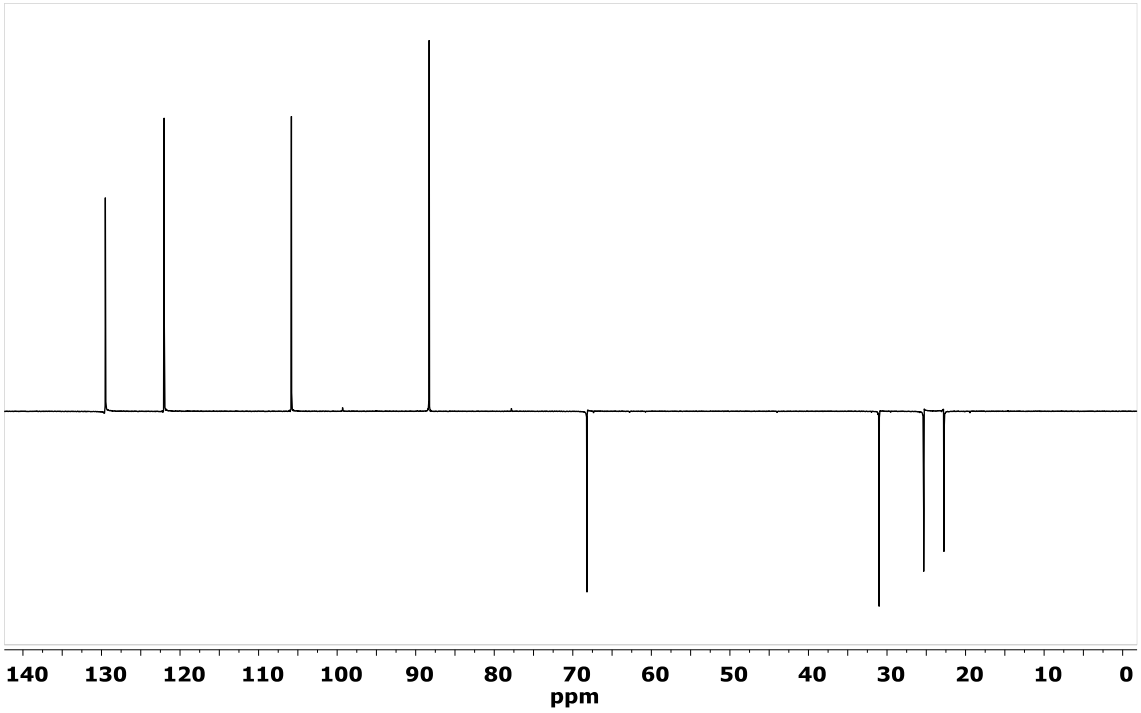

Figure 6.5.4. DEPT-135 of 4-bromo-2,6-bis(1-(tetrahydro-2H-pyran-2-yl)-1H-pyrazol-3-yl)pyridine.

Synthesis of 4-((2,6-bis(1-(tetrahydro-2H-pyran-2-yl)-1H-pyrazol-3-yl)pyridine-4-yl)ethynyl)aniline (3-bpp-THP-L-NH2)

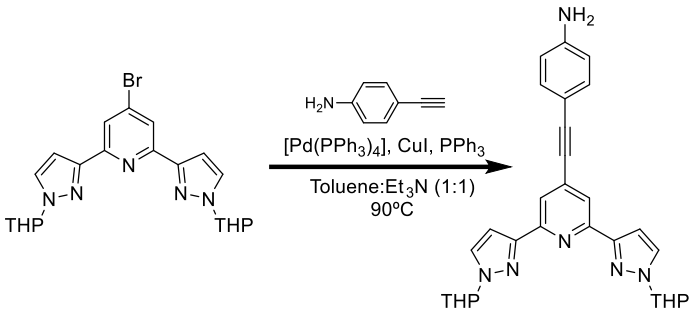

A dry 100 mL Schlenk flask under Ar atmosphere, was charged with 4-bromo-2,6-di(1-THP-pyrazol-1-yl)pyridine (1.69 g, 3.68 mmol, 1.0 eq.), 4-Ethynylaniline (517.0 mg, 4.41 mmol, 1.2 eq.), CuI (29.0 mg, 0.147 mmol, 0.04 eq.), [$Pd(PPh_3)_4$] (85.0 mg, 0.074 mmol, 0.02 eq.) and PPh_3 (96.0 mg, 0.368 mmol, 0.1 eq.) in 10 mL of dry Et_3N and 10 mL of dry toluene and the mixture was stirred at 80 °C for 48 h. The reaction mixture was left to reach RT, poured into a solution of $(NH_4)Cl$ (sat) stirred for 30 min. The aqueous layer was extracted with ethyl acetate (3 x 30 mL). The combined organic layers were washed with brine (80 mL) and dried with $MgSO_4$, after filtration the solvent was removed under vacuum. Product was obtained after to afford the desired compound as an orange solid without further purification (1.58 g, 87%).

^{1}H NMR (500 MHz, Chloroform-*d*) δ 8.02 (d, *J* = 1.1 Hz, 2H), 7.66 (d, *J* = 2.3 Hz, 2H), 7.35 (d, *J* = 8.3 Hz, 2H), 7.07 (dd, *J* = 2.5, 1.0 Hz, 2H), 6.64 (d, *J* = 8.3 Hz, 2H), 5.46 (dd, *J* = 9.6, 2.7 Hz, 2H), 4.11 (m, 2H), 3.73 (td, *J* = 11.1, 2.9 Hz, 2H), 2.19 (ddt, *J* = 13.4, 9.6, 4.0 Hz, 2H), 2.09 (m, 4H), 1.72 (m, 4H), 1.61 (m, 2H).

^{13}C NMR (126 MHz, $CDCl_3$) δ 152.33 (C), 152.11 (C), 147.68 (C), 133.81, 133.31 (C), 132.81 (CH), 129.22 (CH), 120.78 (CH), 115.11 (CH), 112.25 (C), 105.70 (CH), 94.68 (C), 88.30 (CH), 86.27 (C), 68.16 (CH_2), 31.10 (CH_2), 25.40 (CH_2), 22.81 (CH_2).

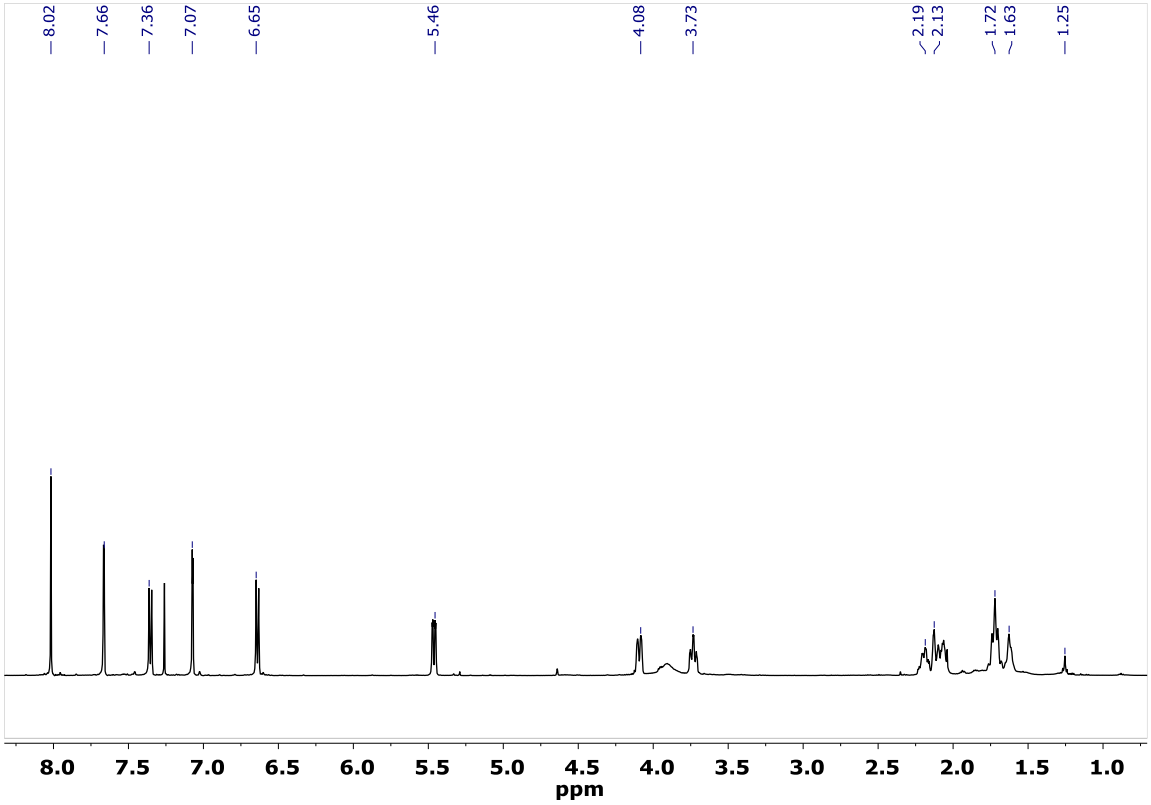

Figure 6.5.5. ^{1}H NMR spectrum of 4-((2,6-bis(1-(tetrahydro-2H-pyran-2-yl)-1H-pyrazol-3-yl)pyridine-4-yl)ethynyl)aniline (3-bpp-THP-L-NH2).

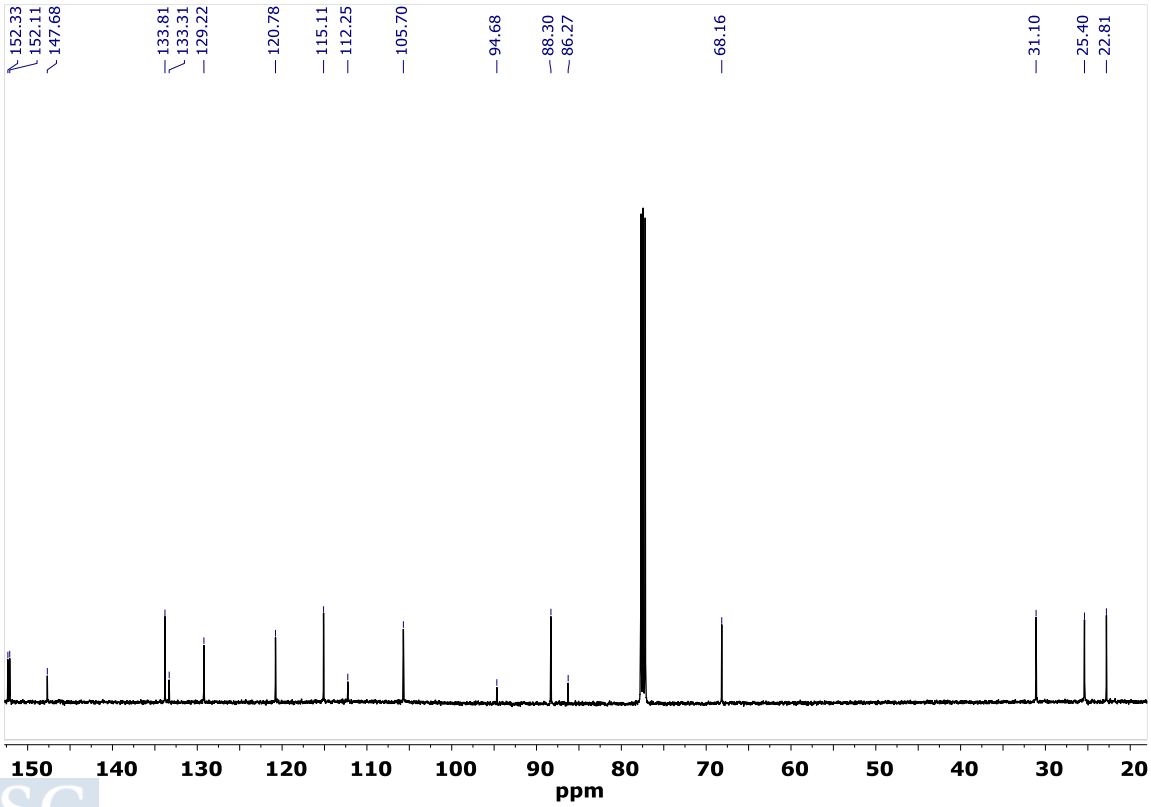

Figure 6.5.6. ^{13}C NMR spectrum of 4-((2,6-bis(1-(tetrahydro-2H-pyran-2-yl)-1H-pyrazol-3-yl)pyridin-4-yl)ethynyl)aniline (3-bpp-THP-L-NH2).

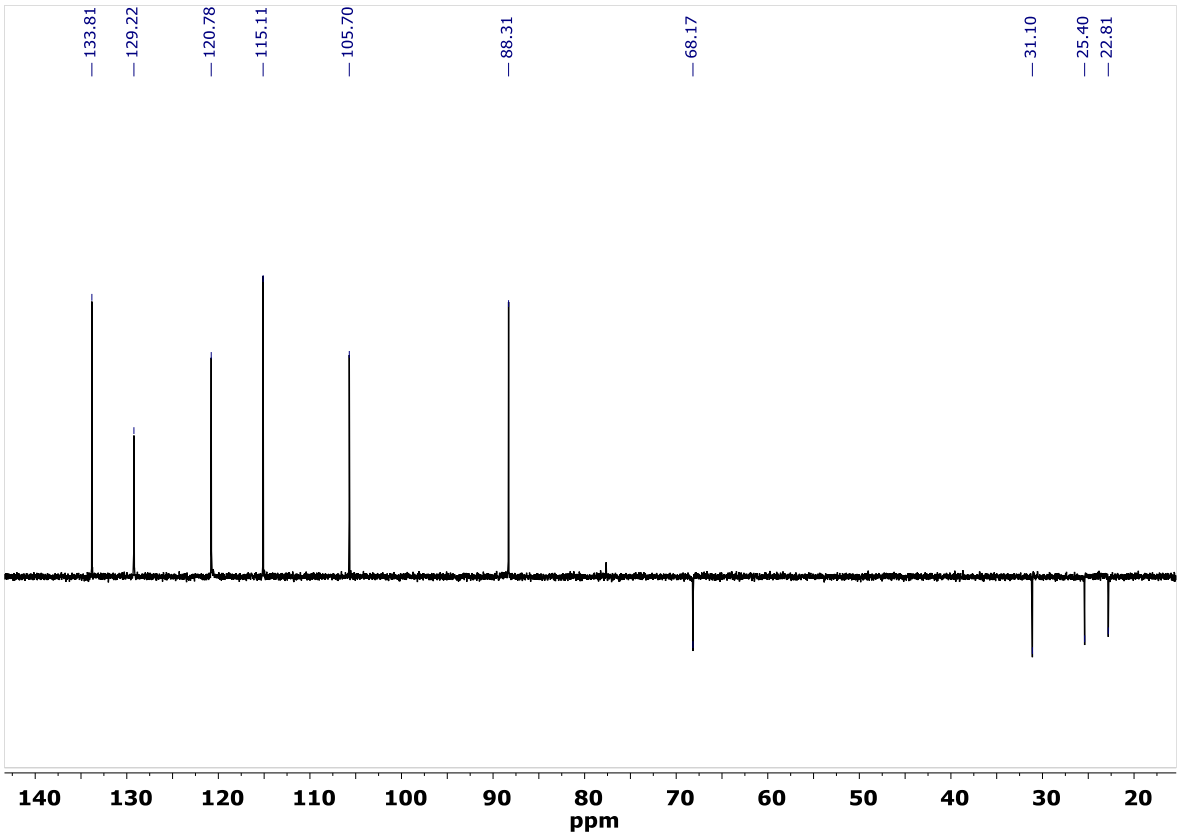

Figure 6.5.7. DEPT-135 spectrum of 4-((2,6-bis(1-(tetrahydro-2H-pyran-2-yl)-1H-pyrazol-3-yl)pyridin-4-yl)ethynyl)aniline (3-bpp-THP-L-NH2).

6.5.1.3 NH2-terminated α-amino acid derivative ligands

Synthesis of (4-((2,6-bis(1*H*-pyrazol-1-yl)pyridin-4-yl)ethynyl)phenyl)glycine (1-bpp-L-Gly)

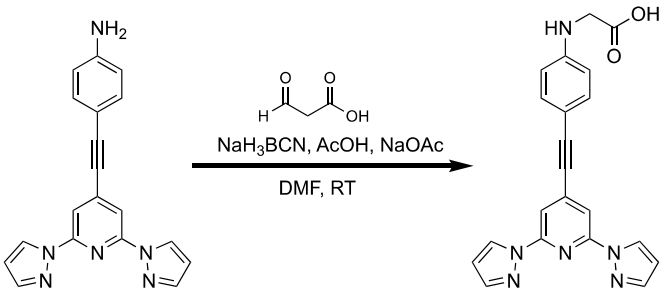

In a 50 mL round bottom flask 4-((2,6-di(1H-pyrazol-1-yl)pyridin-4-yl)ethynyl)aniline (368 mg, 1 eq.), 3-oxopropanoic acid (109 mg, 1.05 eq) and NaOAc (185 mg, 2 eq.) were dissolved in 10 mL of DMF. Then AcOH (387 µL, 6 eq.) were added. Finally, to this mixture the reductant sodium cyanoborohydride (106 mg, 1.5 eq.) was added. The resultant mixture was stirred at room temperature for 24 hours. After this time, water was added and the orange precipitate was collected by centrifugation, washed with water, and dried by lyophilization. (390 mg, 90% yield).

^{1}H NMR (500 MHz, DMSO-d_6) δ 8.95 (dd, *J* = 2.6, 0.7 Hz, 2H), 7.89 (dd, *J* = 1.6, 0.7 Hz, 2H), 7.77 (s, 1H), 7.43 (d, *J* = 8.7 Hz, 2H), 6.66 – 6.64 (m, 3H), 6.63 (s, 1H), 3.90 (s, 3H).

^{13}C NMR (126 MHz, DMSO) δ 172.05, 149.91, 149.85, 142.92, 136.83, 133.51, 128.21, 112.11, 109.48, 108.61, 106.91, 98.07, 84.90, 44.14.

MS-ESI-TOF: m/z calculated for $[C_{21}H_{17}N_6O_2]^+$ 385.14, found 385.16.

Synthesis of (4-((2,6-bis(1-(tetrahydro-2H-pyran-2-yl)-1H-pyrazol-3-yl)pyridin-4-yl)ethynyl)phenyl)glycine (3-bpp-THP-L-Gly)

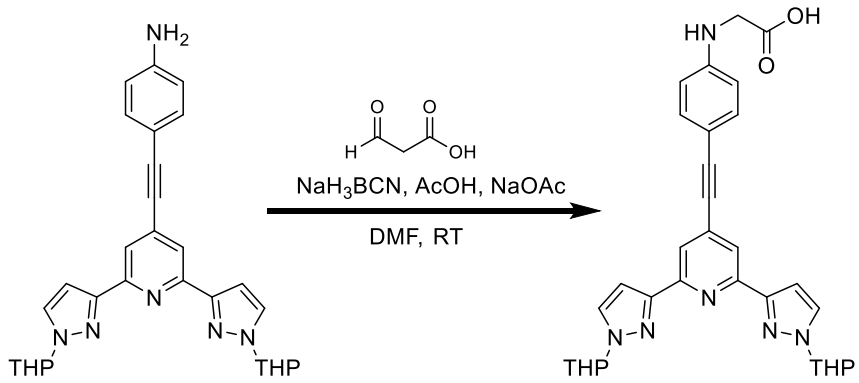

A 100 mL round-bottom flask was charged with 4-((2,6-bis(1*H*-pyrazol-1-yl)pyridin-4-yl)ethynyl)aniline (0.750 g, 1.51 mmol, 1.0 eq.), 3-oxopropanoic acid (0.139 g, 1.59 mmol, 1.05 eq.), $NaBH_3CN$ (0.104 g, 1.661 mmol, 1.1 eq.), NaOAc (0.247 g, 3.02 mmol, 2.0 eq.) and glacial acetic acid (0.362 mL, 9.06 mmol, 6.0 eq.). Under Ar 15 mL of dry DMF were added and the reaction was stirred under inert atmosphere and RT overnight. The solution was

poured into 50 mL of ACN and the solid was isolated by centrifugation to give the final product as a yellowish solid. (0.767 g, 92% yield).

^{1}H NMR (300 MHz, DMSO-d_6) δ 8.00 (d, *J* = 2.4 Hz, 2H), 7.84 (s, 1H), 7.39 (s, 2H), 7.00 (d, *J* = 2.4 Hz, 2H), 6.63 (d, *J* = 8.3 Hz, 2H), 5.50 (dd, *J* = 9.9, 2.1 Hz, 2H), 3.98 (dd, *J* = 11.8, 3.9 Hz, 2H), 3.88 (s, 2H), 3.68 (ddd, *J* = 11.8, 8.5, 5.4 Hz, 2H), 2.19 (tq, *J* = 9.5, 4.6, 3.8 Hz, 2H), 2.00 (m, 4H), 1.71 (m, 4H), 1.58 (hept, *J* = 3.7 Hz, 2H).

^{13}C NMR (75 MHz, DMSO-d_6) δ 172.58 (C), 152.19 (C), 150.81 (C), 149.96 (C), 133.67 (CH_2), 132.91 (C), 131.06 (CH_2), 119.18 (CH_2), 112.59 (CH_2), 108.09 (C), 105.19 (CH_2), 96.34, 87.49 (CH_2), 85.55 (CH), 67.37 (CH), 44.70 (CH), 30.29 (CH), 25.09 (CH), 22.46 (CH_2).

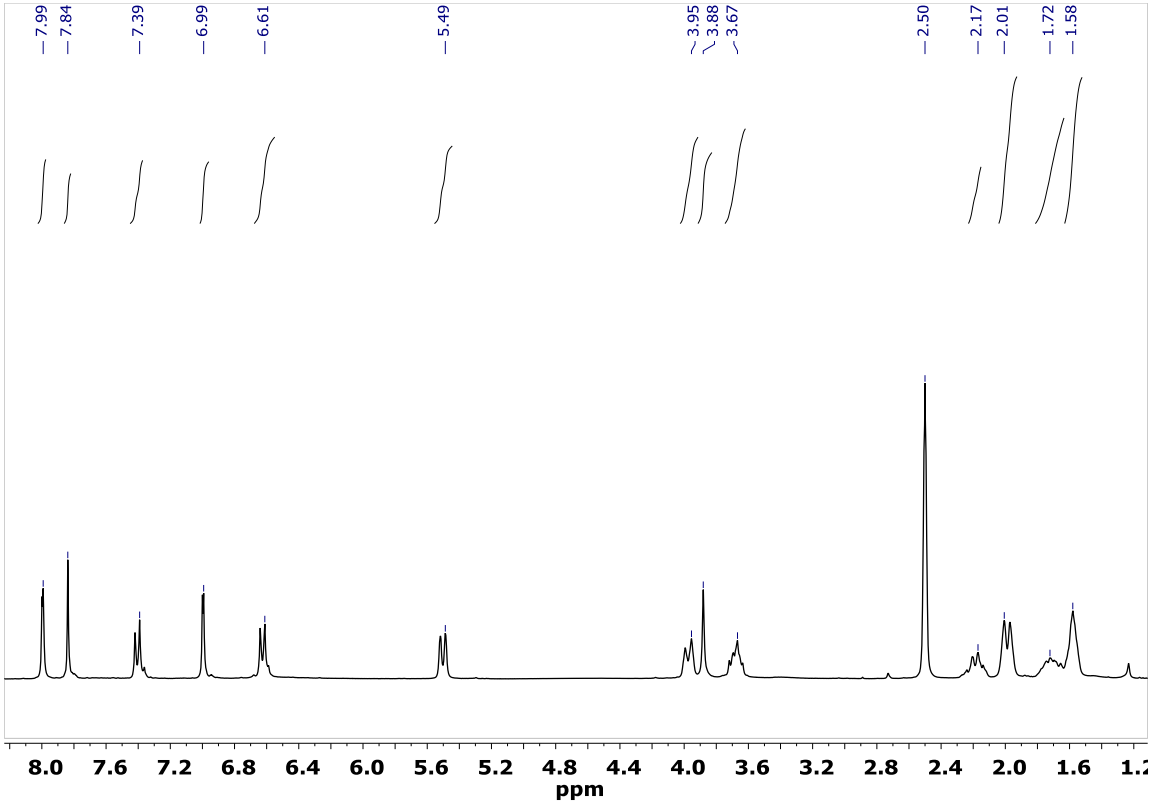

Figure 6.5.8. ^{1}H NMR spectrum of (4-((2,6-bis(1-(tetrahydro-2H-pyran-2-yl)-1H-pyrazol-3-yl)pyridin-4-yl)ethynyl)phenyl)glycine (3-bpp-THP-L-Gly).

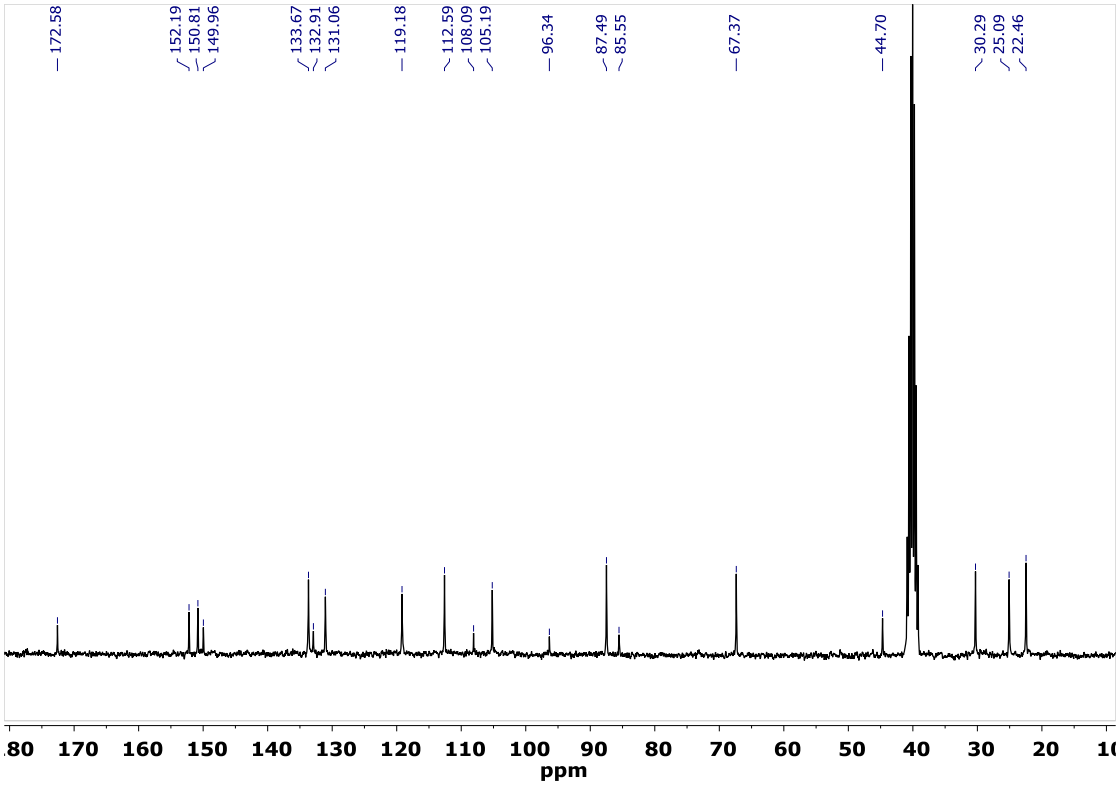

Figure 6.5.9. ^{13}C NMR spectrum of (4-((2,6-bis(1-(tetrahydro-2H-pyran-2-yl)-1H-pyrazol-3-yl)pyridin-4-yl)ethynyl)phenyl)glycine (3-bpp-THP-L-Gly).

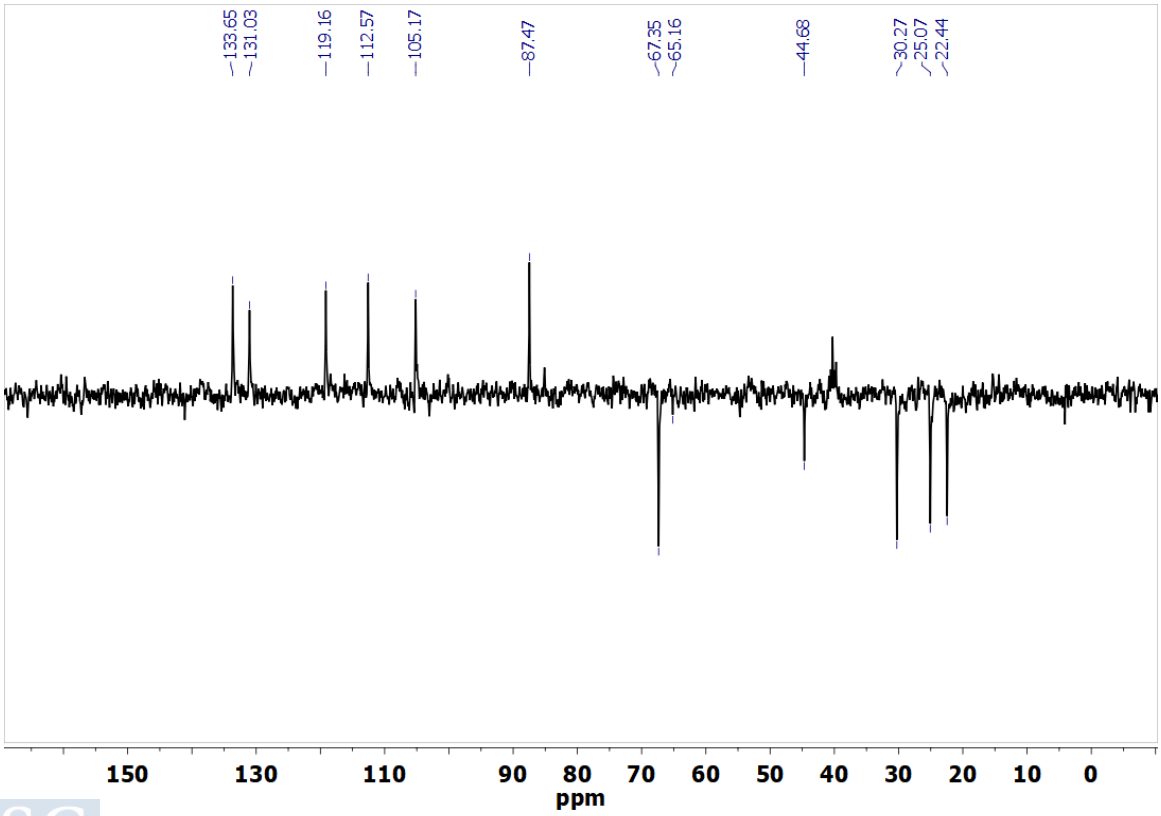

Figure 6.5.10. DEPT-135 spectrum of (4-((2,6-bis(1-(tetrahydro-2H-pyran-2-yl)-1H-pyrazol-3-yl)pyridin-4-yl)ethynyl)phenyl)glycine (3-bpp-THP-L-GLy).

6.5.2 X-ray Photoelectron Spectroscopy (XPS)

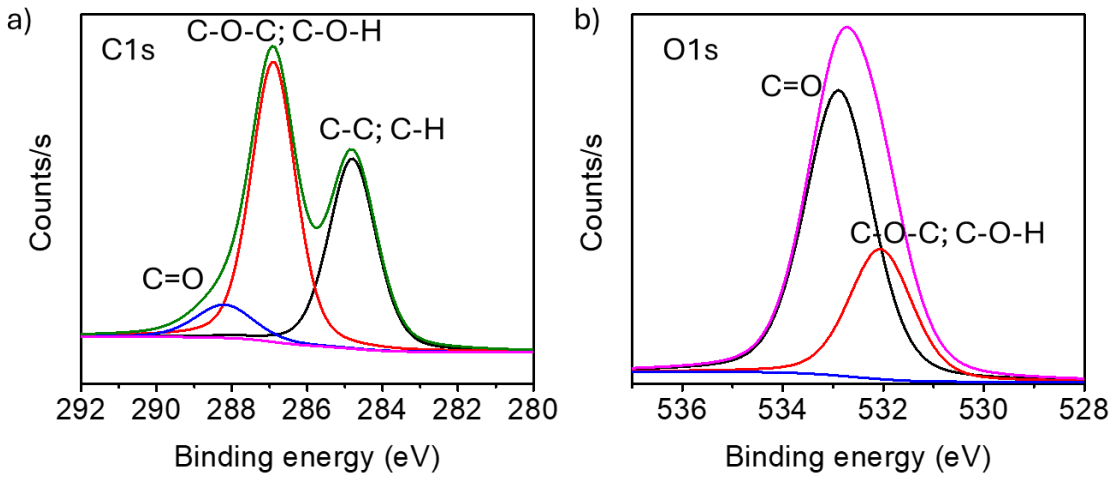

Figure 6.5.11. High resolution XPS spectra of a) C 1s and b) O 1s for hGO . Charge correction for the C 1s spectrum was set at the binding energy of 284.8 eV.

6.5.3 Thermogravimetric Analysis (TGA)

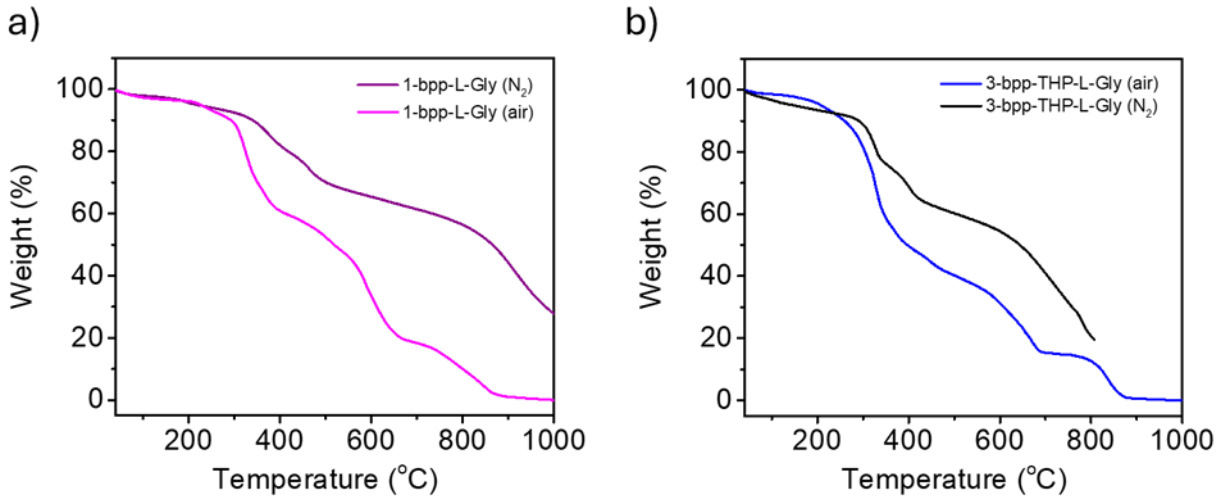

Figure 6.5.12. TGA analysis for 1-bpp-L-Gly (a) and 3-bpp-THP-L-Gly (b). Measurements were performed in the range of 40 – 1000 °C at a scan rate of 4 °C/min under air and nitrogen.

6.5.4 Raman Spectroscopy

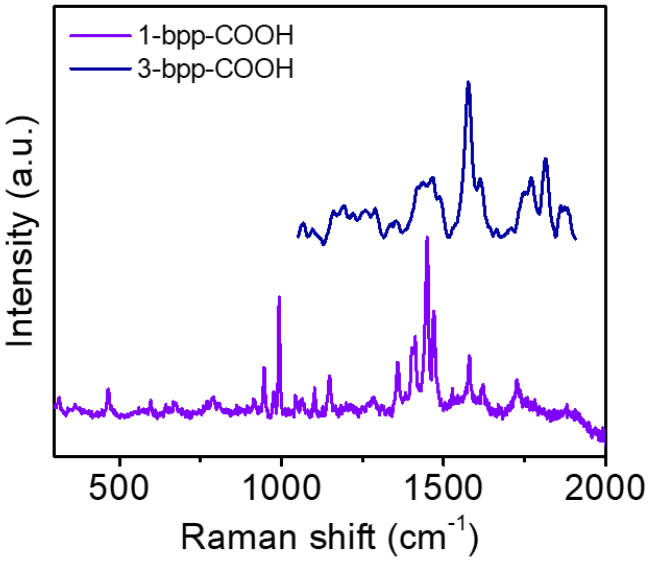

Figure 6.5.13. Raman spectra for 1-bpp-COOH and 3-bpp-COOH.

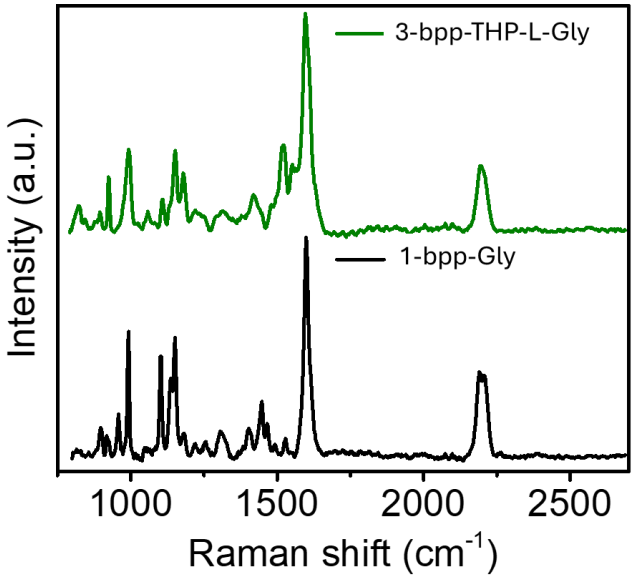

Figure 6.5.14. Raman spectra for 1-bpp-L-Gly and 3-bpp-THP-L-Gly.

6.5.5 Transmission Electron Microscopy (TEM)

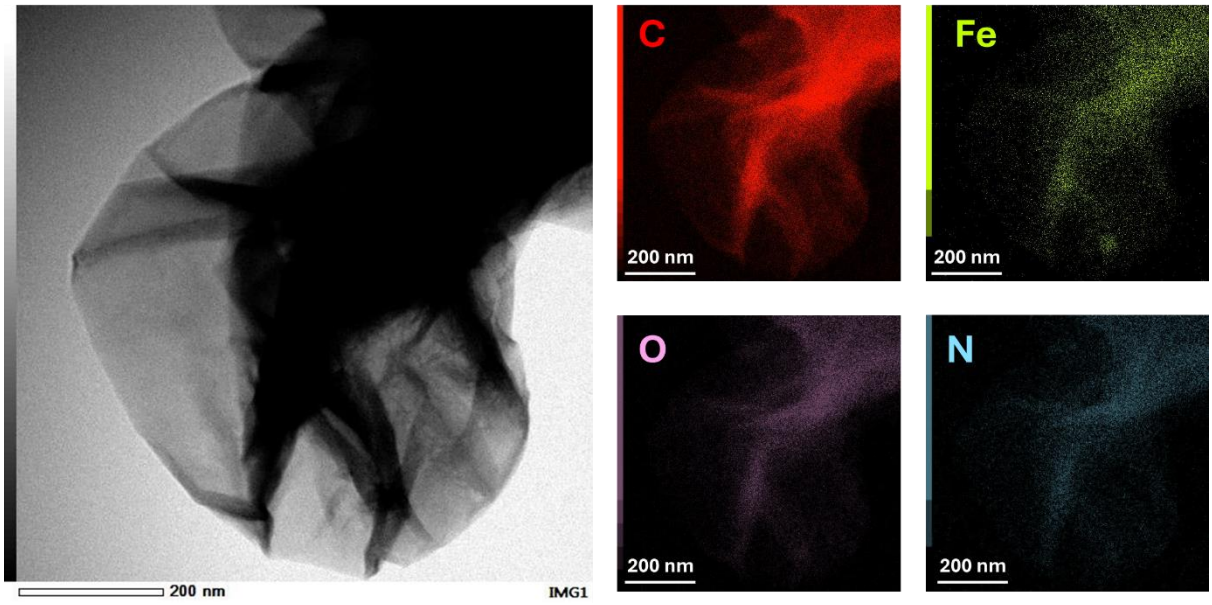

Figure 6.5.15. STEM/EDS elemental mapping of C, Fe, O and N for Fe-3-cGO.

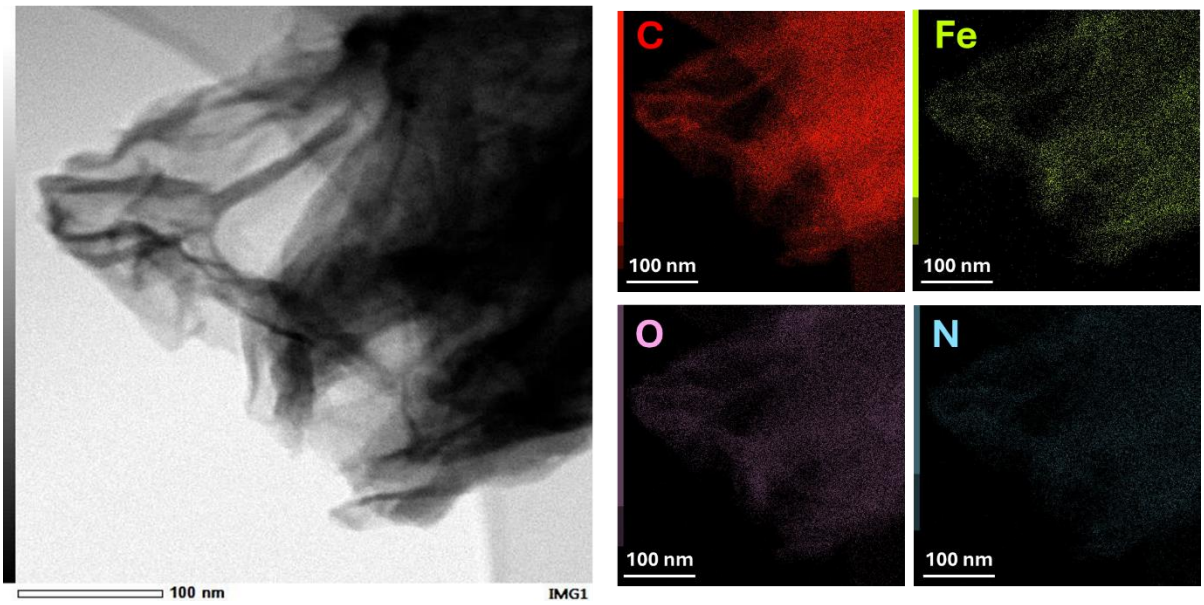

Figure 6.5.16. STEM/EDS elemental mapping of C, Fe, O and N for Fe-5-cGO.

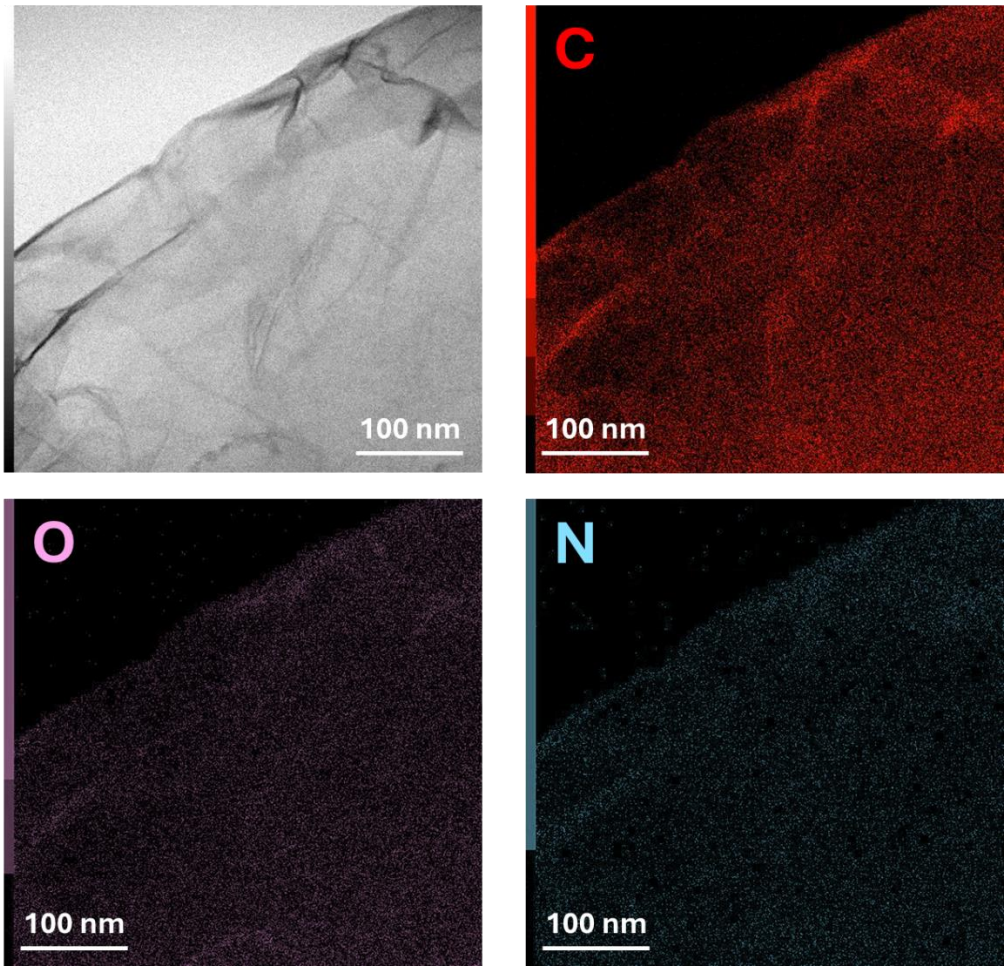

Figure 6.5.17. STEM/EDS elemental mapping of C, O and N for 7-rGO.

6.5.6 Scanning Electron Microscopy (SEM)

Table 6.5.1. Scanning electron microscopy-energy dispersive X-ray analysis for 6-rGO, Fe-6-rGO, 7-rGO and Fe-7-rGO

% (wt)	6-rGO	Fe-6-rGO	7-rGO	Fe-7-rGO
C	77.46	70.76	78.97	67.01
O	20.60	12.52	18.21	18.37
N	1.51	12.38	-	9.27
Fe	-	0.53	-	0.20
Rest	0.43	3.74	2.82	5.15

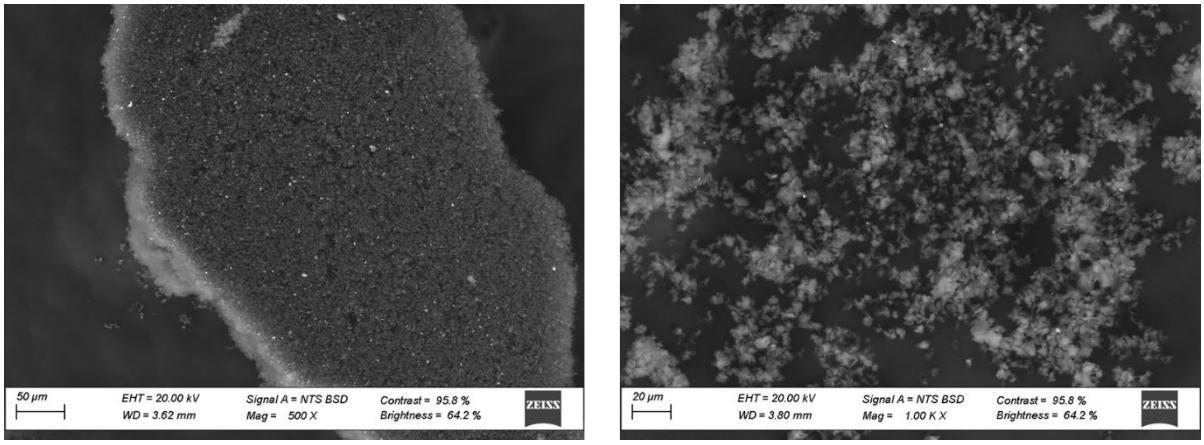

Figure 6.5.18. SEM images of 6-rGO.

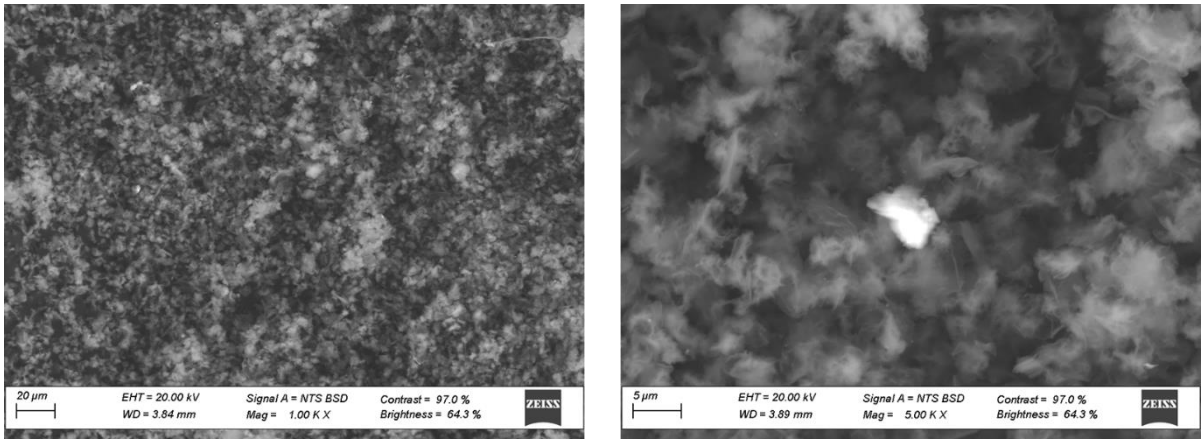

Figure 6.5.19. SEM images of Fe-6-rGO.

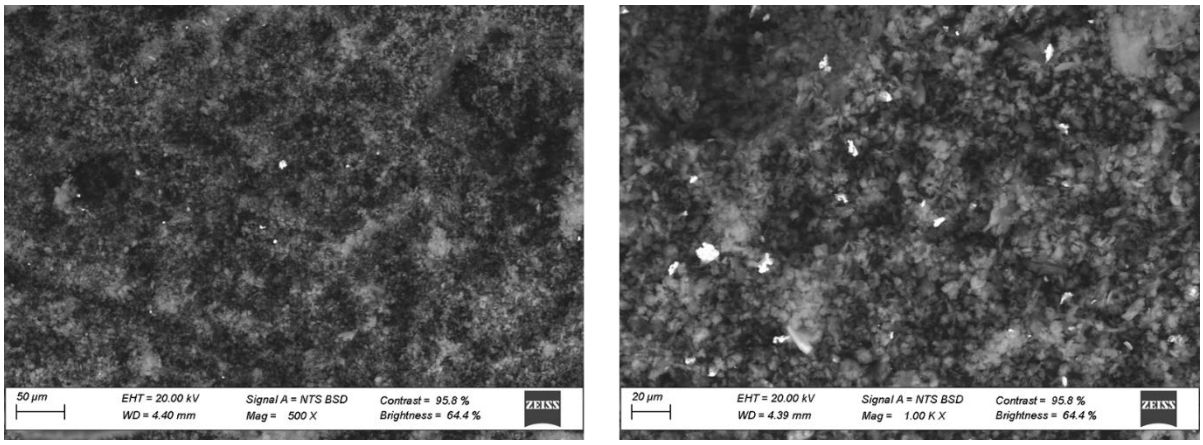

Figure 6.5.20. SEM images of 7-rGO

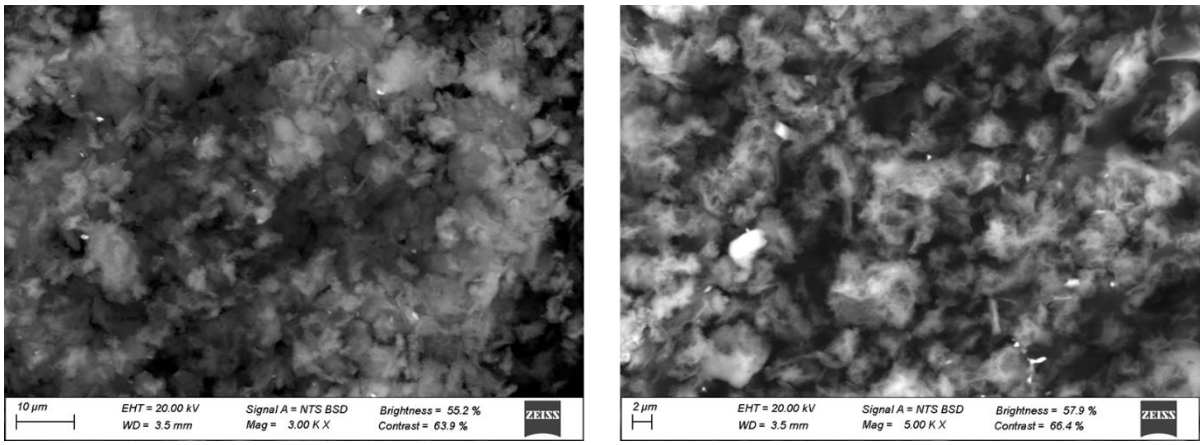

Figure 6.5.21. SEM images of Fe-7-rGO.

7 REFERENCES

1 E. Resines-Urien, E. Fernandez-Bartolome, A. Martinez-Martinez, A. Gamonal, L. Piñeiro-López and J. S. Costa, *Chem. Soc. Rev.*, 2022, **52**, 705–727.

2 J. A. Real, A. B. Gaspar and M. Carmen Muñoz, *Dalton Trans.*, 2005, 2062–2079.

3 K. Senthil Kumar and M. Ruben, *Coord. Chem. Rev.*, 2017, **346**, 176–205.

4 *Magnetism in Condensed Matter*, ed. Stephen Blundell, Oxford University Press, 2001.

5 *Molecular Magnetism*, ed. Olivier Kahn, VCH-Verlag, 1993.

6 *Spin Crossover in Transition Metal Compounds*, in *Topics in Current Chemistry*, ed. P. Gütlich and H. A. Goodwin, Springer, Berlin, 2004, vol. I–III

7 P. Gütlich, Y. Garcia and H. A. Goodwin, *Chem. Soc. Rev.*, 2000, **29**, 419–427.

8 *Spin-Crossover Materials: Properties and Applications*, ed. Malcolm A. Halcrow, John Wiley & Sons, 2013.

9 Y. Garcia and P. Gütlich, *Top Curr. Chem.*, 2004, **234**, 49–62.

10 S. Hayami, Z. Z. Gu, H. Yoshiki, A. Fujishima and O. Sato, *J. Am. Chem. Soc.*, 2001, **123**, 11644–11650.

11 S. Brooker, P. G. Plieger, B. Moubaraki and K. S. Murray, *Angew. Chem., Int. Ed.*, 1999, **38**, 408–410.

12 W. Kläui, W. Eberspach and P. Gütlich, *Inorg. Chem*, 1987, **26**, 3977–3982.

13 R. W. Hogue, S. Singh and S. Brooker, *Chem. Soc. Rev.*, 2018, **47**, 7303–7338.

14 H. S. Scott, R. W. Staniland and P. E. Kruger, *Coord. Chem. Rev.*, 2018, **362**, 24–43.

15 A. Arroyave, A. Lennartson, A. Dragulescu-Andrasi, K. S. Pedersen, S. Piligkos, S. A. Stoian, S. M. Greer, C. Pak, O. Hietsoi, H. Phan, S. Hill, C. J. McKenzie and M. Shatruk, *Inorg. Chem.*, 2016, **55**, 5904–5913.

16 P. N. Martinho, F. F. Martins, N. A. G. Bandeira and M. J. Calhorda, *Sustainability*, 2020, **12**, 2512–2562.

17 G. S. Matouzenko, D. Luneau, G. Molnár, N. Ould-Moussa, S. Zein, S. A. Borshch, A. Bousseksou and F. Averseng, *Eur. J. Inorg. Chem.*, 2006, **2006**, 2671–2682.

18 S. Bonnet, G. Molnár, J. S. Costa, M. A. Siegler, A. L. Spek, A. Bousseksou, W. T. Fu, P. Gamez and J. Reedijk, *Chem. Mat.*, 2009, **21**, 1123–1136.

19 J. Klingele, D. Kaase, M. H. Klingele, J. Lach and S. Demeshko, *Dalton Trans.*, 2010, **39**, 1689–1691.

20 J. Dugay, M. Giménez-Marqués, W. J. Venstra, R. Torres-Cavanillas, U. N. Sheombarsing, N. Manca, E. Coronado and H. S. J. Van Der Zant, *J. Phys. Chem. C*, 2019, **123**, 6778–6786.

21 S. Hayami, S. M. Holmes and M. A. Halcrow, *J. Mater. Chem. C.*, 2015, **3**, 7775–7778.

22 A. Bousseksou and G. Molnár, *C. R. Chim.*, 2003, **6**, 1175–1183.

23 M. Ren, X. Zhu, Q. Luo, X. Li and J. Yang, *Nanoscale*, 2023, **15**, 10661–10666.

24 *Inorganic Chemistry*, ed. C. E. and S. A. G. Housecroft, Pearson, 2012.

25 L. Cambi and L. Szegö, *Berichte der deutschen chemischen Gesellschaft (A and B Series)*, 1931, **64**, 2591–2598.

26 *The Theory of Electric and Magnetic Susceptibilities*, ed. R. Cíni, J. Ciampolini, F. Maggio, P. E. Figgins and D. H. Busch, Oxford Press, 1961.

27 E. J. Halbert, C. M. Harris, E. Sinn and G. J. Sutton, *Aust. J. Chem.*, 1973, **26**, 951–959.

28 C. Sousa, C. De Graaf, A. Rudavskyi, R. Broer, J. Tatchen, M. Etinski and C. M. Marian, *Chem. – Eur. J.*, 2013, **19**, 17541–17551.

29 M. Mörtel, T. Lindner, A. Scheurer, F. W. Heinemann and M. M. Khusniyarov, *Inorg. Chem.*, 2020, **59**, 2659–2666.

30 M. Giménez-Marqués, M. L. García-Sanz De Larrea and E. Coronado, *J. Mater. Chem. C.*, 2015, **3**, 7946–7953.

31 J. Dugay, M. Giménez-Marqués, T. Kozlova, H. W. Zandbergen, E. Coronado and H. S. J. Van Der Zant, *Adv. Mater.*, 2015, **27**, 1288–1293.

32 R. Torres-Cavanillas, L. Lima-Moya, F. D. Tichelaar, H. W. Zandbergen, M. Giménez-Marqués and E. Coronado, *Dalton Trans.*, 2019, **48**, 15465–15469.

33 R. Turo-Cortés, C. Bartual-Murgui, J. Castells-Gil, M. C. Muñoz, C. Martí-Gastaldo and J. A. Real, *Chem. Sci.*, 2020, **11**, 11224–11234.

34 M. J. Murphy, K. A. Zenere, F. Ragon, P. D. Southon, C. J. Kepert and S. M. Neville, *J. Am. Chem. Soc.*, 2017, **139**, 1330–1335.

35 O. I. Kucheriv, S. I. Shylin, V. Ksenofontov, S. Dechert, M. Haukka, I. O. Fritsky and I. A. Guralskiy, *Inorg. Chem.*, 2016, **55**, 4906–4914.

36 F. J. Valverde-Muñoz, M. Seredyuk, M. C. Muñoz, K. Znovjyak, I. O. Fritsky and J. A. Real, *Inorg. Chem.*, 2016, **55**, 10654–10665.

37 C. Hansch, A. Leo and R. W. Taft, *Chem. Rev.*, 1991, **91**, 165–195.

38 A. Kimura and T. Ishida, *ACS Omega*, 2018, **3**, 6737–6747.

39 L. J. Kershaw Cook, R. Kulmaczewski, R. Mohammed, S. Dudley, S. A. Barrett, M. A. Little, R. J. Deeth and M. A. Halcrow, *Angew. Chem.*, 2016, **128**, 4399–4403.

40 H. C. Liang, Y. Pan, H. L. Zhu, Y. S. Meng, C. H. Liu, T. Liu and Y. Y. Zhu, *Inorg. Chem. Front.*, 2022, **9**, 2343–2352.

41 C. F. Wang, Z. S. Yao, G. Y. Yang and J. Tao, *Inorg. Chem.*, 2019, **58**, 1309–1316.

42 C. Bartual-Murgui, S. Vela, M. Darawsheh, R. Diego, S. J. Teat, O. Roubeau and G. Aromí, *Inorg. Chem. Front.*, 2017, **4**, 1374–1383.

43 R. Saiki, H. Miyamoto, H. Sagayama, R. Kumai, G. N. Newton, T. Shiga and H. Oshio, *Dalton Trans.*, 2019, **48**, 3231–3236.

44 M. A. Halcrow, *Coord. Chem. Rev.*, 2005, **249**, 2880–2908.

45 M. A. Halcrow, *Coord. Chem. Rev.*, 2009, **253**, 2493–2514.

46 C. Rajadurai, F. Schramm, S. Brink, O. Fuhr, M. Ghafari, R. Kruk and M. Ruben, *Inorg. Chem.*, 2006, **45**, 10019–10021.

47 C. Rajadurai, O. Fuhr, R. Kruk, M. Ghafari, H. Hahn and M. Ruben, *Chem. Comm.*, 2007, 2636–2638.

48 L. J. Kershaw Cook, J. Fisher, L. P. Harding and M. A. Halcrow, *Dalton Trans.*, 2015, **44**, 9417–9425.

49 R. Chandrasekar, F. Schramm, O. Fuhr and M. Ruben, *Eur. J. Inorg. Chem.*, 2008, **2008**, 2649–2653.

50 V. A. Money, C. Carbonera, J. Elhaïk, M. A. Halcrow, J. A. K. Howard and J. F. Létard, *Chem. – Eur. J.*, 2007, **13**, 5503–5514.

51 C. A. Kilner and M. A. Halcrow, *Acta. Cryst. C*, 2006, **62**, 437–439.

52 K. S. Kumar, I. Šalitroš, N. Suryadevara, E. Moreno-Pineda and M. Ruben, *Eur. J. Inorg. Chem.*, 2018, **2018**, 5091–5097.

53 C. M. Klug, A. M. McDaniel, S. R. Fiedler, K. A. Schulte, B. S. Newell and M. P. Shores, *Dalton Trans.*, 2012, **41**, 12577–12585.

54 M. Tafili-Kryeziu, M. Weil, T. Muranaka, A. Bousseksou, M. Hasegawa, A. Jun and W. Linert, *J. Chem. Soc. Dalton Trans.*, 2013, **42**, 15796–15804.

55 Y. H. Luo, G. J. Wen, L. S. Gu, M. N. Wang and B. W. Sun, *Polyhedron*, 2017, **121**, 101–106.

56 Y. H. Luo, L. Chen, J. W. Wang, M. X. Wang, Y. W. Zhang and B. W. Sun, *Inorganica Chim. Acta*, 2016, **450**, 8–11.

57 J. A. Kitchen, N. G. White, G. N. L. Jameson, J. L. Tallon and S. Brooker, *Inorg. Chem.*, 2011, **50**, 4586–4597.

58 J. H. Askew and H. J. Shepherd, *Dalton Trans.*, 2020, **49**, 2966–2971.

59 L. Navarro and J. Cirera, *Inorg. Chem. Front.*, 2022, **10**, 250–258.

60 A. Bousseksou, M. Verelst, H. Constant-Machado, G. Lemercier, J.-P. Tuchagues and F. Varret, *Inorg. Chem.*, 1996, **35**, 110–115.

61 G. Lemercier, N. Bréfuel, S. Shova, J. A. Wolny, F. Dahan, M. Verelst, H. Paulsen, A. X. Trautwein and J. P. Tuchagues, *Chem. – Eur. J.*, 2006, **12**, 7421–7432.

62 S. A. Barrett and M. A. Halcrow, *RSC Adv.*, 2014, **4**, 11240–11243.

63 V. García-López, H. E. M. El Jastimi, J. Juráková, M. Clemente-León and E. Coronado, *Cryst. Growth. Des.*, 2023, **23**, 2730–2738.

64 M. Palacios-Corella, V. García-López, J. C. Waerenborgh, B. J. C. Vieira, G. Mínguez Espallargas, M. Clemente-León and E. Coronado, *Chem. Sci.*, 2023, **14**, 3048–3055.

65 L. Sun, N. E. I. Belmouri, M. Ndiaye, K. Robeyns, A. Rotaru, K. Boukheddaden and Y. Garcia, *Cryst. Growth. Des.*, 2023, **23**, 3402–3411.

66 R. J. Archer, H. S. Scott, M. I. J. Polson, C. Mathonière, M. Rouzières, R. Clérac and P. E. Kruger, *Chem. Asian J.*, 2019, **14**, 2225–2229.

67 M. del C. Giménez-López, M. Clemente-León and C. Giménez-Saiz, *Dalton Trans.*, 2018, **47**, 10453–10462.

68 X. P. Sun, R. J. Wei, Z. S. Yao and J. Tao, *Cryst. Growth. Des.*, 2018, **18**, 6853–6862.

69 R. Rabelo, L. Toma, N. Moliner, M. Julve, F. Lloret, M. Inclán, E. García-España, J. Pasán, R. Ruiz-García and J. Cano, *Chem. Sci.*, 2023, **14**, 8850–8859.

70 C. Lefter, R. Tan, J. Dugay, S. Tricard, G. Molnár, L. Salmon, J. Carrey, W. Nicolazzi, A. Rotaru and A. Bousseksou, *Chem. Phys. Lett.*, 2016, **644**, 138–141.

71 Q. Zhao, J. P. Xue, Z. K. Liu, Z. S. Yao and J. Tao, *Dalton Trans.*, 2021, **50**, 11106–11112.

72 M. Yamasaki and T. Ishida, *J. Mater. Chem. C*, 2015, **3**, 7784–7787.

73 R. Kulmaczewski, J. Olguín, J. A. Kitchen, H. L. C. Feltham, G. N. L. Jameson, J. L. Tallon and S. Brooker, *J. Am. Chem. Soc.*, 2014, **136**, 878–881.

74 Q. Yang, Y. S. Meng, T. Liu and J. Tang, *Dalton Trans.*, 2022, **51**, 602–607.

75 V. Jornet-Mollá, C. Giménez-Saiz, B. J. C. Vieira, J. C. Waerenborgh and F. M. Romero, *Dalton Trans.*, 2021, **50**, 2536–2544.

76 S. Marcén, L. Lecren, L. Capes, H.A. Goodwin and J.-F. Létard, *Chem. Phys. Lett.*, 2002, **358**, 87–95.

77 L. Zhang, Y. Tong, M. Kelai, A. Bellec, J. Lagoute, C. Chacon, Y. Girard, S. Rousset, M. L. Boillot, E. Rivière, T. Mallah, E. Otero, M. A. Arrio, P. Sainctavit and V. Repain, *Angew. Chem., Int. Ed.*, 2020, **59**, 13341–13346.

78 V. García-López, M. Palacios-Corella, S. Cardona-Serra, M. Clemente-León and E. Coronado, *Chem. Comm.*, 2019, **55**, 12227–12230.

79 V. García-López, M. Palacios-Corella, M. Clemente-León and E. Coronado, *Polyhedron*, 2019, **170**, 95–100.

80 B. Rösner, M. Milek, A. Witt, B. Gobaut, P. Torelli, R. H. Fink and M. M. Khusniyarov, *Angew. Chem.*, 2015, **127**, 13168–13172.

81 I. Šalitroš, O. Fuhr, R. Kruk, J. Pavlik, L. Pogány, B. Schäfer, M. Tatarko, R. Boča, W. Linert and M. Ruben, *Eur. J. Inorg. Chem.*, 2013, **2013**, 1049–1057.

82 J. Klingele, D. Kaase, M. Schmucker, Y. Lan, G. Chastanet and J. F. Létard, *Inorg. Chem.*, 2013, **52**, 6000–6010.

83 E. Codjovi, N. Menéndez, J. Jeftic and F. Varret, *Chemistry*, 2001, **4**, 181–188.

84 G. Molnár, V. Niel, J. A. Real, L. Dubrovinsky, A. Bousseksou and J. J. McGarvey, *J. Phys. Chem. B*, 2003, **107**, 3149–3155.

85 A. Galet, A. B. Gaspar, M. C. Muñoz, G. V. Bukin, G. Levchenko and J. A. Real, *Adv. Mater.*, 2005, **17**, 2949–2953.

86 A. Galet, A. B. Gaspar, G. Agusti, M. C. Muñoz, G. Levchenko and J. A. Real, *Eur J Inorg. Chem.*, 2006, **2006**, 3571–3573.

87 A. B. Gaspar, G. Levchenko, S. Terekhov, G. Bukin, J. Valverde-Muñoz, F. J. Muñoz-Lara, M. Seredyuk and J. A. Real, *Eur. J. Inorg. Chem.*, 2014, **2014**, 429–433.

88 B. Ll, R. J. Wei, J. Tao, R. Bin Huang and L. S. Zheng, *Inorg. Chem.*, 2010, **49**, 745–751.

89 V. Ksenofontov, H. Spiering, A. Schreiner, G. Levchenko, H. A. Goodwin and P. Gütlich, *J. of Phys. Chem. Solids*, 1999, **60**, 393–399.

90 C. P. Köhler, R. Jakobi, E. Meissner, L. Wiehl, H. Spiering and P. Gütlich, *J. of Phys. Chem. Solids*, 1990, **51**, 239–247.

91 J. Bin Lin, W. Xue, B. Y. Wang, J. Tao, W. X. Zhang, J. P. Zhang and X. M. Chen, *Inorg. Chem.*, 2012, **51**, 9423–9430.

92 N. F. Sciortino, F. Ragon, K. A. Zenere, P. D. Southon, G. J. Halder, K. W. Chapman, L. Piñeiro-López, J. A. Real, C. J. Kepert and S. M. Neville, *Inorg. Chem.*, 2016, **55**, 10490–10498.

93 D. J. Mondal, N. Mukherjee and S. Konar, *Cryst. Growth. Des.*, 2023, **23**, 1832–1839.

94 Th. Strässle, A. Furrer and K.A. Müller, *Physica B*, 2000, **276–278**, 944–945.

95 S. Yuce, M. Barrio, B. Emre, E. Stern-Taulats, A. Planes, J. L. Tamarit, Y. Mudryk, K. A. Gschneidner, V. K. Pecharsky and L. Mañosa, *Appl. Phys. Lett.*, 2012, **101**, 071906.

96 K. G. Sandeman, *APL Mater.*, 2016, **4**, 111102.

97 P. J. Von Ranke, B. P. Alho, R. M. Ribas, E. P. Nobrega, A. Caldas, V. S. R. De Sousa, M. V. Colaço, L. F. Marques, D. L. Rocco and P. O. Ribeiro, *Phys. Rev. B*, 2018, **98**, 224408.

98 P. J. Von Ranke, *Appl. Phys. Lett.*, 2017, **110**, 181909.

99 S. P. Vallone, A. N. Tantillo, A. M. dos Santos, J. J. Molaison, R. Kulmaczewski, A. Chapoy, P. Ahmadi, M. A. Halcrow and K. G. Sandeman, *Adv. Mater.*, 2019, **31**, 1807334.

100 P. J. Von Ranke, B. P. Alho, P. H. S. Da Silva, R. M. Ribas, E. P. Nobrega, V. S. R. De Sousa, M. V. Colaço, L. F. Marques, M. S. Reis, F. M. Scaldini, L. B. L. Escobar and P. O. Ribeiro, *J. Appl. Phys.*, 2020, **127**, 165104.

101 M. Romanini, Y. X. Wang, K. Gürpinar, G. Ornelas, P. Lloveras, Y. Zhang, W. Zheng, M. Barrio, A. Aznar, A. Gràcia-Condal, B. Emre, O. Atakol, C. Popescu, H. Zhang, Y. Long, L. Balicas, J. Lluís Tamarit, A. Planes, M. Shatruk and L. Mañosa, *Adv. Mater.*, 2021, **33**, 2008076.

102 P. J. von Ranke, B. P. Alho, P. H. S. da Silva, R. M. Ribas, E. P. Nobrega, V. S. R. de Sousa, A. M. G. Carvalho and P. O. Ribeiro, *Phys. Status Solidi B Basic Res.*, 2021, **258**, 2100108.

103 J. Seo, J. D. Braun, V. M. Dev and J. A. Mason, *J. Am. Chem. Soc.*, 2022, **144**, 6493–6503.

104 A. Caneschi, D. Gatteschi, R. Sessoli, A.-L. Barra, L. C. Brunel and M. Guillot, *J. Am. Chem. Soc.*, 1991, **113**, 5873–5874.

105 M. Cavallini, J. Gomez-Segura, D. Ruiz-Molina, M. Massi, C. Albonetti, C. Rovira, J. Veciana and F. Biscarini, *Angew. Chem., Int. Ed.*, 2005, **44**, 888–892.

106 L. Bogani and W. Wernsdorfer, *Nat. Mater.*, 2008, **7**, 179–186.

107 A. Gaita-Ariño, F. Luis, S. Hill and E. Coronado, *Nat. Chem.*, 2019, **11**, 301–309.

108 G. A. Craig and M. Murrie, *Chem. Soc. Rev.*, 2015, **44**, 2135–2147.

109 Frost, K. L. M. Harriman and M. Murugesu, *Chem. Sci.*, 2016, **7**, 2470–2491.

110 G. Peng, Y. F. Qian, Z. W. Wang, Y. Chen, T. Yadav, K. Fink and X. M. Ren, *Cryst. Growth Des.*, 2021, **21**, 1035–1044.

111 Z. Y. Ding, Y. S. Meng, Y. Xiao, Y. Q. Zhang, Y. Y. Zhu and S. Gao, *Inorg. Chem. Front.*, 2017, **4**, 1909–1916.

112 D. Shao, S. L. Zhang, L. Shi, Y. Q. Zhang and X. Y. Wang, *Inorg. Chem.*, 2016, **55**, 10859–10869.

113 D. Shao, S. Y. She, L. F. Shen, X. Yang and Z. Tian, *Polyhedron*, 2022, **213**, 115614.

114 L. Shi, D. Shao, H. Y. Wei and X. Y. Wang, *Cryst. Growth Des.*, 2018, **18**, 5270–5278.

115 Y. F. Deng, M. K. Singh, D. Gan, T. Xiao, Y. Wang, S. Liu, Z. Wang, Z. Ouyang, Y. Z. Zhang and K. R. Dunbar, *Inorg. Chem.*, 2020, **59**, 7622–7630.

116 S. Roy, I. Oyarzabal, J. Vallejo, J. Cano, E. Colacio, A. Bauza, A. Frontera, A. M. Kirillov, M. G. B. Drew and S. Das, *Inorg. Chem.*, 2016, **55**, 8502–8513.

117 L. Rigamonti, N. Bridonneau, G. Poneti, L. Tesi, L. Sorace, D. Pinkowicz, J. Jover, E. Ruiz, R. Sessoli and A. Cornia, *Chem. – Eur. J.*, 2018, **24**, 8857–8868.

118 V. García-López, F. J. Orts-Mula, M. Palacios-Corella, J. M. Clemente-Juan, M. Clemente-León and E. Coronado, *Polyhedron*, 2018, **150**, 54–60.

119 C. Rajnák, J. Titiš, J. Miklovič, G. E. Kostakis, O. Fuhr, M. Ruben and R. Boča, *Polyhedron*, 2017, **126**, 174–183.

120 A. A. Fursina and A. Sinitskii, *ACS App. Electron. Mater.*, 2023, **5**, 3531–3545.

121 E. Coronado, *Nat. Rev. Mater.*, 2020, **5**, 87–104.

122 V. Georgakilas, M. Otyepka, A. B. Bourlinos, V. Chandra, N. Kim, K. C. Kemp, P. Hobza, R. Zboril and K. S. Kim, *Chem. Rev.*, 2012, **112**, 6156–6214.

123 A. Criado, M. Melchionna, S. Marchesan and M. Prato, *Angew. Chem.*, 2015, **127**, 10882–10900.

124 K. S. Novoselov, A. K. Geim, S. V Morozov, D. Jiang, Y. Zhang, S. V Dubonos, I. V Grigorieva and A. A. Firsov, *Phys. Rev. Lett*, 2004, **404**, 3824.

125 K. S. Novoselov, A. K. Geim, S. V. Morozov, D. Jiang, M. I. Katsnelson, I. V. Grigorieva, S. V. Dubonos and A. A. Firsov, *Nature*, 2005, **438**, 197–200.

126 D. Qiu, D. H. Ren, L. Gu, X. L. Sun, T. T. Qu, Z. G. Gu and Z. Li, *RSC Adv.*, 2014, **4**, 31323–31327.

127 M. Bernien, H. Naggert, L. M. Arruda, L. Kipgen, F. Nickel, J. Miguel, C. F. Hermanns, A. Krüger, D. Krüger, E. Schierle, E. Weschke, F. Tuczek and W. Kuch, *ACS Nano*, 2015, **9**, 8960–8966.

128 Y. Murashima, M. R. Karim, N. Saigo, H. Takehira, R. Ohtani, M. Nakamura, M. Koinuma, L. F. Lindoy, K. Kuroiwa and S. Hayami, *Inorg. Chem. Front.*, 2015, **2**, 886–892.

129 J. Dugay, M. Aarts, M. Gimenez-Marqués, T. Kozlova, H. W. Zandbergen, E. Coronado and H. S. J. Van Der Zant, *Nano Lett.*, 2017, **17**, 186–193.

130 A. Holovchenko, J. Dugay, M. Giménez-Marqués, R. Torres-Cavanillas, E. Coronado and H. S. J. van der Zant, *Adv. Mater.*, 2016, **28**, 7228–7233.

131 K. Senthil Kumar, I. Šalitroš, Z. Boubegtiten-Fezoua, S. Moldovan, P. Hellwig and M. Ruben, *Dalton Trans.*, 2018, **47**, 35–40.

132 C. Boix-Constant, V. García-López, E. Navarro-Moratalla, M. Clemente-León, J. L. Zafra, J. Casado, F. Guinea, S. Mañas-Valero and E. Coronado, *Adv. Mater.*, 2022, **34**, 2110027.

133 M. Gavara-Edo, R. Córdoba, F. J. Valverde-Muñoz, J. Herrero-Martín, J. A. Real and E. Coronado, *Adv. Mater.*, 2022, **34**, 2202551.

134 H. J. Shepherd, G. Molnár, W. Nicolazzi, L. Salmon and A. Bousseksou, *Eur. J. Inorg. Chem.*, 2013, 653–661.

135 F. L. Liu and J. Tao, *Chem. – Eur. J.*, 2017, **23**, 18252–18257.

136 G. Molnár, T. Guillon, N. O. Moussa, L. Rechignat, T. Kitazawa, M. Nardone, A. Bousseksou, N. Ould Moussa and T. Kitazawa, *Chem. Phys. Lett.*, 2006, **423**, 152–156.

137 R. Akiyoshi, K. Kuroiwa, S. Alao Amolegbe, M. Nakaya, R. Ohtani, M. Nakamura, L. F. Lindoy and S. Hayami, *Chem. Comm.*, 2017, **53**, 4685–4687.

138 S. Hayami, N. Motokawa, A. Shuto, N. Masuhara, T. Someya, Y. Ogawa, K. Inoue and Y. Maeda, *Inorg. Chem.*, 2007, **46**, 1789–1794.

139 P. Grondin, O. Roubeau, M. Castro, H. Saadaoui, A. Colin and R. Clérac, *Langmuir*, 2010, **26**, 5184–5195.

140 I. A. Gural'skiy, V. A. Reshetnikov, A. Szebesczyk, E. Gumienna-Kontecka, A. I. Marynin, S. I. Shylin, V. Ksenofontov and I. O. Fritsky, *J. Mater. Chem. C*, 2015, **3**, 4737–4741.

141 L. Pukenas, F. Benn, E. Lovell, A. Santoro, L. J. Kershaw Cook, M. A. Halcrow and S. D. Evans, *J. Mater. Chem. C*, 2015, **3**, 7890–7896.

142 F. Armand, C. Badoux, P. Bonville and A. Ruaudel-Teixier, *Langmuir*, 1995, **11**, 3467–3472.

143 J. A. Kitchen, N. G. White, C. Gandolfi, M. Albrecht, G. N. L. Jameson, J. L. Tallon and S. Brooker, *Chem. Comm.*, 2010, **46**, 6464–6466.

144 D. Rosario-Amorin, P. Dechambenoit, A. Bentaleb, M. Rouzières, C. Mathonière and R. Clérac, *J. Am. Chem. Soc.*, 2018, **140**, 98–101.

145 R. Akiyoshi, R. Ohtani, L. F. Lindoy and S. Hayami, *Dalton Trans.*, 2021, **50**, 5065–5079.

146 J. Weihermüller, S. Schlamp, W. Milius, F. Puchtler, J. Breu, P. Ramming, S. Hüttner, S. Agarwal, C. Göbel, M. Hund, G. Papastavrou and B. Weber, *J. Mater. Chem. C*, 2019, **7**, 1151–1163.

147 S. Hayami, Y. Shigeyoshi, M. Akita, K. Inoue, K. Kato, K. Osaka, M. Takata, R. Kawajiri, T. Mitani and Y. Maeda, *Angew. Chem.*, *Int. Ed.*, 2005, **44**, 4899–4903.

148 S. Hayami, Y. Yamamoto, Y. Kojima and K. Inoue, in *Journal of Physics: Conference Series*, Institute of Physics Publishing, 2010, vol. 200.

149 Y. Galyametdinov, V. Ksenofontov, A. Prosvirin, I. Ovchinnikov, G. Ivanova, P. Gütlich, W. Haase, Y. Galyametdinov, A. Prosvirin, I. Ovchinnikov, Dipl.-E. G. Ivanova, P. Gütlich, V. Ksenofontov and W. Haase, *Angew. Chem.*, *Int. Ed.*, 2001, **40**, 4269.

150 A. B. Gaspar and M. Seredyuk, *Coord. Chem. Rev.*, 2014, **268**, 41–58.

151 I. Galadzhun, R. Kulmaczewski, N. Shahid, O. Cespedes, M. J. Howard, M. A. Halcrow, R. Li, / Chemcomm and C. Communication, *Chem. Commun.*, 2021, **57**, 4039.

152 J. Lin, P. Tong, K. Zhang, K. Tao, W. Lu, X. Wang, X. Zhang, W. Song and Y. Sun, *Nat. Commun.*, 2022, **13**, 1–7.

153 R. Akiyoshi, Y. Hirota, D. Kosumi, M. Tsutsumi, M. Nakamura, L. F. Lindoy and S. Hayami, *Chem. Sci.*, 2019, **10**, 5843–5848.

154 Y. Lin and S. A. Lang, *J. Heterocycl. Chem.*, 1977, **14**, 345–347.

155 L. Zhao, K. M. C. Wong, B. Li, W. Li, N. Zhu, L. Wu and V. W. W. Yam, *Chem. – Eur. J.*, 2010, **16**, 6797–6809.

156 I. C. Berdiell, T. Hochdörffer, C. Desplanches, R. Kulmaczewski, N. Shahid, J. A. Wolny, S. L. Warriner, O. Cespedes, V. Schünemann, G. Chastanet and M. A. Halcrow, *J. Am. Chem. Soc.*, 2019, **141**, 18759–18770.

157 M. A. Halcrow, *Chem. Soc. Rev.*, 2011, **40**, 4119–4142.

158 S. Schlamp, P. Thoma and B. Weber, *Chem. – Eur. J.*, 2014, **20**, 6462–6473.

159 *Textures of liquid crystals*, ed. I. Dierking, Wiley-VCH, 2003.

160 C. López-Bueno, M. R. Bittermann, B. Dacuña-Mariño, A. L. Llamas-Saiz, M. Del Carmen Giménez-López, S. Woutersen and F. Rivadulla, *Phys. Chem. Chem. Phys.*, 2020, **22**, 20524–20530.

161 S. Liu, Z. Zhu, X. L. Li and J. Tang, *Inorg. Chem. Front.*, 2022, **9**, 267–274.

162 W. H. Chen, W. T. Chuang, U. S. Jeng, H. S. Sheu and H. C. Lin, *J. Am. Chem. Soc.*, 2011, **133**, 15674–15685.

163 M. Martínez-Abadía, R. Giménez and M. B. Ros, *Adv. Mater.*, 2018, **30**, 1704161.

164 E. J. Devid, P. N. Martinho, M. V. Kamalakar, I. Šalitroš, Ú. Prendergast, J. F. Dayen, V. Meded, T. Lemma, R. González-Prieto, F. Evers, T. E. Keyes, M. Ruben, B. Doudin and S. J. Van Der Molen, *ACS Nano*, 2015, **9**, 4496–4507.

165 C. Matthias Grunert, H. A. Goodwin, C. Carbonera, J. F. Létard, J. Kusz and P. Gütlich, *J. Phys. Chem. B*, 2007, **111**, 6738–6747.

166 N. F. Sciortino, K. R. Scherl-Gruenwald, G. Chastanet, G. J. Halder, K. W. Chapman, J. F. Létard and C. J. Kepert, *Angew. Chem.*, *Int. Ed.*, 2012, **51**, 10154–10158.

167 C. P. Bean and D. S. Rodbell, *Phys. Rev.*, 1961, **126**, 104–115.

168 *Introduction to Phase Transitions and Critical Phenomena*, ed. H. E. Stanley, Oxford University Press, 1971.

169 D. Chernyshov, H. B. Bürgi, M. Hostettler and K. W. Tösrnroos, *Phys. Rev. B.*, 2004, **70**, 094116.

170 M. Paez-Espejo, M. Sy and K. Boukheddaden, *J. Am. Chem. Soc.*, 2016, **138**, 3202–3210.

171 M. W. Haverkort, Z. Hu, J. C. Cezar, T. Burnus, H. Hartmann, M. Reuther, C. Zobel, T. Lorenz, A. Tanaka, N. B. Brookes, H. H. Hsieh, H. J. Lin, C. T. Chen and L. H. Tjeng, *Phys. Rev. Lett.*, 2006, **97**, 176405.

172 J. Cruddas and B. J. Powell, *Inorg. Chem. Front.*, 2020, **7**, 4424–4437.

173 V. A. Money, J. Elhaïk, M. A. Halcrow and J. A. K. Howard, *J. Chem. Soc. Dalton Trans.*, 2004, **4**, 1516–1518.

174 T. Vermonden, D. Branowska, A. T. M. Marcelis and E. J. R. Sudhölter, *Tetrahedron*, 2003, **59**, 5039–5045.

175 J. Elhaïk, V. A. Money, S. A. Barrett, C. A. Kilner, I. R. Evans and M. A. Halcrow, *Dalton Trans.*, 2003, **2003**, 2053–2060.

176 R. J. Deeth, M. A. Halcrow, L. J. Kershaw Cook and P. R. Raithby, *Chem. – Eur. J.*, 2018, **24**, 5204–5212.

177 A. L. Gérard, C. Mahatsekake, V. Collot and S. Rault, *Tetrahedron Lett.*, 2007, **48**, 4123–4126.

178 R. Bernardi, F. Bertini, R. Galli and M. Perchinijmmo, *Tetrahedron*, 1971, **27**, 3575–3579.

179 D. Gygi, S. J. Hwang and D. G. Nocera, *J. Org. Chem.*, 2017, **82**, 12933–12938.

180 P. Guionneau, M. Marchivie, G. Bravic, J. F. Létard and D. Chasseau, *J. Mater. Chem.*, 2002, **12**, 2546–2551.

181 X. Zhang, X. F. Qiao, W. Shi, J. Bin Wu, D. S. Jiang and P. H. Tan, *Chem. Soc. Rev.*, 2015, **44**, 2757–2785.

182 C. Lochenie, W. Bauer, A. P. Railliet, S. Schlamp, Y. Garcia and B. Weber, *Inorg. Chem.*, 2014, **53**, 11563–11572.

183 M. Feng and M. L. Tong, *Chem. – Eur. J.*, 2018, **24**, 7574–7594.

184 R. Mitsuhashi, S. Hosoya, T. Suzuki, Y. Sunatsuki, H. Sakiyama and M. Mikuriya, *RSC Adv.*, 2020, **10**, 43472–43479.

185 A. Sarkar, S. Dey and G. Rajaraman, *Chem. – Eur. J.*, 2020, **26**, 14036–14058.

186 A. K. Bar, C. Pichon, N. Gogoi, C. Duhayon, S. Ramasesha and J. P. Sutter, *Chem. Comm.*, 2015, **51**, 3616–3619.

187 F. R. Fortea-Pérez, J. Vallejo, T. F. Mastropietro, G. De Munno, R. Rabelo, J. Cano and M. Julve, *Molecules*, 2023, **28**, 4423.

188 Y. Rechkemmer, F. D. Breitgoff, M. Van Der Meer, M. Atanasov, M. Hakl, M. Orlita, P. Neugebauer, F. Neese, B. Sarkar and J. Van Slageren, *Nat. Commun.*, 2016, **7**, 10467.

189 B. Yao, M. K. Singh, Y. F. Deng, Y. N. Wang, K. R. Dunbar and Y. Z. Zhang, *Inorg. Chem.*, 2020, **59**, 8505–8513.

190 Y. Z. Zhang, A. J. Brown, Y. S. Meng, H. L. Sun and S. Gao, *Dalton Trans.*, 2015, **44**, 2865–2870.

191 X. N. Yao, J. Z. Du, Y. Q. Zhang, X. B. Leng, M. W. Yang, S. Da Jiang, Z. X. Wang, Z. W. Ouyang, L. Deng, B. W. Wang and S. Gao, *J. Am. Chem. Soc.*, 2017, **139**, 373–380.

192 J. Vallejo, M. Viciano-Chumillas, F. Lloret, M. Julve, I. Castro, J. Krzystek, M. Ozerov, D. Armentano, G. De Munno and J. Cano, *Inorg. Chem.*, 2019, **58**, 15726–15740.

193 J. R. Jiménez, B. Xu, H. El Said, Y. Li, J. Von Bardeleben, L. M. Chamoreau, R. Lescouëzec, S. Shova, D. Visinescu, M. G. Alexandru, J. Cano and M. Julve, *Dalton Trans.*, 2021, **50**, 16353–16363.

194 D. Valigura, C. Rajnák, J. Moncol, J. Titiš and R. Boča, *Dalton Trans.*, 2017, **46**, 10950–10956.

195 A. Eichhöfer, Y. Lan, V. Mereacre, T. Bodenstein and F. Weigend, *Inorg. Chem.*, 2014, **53**, 1962–1974.

196 I. Nemec, O. F. Fellner, B. Indruchová and R. Herchel, *Mater.*, 2022, **15**, 1064.

197 P. S. Perlepe, D. Maniaki, E. Pilichos, E. Katsoulakou and S. P. Perlepes, *Inorganics*, 2020, 8, 1–45.

198 J. Vallejo, F. R. Fortea-Pérez, E. Pardo, S. Benmansour, I. Castro, J. Krzystek, D. Armentano and J. Cano, *Chem. Sci.*, 2016, **7**, 2286–2293.

199 L. J. Kershaw Cook, F. L. Thorp-Greenwood, T. P. Comyn, O. Cespedes, G. Chastanet and M. A. Halcrow, *Inorg. Chem.*, 2015, **54**, 6319–6330.

200 S. Hayami, Y. Komatsu, T. Shimizu, H. Kamihata and Y. H. Lee, *Coord. Chem. Rev.*, 2011, **255**, 1981–1990.

201 L. T. Birchall, G. Truccolo, L. Jackson and H. J. Shepherd, *Chem. Sci.*, 2022, **13**, 3176–3186.

202 R. Ketkaew, Y. Tantirungrotechai, P. Harding, G. Chastanet, P. Guionneau, M. Marchivie and D. J. Harding, *Dalton Trans.*, 2021, **50**, 1086–1096.

203 Z. Zhu, G. Wang, Z. Xu, Z. Chen, J. Wang, J. Shi and W. Zhu, *Phys. Chem. Chem. Phys.*, 2019, **21**, 15106–15119.

204 R. Boča, *Coord. Chem. Rev.*, 2004, **248**, 757–815.

205 N. F. Chilton, R. P. Anderson, L. D. Turner, A. Soncini and K. S. Murray, *J. Comput. Chem.*, 2013, **34**, 1164–1175.

206 *Organometallic Magnets*, ed. S. Tripathi, A. Dey, M. Shanmugam, R. S. Narayanan, V. Chandrasekhar, V. Chandrasekhar and F. Pointillart, Springer, 2019.

207 A. Świtlicka, B. Machura, M. Penkala, A. Bieńko, D. C. Bieńko, J. Titiš, C. Rajnák, R. Boča, A. Ozarowski and M. Ozerov, *Inorg. Chem.*, 2018, **57**, 12740–12755.

208 H. H. Cui, F. Lu, X. T. Chen, Y. Q. Zhang, W. Tong and Z. L. Xue, *Inorg. Chem.*, 2019, **58**, 12555–12564.

209 Y. Cui, Y. Xu, X. Liu, Y. Li, B. L. Wang, Y. Dong, W. Li and S. Lei, *Chem. Asian J.*, 2019, **14**, 2620–2628.

210 M. Yang, Z. J. Ouyang, Y. J. Zhong, J. W. Cai, X. H. Li and W. Dong, *Dalton Trans.*, 2020, **49**, 17017–17025.

211 F. Yang, Q. Zhou, Y. Zhang, G. Zeng, G. Li, Z. Shi, B. Wang and S. Feng, *Chem. Comm.*, 2013, **49**, 5289–5291.

212 H. H. Cui, Y. Q. Zhang, X. T. Chen, Z. Wang and Z. L. Xue, *Dalton Trans.*, 2019, **48**, 10743–10752.

213 D. Reta and N. F. Chilton, *Phys. Chem. Chem. Phys.*, 2019, **21**, 23567–23575.

214 W. J. A. Blackmore, G. K. Gransbury, P. Evans, J. G. C. Kragskow, D. P. Mills and N. F. Chilton, *Phys. Chem. Chem. Phys.*, 2023, **25**, 16735–16744.

215 A. B. Andreeva, K. N. Le, K. Kadota, S. Horike, C. H. Hendon and C. K. Brozek, *Chem. Mater.*, 2021, **33**, 8534–8545.

216 M. G. Reeves, E. Tailleur, P. A. Wood, M. Marchivie, G. Chastanet, P. Guionneau and S. Parsons, *Chem Sci*, 2021, **12**, 1007–1015.

217 K. A. Zenere, S. G. Duyker, E. Trzop, E. Collet, B. Chan, P. W. Doheny, C. J. Kepert and S. M. Neville, *Chem Sci*, 2018, **9**, 5623–5629.

218 N. Nassirinia, S. Amani, S. J. Teat, O. Roubeau and P. Gamez, *Chemical Communications*, 2014, **50**, 1003–1005.

219 L. Trevisan, A. D. Bond and C. A. Hunter, *J. Am. Chem. Soc.*, 2022, **144**, 19499–19507.

220 C. Y. Niu, B. L. Wu, X. F. Zheng, X. S. Wan, H. Y. Zhang, Y. Y. Niu and L. Y. Meng, *CrystEngComm*, 2009, **11**, 1373–1382.

221 C. A. Simosono, R. M. R. da Silva, N. R. De Campos, M. A. R. Silva, A. C. Doriguetto, L. S. Flores, C. C. Correa, T. R. G. Simões, A. K. S. M. Valdo, F. T. Martins, F. Garcia, G. P. Guedes, B. R. L. Galvão, J. Cancino-Bernardi, R. D. dos Reis, H. O. Stumpf, D. D. Justino, P. F. R. Ortega, W. D. do Pim, M. Julve and M. V. Marinho, *Molecules*, 2023, **28**, 2086.

222 K. H. Sugiyarto and H. A. Goodwin, *Aust. J. Chem*, 1988, **41**, 1645–63.

223 H. A. Goodwin and K. H. Sugiyarto, *Chem. Phys. Lett.*, 1987, **139**, 470–474.

224 J. D. Oliver, D. F. Mullica, B. B. Hutchinson and W. O. Milligan, *Inorg. Chem.*, 1980, **19**, 165–169.

225 B. Li, R. J. Wei, J. Tao, R. Bin Huang, L. S. Zheng and Z. Zheng, *J. Am. Chem. Soc.*, 2010, **132**, 1558–1566.

226 K. H. Sugiyarto, K. Weitzner, D. C. Craig and H. A. Goodwin, *Aust. J. Chem.*, 1997, **50**, 869–873.

227 M. C. Giménez-López, M. Clemente-León, E. Coronado, F. M. Romero, S. Shova and J. P. Tuchagues, *Eur. J. Inorg. Chem.*, 2005, **2005**, 2783–2787.

228 E. Coronado, M. C. Giménez-López, C. Gimenez-Saiz, J. M. Martínez-Agudo and F. M. Romero, *Polyhedron*, 2003, **22**, 2375–2380.

229 H. Y. Sun, Y. S. Meng and T. Liu, *Chem. Comm.*, 2019, **55**, 8359–8373.

230 B. Brachňaková and I. Šalitroš, *Chemical Papers*, 2018, **72**, 773–798.

231 G. Chastanet, M. Lorenc, R. Bertoni and C. Desplanches, *C. R. Chim.*, 2018, **21**, 1075–1094.

232 G. A. Craig, O. Roubeau and G. Aromí, *Coord. Chem. Rev.*, 2014, **269**, 13–31.

233 S. Vela, M. Fumanal and C. Sousa, *J. Mater. Chem. C*, 2022, **11**, 235–243.

234 M. Attwood, H. Akutsu, L. Martin, T. J. Blundell, P. Le Maguere and S. S. Turner, *Dalton Trans.*, 2021, **50**, 11843–11851.

235 Z. G. Lada, *Magnetochemistry*, 2022, **8**, 1–29.

236 H. J. Shepherd, G. Tonge, L. E. Hatcher, M. J. Bryant, J. V. Knichal, P. R. Raithby, M. A. Halcrow, R. Kulmaczewski, K. J. Gagnon and S. J. Teat, *Magnetochemistry*, 2016, **2**, 1–9.

237 A. Abhervé, M. J. Recio-Carretero, M. López-Jordá, J. M. Clemente-Juan, J. Canet-Ferrer, A. Cantarero, M. Clemente-León and E. Coronado, *Inorg. Chem.*, 2016, **55**, 9361–9367.

238 M. Lu, T. Chen, M. Wang, G. Jiang, T. Lu, G. Jiang and J. Du, *J. Mol. Struct.*, 2014, **1060**, 131–137.

239 H. Kim, K. Y. Park, J. Hong and K. Kang, *Sc.i Rep.*, 2014, **4**, 1–8.

240 N. Baig, Ihsanullah, M. Sajid and T. A. Saleh, *J. Environ. Manage.*, 2019, **244**, 370–382.

241 Q. He, S. Wu, Z. Yin and H. Zhang, *Chem. Sci.*, 2012, **3**, 1764–1772.

242 W. Han, R. K. Kawakami, M. Gmitra and J. Fabian, *Nat. Nanotechnol.*, 2014, **9**, 794–807.

243 H. J. Hwang, S. Y. Kim, S. K. Lee and B. H. Lee, *Carbon*, 2023, **201**, 467–472.

244 Y. Hernandez, V. Nicolosi, M. Lotya, F. M. Blighe, Z. Sun, S. De, I. T. McGovern, B. Holland, M. Byrne, Y. K. Gun'ko, J. J. Boland, P. Niraj, G. Duesberg, S. Krishnamurthy, R. Goodhue, J. Hutchison, V. Scardaci, A. C. Ferrari and J. N. Coleman, *Nat. Nanotechnol.*, 2008, **3**, 563–568.

245 S. Stankovich, D. A. Dikin, R. D. Piner, K. A. Kohlhaas, A. Kleinhammes, Y. Jia, Y. Wu, S. B. T. Nguyen and R. S. Ruoff, *Carbon*, 2007, **45**, 1558–1565.

246 S. Park, J. An, J. R. Potts, A. Velamakanni, S. Murali and R. S. Ruoff, *Carbon*, 2011, **49**, 3019–3023.

247 Y. Zhu, S. Murali, W. Cai, X. Li, J. W. Suk, J. R. Potts and R. S. Ruoff, *Adv. Mater.*, 2010, **22**, 3906–3924.

248 A. Wang, W. Yu, Z. Huang, F. Zhou, J. Song, Y. Song, L. Long, M. P. Cifuentes, M. G. Humphrey, L. Zhang, J. Shao and C. Zhang, *Sci. Rep.*, 2016, **6**, 1–12.

249 A. Sinitskii, A. Dimiev, D. A. Corley, A. A. Fursina, D. V. Kosynkin and J. M. Tour, *ACS Nano*, 2010, **4**, 1949–1954.

250 H. Li and R. Papadakis, *Polymers*, 2021, **13**, 1–19.

251 D. Yu, Y. Yang, M. Durstock, J. B. Baek and L. Dai, *ACS Nano*, 2010, **4**, 5633–5640.

252 Z. Liu, J. T. Robinson, X. Sun and H. Dai, *J. Am. Chem. Soc.*, 2008, **130**, 10876–10877.

253 M. Quintana, K. Spyrou, M. Grzelczak, W. R. Browne, P. Rudolf and M. Prato, *ACS Nano*, 2010, **4**, 3527–3533.

254 V. Georgakilas, A. B. Bourlinos, R. Zboril, T. A. Steriotis, P. Dallas, A. K. Stubos and C. Trapalis, *Chem. Comm.*, 2010, **46**, 1766–1768.

255 L. H. Liu, M. M. Lerner and M. Yan, *Nano Lett.*, 2010, **10**, 3754–3756.

256 J. Chen, Y. Zhang, M. Zhang, B. Yao, Y. Li, L. Huang, C. Li and G. Shi, *Chem. Sci.*, 2016, **7**, 1874–1881.

257 K. Phasuksom, W. Prissanaroon-Ouajai and A. Sirivat, *RSC Adv.*, 2020, **10**, 15206–15220.

258 D. López-Díaz, J. A. Delgado-Notario, V. Clericò, E. Diez, M. D. Merchán and M. M. Velázquez, *Coatings*, 2020, **10**, 1–12.

259 C. Wetzl, A. Silvestri, M. Garrido, H. L. Hou, A. Criado and M. Prato, *Angew. Chem., Int. Ed.*, 2023, **62**, 1–20.

260 I. Y. Jeon, H. J. Choi, M. J. Ju, I. T. Choi, K. Lim, J. Ko, H. K. Kim, J. C. Kim, J. J. Lee, D. Shin, S. M. Jung, J. M. Seo, M. J. Kim, N. Park, L. Dai and J. B. Baek, *Sci. Rep.*, 2013, **3**, 1–7.

261 G. Yasin, M. Arif, M. Shakeel, Y. Dun, Y. Zuo, W. Q. Khan, Y. Tang, A. Khan and M. Nadeem, *Adv. Eng. Mater.*, 2018, **20**, 1701166.

262 A. Naranjo, N. Martín Sabanés, M. Vázquez Sulleiro and E. M. Pérez, *Chem. Comm.*, 2022, **58**, 7813–7816.

263 Y. Zhou, D. Yang, L. Li, F. Li and J. F. Li, *Rev. Sci. Instrum.*, 2014, **85**, 054904.

264 J. Choi, N. D. K. Tu, S. S. Lee, H. Lee, J. S. Kim and H. Kim, *Macromol Res*, 2014, **22**, 1104–1108.

8 APPENDICES – RIGHTS & PERMISSIONS

Appendix I: Conflict of interest

Yolanda Sabater Algarra, the doctoral candidate, declares that there is no conflict of interest associated with this Doctoral Thesis.

Santiago de Compostela, May 19th, 2024

Appendix II: Rights and permissions

Figure 3.1.2. Different types of spin crossover curves: Left to right — abrupt and complete, gradual and complete, stepped and complete, abrupt and complete with hysteresis, and gradual and incomplete. Reproduced with permission from [16]. Copyright 2020, MDPI.

Figure 3.2.1. SCO temperature $T1_{/2\ for}$ [Fe(X-pybox)$_2$] vs ρ (Npy) [Fe(X-1-bpp)$_2$](BF4)$_2$ vs ρ (Npy) and [FeII(Lazinyl$_)$2(NCBH3$_)$2] vs ρ (NA). Reproduced with permission from [38]. Copyright 2018, American Chemical Society.

Figure 3.2.2. Top: 3D supramolecular disposition highlighting the N···N distance (hydrogens are omitted for clarity). Bottom: variable temperature magnetic measurements. Image reproduced from [46], Copyright 2016, American Chemical Society.

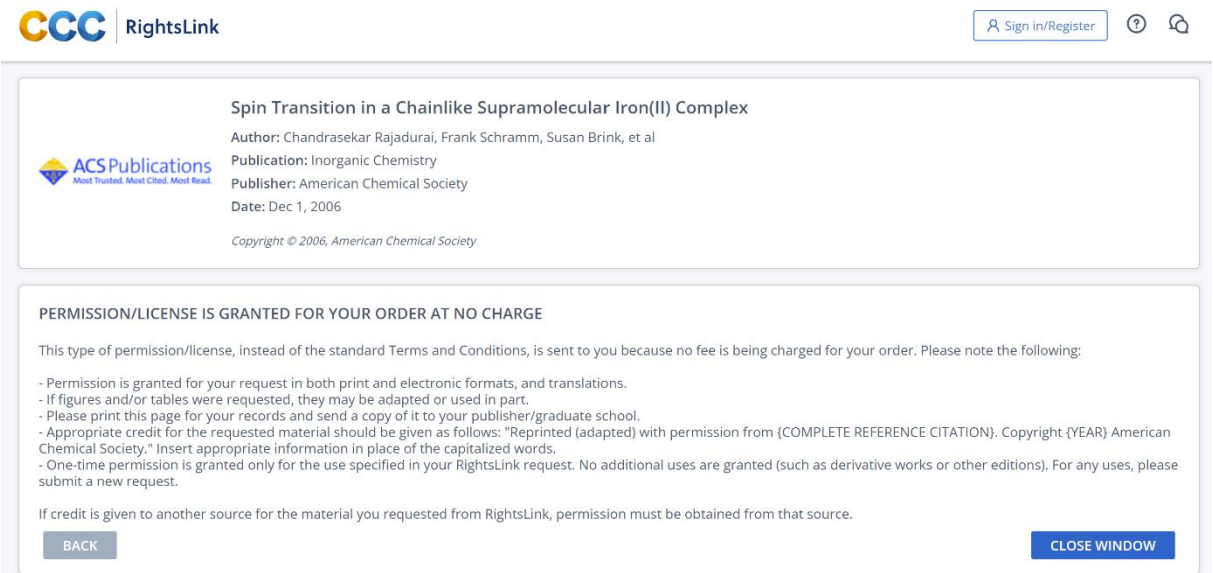

Figure 3.2.4. Temperature dependence of $\chi_M T$ for 1–4. Reproduced with permission from [53]. Copyright 2012, Royal Society of Chemistry.

Figure 3.2.5. The spin-crossover equilibrium midpoint temperature ($T1_{/2}$) in $[Fe(3\text{-bpp})_2]X2$ (3-bpp = 2,6-di{pyrazol-3-yl}pyridine) varies from 259 K when X^- = $BPh4^-$ to 277 K when X^- = Br^- , in a polar acetone:water solvent mixture. Reproduced with permission from [62]. Copyright 2014, Royal Society of Chemistry.

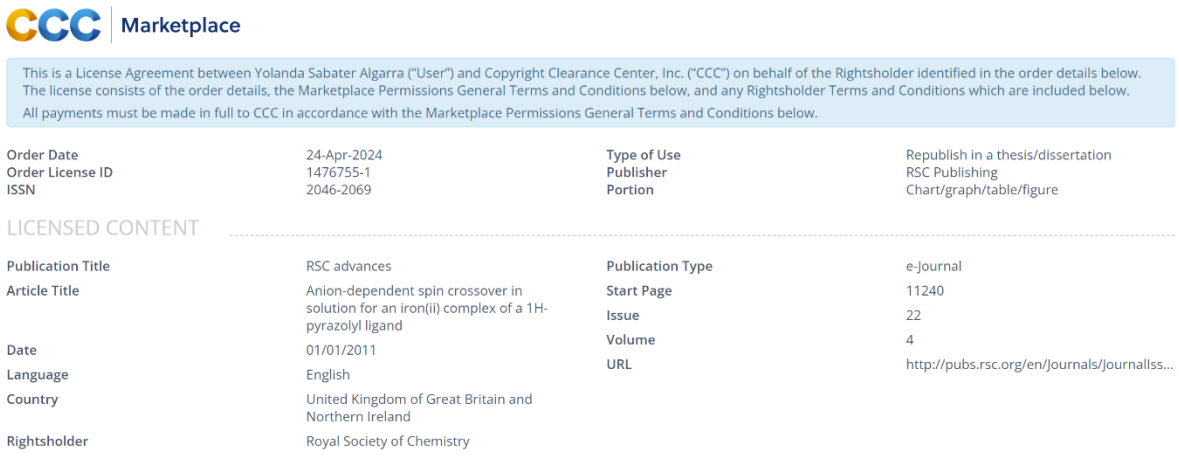

CCC Marketplace

This is a License Agreement between Yolanda Sabater Algarra ("User") and Copyright Clearance Center, Inc. ("CCC") on behalf of the Rightsholder identified in the order details below. The license consists of the order details, the Marketplace Permissions General Terms and Conditions below, and any Rightsholder Terms and Conditions which are included below.
All payments must be made in full to CCC in accordance with the Marketplace Permissions General Terms and Conditions below.

Order Date	24-Apr-2024	Type of Use	Republish in a thesis/dissertation
Order License ID	1476755-1	Publisher	RSC Publishing
ISSN	2046-2069	Portion	Chart/graph/table/figure

LICENSED CONTENT

Publication Title	RSC advances	Publication Type	e-Journal
Article Title	Anion-dependent spin crossover in solution for an iron(ii) complex of a 1H-pyrazolyl ligand	Start Page	11240
		Issue	22
Date	01/01/2011	Volume	4
Language	English	URL	http://pubs.rsc.org/en/Journals/Journallss...
Country	United Kingdom of Great Britain and Northern Ireland		
Rightsholder	Royal Society of Chemistry		

Figure 3.2.6. a) Magneto-structural correlations for 1 and 5 showing the relationship between the different packing diagrams and the variable-temperature magnetic susceptibility (2–400 K) towards the desolvation process. π– π stacking interactions are shown in yellow. Reproduced with permission from [67]. Copyright 2018, Royal Society of Chemistry. b) χMT versus T plots (per Fe unit) of 1·CH3OH, 1·C2H5OH, 1·H2O, 1·CH3CN-A, 1·CH3CN-B, and 1·CH2Cl2. Reproduced with permission from [68]. Copyright 20218, American Chemical Society.

CCC Marketplace

This is a License Agreement between Yolanda Sabater Algarra ("User") and Copyright Clearance Center, Inc. ("CCC") on behalf of the Rightsholder identified in the order details below. The license consists of the order details, the Marketplace Permissions General Terms and Conditions below, and any Rightsholder Terms and Conditions which are included below.
All payments must be made in full to CCC in accordance with the Marketplace Permissions General Terms and Conditions below.

Order Date	24-Apr-2024	Type of Use	Republish in a thesis/dissertation
Order License ID	1476790-1	Publisher	ROYAL SOCIETY OF CHEMISTRY
ISSN	1477-9234	Portion	Chart/graph/table/figure

LICENSED CONTENT

Publication Title	Dalton transactions	Rightsholder	Royal Society of Chemistry
Article Title	Unravelling the spin-state of solvated [Fe(bpp)2]2+ spin-crossover complexes: structure-function relationship.	Publication Type	e-Journal
		Start Page	10453
Author/Editor	Royal Society of Chemistry (Great Britain)	End Page	10462
Date	01/01/2003	Issue	31
Language	English	Volume	47
Country	United Kingdom of Great Britain and Northern Ireland		

Figure 3.2.6. a) Magneto-structural correlations for 1 and 5 showing the relationship between the different packing diagrams and the variable-temperature magnetic susceptibility (2–400 K) towards the desolvation process. π– π stacking interactions are shown in yellow. Reproduced with permission from [67]. Copyright 2018, Royal Society of Chemistry. b) χMT versus T plots (per Fe unit) of 1·CH3OH, 1·C2H5OH, 1·H2O, 1·CH3CN-A, 1·CH3CN-B, and 1·CH2Cl2. Reproduced with permission from [68]. Copyright 20218, American Chemical Society.

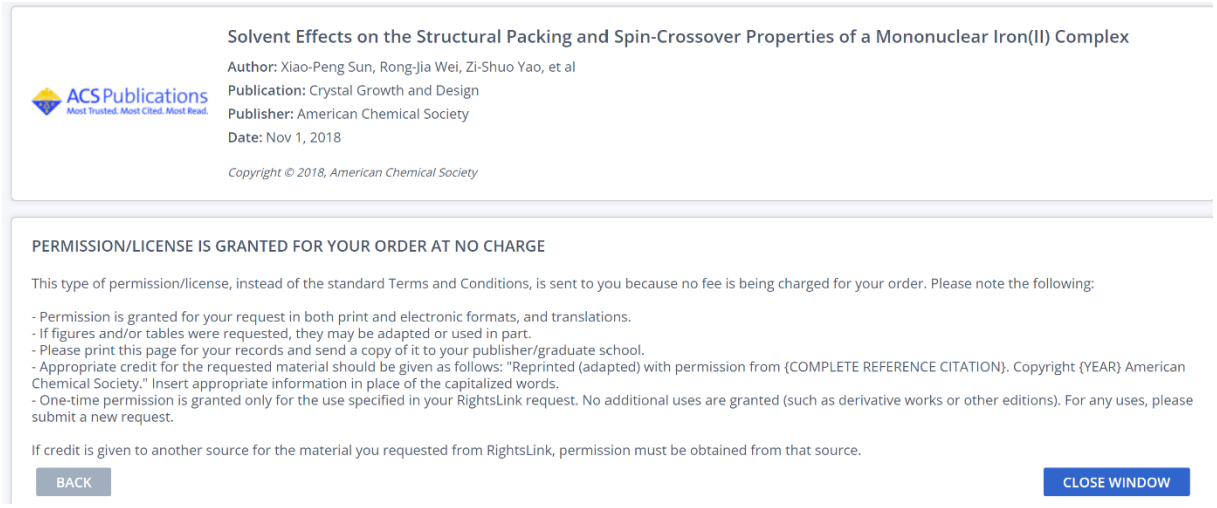

ACS Publications
Most Trusted. Most Cited. Most Read.

Solvent Effects on the Structural Packing and Spin-Crossover Properties of a Mononuclear Iron(II) Complex

Author: Xiao-Peng Sun, Rong-Jia Wei, Zi-Shuo Yao, et al
Publication: Crystal Growth and Design
Publisher: American Chemical Society
Date: Nov 1, 2018

Copyright © 2018, American Chemical Society

PERMISSION/LICENSE IS GRANTED FOR YOUR ORDER AT NO CHARGE

This type of permission/license, instead of the standard Terms and Conditions, is sent to you because no fee is being charged for your order. Please note the following:

- Permission is granted for your request in both print and electronic formats, and translations.
- If figures and/or tables were requested, they may be adapted or used in part.
- Please print this page for your records and send a copy of it to your publisher/graduate school.
- Appropriate credit for the requested material should be given as follows: "Reprinted (adapted) with permission from {COMPLETE REFERENCE CITATION}. Copyright {YEAR} American Chemical Society." Insert appropriate information in place of the capitalized words.
- One-time permission is granted only for the use specified in your RightsLink request. No additional uses are granted (such as derivative works or other editions). For any uses, please submit a new request.

If credit is given to another source for the material you requested from RightsLink, permission must be obtained from that source.

BACK CLOSE WINDOW

Figure 3.3.1. Jablonski diagram displaying the mechanism of LIESST. Reproduced with permission from [8]. Copyright 2020, Wiley.

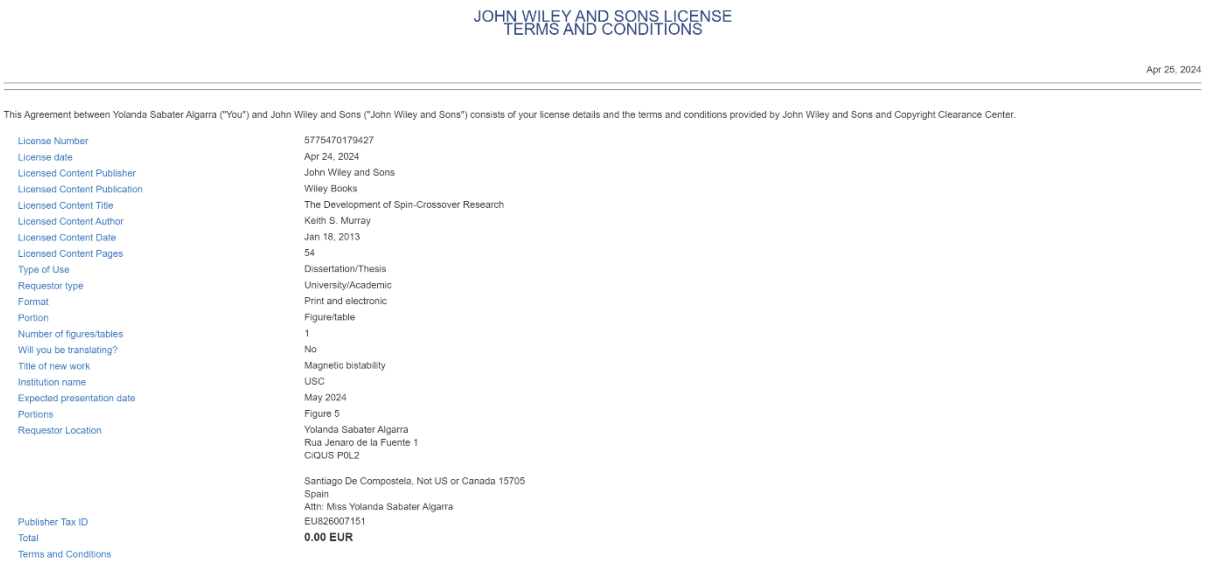

JOHN WILEY AND SONS LICENSE
TERMS AND CONDITIONS

Apr 25, 2024

This Agreement between Yolanda Sabater Algarra ("You") and John Wiley and Sons ("John Wiley and Sons") consists of your license details and the terms and conditions provided by John Wiley and Sons and Copyright Clearance Center.

License Number	5775470179427
License date	Apr 24, 2024
Licensed Content Publisher	John Wiley and Sons
Licensed Content Publication	Wiley Books
Licensed Content Title	The Development of Spin-Crossover Research
Licensed Content Author	Keith S. Murray
Licensed Content Date	Jan 18, 2013
Licensed Content Pages	54
Type of Use	Dissertation/Thesis
Requestor type	University/Academic
Format	Print and electronic
Portion	Figure/table
Number of figures/tables	1
Will you be translating?	No
Title of new work	Magnetic bistability
Institution name	USC
Expected presentation date	May 2024
Portions	Figure 5
Requestor Location	Yolanda Sabater Algarra Rua Jenaro de la Fuente 1 CIQUS P0L2 Santiago De Compostela, Not US or Canada 15705 Spain Attn: Miss Yolanda Sabater Algarra
Publisher Tax ID	EU826007151
Total	**0.00 EUR**
Terms and Conditions	

Figure 3.3.2. 4 K X-ray absorption spectra of the FeIIL3 edge before and after illumination of the sample with a blue light for Cu(111) (a), Ag(111) (b) and Au(111) (c). d) Reference spectra recorded at 4 K and 290 K on a 130 nm thick film on a SiO2 substrate. Reproduced with permission from [77]. Copyright 2020, Wiley

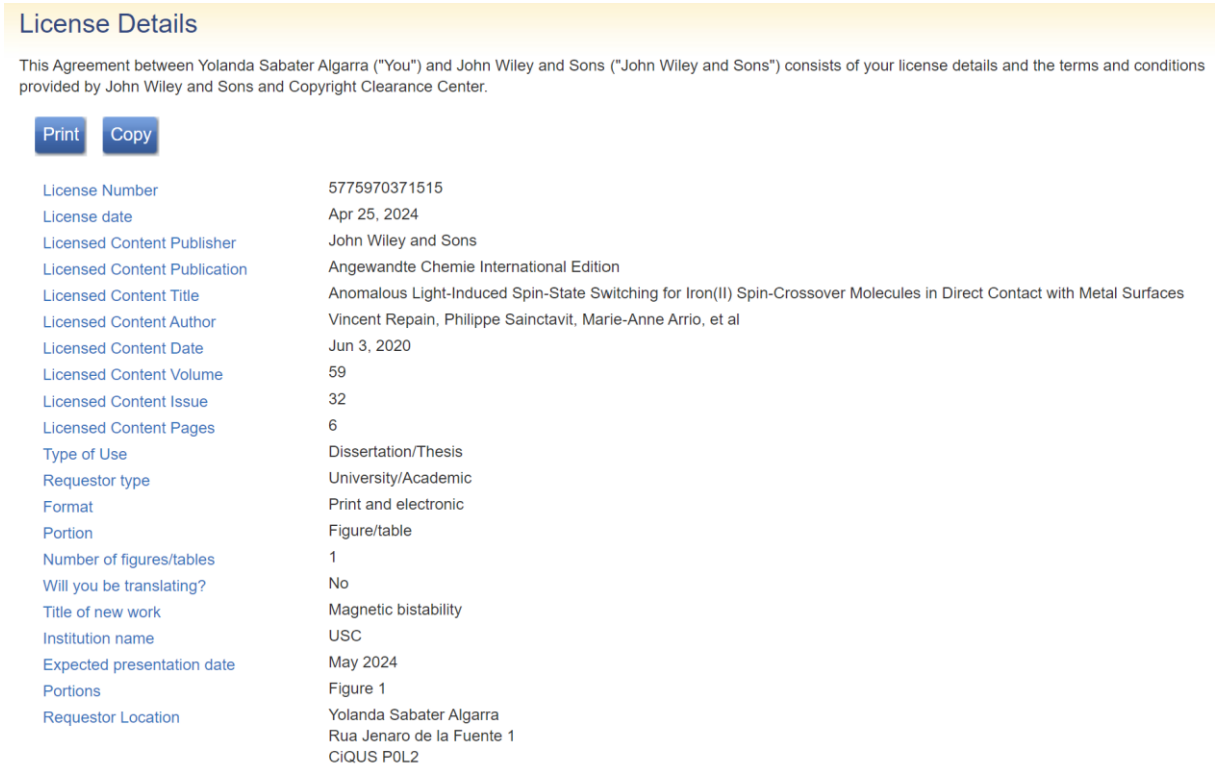

License Details

This Agreement between Yolanda Sabater Algarra ("You") and John Wiley and Sons ("John Wiley and Sons") consists of your license details and the terms and conditions provided by John Wiley and Sons and Copyright Clearance Center.

Print Copy

License Number	5775970371515
License date	Apr 25, 2024
Licensed Content Publisher	John Wiley and Sons
Licensed Content Publication	Angewandte Chemie International Edition
Licensed Content Title	Anomalous Light-Induced Spin-State Switching for Iron(II) Spin-Crossover Molecules in Direct Contact with Metal Surfaces
Licensed Content Author	Vincent Repain, Philippe Sainctavit, Marie-Anne Arrio, et al
Licensed Content Date	Jun 3, 2020
Licensed Content Volume	59
Licensed Content Issue	32
Licensed Content Pages	6
Type of Use	Dissertation/Thesis
Requestor type	University/Academic
Format	Print and electronic
Portion	Figure/table
Number of figures/tables	1
Will you be translating?	No
Title of new work	Magnetic bistability
Institution name	USC
Expected presentation date	May 2024
Portions	Figure 1
Requestor Location	Yolanda Sabater Algarra Rua Jenaro de la Fuente 1 CiQUS P0L2

Figure 3.3.3. Pressure effect on the SCO behaviors of (a) 1·EtOH, (b) 1·MeOH, and (c) 1. Reproduced with permission from [91]. Copyright 2012, American Chemical Society.

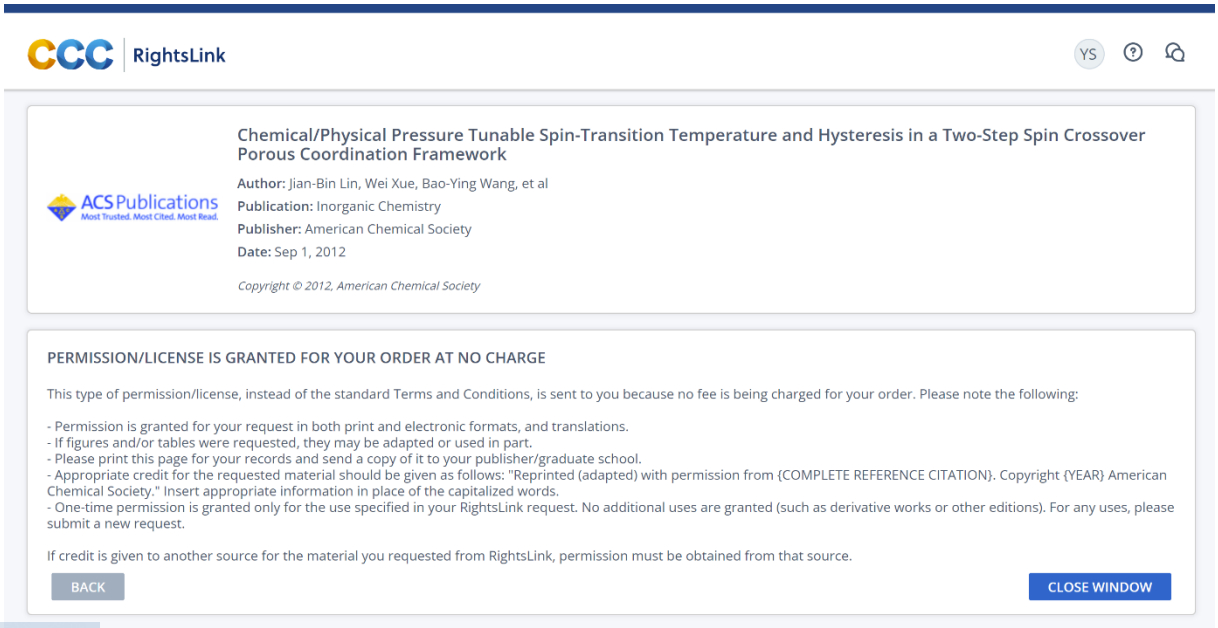

CCC RightsLink YS

ACS Publications Most Trusted. Most Cited. Most Read.

Chemical/Physical Pressure Tunable Spin-Transition Temperature and Hysteresis in a Two-Step Spin Crossover Porous Coordination Framework

Author: Jian-Bin Lin, Wei Xue, Bao-Ying Wang, et al
Publication: Inorganic Chemistry
Publisher: American Chemical Society
Date: Sep 1, 2012

Copyright © 2012, American Chemical Society

PERMISSION/LICENSE IS GRANTED FOR YOUR ORDER AT NO CHARGE

This type of permission/license, instead of the standard Terms and Conditions, is sent to you because no fee is being charged for your order. Please note the following:

- Permission is granted for your request in both print and electronic formats, and translations.
- If figures and/or tables were requested, they may be adapted or used in part.
- Please print this page for your records and send a copy of it to your publisher/graduate school.
- Appropriate credit for the requested material should be given as follows: "Reprinted (adapted) with permission from {COMPLETE REFERENCE CITATION}. Copyright {YEAR} American Chemical Society." Insert appropriate information in place of the capitalized words.
- One-time permission is granted only for the use specified in your RightsLink request. No additional uses are granted (such as derivative works or other editions). For any uses, please submit a new request.

If credit is given to another source for the material you requested from RightsLink, permission must be obtained from that source.

BACK CLOSE WINDOW

Figure 3.3.4. $Fe[HB(tz)_3]_2$ experiences a thermally triggered spin crossover (SCO) accompanied by a rise in both electronic entropy (ΔSelec) and vibrational entropy (ΔSvib). (b) Differential scanning calorimetry (DSC) conducted at ambient pressure, with heating and cooling rates set at 2 $K \cdot min^{-1}$ (top), along with helium pycnometry measurements (bottom), underscore the significant alterations in entropy and volume during the SCO transition, with minimal hysteresis observed. Reproduced with permission from [103]. Copyright 2022, American Chemical Society.

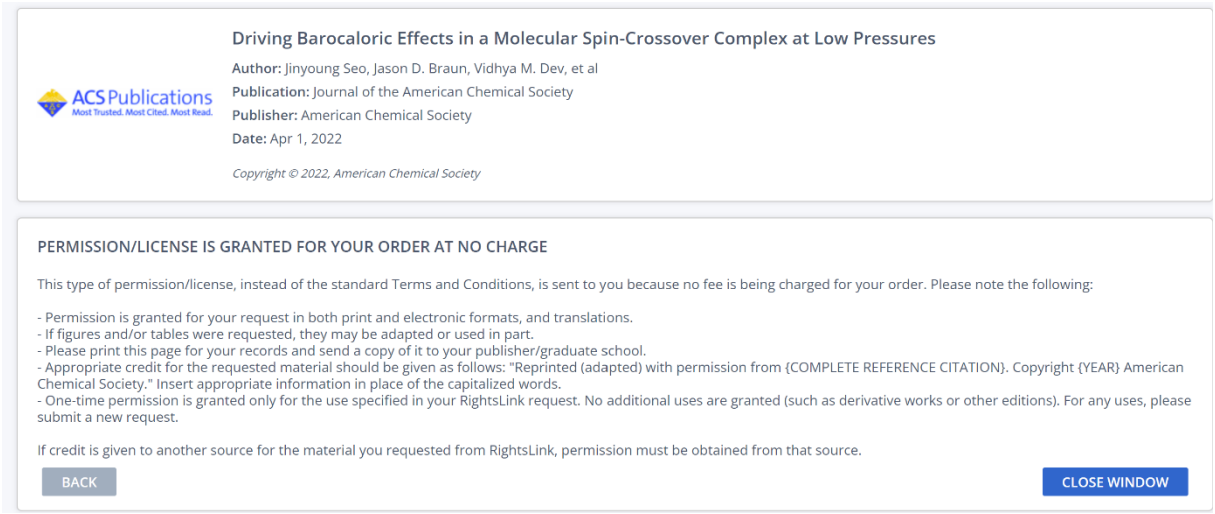

Driving Barocaloric Effects in a Molecular Spin-Crossover Complex at Low Pressures

Author: Jinyoung Seo, Jason D. Braun, Vidhya M. Dev, et al
Publication: Journal of the American Chemical Society
Publisher: American Chemical Society
Date: Apr 1, 2022

Copyright © 2022, American Chemical Society

PERMISSION/LICENSE IS GRANTED FOR YOUR ORDER AT NO CHARGE

This type of permission/license, instead of the standard Terms and Conditions, is sent to you because no fee is being charged for your order. Please note the following:

- Permission is granted for your request in both print and electronic formats, and translations.
- If figures and/or tables were requested, they may be adapted or used in part.
- Please print this page for your records and send a copy of it to your publisher/graduate school.
- Appropriate credit for the requested material should be given as follows: "Reprinted (adapted) with permission from {COMPLETE REFERENCE CITATION}. Copyright {YEAR} American Chemical Society." Insert appropriate information in place of the capitalized words.
- One-time permission is granted only for the use specified in your RightsLink request. No additional uses are granted (such as derivative works or other editions). For any uses, please submit a new request.

If credit is given to another source for the material you requested from RightsLink, permission must be obtained from that source.

BACK CLOSE WINDOW

Figure 3.4.1. a) Double-well energy diagram for negative (left) and positive (right) D. b) Schematic representation of possible relaxation pathways in SMM/SIM. Reproduced with permission from [109]. Copyright 2016, Royal Society of Chemistry.

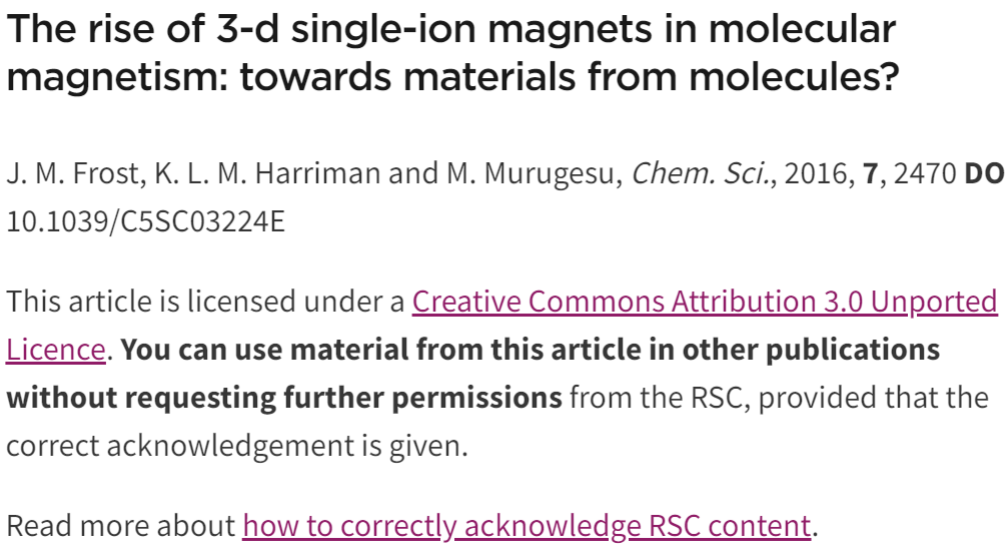

The rise of 3-d single-ion magnets in molecular magnetism: towards materials from molecules?

J. M. Frost, K. L. M. Harriman and M. Murugesu, *Chem. Sci.*, 2016, **7**, 2470 **DOI:** 10.1039/C5SC03224E

This article is licensed under a Creative Commons Attribution 3.0 Unported Licence. **You can use material from this article in other publications without requesting further permissions** from the RSC, provided that the correct acknowledgement is given.

Read more about how to correctly acknowledge RSC content.

Figure 3.4.2. Orientations of gx, gy, and gz (hard axis) on CoII of complexes 1-4 (a-d). Frequency dependence of the in-phase (χ′) and out-of-phase (χ″) parts of the ac magnetic susceptibilities for 1-4 collected under a 1.5 kOe dc field over the temperature range of 1.8-6.0 K. Reproduced with permission from [112]. Copyright 2016, American Chemical Society.

ACS Publications
Most Trusted. Most Cited. Most Read.

Probing the Effect of Axial Ligands on Easy-Plane Anisotropy of Pentagonal-Bipyramidal Cobalt(II) Single-Ion Magnets

Author: Dong Shao, Shao-Liang Zhang, Le Shi, et al
Publication: Inorganic Chemistry
Publisher: American Chemical Society
Date: Nov 1, 2016

Copyright © 2016, American Chemical Society

PERMISSION/LICENSE IS GRANTED FOR YOUR ORDER AT NO CHARGE

This type of permission/license, instead of the standard Terms and Conditions, is sent to you because no fee is being charged for your order. Please note the following:

- Permission is granted for your request in both print and electronic formats, and translations.
- If figures and/or tables were requested, they may be adapted or used in part.
- Please print this page for your records and send a copy of it to your publisher/graduate school.
- Appropriate credit for the requested material should be given as follows: "Reprinted (adapted) with permission from {COMPLETE REFERENCE CITATION}. Copyright {YEAR} American Chemical Society." Insert appropriate information in place of the capitalized words.
- One-time permission is granted only for the use specified in your RightsLink request. No additional uses are granted (such as derivative works or other editions). For any uses, please submit a new request.

If credit is given to another source for the material you requested from RightsLink, permission must be obtained from that source.

BACK CLOSE WINDOW

Figure 3.5.1. Schematic of the device with CVD graphene on top of a silicon-silicon oxide substrate and after deposition of a bistable SCO. Resistance per square at the Dirac point as a function of temperature for heating and cooling modes. A wide clockwise hysteresis loop is observed between 327 and 374 K. Reproduced with permission from [129]. Copyright 2016, American Chemical Society.

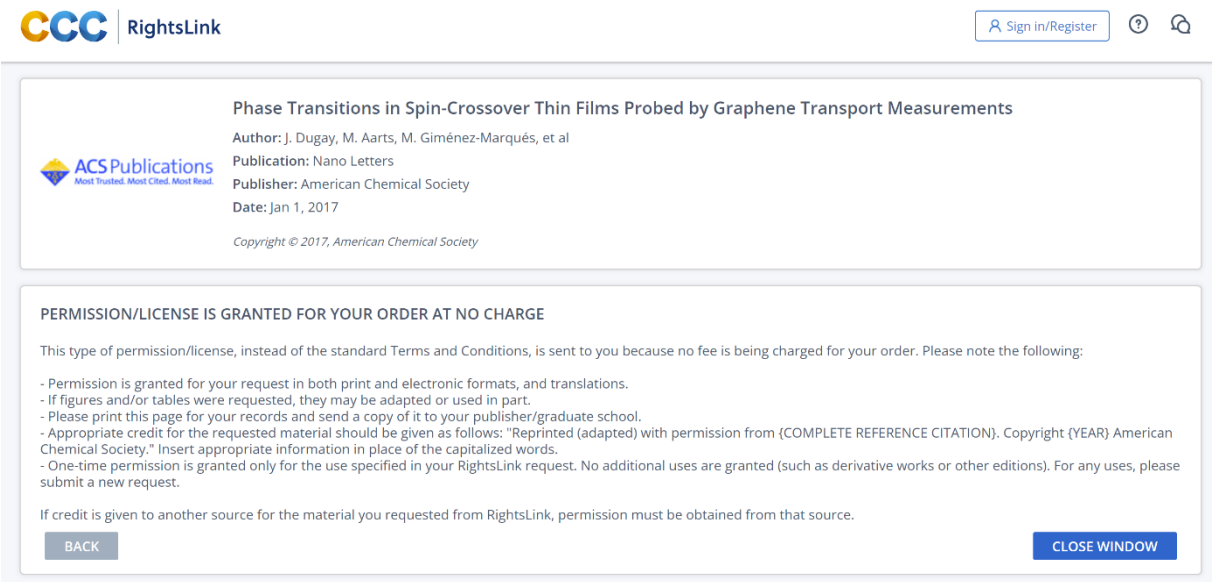

CCC RightsLink Sign in/Register

ACS Publications
Most Trusted. Most Cited. Most Read.

Phase Transitions in Spin-Crossover Thin Films Probed by Graphene Transport Measurements

Author: J. Dugay, M. Aarts, M. Giménez-Marqués, et al
Publication: Nano Letters
Publisher: American Chemical Society
Date: Jan 1, 2017

Copyright © 2017, American Chemical Society

PERMISSION/LICENSE IS GRANTED FOR YOUR ORDER AT NO CHARGE

This type of permission/license, instead of the standard Terms and Conditions, is sent to you because no fee is being charged for your order. Please note the following:

- Permission is granted for your request in both print and electronic formats, and translations.
- If figures and/or tables were requested, they may be adapted or used in part.
- Please print this page for your records and send a copy of it to your publisher/graduate school.
- Appropriate credit for the requested material should be given as follows: "Reprinted (adapted) with permission from {COMPLETE REFERENCE CITATION}. Copyright {YEAR} American Chemical Society." Insert appropriate information in place of the capitalized words.
- One-time permission is granted only for the use specified in your RightsLink request. No additional uses are granted (such as derivative works or other editions). For any uses, please submit a new request.

If credit is given to another source for the material you requested from RightsLink, permission must be obtained from that source.

BACK CLOSE WINDOW

Figure 4.5.1. General scheme of the experimental procedure of Hummer's method. Reproduced with permission from [257]. Copyright 2020, Royal Society of Chemistry.

A highly responsive methanol sensor based on graphene oxide/polyindole composites

K. Phasuksom, W. Prissanaroon-Ouajai and A. Sirivat, *RSC Adv.*, 2020, **10**, 15206 **DOI:** 10.1039/D0RA00158A

Yolanda Sabater Algarra, the doctoral candidate, declares that all the other images, tables, and figures shown in this Doctoral Thesis have been personally elaborated.

In this doctoral thesis, novel synthetic methodologies are established for obtaining bistable magnetic materials, including spin crossover compounds and single ion magnets. These insights have paved the way for designing and fabricating graphene hybrids by incorporating switchable molecules via covalent functionalization. A variety of physicochemical techniques have been employed to precisely evaluate magneto-structural correlations and identify functional groups on graphene. These results open the route for a wider range of applications involving barocalorics, data storage, or spintronics, among others.